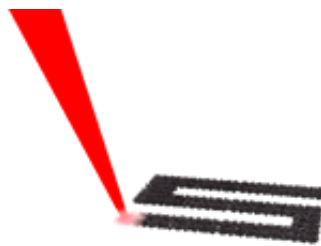


Aus dem Max-Planck-Institut für Kolloid- und Grenzflächenforschung

Laser-Induced Carbonization – From Fundamentals to Applications



Habilitationsschrift (kumulativ)

zur Erlangung des akademischen Grades
Doktor rerum naturalium habitatus
(Dr. rer. nat. habil.)

in der Wissenschaftsdisziplin Kolloid- und Polymerchemie

eingereicht an der
Mathematisch-Naturwissenschaftlichen Fakultät
der Universität Potsdam

von

Dr. Volker Strauß

geboren am 24.11.1983 in Schwabach
fertiggestellt im April 2022

Disputation: 25. November 2022

Probevorlesung: 30. März 2023

Die Publikation ist durch das Urheberrecht und/oder verwandte Schutzrechte geschützt. Nutzende sind berechtigt, die Publikation in jeder Form zu nutzen, die das Urheberrechtsgesetz (UrhG) und/oder einschlägige verwandte Schutzrechte gestatten. Für weitere Nutzungsarten ist die Zustimmung der Rechteinhaber*innen einzuholen.
<https://rightsstatements.org/page/InC/1.0/>

Online veröffentlicht auf dem
Publikationsserver der Universität Potsdam:
<https://doi.org/10.25932/publishup-59199>
<https://nbn-resolving.org/urn:nbn:de:kobv:517-opus4-591995>

Betreuer:

Prof. Dr. Markus Antonietti

Max-Planck-Institut für Kolloid- und Grenzflächenforschung, Golm

Gutachter:

Prof. Dr. Markus Antonietti

Max-Planck-Institut für Kolloid- und Grenzflächenforschung, Golm

Prof. Dr. Georg Garnweitner

Institut für Partikeltechnik, Technische Universität Braunschweig

Prof. Dr. Zdeněk Sofer

Department of Inorganic Chemistry, University of Chemistry and Technology Prague

Table of Contents

Abstract	I
Zusammenfassung	III
Acknowledgements	V
Motivation	VII
General Part	1
<i>The Complexity of Carbonization</i>	<i>1</i>
Carbonization – General Aspects.....	1
Pyrolysis – Microstructure and Properties of Carbonized Materials.....	4
Porous Carbons.....	7
Nitrogen-Doped Carbons.....	9
Carbothermic Reduction.....	10
Pore Engineering.....	11
Principles of Combustion	13
Alternative Carbonization Methods.....	14
<i>Laser-Carbonization – Context</i>	<i>16</i>
On-Substrate Carbonization.....	16
Terminology.....	18
Laser-Carbonization – Historical Overview.....	19
Laser-Processing of Materials – General Aspects	21
Mechanistic Studies – Literature Survey	28
Applications – Overview and Literature Survey	36
Results Part	51
<i>Scope</i>	<i>51</i>
<i>Laser-carbonization – Approach</i>	<i>53</i>
Overview	53
Carbon Network-Forming Agents.....	55
Solvents.....	56
Film-forming Agents	57
Reactants, Additives, Porogens.....	57
Substrates	60
<i>Laser-carbonization – Implementation</i>	<i>61</i>
Principles of Laser-Carbonization.....	61
Laser-Patterned Carbon in Sensing.....	63
Laser-Patterned Carbon for Electrocatalysis	66
Laser-Patterned Carbon for Supercapacitors	66
Conclusions and Future Directions	69
References	71
List of Abbreviations	79
Appendix – Publications	81

Abstract

Fabricating electronic devices from natural, renewable resources has been a common goal in engineering and materials science for many years. In this regard, carbon is of special significance due to its biological compatibility. In the laboratory, carbonized materials and their composites have been proven as promising solutions for a range of future applications in electronics, optoelectronics, or catalytic systems. On the industrial scale, however, their application is inhibited by tedious and expensive preparation processes and a lack of control over the processing and material parameters. Therefore, we are exploring new concepts for the direct utilization of functional carbonized materials in electronic applications. In particular, laser-induced carbonization (carbon laser-patterning (CLaP)) is emerging as a new tool for the precise and selective synthesis of functional carbon-based materials for flexible on-chip applications.

We developed an **integrated approach** for on-the-spot laser-induced synthesis of flexible, carbonized films with specific functionalities. To this end, we design versatile precursor inks made from naturally abundant starting compounds and reactants to cast films which are carbonized with an infrared laser to obtain functional patterns of conductive porous carbon networks. In our studies we obtained deep mechanistic insights into the **formation process** and the **microstructure** of laser-patterned carbons (LP-C). We shed light on the kinetic reaction mechanism based on the interplay between the precursor properties and the reaction conditions. Furthermore, we investigated the use of porogens, additives, and reactants to provide a **toolbox** for the chemical and physical fine-tuning of the electronic and surface properties and the targeted integration of functional sites into the carbon network. Based on this knowledge, we developed **prototype resistive chemical and mechanical sensors**. In further studies, we show the applicability of LP-C as electrode materials in **electrocatalytic** and charge-storage **applications**.

To put our findings into a common perspective, our results are embedded into the context of general carbonization strategies, fundamentals of laser-induced materials processing, and a broad literature review on state-of-the-art laser-carbonization, in the general part.

|| **Zusammenfassung**

Die Herstellung elektronischer Geräte aus natürlichen, erneuerbaren Ressourcen ist seit vielen Jahren ein gemeinsames Ziel in den Ingenieurs- und Materialwissenschaften. Kohlenstoff kommt dabei aufgrund seiner biologischen Verträglichkeit eine besondere Bedeutung zu. Im Labor haben sich karbonisierte Materialien und ihre Verbundwerkstoffe als vielversprechende Lösungen für eine Reihe zukünftiger Anwendungen in der Elektronik, Optoelektronik oder katalytischen Systemen erwiesen. Im industriellen Maßstab wird ihre Anwendung jedoch durch langwierige und teure Herstellungsverfahren und mangelnde Kontrolle über die Verarbeitungs- und Materialparameter gehemmt. Daher erforschen wir neue Konzepte für die direkte Nutzung funktionaler karbonisierter Materialien in elektronischen Anwendungen. Insbesondere die laserinduzierte Karbonisierung / Kohlenstoff-Laserstrukturierung (KoLaSt) entwickelt sich zu einem neuen Werkzeug für die präzise und selektive Synthese von funktionellen Materialien auf Kohlenstoffbasis für flexible On-Chip-Anwendungen.

Wir haben einen integrierten Ansatz für die direkte laserinduzierte Synthese von flexiblen, karbonisierten Filmen mit spezifischen Funktionalitäten entwickelt. Zu diesem Zweck haben wir vielseitige Vorläufertinten aus natürlich vorkommenden organischen Ausgangsstoffen und Reaktanten entwickelt, um Filme aufzutragen, die mit einem Infrarotlaser karbonisiert werden um dadurch funktionelle Muster aus leitfähigen porösen Kohlenstoffnetzwerken zu erhalten. In unseren Studien haben wir tiefe mechanistische Einblicke in den Bildungsprozess und die Mikrostruktur von laserstrukturierten Kohlenstoffen (LP-C) erhalten. Wir beleuchten den kinetischen Reaktionsmechanismus basierend auf dem Zusammenspiel zwischen den Vorläufereigenschaften und den Reaktionsbedingungen. Darüber hinaus untersuchen wir die Verwendung von Porogenen, Additiven und Reaktanten, um eine Toolbox für die chemische und physikalische Feineinstellung der elektronischen und Oberflächeneigenschaften und die gezielte Integration von funktionellen Einheiten in das Kohlenstoffnetzwerk bereitzustellen. Basierend auf diesem Wissen haben wir Prototypen resistiver chemischer und mechanischer Sensoren entwickelt. In weiteren Studien zeigen wir die Anwendbarkeit von LP-C als Elektrodenmaterialien in elektrokatalytischen und Ladungsspeicheranwendungen.

Um unsere Erkenntnisse in eine allgemeine Perspektive zu bringen, betten wir unsere Ergebnisse im allgemeinen Teil in den Kontext bekannter Karbonisierungsstrategien, Grundlagen der laserinduzierten Materialbearbeitung und einer breiten Literaturübersicht zum Stand der Technik der Laserkarbonisierung ein.

Acknowledgements

As an enabler of this work, I would like to thank Prof. Markus Antonietti for his continuous support and mentoring during the past three years. His passion for and deep understanding of sustainable materials chemistry and science, in general, is a guide for all growing scientists. He made the colloid department at MPICI an extremely efficient place to learn and develop.

My greatest thanks go to my group members and especially my colleague Huize Wang who developed and maintained an inspiring enthusiasm for our common research since we started working together. This quality together with his balanced hard-working character made our research successful. I deeply appreciate the contribution and scientific support from my colleague Dr. Simon Delacroix who worked hard with devotion and competence. For one year, he was a highly active member of our lab and initiated a great number of projects. Certainly, Simon raised the bars in our little sub-field of materials research. I would like to express my gratitude to Ines-Below Lutz who is responsible for a significant decrease of my personal stress level. She is a highly skilled co-worker and an extremely pleasant person to work with. Thanks to Sanghwa Moon we made substantial progress in engineering laser-patterned carbons. Her hard work and substantial questions foster our current pursuit of new directions.

I am very happy that I can look back to a number of collaborators with whom I shared so many fruitful meetings and discussions. Without the strong support of many of these groups and individuals, we would have not been able to complete this work:

Deep visual insights into our laser-carbonized materials were gained with unprecedented high-resolution microscopic and spectroscopic analyses that was carried out in a close and friendly collaboration with the Micro and Nano-analytics group at Siegen University. Prof. Benjamin Butz is not only a great scientist with devotion to the tiniest details but also a great teacher who enjoys passing his knowledge to his collaborators and co-workers. Thanks to their detailed analysis conducted by Marco Hepp, Charles Otieno Ogolla, and Katharina Derr, the academic value of our studies and interpretations were lifted to a higher level. One aspect, we became very much interested in was the investigation of the charge-carrier properties of our LCMs. Certainly, we would not have been able to understand our sensor performance without the competent support of the Chemistry and Nanoscience Center at NREL/Colorado with Dr. Anna Zieleniewska, Dr. Andrew Ferguson, Dr. Jeffrey Blackburn and the Department Dynamics and Transport in Quantum Materials at Helmholtz Zentrum Berlin with Dr. Klaus Habicht, Dr. Danny Kojda, and Gyanendra Panchal. In a pleasant collaboration with Andreas Hoffmann and

Prof. Alexander Kühne we learned about the fundamentals of laser-carbonization of polyacrylonitrile, which provided an insightful knowledge. The collegial atmosphere is highly appreciated. In the same manner, I would like to thank Oliver Oßwald and Prof. Bernd Smarsley for their fundamental and comprehensive WAXS analysis. Thanks to their contribution, we achieved deep insights into the microstructure of our laser-patterned carbons. Moreover, I would like to thank Dr. Nadja Tarakina, Dr. Tobias Heil, Dr. Jing Hou for their scientific contribution to several of our studies and their extremely insightful microscopic characterizations. Throughout the past years, I have had many fruitful conversations and shared many common studies on laser-induced materials processing with my colleague Dr. Felix Löffler and his group. Also, I would like to thank for friendly and effective collaborations with Dr. Nieves Lopez-Salas, Enrico Lepre, Janina Koßmann, and Maria Jerigova as well as Svitlana Filonenko and Helen Schneider that enabled the completion of several interesting research studies. I am particularly grateful to Nieves, Svitlana, and Felix, for the mutual mental support during these years. None of our research studies would have been possible without the support of several X-ray absorption spectroscopy facilities. I would like to thank for their support in comprehensively characterizing several of our samples to Mackenzie Anderson and Prof. Richard Kaner, Daniel Cruz, and Mark Isaacs. I would like to thank Chenxiang Wang and Mit Muni from the Kaner group at UCLA for their hard work on summarizing the use of graphene in supercapacitors. Since 2019, we started several projects, for which we build up new experimental setups. These were always accompanied by the competent technical support from Klaus Bienert. He provides more than just his work force. The MPICI is scientifically successful because of a strong permanent fundament. There is a number of people that I loved to work with and I am very thankful for their active support, expertise, and collegial atmosphere. In the colloid chemistry department especially: Carolin Nuglisch, Luisa Nishimura, Annemarie Schulz, Katharina ten Brummelhuis, Jessica Brandt, Antje Völkel, Heike Runge, Ursula Lubahn, Rona Pitschke, Regina Rothe, Marlies Gräwert, Bolortuya Badamdorj, Irina Shekova, Sven Hühnerfuß, Maik Wolfram, and all the members of the administration and the workshops. Thank you all!

Motivation

Since I started my active research, it has been a main driving force to **study** and identify routes to alternative **sustainable materials** and processes. This originates from the obvious need to change the existing environmental and societal situation, on the one hand, and from a deep fascination about **nature's role model**, on the other. The latter should be the **guideline** for the design of our industrial and economic processes to ultimately achieve a full **integration** of the manufactured world **into the natural organism**. There are principally two ways to achieve a **stable equilibrium** between human desires (economy, energy, wealth) and the conservation of environmental conditions (climate, environment): change manufacturing (materials and processes) or change society. Since the latter option is extremely difficult to achieve due to social psychological reasons, the first option becomes the only viable choice. This brings **natural sciences** and engineering to the scene, as the very fundamental industrial processes and basic infrastructure of the world's economies need to be **revised**. That implies that current materials research should strictly focus on **processes and materials** that 1) reduce the use of resources, 2) replace expensive and hazardous materials, 3) support circular value creation, and 4) reduce transport.

From experience, we know that every technology that brings a **solution** also brings a **problem**, which, in turn, brings an **opportunity**. We should take this as a **principle** for a **dynamic industry** with temporary technological solutions to drive a steady development towards integration into natural processes. In this regard, carbon in its various forms plays a central role.

Humankind was given the present of huge oil and coal reservoirs to develop a fast-growing chemical knowledge of carbon. As a result, tremendous materials advances have been made and nowadays a majority of industrial products are made of **plastics** or **crude-oil based materials**. Changing their production and disposal is a **long lever** for making a difference. Rather than focusing on unidirectional synthesis of functional materials, we have to take a **holistic view** on origin, production, and fate of the materials.

In the past years, these relationships have moved into collective awareness and are gaining economic value. The importance of carbon in the **delicate global chemical system** is demonstrated by its double role at the **global market places** in the form of positive (minerals, coal, oil, grain, wood) and negative resources (CO₂-certificates). At the same time it demonstrates the need of **implementing artificial circular carbon economies**. To wisely integrate our industrial processes into natural carbon cycles we need to adopt strategies for carbon utilization on the large and the

small scale. Such application gaps are, for example, the valorization of biomass through direct production of useful products, e.g. by carbonization.

Tailor-made functional carbonized materials are used in many fields of industry, such as filtration, electrodes, construction etc. There is even great potential for the use of carbonized materials as active materials in electronic devices. With the **advent of the carbon nano-allotropes** graphene and carbon nanotubes in the past decades advances in carbon-based electronic applications have been made and are now even finding their way into commercialization. The scarce utilization of carbonized biomass, however, is mainly due to a lack of suitable processing methods, poor reproducibility, and often low performance.

With **Laser-induced carbonization** a new processing technology evolves which promises to solve many of the current issues about application of carbonized materials. Laser-induced carbonization provides many advantages, such as high-speed processing, low energy consumption, and direct device integration. Of course, every application demands different requirements. For instance, the large scale production of bulk carbon materials for high-throughput applications (filtration) are hardly realizable with laser-carbonization. However, for small-scale electronics laser-carbonization can be considered a green method for the direct valorization of biomass or carbon waste. In contrast to many other synthetic routes, only little use of solvents or petrochemicals are required.

Early **investigations on laser-induced carbonization** were conducted already in the 1980s and 90s, but the discovery of carbon nanotubes and graphene drew the attention to their investigation. With the rising interest and advances in **flexible electronics** and the trending topic of biomass valorization in the past decade, laser-carbonization moved back into the focus of materials scientists as it displays an interesting approach to achieve functional carbon films for a range of applications.

This work aims to explain the fundamentals of laser-induced carbonization at the current state of our research and some prospective applications. It is meant to provide a comprehensive picture of the underlying principles and move the topic into the context of carbon materials synthesis. In the General Part a survey on the **fundamentals of carbonization** and methods for the selective tailoring of the properties of carbons are given. Throughout this section important terminology is explained. Then the **state-of-the-art** in laser-induced carbonization will be discussed based on a broad literature review and will be put into perspective of fundamentals known from laser-assisted materials processing. In the Results Part our insights into materials properties and their applications are discussed. Remaining questions and future directions are presented in the Conclusions and Future Directions section.

General Part

The Complexity of Carbonization

Carbonization – General Aspects

Carbonization is a process of converting organic compounds or molecules into carbon-rich materials. This is a process occurring naturally during the evolution of mineral coals, which are mined on large scales for energy generation (**Figure 1A**). Such natural carbons contain between 25 and 100% carbon and are classified into different categories based on their carbon content and heating value according to the American Society for Testing and Materials (ASTM). The categories range from lignite (25-35%) through subbituminous and bituminous coal (35-86%) to anthracite (86-97%) and finally graphite (97-100%). Other major components of natural coals and mineral carbon are moist, polyaromatic hydrocarbons (PAH), volatile organic compounds (VOC), or polymeric residues.⁽¹⁾

Artificial carbonization processes are also used for the commercial production of fuels. The most common artificially carbonized materials, which have been known for millennia are charcoals, which are made by pyrolysis of wood at temperatures of ~300-400°C under exclusion of oxygen from the reaction atmosphere (**Figure 1B**).⁽²⁾ In this process, the mass fraction of carbon is increased to >80% from originally ~50%. The properties and composition of the carbonized wood are dependent on several factors, such as the drying grade, the contents of pitch, or the reaction temperature. An overview to the commonly used terminology used for the description of carbons and their components is given in a IUPAC recommendation.⁽³⁾



Figure 1. Photographs of A) a lignite coal mine, B) an ancient charcoal production process, C) a bonfire, and D) a flame of a candle.

As an illustration of an every-day carbonization process the phenomenon of a flame evolving in a fire or a candle. Volatile compounds evolving from the precursor material (e.g. wood or wax) evaporate as they are heated by the flame (**Figure 1C** and **D**). Once they reach

temperatures $>200\text{ }^{\circ}\text{C}$, these compounds decompose and form volatile reactive intermediates. At the outer zones of the flame complete combustion leads to the release of the gaseous thermodynamic products H_2O and CO_2 and the release of heat which feeds the reaction with activation energy. A limited supply of oxygen towards the center of the flame leads to incomplete combustion and the promotion of C-C bond formation of the evaporated precursors, following different polymerization schemes (e.g. conjunct polymerization).⁽⁴⁾ At temperatures of $1000\text{-}1200\text{ }^{\circ}\text{C}$ in the center of the flame, ionic carbon clusters (soot) are formed. The appearance of the flame is due to the phenomenon of thermal emission (black body radiation) of these carbon clusters at temperatures of $\sim 1400\text{ }^{\circ}\text{C}$. The structure of the carbon clusters (the carbonized product) is complex and varies with the type of precursors and temperature fluctuations in the flame.

The previous example illustrates that carbonization is generally a **complex process** in which many reactions occur simultaneously and/or sequentially, such as dehydrogenations, condensations, isomerizations, decarboxylations, polymerizations, aromatizations, deoxygenations, denitrogenations etc. Each of these reactions is favored in a specific temperature window and is highly sensitive to the reaction environment, meaning such complex reaction cascades are based on a very delicate energy balance.⁽⁵⁾

One of the main characteristics of carbonized materials, natural or artificial, is the **degree of carbonization**, i.e. the increase in carbon content during the reaction. The degree of carbonization can be quantified and visualized in the H/C–O/C diagram developed by Van Krevelen.⁽⁶⁾ It was originally developed to assess the maturity and workability of kerogen and petroleum.⁽⁷⁾

Artificially carbonized materials are commercially used in a variety of applications, for example in construction, as sorption materials, catalyst supports, electrodes, or electronic sensors. The research on carbonized materials as active catalysts, electrodes for energy storage, semiconductors, or flexible electronics is currently blooming. One of the biggest challenges about carbonization reactions is to control the properties of the reaction product by understanding the influence of the precursors and reaction parameters (**Figure 2**).

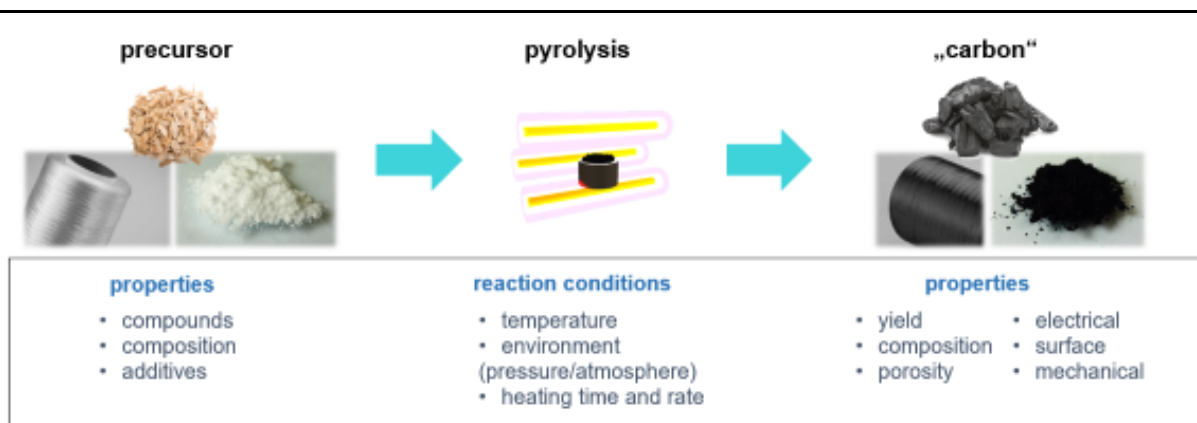


Figure 2. Illustration of the carbonization process using wood, polymers, or organic molecules as precursors. The properties of the final “carbon” depends on the properties of the precursors and the reaction conditions during pyrolysis.

As any chemical reaction strongly depends on the temperature, the manifold of chemical reactions during carbonization naturally make a strong difference in the reaction product. In a

Temperature dependence of chemical reactions

- Arrhenius-equation

pyrolysis (see Pyrolysis) process the precursor properties (composition, compounds, additives) as well as the reaction conditions (temperature, heating rate, environment) govern the properties of the final carbon materials, such as yield, composition, structure, and electronic or mechanical properties (**Figure 2**).

A famous example are **carbon fibers** produced from polyacrylonitrile (PAN) that are used as mechanical construction elements due to their extraordinary materials properties (tensile strength, stiffness, light-weight, chemical and thermal resistance).⁽⁸⁾ Carbon fibers are made by electrospinning PAN into fibers and subsequent pyrolysis. A special feature of PAN as a precursor is its duroplastic nature, i.e. it degrades before it melts, therefore, its shape is retained during thermal pyrolysis. The reaction to carbon fibers is well understood. It occurs in three steps: cyclization, dehydration, and denitrogenation (N_2 -elimination). The first reaction is slow and occurs in a temperature range between 200 and 300 °C in air. The latter two reactions occur at higher temperatures up to 1100 °C under exclusion of O_2 in the atmosphere and depend strongly on the molecular weight and crosslinking of the precursor. To ensure a complete reaction, slow heating rates of 30 – 120 °C h⁻¹ are used. This example illustrates the importance and the role of the reaction parameters, such as temperature, atmosphere, heating rate, and precursors.

Besides the extraordinary properties of carbonized materials and their sheer endless possibilities for tuning, carbon bears the great advantage of being a ubiquitous element. Especially carbons

made from biomass have the potential of becoming game changers in avoiding inconvenient global supply chains.⁽⁹⁾ In the following sections, the general synthetic approaches to carbonized materials and their properties as well as some examples of the tuning knobs in the production of carbon materials are discussed. This section is meant to provide the basis for understanding laser-induced carbonization discussed in the main part.

Pyrolysis – Microstructure and Properties of Carbonized Materials

The most commonly used technique to produce carbon materials is pyrolysis (thermolysis).⁽¹⁰⁾ Pyrolysis generally describes the thermally induced chemical decomposition of organic matter in absence of oxygen (O_2). As outlined in the introductory section, high enough temperatures cause the breaking of covalent bonds and induce rearrangements of bonds to form thermodynamically stable products. This principle has been applied to a vast number of starting materials, both polymers and molecular precursors.⁽¹¹⁾

In the following sections, concepts of tuning and manipulating the properties of carbons are highlighted. Primary parameters are heating time, reaction temperature, heating rate, and pressure. It is important to view into the chemistry of each carbonization reaction individually. However, some generalizations can be made.

During pyrolysis, several intermediate states of carbon are passed through. The different phases are structurally distinguished by the degree of graphitization. An illustration of a generalized transformation scheme from organic precursors through the different “carbon” stages to graphitic carbon was originally provided in “Fibre Reinforcements For Composite Materials” by Bunsell.⁽¹²⁾ The graphic in **Figure 3** shows an adopted version of this scheme by Schuepfer et al.⁽¹³⁾

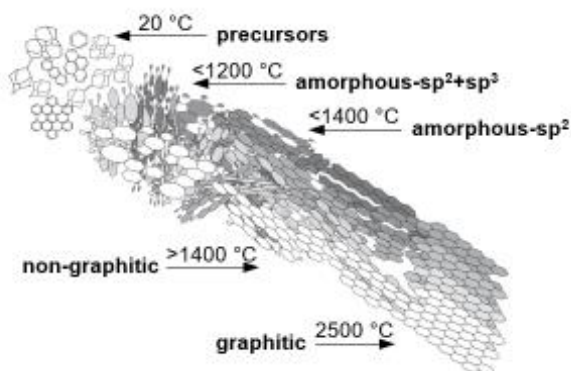


Figure 3. Illustration of the different stages of crystallinity during a carbonization process from molecular precursors to graphitic carbon.^(12,13)

As this figure shows, the structure and composition of carbonized materials is strongly dependent on the reaction conditions, especially the temperature. To estimate and understand the structure and properties of carbonized materials, a comparison to the properties of the reference materials, i.e. the precursors and the respective carbon allotropes, **graphite** and **diamond**, should be made.

As outlined above, **graphitic carbon** is composed of purely sp^2 -hybridized carbon. Since sp^2 -hybridization entails a planar structure, graphitic carbon occurs in a layered ordering with a simple hexagonal crystal structure in each plane (**Figure 4A**). Pure graphite is known for its black/silverish appearance and its anisotropic physical properties due to covalent versus non-covalent bonding in the different crystal directions. Along the crystal planes of graphite it is electrically and thermally conductive. Graphite has a sublimation point of ~ 3600 °C and is the thermodynamically stable carbon allotrope.⁽¹⁴⁾ Naturally, it forms under unoxic conditions in millions of years at high pressures and temperatures from organic materials.⁽¹³⁾

Basics

- orbital hybridization
- crystal structures

Synthetically, graphite is produced by heating carbon-rich precursors, such as coals or coal tar pitch to temperatures of ~ 3000 °C.⁽¹⁵⁾ Synthetic graphite offers usually a poly-crystalline texture. Generalizations on the graphitization process of different precursors are extremely difficult to make. However, some boundary conditions in terms of structure are commonly observed. While the term carbonization generally describes an increase of the carbon content and subsequently the formation of more or less extended graphitic domains, a true **graphitization**⁽¹⁶⁾ is observed at temperatures higher than ~ 2200 °C (atmospheric pressure). The degree of graphitization is controlled by the chemical structure of the starting materials. Importantly, not every starting material graphitizes. Therefore, the starting materials are distinguished as **graphitizing** or **non-graphitizing carbons**⁽¹⁷⁾. The latter convert into non-crystalline, glass-like carbon (**glassy carbon**⁽¹⁸⁾) with significant portions of fullerene-like domains and some sp^3 - or sp -hybridized carbons. Graphitizing carbons pass through a so-called liquid crystal phase (**mesophase**⁽¹⁹⁾) at intermediate temperatures (**Figure 4B**). So-called **non-graphitic carbon**⁽²⁰⁾ is often observed to form in the temperature range between 1400 – 1700 °C.

In these intermediate phases graphitic domains (crystallites) of different extensions are found. Descriptors of these phases are the **stacking thickness** (L_c) and **crystallite diameter** (L_a) of the graphitic domains, and their defect density (**Figure 4C**).⁽¹³⁾ Among the most prominent **structural defects** are vacancies, five- or seven rings (Stone-Wales) defects, edge sites,

deformations, or heteroatoms.⁽²¹⁾ The overall electron mobility of ideal graphite is on the order of $3000 \text{ cm}^2 \cdot (\text{Vs})^{-1}$ at liquid nitrogen temperature.⁽²²⁾ In contrast, the electron mobility in glassy carbon with a higher defect density is on the order of $100 \text{ cm}^2 \cdot (\text{Vs})^{-1}$.⁽²³⁾

As mentioned above, graphite exhibits a high intrinsic **electric conductivity** of $\sim 2 \times 10^5 \text{ S} \cdot \text{m}^{-1}$ in the basal plane. Therefore, graphitic carbons as such are interesting materials for electronic or electrochemical applications. As a fundamental part of the structure in graphite, the properties of a single sheet – graphene – have been investigated intensively. In contrast to conventional semiconductor materials, isolated defect-free graphene exhibits very high charge-carrier mobilities of up to $200\,000 \text{ cm}^2 \cdot (\text{Vs})^{-1}$.⁽²⁴⁾ In graphite, interplane interactions and **defects** in the sp^2 -carbon lattice have a drastic impact on the electronic properties due to charge-carrier scattering.

Basics

- electrical conductivity in metals and semiconductors

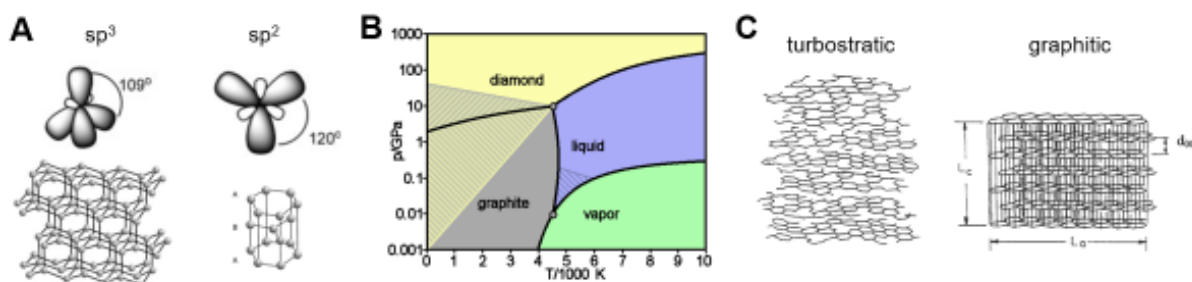


Figure 4. A) Visualization of the carbon crystal structure (left: graphite; right: diamond) as a result of the atomic hybridization,⁽²⁵⁾ B) Phase diagram of carbon,⁽¹¹⁾ C) Illustration of turbostratic graphite versus oriented graphite.⁽²⁶⁾

At the other extreme, **diamond** is a purely sp^3 -hybridized form of carbon with a whitish or transparent appearance due to an electronic band-gap of 5.45 eV (**Figure 4A**). Importantly, under ambient conditions, pure diamond is metastable and transforms into graphite at pyrolysis temperatures of $\sim 1500 \text{ }^\circ\text{C}$ (**Figure 4B**). Mineral diamond is formed at extreme pressures and temperatures between 1200 and $1400 \text{ }^\circ\text{C}$. Mimicking the natural formation, synthetic diamond is produced from graphite in the so-called “high-pressure high-temperature process” at pressures of >60 kbar and temperatures of $>1500 \text{ }^\circ\text{C}$. The transformation process takes typically several weeks. Alternatively, films of diamond are produced by chemical vapor deposition (CVD) from methane in a hydrogen plasma atmosphere.⁽²⁷⁾

Basics

- band structure of semiconductors

A mixture of sp^2 - and sp^3 -hybridized carbon without any appreciable long-range order is referred to as **amorphous carbon (a-C)**⁽²⁸⁾. The materials properties mostly transition smoothly

between those of graphite and diamond. Amorphous carbon is typically obtained at pyrolysis temperatures of 700 – 1200 °C. In a-C, several phases co-exist. For example, small graphitic domains on the order of a few nanometers are present in a-C in an overall disordered fashion. Moreover, the graphitic domains may be disordered or twisted (randomly oriented), meaning that the graphite planes do not follow a stacking order. This arrangement of the microstructure is called **turbostratic graphite (Figure 4C)**.⁽²⁷⁾ Such intermediate carbons (carbonized materials) offer a wide variety of properties which are interesting for different applications.⁽²⁹⁾

Porous Carbons

As the process of carbonization is accompanied by decomposition reactions, i.e. creating gaseous leaving groups, every carbonization reaction comes with a mass loss of the material. Thereby, in most materials **porosity** is generated during carbonization. For many applications, this is an advantage as the porosity brings a high surface area to the material. Due to their intrinsic light weight and high surface areas, such materials are used in technologies such as filtration, separation, construction, energy storage, catalyst supports etc. The production and tuning of specifically porous carbon materials has become a separate field of materials science and engineering.

The most prominent example of porous carbon materials are **activated carbons**⁽³⁰⁾ (**Figure 5A** and **B**). These are typically made by oxidative treatment of coals from different precursors, most commonly coconut husks, bamboo, or wood.⁽³¹⁾ First, thermal pyrolysis at temperatures of 600-1200 °C in inert atmospheres is used to carbonize the starting materials. A subsequent chemical treatment – activation – of the carbonized material with strong acids or bases and repeated thermolysis produces materials with specific surface areas of up to 3000 m²·g⁻¹ due to micropores (<2 nm).⁽³²⁾ A typical feature of porous carbons is a **hierarchical porosity** where the pores are hierarchically arranged spanning pore scales from macro over meso to micropores (**Figure 5C**). Thereby, the entire surface area of the porous materials is accessible for liquid or gaseous adsorptives. Such highly light-weight carbons are often referred to as **carbon aerogels**⁽³³⁾ or **carbon foams**, with reference to their solid state porous morphology dispersed in a gas.⁽³⁴⁾

Definitions (IUPAC)

- micropores: < 2 nm
- mesopores: 2 - 50 nm
- macropores: > 50 nm

Surface Area

- freestanding graphene: 2600 m²·g⁻¹
- football field: 6400 m²

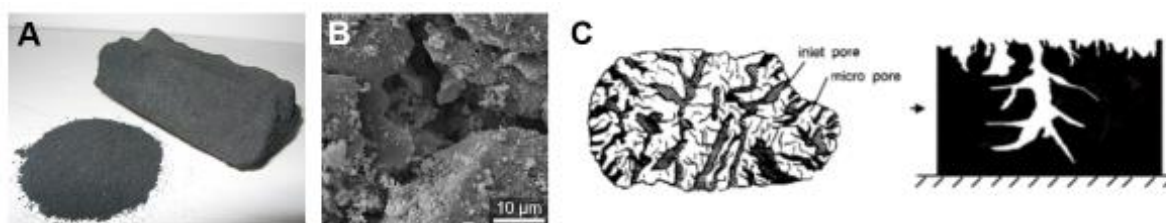


Figure 5. A) Photograph of activated carbon powder and pellet,⁽³⁵⁾ B) Scanning electron micrograph of activated carbon,⁽³⁶⁾ C) Illustration of the hierarchical porous structure of porous carbons.⁽⁹⁾⁽³⁷⁾

Another important feature of carbons besides their physical surface structure, is their chemical surface properties. In any surface or interface application, the surface functionalities play an important role. As carbons are typically derived from oxygenated hydrocarbons as precursors, a high degree of oxygenation of the surface is observed. Noteworthy, the presence of defects and **dangling bonds** obtained in low temperature (<1000 °C) carbonized materials also affect the surface properties and facilitates the adsorption of or reaction with environmental oxygen. Depending on the precursors and the involved reactions during the carbonization process,⁽³⁸⁾ different surface oxide groups evolve (**Figure 6A**). Among them are acidic groups, such as carboxylic acids, phenols, lactols or basic groups like anhydrides, quinones, ketones, or ethers. The amount of oxygen on the surface of a carbon material influences the **surface polarity**. This, in turn, has an impact on the sorption behavior of adsorptives (analytes or reactants) to the surface of the adsorbent (carbon material). The adsorption characteristics of gases of different polarity, for example N₂, SO₂, CH₃OH, H₂O, show a clear dependence on the type and number of oxygen-containing functional groups.⁽³⁹⁾

Definitions (IUPAC)

- adsorptive: substance to be adsorbed⁽⁴¹⁾
- adsorbent: a adsorbing surface (substrate)⁽⁴⁰⁾
- adsorbate: adsorptive on adsorbent⁽⁴²⁾

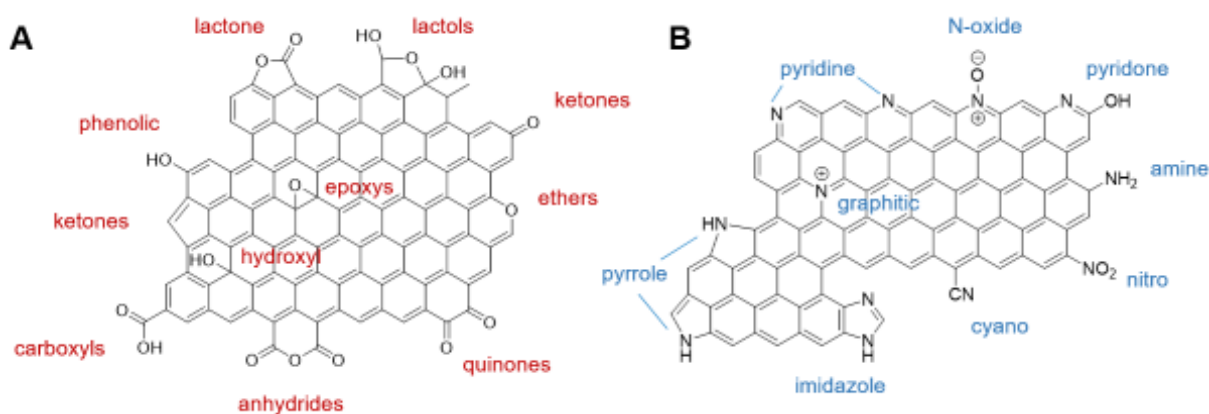


Figure 6. Hypothetical schemes summarizing the most important A) surface oxide groups in carbons⁽⁴³⁾ and B) nitrogen-functionalities in carbons.⁽⁴⁴⁾

Nitrogen-Doped Carbons

Besides oxygenation, any other functionalities that form covalent bonds with carbon can change the structure and the properties of the carbons. Similar to oxygen, nitrogen can be incorporated into the bulk and surface structure of carbons. The most prominent nitrogen species found in so-called **nitrogen-doped carbons** (NC) are pyridinic, pyrrolic, and graphitic nitrogen as well as surface functional groups like amines, nitro, nitrogen oxide or cyano groups (**Figure 6B**).

Nitrogen doping of carbons is typically achieved by carbonization of nitrogen-containing precursors at temperatures lower than 1000 °C.⁽⁴⁴⁾ Again, a prominent example is PAN pyrolyzed at temperatures < 1000 °C.⁽⁸⁾ Other well-known precursors are nitrogen-containing biomass, such as gelatine, amino acids, etc or nitrogen containing polymers.⁽⁴⁵⁾ Specific doping of porous carbon materials is also achieved by co-pyrolysis with small reactive nitrogen-rich precursors like urea, melamine, or nucleobases. Another common route for the synthesis of NCs is the pyrolysis of carbon precursors in reductive ammonia atmosphere. Typical nitrogen contents of such NCs range between 1 and 10 at%.

The binding and the chemical configuration of the nitrogen groups in the carbons depends on the synthesis (carbonization) temperature. Typically a decrease in the nitrogen content is observed with increasing temperatures.⁽⁴⁶⁾ The temperature range between 700 and 1000 °C is characteristic for the largest changes in nitrogen content and configuration, for which the pyrolysis of PAN is an illustrative example.⁽⁴⁷⁾ The different N configurations show different temperature stability. It is generally observed that both pyrrolic and pyridinic N convert to graphitic N starting at temperatures > 500 °C.

Nitrogen functionalities not only change the surface structure of carbons but also influence the electrical conductivity and the stability against environmental oxidation. A big impact of NCs was noted in application as high-capacity electrodes in electric double-layer capacitors. On the other hand, the nitrogen functionalities provide specific binding sites for the adsorption of small molecules from the gas or liquid phase. A multitude of research studies described high adsorption capacities to CO₂ in NCs.⁽⁴⁸⁾

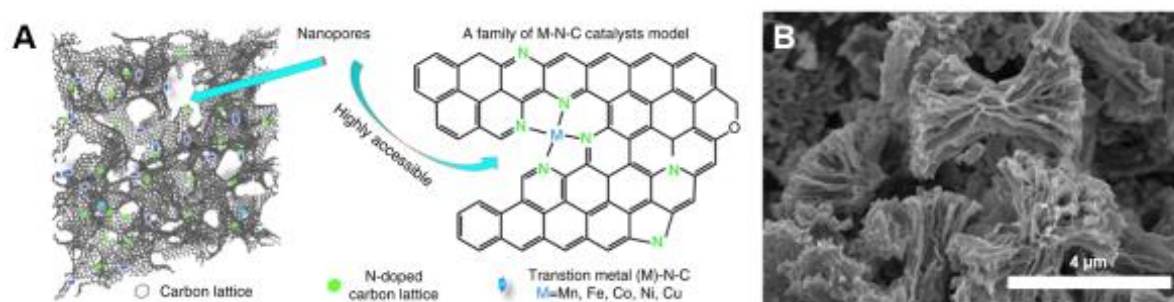
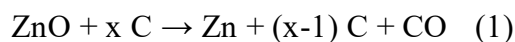


Figure 7. A) Model and schematic local structure of a single-metal active centers coordinated in NCs; B) Typical SEM image of the family of N-coordinated metal-doped (M–N–C) carbon electro-catalysts.⁽⁴⁹⁾

A potential field of application for NCs is as supports or substrates in electrocatalytic systems. For example, the carbonization of polyaniline (PANI) supported with a high-surface area activated carbon (ketjenblack-600) at 900 °C is a neat method for the reproducible production of high-surface area NCs. Furthermore, this carbonization procedure can be simply modified by adding metal salts to PANI to yield single-metal atom sites as active centers for catalytic reactions.^(50,51) The direct carbonization (pyrolysis) of bipyridine-based coordinated polymers with a variety of transition metals is an alternative method to selectively incorporate single-metal atom sites into NCs. Such electrocatalysts show a high performance towards the selective reduction of CO₂ to CO (**Figure 7**).⁽⁴⁹⁾

Carbothermic Reduction

A well-known concept to increase the graphitization degree and the carbonization yields is by utilizing **carbothermic reduction** reactions. This method is commonly used to recover metals from metal oxides in the presence of carbon as a reducing agent.⁽⁵²⁾ In carbon chemistry, oxidized metal compounds, mostly metal oxides, are added to the precursor mixtures. In the carbothermic reduction, metal oxides are reduced to their respective metals in the presence of carbon during which the carbon is oxidized to gaseous CO(g) (**equation (1)**). This reaction catalyzes the rearrangement and crystallization of the remaining amorphous carbon into graphitic carbon. The reduced metal is either washed out of the carbon phase or evaporates at temperatures above its boiling point. The most prominent examples for carbothermic reduction agents are ZnO or Fe₂O₃.^(53,54) The former is well-known to undergo carbothermic reduction at temperatures ≥ 670 °C. At temperatures ≥ 907 °C, the boiling point of zinc, the metallic zinc evaporates.⁽⁵³⁾ Iron has a much higher boiling point of ≥ 3000 °C and needs to be chemically removed from the carbon, if not desired as an integral part.



In addition to the supporting graphitization, ZnO has been used as a hard-templating (see Pore Engineering) agent for the synthesis of hierarchical porous carbon with tailored porosities made from sucrose.⁽⁵⁵⁾ The carbothermic reduction at temperatures up to 950 °C initiated the formation of micropores which lead to specific surface areas of ~3000 m²·g⁻¹, which proved useful as anodes in lithium-sulfur batteries. These carbon materials served also as a support for ordered N-doped carbons based on hexaazatriphenylene-hexacarbonitrile (HAT-CN), which was used in sodium-ion capacitors.⁽⁵⁶⁾

Pore Engineering

Besides the abovementioned method of **activation** (in activated carbons) a number of strategies to modify the porosity in carbons have been developed. A common technique is the addition of **porogens** or **templating agents**, where pre-organization, growth, or alignment of the carbon phase is achieved using structure-directing agents (SDA) with specific geometries.⁽⁵⁷⁾ Thereby, control over the pore structure and the textural properties is gained. The templating approaches are categorized into three groups: soft-, hard-, and salt-templating (**Figure 8** and **Figure 9**).

Structure formation via **soft-templating** is typically achieved by the ordered assembly of carbon precursors supported by amphiphilic compounds such as surfactants or polymers.⁽⁵⁸⁾ The handling of soft templates is delicate for the synthesis of carbon materials.⁽⁵⁹⁾ Universally, strong interactions (e.g. hydrogen-bonding) between the carbon precursor and the SDA are required to prevent phase separation. A requirement to the carbon precursor is an ability to crosslink and form a precursor “backbone” with a higher thermal stability than the SDA to facilitate the removal of the SDA prior to carbonization. Many synthesis routes for mesoporous carbons using soft-templating methods have been developed.⁽⁵⁷⁾ For example, carbonization of self-assembled of organic molecular species (resorcinol-formaldehyde) in a composite consisting of a resin and a block copolymer.

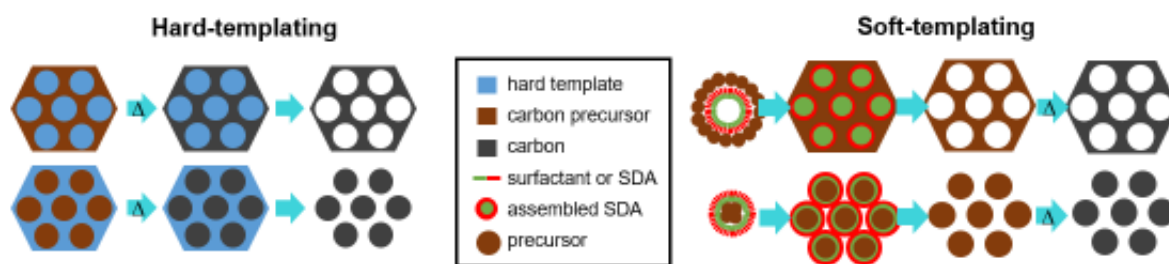


Figure 8. A) Schematic illustration of the hard- and soft-templating approach.

Hard-templating (also-called nanocasting) is a method where rigid templates (nanoparticles) are impregnated into the precursor during carbonization.⁽⁵⁹⁾ The carbonization occurs around the sacrificial hard-templates and afterwards the template is chemically removed. The thus created pores typically adopt the shape of the hard template. This allows for specific pore engineering. Examples of hard templates are zeolites or mesoporous silica. The most prominent examples are mesoporous carbons such as the famous CMK-1.⁽⁶⁰⁾ Two types of hard-templates are distinguished, the endo- and exotemplates, where the carbon network is either formed around or within the pores of a template, respectively.

Salt-templating is another method for the engineering of the pore structure in carbon materials.⁽⁶¹⁾ Typically, non-carbonizable inorganic salts are homogeneously blended with the carbon precursors. Upon heating, the salt melts and mixes with the carbon precursors or the carbon precursors dissolve into the molten salt phase. At high enough temperatures, carbonization occurs in a sol-gel mechanism. After carbonization, the remaining salt phase is removed by washing with H₂O. The porosity is principally dependent on the concentration of the solubilized carbon precursors in the salt phase. Also, the type and the size of the salt ions are discussed as a critical parameter for the lower limit of the resulting pore size of the final carbons. The melting points of various alkali halide salts range between 470 and 800 °C and are significantly reduced in eutectic mixtures with zinc halide salts. Typical examples are eutectics of lithium chloride/zinc chloride (294 °C), sodium chloride/zinc chloride (270 °C), or potassium chloride/zinc chloride (230 °C).⁽⁶¹⁾ Thereby, meso- and microporous carbons from ionic liquids with surface areas of up to 2000 m²·g⁻¹ were achieved.

An example is given by the carbonization of adenine at 900 °C in a mixture of NaCl/ZnCl₂ as a salt-porogen to yield NCs with very high specific surface areas of ~2900 m²·g⁻¹.⁽⁶²⁾ The eutectic mixture of NaCl/ZnCl₂ was a prerequisite for the successful formation of micropores during carbonization and the mass fraction of NaCl was critical to the morphology of the final

NC (**Figure 9**). These NCs were optimized for the performance as catalyst (active and support) for the oxygen reduction reaction in fuel cells.

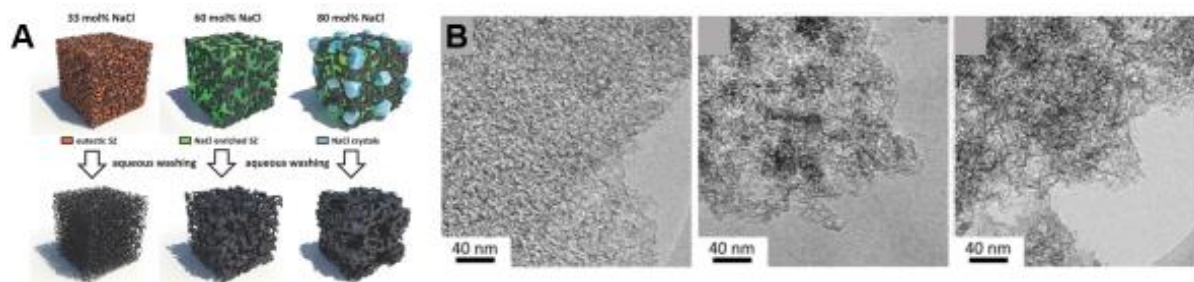


Figure 9. A) Schematic illustration of the pore formation depending on the amount of NaCl present in the NaCl/ZnCl₂ mixture; B) HRTEM images of adenine-based NCs carbonized in the NaCl/ZnCl₂ salt melt with different fractions of NaCl – 33, 60, and 80 mol%.⁽⁶²⁾

Principles of Combustion

Carbonization is achieved through pyrolysis, a high-temperature process conducted in the absence of oxygen. On the contrary, in the presence of oxygen combustion reactions take place, i.e. the reaction of the carbon structure with oxygen to the thermodynamic products H₂O, CO₂, under liberation of heat.⁽⁶³⁾ In most industrial applications, the desired reaction product of a combustion reaction is heat, as for example, in power plants, steam engines, boilers, furnaces, gas turbines, jet, car or rocket engines, etc.

In carbon chemistry, and particularly with regard to laser-induced carbonization, it is essential to understand the fundamentals of combustion reactions. Most elements or materials undergo reactions with oxygen. Here, it will be described by the example of carbon materials. The combustion process follows certain principles. Every carbon material adsorbs oxygen from the environment which is described as additive oxidation. This is followed by so-called over-oxidation, by which the carbon material decomposes and reacts to CO₂. This principle was described in the early last century: “the combustion of carbon compounds and fuels is an elementary oxidation that is initiated by an additive oxidation and over-oxidation, that is the ignition.”⁽⁶⁴⁾

Once ignition occurs the combustion proceeds in a self-accelerating manner. This process is often described as autocatalysis, as the reaction product “heat” acts as a catalyzer. The heat generated during combustion increases the reaction temperature which further increases the reaction rate of combustion. As a practical example, the ignition temperature of coal is ~450 °C. Above this temperature, the combustion reaction is self-sustaining.

Notably, the reaction rate depends on the temperature. At room temperature the reaction rate of any carbon with molecular oxygen is extremely small but not zero. The reaction rate increases with temperature and upon ignition the reaction rate increases rapidly. The reaction rate after ignition depends on whether oxygen is homogeneously distributed in the bulk phase of the carbon or only present in the gas phase above the carbon surface. In the latter case the reaction rate of combustion is diffusion limited. The apparent flames in such a **heterogeneous combustion** origin from heat and reaction products that diffuse out of the carbon phase. In case of a **homogeneous combustion**, the oxidation occurs simultaneously throughout the entire bulk phase. This type of combustion often leads to explosive propagation.

Alternative Carbonization Methods

A recent review article on sustainable materials stated that “the development of synthesis processes with lower energy penalties coupled with the search for sustainable, greener catalysts (i.e., catalytic graphitization) and reducing agents (for graphene production) are challenges that need to be overcome”.⁽⁶⁵⁾ It describes the **paradox of carbon materials**. On the one hand, carbon materials are considered a sustainable alternative. On the other hand, the high-energy demand of their synthesis and their processing to achieve reproducible standards in device performance are still major drawbacks for their widespread application. Common approaches towards lowering the production costs are reducing the carbonization temperatures or the energy input.

An alternative method towards lowering of the reaction temperatures and using milder conditions in general, is **hydrothermal carbonization** (HTC), which has been extensively investigated in the past decade.^(66,67) It generally describes the carbonization of materials in the presence of water at temperatures between 150 and 350 °C. In the HTC process, typically water-soluble carbohydrates or other polar carbon precursors are used as starting materials to obtain micron-sized particulate carbonized materials. To this end, autoclave setups are used. It is worth mentioning that this type of heating can be achieved by **microwave reactors**, which is a major benefit in terms of energy consumption.⁽⁶⁸⁾ The reaction sequence proceeds typically through three stages: dehydration, polymerization, and carbonization. Conducting the reaction in aqueous media promotes the formation of colloidal carbon with an abundance of polar functional groups on their surface. This, in turn, provides a good degree of dispersibility in polar media.

For example, porous NC was synthesized from glucoseamine hydrochloride as precursor by hydrothermal treatment at 180 °C.⁽⁶⁹⁾ After synthesis, the dried material was activated by KOH

treatment to increase the porosity and even induce the formation of micropores. Under these conditions, the oxygen content in the NCs was retained at a high level of ~ 40 wt% giving the NCs a high polarity which was beneficial for the charge storage in aqueous electrolyte-based electric double-layer capacitors (EDLCs).

Another alternative heating process that can be utilized for direct on-substrate carbonization is the so-called **rapid thermal processing (RTP)**. As a heat source, a number of high-power halogen lamps are used. Thereby, very fast heating rates of up to $400 \text{ K}\cdot\text{s}^{-1}$ and cooling rates of $50 \text{ K}\cdot\text{s}^{-1}$ can be achieved.⁽⁷⁰⁾ Since, many sub-reactions during carbonization proceed slower, RTP is only applicable for dispersed precursors or film-based applications where rapid heat transfer through the entire bulk of the material is facilitated.⁽⁷¹⁾ Therefore, in terms of carbon preparation, RTP is mainly used for the synthesis of single- or few layer graphene on catalytic surfaces.^(72,73) However, the energy-inefficiency of conventional carbon preparation routes (pyrolysis) prompts for the study of RTP as an alternative direct processing method of porous carbon.

A recent example demonstrates the synthesis of microporous carbons in a film-based soft-templating approach (**Figure 10**). Phenol formaldehyde, as a carbon precursor, was embedded in a sacrificial template based on polydimethylsiloxane-b-poly(ethylene oxide).⁽⁷¹⁾ The films with a thickness of $\sim 0.5 \mu\text{m}$ were annealed at $950 \text{ }^\circ\text{C}$ for a few minutes with heating rates of $\sim 150 \text{ K}\cdot\text{s}^{-1}$. In a first annealing step at $450 \text{ }^\circ\text{C}$, the template degradation was accomplished, while the second annealing step at $950 \text{ }^\circ\text{C}$ ensured the complete carbonization.

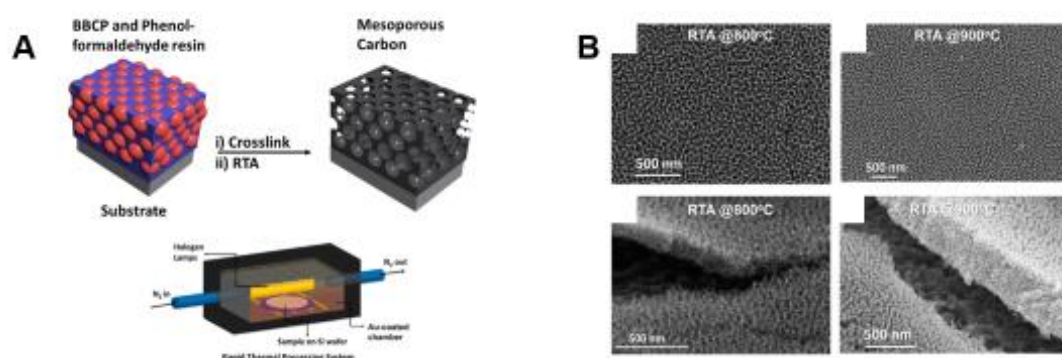


Figure 10. A) Schematic diagram of the preparation of a mesoporous carbons via RTP (b) RTP system.

Summary – Methods for tuning the properties of carbon

- *reaction conditions*
- *post-activation*
- *selecting precursors*
- *incorporation of heteroatoms*
- *pore engineering / templating*
- *carbothermic reductions / chemical activation*

Laser-Carbonization – Context**On-Substrate Carbonization**

The fundamentals described in the previous section demonstrate the complexity of carbonization and introduce some of the most essential tuning knobs for the selective modification of the properties of carbonized materials. Especially, with regard to alternative carbonization methods direct, on-substrate fabrication methods are highly demanded. One upcoming alternative method is laser-induced carbonization. In fact, carbonized materials and carbonized biomass, in particular, are mainly investigated for bulk material applications, such as sorption materials, construction materials, or bulk electrodes (**Figure 11**). In film-based or flexible electronics, their application is often hindered by their processing limitations due to their general insolubility and delicate surface chemistry. Such limitations are avoided by direct carbonization of precursor materials on the spot of application. Lasers provide a versatile and precise (photonic) heat source for carbonization and, therefore, bear the potential for local processing to fill the application gap of carbonized materials.

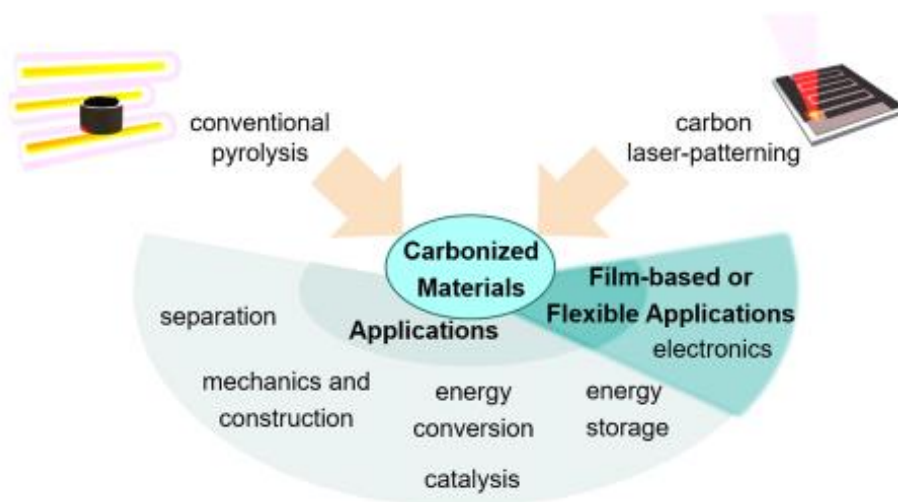


Figure 11. Outline of the application fields of conventionally carbonized materials and potential application fields of laser-patterned carbons.

In light of the advantages of laser-induced carbonization it is worth investigating the underlying fundamental mechanisms and the possibilities for tuning and modulating the properties of carbonized films. Many everyday applications rely on small amounts or film-based materials, such as electrodes in batteries, sensors, or catalytic surfaces (e.g. in fuel cells). In these cases, direct on-chip fabrication techniques are an advantage over classical bulk synthesis. This is probably the most important benefit of laser-induced carbonization: the direct production of active carbonized materials **on the spot of application** and the ability to create desired **patterns** (**Figure 12**).

Additionally, by direct laser-induced carbonization the use of **solvents and reagents** can be drastically reduced. In contrast to conventional bulk-carbonization methods, tedious post-processing procedures are avoided. As outlined in the previous section, carbonization only occurs at high temperatures, although several alternative concepts have been shown to reduce the reaction temperatures. In this regard, laser-induced carbonization bears a significant advantage of **reduced energy costs**. For example, the thermal pyrolysis of a material in a tube furnace at ~ 1000 °C (operated at 1000 W for 2 h) per month would amount up to 60 kWh. In contrast, operating a CO₂-laser at 1 W (high estimate) for 2 h per day would make only 0.06 kWh, only $\sim 1/1000$ of the respective energy costs.

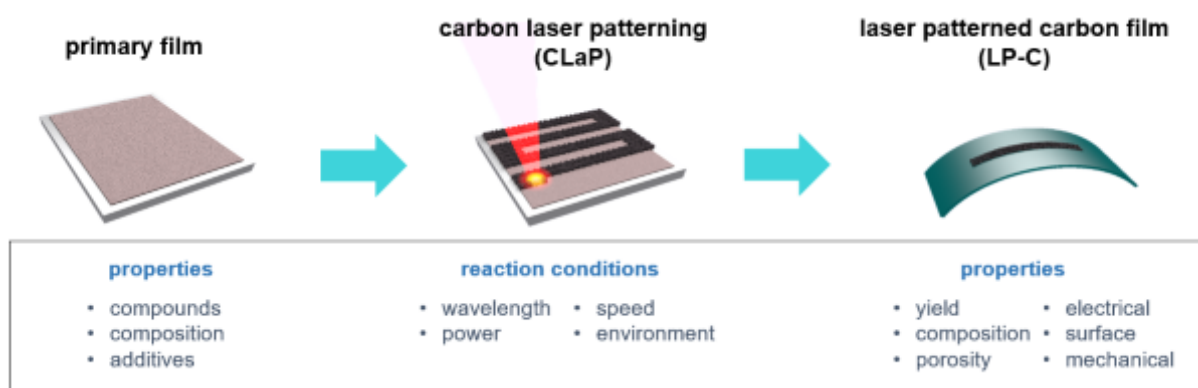


Figure 12. Illustration of the laser-carbonization/ laser-patterning process and the dependencies of LP-C to the properties of the primary film and the reaction conditions.

However, this approach also bears challenges which require fundamental investigations. A major challenge is the precise control over the reaction conditions and laser parameters. The laser power is the most critical parameter in laser-processing of materials. Typically, **power** values on the order of 1 mW are used to sufficiently carbonize organic precursor films. However, in this power regime lasers are often subject to intensity **fluctuations** which may result in large deviations of their product materials properties. Another major critical aspect is the **rapid energy impact** which leads to

several side effects, most importantly, evaporation and ejection of parts of the precursor film. Moreover, the **unidirectional energy input** and the **limited penetration depth** of the laser beam lead to structural and chemical gradients within the product film. Finally, regarding the production of LCMs for direct use in their respective applications, some precautions regarding the **substrate** have to be taken into account. Each substrate responds differently to heat or beam impact and thus influences the properties of the product film (see Beam–Material Interactions).

Advantages of laser-induced carbonization:

- + fast and direct production of carbonized materials
- + localized and precise printing of carbonized structures
- + reduced use of solvents and reagents
- + reduced energy consumption
- + structural and chemical gradient in the product film

Disadvantages or **Challenges** of laser-induced carbonization:

- requires a precise laser-setup to control the reaction temperature
- no bulk production
- substrate dependent
- structural and chemical gradient in the product film

Terminology

In recent years, the sub-field of using lasers to synthesize carbon patterns for film-based applications has been established in materials science. It has become increasingly popular as a fast and precise method to create 2D-patterns of functional materials. A variety of starting materials and precursors have been identified. These are referred to as **primary films**. In all cases, organic starting materials were converted into functional solid-state materials with an increased carbon content. Therefore, the term laser-induced carbonization or simply **laser-carbonization** is an appropriate description which summarizes all materials studied. The term **carbon laser-patterning (CLaP)** may be used to describe the general process of “writing” carbon patterns with a laser beam. The resulting functional carbonized films will be generally referred to as **laser-patterned carbon (LP-C)**. In case of specifically addressing particular properties, for instance intrinsic functionalization or composite materials, variations e.g. **laser-patterned nitrogen-doped carbon (LP-NC)** are used. The material itself regardless of the pattern or structure is referred to as **laser-carbonized materials (LCM)**. It applies generally, also when materials are carbonized with a laser beam, but not obtained in 2D-patterns. This

term also accounts generally for carbon composite materials that were produced in presence of additives or reactants. Alternative terminology used in the literature includes laser induced graphene (LIG) which was established to describe laser-carbonized polyimides. For consistency, the term laser-carbonized polyimide (LC-PI) will be used in this text. Another special case is laser-reduced graphene oxide (LR-GO), which is an accurate description of the laser-carbonization (laser-reduction) of graphene oxide films.

Laser-Carbonization – Historical Overview

The first reports on the laser-induced structural modification of organic materials (polyimide) appeared in the 1980s.^(74,75) Throughout the following decades publications on the topic appeared sparingly and mostly with focus on investigating the laser-induced decomposition of polymers for materials processing.^(76–81) The potential of the general method to specifically apply carbonized patterns has been recognized with the rise of interest in carbon-based printed and flexible electronics during the 2010s (**Figure 13**).⁽⁸²⁾ Especially, the utilization of so-called **LC-PI** from polyimides (Kapton) and **LR-GO** in flexible electronic devices inspired the research on direct laser-writing or laser-patterning of carbon films. Several review articles on laser-reduction / laser-carbonization of PI or GO exist.^(82–89)

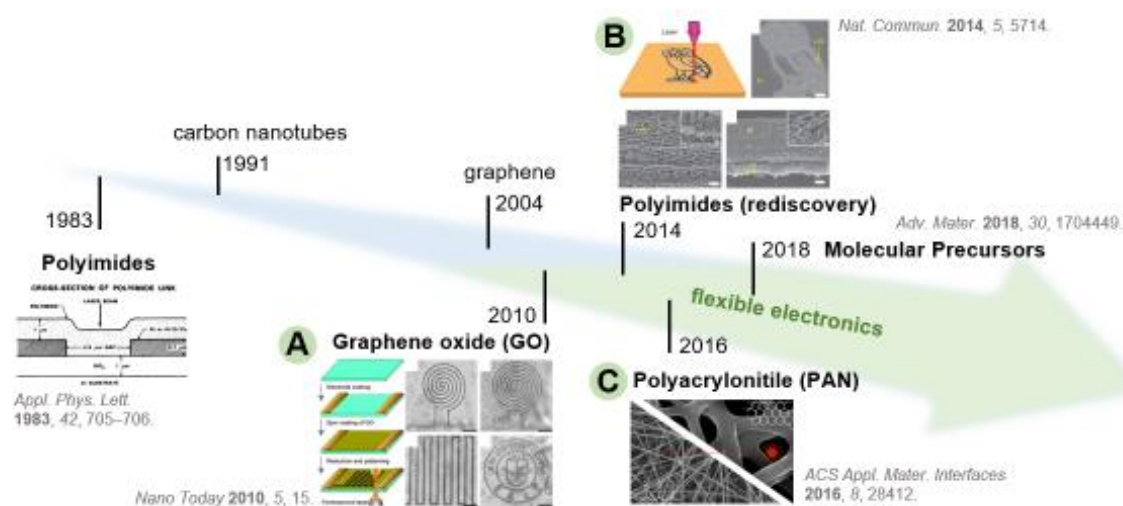


Figure 13. Timeline of laser-patterned carbons showing some examples of modern kick-off studies on the topic of laser-carbonization. A) “Writing” conductive patterns of graphene into graphene oxide primary films with a 790 nm femtosecond laser in 2010⁽⁹⁰⁾; B) “Writing” conductive patterns of LC-PI into commercial PI primary films with a 10.6 μm CO₂-laser in 2014⁽⁹¹⁾; C) Laser-induced carbonization of carbon nano-fabrics based on PAN⁽⁹⁰⁾.

The research in the field experienced a great acceleration more than ten years ago after the publication of the first reports on using lasers to reduce primary films of GO.^(92,93) In these

studies LR-GO films were obtained either in the form of stacked few-layer graphene or as 3D-graphene foams.^(90,94) This discovery fell into a period where extensive research on the fundamental properties of graphenes and their processing methods was conducted.⁽⁹⁵⁾ A few years later in 2014, the first modern report on laser-induced carbonization from commercial PI films sparked the interest in the scientific elucidation of the laser-carbonization process⁽⁹¹⁾, although, the first reports on laser-carbonization of PI date back to 1983.⁽⁷⁴⁾ Originally, an argon laser was used to convert PI into a conductive structure. During that time the carbonization of PI was broadly investigated.^(96,97) In 2016, laser-induced carbonization has also been suggested as an alternative strategy to induce the carbonization of **polyacrylonitrile** (PAN) fiber mats. The latter demonstrates several limitations of laser-induced carbonization (see Laser-Processing of Materials). For example, the cyclization reaction is too slow to be induced by the rapid temperature increase of the laser-beam as it is limited by the diffusion of O₂. To achieve effective carbonization, the heating rate by the laser was finely adjusted to ~50 K·s⁻¹. Secondly, the absorption of the infrared laser beam (968 and 998 nm) in the PAN precursor needed to be enhanced by impregnation with IR-absorbers (graphene nanoplatelets).

The laser-induced carbonization of other polymers as starting materials for efficient laser-carbonization, such as **polysulfones**, were also reported.⁽⁹⁸⁾ Around the same time as the revival article on LC-PI appeared, the laser-induced carbonization of **polyfluorene** was reported.⁽⁹⁹⁾ Another prominent precursor for laser-induced degradation is **poly-dimethylsiloxane** (PDMS) which converts into silicon carbide structures upon laser-irradiation.^(100–102) In the past few years, the approach of laser-carbonization has been applied to other natural polymeric materials, such as **cellulose**, **wood**, **paper** or **coconut fibers** directly.^(103–105)

Direct carbonization of **molecular starting materials** has not been reported. Generally, the high energy impact of the laser beam causes the evaporation of volatile molecular species and prevents the effective formation of a carbon network. In our report in 2018, we described the thermal conversion of molecular precursors into so-called carbon nanodots (CND), which is considered a **pre-carbonized** or a pre-condensed intermediate. After pre-carbonization at ~300 °C, organic materials are less volatile and, additionally, the energetically unfavorable dehydration reactions are completed (see Results Part: Carbon Network-Forming Agents). Laser treatment of such pre-carbonized products lead to conductive porous carbon films. This discovery prompted us to study the process and mechanisms of laser-carbonization to improve the materials performance in film-based electronic devices (see Results Part: Laser-carbonization – Approach).

To obtain a fundamental view and understand the complexity of laser-carbonization, especially the processing parameters and the beam–precursor interactions (**Figure 12**), the most relevant fundamentals of laser processing in a general sense will be highlighted in the next section.

Laser-Processing of Materials – General Aspects

Beam–Material Interactions

Laser-processing of materials is a complex field of many different aspects. Several challenges of material processing have been solved by using lasers as a processing tool. Nowadays, lasers are commonly used in industrial materials processing for different purposes. The

Definition

LASER: light amplification by stimulated emission of radiation

Basics

- working principles of lasers

processes enabled by lasers can be categorized into vaporization of material (cutting, drilling or piercing) melting of materials (welding) or microstructural optimization (patterning or finishing) (**Figure 17A**).⁽¹⁰⁶⁾ Here, a general overview of the main aspects of materials processing with significance to laser-carbonization will be given.

Different models describing the **beam-materials interactions** have been discussed. Some fundamental aspects are commonly described as depicted in **Figure 14**⁽¹⁰⁶⁾: A laser beam provides sufficient energy to evaporate material to form a keyhole. Around the keyhole, the material may be molten (melt pool). The energy impact causes plastic deformation to the surrounding material. Within the keyhole, the laser beam undergoes multiple reflections and is eventually (re)absorbed. Above the keyhole, a plasma plume consisting of ejected material and gases is present.

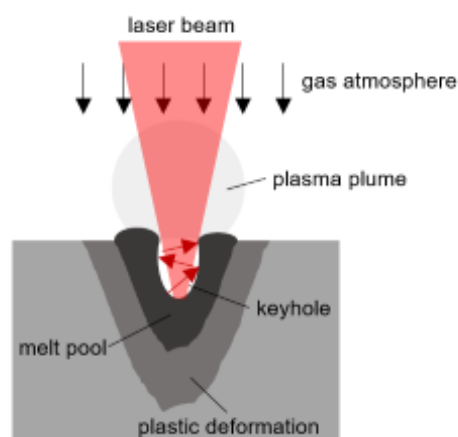


Figure 14. Illustration of some common beam-material interactions.⁽¹⁰⁶⁾

Mechanistically, laser-carbonization may be described with the same principle models. Similar to general observations during materials laser-processing, tentatively, the processes occurring during laser-carbonization may be divided into three steps: Absorption of the high energy of the laser beam causes evaporation of the precursor materials forming the keyhole. From there, the process gets very complex. Competing processes such as melting, bond-dissociation, plasma absorption, and high gas pressure occur simultaneously. The evaporated material most likely consists of ionic carbon clusters or a colloidal carbon plasma. The complexity of the process and the consideration of all reaction parameters and materials properties makes modeling of the processes occurring during laser-carbonization highly challenging.

Due to this complexity, processing materials with laser beams requires a solid knowledge about the underlying **beam-matter interactions**. It is known from industrial materials processing that every material shows a different response to the impact of a laser beam due to their materials characteristics. Primarily, the direct laser beam–materials interactions need to be considered, i.e. primary light-matter interactions such as absorptivity and reflectivity. These two parameters depend on the materials and surface properties and define the so-called **laser coupling** according to equation (2).

$$\begin{aligned} P &= \alpha P_A + \beta P_R \\ \alpha + \beta &= 1 \end{aligned} \quad (2)$$

P is the incident laser power, P_A is the portion of power absorbed and P_R is the portion reflected, while α and β are the absorptivity or reflectivity, respectively. Several examples for the interplay between materials parameters (e.g. aluminum, stainless steel, etc.) and laser irradiation are given in the literature.⁽¹⁰⁷⁾ The same principle applies for organic or carbon precursor films. However, as laser-carbonization has been scarcely investigated mechanistically, comprehensive databases are still lacking.

Once absorbed, the thermal properties of the materials, such as **heat capacity** and **heat conductivity** are decisive for the energy conversion and transport within the material. Moreover, intrinsic materials properties like **melting point** and **evaporation point** are essential. For example, a low melting point lead to a strongly different heat dissipation during the reaction due to enthalpic effects during melting.

Finally, **gases** or **volatile species** evolving during the laser beam induced reactions form a **colloidal plasma** that interacts with the laser beam and reacts with the product material. Therefore, evaporation rates, the density of the evaporated products, their reactivity and their

interaction with the laser beam need to be considered. All these parameters also apply for carbonization reactions.

In this regard, the **reaction atmosphere** is another critical parameter especially in carbonization reactions. Despite the fast reaction rates induced by the laser, the reaction is largely dependent on the presence of reactive gases such as oxygen, ammonia, or hydrogen in the atmosphere.

To summarize, the key materials characteristics that are essential to understand or tune a reaction are:

- 1) absorptivity / reflectivity of the laser beam (reflectivity very low in organic materials)
- 2) thermal properties - heat capacity and heat conductivity
- 3) melting point and evaporation point
- 4) interaction with the products (absorption, reflection, e.g. plasma, gases, dust, or melt)
- 5) reaction atmosphere

Laser Parameters

Lasers are primarily a light source and provide photonic energy. In most materials the high photonic energy density is absorbed and converted to heat. Therefore, lasers are considered an alternative localized heat source. A picture or a simple experiment to have in mind when thinking about laser-induced heat or specifically laser-carbonization is condensing sunlight with a magnification lens to burn a piece of paper (**Figure 15A**). The black residue at the rims of the burned spot is carbonized cellulose fiber (paper).

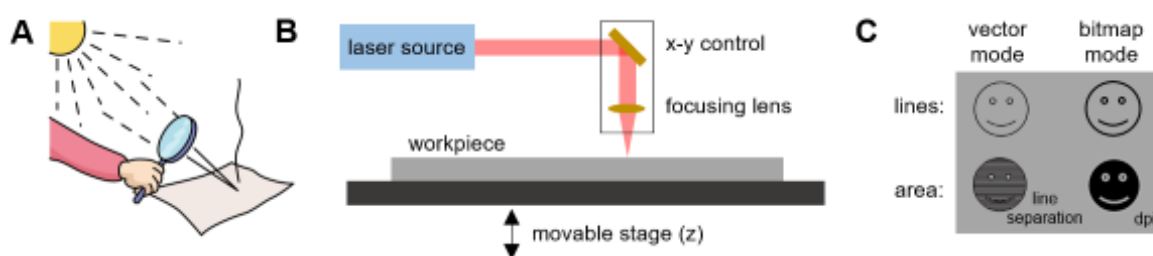


Figure 15. A) Focusing sun light onto a piece of paper with a magnification lens (<https://www.labbe.de>); B) Schematic illustration of the working principle of a processing laser.

Lasers used for materials processing function in a similar manner. A laser source generates a beam with tunable intensity which is directed along a mirror system and a focusing lens to the workpiece (**Figure 15B**). The position and speed of the laser beam is controlled by a moveable x-y axis while the focal distance and focal length is controlled by the specifications of the focusing lens and a movable specimen stage. These laser-setups are operated either in the **vector mode** or in the **bitmap mode**. In the former, the x-y-control follows the lines or paths

in a vector graphic while in the image mode a bitmap with a certain resolution, given in dots per inch (dpi), is rastered (**Figure 15C**). The bitmap mode is generally applicable for scanning (converting) larger areas (engraving). However, higher precision in the patterns and the power control is achieved in the vector mode. When using the vector mode to carbonize larger areas, the **line separation** needs to be defined (**Figure 15C**). Noteworthy, the interaction cross-section is dependent on the materials specific absorption at the laser energy and the thermal diffusivity, therefore the line separation varies with the material in the primary film.

As mentioned above, laser radiation can be considered an alternative heat source to synthesize carbonized materials. Similar to conventional heating methods, the temperature of the laser-induced carbonization reaction is adjusted by the energy input which is a direct result of the power density and the reaction time, i.e. the time the laser beam resides on a spot. In comparison to conventional heating a laser-induced reaction is extremely fast, i.e. occurring on the **time scale of milliseconds**. To understand the heat-induction, some fundamental aspects distinguishing laser heating from conventional joule heating need to be considered. For the sake of conciseness of this text, a laser should just be simply viewed as a source of bundled photonic energy.⁽¹⁰⁸⁾

Lasers are among the **energy sources** with the highest power density. The high power densities in a laser beam are a result of the condensation of photons of a certain wavelength. These properties, the **power density** and the **wavelength**, are the two main criteria that are relevant for (carbon-)materials processing. The power density depends on the **beam diameter** (spot size) in the focus of the laser. The beam diameter is determined by the focusing lens and the wavelength of the laser.⁽¹⁰⁷⁾ For example, a 1 W laser that is focused to a spot size of 0.2 mm results in a power density of $3200 \text{ W} \cdot \text{cm}^{-2}$ according to equation (3).

$$\frac{1 \text{ W}}{\pi \cdot (0.01 \text{ cm})^2} \quad (3)$$

This is to be compared to a value of 1000 – 15000 W that are used in conventional tube furnaces for laboratory use carbonization reactions.

In materials processing, the **fluence** (energy density) is provided as a figure of merit. As a universal value, the fluence, i.e. the energy delivered per unit area, is a direct result of the laser power and the spot size (the focus). The laser fluence F is adjusted by setting the incident power P and the scanning speed v (**Figure 16A**). The fluence is given as either lineal F_L or areal F_A in

$\text{J}\cdot\text{cm}^{-1}$ or $\text{J}\cdot\text{cm}^{-2}$, respectively. The values are determined directly from the preset output power, the scanning speed, and the focal diameter (spot size) according to equations (4) or (5).⁽¹⁰⁷⁾

$$F_L = \frac{P}{v} \quad (4) \qquad F_A = \frac{P}{v \cdot d} \quad (5)$$

Thereby, precise and reproducible fluence values for the area of a laser-carbonized line on a primary film are given (**Figure 16B**).

Notably, the effective energy distribution is also dependent on the **beam profile** with either **Gaussian** or non-Gaussian (**flat-top**) intensity distributions (**Figure 16C**). The profile of the beam largely influences the energy density distribution delivered to the workpiece (precursor film). For Gaussian beams often the peak energy density is provided as it is significantly higher than the average energy density.⁽¹⁰⁸⁾ Moreover, techniques to produce **line shaped beams** with cylindrical lenses are sometimes used to expose a larger focus onto the workpiece.

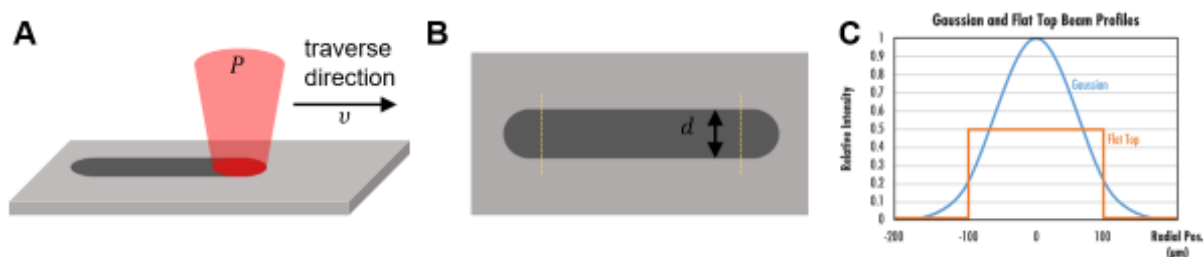


Figure 16. A) Graph illustrating the Gaussian or flat-top beam profiles of a laser beam⁽¹⁰⁹⁾; B) Laser-beam scanned over the surface of a workpiece; C) Laser-modified area determined by the scanning speed and the beam diameter.

The effective **output power** (incident power) is determined directly with a power meter prior to processing, since each laser system has its own specifications. In many commercial laser setups, the output power is generically given in % of the maximum power. However, the real output power often scales non-linearly with the user settings as it is dependent on the repetition rate or scanning speed.

The **scanning speed** enters directly into the equation of the exposed energy density and is therefore a critical parameter. In terms of laser-carbonization, however, the **reaction time** plays a pivotal role. Therefore, the scanning speed should be viewed as a parameter with an individual impact on the processing as it determines the reaction time. Material characteristics such as heat capacity and heat conductivity are dependent on the scanning speed and determine the reactivity of a material.

The **spot size**, or more specifically the beam diameter, is determined by the characteristics of the focusing lens and the laser wavelength. The wavelength depends on the laser source and its active medium and ranges from the ultraviolet (100-380 nm) over the visible (380-780 nm) and the near infrared (780-3000 nm) to the mid-infrared (3-50 μm). An overview of laser sources commonly used in materials processing is given in **Figure 17A**. Among the many classes of lasers, the most relevant for materials processing are:

- 6) gas-laser (e.g. CO₂-laser, $\lambda = 10.6 \mu\text{m}$)
- 7) rare-earth solid-state lasers (e.g. Nd:YAG, $\lambda = 1064 \text{ nm}$)
- 8) diode lasers (e.g. diode GaP, $\lambda = 540 \text{ nm}$)
- 9) excimer lasers (e.g. KrF, $\lambda = 248 \text{ nm}$)

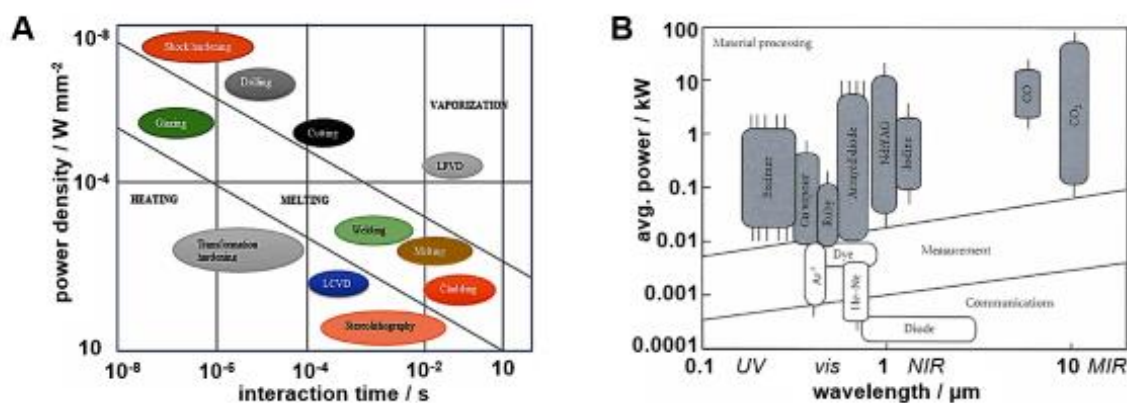


Figure 17. A) Chart of commercial lasers categorized by their average power and wavelength indicating their common fields of application,⁽¹¹⁰⁾ B) Map of typical laser processes as a function of power density per unit interaction.⁽¹¹¹⁾

Notably, the **CO₂-laser** is the most widely used type in materials processing, in general, and for carbonization reactions, in particular. It is available for different power ranges from the microwatt (mW) to the megawatt (MW) regime, making it the work-horse in materials processing. With regard to CO₂-lasers, significant offsets and fluctuations in the low energy regime are typical for direct current (DC)-pumped laser sources. Since laser-carbonization is conducted in the low output power regime between 0.1 – 5 W, radiofrequency (RF) laser sources are the preferred choice, as these provide a higher laser beam stability in the low power regime. Reactions in the material, especially when using long wavelength lasers, are induced by the so-called **photothermal effect**: Photonic energy is absorbed by the material and transformed into lattice vibrations. This effect is dominant at long wavelength excitation. Upon excitation, e.g. in the infrared (CO₂-lasers), specific molecular bond vibrations may be directly excited when in resonance.

The absorptivity of **short wavelengths** (e.g. ultraviolet light) by organic materials or semiconductors is generally higher than for long wavelength, because the photonic excitation energy in the UV is in the resonant range of chemical bond energies and is thus able to directly induce bond dissociation (photolysis). Additionally, shorter wavelengths are generally stronger absorbed due to plasmonic resonance of most materials at higher energies. Moreover, in short wavelengths excitation, nonlinear optical effects like multiphoton absorption have to be taken into account (**Figure 18**).

Although the effective focal diameter strongly depends on the laser optics, shorter wavelengths can be generally focused to smaller spot sizes, which is an advantage for miniaturization in small-scale materials synthesis. However, also the response (absorptivity, reactivity) of the materials is largely dependent on the wavelengths. Some materials are transparent or show a high reflectivity for certain wavelengths.

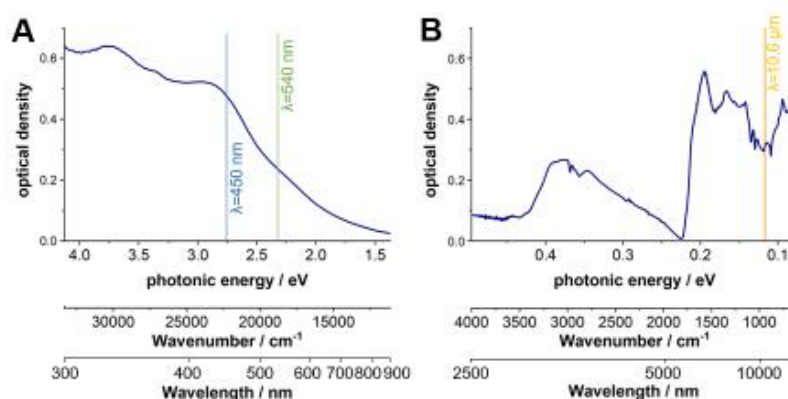


Figure 18. Absorption spectra of an organic precursor for laser-carbonization (CA/U(300)); see Results Part: Carbon Network-Forming Agents) in the UV/vis/NIR and MIR regions.

Another non-negligible beam property that should be considered is the operation mode of the laser, i.e. **continuous wave (CW)** or **pulsed mode**. Especially for the latter, the energy per pulse is an important criterion for the product properties. Typical repetition rates in pulsed lasers range between Hz and GHz depending on the type of laser. For example, a beam propagation speed of $500 \text{ ms} \cdot \text{mm}^{-1}$ ($2 \text{ mm} \cdot \text{s}^{-1}$) and a pulse repetition rate of 1000 Hz, would result in 500 pulses/mm. Changing the propagation speed to $50 \text{ ms} \cdot \text{mm}^{-1}$ gives 50 pulses per mm. This may have a significant impact on the product properties. In many commercial engraving setups the repetition rate is given either in pulses per distance (e.g. per inch: **PPI**) or pulses per time (e.g. per second in Hz).

To summarize, the most important beam properties (laser parameters) that account for laser-induced materials processing in general, and laser-carbonization, in particular, are:

- 1) photon-energy/wavelength of the laser
- 2) incident power
- 3) processing speed
- 4) pulse sequence, repetition rate
- 5) spot size and focal position

Systematic mechanistic studies based on a statistical range of materials and process parameters are still lacking. A comprehensive model for laser-carbonization based on different precursor materials and laser setups would certainly help to understand the principle mechanisms and gain control over the materials properties. In the next section, a survey over individual mechanistic studies on laser-carbonization will be introduced.

Mechanistic Studies – Literature Survey

A good number of studies were devoted to the investigation of the laser-induced carbonization **mechanism**. Among the best studied materials are LC-PI and LR-GO. Notably, the reaction mechanism for all precursors, and these most prominent ones in particular, is highly individual. The laser-induced reaction of GO is considered a deoxygenation or a reduction rather than a classic carbonization as described in the first section. On the other hand, the carbonization mechanism for PI is very specific and not directly transferable to other polymers or precursors as the intrinsic materials properties of each precursor are substantial. Notably, PI is a polymer with an extraordinary thermal stability and duroplastic properties, i.e. without melting point.

Table 1 provides an overview of the essential laser parameters that were used in different studies. The properties of the LCMs such as morphology, crystallinity, surface area, conductivity etc. are largely dependent on the reaction parameters. Especially the laser parameters like **wavelength** (λ), **incident power** (P), **scanning speed** (v), **fluence** (E), **pulse duration** (τ), **pulse frequency** or repetition rate (f), **spot size** (d) and **beam shape** were in the center of the studies. Other reaction parameters like **reaction atmosphere** and **pressure** are also critical. Moreover, the properties of the precursor materials, like **extinction coefficients**, **composition**, **heat conductivity** and **heat capacity** as well as **reactivity** of the precursor films are important to consider. Some insights into the decomposition mechanism of the precursor films were also obtained by analyzing the composition of the **ejected material** or **gases** during laser-carbonization. In the following paragraphs, the influence of these parameters on the properties of the LCMs are briefly described.

A first comprehensive mechanistic study on the laser-carbonization of PI was published in 1985, in which several process components, such as laser wavelength, fluence, or the composition of the ejected materials were individually studied.⁽⁷⁵⁾ In principle, laser-

carbonization, although performed with UV or visible lasers, followed a photo-thermal rather than a photo-chemical mechanism which was confirmed by a sharp reaction threshold in the excitation energy. In other words, the initially induced electronic absorption leads to a rapid transformation into vibrational heating of the precursor film and subsequently a temperature-catalyzed carbonization reaction.

Table 1. Overview on selected studies on laser-carbonization listing the type of precursors used, the target of study (application), and the laser parameters. In case various laser settings were tested in a study, the maximum energy densities or parameter for best device performance were selected.

prec.	target of study	λ nm	v mm·s ⁻¹	P W	τ	f Hz	d μ m	F_A J·cm ⁻²	atm	ref.
cellulose	force sensors	10600	15	2.4	-	-	-	-	-	2019 ⁽¹¹²⁾
cellulose (fiber)	mechanism	10600	40	5	-	-	40	-	-	2019 ⁽¹¹³⁾
cellulose (fiber)	mechanism	522	0.25	0.2	192 fs	63 M	1.6	-	-	2021 ⁽¹¹⁴⁾
GO	mEDLC	1030 /515	125	-	220 fs	500 k	-	-	-	2018 ⁽¹¹⁵⁾
GO	mEDLC	780	-	-	-	-	-	-	amb.	2012 ⁽⁹⁴⁾
GO	optoelectronics	800	-	10	100 fs	1 k	170	0.035	-	2014 ⁽⁸⁴⁾
GO	mEDLC	10600	200	26.5	500 μ s	1 k	line	-	-	2018 ⁽¹¹⁶⁾
GO	mechanism	780	0.005	0.013	70 fs	50 M	2	0.0083	-	2019 ⁽¹¹⁷⁾
GO	fl. electronics	790	-	0.003	120 fs	80 M	-	-	-	2010 ⁽⁹⁰⁾
GO	mechanism	1064 532 355 266	1	-	6 ns	30	5k	0.38 0.15 0.085 0.05	-	2020 ⁽¹¹⁸⁾
lignin	mEDLC	10600	-	-	-	-	100	-	-	2018 ⁽¹¹⁹⁾
lignin/PVA/urea	biosensors	10600	-	-	-	-	-	-	amb.	2020 ⁽¹²⁰⁾
ligno-sulfonate	fl. electronics	10600	-	-	-	-	-	-	-	2020 ⁽¹²¹⁾
ligno-sulfonate	mEDLC	10600	80	-	-	-	-	-	-	2021 ⁽¹²²⁾
PAN	mechanism	968 /998	spot	800	-	-	30k	-	N ₂	2016 ⁽¹²³⁾
paper	multi-sensors	532	15	0.4	-	CW	18	-	-	2020 ⁽¹⁰⁴⁾
PI	strain sensors	10600	1300	6.75	-	-	60	6.2	-	2015 ⁽¹²⁴⁾
PI	acoustic sensors	450	8.5	0.5	-	CW	100	-	-	2017 ⁽¹²⁵⁾
PI	mEDLC	10600	150	6	-	20 k	220	-	-	2016 ⁽¹²⁶⁾
PI	mEDLC	10600	-	4.8	14 μ s	-	-	-	amb.	2015 ⁽¹²⁷⁾
PI	mEDLC/photodet	405	-	0.27	-	CW	-	-	Ar	2016 ⁽¹²⁸⁾
PI	mEDLC	405	-	0.22	-	-	3	-	-	2016 ⁽¹²⁹⁾
PI	mEDLC	10600	-	4.8	-	-	-	-	amb.	2016 ⁽¹³⁰⁾
PI	biosensors	1030	1.0	0.6	-	-	-	-	-	2018 ⁽¹³¹⁾
PI	biosensors	10600	127	0.3	-	-	-	-	-	2020 ⁽¹³²⁾
PI	gas-sensors	10600	180	-	-	-	-	-	-	2019 ⁽¹³³⁾
PI	biosensors	10600	59	5.6	-	-	180	2.3	-	2019 ⁽¹³⁴⁾
PI	humidity sensor	405	none	0.16	>2 μ s	-	-	-	-	2020 ⁽¹³⁵⁾
PI	biosensors	1030 532	0.5	0.23 0.085	400 fs	120 k	5	5	amb.	2016 ⁽¹³⁶⁾
PI	gas-sensors	10600	1.6	0.57	357 μ s	-	100	-	-	2018 ⁽¹³⁷⁾
PI	mEDLC	800	1	0.08	35 fs	1 k 80 M	100	-	-	2021 ⁽¹³⁸⁾
PI (boron)	mEDLC	10600	89	4.8	14 μ s	-	120	-	amb.	2015 ⁽¹³⁹⁾
PI (doped)	biosensors	10600	500	12.5	-	-	-	-	-	2022 ⁽¹⁴⁰⁾
PI (Pt)	electrocatalysis	10600	-	-	-	-	-	-	-	2017 ⁽¹⁴¹⁾
PI (tube)	multi-mech.	10600	15.3	0.85	-	20 k	62.7	-	-	2019 ⁽¹⁴²⁾
wood	electrocatalysis	10600	150	8.6	-	-	1000	-	Ar/ H ₂	2017 ⁽¹⁰³⁾
wood, coconut, potatoes, cardboard	mechanism	10600 9300 1060	150	-	-	-	-	-	N ₂	2018 ⁽¹⁴³⁾
wood/leaves	fl. electronics/ mEDLC/T-sens.	10600	10	0.8	-	-	-	-	-	2019 ⁽¹⁰⁵⁾

* λ : laser wavelength, v : scanning speed, P : laser power, τ : pulse duration, f : frequency, d : spot diameter, F_A : areal energy fluence, atm: reaction atmosphere, ref: reference.

Extinction Coefficients

The thermochemical decomposition of the precursor films (PI) with particular emphasis on the light-matter interactions and the extinction coefficients have been investigated in an exemplary study in 2019.⁽¹³⁴⁾ The absorbance of the incident beam by the film is critical for the efficient transformation of photonic into thermal energy. According to this study, the extinction of the laser beam in the PI film follows the Beer-Lambert law. The extinction coefficients are typically determined at the laser excitation energy ($10.6 \mu\text{m} \triangleq 940 \text{ cm}^{-1}$) by Fourier-transform infrared spectroscopy (FT-IR). This is the resonant energy range of C-H and C-H₂ vibrations. However, plasmonic absorption of particulate or polymeric precursors is also present in this energy regime. A quantitative analysis of the extinction coefficients of PI are still lacking.

Ejected Material

The type and properties of the ejected material during laser impact onto PI was first qualitatively analyzed by gas chromatography–mass spectrometry (GC-MS).⁽⁷⁵⁾ Besides soot (colloidal carbon plasma) that evolves during the laser-carbonization reaction, typical pyrolysis reaction products such as H₂O, CO₂, CO were observed and trace amounts of hydrocarbons. The soot re-condenses to form a carbon-like material, which deposits at the cooler zones. The formation of soot is effectively suppressed in the presence of O₂ as a combustion accelerator.

Composition and Additives

The extinction coefficients and other materials properties such as heat capacity and heat conductivity but also reactivity depend on the chemical **composition** of the precursor films. **Additives** play an important role in the laser-carbonization process as they change both the chemical and the physical properties of the precursor material. For example, a study in which cellulose nanofibers (CNF) were carbonized with a 10.6 μm laser showed efficient conversion only in the presence of sodium as a counter ion in the CNF.⁽¹¹³⁾ It was argued, that the sodium lowers the activation energy of the dehydration step during carbonization. It is, however, more likely that sodium transforms into sodium oxide during laser-carbonization and induces a carbothermic reduction.

Effective carbonization of a variety of precursor materials (filter paper, cloth, and other cellulose-based materials) were enabled by previous heat pretreatment, for instance, exposure to a propane torch.⁽¹⁴³⁾ Thereby, the precursor materials were partly carbonized (charred, pre-carbonized) into amorphous carbon. The materials with an amorphous carbon surface absorbed

enough laser energy to be fully carbonized. This illustrates also the effect of product absorption during laser-carbonization.

Scanning speed, Incident power, and Fluence

In most studies, the primary laser settings like power P [W], scanning speed v [mm·s⁻¹], or fluence F [J·cm⁻²] have been optimized. According to several studies, the efficiency of laser-carbonization is predominantly dependent on the fluence F exposed to the precursor film, and is usually given as areal F_A in J·cm⁻² (**Table 1**).⁽¹⁰⁷⁾ Commonly, the laser parameters are optimized for fluence values in the range between 0.01 – 5 J·cm⁻² for different wavelengths. The divergent range of these values is attributed to inconsistencies in the methods of determination and varying laser technology.

Specific investigations on the influence of the laser parameters on the structural properties of LR-GO prepared with a 10.6 μm laser were included in a study from Tran et al.⁽¹¹⁶⁾ The scanning speed was varied between 100 and 200 mm·s⁻¹ and the power between 18.6 and 26.5 W. These parameters result in linear fluences between 0.93 and 2.65 J·cm⁻¹ or areal fluences between 238 and 680 J·cm⁻², respectively (line beam shape), according to equations (4) and (5). A threshold fluence was necessary to induce sufficient laser reduction, which again points to a thermal rather than a photo-chemical mechanism. The highest capacitance was achieved at the energy density around the minimum threshold, showing that milder reduction conditions yield a higher integrity of the LR-GO network. In a study from Wan et al. the parameters of a femtosecond laser used to reduce GO films were systematically investigated.⁽¹¹⁷⁾ The specifications of the laser are $\lambda = 780$ nm and 70 fs pulse width at a repetition rate of 50 MHz. The power was varied between 3 and 13 mW and a clear dependence of the degree of carbonization, i.e. the portion of carbon, on the laser power was found. In a more recent study, the scanning speed and output power were screened and correlated into matrices showing the effectiveness of laser-carbonization in dependence of output power and scanning speed.⁽¹⁴⁰⁾ By testing a set of three precursors (molecularly engineered PIs), the authors demonstrated that the precursor material is sensitive for both parameters individually. The final morphologies, electrical conductivities, and sensitivities towards dopamine of the LC-PIs vary strongly with these parameters (**Figure 19A**).

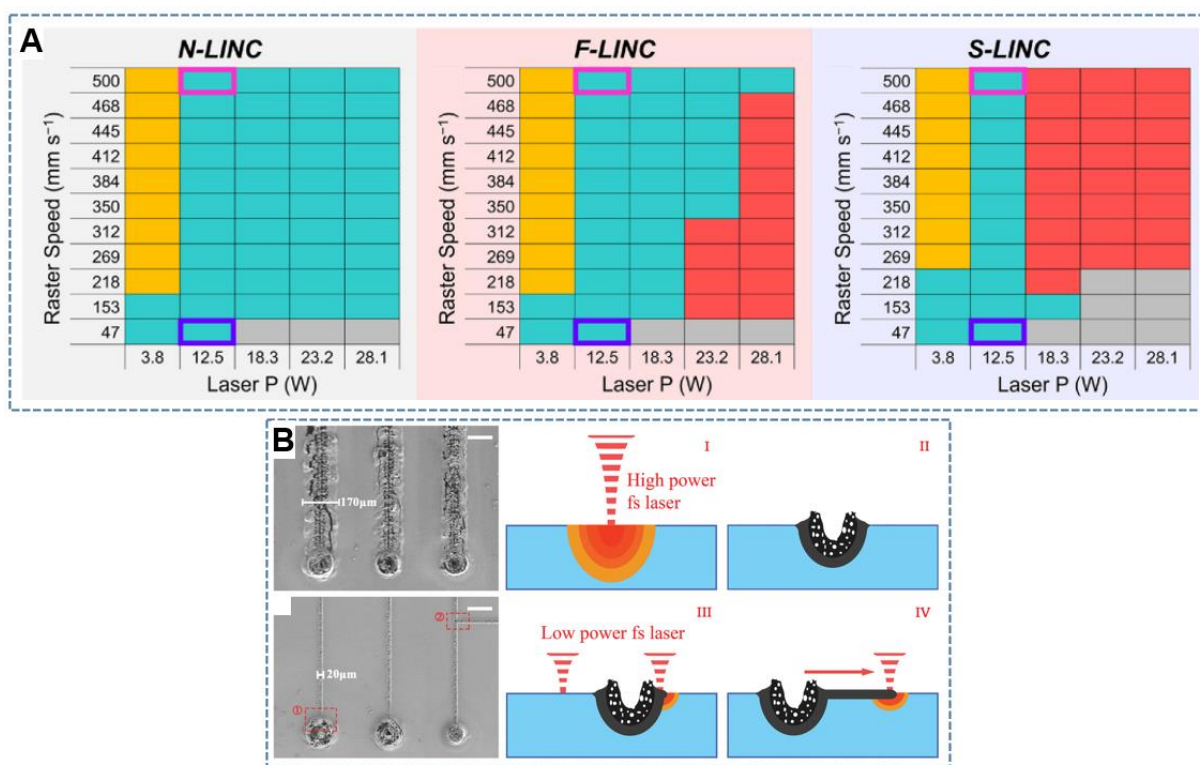


Figure 19. A) Upper: Carbon lines written with laser power of 180 to 200 mW (scale bar: 100 μm); Lower: Carbon lines written with 30 mW starting from carbonized points (scale bar: 100 μm); Right: Schematic of the point-to-line strategy;⁽¹³⁸⁾ B) Correlation map of laser power with scanning speed on different PIs. Yellow: Non-carbonized, green: electrically conducting porous morphology, red: resistive wooly nanofibers.⁽¹⁴⁰⁾

An interesting phenomenon demonstrating the influence and limitations of the precursor film in terms of heat capacitance and heat conductivity was described recently by Guo et al.⁽¹³⁸⁾ In this study, PI was carbonized with an 800 nm femtosecond laser. It was found that a **critical lower threshold value for fluence** and certain repetition rate were necessary to achieve effective heat accumulation and thus carbonization of the PI. An initial carbonization point with fluence above the threshold was set. All subsequent carbonization lines starting from this point were “written” at fluences three times lower than the fluence threshold for bare PI (**Figure 19B**). Thereby, the effective power consumption was reduced and the line width was minimized to only 6.5 μm. Generally, **lower** and **upper threshold** values for effective **laser-carbonization** or **ablation**, respectively, are found in several studies. The thresholds are dependent on the extinction at the wavelength of the laser. An overview is given in **Table 2**. Notably, the threshold was also found to be dependent on the scanning speed.^(116,140) For the laser-induced reduction of GO a lower threshold was determined to be significantly lower than for the carbonization of PI. The lower carbonization fluence threshold may be correlated to the threshold temperature of 200-230 °C for the reduction of GO obtained in reference experiments.⁽¹¹⁷⁾

Table 2. Overview on the threshold values of the laser fluence found in different studies.

precursor	wavelength nm	fluence	fluence	ref.
		(lower threshold) J·cm ⁻²	(upper threshold) J·cm ⁻²	
GO	243	0.010		(84)
GO	243	0.006		(144)
GO	248	0.07		(145)
GO	266		0.050	(118)
GO	355		0.085	(118)
GO	532		0.15	(118)
GO	1064		0.38	(118)
PI	248	0.027		(75)
PI	308	0.070		(75)
PI	351	0.12		(75)
PI	800	0.9		(138)
PI	10600	1.3		(134)
PI	405	83.4 (single pulse)		(135)

The laser fluence is principally a measure for the reaction temperature and has thus a significant influence on the properties of the LCM films such as their structural and electronic properties. For example, the decomposition temperature of PI (commercial Kapton) is ~ 500 °C in air and decomposes almost exclusively to CO₂ and CO.⁽¹⁴⁶⁾ The energy threshold could be a measure for the decomposition temperature. The fluence range within the lower and upper thresholds determines the effective temperature window. Within this window the film composition, morphology, and electronic properties are directly dependent on the fluence. For example, the porosity of LC-PI shows significant differences depending on the fluence.⁽¹³⁴⁾ Also for GO, the reduction efficiency is clearly dependent on the laser fluence. The lower and upper fluence thresholds were determined in systematic studies.^(84,118)

Wavelength and Resolution

Systematic studies on the effect of the **laser wavelength** to the reduction of GO show that deoxygenation is more effective in the short wavelengths region towards the UV while the reduction to the sp²-carbon lattice is more effective at longer wavelengths. These insights enable a differentiation between photochemical and thermochemical effects.⁽¹¹⁸⁾

Although, in the early investigations on the laser-carbonization mechanism of PI short UV-lasers (248, 308, and 351 nm) were used, the most commonly used laser source for laser-carbonization of PI is the CO₂ laser ($\lambda = 10.6$ μm) (**Table 1**). Other wavelength such as 405 nm are increasingly used due to the higher achievable patterning **resolutions**. The resolution of LC-PI has been improved from ~ 100 μm to ~ 12 μm and even 6.5 μm .^(135,138) A comparison of these

studies clearly shows that the effective power / fluence threshold is largely dependent on the wavelength of the laser.

Focus

The effective reaction temperature is varied with the fluence, which peaks in the **focus** of the laser beam. The effective fluence exposed on the precursor film can be reduced by defocusing the laser beam. Chyan et al. demonstrated that defocusing of a 10.6 μm laser has a strong influence on the properties of LCMs from different precursors, such as PI, Kevlar, cardboard etc (**Figure 20A**).⁽¹⁴³⁾ The overlapping regions of the individual laser lines thus experienced multiple exposure which enhanced the electrical sheet conductivity of the product films.

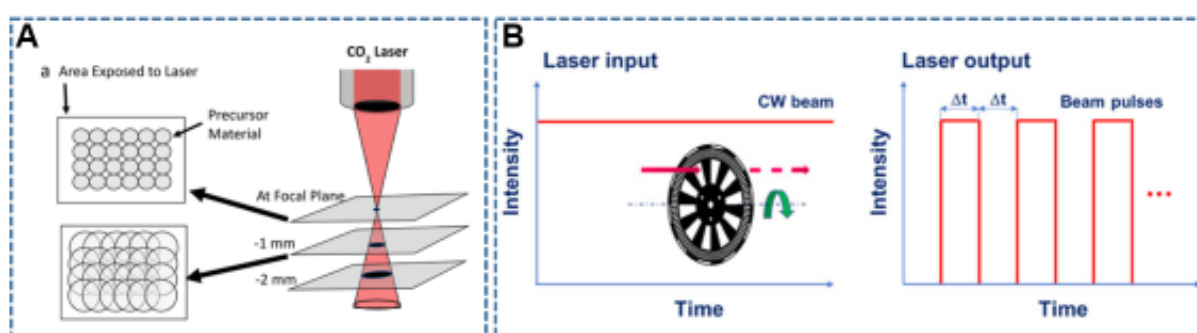


Figure 20. A) Image visualizing the influence of the focus of the effectively irradiated area⁽¹⁴³⁾; B) Image visualizing the difference between CW and pulsed laser modes, the pulse duration and repetition rate.⁽¹¹⁶⁾

Repetition rate / Pulse Duration

Pulsed lasers are frequently used for laser-carbonization. Their characteristics are defined by the **pulse frequency** (repetition rate) and the **pulse duration** (**Figure 20B**). Both parameters were shown to have an influence on the properties of the LCMs. Pulsed laser beams show decisive advantages in terms of power control over continuous wave (CW) operated lasers.⁽¹¹⁶⁾ To test this effect, the pulse duration and repetition rate of a CW CO₂-laser was modulated by a beam chopper and studied towards the performance of LR-GO in EDLCs (**Figure 20B**).⁽¹¹⁶⁾ It was found that the beam modulation from 100 Hz to 1 kHz resulted in a better laser-reduction efficiency as indicated by an improved capacitance. The laser-reduction mechanism of GO was systematically studied in 2014 and optimized for the application of LR-GO films as electrodes in transparent organic photovoltaics.⁽⁸⁴⁾ Here, the effective fluence was varied between 3.5 and 35 $\text{mJ}\cdot\text{cm}^{-2}$. Moreover, the number of pulses of a 248 nm KrF laser showed a significant influence on the efficiency of the laser reduction especially in terms of charge-carrier mobility. A 405 nm fiber-coupled laser integrated into a scanning electron microscope (SEM) chamber

allowed for the *in situ* investigation of the laser-carbonization process of PI.⁽¹³⁵⁾ The carbonization upon applying single pulses with pulse widths between 2 μ s to 100 ms were investigated. The results provide insights into the reaction kinetics of PI. Short pulses of <100 μ s no effective carbonization was observed. The diameter of the irradiated spot increases with increasing pulse width up to pulse durations of <1 ms.

Beam Shape

Besides the beam profile, the **beam shape** is a variable in the laser-carbonization process. To improve the throughput of laser-carbonization a **line-beam** CO₂ laser reduction process of GO was investigated in 2018.⁽¹¹⁶⁾ To this end, a cylindrical lens was employed to achieve an effective line shape of 3.9×0.23 mm². Parameters such as pulse duration and repetition rate of the 10.6 μ m laser were finely adjusted to meet the optimum requirements of the laser-reduction, with the pulse-to-pulse pitch being the effective critical parameter.

Reaction Atmosphere

The presence of O₂ during laser-carbonization was initially found to play no direct role in the reaction rate or the ablation process.⁽⁷⁵⁾ However, later it was found that the reaction atmosphere has a significant influence on the surface properties of the carbonized film. Differences appear mainly in the oxygen content on the surface, which is significantly higher in the presence of oxygen. Subsequently, the surface polarity is much higher which was confirmed by contact angle measurements.^(134,147) In general, the presence of O₂ promotes the combustion reaction at high reaction temperatures (see Principles of Combustion). Due to a more complete combustion reaction the remaining carbon shows a higher degree of graphitization which is reflected lower defect and disorder related signals (D, D3, and D4) in the Raman spectrum.⁽¹³⁴⁾

Applications – Overview and Literature Survey

Overview

The electrically conductive carbon materials obtained from laser-carbonization are generally useful for **application** in film-based or flexible electronics. Their intrinsic porous structure makes them applicable in high-surface area applications such as electrodes in electric double-layer capacitors (EDLC) or batteries, electrocatalysts, electrochemical sensors etc. All these applications rely on large interface materials and the interaction of gaseous or liquid media with the electronic surface or specific active sites on the surface of the materials.

In this section, the most prominent fields of application for LP-Cs will be introduced, namely EDLCs, electrocatalysis, and sensors. These are also the applications of the LP-Cs developed and investigated in this thesis (**Figure 21**).

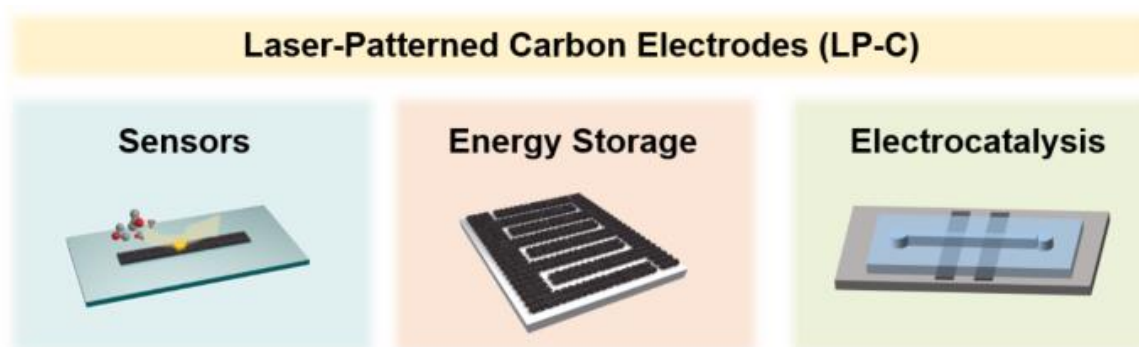


Figure 21. Overview of the most prominent fields of application for laser-carbonized materials: Electrochemical sensors, electrochemical energy storage, and electrocatalysis.

LP-C in Electric Double-Layer Capacitors

Introduction

Among the most widely studied applications of high-surface area carbons in flexible electronics are **EDLCs**. EDLCs are energy storage devices where the energy storage is achieved through electrostatic charge deposition

at the electrode/electrolyte interface.⁽¹⁴⁸⁾ The charge stored at the biased electrode surfaces and the proximate layer with an equivalent counter ion population continuously increases with the potential difference between the two, limited only by the standard electrochemical potentials of the electrolyte ions and/or the stable voltage range of the electrolyte solvent (**Figure 22A**). Therefore, for high-performance EDLCs, high surface areas with a hierarchical porous structure

Basics

- electrochemical double-layers
- ionic conduction
- interface reactions

are preferred. Such requirements are generally fulfilled in LCMs.⁽¹⁴⁹⁾ In the light of future flexible and wearable electronics as well as on-chip fabrication of electronic devices, particular focus was laid on the development of so-called micro-EDLCs (mEDLC). mEDLCs are developed in a planar fashion in order to be integrated onto different substrates in form of in-plane interdigitated electrodes (**Figure 22B**). For further reading on the operation principles, device performance parameters, engineering and limitations one of the plenty review articles on the topic is recommended.^(150,151) Laser-carbonization is a direct synthesis method suitable for the fabrication of porous carbon-based electrodes on different substrates.

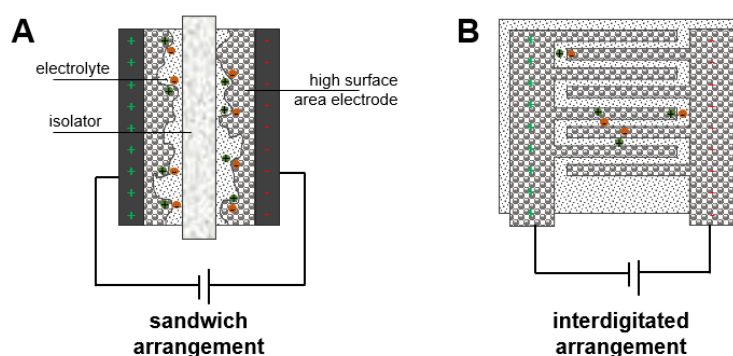


Figure 22. Schematic illustrations of the working principle of an electrochemical capacitor in the sandwich or the 2D printed – interdigitated arrangement.

State-of-the-art

In an early report on using LR-GO as an active electrode material interdigitated electrodes were prepared with a simple commercial Lightscribe drive ($\lambda = 780 \text{ nm}$).^(94,152) Homogeneous GO films with thicknesses of up to $10 \mu\text{m}$, cast from aqueous GO dispersions, were applied onto a flexible substrate and mounted onto a DVD (digital versatile disc). In the disk drive, the GO was reduced by the laser to obtain porous 3D-graphene films (**Figure 23**). The electrode performance was tested in a sandwich or in a 2D-interdigitated electrode arrangement resulting in areal capacitances of $2.3 \text{ mF}\cdot\text{cm}^{-2}$ (at $16.8 \text{ mA}\cdot\text{cm}^{-3}$). In 2016, a laser-reduced rGO/ZnO composite was prepared by laser-treatment of a $\text{Zn}(\text{NO}_3)_2$ impregnated GO film.⁽¹⁵³⁾ Interdigitated electrodes were laser-patterned on PET substrates with a 780 nm LightScribe drive and showed a high capacitance retention at random bending angles. To improve the flexibility and stretchability of the LR-GO electrodes, a femtosecond laser ($\lambda = 1030$ or 515 nm) was used to pattern GO films into vertically oriented LR-GO in the shape of interdigitated electrodes.⁽¹¹⁵⁾ A gold layer was sputter deposited on top of the LR-GO to reinforce the electrical connections during mechanical deformation.

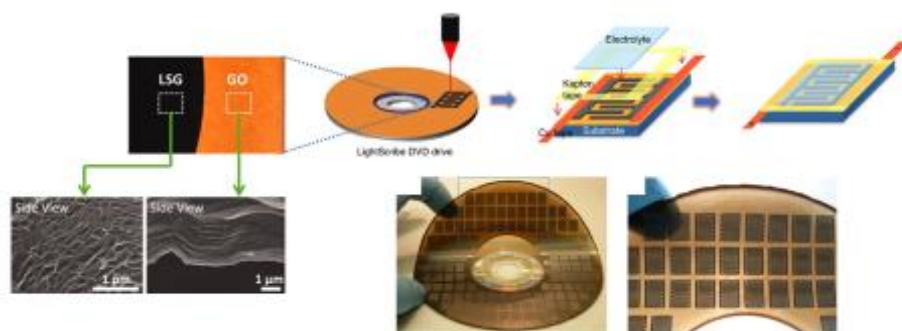


Figure 23. Schematic diagram showing the fabrication process for an LR-GO based mEDLC applied on a PET substrate produced in a commercial LightScribe DVD drive. Copper tape is applied along the edges to improve the electrical contacts, and the interdigitated area is defined by Kapton tape. An electrolyte overcoat is then added to create a planar mEDLC.^(94,152)

To increase the throughput of the laser-fabrication technique, a line-beam shape was utilized in a CO₂-laser to reduce GO films.⁽¹¹⁶⁾ The LR-GO exhibits capacitive behavior reflected in quasi-rectangular cyclic voltammograms at even very high scan rates of 5 V·s⁻¹. Areal capacitances of ~90 mF·cm⁻² (at 1 A/g) were achieved.

Standard electrochemical characterization

- cyclic voltammetry
- galvanostatic and potentiostatic impedance spectroscopy
- chronoamperometry
- etc.

In 2015, it was demonstrated, that LC-PI, processed with a 10.6 μm CO₂-laser from commercial Kapton tapes show a high electrochemical performance in both vertically stacked and in an in-plane arrangement.⁽¹²⁷⁾ Stable areal capacitances of ~10 mF·cm⁻² (at 0.01 mA·cm⁻²) were achieved. The vertical stacking was enabled by laser-carbonization on both sides of the PI tapes and using polyvinyl alcohol (PVA) membranes as separators. On the other hand, in-plane geometry was realized by laser-patterning interdigitated electrodes on one side of the membrane and applying PVA as a polymeric electrolyte.

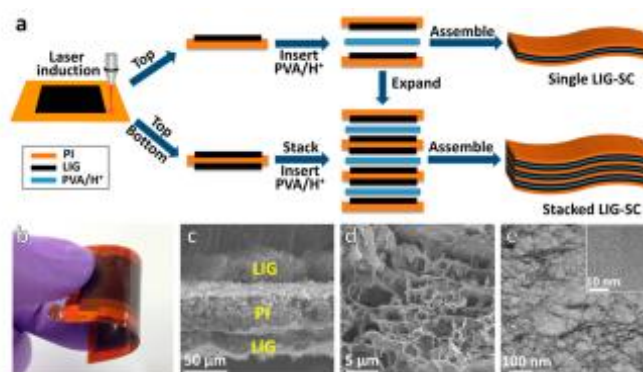


Figure 24. Fabrication and characterization of LC-PI-based mEDLCs. (a) Schematic illustration showing the fabrication process for assembling a single and stacked LC-PI-based mEDLCs; (b) Optical image of a fully assembled single LC-PI-based mEDLCs manually bent. (c) Cross-sectional SEM image of a PI substrate with both sides laser-induced to form graphene. (d) SEM image of the LC-PI films showing a porous 3D network. (e) TEM image of a LC-PI film showing nano-sized wrinkles and ripples. Inset is a HRTEM image of a LIG nanosheet showing graphene edges.

The performance of the LC-PI-based mEDLCs was improved by electrodeposition of pseudo-capacitive components, such as MnO_2 , FeOOH , or polyaniline (PANI) onto the laser-carbonized PI to reach energy densities comparable to micro-batteries.⁽¹³⁰⁾ Similarly, boron doping of the LC-PI electrodes by adding boric acid to the PI precursor, improves the capacitance and the energy density.⁽¹³⁹⁾ Similar performance is achieved with a 405 nm laser, by which a much smaller spot size of only 3 μm was realized.⁽¹²⁹⁾ Notably, the performance of the mEDLCs was significantly improved by air-plasma etching of the LC-PI electrodes, which modifies the surface properties and the porosity of the LC-PI. To test and improve the mechanical flexibility, LC-PI was transferred to a stretchable PDMS substrate and showed only little impact on the performance in the bent or in the stretched state.⁽¹²⁶⁾ It has been shown, that the capacitive performance of LC-PI-based mEDLCs can be significantly improved by conducting the laser-carbonization in an inert gas atmosphere.⁽¹²⁸⁾ Thereby, higher conductivity, higher surface area and a change in the pore-size distribution were achieved.

Challenges

Obvious challenges are improving the **electrochemical performance** of the mEDLCs in terms of energy and power densities, cyclability, high retention upon bending, high flexibility etc. Clearly, energy densities in energy storage devices needs to be improved to meet the requirements of long-term energy storage. To be applicable in future flexible electronic devices a **fundamental understanding** of the surface properties of LP-Cs is necessary. The specifications of any device needs to be adopted to the market-specific demands. Every commercial EDLC is designed for the specific demands of the intended application. For example, the capacitive frequency window is crucial. Therefore, universal strategies for **selective tuning** of the LP-C **materials parameters** must be a goal of current research. The applicability of LP-Cs on **different substrates** is another requirement. To adopt a general concept for a variety of precursors, universal strategies to apply carbon precursor films on different substrates need to be identified. Although **minimal feature sizes** of only a few μm have been achieved, miniaturization is still a challenge in most LCMs. The abovementioned examples, PI and GO have been widely investigated as precursors of LP-Cs, however, their **high costs** may be a limiting factor for widespread application. Additionally, **limited tunability** in terms of surface and electronic structure are inherent.

LP-C in Electrocatalysts

Introduction

In electrocatalysis, the rates of chemical reactions at the surface of an electrode are enhanced by the potential of the electrode. Here, the activation energy of an electrochemical reaction is dependent on the potential of the electrode. The type of reactions commonly catalyzed with electrocatalyst electrodes range from the selective organic reactions over fuel cells, CO₂ reduction, or N₂ activation to materials synthesis, to name only a few.^(154,155)

Basics

- electrochemical double layers
- heterogeneous catalysis
- standard electrode potential

The concept of electrocatalysis may be best explained using the example of **water splitting** (electrolysis) or hydrogen-oxygen **fuel cells** (proton exchange membrane (PEM) fuel cell **Figure 25**). Electrodes can be used to facilitate the decomposition of H₂O into H₂ and O₂ or the controlled synthesis of H₂O from H₂ and O₂, respectively, using electrical energy. In this first case two electrodes immersed in H₂O are connected by a DC power supply. At high enough potential, the reduction reaction, the hydrogen evolution reaction (**HER**: $2 \text{H}_2\text{O}(\text{l}) + 2 \text{e}^- \rightarrow \text{H}_2(\text{g}) + 2 \text{OH}^-(\text{aq})$) occurs at the cathode (negatively charged) while the oxidation, the oxygen evolution reaction (**OER**: $2 \text{OH}^-(\text{aq}) \rightarrow \frac{1}{2} \text{O}_2(\text{g}) + \text{H}_2\text{O}(\text{l}) + 2 \text{e}^-$) occurs at the anode (positively charged) (**Figure 25A**). In the reverse reaction, the excess of energy stored in the gaseous components H₂ and O₂, is used in a controlled fashion to gain electrical energy in fuel cells. Here, the hydrogen oxidation reaction (**HOR**: $\text{H}_2(\text{g}) \rightarrow 2 \text{H}^+ + 2 \text{e}^-$) occurs at the anode and the oxidation reduction reaction (**ORR**: $\frac{1}{2} \text{O}_2(\text{g}) + 2 \text{H}^+ + 2 \text{e}^- \rightarrow \text{H}_2\text{O}$) occurs at the cathode (**Figure 25B**).⁽¹⁵⁶⁾

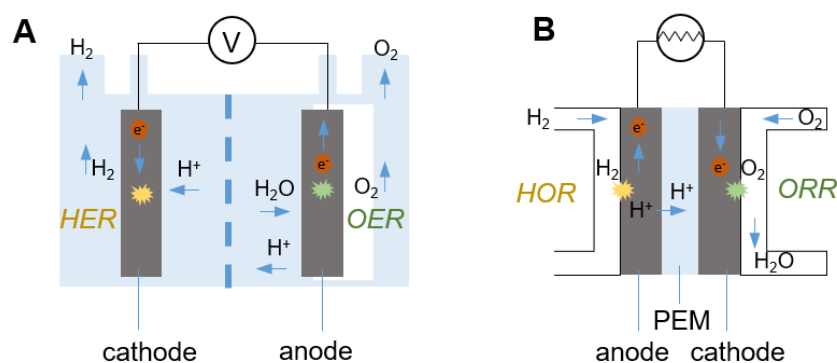


Figure 25. A) Working principle of a PEM fuel cell involving the hydrogen oxidation reaction (HOR) and the oxygen reduction reaction (ORR); Working principle of a water electrolyzer involving the hydrogen evolution reaction (HER) and the oxygen evolution reaction (OER).

The most important assets of electrocatalysts is their **activity** and **selectivity** for specific reactions, but also **stability** for commercial applications.^(157,158) The **activity** is measured by the current density generated during the reaction. It is related to the accessible number of active sites, i.e. the available surface area of the catalyst or catalyst support (see Results Part: **Figure 30**). Other factors are the type of active sites and the quality of mass, ion, and electron transport phenomena by modulating the electronic, and structural properties of the active material or the diffusion processes of the electrolyte. Therefore, efforts towards strategic performance improvements focus mainly on the identification of new active sites or stabilizing nanostructuring of the catalyst support. A common way to increase the activity of electrocatalysts is the dispersion of active sites on high-surface area electrode supports. Another common feature influencing the performance of an electrocatalytically active material are their electronic properties, such as work function, or charge-carrier properties.⁽¹⁵⁹⁾

Notably, for economic reasons, the fabrication costs are an essential criterion for the widespread availability of commercially used electrodes. Therefore, a good amount of research is devoted to the identification of **cost-effective materials** and **processes**.

In the past decades, carbon nanomaterials such as **carbon nanotubes** or **graphene** have been extensively studied as electrocatalyst materials or conductive supports for electrocatalysts and contributed to a fundamental understanding of electrochemical carbon-electrolyte interfaces.⁽¹⁶⁰⁾ Both these materials exhibit very large surface areas and chemically reactive sites for the deposition of electrocatalytic sites. Moreover, their intrinsic electric conductivity enables them to act as electrode materials.

Besides carbon allotropes, other carbon-based electrodes based on, for example, pyrolyzed carbons or carbonized materials, in general, are moving into the focus of attention.⁽¹⁶¹⁾ The simplicity and versatility of their synthesis enabled the discovery of highly active, yet cost-effective catalyst electrodes. General strategies to improve the activity in carbonized materials include the introduction of active sites by heteroatom doping, nano-structuring, pore engineering, surface functionalization, defect engineering, or hybridization and composite synthesis.

State-of-the-art

Only a few examples of LCMs applied in electrocatalytic systems have been published. In a study from 2017, a double-sided LC-PI membrane was used as electrodes to facilitate full water-splitting (**Figure 26**). The membrane was fabricated by direct laser-carbonization of PI

and subsequent electrodeposition of either a $\text{Ni}_x\text{Fe}_y(\text{OH})_{2x+3y}$ (NiFe) catalyst or a combination of $\text{Co}_3(\text{PO}_4)_2$ and CoO_x (Co-P) catalysts to facilitate either the hydrogen evolution reaction (HER) or and the oxygen evolution reaction (OER), respectively. Alternatively, *in situ* formation of Pt nanoparticles during laser-carbonization of PI was studied as HER electrode by mixing Pt(II)acetylacetonate (Pt(acac)) and polyamic acid as precursors and subsequent drying and thermal curing.⁽¹⁴¹⁾ In a separate study, it was shown that laser-carbonized natural wood also serves as a support material for the electrodeposition of the aforementioned HER or OER catalysts showing similar performance.⁽¹⁰³⁾

Basics

- electrodeposition

The importance of surface oxidation of the LP-C by exposure to an oxygen atmosphere during the laser-carbonization for efficient OER or ORR was highlighted in 2018. The oxygen-containing functional groups on the surface provide active sites, on the one hand, and reduce the activation energy by facilitating adsorption of reaction intermediates.⁽¹⁶²⁾

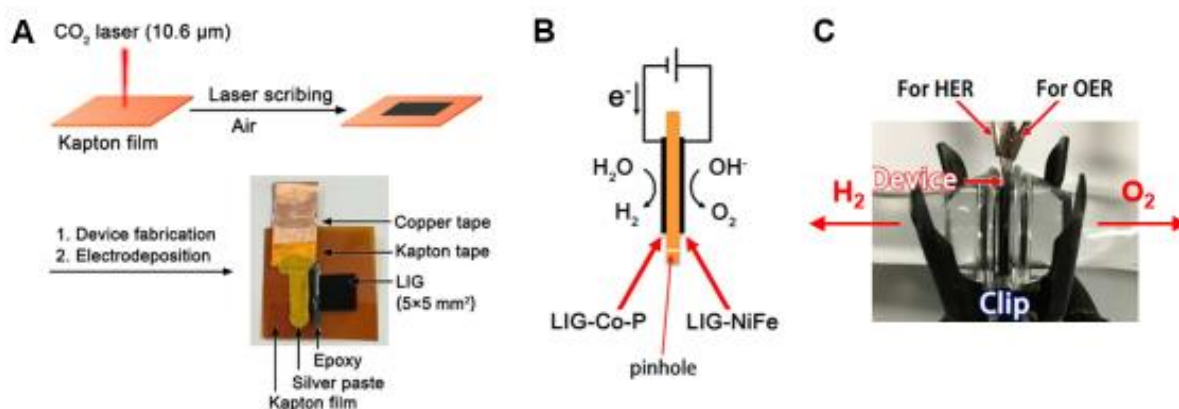


Figure 26. A) Fabrication process of the laser-carbonized PI/NiFe or Co-P electrodes. Commercially available Kapton (PI) was directly laser-carbonized. Then the catalysts were electrochemically deposited on the laser-patterned carbon; B) Schematic drawing of the integrated water-splitting electrode membrane; C) A photograph of the water-splitting electrode membrane.⁽¹⁴¹⁾

Challenges

In the light of oxidation or reduction reactions utilized in fuel cells, current scientific challenges are among others improvements of the **catalytic performance** of carbons and their composites. Although, many carbon or carbon composite materials show a decent performance, the exact mechanisms are still unknown. **Systematic mechanistic studies** to derive universal principles would help to develop the field of carbon-based electrocatalysis but are largely missing. **Reproducibility** is another critical issue. The synthesis conditions of the carbon materials, in particular, the composite materials need to show a high experimental batch-to-batch control. This counts especially for heteroatom-doped carbons. The synthesis strategies need to come

along with high **economic efficiency** to avoid the use of expensive fabrication methods and the use of extensive amounts of solvents.

LP-C in Sensors

General Principles of Sensors

The **working principle of any sensor**, i.e. the detection of a stimulus, is based on three steps: signal detection (stimulus), transduction (information), and processing (data) as presented in **Figure 27**. In biological (ionic) systems, e.g. the human body, signal detection occurs in the cells, the information is transduced in form of an action potential along the nerve system, and the data is processed in the brain. In artificial (electronic) sensor systems, the signal detection happens at the interface of a sensor material and the information is transduced by electrical connections and processed with a computer.

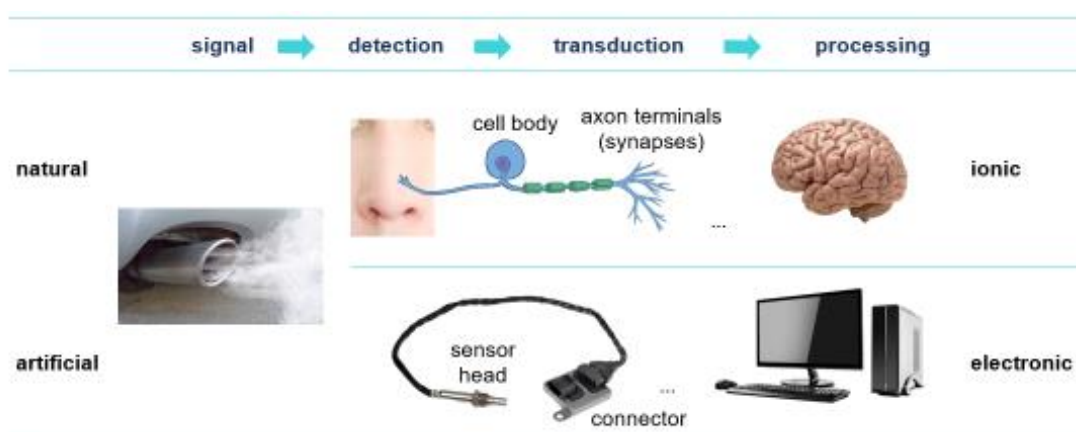


Figure 27. Scheme explaining the working principle of natural and artificial sensors by the example of olfactory detection.

The general **types of signals** or **stimuli** that are detected can be categorized into five groups: electromagnetic radiation, electromagnetic fields, temperature, mechanical, and chemical. For a range of these stimuli, the human body is equipped with specifically trained organs providing our five known senses: visual, auditory, olfactory, gustatory, somatosensory. However, all artificial or natural sensors, and particularly the human senses, are limited to certain detection ranges. For example, the reception of electromagnetic radiation by the human eyes is limited to the visible part of the spectrum. Another example is the limitation of the gustatory or olfactory senses to certain molecular receptors where specific molecular such as CO_2 are excluded.

Artificial sensors provide information about the environment that is not detected by our human senses and thus allow to create **awareness** and enable forecasts, for example, in medical diagnostics, weather monitoring, safety, security, emission control, robotics, or bionics.

Carbon materials have been investigated as active sensor materials mainly for chemical and mechanical sensors. However, their general responsiveness to external stimuli makes them applicable also in other sensor types. Here, nano-carbon allotropes, such as graphene and carbon nanotubes have been intensively investigated as active materials in these devices.⁽¹⁶³⁾ As a viable alternative LP-Cs offer all the benefits like large surface areas and tunable surface chemistry, but come with much lower costs.

Introduction – Mechanical sensors

Mechanical sensors are devices sensitive to mechanical environmental changes like displacement, movement, pressure, flow, acceleration etc. Typical measurement principles are based on the quantitative monitoring of changes of a physical parameter of a material upon deformation such as electric properties, resonance, density, etc.

Typical functional (semi)conductive materials for flexible electronics include metal or semiconductor nanowires or nanoparticles (e.g., silver, gold, metal oxides).^(164–167) Their nanoscale morphology and properties are decisive for their flexible performance and advantageous for their utilization in thin skin-like devices.⁽¹⁶⁸⁾ For the fabrication of reliable devices, methods such as chemical vapor deposition, photolithography, screen printing, PDMS transfer techniques, or transfer printing are commonly used.⁽¹⁶⁹⁾ In most cases, these nanomaterials are coupled with or processed into flexible and stretchable polymers such as PDMS matrices.^(170,171) For film thicknesses on the micrometer scale inner material shear forces typically cause cracking or delamination.⁽¹⁷²⁾

A great potential is attributed to organic electronic materials based on conductive polymers, such as poly(3,4-ethylenedioxythiophene) polystyrene sulfonate (PEDOT:PSS), polyaniline, or polyacetylene due to their easy processability, structural tunability, and light-weight.^(173–175) However, several drawbacks, such as poor environmental stability, poor repeatability, or low mechanical stability, arise with their utilization.⁽¹⁷⁶⁾ Great achievements in developing flexible electronic devices have been made with nanocarbons such as carbon nanotubes or graphene.^(177–180) These materials are generally well-suited for thin-film flexible electronic devices due to their intrinsically low dimensions and tunable electronic properties, which has been demonstrated in a plethora of studies.^(181,182) A broad overview about carbon-based materials

used in flexible electronics is covered in a recent book on “flexible carbon-based electronics”.⁽¹⁷⁶⁾ Among the greatest challenges for the production of flexible devices are long-term stability and large-scale production. In the course of the past decade, mechanical sensor devices based on LP-C have been developed.

State-of-the-art – Mechanical Sensors

In 2017 a concept of detecting sound waves with LC-PI films ($\lambda = 450$ nm) was reported.⁽¹²⁵⁾ Acoustic wave detection is usually realized with piezoelectric sensors. The LC-PI acts as a sensitive electrically resistive membrane and is able to detect vibrations in the frequency range between 100 and 40,000 Hz. It was shown, that the thickness of the membrane controls the frequency range.

In 2015 a concept of producing strips (2×30 mm) of LC-PI films ($\lambda = 10.6$ μm) and embedding them into elastic membranes such as PDMS or silicone was developed.⁽¹²⁴⁾ The LC-PI showed a high conductivity and stable electric conductivity towards stretching to up to 100% longitudinal strain.

Introduction – Chemical sensors

Chemical sensors are devices for the specific detection of **chemical species**, thus the mimicking of the gustatory or olfactory senses. Famous **examples** of synthetic chemical sensors are devices for the global and local monitoring of emission of toxic or greenhouse gases or the indoor air quality control towards hazardous volatile organic compounds (VOC). On the other hand, devices for the quantitative detection of biomarkers in body fluid analysis are used for medical diagnostics, like the monitoring of human vital parameters.⁽¹⁸³⁾

Modern, portable and wearable sensors become increasingly important for non-invasive medical diagnosis and physical performance optimization. Therefore, a high interest in the development of new inexpensive and sustainable materials for modern sensors exists.⁽¹⁸⁴⁾

Important **assets** of modern sensors are flexibility, portability, integratability, sensitivity, selectivity, accuracy, short response time, and reliability.^(185,186) As a matter of course, such devices should be available at low cost and be based on sustainable materials and manufacturing processes. An ideal sensor device fulfils all requirements but in reality each sensor device is designed to fulfil the requirements for a specific application.

As mentioned above, important classes of analytes are environmental and industrial gases such as CO₂, CO, NO_x, SO_x etc, as well as biomolecules and biomarkers, such as glucose, acetone,

urea etc. For different applications, chemical sensors rely on different **operation principles** based on signals, such as electronic/electrochemical measurement, spectroscopic, or chemical reactions. Typical electronic sensor architectures, distinguished by their operation mode, are chemiresistors, chemical capacitors, or electrochemical sensors, field-effect transistors, or chemical diodes.⁽¹⁸⁷⁾ For widespread untrained application the most promising, because simple, are electronic sensors and chemiresistors, in particular. Here, interaction of an analyte with an active material leads to a change of the **electronic properties** of the material, which is read out and translated to a quantitative value (**Figure 28A**). Examples are liquid/solid or gas/solid adsorption of analytes to the surface and a subsequent change in either conductivity, capacitance, work function, or permittivity (**Figure 28B**).

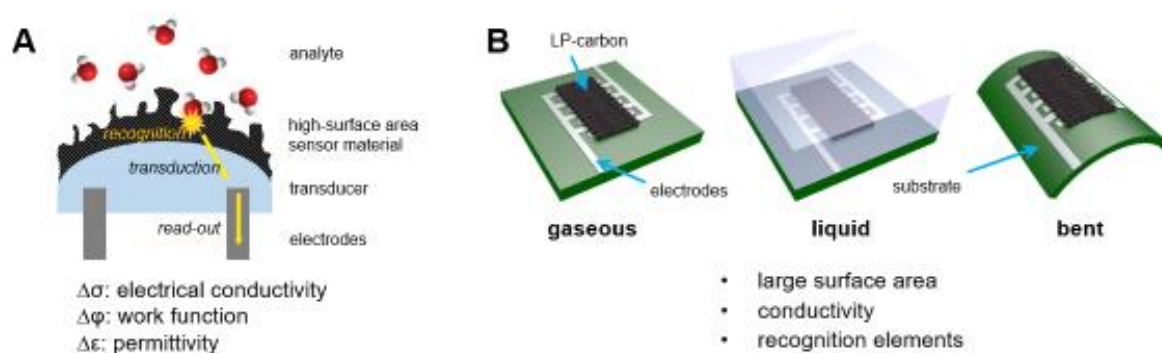


Figure 28. A) Working principle of a chemical sensor; B) Illustration of chemical sensors used for gaseous or liquid detection or on flexible substrates.

Importantly, the field of flexible electronic sensor devices experienced a notable acceleration due to the rapid development of artificial intelligence (AI) and machine learning algorithms. These allow for the efficient training and utilization of small scale **sensor array technologies** that are the basis for the realization of so-called **electronic noses** (**Figure 29**).^(188,189) First mobile commercial products based on sophisticated nanotechnology are currently in the final phase of development.

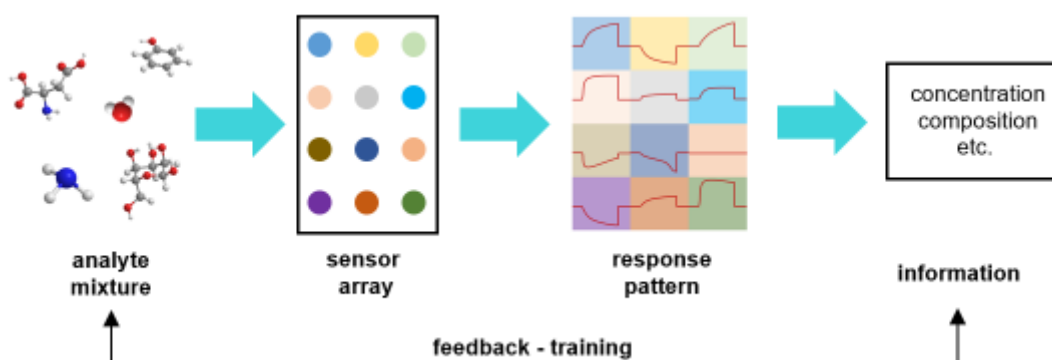


Figure 29. Schematic illustration of the working principle of sensor arrays: Analyte mixtures interact with individual sensors in the array and their responses give a response pattern. The read-out is trained with known data sets.

Common commercial materials used for the detection of chemical species are mostly based on **metal semiconductors**, especially metal oxides. Operation temperatures of 200 – 400 °C make these materials highly sensitive indeed but their devices energy-consuming and expensive. Alternative materials, such as carbon nanotubes and nanoparticle composites are promising for room-temperature detection of volatile analytes, however, those typically come along with high production costs.⁽¹⁹⁰⁾

New functional materials, such as **hierarchical porous carbons** constitute interesting alternatives for the use in everyday-use or disposable sensor arrays.^(191–193) As outlined above, CLaP is a well suited method to produce electronically conductive porous carbon films and provide the possibility to incorporate functional sites for the selective interaction with analytes.⁽¹⁹⁴⁾ This process avoids the inherent difficulties of processing carbonized materials into flexible conductive films and provides a scalable method for the production of stable electronic sensors. In particular the possibility for tuning the properties of LP-C by simple modification of the precursor formulas has demonstrated a significant enhancement of the sensitivity of LP-C.⁽¹⁹⁵⁾ A common strategy to tune the electronic properties of carbon materials is the integration of electronic heterojunctions, e.g. Schottky barriers or p-n-junctions and thereby modulate the charge-carrier density to achieve higher response upon electronic/chemical interaction with analytes.⁽¹⁹⁶⁾ These aspects make this process generally interesting for commercial applications.

Basics

- semi-conductors
- Schottky-junctions
- p-n-junctions
- charge-carrier properties

State-of-the-art – Chemical Sensors

A 1030 nm femtosecond laser system was used to produce laser-carbonized interdigitated electrodes in a PI film.⁽¹³¹⁾ Each of the electrodes (sensor units) were post-functionalized with

either Au-nanoparticles, rGO, or polyaniline (PANI) and the impedance of each of the electrodes was analyzed in the presence of different analytes, namely salt (NaCl), sugar (sucrose), or vinegar. Thereby a cross-sensitive sensor array for the selective detection of different flavors was fabricated and read out by statistical principal component analysis (PCA).

The principle of capacitive sensing with interdigitated LC-PI based on the electroosmotic effect was also utilized for the selective sensing of Bisphenol A.⁽¹³⁶⁾ To achieve a higher surface polarity the laser-carbonized electrodes were plasma treated. Subsequently, aptamer-receptors were immobilized on the LC-PI electrodes. In this study, laser-carbonization was accomplished with a dual laser irradiation using a 532 nm CW and a 1030 nm femtosecond laser.

Another example demonstrates the quantitative detection of gaseous ammonia in a simple resistive device architecture based on LC-PI ($\lambda = 10.6 \mu\text{m}$).⁽¹³⁷⁾ The sensors response was $\Delta R/R_0 = 3.5\%$ at a concentration of 75 ppm ammonia. The response and recovery times were 214 and 222 s, respectively, with a sensitivity of $0.087 \text{ \%} \cdot \text{ppm}^{-1}$.

In a similar fashion gas sensors were fabricated for distinguishing gases based on their thermal conductivities.⁽¹³³⁾ To this end ultrafine filaments of LC-PI in $60 \mu\text{m}$ wide channels produced and their resistance was measured in different gaseous environments, namely CO_2 , argon, air, or helium. A voltage applied across the channels causes Joule heating which depends on the thermal conductivity of the gases. For example, the sensors detected 3600 ppm Ar in He and the response times were as low as 8 s.

Furthermore, LC-PI served as an electrocatalyst support for Pd nanoparticles for the selective amperometric detection of methane gas.⁽¹⁹⁷⁾ The Pd nanoparticles serve as electrocatalysts for the electro-oxidation of methane. A porous quasi-solid state electrolyte, namely ionic liquid/polyvinylidene fluoride provided a permeable membrane to support the diffusion of methane to the electrode. The cell was operated at 0.6 V. With this architecture, a sensitivity of $1.1 \mu\text{A/ppm}$ towards methane with a response time of 40 s was achieved.

Direct gas sensing with LCMs by detecting adsorption events has not been described (to the best of current knowledge).

Challenges

A general difficulty is the design of specific active sites in a sensor material that show a sensitive response and is broadly applicable. Challenges for the application of LP-C in sensor architectures are primarily the **tuning of the surface properties**. Thereby, the chemical adsorption characteristics can be modified. **Functional groups** are responsible for any kind of

interaction between analytes and the active material. Therefore, it is of pronounced importance to identify **new precursor materials** for the selective integration of functional groups. Mechanistic carbonization studies are necessary to create a fundamental understanding of the sensor detection principles, i.e. the analyte-material interactions and the electronic transduction. This entails a combination of mechanistic studies with systematic tuning of the chemical composition and surface chemistry of LP-Cs.

Importantly, the sensing principle based on adsorption and desorption typically proceeds at low response times. Mechanisms for improving the **response times** need to be identified.

As outlined above, the major features of chemical as well as mechanical sensors are flexibility, portability, integratability, sensitivity, selectivity, accuracy, short response time, and reliability. With regard to all these assets, the engineering aspect is to improve the **mechanical properties** towards high flexibility and stretchability as well as optimized substrate interactions.

Summary – Challenges for LP-Cs in electronic interface applications

- control the porosity and surface area
- control the mechanical properties
- control the surface chemistry
- control the integration of active sites
- control the charge-carrier properties

Results Part

Scope

With regard to the challenges described in the previous section, the aim of this work is the identification of universal synthetic strategies to modify LP-Cs for the application in flexible electronic devices. As outlined in the General Part, molecular precursors are generally difficult to be carbonized with a laser beam. Also, the lessons learned from the experience in conventional carbonization reactions and strategies to engineering the properties of carbons (The Complexity of Carbonization) are only partly transferrable to laser-carbonization. The fundamental knowledge from laser-carbonization of polymeric precursor materials, mainly PI and GO, provide a basis for selecting the approaches in our studies. However, as described in the literature review (Laser-Carbonization – Context) clear distinctions between the starting materials, exemplarily shown for GO and PI, in terms of formation mechanism and product properties have to be made.

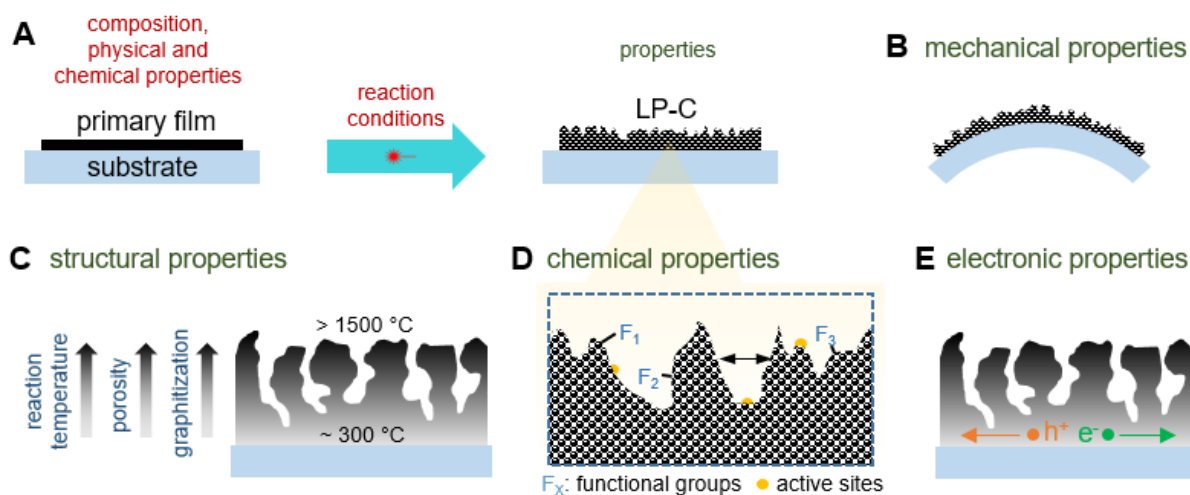


Figure 30. Schematic illustration of the properties of LP-C (mechanical (B), structural (C), chemical (D), electronic (E)) in dependence of the composition and properties of the primary film, the substrate, and the reaction conditions (A).

Generally, laser-carbonization affords carbon films with a hierarchical porous morphology as depicted in **Figure 30C-E**. Depending on the composition and physical and chemical properties of the primary film as well as the reaction conditions different **structural properties**, like porosity, surface area, crystallinity, and morphology are obtained. The resulting **mechanical properties** are dependent on the degree of carbonization and the structural properties, but also on the substrate properties (**Figure 30B**). In fact, the LP-C / substrate interactions are a critical

component of the overall mechanical performance. A general observation is the formation of a **structural and chemical gradient** across the film (**Figure 30C**) due to the effective reaction temperature gradient induced by the unidirectional energy impact of the laser beam. The **chemical composition** and the chemical surface properties, like functional groups, active sites, and composite structures are mainly dependent on the type of precursor and additional reactants (**Figure 30D**). The principle **electronic structure** of the LP-C, i.e. conductivity, charge carrier properties, and electronic band-gap depends on mainly the precursors and the reaction conditions. The latter are also decisive for the **degree of carbonization** or graphitization, which influences the conductivity (**Figure 30E**). Moreover, additives or reactants are used to implement heterostructures (nanoparticles) into the LP-C, by which electronic heterojunctions are incorporated.

Designing properties:

- + chemical (surface groups, active sites, composites)
 - *precursors, reactants*
- + structure (morphology, surface area, porosity)
 - *precursors, reaction conditions*
- + electronic (conductivity, hetero junctions)
 - *precursors, reaction conditions, additives*
- + mechanical (flexibility)
 - *precursors, reaction conditions, additives, substrate*
- + substrate interaction
 - *precursors, substrate, additives, reactants*

We strive to identify new strategies for the application and modification of LCMs and to derive universal laws for the rational design of new functional LP-Cs. With respect to the broad fundamental knowledge on engineering of specific properties of conventionally carbonized materials, we make an effort for its transfer to laser-carbonized materials. To serve a wide field of applications, especially in future electronic devices, several challenges regarding the tuning of the materials properties are addressed.

In the herein introduced studies, we aimed on investigating methods to influence the above mentioned properties. In the past three years, we focused on the following aspects:

- new precursor materials
- precursor preparation
- new porogens and structure-directing agents (SDA)
- laser-parameters
- tuning the electronic properties
- mechanistic studies

In the following section (Laser-carbonization – Approach) the development of the individual process components in our laser-carbonization approach will be outlined. In the section (Laser-carbonization – Implementation) the results of our completed studies will be summarized and each of the aforementioned aspects – fundamental properties and applications – will be addressed.

Laser-carbonization – Approach

Overview

An integrated **two-step approach** to prepare functionalized LP-Cs was developed (**Figure 31**). The central element of the **first step** is the preparation of the primary inks which mainly consist of carbonizable precursors, the so-called carbon network-forming agents (CNFA), and additional components such as film-forming agents (FFA), porogens, additives, or reactants. The CNFAs are prepared by pre-carbonization of organic precursors, typically in a temperature regime between 300 and 400 °C under anaerobic conditions in a tube furnace (**Figure 31A**). For some precursors, like lignosulfonates, the pre-carbonization step is unnecessary. The CNFAs are dispersed in a solvent to produce an ink or a dispersion suitable for the selected film-casting technique. A film-forming agent (FFA) is typically added to the ink to facilitate a homogeneous film-formation or to improve the contact with the substrate. Additives, reactants, or porogens may be added either directly to the ink, given their solubility or dispersibility in the solvent, or to the precursor prior to the pre-carbonization step (**Figure 31A**).

Basics

- film-casting techniques

In the **second step**, these inks are cast as primary films onto a substrate, by film-casting techniques like doctor-blading, spray coating, dip-coating, or drop-casting (**Figure 31B**). A laser beam is then used to carbonize the primary films in the desired patterns. Subsequently, the parts of the primary film not exposed to the laser beam are removed by rinsing with a solvent (H₂O). As outlined in **Figure 30**, the properties of the LP-Cs (composition, structure, electronic properties, mechanical properties) are controlled by the characteristics of the primary film (compounds, composition, additives) and the reaction conditions (laser settings, environment).

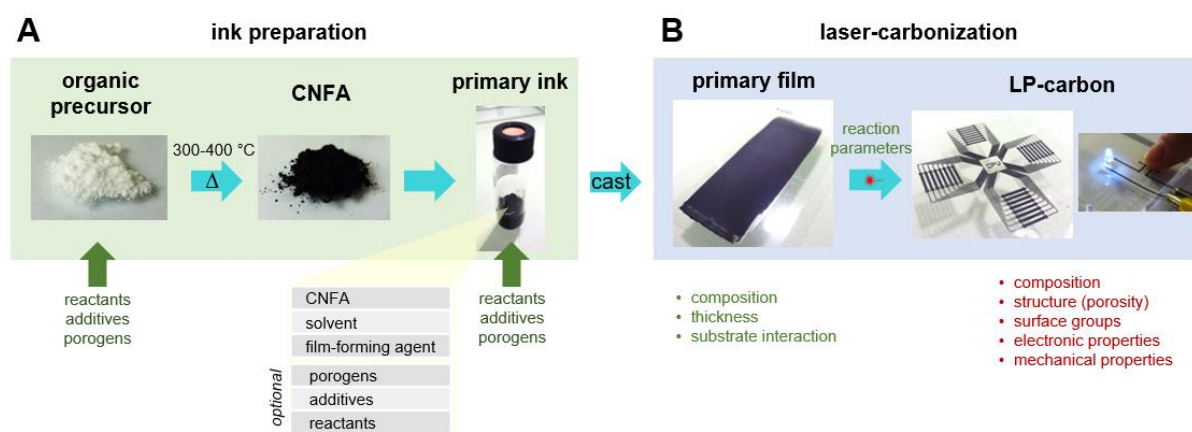


Figure 31. Schematic illustration of the integrated two-step approach to prepare LP-C. Organic precursors are pre-carbonized to form CNFAs. The CNFAs are processed into primary inks together with a solvent a film-forming agent and optionally porogens and additives. Reactants are added either before pre-carbonization or into the “carbon ink” before film-casting. Films are cast from the inks and the solvent is removed subsequently. A laser beam is used to carbonize the film in the desired patterns.

Based on our discovery in 2018⁽¹⁹⁸⁾, we established a standard ink recipe that is composed of a CNFA, a film-forming agent (FFA), and a solvent. In the past three years we systematically investigated the influence of several ink components on the properties of the LP-Cs. An overview of the components used in the presented studies is given in **Table 3** and their role is explained in the following paragraphs.

Table 3. Overview on the components of the inks used in the different studies.

reference	CNFA	solv.	FFA	porogen	reactants	additive	substrate	ref.
fl. electronics	CA/U(300)	EtGly	PVP				PET Si-wafer Al	S1
microstructure	Glu(300) Cyt(300) CA/U(300)	EtGly					PET Si-wafer	S3
humidity sen.	CA/U(300)	EtGly	PVP				PET	S4
VOC sensors	CA/U(300)		PVP		(NH ₄) ₆ Mo ₇ O ₂₄		PET	S5
VOC sensors	CA/U(300)	EtGly	PVP	Zn(NO ₃) ₂ ZnO			PET	S6
mech. sensor	CA/U(300)	EtGly	PVP	NaI			PET	S7
CO ₂ sensor	Ade(380)	EtGly	PVP	Glu(300)			PET	S8
ORR catalyst	CA/U(300) CA/U_Fe(300)	EtGly	PVP	NaI	Fe(NO ₃) ₃		PET Si-wafer	S9
mEDLC	CA/U(300)	NMP					stl. steel	S10
Patching	GO CA/U(300)	H ₂ O					stl. steel	S11
mEDLC	PAN					CNT	PCB board	S12
unpublished	CA/U(300)	CHCl ₃			Pt(acac) ₂		PET	
unpublished	Na-LigS	EtGly					diverse	

Carbon Network-Forming Agents

The CNFA is the central component of the primary ink. The principle chemical characteristics of the final LP-C, like surface functional groups and internal bonding are defined by the characteristics of the CNFA. As mentioned above, most molecular precursors evaporate upon rapid heating in a laser beam. In our initial study, we found that evaporation can be prevented by thermal **pre-carbonization** of the molecular starting materials.⁽¹⁹⁸⁾ In most cases, this is an essential step for the laser-induced formation of a conductive carbon network. In a similar manner, the necessity of this step was described around the same time in a study from Chyan et al.⁽¹⁴³⁾ Several natural compounds were only effectively carbonized in a laser beam after pre-heating with a torch to initiate a pre-carbonization. The thus formed amorphous carbon was then efficiently carbonized in the laser beam.

Pre-carbonization is a process comparable to torrefaction, i.e. mild pyrolysis of biomass at 200-320°C. By pre-carbonization, three positive effects are evoked: 1) water is removed from the precursors which would disturb the enthalpic balance of laser-carbonization reaction, 2) the hygroscopy of the precursors is reduced, making the pre-carbonized products easier to handle in ambient environments, 4) the increased molecular weight during cross-linking of the molecular precursors prevents full evaporation upon laser impact.⁽²⁾

In the comparably low temperature regime in which pre-carbonization takes place, several temperature-induced reactions (polymerizations, dehydrations, etc) occur simultaneously or in cascades. Typical reactions of biomass observed in the low temperature range are Maillard reactions, i.e. the condensation of amino groups and reducing sugars, an effect that is observed for most organic substances upon heating in this temperature regime.⁽¹⁹⁹⁾ These reactions are also referred to as non-enzymatic browning reactions. As a consequence of these reactions, the educts grow into micron-sized particles and become insoluble. To guarantee a fine dispersion in the ink and a homogeneous casting of the precursor films, the CNFA is grinded in a ball mill prior to dispersing in the ink. In our studies, we tested the following molecular precursors as CNFAs: a combination of citric acid and urea (CA/U(300)), adenine (ade380), cytosine (cyt300), glucose (glu(300)), and sodium lignosulfonate. Polymeric precursors include: polyacrylonitrile (PAN) and graphene oxide (GO). The number in brackets indicates the pre-carbonization temperature (**Table 3**).

Solvents

The film-formation of the inks largely depends on the properties of the solvent such as boiling point, vapor pressure, polarity, viscosity, and surface tension. A list with relevant properties of selected solvents is given in **Table 4**. Our standard ink recipe was optimized for the application of primary films by doctor blade coating on different substrates. This technique requires the use of solvents/inks with high viscosity.

On the one hand, ethylene glycol (EtGly) as a solvent was chosen for its high viscosity. On the other hand, its inherent polarity provides good dispersibility of most CNFAs and high solubility for additives and reactants. Another advantage of EtGly is its low vapor pressure to avoid solvent evaporation during the ink preparation. To obtain homogenous inks, the mixtures were stirred in closed vials for 24 h prior to use.

Notably, other casting techniques, like spray coating, require the use of highly volatile solvents. For example, suitable reactants for the incorporation of Pt nanoparticles are not soluble in polar solvents like EtGly. The Pt precursor platinum(II) acetylacetonate (Pt(acac)) is soluble in non-polar solvents such as methylene chloride (CH_2Cl_2). In this case, a dispersion of the CNFA (CA/U(300)) was prepared in a solution of Pt(acac) in CH_2Cl_2 , which was then applied onto the substrate by spray casting.

Table 4. Overview on the relevant properties of selected solvents for film-casting.

Solvent	boiling point (°C)	vapor pressure @ 20 °C (hPa)	dipole moment (D)	viscosity (mPa·s)	surface tension @ 20 °C in (mN·m ⁻¹)
1-butanol	118	6	1.7	2.59	25
2-butanone	80	105	2.8	0.41	24.6
2-propanol	82	44	1.66	2.07	23
acetic acid	118	15	1.68	1.12	27
acetone	56	240	2.85	0.3	25.2
acetonitrile	82	97	3.5	0.34	29
chlorobenzene	132	12	1.54	0.75	33
chloroform	61	210	1	0.54	27.5
cyclohexane	81	104	0	0.89	24.9
dimethylformamide (DMF)	153	4	3.8	0.8	37.1
dimethylsulfoxide (DMSO)	189	0.61	3.9	2	44
ethanol	79	59	1.7	1.08	22.1
ethyl acetate	77	97	1.78	0.43	24
ethylene glycol (EtGly)	197	0.092	2.3	16.1	47.7
hexane	69	160	0	0.29	18
methanol	65	128	1.6	0.54	22.7
methylene chloride	40	475	1.6	0.42	26.5
t-butyl alcohol	82	41	1.7	3.35	25
tetrahydrofuran(THF)	66	200	1.63	0.46	26.4
toluene	111	29	0.36	0.55	28.4
water	100	17.5	1.85	0.89	72.8
N-Methyl-2-pyrrolidone (NMP)	203	0	4.09	1.67	40.7

N-Methyl-2-pyrrolidone (NMP) has also been used as a processing solvent in the primary inks. In comparison to EtGly the viscosity is rather unfavorable. Additionally, NMP is reactive at higher temperatures. During the solvent evaporation step, the temperatures must not exceed 120 °C.

Film-forming Agents

In our standard recipe a film-forming agent (FFA) was added for two reasons: The energy balance and the beam-material interactions strongly depend on the quality and homogeneity of the primary films (see Laser-Processing of Materials). Topological irregularities increase the surface scattering and random reflections of the laser beam. The addition of a FFA ensures a high degree of homogeneity of the films and thus reproducible conditions. The selected FFA, polyvinylpyrrolidone (PVP) exhibits high solubility in EtGly and water. The presence of water-soluble PVP in the primary films helps in removing the unexposed parts of the film from the substrate after laser-carbonization.

Reactants, Additives, Porogens

In order to functionalize LP-Cs or tune their properties, additives, porogens, or reactants are added. As indicated in **Figure 31**, two principle routes for the addition of reactants exist: 1) addition of the reactants/additives/porogens to the organic precursors prior to pre-carbonization and 2) addition of the reactants/additives/porogens to the primary ink (**Figure 32**).

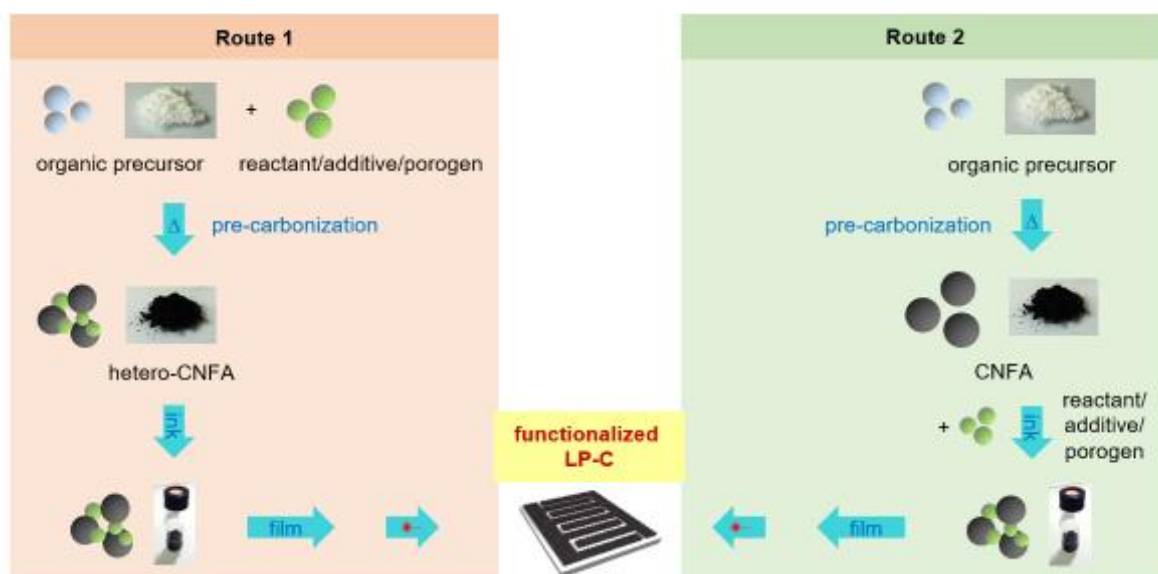


Figure 32. Schematic illustration of the ink preparation. 1) The additive, reactant, or porogen is added to the precursor prior to pre-carbonization; 2) The additive, reactant, or porogen is directly added to the primary ink.

The surface properties and porosity of the LP-C are influenced by the presence of **porogens** in the CNFA during laser-carbonization. Due to the extremely fast reaction occurring on the order of milliseconds and photo-induced effects, many conventional templating strategies are not applicable. Soft-templating is generally difficult for the little control over the exact temperature during the reaction. Hard-templates in the form of nanoparticles or salt-templating are better suitable.

In our studies, we investigated two types of porogens: alkali metal halide salts and zinc oxide nanoparticles. Alkali metal halide (AMH) salts oxidize at high temperatures to their respective oxides. AM-oxides are principally highly reactive. In the presence of H₂O they decompose to the respective hydroxides. In the presence of carbon at high temperatures they undergo a carbothermic reduction producing their reduced metal states while the carbon acts as a reducing agent (see Carbothermic Reduction).

Sodium-halides are particularly well suited as porogenic agents for laser-carbonization. During laser-carbonization temperatures >1500 °C are induced. The melting point of the sodium-halide salts are between 661 and 802 °C (**Table 5**). However, in this temperature regime oxidation and carbothermic reactions occur. The reactions are most likely faster than the formation of liquid phases above the melting point. All high-temperature reaction products of the Na-halides, i.e. Na₂O and Na, exhibit boiling points lower than the surface temperature of the LP-Cs. Therefore, Na-halides perfectly fulfil the role of a porogen.

Table 5. Overview on some properties of metal salts suitable for the use as porogenic agents.

alkali metal halide salt	melting point °C	solubility in H ₂ O (20 °C) g·L ⁻¹	alkali metal halide oxide	boiling point °C	alkali metal halide	boiling point °C
NaCl	802	358	Na ₂ O	1275	Na	890
NaBr	747	905				
NaI	661	1793				
KCl	771	347	K ₂ O		K	759
KBr	734	650				
KI	681	1430				
LiCl	610	832	Li ₂ O	2600	Li	1330
LiBr	550	1450				
LiI	469	1650				
ZnCl ₂	325	4300	ZnO	1974	Zn	907
ZnBr ₂	402	4470				
ZnI ₂	450	4500				
Zn(NO ₃) ₂	< 50	1843				

Another property of AMHs, which makes them beneficial for their porogenic activity in laser-carbonization reactions is their intrinsic optical transparency ranging from the visible to the

mid-infrared. Only a little fraction of the incident laser energy is absorbed by the AMH. When added to the ink, these salts are dissolved and homogeneously distributed in the primary ink. Upon drying, nano- or micro crystals of these AMH are formed. When irradiated with laser light, the crystals transmit the laser energy to the CNFA surrounding the crystals. Therefore, deeper penetration depth of the laser beam is achieved.

Similar behavior is observed for zinc salts. The ZnO hard-templating effect based on carbothermic reduction of ZnO is well understood and is commonly used in thermally induced carbonization reactions (see Carbothermic Reduction).⁽⁵³⁾ In laser-carbonization, the formation of ZnO used for the hard-templating effect occurs *in situ* within the timeframe of the laser-induced reaction: The homogeneously distributed zinc salt in the primary films forms ZnO nanoparticles upon elevating the temperature. When the laser-induced temperature reaches $\sim 670^\circ\text{C}$ the ZnO is reduced to Zn by carbothermal reduction, during which the carbon is oxidized to gaseous CO(g). The remaining carbon is rearranged and recrystallized and thus forms highly graphitized domains. At temperatures above the boiling point of zinc (907°C), the liquid zinc evaporates.

A special case of porogen is glucose, which increases the surface of the LP-(N)C by **foaming** rather than acting as a regular porogen. Glucose is a well-known precursor for carbonized materials that generates high surfaces by foaming. The foaming, i.e. formation of bubbles, is commonly observed in thermally treated carbohydrates.⁽²⁰⁰⁾ When using glucose pre-carbonized at 300°C (glu300) as a CNFA in laser-patterning, a carbon foam is obtained. Bubbles in a size range between tens of nanometers up to several microns are observed.

If the additive forms useful reaction products that remain in the LP-C, we refer to them as **reactants**. The reactants are of either molecular or particulate nature and upon their addition a composite LP-C is formed. For example, by addition of metal salts or complexes (e.g. $\text{Fe}(\text{NO}_3)_3$, $\text{Pt}(\text{acac})_2$, or $(\text{NH}_4)_6\text{Mo}_7\text{O}_{24}$), nanoparticles are formed *in situ* and are incorporated into the LP-C network. Depending on the reaction conditions and the thermal reactivity of the metal salts, the respective oxide or carbide nanoparticles are formed. These nanoparticles exhibit active sites for electrochemical reactions that are utilized in electrocatalytic reactions or pseudocapacitive energy storage or are influence the intrinsic electronic structure of the LP-C.⁽²⁰¹⁾ Due to the chemical and structural gradient obtained in the LP-C (**Figure 30C**), the formed nanoparticles are heterogeneous in terms of structure and size. For example, different oxide phases are obtained in the different temperature regions of the LP-C film. Moreover, the

formation and incorporation of nanoparticulate species influences the formation mechanism of the LP-C.

Additives are compounds that do not react during laser-carbonization but enhance or alter the physical or chemical properties of the LP-C. For example, the presence of carbon nanotubes greatly enhances the absorption of the laser energy and supports the dissipation of the thermal energy into the primary film and, thereby, support the reaction of the CNFA. Moreover, the incorporation of CNTs enhances the mechanical stability of LP-C.

Substrates

Depending on the targeted application, the choice of the **substrate** is critical. The penetration depth of the laser energy is limited by the absorptivity (extinction coefficients), the heat conductivity, and the heat capacity of the primary film. The remaining thermal energy arriving at the substrate is either absorbed by, reflected from or dissipated through the substrate (see Beam–Material Interactions). Similar to the primary film the fate of the thermal energy is quantified by absorptivity, heat conductivity, and heat capacity of the substrate. The absorbed thermal energy is either dissipated across the substrate or leads to reactions of the substrate itself, such as physical melting, evaporation, or reactions (carbonization). In reverse, the heat dissipation within the primary film also depends on the same physical properties of the substrate, i.e. more heat is generated within the primary film when reflective substrates are used. On the other hand, thermally conductive substrates may absorb the thermal energy and dissipate it. Therefore, the intrinsic thermal properties of the substrate influence the carbonization and the properties of the primary film.

The primary film formation and interaction (bonding) with the substrate also depend on the surface tension (hydrophilicity) of the substrate. Decisive is the interfacial tension, between ink and substrate. Substrates may be grouped into different categories according to their properties: electronically conductive, mechanically flexible or stretchable. In our studies, we focused on the substrates listed in **Table 6**.

Table 6. Overview on some properties of the substrates used.⁽²⁰²⁾ The values for absorptivity are taken from a comparative study.⁽⁹⁴⁾

material	thermal conductivity $\text{W}\cdot(\text{m}\cdot\text{K})^{-1}$	heat capacity $\text{J}\cdot(\text{g}\cdot\text{K})^{-1}$	absorptivity @ 10.6 μm %	melting point $^{\circ}\text{C}$	boiling point $^{\circ}\text{C}$	electrically conductive
Al	237	0.90	~3 (reflective)	660		✓
PET	0.24	1.03	high	264	~350	
graphite	~400	0.70		3600		✓
Si-wafer	149	0.71	reflective	1410	3260	
glass	0.8	0.75	high	~1500	~2200	
Cu	401	0.39	~2 (reflective)	1084		✓
StSt	16	0.49	~11 (reflective)	1510		✓
PI (Kapton)	0.75	1.09	~92	-	~520	

Laser-carbonization – Implementation

Taking the abovementioned aspects into concert, the synthesis of LP-C can be considered a complex interplay of several variables. In a series of studies, we investigated the influence of these parameters on the structural, chemical, electronic, and mechanical properties of LP-Cs. To improve and optimize the performance as active electrodes in electrochemical double-layer capacitors, electrocatalytic oxygen-reduction reactions, and, especially, resistive sensors.

Principles of Laser-Carbonization

S1. Laser-Induced Carbonization of Natural Organic Precursors for Flexible Electronics ([link to article](#))

S. Delacroix, H. Wang, T. Heil, V. Strauss, *Adv. Electron. Mater.* **2020**, 6, 2000463.

Our fundamental universal approach for laser-carbonization, i.e. the primary ink formulation and laser-patterning on flexible substrates was developed based on the standard CNFA – CA/U(300). The CNFA was chemically and structurally characterized. A simple recipe for the ink is then described for the creation of highly reproducible LP-C structures on different substrates. Homogeneous ~20 μm thick primary films were cast on different substrates and characterized before and after laser-carbonization. The carbon content on top of the final films is 97% and is of turbostratic graphitic nature. The penetration depth was first analyzed by micro-tomography measurements. As reproducible laser-induced reactions depend on precise reaction conditions, the influence of material properties, film thickness, and laser fluence were thoroughly analyzed. Films on three different substrates, namely aluminum sheets, silicon wafers, and polyethylene terephthalate (PET) are characterized by electrical impedance measurements. Electrical conductivities of up to $5.21 \text{ S}\cdot\text{cm}^{-1}$ and maximum current densities of $44 \text{ A}\cdot\text{cm}^{-2}$ are achieved, which proved applicable as fine carbon circuits on PET as a flexible

substrate. This study laid the foundations for the investigation of synthetic procedures to producing conductive circuit elements based on carbon.

S2. Carbon nanodots revised: the thermal citric acid/urea reaction ([link to article](#))

V. Strauss, H. Wang, S. Delacroix, M. Ledendecker, P. Wessig *Chem. Sci.* **2020**, *11*, 8256–8266.

The standard CNFA used in our studies – (CA/U(300)) – is made from a mixture of citric acid (CA) and urea (U). The products of the thermal reaction of CA and U contain soluble reaction intermediates with interesting fluorescent properties, commonly referred to as carbon nanodots (CNDs), as well as insoluble carbonaceous products (char). The insoluble product of the thermal reaction was the first CNFA used for laser-carbonization.⁽¹⁹⁸⁾

This study aimed for the investigation of the thermal reaction mechanism of CA and U in a temperature range of 100-300 °C. Autoclave–microwave reactions in the melt were thoroughly investigated as a function of the reaction temperature and the reaction products were subsequently separated by a series of solvent extractions and column chromatography. The insoluble reaction product (CA/U(300)) forms upon condensation of the soluble reaction intermediates namely HPPT (4-hydroxy-1*H*-pyrrolo[3,4-*c*]pyridine-1,3,6(2*H*,5*H*)-trione) and oligomeric ureas. These two components form strong hydrogen-bond networks which eventually react to form solid, semi-crystalline particles with a size of ~7 nm and an elemental composition of 46% C, 22% N, and 29% O.

S3. Laser-carbonization: Peering into the formation of micro-thermally produced (N-doped)carbons ([link to article](#))

H. Wang, S. Delacroix, O. Osswald, M. Anderson, T. Heil, E. Lepre, N. Lopez-Salas, R. B. Kaner, B. Smarsly, V. Strauss, *Carbon* **2021**, *176*, 500–510.

In this study, we identified and characterized additional precursors for the use in laser-carbonization, namely cytosine and glucose, pre-carbonized at 300 °C to the respective CNFAs: cyt(300) and glu(300). Together with CA/U(300), this set of CNFAs enabled a comparative study to learn about the interplay between the laser parameters and the CNFAs. We conducted an in-depth morphological and compositional study to understand how molecular precursors must be prepared for the high-speed laser-induced carbonization reactions. The resulting LP-Cs or LP-NCs are different from their conventionally pyrolyzed reference products (pyrolyzed at 950 °C) mostly in terms of morphology and surface structure. A generally porous structure

and a carbonization gradient induced by the top-to-bottom energy input were identified as the most remarkable features of LP-Cs or LP-NCs, in general. Additionally, the microstructure, the elemental composition and the resulting electronic properties differ to their respective conventionally pyrolyzed reference products as demonstrated by X-ray photoelectron spectroscopy (XPS) and wide-angle X-ray scattering (WAXS) analysis.

Moreover, we demonstrated that each precursor shows characteristic reaction response to the laser-parameters like incident power and scanning speed by testing a variety of settings and correlating them to the obtained electric conductivity of the LP-C/LP-NC films. These response patterns are plotted as 2D-maps and clearly show an individual dependence of the scanning speed, which indicates a kinetic reaction mechanism.

Laser-Patterned Carbon in Sensing

S4. Using Carbon Laser Patterning to Produce Flexible, Metal-Free Humidity Sensors ([link](#) to article)

S. Delacroix, A. Zieleniewska, A. J. Ferguson, J. L. Blackburn, S. Ronneberger, F. F. Loeffler, V. Strauss, *ACS Appl. Electron. Mater.* **2020**, *2*, 4146–4154.

The standard procedure, based on CA/U(300) as a CNFA, was utilized to fabricate a relative humidity sensor and investigate the fundamental electronic properties of LP-C. First information on the electronic charge-carrier properties were obtained by Hall measurements, which confirmed an intrinsic p-type semiconducting behavior. The resistance of defined porous LP-C films is sensitive to atmospheric variations, namely, temperature and relative humidity ($\approx 5 \Omega \cdot \%$). Under dry atmosphere, the LP-C film act as a thermometer with a linear relationship between temperature and relative variation of resistance ($0.07\% \cdot \text{K}^{-1}$). The change in sensor resistance at different relative humidities and temperatures, studied by electrical impedance measurements, yielded a kinetic transitory regime of water desorption from the carbonaceous surface. The equilibrium constants of water sorption K_{ads} was determined, and the standard enthalpy of adsorption of water on the sensor surface was estimated to $\Delta_{\text{ads}}H^\circ = -42.6 \text{ kJ} \cdot \text{mol}^{-1}$.

S5. In Situ Synthesis of Molybdenum Carbide Nanoparticles Incorporated into Laser-Patterned Nitrogen-Doped Carbon for Room Temperature VOC Sensing ([link](#) to article)

H. Wang, S. Delacroix, A. Zieleniewska, J. Hou, N. V. Tarakina, D. Cruz, I. Lauemann, A. J. Ferguson, J. L. Blackburn, V. Strauss, *Adv. Funct. Mater.* **2021**, 2104061.

The insights gained from the previous study prompted for the selective modification of the structural and electronic properties of LP-C to enhance its applicability for sophisticated resistive gas-sensing applications. To this end, a porogen, namely sodium iodide (NaI) was employed to increase the specific surface areas of the LP-C. An increase in electronic conductivity and surface area corroborate a deeper penetration of the laser-beam into the film in the presence of NaI. Furthermore, the LP-C was impregnated with metallic MoC_{1-x} (<10 nm) nanoparticles by adding ammonium heptamolybdate ($(\text{NH}_4)_6\text{Mo}_7\text{O}_{24}$) as a reactant to the primary ink (route 2, see Laser-carbonization – Approach). Thereby, doping-sensitive nano-grain boundaries, i.e. Schottky junctions, between the p-type LP-C and metallic MoC_{1-x} nanoparticles lead to an improvement of the sensing response of $\Delta R/R_0 = -3.7\%$ or -0.8% for 1250 ppm acetone or 900 ppm toluene at room temperature, respectively. The positive effect of the nano-Schottky junctions was confirmed by a significant decrease of the charge-carrier densities in the conductive LP-C films determined by Hall-measurements. These response values are competitive with other carbon-based sensor materials.

S6. Laser-Patterned Porous Carbon/ZnO Nanostructure Composites for Selective Room-Temperature Sensing of Volatile Organic Compounds ([link to article](#))

H. Wang, P. Jiménez-Calvo, M. Hepp, M. Isaacs, I. Below-Lutz, B. Butz, V. Strauss, *ACS Appl. Nano Mater.* **2023**, 6, 2, 966–975.

To prepare LP-Cs for the selective detection of VOCs, the surface properties were modified. CA/U(300)-based primary films were converted by CLaP in the presence of different concentrations of $\text{Zn}(\text{NO}_3)_2$. The impact of $\text{Zn}(\text{NO}_3)_2$ on the fundamental properties such as electrical conductivity and surface area were determined. The highest specific surface area obtained was $\sim 700 \text{ m}^2 \text{ g}^{-1}$. Subsequently, the resistive response upon exposure of acetone as a polar analyte and toluene a non-polar analyte was evaluated for a series of samples. The best performing LP-C sensors were characterized by transmission/scanning electron microscopy and X-ray photoelectron/energy-dispersive X-ray/Raman spectroscopies. Cross-sectional HRTEM analysis reveals the presence of ZnO particles embedded in the lower layer of the film with a profile distribution along the graphitization gradient. The final optimized composites exhibited a room temperature response of $\Delta R/R_0 = 18.5\%$ and 0.9% for acetone and toluene, using concentrations of 2.5 and 0.4%, respectively. As a reference, LP-C sensors prepared with readily prepared ZnO nanorods show a preferential response to non-polar toluene, which is attributed to the formation of large graphitic domains on the surface of LP-C. A physisorption

mechanism is suggested based on the polar and non-polar nature of the analytes used and their surface interaction with the LP-C/ZnO composite materials.

S7. Trained Laser-Patterned Carbon for High-Performance Mechanical Sensors ([link](#) to article)

M. Hepp, H. Wang, K. Derr, S. Delacroix, S. Ronneberger, F. Loeffler, B. Butz, V. Strauss, *npj Flex. Electron.* **2022**, *6*, 3.

The electronic properties of LP-C films on flexible PET substrates upon defined mechanical deformation were investigated in this study. The porous conductive LP-C films show a quantitative and reversible change in resistance upon bending or application of pressure in normal loading direction. Such properties enable their application as bending or mechanical pressure sensors. Maximum response values of $\Delta R/R_0 = 388\%$ upon positive bending (tensile stress) and -22.9% upon negative bending (compression) are implicit for their high sensitivity towards mechanical deformation. Normal mechanical loading in a range between 0 and 500 kPa causes a response between $\Delta R/R_0 = 0$ and -15% . The reversible increase or decrease in resistance is attributed to compression or tension of the turbostratically graphitized domains on top of the film, respectively. A detailed high-resolution transmission electron microscopic analysis of the cross-section of the LP-C films provides unprecedented insights into the microstructure and chemical properties.

S8. Flexible CO₂ sensor architecture with selective nitrogen functionalities by one-step laser-induced conversion of versatile organic ink ([link](#) to article)

H. Wang, C. Otieno Ogolla, G. Panchal, M. Hepp, S. Delacroix, D. Cruz, D. Kojda, Jim Ciston, Colin Ophus, A. Knop-Gericke, K. Habicht, B. Butz, V. Strauss, *Advanced Functional Materials* **2022**, *32* (51), 2207406.

The chemical and structural gradient of the LP-C films induced by laser-carbonization enables the fabrication of a layered sensor heterostructure with a porous graphitic transducer layer and an active sensor layer. The lower effective temperatures in the sensor layer allow for the preservation of thermally-metastable functional groups that serve as binding sites for specific analytes. We used this concept to fabricate a layered nitrogen-doped carbon film with a high content of pyrrolic or imidazolic nitrogen by laser-patterning of adenine-CNFA (ade380) for selective sensing of CO₂. Detailed, comprehensive microscopic and spectroscopic cross-sectional analyses reveals the unique microstructure and chemical bonding within the LP-NC film. The LP-NC films were optimized in terms of precursor preparation, laser-parameters,

reaction atmosphere, porosity, and film thickness to achieve a linear response of up to $\Delta R/R_0 = -14.3\%$ (10% of CO_2). The access of gaseous CO_2 to the sensor layers was improved by adding pre-carbonized glucose (glu(300) as a foaming agent, which was confirmed by elemental HR-(S)TEM analysis. The thermodynamic analysis yields $\Delta_{\text{ads}}H$ values of $-35.6 \text{ kJ}\cdot\text{mol}^{-1}$ and $34.1 \text{ kJ}\cdot\text{mol}^{-1}$ for H_2O and CO_2 , respectively. In humid environments, for example, $\text{RH} = 80\%$ the selective response to 10% CO_2 is still $\Delta R/R_0 = 0.53\%$. The CO_2 sensing performance of the LP-NC sensors is mechanistically largely unaffected by bending of the material and shows a stable response.

Laser-Patterned Carbon for Electrocatalysis

S9. Modulating between $2e^-$ and $4e^-$ pathway in the oxygen reduction reaction with laser-synthesized iron oxide-grafted nitrogen-doped carbon ([link](#) to article)

H. Wang, M. Jerigova, J. Hou, N. Tarakina, S. Delacroix, N. Lopez-Salas, V. Strauss, *J. Mater. Chem. A* **2022**, *10*, 24156-24166.

In this study, we demonstrate the tuning of the oxygen reduction reaction (ORR) by iron/iron oxide nanoparticle grafted LP-C electrodes. Depending on the preparation route, i.e. addition of a molecular $\text{Fe}(\text{NO}_3)_2$ precursor before (Route 1) or after pre-carbonization (Route 2) of the citric acid / urea precursors, either the $2e^-$ or the $4e^-$ pathway in the oxygen reduction reaction is facilitated leading to either H_2O_2 or H_2O as a reaction product, respectively. The kinetic reaction conditions afford rarely observed $\text{Fe}(0)/\text{Fe}_2\text{O}_3$ core-shell nanoparticles embedded in LP-Cs with Fe_2O_3 occurring in the η - or α - phase, in dependence of the preparation route. The *in situ* formation of $\text{Fe}(0)/\text{Fe}_2\text{O}_3$ core-shell nanoparticles from $\text{Fe}(\text{NO}_3)_2$ is facilitated by a carbothermic reduction during the graphitization of the carbon network-forming agent (CNFA) leading to a graphitized shell around the nanoparticles. Onset potentials for the $2e^-$ or $4e^-$ mediated ORR are as low as 0.77 or 0.70 V (vs. RHE) with a H_2O_2 production efficiency of 4 or 99% respectively for electrodes with $\sim 3 \text{ wt}\%$ iron.

Laser-Patterned Carbon for Supercapacitors

S10. Fast response electrochemical capacitor electrodes created by laser-reduction of carbon nanodots ([link](#) to article)

V. Strauss, M. Anderson, C. L. Turner, R. B. Kaner, *Mater. Today Energy* **2019**, *11*, 114–119.

LP-C electrodes based on CA/U(300) were fabricated on stainless steel substrates and tested for their performance in electrochemical double-layer capacitors. The effect of the reaction atmosphere, Ar or O₂, on the electrochemical characteristics was investigated. The electric conductivity and the specific surface areas are only marginally affected by the reaction atmosphere. The surface properties, on the other hand, are significantly altered as shown in a drastic change of the frequency response of the EDLCs. Remarkable are the extremely fast RC (resistance-capacitance) time constant of $\tau = 0.29$ ms and a capacitance of 0.259 mF cm^{-2} at 120 Hz.

S11. Patching laser-reduced graphene oxide with carbon nanodots ([link to article](#))

V. Strauss, M. Muni, A. Borenstein, B. Badamdorj, T. Heil, M. D. Kowal, R. Kaner, *Nanoscale* **2019**, *11*, 12712–12719.

The CA/U(300) CNFA was used to improve the structural integrity of 3D-graphenes obtained from laser-reduction of GO. To this end, different mass ratios of CA/U(300) and GO were mixed in the primary films. At a mass percentage of ~32%, the active surface area in the hybrid starting materials was increased to 130% and the electrical conductivity enhanced by nearly an order of magnitude compared to pure LR-GO. These improved material parameters lead to enhanced device performance of the EDLC electrodes on stainless steel substrates. The frequency response, *i.e.* the minimum phase angle and the relaxation time, were significantly improved from -82.2° and 128 ms to -84.3° and 7.6 ms, respectively. For the same devices the specific gravimetric device capacitance was increased from 110 to a maximum value of 214 F g⁻¹ at a scan rate of 10 mV s⁻¹.

S12. On-Chip Direct Laser Writing of PAN-Based Carbon Supercapacitor Electrodes ([link to article](#))

A. Hoffmann, P. Jiménez-Calvo, J. Bansmann, V. Strauss, A. J. C. Kuehne, *Macromol. Rapid Commun.* **2022**, 2100731.

The direct laser-induced carbonization of polyacrylonitrile (PAN) has been impeded by the slow reaction kinetics of the cyclization step of PAN (see Laser-Carbonization – Historical Overview). In this study, we demonstrate direct laser-carbonization of PAN films by integrating carbon nanotubes as additives to support the absorption of the infrared laser beam. The PAN/CNT films were deposited on a printed circuit board (PCB) as substrate and directly laser-patterned into interdigitated electrodes which were characterized for their performance as

mEDLCs. By varying the laser power, the process can be tuned from carbonization to material ablation. This allows to not only to convert pristine PAN films into carbon electrodes, but also to pattern and cut away non-carbonized material to produce completely freestanding LP-C electrodes. While the LP-C electrodes adhere well to the printed circuit board, non-carbonized PAN is peeled off the substrate. Specific capacities as high as $260 \mu\text{F}\cdot\text{cm}^{-2}$ are achieved in a mEDLC with 16 fingers.

|| Conclusions and Future Directions

This work summarizes and contextualizes our investigations on laser-carbonization as a synthesis tool for functional materials in flexible electronic devices. We developed an **integrated approach** for laser-carbonization of molecular and polymeric precursors. With regard to molecular precursors, we elucidated the fundamental importance of pre-carbonization (condensation, polymerization) for their use as starting materials. In a series of studies we created a **comprehensive understanding** of the formation mechanism of carbonized films facilitated by the rapid photo-thermal reactions on the millisecond (kinetic) time-scale. We provided insights into the film formation with chemical and structural gradients and investigated the mechanical and electronic flexibility of laser-patterned carbon films on flexible substrates. Furthermore, we developed a **toolbox** for the selective tuning of the properties of laser-patterned carbons by addition of porogens, additives, or reactants to the primary films. Thereby, properties like porosity, surface polarity, charge-carrier density, or chemical composition are selectively modified. Based on the fundamental understanding of these factors we developed **prototype devices** for chemical or mechanical sensors, electrocatalytic electrodes, and capacitive charge-storage devices.

During the conduct of the herein presented studies, we faced several **challenges**. In particular, the complex interplay of the many processing parameters (power, speed, atmosphere, focus, substrate, precursors, pressure etc.) make generalizations on the precursor–product relationship difficult. The analysis of the microstructure (porosity) and its correlation with the chemical and electronic properties for such small amounts of material is highly challenging. Advanced *in situ* characterization methods are required to create a comprehensive and fundamental knowledge for the customized design of functional material films.

As outlined in the General Part, **comprehensive mechanistic studies** including all aforementioned aspects to derive universal processing parameters are still lacking. Understanding the **physics** of laser-carbonization, similar to the insights generated in other disciplines of laser-assisted materials processing, would greatly help in improving the design of devices. For example, a systematic study on the beam-precursor interactions (wavelengths – extinction coefficients, heat conductivity, etc) for a representative set of precursors is necessary to establish a quick method to pre-determine the suitability of precursors. Based on the experience from decades of carbonization research, we know that each system brings its individual challenges. However, systematic studies to identify universal laws should be carried out.

In our studies, the mutual dependencies between precursors, processing parameters, and the properties of the LP-(N)Cs were evaluated and correlations to their functionality were established. Our fundamental cross-sectional analyses revealed the most remarkable feature of LP-(N)C, namely the chemical and structural gradient due to the unidirectional energy input. In many applications, e.g. chemical sensors, this gradient may be a decisive advantage. Sophisticated, selective spectroscopic characterization of the individual layers would enhance the understanding of the formation mechanism and enable the tuning of the functional properties. Furthermore, studies on the **correlation between the surface properties and the electronic properties** on the micro and macroscale may provide important information on how to design simple functional carbon-based sensors. Similarly, a systematic **correlation between pore size and functional groups** are necessary to understand the chemical bonding and activation of gaseous or liquid analytes. Furthermore, the specific **LP-C/substrate interactions** have a major influence on the film properties and device performance. To this end, alternative film-casting strategies should be developed. Importantly, the **determination of the active surface areas** of such low amounts of material is still difficult to achieve with conventional sorption-isotherm analysis. Simple lab-based alternative methods are highly demanded.

Challenges

- comprehensive mechanistic studies
- beam-precursor interactions (extinction coefficients, heat conductivity, wavelengths, etc)
- LP-(N)C/substrate interactions
- determination of the active surface areas
- correlation between pore size and functional groups
- correlation of functional groups and charge-carrier properties

The fundamental insights provided in this work initiate future directions for both academic research and potential commercial applications. Two summarizing conclusions can be drawn:

- 1) Laser-carbonization is a potential method for the direct synthesis and utilization of functional carbonized materials in film-based or flexible devices. It is competitive to conventional pyrolysis. However, tailoring strategies need to be adopted to the (kinetic) reaction conditions.
- 2) Besides being a new fabrication and processing method, the kinetic reaction conditions of laser-carbonization offer a unique opportunity to access new materials with unknown properties.

References

- 1 M. W. Haenel, "Recent progress in coal structure research" *Fuel* **1992**, *71*, 1211–1223.
- 2 M. Kaltschmitt, H. Hartmann, H. Hofbauer, Eds. , "Energie aus Biomasse" Springer Berlin Heidelberg, Berlin, Heidelberg, **2009**.
- 3 E. Fitzer, K.-H. Kochling, H. P. Boehm, H. Marsh, "Recommended terminology for the description of carbon as a solid (IUPAC Recommendations 1995)" *Pure Appl. Chem.* **1995**, *67*, 473–506.
- 4 L. Schmerling, V. N. Ipatieff, "The Mechanism of the Polymerization of Alkenes" **1950**, pp. 21–80.
- 5 I. C. Lewis, "Chemistry of carbonization" *Carbon N. Y.* **1982**, *20*, 519–529.
- 6 A. K. Burnham, "Van Krevelen Diagrams" in *Encycl. Pet. Geosci.*, **2018**, pp. 1–5.
- 7 D. W. van Krevelen, "Coal: Typology - Physics - Chemistry - Constitution" Elsevier, **1993**.
- 8 E. Frank, F. Hermanutz, M. R. Buchmeiser, "Carbon Fibers: Precursors, Manufacturing, and Properties" *Macromol. Mater. Eng.* **2012**, *297*, 493–501.
- 9 R. J. White, Ed. , "Porous Carbon Materials from Sustainable Precursors" Royal Society Of Chemistry, Cambridge, **2015**.
- 10 "pyrolysis" in *IUPAC Compend. Chem. Terminol.*, International Union Of Pure And Applied Chemistry (IUPAC), Research Triangle Park, NC, **2014**.
- 11 D. D. L. Chung, "Carbon Materials" WORLD SCIENTIFIC, **2019**.
- 12 A. R. Bunsell, Ed. , "Fibre Reinforcements For Composite Materials" **1988**.
- 13 D. B. Schuepfer, F. Badaczewski, J. M. Guerra-Castro, D. M. Hofmann, C. Heiliger, B. Smarsly, P. J. Klar, "Assessing the structural properties of graphitic and non-graphitic carbons by Raman spectroscopy" *Carbon N. Y.* **2020**, *161*, 359–372.
- 14 J. Abrahamson, "Graphite sublimation temperatures, carbon arcs and crystallite erosion" *Carbon N. Y.* **1974**, *12*, 111–141.
- 15 A. D. Jara, A. Betemariam, G. Woldetinsae, J. Y. Kim, "Purification, application and current market trend of natural graphite: A review" *Int. J. Min. Sci. Technol.* **2019**, *29*, 671–689.
- 16 "graphitization" in *IUPAC Compend. Chem. Terminol.*, International Union Of Pure And Applied Chemistry (IUPAC), Research Triangle Park, NC, **2012**.
- 17 "non-graphitizable carbon" in *IUPAC Compend. Chem. Terminol.*, International Union Of Pure And Applied Chemistry (IUPAC), Research Triangle Park, NC, **2014**.
- 18 "glass-like carbon" in *IUPAC Compend. Chem. Terminol.*, International Union Of Pure And Applied Chemistry (IUPAC), Research Triangle Park, NC, **2014**.
- 19 "carbonaceous mesophase" in *IUPAC Compend. Chem. Terminol.*, International Union Of Pure And Applied Chemistry (IUPAC), Research Triangle Park, NC, **2014**.
- 20 "non-graphitic carbon" in *IUPAC Compend. Chem. Terminol.*, International Union Of Pure And Applied Chemistry (IUPAC), Research Triangle Park, NC, **2014**.
- 21 P. T. Araujo, M. Terrones, M. S. Dresselhaus, "Defects and impurities in graphene-like materials" *Mater. Today* **2012**, *15*, 98–109.
- 22 C. A. Klein, W. D. Straub, "Carrier Densities and Mobilities in Pyrolytic Graphite" *Phys. Rev.* **1961**, *123*, 1581–1583.
- 23 R. Shinzawa, A. Otsuka, A. Nakamura, "Growth of glassy carbon thin films and its pH sensor applications" *SN Appl. Sci.* **2019**, *1*, 171.
- 24 X. Du, I. Skachko, A. Barker, E. Y. Andrei, "Approaching ballistic transport in suspended graphene" *Nat. Nanotechnol.* **2008**, *3*, 491–495.
- 25 A. Krueger, "Carbon Materials and Nanotechnology" Wiley, **2010**.
- 26 K. Dasgupta, D. Sathiyamoorthy, "Disordered carbon—its preparation, structure, and characterisation" *Mater. Sci. Technol.* **2003**, *19*, 995–1002.
- 27 H. Jäger, W. Frohs, Eds. , "Industrial Carbon and Graphite Materials, Volume I" Wiley, **2021**.
- 28 "amorphous carbon" in *IUPAC Compend. Chem. Terminol.*, International Union Of Pure And Applied Chemistry (IUPAC), Research Triangle Park, NC, **2008**.
- 29 M. P. Ho, A. K.-T. Lau, "Amorphous carbon nanocomposites" in *Fill. Reinf. Adv. Nanocomposites*, Elsevier, **2015**, pp. 309–328.
- 30 "activated carbon" in *IUPAC Compend. Chem. Terminol.*, International Union Of Pure And Applied Chemistry (IUPAC), Research Triangle Park, NC, **2008**.
- 31 Z. Heidarinejad, M. H. Dehghani, M. Heidari, G. Javedan, I. Ali, M. Sillanpää, "Methods for preparation and activation of activated carbon: a review" *Environ. Chem. Lett.* **2020**, *18*, 393–415.
- 32 "microporous carbon" in *IUPAC Compend. Chem. Terminol.*, International Union Of Pure And Applied Chemistry (IUPAC), Research Triangle Park, NC, **2014**.

References

- 33 "aerogel" in *IUPAC Compend. Chem. Terminol.*, International Union Of Pure And Applied Chemistry (IUPAC), Research Triangle Park, NC, **2014**.
- 34 "foam" in *IUPAC Compend. Chem. Terminol.*, International Union Of Pure And Applied Chemistry (IUPAC), Research Triangle Park, NC, **2014**.
- 35 Ravedave, "Wikimedia Commons" can be found under https://commons.wikimedia.org/wiki/File:Activated_Carbon.jpg.
- 36 Mydriatic, "Wikimedia Commons" can be found under https://commons.wikimedia.org/wiki/File:Activated_Charcoal.jpg.
- 37 D. Liang, Q. Xie, J. Liu, F. Xie, D. Liu, C. Wan, "Mechanism of the evolution of pore structure during the preparation of activated carbon from Zhundong high-alkali coal based on gas–solid diffusion and activation reactions" *RSC Adv.* **2020**, *10*, 33566–33575.
- 38 "Test" .
- 39 F. Rodríguez-Reinoso, M. Molina-Sabio, M. A. Munecas, "Effect of microporosity and oxygen surface groups of activated carbon in the adsorption of molecules of different polarity" *J. Phys. Chem.* **1992**, *96*, 2707–2713.
- 40 "adsorbent" in *IUPAC Compend. Chem. Terminol.*, International Union Of Pure And Applied Chemistry (IUPAC), Research Triangle Park, NC, **2014**.
- 41 "adsorptive" in *IUPAC Compend. Chem. Terminol.*, International Union Of Pure And Applied Chemistry (IUPAC), Research Triangle Park, NC, **2014**.
- 42 "adsorbate" in *IUPAC Compend. Chem. Terminol.*, International Union Of Pure And Applied Chemistry (IUPAC), Research Triangle Park, NC, **2014**.
- 43 E. Fuente, J. A. Menéndez, D. Suárez, M. A. Montes-Morán, "Basic Surface Oxides on Carbon Materials: A Global View" *Langmuir* **2003**, *19*, 3505–3511.
- 44 M. Inagaki, M. Toyoda, Y. Soneda, T. Morishita, "Nitrogen-doped carbon materials" *Carbon N. Y.* **2018**, *132*, 104–140.
- 45 J. Lahaye, G. Nansé, A. Bagreev, V. Strelko, "Porous structure and surface chemistry of nitrogen containing carbons from polymers" *Carbon N. Y.* **1999**, *37*, 585–590.
- 46 J. R. Pels, F. Kapteijn, J. A. Moulijn, Q. Zhu, K. M. Thomas, "Evolution of nitrogen functionalities in carbonaceous materials during pyrolysis" *Carbon N. Y.* **1995**, *33*, 1641–1653.
- 47 M. Gehring, H. Tempel, A. Merlen, R. Schierholz, R.-A. Eichel, H. Kungl, "Carbonisation temperature dependence of electrochemical activity of nitrogen-doped carbon fibres from electrospinning as air-cathodes for aqueous-alkaline metal–air batteries" *RSC Adv.* **2019**, *9*, 27231–27241.
- 48 M. Oschatz, M. Antonietti, "A search for selectivity to enable CO₂ capture with porous adsorbents" *Energy Environ. Sci.* **2018**, *11*, 57–70.
- 49 W. Ju, A. Bagger, G.-P. Hao, A. S. Varela, I. Sinev, V. Bon, B. Roldan Cuenya, S. Kaskel, J. Rossmeisl, P. Strasser, "Understanding activity and selectivity of metal-nitrogen-doped carbon catalysts for electrochemical reduction of CO₂" *Nat. Commun.* **2017**, *8*, 944.
- 50 N. R. Sahraie, U. I. Kramm, J. Steinberg, Y. Zhang, A. Thomas, T. Reier, J.-P. Paraknowitsch, P. Strasser, "Quantifying the density and utilization of active sites in non-precious metal oxygen electroreduction catalysts" *Nat. Commun.* **2015**, *6*, 8618.
- 51 F. Luo, A. Roy, L. Silvioli, D. A. Cullen, A. Zitolo, M. T. Sougrati, I. C. Oguz, T. Mineva, D. Teschner, S. Wagner, J. Wen, F. Dionigi, U. I. Kramm, J. Rossmeisl, F. Jaouen, P. Strasser, "P-block single-metal-site tin/nitrogen-doped carbon fuel cell cathode catalyst for oxygen reduction reaction" *Nat. Mater.* **2020**, *19*, 1215–1223.
- 52 S. S. Naboychenko, I. B. Murashova, O. D. Neikov, "Production of Refractory Metal Powders" in *Handb. Non-Ferrous Met. Powders*, Elsevier, **2009**, pp. 436–484.
- 53 B. Yan, J. Zheng, F. Wang, L. Zhao, Q. Zhang, W. Xu, S. He, "Review on porous carbon materials engineered by ZnO templates: Design, synthesis and capacitance performance" *Mater. Des.* **2021**, *201*, 109518.
- 54 M. Bystyrzewski, "Synthesis of carbon-encapsulated iron nanoparticles via solid state reduction of iron oxide nanoparticles" *J. Solid State Chem.* **2011**, *184*, 1492–1498.
- 55 P. Strubel, S. Thieme, T. Biemelt, A. Helmer, M. Oschatz, J. Brückner, H. Althues, S. Kaskel, "ZnO Hard Templating for Synthesis of Hierarchical Porous Carbons with Tailored Porosity and High Performance in Lithium-Sulfur Battery" *Adv. Funct. Mater.* **2015**, *25*, 287–297.
- 56 R. Yan, K. Leus, J. P. Hofmann, M. Antonietti, M. Oschatz, "Porous nitrogen-doped carbon/carbon nanocomposite electrodes enable sodium ion capacitors with high capacity and rate capability" *Nano Energy* **2020**, *67*, 104240.
- 57 T.-Y. Ma, L. Liu, Z.-Y. Yuan, "Direct synthesis of ordered mesoporous carbons" *Chem. Soc. Rev.* **2013**, *42*, 3977–4003.
- 58 L. Chuenchom, R. Kraehnert, B. M. Smarsly, "Recent progress in soft-templating of porous carbon materials" *Soft Matter* **2012**, *8*, 10801.
- 59 Y. Xia, Z. Yang, R. Mokaya, "Templated nanoscale porous carbons" *Nanoscale* **2010**, *2*, 639.
- 60 R. Ryoo, S. H. Joo, S. Jun, "Synthesis of Highly Ordered Carbon Molecular Sieves via Template-Mediated Structural Transformation" *J. Phys. Chem. B* **1999**, *103*, 7743–7746.
- 61 N. Fechler, T.-P. Fellingner, M. Antonietti, "'Salt Templating': A Simple and Sustainable Pathway toward Highly Porous Functional Carbons from Ionic Liquids" *Adv. Mater.* **2013**, *25*, 75–79.
- 62 J. Pampel, T.-P. Fellingner, "Opening of Bottleneck Pores for the Improvement of Nitrogen Doped Carbon Electrocatalysts" *Adv. Energy Mater.* **2016**, *6*, 1502389.
-

-
- 63 F. A. Williams, "Combustion" in *Encycl. Phys. Sci. Technol.*, Elsevier, **2003**, pp. 315–338.
- 64 D. Aufhäuser, "Die Verbrennung als katalytische Reaktion" in *Brennst. Und Verbrennung*, Springer Berlin Heidelberg, Berlin, Heidelberg, **1928**, pp. 48–60.
- 65 M.-M. Titirici, S. Baird, T. Sparks, S. M. Yang, A. Brandt-Talbot, O. Hosseinaei, D. P. Harper, R. Parker, S. Vignolini, L. Berglund, Y. Li, H.-L. Gao, L.-B. Mao, S. Yu, N. Díez, G. Alvarez.ferrero, M. Sevilla Solis, P. Szilagyi, C. Stubbs et al., "The Sustainable Materials Roadmap" *J. Phys. Mater.* **2022**, DOI 10.1088/2515-7639/ac4ee5.
- 66 M.-M. Titirici, M. Antonietti, "Chemistry and materials options of sustainable carbon materials made by hydrothermal carbonization" *Chem. Soc. Rev.* **2010**, *39*, 103–116.
- 67 M.-M. TITIRICI, Ed. , "Sustainable Carbon Materials from Hydrothermal Processes" John Wiley & Sons, Ltd, Oxford, UK, **2013**.
- 68 R. Sharma, K. Jasrotia, N. Singh, P. Ghosh, S. Srivastava, N. R. Sharma, J. Singh, R. Kanwar, A. Kumar, "A Comprehensive Review on Hydrothermal Carbonization of Biomass and its Applications" *Chem. Africa* **2020**, *3*, 1–19.
- 69 L. Zhao, L.-Z. Fan, M.-Q. Zhou, H. Guan, S. Qiao, M. Antonietti, M.-M. Titirici, "Nitrogen-Containing Hydrothermal Carbons with Superior Performance in Supercapacitors" *Adv. Mater.* **2010**, *22*, 5202–5206.
- 70 V. E. Borisenko, P. J. Hesketh, "Rapid Thermal Processing of Semiconductors" Springer US, Boston, MA, **1997**.
- 71 A. Bhardwaj, J. N. Pagaduan, Y.-G. Yu, V. J. Einck, S. Nuguri, R. Katsumata, J. J. Watkins, "Large-Pore Ordered Mesoporous Turbostratic Carbon Films Prepared Using Rapid Thermal Annealing for High-Performance Micro-pseudocapacitors" *ACS Appl. Mater. Interfaces* **2021**, *13*, 61027–61038.
- 72 J. Hofrichter, B. N. Szafrank, M. Otto, T. J. Echtermeyer, M. Baus, A. Majerus, V. Geringer, M. Ramsteiner, H. Kurz, "Synthesis of Graphene on Silicon Dioxide by a Solid Carbon Source" *Nano Lett.* **2010**, *10*, 36–42.
- 73 J. H. Chu, J. Kwak, T.-Y. Kwon, S.-D. Park, H. Go, S. Y. Kim, K. Park, S. Kang, S.-Y. Kwon, "Facile Synthesis of Few-Layer Graphene with a Controllable Thickness Using Rapid Thermal Annealing" *ACS Appl. Mater. Interfaces* **2012**, *4*, 1777–1782.
- 74 J. I. Raffel, J. F. Freidin, G. H. Chapman, "Laser-formed connections using polyimide" *Appl. Phys. Lett.* **1983**, *42*, 705–706.
- 75 J. H. Brannon, J. R. Lankard, A. I. Baise, F. Burns, J. Kaufman, "Excimer laser etching of polyimide" *J. Appl. Phys.* **1985**, *58*, 2036–2043.
- 76 M. Schumann, R. Sauerbrey, M. C. Smayling, "Permanent increase of the electrical conductivity of polymers induced by ultraviolet laser radiation" *Appl. Phys. Lett.* **1991**, *58*, 428–430.
- 77 R. Srinivasan, "Ablation of polyimide (Kapton?) films by pulsed (ns) ultraviolet and infrared (9.17 ?m) lasers" *Appl. Phys. A Solids Surfaces* **1993**, *56*, 417–423.
- 78 R. Srinivasan, R. R. Hall, D. C. Allbee, "Generation of electrically conducting features in polyimide (Kapton T M) films with continuous wave, ultraviolet laser radiation" *Appl. Phys. Lett.* **1993**, *63*, 3382–3383.
- 79 T. Feurer, R. Sauerbrey, M. C. Smayling, B. J. Story, "Ultraviolet-laser-induced permanent electrical conductivity in polyimide" *Appl. Phys. A Solids Surfaces* **1993**, *56*, 275–281.
- 80 R. Srinivasan, R. R. Hall, W. D. Wilson, W. D. Loehle, D. C. Allbee, "Formation of a Porous, Patternable, Electrically Conducting Carbon Network by the Ultraviolet Laser Irradiation of the Polyimide PMDA-ODA (Kapton)" *Chem. Mater.* **1994**, *6*, 888–889.
- 81 E. E. Orтели, F. Geiger, T. Lippert, J. Wei, A. Wokaun, "UV-Laser-Induced Decomposition of Kapton Studied by Infrared Spectroscopy" *Macromolecules* **2000**, *33*, 5090–5097.
- 82 A. Kothuru, C. Hanumanth Rao, S. B. Puneeth, M. Salve, K. Amreen, S. Goel, "Laser-Induced Flexible Electronics (LIFE) for Resistive, Capacitive and Electrochemical Sensing Applications" *IEEE Sens. J.* **2020**, *20*, 7392–7399.
- 83 Z. Wan, E. W. Streed, M. Lobino, S. Wang, R. T. Sang, I. S. Cole, D. V. Thiel, Q. Li, "Laser-Reduced Graphene: Synthesis, Properties, and Applications" *Adv. Mater. Technol.* **2018**, *3*, 1700315.
- 84 E. Kymakis, C. Petridis, T. D. Anthopoulos, E. Stratakis, "Laser-Assisted Reduction of Graphene Oxide for Flexible, Large-Area Optoelectronics" *IEEE J. Sel. Top. Quantum Electron.* **2014**, *20*, 106–115.
- 85 P. Zhang, Z. Li, S. Zhang, G. Shao, "Recent Advances in Effective Reduction of Graphene Oxide for Highly Improved Performance Toward Electrochemical Energy Storage" *Energy Environ. Mater.* **2018**, *1*, 5–12.
- 86 L. Cheng, W. Guo, X. Cao, Y. Dou, L. Huang, Y. Song, J. Su, Z. Zeng, R. Ye, "Laser-induced graphene for environmental applications: progress and opportunities" *Mater. Chem. Front.* **2021**, *5*, 4874–4891.
- 87 R. Ye, D. K. James, J. M. Tour, "Laser-Induced Graphene: From Discovery to Translation" *Adv. Mater.* **2019**, *31*, 1803621.
- 88 W. Ma, J. Zhu, Z. Wang, W. Song, G. Cao, "Recent advances in preparation and application of laser-induced graphene in energy storage devices" *Mater. Today Energy* **2020**, *18*, 100569.
- 89 Z. Wan, N.-T. Nguyen, Y. Gao, Q. Li, "Laser induced graphene for biosensors" *Sustain. Mater. Technol.* **2020**, *25*, e00205.
- 90 Y. Zhang, L. Guo, S. Wei, Y. He, H. Xia, Q. Chen, H.-B. Sun, F.-S. Xiao, "Direct imprinting of microcircuits on graphene oxides film by femtosecond laser reduction" *Nano Today* **2010**, *5*, 15–20.
- 91 J. Lin, Z. Peng, Y. Liu, F. Ruiz-Zepeda, R. Ye, E. L. G. Samuel, M. J. Yacaman, B. I. Yakobson, J. M. Tour, "Laser-induced porous graphene films from commercial polymers" *Nat. Commun.* **2014**, *5*, 5714.
- 92 D. A. Sokolov, K. R. Shepperd, T. M. Orlando, "Formation of Graphene Features from Direct Laser-Induced Reduction of Graphite Oxide" *J. Phys. Chem. Lett.* **2010**, *1*, 2633–2636.
-

References

- 93 W. Gao, N. Singh, L. Song, Z. Liu, A. L. M. Reddy, L. Ci, R. Vajtai, Q. Zhang, B. Wei, P. M. Ajayan, "Direct laser writing of micro-supercapacitors on hydrated graphite oxide films" *Nat. Nanotechnol.* **2011**, *6*, 496–500.
- 94 M. F. El-Kady, V. Strong, S. Dubin, R. B. Kaner, "Laser Scribing of High-Performance and Flexible Graphene-Based Electrochemical Capacitors" *Science (80-.)* **2012**, *335*, 1326–1330.
- 95 T. Barkan, "Graphene: the hype versus commercial reality" *Nat. Nanotechnol.* **2019**, *14*, 904–906.
- 96 A. Bürger, E. Fitzer, M. Heym, B. Terwiesch, "Polyimides as precursors for artificial carbon" *Carbon N. Y.* **1975**, *13*, 149–157.
- 97 M. Inagaki, S. Harada, T. Sato, T. Nakajima, Y. Horino, K. Morita, "Carbonization of polyimide film "Kapton"" *Carbon N. Y.* **1989**, *27*, 253–257.
- 98 S. P. Singh, Y. Li, J. Zhang, J. M. Tour, C. J. Amusch, "Sulfur-Doped Laser-Induced Porous Graphene Derived from Polysulfone-Class Polymers and Membranes" *ACS Nano* **2018**, *12*, 289–297.
- 99 N. Morita, Y. Shimotsuma, M. Nishi, M. Sakakura, K. Miura, K. Hirao, "Direct micro-carbonization inside polymer using focused femtosecond laser pulses" *Appl. Phys. Lett.* **2014**, *105*, 201104.
- 100 N. E. Stankova, P. A. Atanasov, N. N. Nedyalkov, T. R. Stoyanchov, K. N. Kolev, E. I. Valova, J. S. Georgieva, S. A. Aramyanov, S. Amoroso, X. Wang, R. Bruzzese, K. Grochowska, G. Śliwiński, K. Baert, A. Hubin, M. P. Delplancke, J. Dille, "fs- and ns-laser processing of polydimethylsiloxane (PDMS) elastomer: Comparative study" *Appl. Surf. Sci.* **2015**, *336*, 321–328.
- 101 P. A. Atanasov, N. E. Stankova, N. N. Nedyalkov, N. Fukata, D. Hirsch, B. Rauschenbach, S. Amoroso, X. Wang, K. N. Kolev, E. I. Valova, J. S. Georgieva, S. A. Aramyanov, "Fs-laser processing of medical grade polydimethylsiloxane (PDMS)" *Appl. Surf. Sci.* **2016**, *374*, 229–234.
- 102 N. E. Stankova, P. A. Atanasov, R. G. Nikov, R. G. Nikov, N. N. Nedyalkov, T. R. Stoyanchov, N. Fukata, K. N. Kolev, E. I. Valova, J. S. Georgieva, S. A. Aramyanov, "Optical properties of polydimethylsiloxane (PDMS) during nanosecond laser processing" *Appl. Surf. Sci.* **2016**, *374*, 96–103.
- 103 R. Ye, Y. Chyan, J. Zhang, Y. Li, X. Han, C. Kittrell, J. M. Tour, "Laser-Induced Graphene Formation on Wood" *Adv. Mater.* **2017**, *29*, 1702211.
- 104 K. Ju, Y. Gao, T. Xiao, C. Yu, J. Tan, F. Xuan, "Laser direct writing of carbonaceous sensors on cardboard for human health and indoor environment monitoring" *RSC Adv.* **2020**, *10*, 18694–18703.
- 105 T. D. Le, S. Park, J. An, P. S. Lee, Y. Kim, "Ultrafast Laser Pulses Enable One-Step Graphene Patterning on Woods and Leaves for Green Electronics" *Adv. Funct. Mater.* **2019**, *29*, 1902771.
- 106 W. M. Steen, J. Mazumder, "Laser Material Processing" Springer London, London, **2010**.
- 107 E. T. Akinlabi, R. M. Mahamood, S. A. Akinlabi, "Advanced Manufacturing Techniques Using Laser Material Processing" IGI Global, **2016**.
- 108 G. G. Gladush, I. Smurov, "Physics of Laser Materials Processing" Springer Berlin Heidelberg, Berlin, Heidelberg, **2011**.
- 109 "Why Use a Flat Top Laser Beam?" can be found under <https://www.edmundoptics.de>.
- 110 T. N. Baker, "Laser surface modification of titanium alloys" in *Surf. Eng. Light Alloy.*, Elsevier, **2010**, pp. 398–443.
- 111 "Laser Surface Engineering" Elsevier, **2015**.
- 112 Y. Yao, X. Duan, M. Niu, J. Luo, R. Wang, T. Liu, "One-step process for direct laser writing carbonization of NH₄H₂PO₄ treated cellulose paper and its use for facile fabrication of multifunctional force sensors with corrugated structures" *Cellulose* **2019**, *26*, 7423–7435.
- 113 S. Lee, S. Jeon, "Laser-Induced Graphitization of Cellulose Nanofiber Substrates under Ambient Conditions" *ACS Sustain. Chem. Eng.* **2019**, *7*, 2270–2275.
- 114 F. Morosawa, S. Hayashi, M. Terakawa, "Femtosecond Laser-Induced Graphitization of Transparent Cellulose Nanofiber Films" *ACS Sustain. Chem. Eng.* **2021**, *9*, 2955–2961.
- 115 S. Park, H. Lee, Y.-J. Kim, P. S. Lee, "Fully laser-patterned stretchable microsupercapacitors integrated with soft electronic circuit components" *NPG Asia Mater.* **2018**, *10*, 959–969.
- 116 T. X. Tran, H. Choi, C. H. Che, J. H. Sul, I. G. Kim, S.-M. Lee, J.-H. Kim, J. Bin In, "Laser-Induced Reduction of Graphene Oxide by Intensity-Modulated Line Beam for Supercapacitor Applications" *ACS Appl. Mater. Interfaces* **2018**, *10*, 39777–39784.
- 117 Z. Wan, S. Wang, B. Haylock, J. Kaur, P. Tanner, D. Thiel, R. Sang, I. S. Cole, X. Li, M. Lobino, Q. Li, "Tuning the sub-processes in laser reduction of graphene oxide by adjusting the power and scanning speed of laser" *Carbon N. Y.* **2019**, *141*, 83–91.
- 118 B. S. de Lima, M. I. B. Bernardi, V. R. Mastelaro, "Wavelength effect of ns-pulsed radiation on the reduction of graphene oxide" *Appl. Surf. Sci.* **2020**, *506*, 144808.
- 119 W. Zhang, Y. Lei, F. Ming, Q. Jiang, P. M. F. J. Costa, H. N. Alshareef, "Lignin Laser Lithography: A Direct-Write Method for Fabricating 3D Graphene Electrodes for Microsupercapacitors" *Adv. Energy Mater.* **2018**, *8*, 1801840.
- 120 Y. Lei, A. H. Alshareef, W. Zhao, S. Inal, "Laser-Scribed Graphene Electrodes Derived from Lignin for Biochemical Sensing" *ACS Appl. Nano Mater.* **2020**, *3*, 1166–1174.
- 121 J. Edberg, R. Brooke, O. Hosseinaei, A. Fall, K. Wijeratne, M. Sandberg, "Laser-induced graphitization of a forest-based ink for use in flexible and printed electronics" *npj Flex. Electron.* **2020**, *4*, 17.
- 122 M. Yuan, F. Luo, Y. Rao, Y. Wang, J. Yu, H. Li, X. Chen, "Laser synthesis of superhydrophilic O/S co-doped porous graphene derived from sodium lignosulfonate for enhanced microsupercapacitors" *J. Power Sources* **2021**, *513*, 230558.

- 123 D. Go, P. Lott, J. Stollenwerk, H. Thomas, M. Möller, A. J. C. Kuehne, "Laser Carbonization of PAN-Nanofiber Mats with Enhanced Surface Area and Porosity" *ACS Appl. Mater. Interfaces* **2016**, *8*, 28412–28417.
- 124 R. Rahimi, M. Ochoa, W. Yu, B. Ziaie, "Highly Stretchable and Sensitive Unidirectional Strain Sensor via Laser Carbonization" *ACS Appl. Mater. Interfaces* **2015**, *7*, 4463–4470.
- 125 L.-Q. Tao, H. Tian, Y. Liu, Z.-Y. Ju, Y. Pang, Y.-Q. Chen, D.-Y. Wang, X.-G. Tian, J.-C. Yan, N.-Q. Deng, Y. Yang, T.-L. Ren, "An intelligent artificial throat with sound-sensing ability based on laser induced graphene" *Nat. Commun.* **2017**, *8*, 14579.
- 126 A. Lamberti, F. Clerici, M. Fontana, L. Scaltrito, "A Highly Stretchable Supercapacitor Using Laser-Induced Graphene Electrodes onto Elastomeric Substrate" *Adv. Energy Mater.* **2016**, *6*, 1600050.
- 127 Z. Peng, J. Lin, R. Ye, E. L. G. Samuel, J. M. Tour, "Flexible and Stackable Laser-Induced Graphene Supercapacitors" *ACS Appl. Mater. Interfaces* **2015**, *7*, 3414–3419.
- 128 J. Cai, C. Lv, A. Watanabe, "Laser direct writing of high-performance flexible all-solid-state carbon micro-supercapacitors for an on-chip self-powered photodetection system" *Nano Energy* **2016**, *30*, 790–800.
- 129 J. Cai, C. Lv, A. Watanabe, "Cost-effective fabrication of high-performance flexible all-solid-state carbon micro-supercapacitors by blue-violet laser direct writing and further surface treatment" *J. Mater. Chem. A* **2016**, *4*, 1671–1679.
- 130 L. Li, J. Zhang, Z. Peng, Y. Li, C. Gao, Y. Ji, R. Ye, N. D. Kim, Q. Zhong, Y. Yang, H. Fei, G. Ruan, J. M. Tour, "High-Performance Pseudocapacitive Microsupercapacitors from Laser-Induced Graphene" *Adv. Mater.* **2016**, *28*, 838–845.
- 131 Y. Yu, P. C. Joshi, J. Wu, A. Hu, "Laser-Induced Carbon-Based Smart Flexible Sensor Array for Multiflavors Detection" *ACS Appl. Mater. Interfaces* **2018**, *10*, 34005–34012.
- 132 P. Puetz, A. Behrent, A. J. J. Baeumner, J. Wegener, "Laser-scribed graphene (LSG) as new electrode material for impedance-based cellular assays" *Sensors Actuators B Chem.* **2020**, *321*, 128443.
- 133 M. G. Stanford, K. Yang, Y. Chyan, C. Kittrell, J. M. Tour, "Laser-Induced Graphene for Flexible and Embeddable Gas Sensors" *ACS Nano* **2019**, *13*, 3474–3482.
- 134 E. R. Mamleyev, S. Heissler, A. Nefedov, P. G. Weidler, N. Nordin, V. V. Kudryashov, K. Länge, N. MacKinnon, S. Sharma, "Laser-induced hierarchical carbon patterns on polyimide substrates for flexible urea sensors" *npj Flex. Electron.* **2019**, *3*, 2.
- 135 M. G. Stanford, C. Zhang, J. D. Fowlkes, A. Hoffman, I. N. Ivanov, P. D. Rack, J. M. Tour, "High-Resolution Laser-Induced Graphene. Flexible Electronics beyond the Visible Limit" *ACS Appl. Mater. Interfaces* **2020**, *12*, 10902–10907.
- 136 C. Cheng, S. Wang, J. Wu, Y. Yu, R. Li, S. Eda, J. Chen, G. Feng, B. Lawrie, A. Hu, "Bisphenol A Sensors on Polyimide Fabricated by Laser Direct Writing for Onsite River Water Monitoring at Attomolar Concentration" *ACS Appl. Mater. Interfaces* **2016**, *8*, 17784–17792.
- 137 D. Wu, Q. Peng, S. Wu, G. Wang, L. Deng, H. Tai, L. Wang, Y. Yang, L. Dong, Y. Zhao, J. Zhao, D. Sun, L. Lin, "A Simple Graphene NH₃ Gas Sensor via Laser Direct Writing" *Sensors* **2018**, *18*, 4405.
- 138 H. Guo, J. Yan, L. Jiang, L. Qu, J. Yin, J. Lu, "Conductive Writing with High Precision by Laser-Induced Point-to-Line Carbonization Strategy for Flexible Supercapacitors" *Adv. Opt. Mater.* **2021**, *9*, 2100793.
- 139 Z. Peng, R. Ye, J. A. Mann, D. Zakhidov, Y. Li, P. R. Smalley, J. Lin, J. M. Tour, "Flexible Boron-Doped Laser-Induced Graphene Microsupercapacitors" *ACS Nano* **2015**, *9*, 5868–5875.
- 140 K.-H. Nam, M. Abdulhafez, E. Castagnola, G. N. Tomaraei, X. T. Cui, M. Bedewy, "Laser direct write of heteroatom-doped graphene on molecularly controlled polyimides for electrochemical biosensors with nanomolar sensitivity" *Carbon N. Y.* **2022**, *188*, 209–219.
- 141 J. Zhang, C. Zhang, J. Sha, H. Fei, Y. Li, J. M. Tour, "Efficient Water-Splitting Electrodes Based on Laser-Induced Graphene" *ACS Appl. Mater. Interfaces* **2017**, *9*, 26840–26847.
- 142 X. Duan, Y. Yao, M. Niu, J. Luo, R. Wang, T. Liu, "Direct Laser Writing of Functional Strain Sensors in Polyimide Tubes" *ACS Appl. Polym. Mater.* **2019**, *1*, 2914–2923.
- 143 Y. Chyan, R. Ye, Y. Li, S. P. Singh, C. J. Arnusch, J. M. Tour, "Laser-Induced Graphene by Multiple Lasing: Toward Electronics on Cloth, Paper, and Food" *ACS Nano* **2018**, *12*, 2176–2183.
- 144 P. Malinský, A. Macková, M. Cutroneo, J. Siegel, M. Boháčová, K. Klímová, V. Švorčík, Z. Sofer, "Laser modification of graphene oxide layers" *EPJ Web Conf.* **2018**, *167*, 04010.
- 145 K. C. Yung, H. Liem, H. S. Choy, Z. C. Chen, K. H. Cheng, Z. X. Cai, "Laser direct patterning of a reduced-graphene oxide transparent circuit on a graphene oxide thin film" *J. Appl. Phys.* **2013**, *113*, 244903.
- 146 "DuPont - Kapton Thermal Properties" can be found under <https://www.dupont.com/content/dam/dupont/amer/us/en/products/ei-transformation/documents/EL-10145-Kapton-Products-of-Decomposition.pdf>.
- 147 Y. Li, D. X. Luong, J. Zhang, Y. R. Tarkunde, C. Kittrell, F. Sargunaray, Y. Ji, C. J. Arnusch, J. M. Tour, "Laser-Induced Graphene in Controlled Atmospheres: From Superhydrophilic to Superhydrophobic Surfaces" *Adv. Mater.* **2017**, *29*, 1700496.
- 148 C. Wang, V. Strauss, R. B. R. B. Kaner, "Carbon Nanodots for Capacitor Electrodes" *Trends Chem.* **2019**, *1*, 858–868.
- 149 F. Bu, W. Zhou, Y. Xu, Y. Du, C. Guan, W. Huang, "Recent developments of advanced micro-supercapacitors: design, fabrication and applications" *npj Flex. Electron.* **2020**, *4*, 31.
- 150 M. F. El-Kady, Y. Shao, R. B. Kaner, "Graphene for batteries, supercapacitors and beyond" *Nat. Rev. Mater.* **2016**, *1*, 16033.
- 151 P. Simon, Y. Gogotsi, B. Dunn, "Where Do Batteries End and Supercapacitors Begin?" *Science (80-.).* **2014**, *343*, 1210–1211.
- 152 M. F. El-Kady, R. B. Kaner, "Scalable fabrication of high-power graphene micro-supercapacitors for flexible and on-chip energy

References

- storage" *Nat. Commun.* **2013**, *4*, 1475.
- 153 M. H. Amiri, N. Namdar, A. Mashayekhi, F. Ghasemi, Z. Sanaee, S. Mohajerzadeh, "Flexible micro supercapacitors based on laser-scribed graphene/ZnO nanocomposite" *J. Nanoparticle Res.* **2016**, *18*, 237.
- 154 A. P. O'Mullane, M. Escudero-Escribano, I. E. L. Stephens, K. Krischer, "The Role of Electrocatalysis in a Sustainable Future: From Renewable Energy Conversion and Storage to Emerging Reactions" *ChemPhysChem* **2019**, *20*, 2900–2903.
- 155 Z. J. Xu, X. Wang, "Electrocatalysis: A Core Technique for a Sustainable Future" *Chem. – A Eur. J.* **2020**, *26*, 3897–3897.
- 156 G. Zini, P. Tartarini, "Electrolysis and Fuel Cells" in *Sol. Hydrog. Energy Syst.*, Springer Milan, Milano, **2012**, pp. 29–52.
- 157 M. K. Debe, "Electrocatalyst approaches and challenges for automotive fuel cells" *Nature* **2012**, *486*, 43–51.
- 158 E. Roduner, "Selected fundamentals of catalysis and electrocatalysis in energy conversion reactions—A tutorial" *Catal. Today* **2018**, *309*, 263–268.
- 159 N. Govindarajan, G. Kastlunger, H. H. Heenen, K. Chan, "Improving the intrinsic activity of electrocatalysts for sustainable energy conversion: where are we and where can we go?" *Chem. Sci.* **2022**, *13*, 14–26.
- 160 D. He, H. Tang, Z. Kou, M. Pan, X. Sun, J. Zhang, S. Mu, "Engineered Graphene Materials: Synthesis and Applications for Polymer Electrolyte Membrane Fuel Cells" *Adv. Mater.* **2017**, *29*, 1601741.
- 161 J. Wang, H. Kong, J. Zhang, Y. Hao, Z. Shao, F. Ciucci, "Carbon-based electrocatalysts for sustainable energy applications" *Prog. Mater. Sci.* **2021**, *116*, 100717.
- 162 J. Zhang, M. Ren, L. Wang, Y. Li, B. I. Yakobson, J. M. Tour, "Oxidized Laser-Induced Graphene for Efficient Oxygen Electrocatalysis" *Adv. Mater.* **2018**, *30*, 1707319.
- 163 H. Jiang, L. Zheng, Z. Liu, X. Wang, "Two-dimensional materials: From mechanical properties to flexible mechanical sensors" *InfoMat* **2020**, *2*, 1077–1094.
- 164 S. Gong, W. Schwalb, Y. Wang, Y. Chen, Y. Tang, J. Si, B. Shirinzadeh, W. Cheng, "A wearable and highly sensitive pressure sensor with ultrathin gold nanowires" *Nat. Commun.* **2014**, *5*, 3132.
- 165 M. Amjadi, A. Pichitpajongkit, S. Lee, S. Ryu, I. Park, "Highly Stretchable and Sensitive Strain Sensor Based on Silver Nanowire–Elastomer Nanocomposite" *ACS Nano* **2014**, *8*, 5154–5163.
- 166 B. Wang, A. Thukral, Z. Xie, L. Liu, X. Zhang, W. Huang, X. Yu, C. Yu, T. J. Marks, A. Facchetti, "Flexible and stretchable metal oxide nanofiber networks for multimodal and monolithically integrated wearable electronics" *Nat. Commun.* **2020**, *11*, 2405.
- 167 S. Yao, Y. Zhu, "Wearable multifunctional sensors using printed stretchable conductors made of silver nanowires" *Nanoscale* **2014**, *6*, 2345.
- 168 D. Corzo, G. Tostado-Blázquez, D. Baran, "Flexible Electronics: Status, Challenges and Opportunities" *Front. Electron.* **2020**, *1*, DOI 10.3389/felec.2020.594003.
- 169 M. Zou, Y. Ma, X. Yuan, Y. Hu, J. Liu, Z. Jin, "Flexible devices: from materials, architectures to applications" *J. Semicond.* **2018**, *39*, 011010.
- 170 X. Wang, Y. Gu, Z. Xiong, Z. Cui, T. Zhang, "Silk-Molded Flexible, Ultrasensitive, and Highly Stable Electronic Skin for Monitoring Human Physiological Signals" *Adv. Mater.* **2014**, *26*, 1336–1342.
- 171 D. J. Lipomi, M. Vosgueritchian, B. C.-K. Tee, S. L. Hellstrom, J. A. Lee, C. H. Fox, Z. Bao, "Skin-like pressure and strain sensors based on transparent elastic films of carbon nanotubes" *Nat. Nanotechnol.* **2011**, *6*, 788–792.
- 172 X. Wang, W. Fu, G. Gao, M. S. Mehay, L. Zheng, H. Wang, W. Zhao, K. P. Loh, T. Zhang, W. Huang, Z. Liu, "Self-cross-linked arrays enabled flexible mechanical sensors for monitoring the body tremor" *npj Flex. Electron.* **2020**, *4*, 8.
- 173 C. Liao, M. Zhang, M. Y. Yao, T. Hua, L. Li, F. Yan, "Flexible Organic Electronics in Biology: Materials and Devices" *Adv. Mater.* **2015**, *27*, 7493–7527.
- 174 F. Zhang, Y. Zang, D. Huang, C. Di, D. Zhu, "Flexible and self-powered temperature–pressure dual-parameter sensors using microstructure-frame-supported organic thermoelectric materials" *Nat. Commun.* **2015**, *6*, 8356.
- 175 G. Ge, Y. Lu, X. Qu, W. Zhao, Y. Ren, W. Wang, Q. Wang, W. Huang, X. Dong, "Muscle-Inspired Self-Healing Hydrogels for Strain and Temperature Sensor" *ACS Nano* **2020**, *14*, 218–228.
- 176 P. Samori, V. Palermo, "Flexible Carbon-based Electronics" Wiley-VCH Verlag GmbH & Co. KGaA, Weinheim, Germany, **2018**.
- 177 A. Rakitin, C. Papadopoulos, J. M. Xu, "Carbon nanotube self-doping: calculation of the hole carrier concentration" *Phys. Rev. B* **2003**, *67*, 33411.
- 178 H. Kuzmany, W. Plank, M. Hulman, C. Kramberger, A. Grüneis, T. Pichler, H. Peterlik, H. Kataura, Y. Achiba, "Determination of SWCNT diameters from the Raman response of the radial breathing mode" *Eur. Phys. J. B - Condens. Matter Complex Syst.* **2001**, *22*, 307–320.
- 179 F. Wang, G. Dukovic, L. Brus, T. Heinz, "Time-Resolved Fluorescence of Carbon Nanotubes and Its Implication for Radiative Lifetimes" *Phys. Rev. Lett.* **2004**, *92*, 17–20.
- 180 P. H. Tan, A. G. Rozhin, T. Hasan, P. Hu, V. Scardaci, W. I. Milne, A. C. Ferrari, "Photoluminescence Spectroscopy of Carbon Nanotube Bundles: Evidence for Exciton Energy Transfer" *Phys. Rev. Lett.* **2007**, *99*, 137402.
- 181 Y. Gu, X. Wang, W. Gu, Y. Wu, T. Li, T. Zhang, "Flexible electronic eardrum" *Nano Res.* **2017**, *10*, 2683–2691.
- 182 Y. Yamamoto, S. Harada, D. Yamamoto, W. Honda, T. Arie, S. Akita, K. Takei, "Printed multifunctional flexible device with an
-

- integrated motion sensor for health care monitoring" *Sci. Adv.* **2016**, *2*, e1601473.
- 183 T. M. Swager, K. A. Mirica, "Introduction: Chemical Sensors" *Chem. Rev.* **2019**, *119*, 1–2.
- 184 A. J. Bhandarkar, J. Wang, "Non-invasive wearable electrochemical sensors: a review" *Trends Biotechnol.* **2014**, *32*, 363–371.
- 185 S. Mulmi, V. Thangadurai, "Editors' Choice—Review—Solid-State Electrochemical Carbon Dioxide Sensors: Fundamentals, Materials and Applications" *J. Electrochem. Soc.* **2020**, *167*, 037567.
- 186 X.-H. Zhao, S.-N. Ma, H. Long, H. Yuan, C. Y. Tang, P. K. Cheng, Y. H. Tsang, "Multifunctional Sensor Based on Porous Carbon Derived from Metal–Organic Frameworks for Real Time Health Monitoring" *ACS Appl. Mater. Interfaces* **2018**, *10*, 3986–3993.
- 187 Z. Meng, R. M. Stolz, L. Mendecki, K. A. Mirica, "Electrically-Transduced Chemical Sensors Based on Two-Dimensional Nanomaterials" *Chem. Rev.* **2019**, *119*, 478–598.
- 188 T. Hayasaka, A. Lin, V. C. Copa, L. P. Lopez, R. A. Loberternos, L. I. M. Ballesteros, Y. Kubota, Y. Liu, A. A. Salvador, L. Lin, "An electronic nose using a single graphene FET and machine learning for water, methanol, and ethanol" *Microsystems Nanoeng.* **2020**, *6*, 50.
- 189 L. Guo, T. Wang, Z. Wu, J. Wang, M. Wang, Z. Cui, S. Ji, J. Cai, C. Xu, X. Chen, "Portable Food-Freshness Prediction Platform Based on Colorimetric Barcode Combinatorics and Deep Convolutional Neural Networks" *Adv. Mater.* **2020**, *32*, 2004805.
- 190 R. S. Andre, R. C. Sanfelice, A. Pavinatto, L. H. C. Mattoso, D. S. Correa, "Hybrid nanomaterials designed for volatile organic compounds sensors: A review" *Mater. Des.* **2018**, *156*, 154–166.
- 191 W. Zhang, G. Li, H. Yin, K. Zhao, H. Zhao, T. An, "Adsorption and desorption mechanism of aromatic VOCs onto porous carbon adsorbents for emission control and resource recovery: recent progress and challenges" *Environ. Sci. Nano* **2022**, DOI 10.1039/D1EN00929J.
- 192 K. Kante, M. Florent, A. Temirgaliyeva, B. Lesbayev, T. J. Bandoz, "Exploring resistance changes of porous carbon upon physical adsorption of VOCs" *Carbon N. Y.* **2019**, *146*, 568–571.
- 193 Y. Jiao, S. W. Cho, S. Lee, S. H. Kim, S.-Y. Jeon, K. Hur, S. M. Yoon, M.-W. Moon, A. Wang, "A Hierarchically Porous Carbon Fabric for Highly Sensitive Electrochemical Sensors" *Adv. Eng. Mater.* **2018**, *20*, 1700608.
- 194 X. Zhang, B. Gao, A. E. Creamer, C. Cao, Y. Li, "Adsorption of VOCs onto engineered carbon materials: A review" *J. Hazard. Mater.* **2017**, *338*, 102–123.
- 195 H. Wang, S. Delacroix, A. Zieleniewska, J. Hou, N. V. Tarakina, D. Cruz, I. Lauermann, A. J. Ferguson, J. L. Blackburn, V. Strauss, "In Situ Synthesis of Molybdenum Carbide Nanoparticles Incorporated into Laser-Patterned Nitrogen-Doped Carbon for Room Temperature VOC Sensing" *Adv. Funct. Mater.* **2021**, *31*, 2104061.
- 196 A. Di Bartolomeo, "Graphene Schottky diodes: An experimental review of the rectifying graphene/semiconductor heterojunction" *Phys. Rep.* **2016**, *606*, 1–58.
- 197 M. Dosi, I. Lau, Y. Zhuang, D. S. A. Simakov, M. W. Fowler, M. A. Pope, "Ultrasensitive Electrochemical Methane Sensors Based on Solid Polymer Electrolyte-Infused Laser-Induced Graphene" *ACS Appl. Mater. Interfaces* **2019**, *11*, 6166–6173.
- 198 V. Strauss, K. Marsh, M. D. Kowal, M. F. El-Kady, R. B. Kaner, "A Simple Route to Porous Graphene from Carbon Nanodots for Supercapacitor Applications" *Adv. Mater.* **2018**, *30*, 1704449.
- 199 M. N. Lund, C. A. Ray, "Control of Maillard Reactions in Foods: Strategies and Chemical Mechanisms" *J. Agric. Food Chem.* **2017**, *65*, 4537–4552.
- 200 X. Wang, Y. Zhang, C. Zhi, X. Wang, D. Tang, Y. Xu, Q. Weng, X. Jiang, M. Mitome, D. Golberg, Y. Bando, "Three-dimensional strutted graphene grown by substrate-free sugar blowing for high-power-density supercapacitors" *Nat. Commun.* **2013**, *4*, DOI 10.1038/ncomms3905.
- 201 V. Strauss, M. Anderson, C. Wang, A. Borenstein, R. B. Kaner, "Carbon Nanodots as Feedstock for a Uniform Hematite-Graphene Nanocomposite" *Small* **2018**, *14*, 1803656.
- 202 "The Engineering Toolbox" .

List of Abbreviations

AC	activated carbon	IUPAC	International Union of Pure and Applied Chemistry
a-C	amorphous carbon	kW	kilowatt
Ade(380)	adenine annealed at 380°C	LC-M	laser-carbonized materials
AMH	alkali metal halide	LC-PI	laser-carbonized polyimide
at%	atomic percent	LIG	laser-induced graphene
CA	citric acid	LP-C	laser-patterned carbon
CA/U(300)	citric acid and urea annealed at 300°C	LP-NC	laser-patterned nitrogen-doped carbon
CLaP	carbon laser-patterning	LR-GO	laser-reduced graphene oxide
CND	carbon dot	MS	mass spectrometry
CNP	carbon nanoparticle	mEDLC	micro-electric double-layer capacitor
CNT	carbon nanotubes	mW	milliwatt
CQD	carbon quantum dot	MW	megawatt
CV	cyclic voltammetry	NC	nitrogen-doped carbon
CW	continuous wave	NMP	N-Methyl-2-pyrrolidone
Cyt(300)	cytosine annealed at 300°C	OER	oxygen evolution reaction
DC	direct current	ORR	oxygen reduction reaction
dpi	dots per inch	PAH	polyaromatic hydrocarbons
DVD	digital versatile disc	PAN	polyacrylonitrile
EA	elemental analysis	PANI	polyaniline
EDL	electric double layer	PEM	proton exchange membrane
EDLC	electric double-layer capacitor	PET	polyethylene terephthalate
EDX	energy dispersive X-ray analysis	PCA	principle component analysis
EELS	electron energy loss spectroscopy	PDMS	poly-dimethylsiloxane
EPR	electron paramagnetic resonance	PI	polyimide
FT	Fourier-transformation	PVP	polyvinylpyrrolidone
FT-IR	Fourier-transform infrared spectroscopy	RF	radio frequency
Glu(300)	Glucose annealed at 300°C	rGO	reduced graphene oxide
GO	graphene oxide	RTP	rapid thermal processing
HAT-CN	hexaazatriphenylene-hexacarbonitrile	SDA	structure directing agent
HER	hydrogen evolution reaction	SEM	scanning electron microscope
HOPG	highly ordered pyrolytic graphite	SEM	scanning electron microscopy
HOR	hydrogen oxidation reaction	SSA	specific surface area
HRTEM	high-resolution transmission electron microscopy/microscope	TEM	transmission electron microscope
HTC	hydrothermal carbonization	U	urea
IC	internal conversion	VOC	volatile organic compounds
IR	infrared	VOC	volatile organic compound
		wt%	weight percent

Appendix – Publications

S1. Laser-Induced Carbonization of Natural Organic Precursors for Flexible Electronics

S. Delacroix, H. Wang, T. Heil, V. Strauss, *Adv. Electron. Mater.* **2020**, *6*, 2000463.

S2. Carbon nanodots revised: the thermal citric acid/urea reaction

V. Strauss, H. Wang, S. Delacroix, M. Ledendecker, P. Wessig, *Chem. Sci.* **2020**, *11*, 8256–8266.

S3. Laser-carbonization: Peering into the formation of micro-thermally produced (N-doped)carbons

H. Wang, S. Delacroix, O. Osswald, M. Anderson, T. Heil, E. Lepre, N. Lopez-Salas, R. B. Kaner, B. Smarsly, V. Strauss, *Carbon* **2021**, *176*, 500–510.

S4. Using Carbon Laser Patterning to Produce Flexible, Metal-Free Humidity Sensors

S. Delacroix, A. Zieleniewska, A. J. Ferguson, J. L. Blackburn, S. Ronneberger, F. F. Loeffler, V. Strauss, *ACS Appl. Electron. Mater.* **2020**, *2*, 4146–4154.

S5. In Situ Synthesis of Molybdenum Carbide Nanoparticles Incorporated into Laser-Patterned Nitrogen-Doped Carbon for Room Temperature VOC Sensing

H. Wang, S. Delacroix, A. Zieleniewska, J. Hou, N. V. Tarakina, D. Cruz, I. Lauermann, A. J. Ferguson, J. L. Blackburn, V. Strauss, *Adv. Funct. Mater.* **2021**, 2104061.

S6. Tuning the Surface Properties of Porous Laser-Patterned Carbon with ZnO Hard-Templates for Selective Room Temperature VOC Sensing

H. Wang, P. Jiménez-Calvo, M. Hepp, M. Isaacs, I. Below-Lutz, B. Butz, V. Strauss, *ACS Appl. Nano Mater.* **2023**, *6*, 2, 966–975.

S7. Trained Laser-Patterned Carbon for High-Performance Mechanical Sensors

M. Hepp, H. Wang, K. Derr, S. Delacroix, S. Ronneberger, F. Loeffler, B. Butz, V. Strauss, *npj Flex. Electron.* **2022**, *6*, 3.

S8. Flexible CO₂ sensor architecture with selective nitrogen functionalities by one-step laser-induced conversion of versatile organic ink

H. Wang, C. Otieno Ogolla, G. Panchal, M. Hepp, S. Delacroix, D. Cruz, D. Kojda, Jim Ciston, Colin Ophus, A. Knop-Gericke, K. Habicht, B. Butz, V. Strauss, *Adv. Funct. Mater.* **2022**, *32* (51), 2207406.

S9. Modulating between 2e⁻ and 4e⁻ pathway in the oxygen reduction reaction with laser-synthesized iron oxide-grafted nitrogen-doped carbon

H. Wang, M. Jerigova, J. Hou, N. Tarakina, S. Delacroix, N. Lopez-Salas, V. Strauss, *J. Mater. Chem. A* **2022**, *10*, 24156-24166.

S10. Fast response electrochemical capacitor electrodes created by laser-reduction of carbon nanodots

V. Strauss, M. Anderson, C. L. Turner, R. B. Kaner, *Mater. Today Energy* **2019**, *11*, 114–119.

S11. Patching laser-reduced graphene oxide with carbon nanodots

V. Strauss, M. Muni, A. Borenstein, B. Badamdorj, T. Heil, M. D. Kowal, R. Kaner, *Nanoscale* **2019**, *11*, 12712–12719.

S12. On-chip Direct Laser Writing of PAN-based Carbon Supercapacitor Electrodes

A. Hoffmann, P. Jiménez-Calvo, V. Strauss, A. J. C. Kuehne, *Macromol. Rapid Commun.* **2022**, 2100731.

Laser-Induced Carbonization of Natural Organic Precursors for Flexible Electronics

Simon Delacroix, Huize Wang, Tobias Heil, and Volker Strauss*

A precursor ink for carbon laser-patterning is developed using inexpensive, naturally abundant molecular compounds, namely citric acid and urea, and used to fine-print conductive carbon circuits on a flexible substrate. The precursor in the ink consists of organic nanoparticles obtained from the thermal treatment of citric acid and urea. This precursor is thoroughly characterized chemically and structurally. A simple recipe for the ink is then described for the creation of highly reproducible laser-patterned carbon structures on different substrates. Homogeneous ~ 20 μm thick films are cast on different substrates and characterized before and after laser-carbonization. The carbon content of the final films is 97% and is of turbostratic graphitic nature. As reproducible laser-induced reactions depend on precise laser conditions, the influence of material properties, film thickness, and laser fluence are thoroughly analyzed. Films on three different substrates, namely aluminum sheets, silicon wafers, and polyethylene terephthalate (PET) are characterized by electrical impedance measurements. Electrical conductivities of up to 5.21 S cm^{-1} and maximum current densities of 44 A cm^{-2} are achieved, which proved applicable as fine carbon circuits on PET as a flexible substrate. This study opens a simple synthetic avenue to producing conductive circuit elements based on carbon.

1. Introduction

New fabrication methods for functional materials have driven the development of innovations and new products ever since. In fact, the industrial and commercial application and innovation of new products strongly depends on the identification of new processing methods. In particular, with respect to the processing and applicability of carbon nanomaterials (CNM), such as carbon nanotubes, graphene, and their relatives, new fabrication concepts are required.^[1,2] Although CNMs find commercial applications in, for example, electrochemical sensors or energy storage, they still fall short in expectations in commercial electronics in general.^[3,4] On top of that, it is a desirable goal to

replace toxic, expensive, or conflict materials with environmentally and socially more benign CNMs. Therefore, they are still considered promising candidates for a range of future applications in electronics, optoelectronics, or catalytic systems.


Laser-fabrication methods have been investigated as fast, energy-saving, low-cost, and precise material processing techniques in both science and industry and even a new “age of photon-driven materials manufacturing” has been prognosed.^[5] In industry, laser-processing techniques are mainly used for cutting, welding, cladding, or surface processing.^[6] It allows for high-precision materials modifications with unprecedented accuracy, not only spatially but also temporally, which is of particular interest for the manufacturing of future small-scale electronic and photonic products.

Also direct laser-induced materials synthesis has become an active field of research. For example, laser-induced ablation of graphite, discovered in the 1990s, is

commonly used for the targeted synthesis of CNMs.^[7,8] High-power laser pulses hit a graphite target and create a carbon plasma above the surface, which reacts to crystalline nanocarbons. These laser-assisted synthesis methods differ from conventional thermal methods in the reaction time-scales. Heat transfer within micro- or milliseconds allows for reactions different to conventional heating methods.

Moreover, the precise spatial control with nano- to micrometer resolutions allows also for the fine patterning of materials. Generally, laser-patterning describes the micro-structuring of organic materials like polymers or plastics by evaporating material from their surface.^[9] Directed 2D-film patterning by laser-induced material conversion evolved in the past years as a new synthetic fabrication method.^[10] In particular, the uncomplicated access to laser-assisted patterning of graphene oxide and their relatives has given the field a significant push.^[11–18] In most cases, graphene is produced by laser-induced reduction of graphene oxide (GO). Another famous laser-patternable material is polyimide (PI), which carbonizes at high temperatures.^[19–21] Vast research efforts have been conducted on the characterization and application of laser-patterned GO or PI films.^[22–24] However, the starting materials used are rather expensive and the modification of the resulting materials properties is limited since the starting materials are polymeric. Other materials could be used as precursor like paper or wood but without the possibility of choosing the initial substrate.^[25]

Dr. S. Delacroix, H. Wang, Dr. T. Heil, Dr. V. Strauss
Department of Colloid Chemistry
Max-Planck-Institute of Colloids and Interfaces
Am Mühlenberg 1, Potsdam 14476, Germany
E-mail: volker.strauss@mpikg.mpg.de

 The ORCID identification number(s) for the author(s) of this article can be found under <https://doi.org/10.1002/aelm.202000463>.

© 2020 The Authors. Published by Wiley-VCH GmbH. This is an open access article under the terms of the Creative Commons Attribution License, which permits use, distribution and reproduction in any medium, provided the original work is properly cited.

DOI: 10.1002/aelm.202000463

A promising alternative starting material recently identified is phenolic resin,^[26,27] but molecular starting materials are in fact rarely used. Most organic substances evaporate upon heat treatment with lasers due to the rapid heating to temperatures to well above 1000 °C in just a few milliseconds.

It has to be noted that laser-assisted material modification depends on several parameters, such as laser wavelength, power and energy density, absorptivity, and thermal conductivity of the active material and the substrate. The wavelength is critical for the interaction with the active material and the substrate. For example, a clear advantage of CO₂ lasers is the large penetration depth compared to short-wavelength lasers. A disadvantage, on the other hand, is the rather poor printing resolution due to the long wavelength. Power and energy density are governed by the spot size, the resolution, the laser power, and the scanning speed. The latter two are a result of the chemical and compositional properties of the materials. Therefore, a careful consideration of all these parameters has to be taken when applying laser treatment for materials modifications.

Recently, we identified an inexpensive molecular precursor system that was processed to an ink for laser-assisted carbonization to yield highly conductive carbon networks.^[28] In brief, citric acid and urea are pre-carbonized in an annealing process at 300 °C. Inks produced from their reaction product in viscous solvents were applied onto different substrates and subsequently treated with a CO₂ laser to obtain fully carbonized films. Notably, this carbon laser-processing method does not require the use of catalysts. It became a question of scientific value what makes a precursor system laser-carbonizable as most organic substances evaporate in the high temperature reaction zone of a CO₂ laser.

We take this as a motivation to investigate the components of the inks and systematically investigate the laser-assisted carbonization process. First, we characterized the carbon precursor spectroscopically and microscopically in terms of composition and properties. We present a recipe for the production of a suitable ink and discuss the role of the laser-parameters to produce carbonized films on different substrates. The films were then characterized in terms of structure, composition, and electrical properties in order to make it applicable in thin film electronics.

2. Results and Discussion

2.1. Preparation of the Carbon Precursor

As demonstrated in earlier studies and in the literature, certain materials are suitable as precursors for laser-carbonization reactions. In contrast to conventional heating where carbonization is achieved within minutes or hours, laser-carbonization occurs on a time scale of milliseconds. On this fast time scale, even oxidation reactions by atmospheric oxygen are largely suppressed;^[29,30] however, most organic materials, especially low-molecular-weight compounds evaporate without forming conductive carbon networks. It is still an open question what materials qualify for laser-carbonizations. In our studies, we found that a carbon precursor ink consists of three main components: the carbon-network forming agent (CNFA), the film-forming agent (FFA), and a solvent. In case of polymeric

precursors, the CNFA and FFA are combined in one structure. The FFA is an optional component for improving the wetting and processing properties of the ink.

In the first step, a precursor acting as a CNFA for the laser-assisted carbonization was prepared. A 1:1 mass mixture of citric acid and urea was annealed at 300 °C in a chamber oven producing a solid black foam referred to as CAU300. We refer to this process as pre-carbonization, due to the fact that the carbon content is increased from originally 33% in a 1:3 citric acid/urea mixture to 49% in the precursor for the laser process. The product was ground to a powder and further purified by a multistep washing process in H₂O at 95 °C. The supernatant contains molecular intermediates, which are soluble in H₂O. After two washing steps in H₂O at 95 °C, the supernatant appears still brown but the apparent fluorescence turns from green to blue (Figure 1a). In the first washing step, unreacted low-molecular-weight intermediates were removed from the reaction product as shown in the ¹H-NMR patterns of the supernatants (Figure 1b). The dominant peaks at 5.39 and 9.84 originate from a green fluorophore: 4-hydroxy-1H-pyrrolo[3,4-c]pyridine-1,3,6(2H,5H)-trione (HPPT).^[31] Only traces of these intermediates are found after the second washing step. The same supernatants were probed by UV-vis absorption spectroscopy. In the supernatant of the first washing step, a strong molecular absorption with maxima at 330 and 407 nm appear, which are assigned to the absorption of HPPT (Figure 1c). These absorption features appear as weak peaks in the supernatants of the subsequent washing steps. A closer look reveals a significant red-shift of these peaks after washing. For example, in the supernatants of washing steps 4 and 5, the second maximum appears red-shifted by 18 nm at 425 nm. The absorption features correlate to fluorescence in the visible. After the first washing step, the fluorescence intensity is significantly reduced and notably shifted to the blue (Figure S1, Supporting Information). A trailing absorption into the long wavelength region, between 500 and 900 nm, becomes more pronounced indicating the presence of dispersed particles. The low-intensity feature at 369 nm stems from the particles and may be assigned to an intra-particle charge-transfer band.

After five washing steps, the remaining mass amounts to ~85% of the original mass. This product, referred to as CAU300p (precipitate), was further characterized. Elemental analysis of CAU300p yields 49% C, 20% N, 3% H, and 28% O. The weight loss of CAU300 and CAU300p during heating of the sample in inert atmosphere (Figure 1g) was analyzed. For CAU300, a weight loss of ~3% in the low temperature regime <150 °C is ascribed to adsorbed H₂O. At 343 °C, a large weight loss peak is assigned to HPPT, which amounts 15% of the sample. A further mass loss of 30% is noted in the temperature range between 300 and 800 °C, which is assigned to CAU300p. The residual mass at 1000 °C is 46% of the original weight. Notably, the thermogravimetric analysis of purified CAU300p shows an even more pronounced mass loss due to adsorbed H₂O accounting for ~10% of the original weight. The residual mass is 40% of the original mass. This large decomposition temperature range and the rather large residual mass indicate polymerization at high temperatures.

After drying, the material appears as a light-weighted black powder that is finely dispersible in a range of solvents

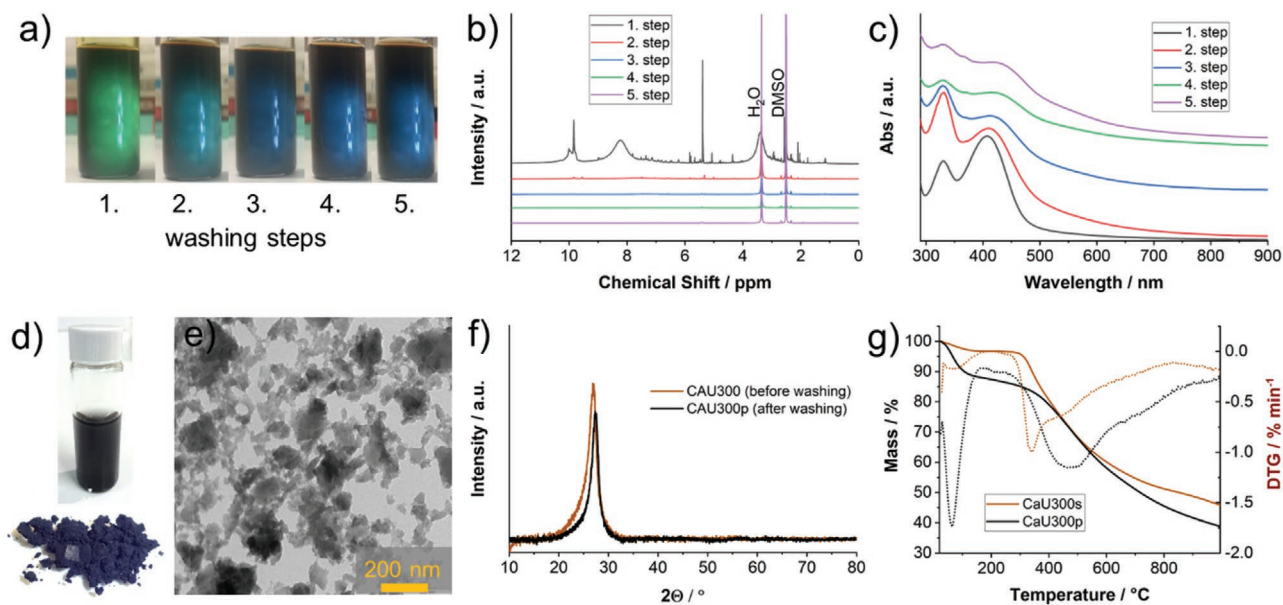


Figure 1. Characterization of CAU300p. a) Photographs depicting the aqueous supernatants after each washing step; b) ¹H-NMR patterns of the supernatants after each washing step in DMSO-d₆; c) UV/vis absorption spectra of the supernatants after each washing step; d) photograph of purified CAU300p (bottom) and freshly dispersed in H₂O; e) TEM image of CAU300p; f) powder X-ray diffraction patterns of CAU300 and CAU300p; g) thermogravimetric analysis of CAU300 and CAU300p.

(Figure S2, Supporting Information). Notably, after 24 h in H₂O or methanol, the solid particles start to settle and the liquid phase turns weakly brown. This color change comes together with a blue fluorescence like the one observed during the last washing step of the process. In dimethyl sulfoxide (DMSO) and dimethylformamide (DMF), CAU300p appears well stabilized, as no solid phase was formed during centrifugation. This difference of dispersibility of CAU300p in water or DMSO is confirmed by dynamic light scattering (DLS) and transmission electron microscopy (TEM) measurements. At 20 °C, the dispersion of CAU300p in water or DMSO showed particles with mean sizes of 240 ± 12 or 5.5 ± 3.5 nm, respectively. The sample in the TEM image in Figure 1e was prepared from an aqueous dispersion of CAU300p and shows amorphous carbonaceous networks. Preparing the same sample from a DMSO solution, finely dispersed individual particles with sizes of 3–8 nm throughout the entire scanned area are seen (Figure S3, Supporting Information). We attribute this effect to the basicity of solvents like DMSO and DMF and their ability to stabilize acidic particles.

In the powder X-ray diffraction (XRD) pattern, a single sharp peak at $26.9^\circ 2\theta$ (Figure 1f) is observed. The peak position indicates a typical graphitic (002) reflection corresponding to a lattice spacing of 3.33 Å. With regard to the peak width and according to the Scherrer-equation the crystallite size is $\approx 5\text{--}6$ nm.

Taking the aforementioned results into concert, we assume an organic particulate structure of CAU300p. The sizes of these nanoparticles are on the order of a few nanometers as determined by TEM and DLS analysis. In most solvents, these nanoparticles aggregate to larger structures. In basic solvents such as DMSO or DMF, the particles are individually stabilized. Structurally, the sample is predominantly amorphous

with small crystalline domains. The green fluorophore HPPT formed during the thermal reaction is present in the product after annealing at 300 °C. Harsh washing conditions remove free HPPT from the product. However, as indicated by the presence of their absorption features in UV-vis spectroscopy, some HPPT may remain in CAU300p and may even be a main component. However, the strong red-shifts indicate a significant electronic interaction with other components. It seems likely that the insoluble CAU300p results as a thermal product from the decomposition or condensation of HPPT.

2.2. Preparation of the Carbon Ink and Printing

Our standard precursor ink is composed of CAU300p (48 wt%), polyvinylpyrrolidone 1000 (PVP) (8 wt%), and ethylene glycol (EtGly) (44 wt%). The first acts as a CNFA, the second as a FFA, and the last is a viscous, non-reactive solvent.

The films were prepared by doctor-blading the ink onto different substrates with a preset wet film thickness (i.e., 50–150 μm). The solvent was carefully evaporated at 80 °C on a precision hotplate. The mass loss during solvent evaporation was monitored for all substrates and found to be consistently $44 \pm 2\%$ of the original mass, which accounts for the content of ethylene glycol. The final film thickness depends on the substrate and ranges between 15–40 μm resulting in areal mass loadings of 1–4 mg cm⁻² (Table 1). In Figure 2, a scanning electron micrograph (SEM) of the dried film cast from our standard CAU300p/PVP/EtGly precursor ink onto aluminum is presented. Upon evaporation of the solvent, cracks of <2 μm in the film evolve; however, these cracks are homogeneous across the entire film (Figure 2b, left). The Raman spectrum of these films shows two broad coalescing peaks at 1350 and 1590 cm⁻¹

Table 1. Quantitative analysis of the precursor and carbonized films in terms of film thickness and mass density and results of the impedance measurements of laser-carbonized films on different substrates.

	Film thickness [μm]	Areal mass density [mg cm^{-2}]	Volumetric mass density [mg cm^{-2}]	Fluence [J cm^{-2}]	Mass loss [%]	Resistivity [$\Omega \text{ cm}$]	Conductivity [S cm^{-1}]	Current limit [mA]	Max. current density [A cm^{-2}]
Al-1	19	1.29	677	7.1	43	0.23	4.38	3.6	38
Al-2	24	1.42	592	7.1	56	0.23	4.33	2.6	22
Al-3	19	1.31	704	3.8	18	—	—	—	—
Al-4	22	1.73	799	9.5	69	0.27	3.72	4.1	38
Si-1	22	3.13	1422	7.1	44	0.19	5.21	4.85	44
Si-2	38	3.87	1027	7.1	32	0.56	1.80	4.1	14
Si-3	25	3.16	1263	3.8	23	—	—	—	—
Si-4	22	3.10	1388	9.5	81	—	—	—	—
PET-1	20	0.95	467	7.1	76	0.74	1.35	1.10	10.9
PET-2	22	1.36	627	7.1	81	0.33	3.06	2.35	22
PET-3	24	1.69	706	3.8	10	—	—	—	—
PET-4	24	1.40	581	9.5	2554	—	—	—	—

indicating the presence of small graphitic domains (compare XRD in Figure 1).

After laser-treatment, the film appears with a metallic gleam, as shown in Figure 2b right. The SEM image in Figure 2c reveals a foam-like appearance with a hierarchical pore structure. The elemental analysis, tested by energy dispersive X-ray analysis (EDX) at seven different areas, yields a composition of $97 \pm 0.2\%$ carbon and $3 \pm 0.2\%$ oxygen (Figure S4, Supporting Information). The Raman spectrum of the laser-treated film (below) shows a pattern typically observed in turbostratic graphite samples.^[32] Most prominent are two sets of peaks at 1336, 1564, and 1602 cm^{-1} and 2430, 2666, and 2906 cm^{-1} . The first set is composed of the D, G, and D' bands and the latter set is composed of the D+D', G', and D+G bands. The pronounced D and D' bands indicate the presence of defects in the graphitic lattice. The G' band was fit with a single Lorentzian with an FWHM of 49 cm^{-1} underlining the turbostratic nature of the graphitic network. To obtain a closer visual insight into the structure of the

laser-carbonized films, a TEM image of a fragment of the film is shown in Figure 2d. A crystalline, porous structure with pore sizes between a few tens and a few hundreds of nanometers is clearly visible. High-resolution TEM images and selected area electron diffraction (SAED) reveal lattices fringes characteristic for graphitic layers and a disordered, turbostratic crystal orientation (Figure S5, Supporting Information). The interplanar distance measured from the lattice fringes is around 3.4 \AA , which corresponds to the interlayer spacing of the graphitic samples.

A reaction mechanism of the laser-induced carbonization has been discussed earlier.^[28,29] In brief, pre-carbonized organic nanoparticles containing significant amounts of functional groups are reduced in the hot reaction zone induced by the laser. Upon rapid cooling, these reduced nanoparticles form carbon-carbon bonds which results in a porous 3D-carbon network. Here, we would like to elucidate on the influence of some process parameters, like film thickness, absorptivity, laser fluence, and substrates.

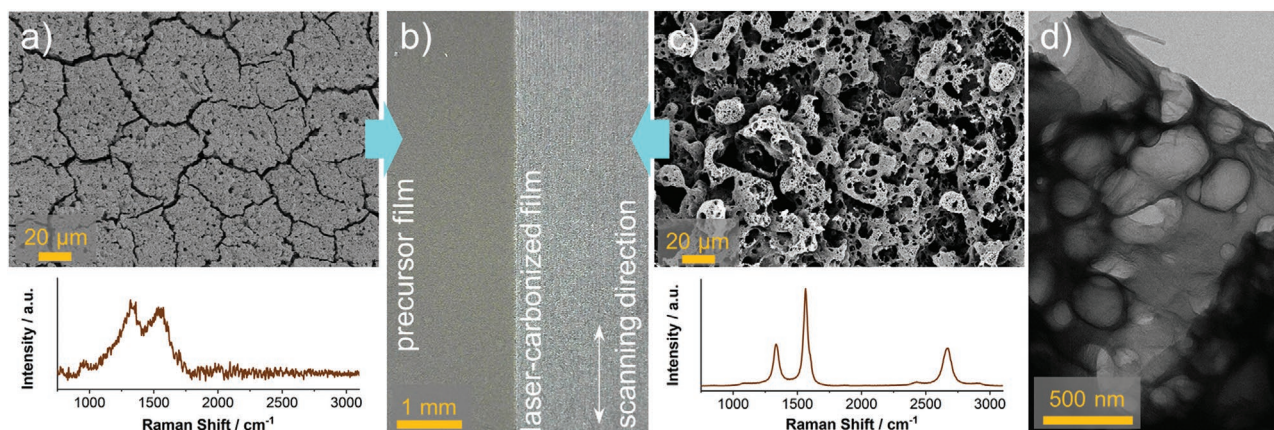


Figure 2. Characterization of films: doctor-bladed precursor films (CAU300p/PVP) and laser-carbonized films on aluminium sheets. a) SEM image of a CAU300p/PVP film and a corresponding Raman spectrum recorded upon excitation at 532 nm; b) low-magnification micrograph showing the precursor film on the left and the laser-carbonized film on the right; c) SEM image of a laser-carbonized CAU300p/PVP film and a corresponding Raman spectrum recorded upon excitation at 532 nm; d) TEM image of a fragment of the laser-carbonized CAU300p/PVP film.

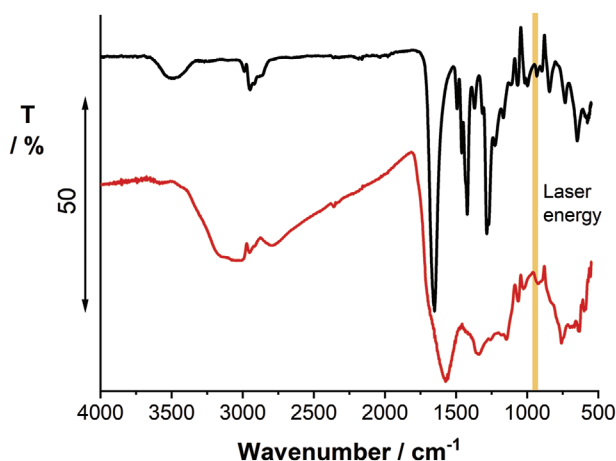


Figure 3. FT-IR spectra of PVP (black) and CAU300p (red). The orange line indicates the laser energy of the CO₂ laser corresponding to 10.6 μm.

A critical parameter for an effective heat transfer from the laser beam to the precursor film is the absorptivity of the laser energy (Figure 3). CAU300p shows a significant laser absorptivity at the characteristic laser energy while the absorptivity of PVP, the film forming agent, is negligible. High absorptivity leads to higher amount of heat transferred from the laser to the precursor material. Thus, for high extinction materials, a successful carbonization is achieved at lower energy input. The extinction coefficient of CAU300p at the laser wavelength 943 cm⁻¹ (10.6 μm) was experimentally determined by transmission Fourier-transform infra-red (FT-IR) absorption spectroscopy to be 0.56 L (g cm⁻¹). Given a mass loading of, for example, 1.3 mg cm⁻² and a thickness of 20 μm, the laser light is absorbed to 81.3% by the film according to the Lambert–Beer law. For a smaller film thickness of, for example, 5 μm and the same volumetric mass loading, the laser light would only be absorbed by 34.2%. That implies that the initial energy density of 5.6 J cm⁻² is reduced to ≈50% after a penetration depth of 8 μm. It has to be taken into account that despite the successful laser-induced carbonization reaction, a significant fraction of precursor material evaporates due to heat absorption.

We tested the penetration depth on a thick precursor film with a mass loading of 4.04 mg cm⁻² prepared on a 11 × 25 cm quartz slide. The quartz slide acts as a flat and solid support for the precursor film during the micro-computer tomography (μ-CT) measurement. The images in Figure S6, Supporting Information, show slices of a μ-CT scan of the precursor film before (left) and after (right) laser treatment. From these scans, a film thickness of 75 μm for the precursor film was obtained. Using a manual digital micrometer (MDM), the thickness was measured to be 73 μm. For the laser-carbonized film, a thickness of 36 μm was obtained from the μ-CT scans, whereas the measurement with the MDM yielded 73 μm.

Considering the high mass loading of 4.04 mg cm⁻² on the quartz slide and the extinction coefficient of the precursor film (0.56 L (g·cm)⁻¹), 92.4% of the laser energy is absorbed after a penetration depth of 35 μm (simplified by Lambert–Beer law). The laser-converted films are highly porous, as seen in the SEM images, and are expected to have a low contrast in the μ-CT scans. Therefore, we conclude that the 36 μm film observed

in the μ-CT scan in Figure S6, Supporting Information, on the right is the remaining unconverted precursor film. The laser-converted film is on top but cannot be seen in the tomograms.

Besides absorptivity, also the heat conductivity of the precursor film and the substrate has to be taken into account. The carbonization reaction from CAU300p to a conductive carbon network, as observed in Figure 2c, occurs in the hot plasma produced in the laser spot, but heat is dissipated across the film. High heat conductivity of the precursor or the substrate is expected to result in higher carbonization yield in the laser spot. To test the influence of the substrate, films with different thicknesses on aluminum sheets, silicon wafers, and polyethylene terephthalate (PET) were prepared by doctor blading. Aluminum sheets are flexible metal substrates with a high thermal conductivity (237 W (m·K)⁻¹) and high transparency for the laser beam.^[33] Silicon wafers are insulating substrates with high thermal conductivities (149 W (m·K)⁻¹) and high reflectivity at the wavelength of the laser beam. In contrast, PET is a flexible substrate with a low thermal conductivity (0.24 W (m·K)⁻¹) and a high absorptivity at the wavelength of the laser beam.

The energy density (fluence) of the laser beam onto the film is dependent on the laser parameters, such as effective output power, scanning speed, and resolution. Notably, these parameters are strongly instrument dependent. Based on the effective scanning speed and output power, we determined the effective fluences in our process to be in the range of 3–10 J cm⁻² (see Experimental Section). These values are slightly higher than typically used in laser-assisted micro and nanofabrication methods used for organic materials.^[5]

The thicknesses of the applied films measured by MDM were in the range between 19 and 60 μm resulting in areal or volumetric mass densities between 1 and 4 mg cm⁻² or 500 and 1500 mg cm⁻³ (Table 1). The different surface tension of the three chosen substrates causes different spreading across the area. For example, a higher volumetric mass density on Si-wafers is observed. Similar spreading properties were observed for aluminum or PET substrates. Notably, lower volumetric and higher areal mass densities were observed for thicker films. For all substrates, the areal mass density increases with higher film thickness. Application of the ink on PET results in thinner films, as spreading is facilitated by its low surface tension.

The films were irradiated with a CO₂ laser using different laser fluences. The mass loss scales with the film thickness and the effective energy density as shown in Table 1. Using the standard laser settings with an effective fluence of 7.1 J cm⁻² results in a mass loss of 43% on aluminum and 44% on Si-wafers. On PET, 76% mass loss is observed due to partial evaporation of the substrate. Higher fluence of, for example, 9.5 J cm⁻² causes larger amounts of material to evaporate during laser treatment. A special case is PET as a substrate, as high fluence leads to its evaporation. In fact, at an effective laser energy density of 9.5 J cm⁻², a significant amount of PET evaporates as evidenced by a mass loss of >2000%.

We tested the electric properties of the laser-carbonized films on the different substrates. Impedance measurements of films with an area of 15 × 20 mm were performed and the serial resistance *R* (Ω) was determined from the impedance values. In the tested frequency range between 0.1 Hz and 100 kHz, probed at a constant current of 0.1 mA, the films performed like

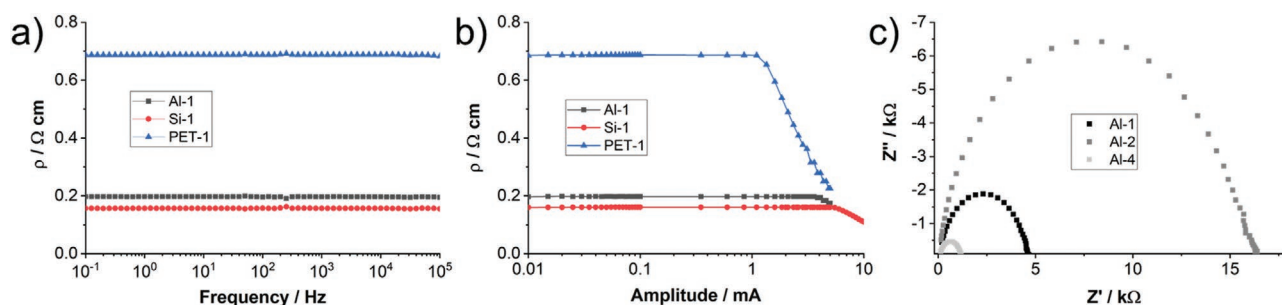


Figure 4. Resistance of the laser-carbonized CAU300p/PVP films in dependence of a) the frequency and b) the current amplitude obtained by impedance measurements on different substrates. c) Nyquist plots of laser-carbonized CAU300p/PVP films of different thicknesses on aluminium substrates.

ideal resistors (Figure 4a). From these measurements, sheet conductivities of $1.3\text{--}5.2\text{ S cm}^{-1}$ were determined. Up to frequencies of 100 kHz, no notable skin effect, that is, increase of resistance at higher frequencies upon current density redistribution, was observed. Last, the maximum current densities for the films were tested, as an important characteristic of conductors in electric or electronic systems for the films on the three chosen substrates. The resistance of the films with respect to the applied electric current densities is plotted against the AC current amplitudes in Figure 4b. Up to a certain threshold, the resistance of the films scales constant with the applied current. In general, the maximum current densities scale with the sheet conductivities. Typical values for maximum current densities of, for example, copper wires are $1 \times 10^5\text{ A cm}^{-2}$.

In Table 1, the above discussed results of the impedance measurements are summarized and the complete set of data is shown in Figure S7, Supporting Information. Here, some interesting effects are observed. Using standard laser fluence of 7.1 J cm^{-2} , the sheet conductivity on Si is significantly higher than on PET which could be attributed to the highest mass density. The conductivity is better if more precursor is reduced by the laser per square centimeter. For thicker films at this fluence, the sheet conductivity decreases, which is attributed to a larger unconverted layer. The lower layers remain unconverted and do not contribute to the overall conductivity of the film.

For aluminium, higher laser fluence leads to lower sheet conductivities, which are ascribed to higher material evaporation and thus lower resulting volumetric mass densities. In contrast to Si and PET as substrates, aluminum-supported films show good electric conductivity when irradiated with higher laser fluence of 9.5 J cm^{-2} , which can be explained by the higher transmissivity of aluminum for the laser beam.

To acquire insights into the interfacial charge transport between the carbonized film and the substrate, we measured the impedance between the carbon film and the aluminium substrate. The charge transfer resistance is expressed in the difference of the two intersections at the Z' -axis of the semicircle in the Nyquist plot (Figure 5c). Clearly, the charge transfer resistance scales with the film thickness as it is reduced from 16 200 (Al-2) to 4600 Ω (Al-1). Larger amounts of unconverted precursors at the film/substrate interface cause higher charge-transfer resistance through the film. Notably, when using higher laser fluences for the carbonization, a smaller charge-transfer resistance of only 1084 Ω is achieved (Al-4).

To demonstrate the applicability of the laser-carbonized films as electronic conductors, we applied precursor films on a PET substrate by doctor blading an area of $100 \times 50\text{ mm}$. Conducting paths with a width of 0.5 mm as shown in Figure 5 were printed by the laser-patterning technique. The remaining material was removed by rinsing with deionized H_2O . Thereby, only the laser-carbonized material remained on the substrate. The conducting path form a circuit connecting a white LED with a 6 V power supply. On one side of the circuit, two strips with a distance of 5 mm were connected by sandwiching with a counter piece, which equally consisted of two 0.5 mm strips separated by 5 mm. Upon applying pressure to the crossover of the two conducting carbon strips, the circuit was closed and the white LED was lit.

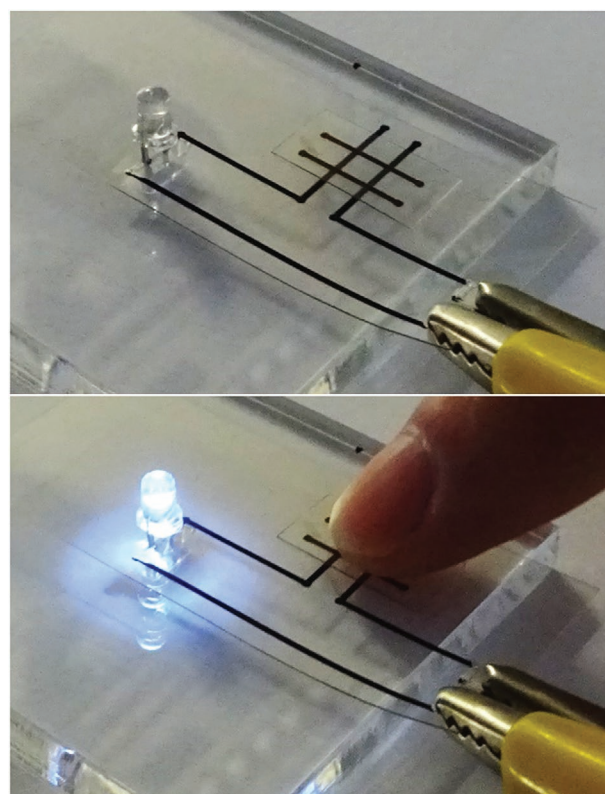


Figure 5. Photographs showing laser-patterned carbon conducting paths printed on a flexible, transparent PET substrate connecting an LED with a 6 V power supply being switched by applying pressure between the paths.

3. Conclusions

We have thoroughly investigated the laser-assisted carbonization reaction of inexpensive, small organic molecules, citric acid and urea. A pre-carbonization at 300 °C is necessary to form organic nanoparticles with an increased carbon content. We described a thorough workup and characterization of this pre-carbonized reaction product of citric acid and urea. A recipe for a precursor ink including these organic nanoparticles as carbon-network forming agents was introduced. Using this “standard ink,” we accomplished a full study on the reaction parameters of the laser-carbonization. Substrates, absorptivity, laser energy density, and film thickness were found to be highly critical parameters for the laser-carbonization process.

The results of this study help to gain an understanding of the criteria for laser-carbonizable materials. Printing fine patterns of conductive carbon on flexible substrates is possible, which makes this process generally attractive for flexible electronics. Fine-tuning of the carbon properties, like surface area and conductivity, will be essential for future applications and is currently under investigation.

4. Experimental Section

Chemicals: Citric acid (99.5% for analysis) and urea (Certified AR for analysis) were obtained from Fisher Scientific GmbH. Ethylene glycol ($\geq 99.7\%$, AnalaR Normapur) was obtained from VWR Chemicals. Polyvinylpyrrolidone (average mol wt. 10 000) was obtained from Sigma-Aldrich.

Substrates: Silicon wafers were obtained from MicroChemicals. Wafers used were either 4-in. boron-doped FZ-Si wafer, orientation (100), with a thickness of 0.5 mm and a generic resistivity of 3–100 k Ω cm or 4-in. FZ-Si wafer, orientation (100), with a thickness of 0.5 mm and a generic resistivity of 10–1000 k Ω cm. Aluminium foil used was 35 μ m thick. The PET substrate was Melinex sheets obtained from Plano GmbH.

Preparation of CAU300p: Citric acid and urea were thoroughly mixed in an alumina crucible or a glass crystallization dish. The vessel was covered with a lid to avoid spilling of the foaming reaction product, and to allow evaporation of evolving gases, a small opening under the lid was placed. The mixtures were annealed at 300 °C in a chamber oven for 2 h. After annealing, the black reaction product was retained and grinded to obtain a fine black powder. The mass of the product (CAU300) is 34% of the original mass of citric acid and urea. Then, CAU300 was dispersed in deionized H₂O and stirred at 95 °C for 24 h. The dispersion was centrifuged to obtain a black precipitate and a brown supernatant. The supernatant was removed and the washing process was repeated four times. After the last washing step, the precipitate was dried to obtain CAU300p, which amounted $\approx 85\%$ of the original mass.

Preparation of the Precursor Films: PVP was dissolved in EtGly to obtain a 200 mg mL⁻¹ solution (PVP/EtGly). CAU300p was then added and stirred for 24 h to obtain a 1 g L⁻¹ dispersion. The resulting slurry was used as a carbon precursor ink. A drop of the ink was applied onto the substrate and the ink was doctor bladed with different wet thicknesses between 50 and 150 μ m. Ethylene glycol was then evaporated at 80 °C on a precision hotplate (PZ2860-SR, Gestigkeit GmbH) to obtain the final films with thicknesses between 15 and 40 μ m.

Laser-Assisted Carbonization: Laser-assisted carbonization was conducted with a high-precision laser engraver setup (Speedy 100, Trotec) equipped with a 60 W CO₂ laser. Focusing was achieved with a 2.5 inch focus lens providing a focal depth of ≈ 3 mm and a focus diameter of 170 μ m. The center wavelength of the laser was 10.6 \pm 0.03 μ m. The scanning speed v , generically given in %, was converted

into s cm⁻². The resulting energy input per area (or fluence) onto the film is given by

$$F = P \times v = P \times \frac{t}{A} \quad (1)$$

where P is the effective power. The laser settings (speed, power, and resolution) were adjusted to meet the requirements of the precursor film and the substrate prior to the experiments (Figure S8, Supporting Information). Typically, 10% power, 20% speed, and a resolution of 1000 dpi were chosen, for which resulted a fluence of $F = 7.1 \frac{J}{cm^2}$. The effective output power of the laser was measured with a Solo 2 (Gentec Electro-Optics) power meter.

Instrumental: Scanning electron microscopy was performed on a Zeiss LEO 1550-Gemini system (acceleration voltage: 3 to 10 kV). An Oxford Instruments X-MAX 80 mm² detector was used to collect the SEM-EDX data. Transmission electron microscopy was performed using an EM 912 Omega from Zeiss operating at 120 kV. To prepare the TEM samples, the carbon material was dispersed in methanol by sonication for 10 min and applying 5 μ L droplets of the dispersion on a carbon-coated copper TEM grid and drying at room temperature. Thermogravimetric analysis was performed using a Thermo Microbalance TG 209 F1 Libra (Netzsch, Selb, Germany). A platinum crucible was used for the measurement of 10 ± 1 mg of samples in a nitrogen flow of 20 mL min⁻¹ and a purge flow of 20 mL min⁻¹ at a heating rate of 10 K min⁻¹. Elemental analysis was performed with a vario MICRO cube CHNOS elemental analyzer (Elementar Analysensysteme GmbH). The elements were detected with a thermal conductivity detector (TCD) for C, H, N, and O and an infrared (IR) detector for sulfur. UV–vis–NIR absorption measurements were performed with a Specord 210 plus from Analytik Jena using 10 mm quartz cuvettes. Fluorescence measurements were performed with a Fluoromax 4 from Horiba. Fourier-transform infrared measurements were performed using a Nicolet iS 5 FT-IR-spectrometer in conjunction with an iD5 ATR unit from ThermoFisher Scientific. Extinction coefficients were determined by measuring a series of transmission infra-red absorption spectra with known concentrations in the range between 1.6 and 7.8 g L⁻¹ pressed into KBr pellets. The absorbance was plotted against the concentration and the extinction coefficients were determined from the slope of the fitting curve. Raman spectra were obtained with a confocal Raman Microscope (alpha300, WITec, Germany) equipped with a piezo-scanner (P-500, Physik Instrumente, Karlsruhe, Germany). The laser, $\lambda = 532$ or 785 nm, was focused on the samples through a 20 \times objective. The laser power on the sample was set to 1.0 mW. The spectra were acquired using a thermoelectrically cooled CCD detector (DU401A-BV, Andor, Belfast, North Ireland) behind a 600 g mm⁻¹ grating spectrograph (UHTS 300, WITec, Ulm, Germany) with a spectral resolution of 3 cm⁻¹. The WITec Control Five software (Version 5.2, WITec, Ulm, Germany) was used for measurement setup. X-ray diffraction was performed on a Bruker D8 Advance diffractometer in the Bragg–Brentano mode at the Cu K α wavelength. Nuclear-magnetic resonance spectroscopy was measured on a 400 MHz Bruker Ascend400. Impedance measurements were performed on a Solartron 1287 potentiostat in combination with a SI 1260 impedance unit. For frequency measurements, the current was kept constant at 0.1 mA, and for current sweeps, a frequency of 1000 Hz was used. Dynamic light scattering was performed on a Zetasizer Nano ZS from Malvern Panalytical at 20 °C (He-Ne laser 633 nm). Micro-computer tomography (μ -CT) was performed on a EasyTom 160 3D Tomography System from RXSolutions. The scans were performed with a sealed microfocus tube equipped with a tungsten filament and a flat panel detector with a CsI (caesium iodide) scintillator. The wavelength of the generated X-rays was 1.5418 Å (Cu K α).

Associated Content: General and supplementary information on synthesis and characterization. Fluorescence spectroscopy of the supernatants during the washing process, photographs of suspensions, transmission electron micrographs, energy-dispersive X-ray analysis, micro-computer tomography measurements, and electrical impedance measurements.

Supporting Information

Supporting Information is available from the Wiley Online Library or from the author.

Acknowledgements

The authors thankfully acknowledge the permanent educational and the financial support from the Max Planck Society and the Fonds financial support from the Fonds der Chemischen Industrie. The authors thank Daniel Werner for performing micro-CT measurements micro-CT measurements, Heike Runge and Rona Pitschke for Microscopy, Antje Völkel for elemental analysis.

Conflict of Interest

The authors declare no conflict of interest.

Keywords

carbon circuits, electrical impedance, flexible electronics, laser carbonization, laser patterning

Received: April 30, 2020

Published online: September 3, 2020

- [1] M. F. L. De Volder, S. H. Tawfick, R. H. Baughman, A. J. Hart, *Science* **2013**, 339, 535.
- [2] R. Rao, C. L. Pint, A. E. Islam, R. S. Weatherup, S. Hofmann, E. R. Meshot, F. Wu, C. Zhou, N. Dee, P. B. Amama, J. Carpena-Nuñez, W. Shi, D. L. Plata, E. S. Penev, B. I. Yakobson, P. B. Balbuena, C. Bichara, D. N. Futaba, S. Noda, H. Shin, K. S. Kim, B. Simard, F. Mirri, M. Pasquali, F. Fornasiero, E. I. Kauppinen, M. Arnold, B. A. Cola, P. Nikolaev, S. Arepalli, et al., *ACS Nano* **2018**, 12, 11756.
- [3] *Nanocarbons for Advanced Energy Conversion* (Ed: X. Feng), Wiley-VCH Verlag, Weinheim **2015**.
- [4] *Nanocarbons for Electroanalysis* (Eds: S. Szunerits, R. Boukherroub, A. Downard, J.-J. Zhu), John Wiley & Sons, Chichester, UK **2017**.
- [5] *Laser-Assisted Fabrication of Materials* (Eds: J. D. Majumdar, I. Manna), Springer Series in Materials Science, Vol. 167, Springer, Berlin **2013**.
- [6] U. S. Springe, *Laser Fabrication and Machining of Materials*, Springer, Boston, MA **2008**.
- [7] Y. Zhang, H. Gu, S. Iijima, *Appl. Phys. Lett.* **1998**, 73, 3827.
- [8] Y. van de Burgt, *J. Laser Appl.* **2014**, 26, 032001.
- [9] W. Pfleging, R. Kohler, I. Südmeyer, M. Rohde, in *Laser-Assisted Fabrication of Materials* (Eds: J. D. Majumdar, I. Manna), **2013**, pp. 319–374.
- [10] D. Zhang, B. Gökce, S. Barcikowski, *Chem. Rev.* **2017**, 117, 3990.
- [11] R. Kumar, R. K. Singh, D. P. Singh, E. Joanni, R. M. Yadav, S. A. Moshkalev, *Coord. Chem. Rev.* **2017**, 342, 34.
- [12] V. Strong, S. Dubin, M. F. El-Kady, A. Lech, Y. Wang, B. H. Weiller, R. B. Kaner, *ACS Nano* **2012**, 6, 1395.
- [13] R. Trusovas, K. Ratautas, G. Račiukaitis, J. Barkauskas, I. Stankevičienė, G. Niaura, R. Mažeikienė, *Carbon N. Y.* **2013**, 52, 574.
- [14] W. Gao, N. Singh, L. Song, Z. Liu, A. L. M. Reddy, L. Ci, R. Vajtai, Q. Zhang, B. Wei, P. M. Ajayan, *Nat. Nanotechnol.* **2011**, 6, 496.
- [15] D. A. Sokolov, C. M. Rouleau, D. B. Geohegan, T. M. Orlando, *Carbon N. Y.* **2013**, 53, 81.
- [16] D. A. Sokolov, K. R. Shepperd, T. M. Orlando, *J. Phys. Chem. Lett.* **2010**, 1, 2633.
- [17] E. Ghoniem, S. Mori, A. Abdel-Moniem, *J. Power Sources* **2016**, 324, 272.
- [18] F. Wang, K. Wang, B. Zheng, X. Dong, X. Mei, J. Lv, W. Duan, W. Wang, *Mater. Technol.* **2018**, 33, 340.
- [19] A. Bürger, E. Fitzer, M. Heym, B. Terwiesch, *Carbon N. Y.* **1975**, 13, 149.
- [20] M. Inagaki, S. Harada, T. Sato, T. Nakajima, Y. Horino, K. Morita, *Carbon N. Y.* **1989**, 27, 253.
- [21] J. Lin, Z. Peng, Y. Liu, F. Ruiz-Zepeda, R. Ye, E. L. G. Samuel, M. J. Yacaman, B. I. Yakobson, J. M. Tour, *Nat. Commun.* **2014**, 5, 5714.
- [22] R. Ye, D. K. James, J. M. Tour, *Adv. Mater.* **2019**, 31, 1803621.
- [23] J. Bin In, B. Hsia, J.-H. Yoo, S. Hyun, C. Carraro, R. Maboudian, C. P. Grigoropoulos, *Carbon N. Y.* **2015**, 83, 144.
- [24] R. Ye, D. K. James, J. M. Tour, *Acc. Chem. Res.* **2018**, 51, 1609.
- [25] Y. Chyan, R. Ye, Y. Li, S. P. Singh, C. J. Arnusch, J. M. Tour, *ACS Nano* **2018**, 12, 2176.
- [26] M. Sopronyi, F. Sima, C. Vaultot, L. Delmotte, A. Bahouka, C. Matei Ghimbeu, *Sci. Rep.* **2016**, 6, 39617.
- [27] J. Liu, L. Zhang, C. Yang, S. Tao, *J. Mater. Chem. A* **2019**, 7, 21168.
- [28] V. Strauss, K. Marsh, M. D. Kowal, M. F. El-Kady, R. B. Kaner, *Adv. Mater.* **2018**, 30, 1704449.
- [29] V. Strauss, M. Anderson, C. L. Turner, R. B. Kaner, *Mater. Today Energy* **2019**, 11, 114.
- [30] Y. Li, D. X. Luong, J. Zhang, Y. R. Tarkunde, C. Kittrell, F. Sargunary, Y. Ji, C. J. Arnusch, J. M. Tour, *Adv. Mater.* **2017**, 29, 1700496.
- [31] W. Kasprzyk, T. Świergosz, S. Bednarz, K. Walas, N. V. Bashmakova, D. Bogdał, *Nanoscale* **2018**, 10, 13889.
- [32] L. M. Malard, M. a. Pimenta, G. Dresselhaus, M. S. Dresselhaus, *Phys. Rep.* **2009**, 473, 51.
- [33] L. Cui, H. J. Butler, P. L. Martin-Hirsch, F. L. Martin, *Anal. Methods* **2016**, 8, 481.

**ADVANCED
ELECTRONIC
MATERIALS**

Supporting Information

for *Adv. Electron. Mater.*, DOI: 10.1002/aelm.202000463

Laser-Induced Carbonization of Natural Organic Precursors
for Flexible Electronics

*Simon Delacroix, Huize Wang, Tobias Heil, and Volker
Strauss**

Supporting Information to

Laser-induced Carbonization of Natural Organic Precursors for Flexible Electronics

Simon Delacroix¹, Huize Wang¹, Volker Strauss^{1*}

Fluorescence spectroscopy of CAU300p	23
Suspension of CAU300p in Different Solvents.....	23
Transmission Electron Microscopy of the CAU300p	24
Energy-Dispersive X-ray Analysis of Laser-Carbonized Films.....	24
High-Resolution Transmission Electron Microscopy Laser-Carbonized Sample.....	25
Micro-Computer-Tomography Measurements	25
Impedance Measurements of Laser-Carbonized Films	26
Quantification of Laser-settings	27

Fluorescence spectroscopy of CAU300p

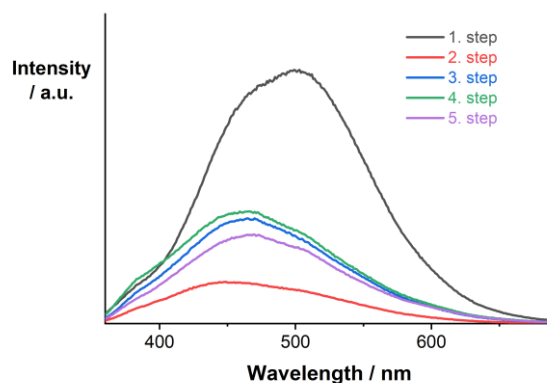


Figure S1. Fluorescence spectra of the supernatants after each washing step obtained in H₂O upon excitation at 350 nm.

Suspension of CAU300p in Different Solvents

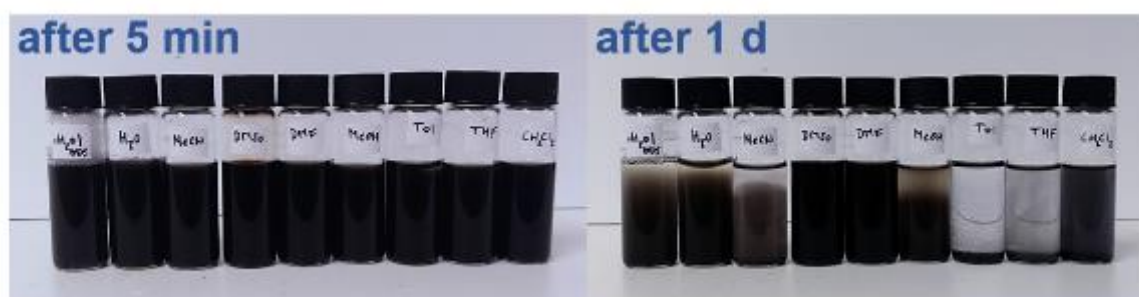


Figure S2. Photographs of suspensions of CAU300p in different solvents.

Transmission Electron Microscopy of the CAU300p

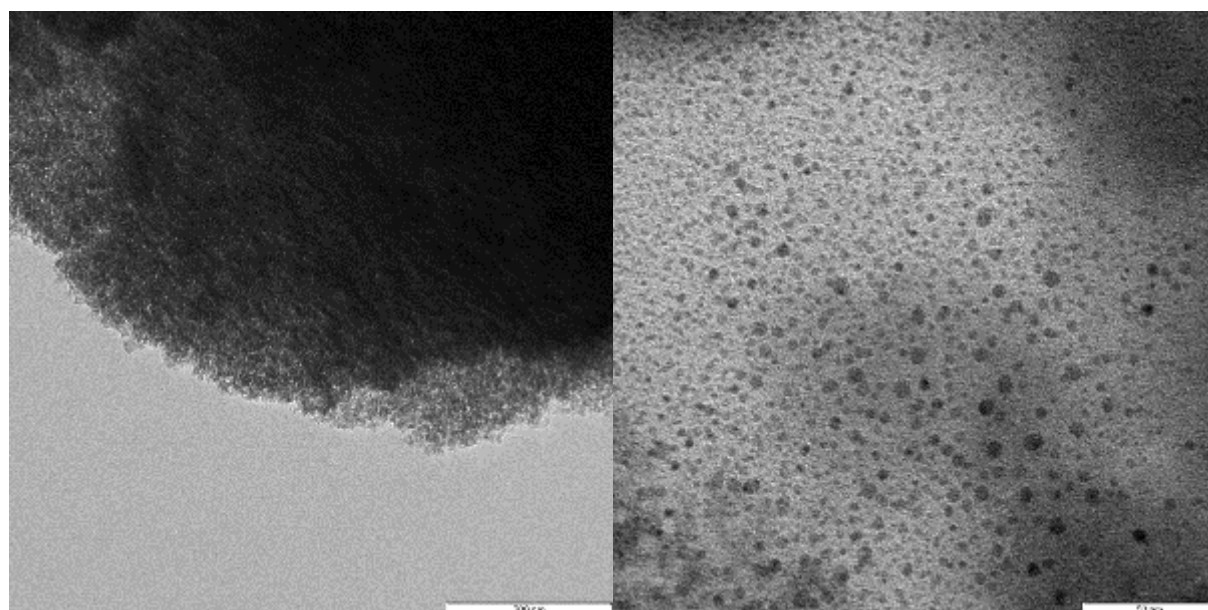


Figure S3. TEM images of CAU300p deposited on a Formvar covered TEM grid from a dispersion in H₂O (left) and (DMSO) right.

Energy-Dispersive X-ray Analysis of Laser-Carbonized Films

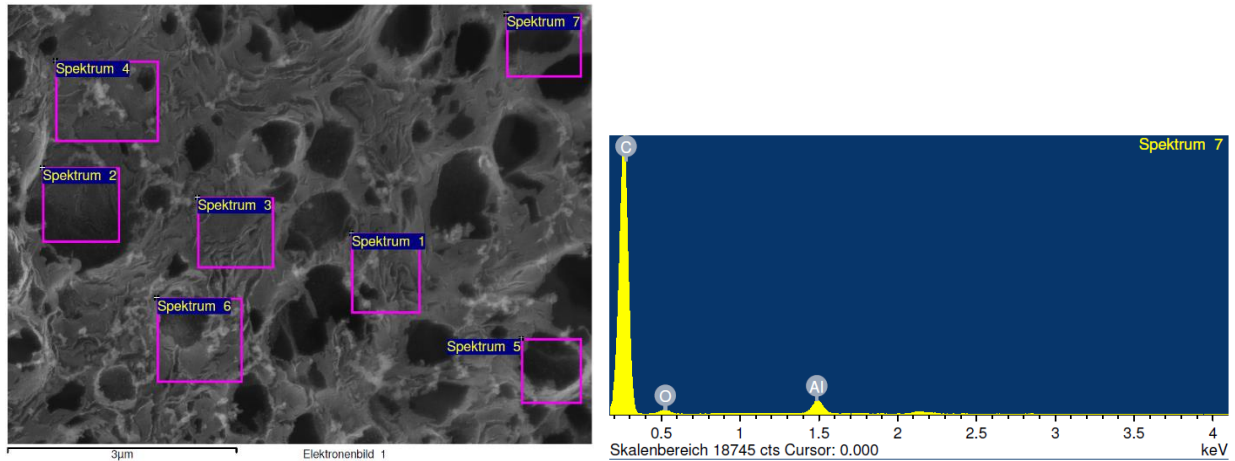


Figure S4. Left: SEM image of a laser-carbonized film on an aluminium substrate showing seven areas which were analyzed by EDX; Right: Representative EDX-spectrum of area 7.

High-Resolution Transmission Electron Microscopy Laser-Carbonized Sample

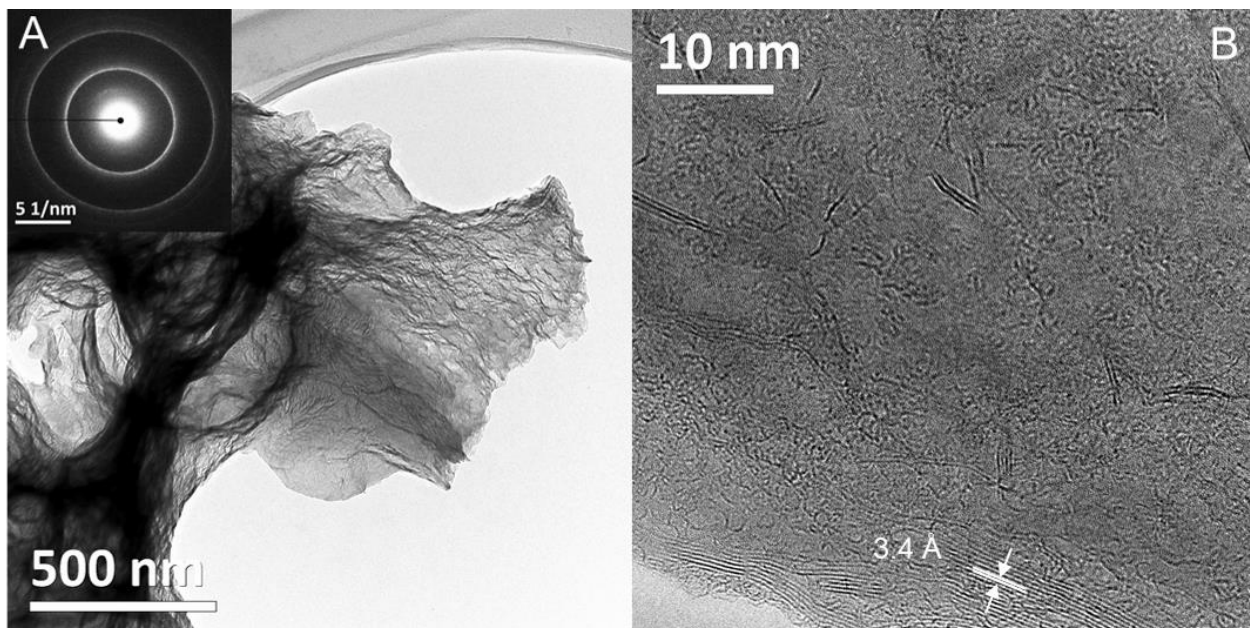


Figure S5. HRTEM pictures of laser-treated CaU300p. The interplanar spacing calculated from the selected area electron diffraction in the insert in (A) and the lattice fringes in (B) are characteristic from graphitic layers.

Micro-Computer-Tomography Measurements

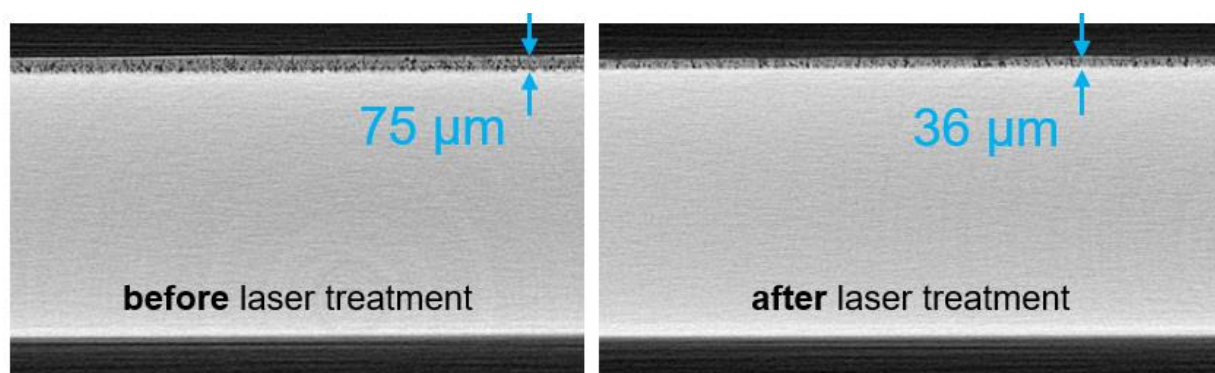
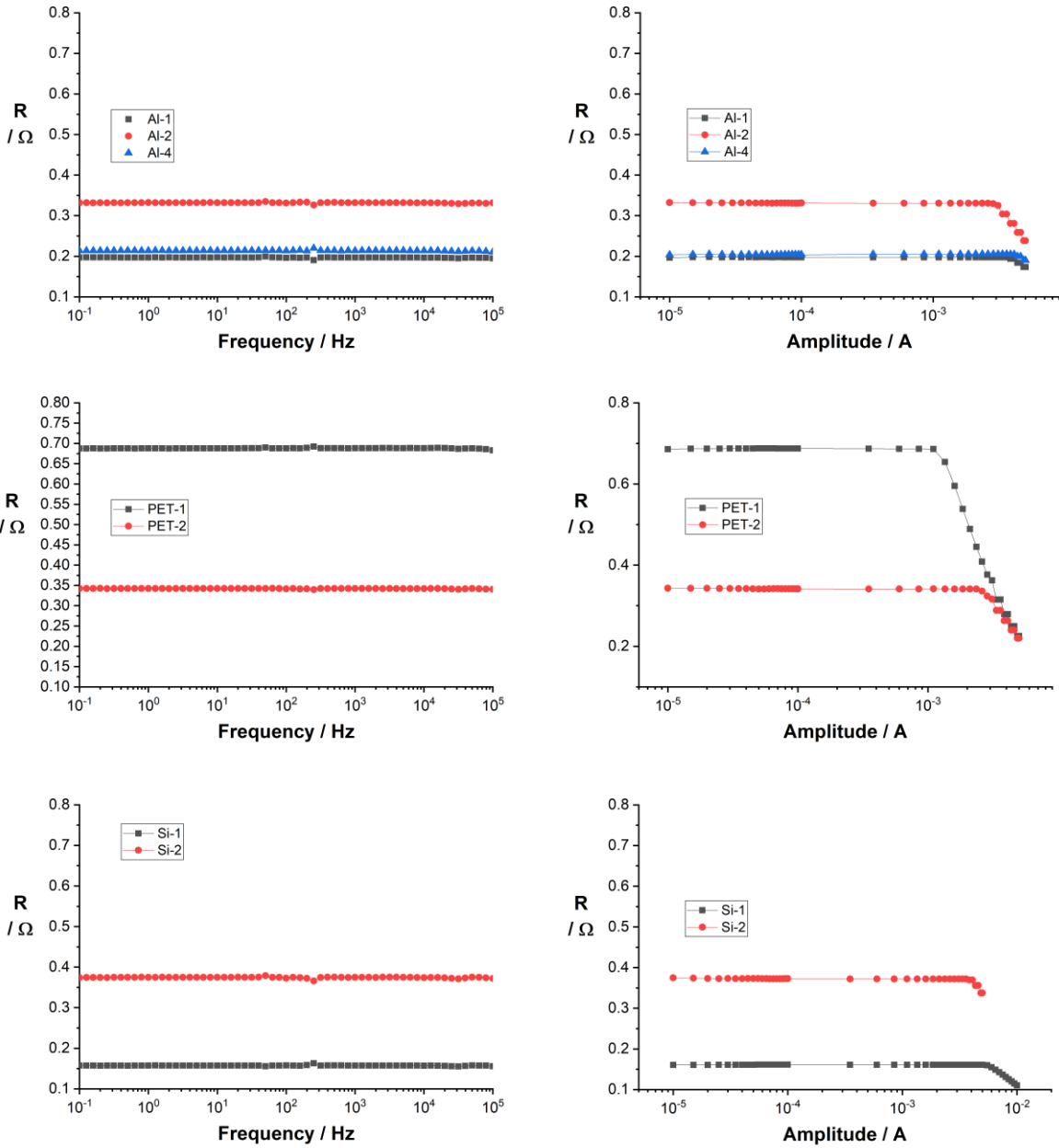


Figure S6. Micro-CT scans of the precursor film (left) and the laser-carbonized film (right).

Impedance Measurements of Laser-Carbonized Films



8

Figure S7. Resistance of the laser-carbonized CAU300p/PVP films in dependence of the frequency (left) and the current amplitude (right) obtained by impedance measurements on Aluminium sheets (top), PET sheets (center), and silicon wafers (bottom).

Quantification of Laser-settings

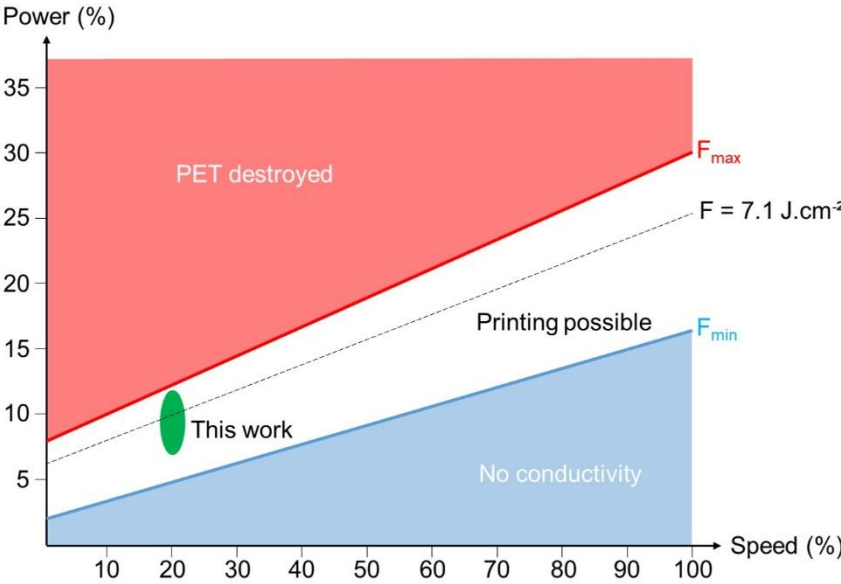


Figure S8. Laser-parameters for printing on PET. $P_{max} = 60 \text{ W}$ and $v_{max} = 1.8 \text{ m s}^{-1}$.

Cite this: *Chem. Sci.*, 2020, **11**, 8256

All publication charges for this article have been paid for by the Royal Society of Chemistry

Carbon nanodots revised: the thermal citric acid/urea reaction†

Volker Strauss, *^a Huize Wang,^a Simon Delacroix, ^a Marc Ledendecker ^b and Pablo Wessig ^c

Luminescent compounds obtained from the thermal reaction of citric acid and urea have been studied and utilized in different applications in the past few years. The identified reaction products range from carbon nitrides over graphitic carbon to distinct molecular fluorophores. On the other hand, the solid, non-fluorescent reaction product produced at higher temperatures has been found to be a valuable precursor for the CO₂-laser-assisted carbonization reaction in carbon laser-patterning. This work addresses the question of structural identification of both, the fluorescent and non-fluorescent reaction products obtained in the thermal reaction of citric acid and urea. The reaction products produced during autoclave–microwave reactions in the melt were thoroughly investigated as a function of the reaction temperature and the reaction products were subsequently separated by a series of solvent extractions and column chromatography. The evolution of a green molecular fluorophore, namely HPPT, was confirmed and a full characterization study on its structure and photophysical properties was conducted. The additional blue fluorescence is attributed to oligomeric ureas, which was confirmed by complementary optical and structural characterization. These two components form strong hydrogen-bond networks which eventually react to form solid, semi-crystalline particles with a size of ~7 nm and an elemental composition of 46% C, 22% N, and 29% O. The structural features and properties of all three main components were investigated in a comprehensive characterization study.

Received 18th March 2020
Accepted 16th July 2020

DOI: 10.1039/d0sc01605e

rsc.li/chemical-science

Introduction

Small organic molecules are common starting materials for hydrothermal or pyrolysis reactions, bringing forth new compounds and materials with intriguing properties which are valuable for a wide range of applications.^{1–7} In particular, the so-called “carbon nanodots (CNDs)” have emerged as an interesting new class of photo- and electroactive materials and have been studied as components in functional systems and devices such as fluorescent sensors,^{8,9} light emitting diodes,¹⁰ drug delivery systems,^{11,12} charge storage systems,¹³

photosensitizers^{9,14} *etc.* However, there has been a consensus among experts in the field that their structural identification and the correlation between their structure and optical properties are the most critical open questions that need to be answered.^{15–17}

As an initial standard model for luminescent organic particles, a carbonized core bearing a number of functional groups, such as amides, carboxylates, hydroxyls and amines, was considered.^{18,19} The presence of a large number of functional groups would facilitate water solubility as shown in molecular dynamics simulations, which is usually not observed for graphitic nanoparticles.²⁰ In the past few years, a variety of thermal reaction products from small organic precursors in the context of CNDs have been discussed and the identified or proposed product palette is wide ranged. For example, the fluorescence of the thermal CA/ethylene diamine reaction product was assigned to a specific molecular species.²¹ Other observations revealed the presence of pure graphitic C₃N₄ phases, when reacting a 1 : 6 mixture of sodium citrate/urea in an autoclave.²² These were documented by characteristic XRD peaks at 27.4 and 13.1° 2θ. In a later report, crystalline phases of β-C₃N₄ were identified by high resolution transmission electron microscopy studies.²³ Recent literature demonstrates the existence of molecular fluorophores occurring in the product mixture.^{24–28} A recently published review article collects studies

^aDepartment of Colloid Chemistry, Max-Planck-Institute of Colloids and Interfaces, Am Mühlenberg 1, 14476 Potsdam, Germany. E-mail: volker.strauss@mpikg.mpg.de

^bDepartment of Technical Chemistry, Technical University Darmstadt, Alarich-Weiss-Straße 8, 64287 Darmstadt, Germany

^cInstitute of Chemistry, University of Potsdam, Karl-Liebknecht-Str. 24-25, D-14476 Potsdam, Germany

† Electronic supplementary information (ESI) available: General and supplementary information on synthesis and characterization. UV-vis and fluorescence spectroscopy of the raw products, nuclear magnetic resonance spectroscopy of the raw products, educts and reference compounds, the separation procedure of the raw products, extinction coefficients, fluorescence lifetime measurements and fluorescence quantum yields, photostability measurements, electron spray ionization mass spectrometry, 2D-correlation nuclear magnetic resonance spectroscopy, thermal mass analysis, and X-ray photoelectron spectroscopy of the isolated products. See DOI: 10.1039/d0sc01605e



on revelations of molecular fluorophores as active species in CND samples based on typical reaction partners such as citric acid (CA)/ammonia, CA/urea (U), CA/cysteine, CA/ethylene diamine, CA/ethanolamine and other non-CA starting materials.²⁹

The thermal reaction of CA and urea is of special importance in this regard, as it brings forth a variety of products with different structural and optical properties.^{22,23,27,30,31} For example, the reaction of CA and U involves the formation of citrazinic acid, a reaction that was described more than hundred years ago³² and, interestingly, it has been shown that citrazinic acid exhibits similar electronic deactivation behavior to that of the hydrothermal CA/urea-reaction product.³³ Depending on the reaction conditions, however, other or additional products have been identified, such as crystalline particles and HPPT, a green fluorophore.^{25,27,34}

Several purification or separation techniques have been proposed, including centrifugation, precipitation, extraction, chromatography and dialysis. Dialysis is the most widely used technique.^{26,35–37} Therefore, it has been demonstrated that the overall fluorescence in these samples originates from molecular fluorophores. The isolation of fluorophores is of pronounced importance to provide easy access to inexpensive and water-soluble photoactive compounds. In fact, new dyes and fluorophores, in particular those featuring a large Stokes shift, are essential for a range of applications, such as fluorescence lifetime imaging microscopy (FLIM), stimulated emission depletion microscopy (STED) and phase-fluorometric sensing (PFS).^{38–40}

Besides water-soluble fluorophores, insoluble, non-fluorescent reaction products are also often produced during solvothermal or thermal reactions, which are typically discarded as carbonaceous particles or larger particles without further use.^{36,41} This insoluble fraction produced during the low-temperature thermal reaction of a CA/U mixture was found to be an excellent precursor material in our recently introduced laser-assisted carbonization process.⁴² A careful analysis of these products is, therefore, meaningful as it reveals the formation of an intermediate product on the way to a fully carbonized material. In general, the structural identification of such intermediate reaction products during low-temperature thermal synthesis may help to achieve a comprehensive understanding of carbonization reactions. The thermal CA/U reaction may be used as an example reaction, as the reaction conditions determine the reaction pathways to a broad product palette and the properties of the final carbonization product are a direct result of the structure of the low-temperature thermal intermediates.

In this study, we analyzed the thermal reaction of citric acid and urea in the melt by varying the reaction temperature. First, the reaction products were analyzed by means of optical spectroscopy and nuclear magnetic resonance (NMR) spectroscopy. Under any reaction conditions, the product consists of three main components, two soluble fractions, referred to as “thermally accessed fluorophores (TAFs)”, and an insoluble fraction (nanoparticles). The three fractions were separated and purified by a series of extractions and column chromatography. The

isolated compounds were structurally characterized by electron spray ionization mass spectrometry (ESI-MS), 2D-correlation nuclear magnetic resonance (2D-NMR) and Fourier-transform infrared (FT-IR) spectroscopies, and thermogravimetric analysis (TGA). The insoluble fraction was characterized by means of transmission electron microscopy (TEM), FT-IR, X-ray diffraction (XRD), X-ray photoelectron spectroscopy (XPS) and TGA. Based on these results, a reaction mechanism is proposed and possible side reactions are discussed.

Results and discussion

Reaction conditions

We started our investigation by analyzing the solid-state mixtures of citric acid and urea. Urea is a well-known hydrogen bond donor that forms strong eutectic mixtures with a variety of compounds.⁴³ We performed differential scanning calorimetry (DSC) with mixtures of citric acid and urea at different compositions (Fig. 1). The mixtures form a eutectic system with melting points significantly lower than those of the pure compounds. The lowest melting points were measured for molar ratios between 1 : 5 and 1 : 3 (CA/U) at ~95 °C.

Mixtures with a molar ratio of 1 : 3 were reacted at different temperatures ranging from 100 °C to 290 °C in a laboratory microwave. Besides the temperature, the reaction time was also found to have an influence on the reaction yields. For comparison, we performed every synthesis for 20 min. To ensure homogeneous blending of the precursors, the mixture was stirred at 100 °C for 5 min, and then the reaction was ramped up to the reaction temperature and kept for 20 min. At temperatures >130°, a yellow product with blue fluorescence was observed (Fig. S1†). However, significant amounts of unreacted precursors were still present in the products up to reaction temperatures of 150 °C, as shown in NMR experiments. At temperatures >150 °C, the visible fluorescence turns green. At 180 °C, the product yield increases dramatically and no reaction educts are contained in the product (Fig. S2†). In aqueous solutions of the raw products, a notable Tyndall scattering effect starts to occur at temperatures >190 °C.

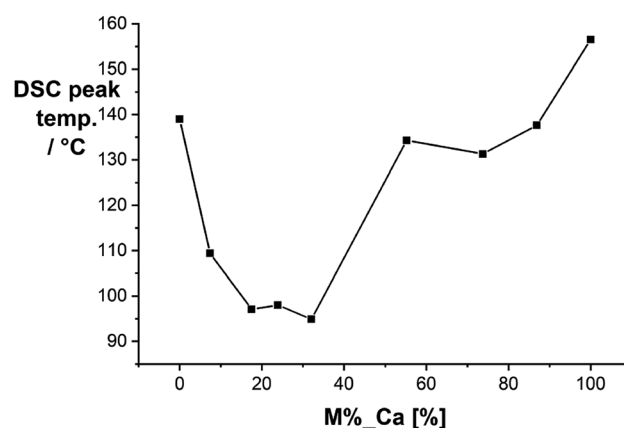


Fig. 1 Melting points of citric acid/urea mixtures obtained by differential scanning calorimetry.



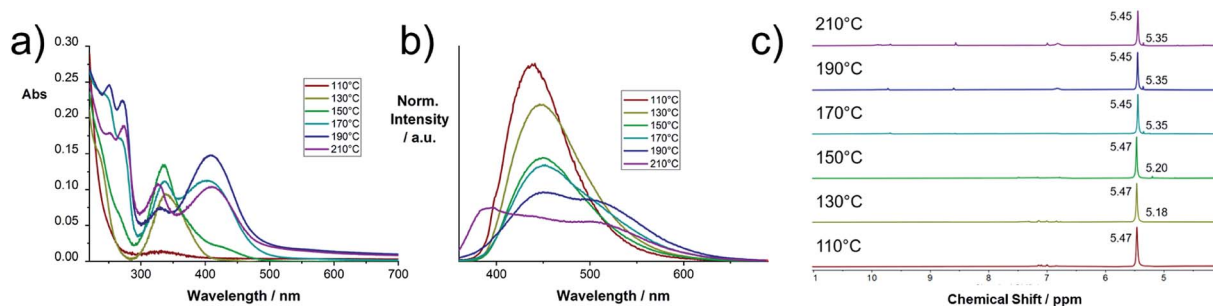


Fig. 2 Characterization of selected raw products of the thermal CA/U reaction (0.013 mg mL^{-1}) at 110–210 °C: (a) UV-vis absorption spectra in H_2O ; (b) fluorescence spectra in H_2O obtained upon excitation at 350 nm; (c) ^1H -NMR spectra recorded in DMSO-d_6 .

In Fig. 2a and b the electronic absorption and fluorescence spectra of selected raw products are shown. The spectra of all raw product samples synthesized at different temperatures between 100 and 290 °C are collected in Fig. S3.† In the low temperature regime between 100 and 140 °C, a distinct absorption peak at 337 nm evolves, which corresponds to the fluorescence peak at 440 nm. At 150 °C a second absorption peak with a maximum at 406 nm starts to evolve together with a set of peaks at <300 nm. The peak at 406 nm causes a second fluorescence peak at 523 nm. At temperatures >180 °C, a notable increase of the absorption at 406 nm with respect to the absorption at 337 nm occurs. Simultaneously, the absorption maxima shift from 337 and 406 to 327 and 411 nm, respectively. These changes occur along with the appearance of a new emission band with a maximum at 394 nm. This effect becomes more pronounced at temperatures >250 °C (Fig. S3†). Given the differences in the electronic absorption of the reaction products after the thermal CA/U reaction, we hypothesize a structural transition of the reaction product, the evolution of a new product, or electronic interaction between the species present. For example, a sample reacted at 230 °C contains all three products, since both the absorption peaks (327 and 411 nm) and all three emission peaks (394, 440, and 523 nm) are present. The correlation between the absorption and emission features has been previously assigned to different nitrogen doping levels of carbon nanodots or clusters of citrazinic acid.^{19,28}

The ^1H -NMR and ^{13}C -NMR spectra of a selection of raw products synthesized at temperatures between 110 and 210 °C are shown in Fig. 2c and S2.† At low temperatures, a peak at 5.47 ppm arises, which remains dominant for any sample. The advent of this peak correlates with the evolution of the previously discussed absorption peak at 340 nm. At a reaction temperature of >150 °C, a peak at 5.18 is observed, which indicates the formation of the compound causing the absorption peak at 410 nm. At higher temperatures, the two peaks shift to 5.45 and 5.35, respectively. In the higher temperature samples (>150 °C), the educts, citric acid and urea, are entirely consumed, as no related NMR signals were observed (see Fig. S4†). Moreover, no evidence for the presence of citrazinic acid was found (see Fig. S5†).

Separation

The product mixtures were separated by a series of solvent extractions followed by column chromatography (see Fig. S6†

and the Experimental section). For example, a reaction of a 1 : 3 mixture of CA/U conducted at 230 °C yields a reaction product containing a minimum of three components. The three main components were isolated and characterized. Initially, the dry reaction product was dissolved in $\text{H}_2\text{O}_{\text{millipore}}$ and stirred well to dissolve the soluble part. The mixture was then centrifuged to separate the soluble part from the insoluble part. The supernatant was dried under reduced pressure and then re-dissolved in methanol (MeOH). The mixture was again centrifuged to remove insoluble materials and the obtained yellowish-brown supernatant was dried. The second washing step in MeOH helps to remove small amounts of residual insoluble particles and to obtain a pure fluorophore fraction. The product was then separated by column chromatography using silica gel as a stationary phase and $\text{H}_2\text{O}_{\text{millipore}}$ as the eluent yielding two fractions, a yellowish-brown fraction showing green emission (citric acid/urea-green: **CUg**) and a colorless fraction showing blue emission (citric acid/urea-blue: **CUB**) under UV light (Fig. 3). Other eluent/stationary phase combinations, such as acetonitrile or methanol failed to separate the reaction products. The precipitate from the initial centrifugation step was washed with $\text{H}_2\text{O}_{\text{millipore}}$ at 95 °C for 24 h and, then, again centrifuged. The larger fraction of the precipitate is a fine black powder (citric acid/urea-particles: **CUp**) that is dispersible in a range of solvents, even non-polar, such as CH_2Cl_2 . The respective yields of the three main components depend on the reaction conditions. For example, a reaction at 180 °C with 20 min reaction time yields 46% **CUB**, 26% **CUg**, and 4% **CUp**. When performing the same reaction at 230 °C, 23% **CUB**, 35% **CUg**, and 36% **CUp** were obtained. The remaining mass corresponds to reaction side products or material losses (product mixtures) from the separation process.

The two fluorescent molecular fractions, **CUg** and **CUB**, are soluble in polar solvents, such as H_2O or MeOH, and have clear NMR patterns; therefore, we refer to those as “thermally accessed fluorophores” (TAFs). The third fraction, **CUp**, is an insoluble, non-fluorescent material which consists of nanoparticles with sizes on the order of a few nanometers and a certain degree of crystallinity as shown by XRD measurements. The TAFs were analyzed by optical absorption and photoluminescence spectroscopies and 2D-correlative ^1H - and ^{13}C - and ^{15}N -NMR spectroscopy, mass spectrometry (MS) and elemental analysis (EA) and X-ray photoelectron spectroscopy



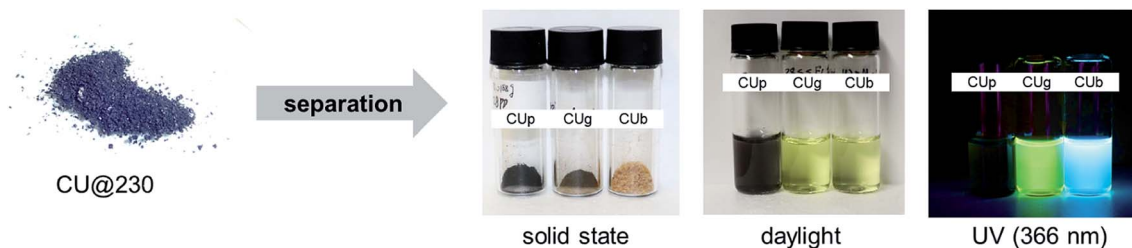


Fig. 3 Separated products, CUb, CUg, and CUp, from the crude thermal reaction product of citric acid and urea; right: isolated reaction products in the solid state, in H₂O in daylight and in H₂O under UV light.

(XPS). CUp was analyzed by a set of characterization methods including XRD, XPS, TEM, EA, FT-IR, TGA and solid-state NMR.

Characterization

TAFs. The electronic absorption and emission spectra of the separated products show, indeed, that the peak at 330 nm originates from CUb (Fig. 4a). The corresponding fluorescence peak appears at 443 nm. CUg shows a set of absorption maxima at a wavelength of < 300 nm and a broad maximum at 410 nm (Fig. S7†) with a corresponding fluorescence maximum at 514 nm. Both fluorescence signals appear as single modes and originate from a single excitation peak as shown in the 2D photoluminescence plots in Fig. 4b and c. Notably, the fluorescence peak at 390 nm as observed in the raw products was not observed in the isolated fractions; therefore, we assume that it originated from the electronic interaction within the mixture or from a minor fraction that was lost during the separation. Fluorescence lifetimes were determined by time-correlated single-photon counting (TCSPC) (Fig. S8†). The fluorescence of CUb decays with two lifetime components of 4.1 and 9.5 ns in H₂O and 3.1 and 7.6 ns in MeOH (Table S1†). The two lifetime components may derive from different species in the mixture of compounds (*vide infra*). The longer lifetimes of CUb in the more polar H₂O are likely due to the higher polarity of their excited states. The opposite trend is observed for CUg, where single-exponential decays with lifetimes of 5.3 or 9.0 ns in H₂O or MeOH, respectively, were obtained. The fluorescence quantum yields of CUg were determined by the gradient method to be 27% in H₂O and 70% MeOH using Na-fluorescein as a standard (Fig. S9†). The results are summarized in Table S2.† Notably,

CUg features remarkable photostability in solution. After 16 h illumination at 410 nm in H₂O, the fluorescence intensity was still 100% (Fig. S10†). For CUb, a quantification of the optical parameters was difficult due to an intrinsic instability of the sample as shown in Fig. S10.†

First structural information was obtained by elemental analysis of the isolated fractions yielding 38% C, 13% N, 3% H and 44% O for CUg. This is in sound agreement with the predicted elemental composition of HPPT·2H₂O (4-hydroxy-1H-pyrrolo[3,4-c]pyridine-1,3,6(2H,5H)-trione) as reported in the literature.²⁵ For CUb an elemental composition of 25% C, 38% N, 6% H and 31% O was determined, which coincides very well with the predicted elemental composition of triuret or tetrauret: 25% C, 38% (37%) N, 4% H, and 33% (34%) O.

Mass spectrometric analysis shows a main molecular fraction with a mass of $m/z = 179$ for CUg, the expected mass for HPPT (Fig. S11†).²⁵ CUb was analyzed in both the positive ion mode and the negative ion mode. When looking at the significant noise in the ESI-MS pattern, CUb seems to contain a variety of small compounds (Fig. S12†). In the negative ion mode, a peak at $m/z = 171$ is dominant, which matches with a cyclic tetrauret species and the signal at $m/z = 121$ matches with the biuret-ammonium adduct. The dominant peak of CUb in the positive ion mode appears at $m/z = 121$ and minor fragments with signals of $m/z = 149$, 186, and 279 are detected. Important are the signals at $m/z = 149$ and 186 as these may originate from melamine·Na⁺ or melaminylguanidine·NH⁴⁺ (Fig. S13†). A minor peak at 128 indicates the presence of cyanuric acid.

Characterization by nuclear magnetic resonance spectroscopy (NMR) was performed in DMSO-d₆ or D₂O. DMSO was found to be a good choice as a solvent for the characterization

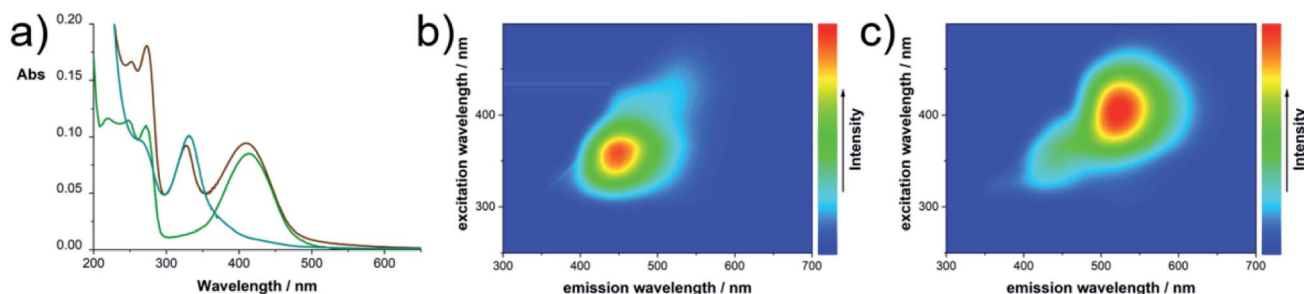


Fig. 4 Optical characterization of TAFs: (a) absorbance of CUg (green), CUb (blue) and the unseparated raw product (brown) in H₂O; (b) 2D photoluminescence plots of CUb and (c) CUg in H₂O at room temperature.



because proton exchange is suppressed to some degree. The ^1H -NMR spectrum of **CUg** shows one dominant signal at 5.40 ppm and two peaks at 9.82 and 10.0 ppm (Fig. 5a). The ^{13}C -NMR spectrum shows seven peaks at 169.6, 168.5, 167.75, 160.3, 147.7, 95.6, and 91.0 ppm. In the ^{15}N -NMR spectrum, two peaks at 176.3 and 156.3 appear, indicating the presence of two imide-like nitrogens. The molecular structure was verified by ^{13}C and ^{15}N heteronuclear single quantum correlation (HSQC) and heteronuclear multiple-bond correlation (HMBC) spectroscopy experiments with ^{15}N -enriched samples (Fig. S14[†]). Only one proton (5.40 ppm) is immediately bonded to carbon (95.6 ppm). Two protons (9.82 and 10.0 ppm) are directly bonded to nitrogens (176.3 and 156.3 ppm), respectively. Using heteronuclear multiple-bond correlation spectroscopy (HMBC), we identified the coupling of protons to ^{13}C or ^{15}N over three bonds within the structure (Fig. S15[†]) and were able to confirm the structure of HPPT.²⁵

The correct tautomeric form of HPPT was confirmed by quantum mechanical calculations in a vacuum and polar solvents. The tautomer B with strong intramolecular H-bonding affinity was found to be the most stable (Fig. S16[†]).

In the ^1H -NMR spectrum of **CUB**, a dominant peak at 5.45 and two weak peaks at 6.84 and 8.64 ppm are observed (Fig. 5b). The ^{13}C -NMR spectrum shows two peaks at 160.1 and 156.0 ppm and the ^{15}N spectrum shows two triplets centered at 76.6 and 83.6 ppm and a weak signal at 123 ppm. All of the ^{15}N peaks appear in the amine-typical region. In neither of the ^1H - ^{13}C 2D-correlation spectroscopies, HSQC and HMBC, coupling between protons and carbon was seen (Fig. S17 and S18[†]); therefore, carbon-hydrogen bonds are excluded. ^1H - ^{15}N HSQC and HMBC experiments were performed with ^{15}N -enriched samples to detect the coupling of ^1H and ^{15}N . A direct coupling between the proton signal at 5.45 and the amine-like ^{15}N signal at 76.6 ppm is confirmed. Direct coupling was also observed between the ^1H at 6.84 and the ^{15}N at 83.6 ppm as well as the ^1H at 8.64 ppm and the ^{15}N at 123 ppm. Three-bond coupling between these ^1H and ^{15}N is also observed (Fig. S18[†]). In general, the NMR pattern resembles the expected pattern of oligomeric ureas such as triuret or tetrauret. A commercial reference for triuret is not available; the peak positions, however, match with a commercial biuret sample, for which similar shifts are expected (Fig. S19[†]). Based on these

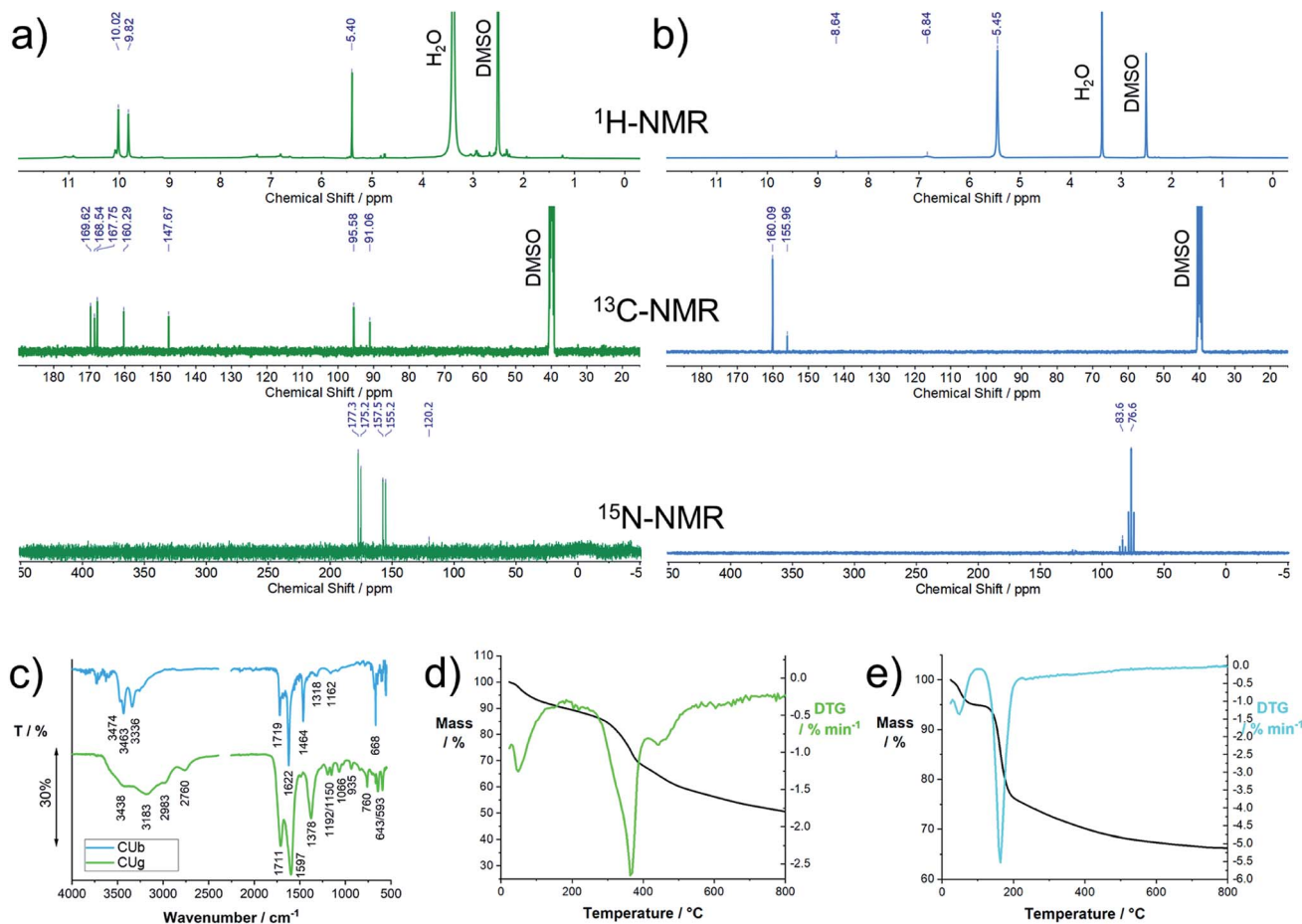


Fig. 5 Structural characterization of TAFs, **CUg** and **CUB**, isolated from the reaction product of the thermal reaction of citric acid and urea: (a) ^1H -, ^{13}C -, and ^{15}N -NMR spectra of **CUB** recorded in $\text{DMSO}-d_6$; for the ^{15}N -NMR spectrum, samples were enriched with ^{15}N ; (b) ^1H -, ^{13}C -, and ^{15}N -NMR spectra of **CUg** recorded in $\text{DMSO}-d_6$; for the ^{15}N -NMR spectrum, samples were enriched with ^{15}N ; (c) solid state FT-IR spectra of **CUB** and **CUg**; (d) thermogravimetric analysis of **CUg**; (e) thermogravimetric analysis of **CUB**.



results, we assume small oligomeric ureas to be the dominant species in **CUB**. A positive “biuret test” confirmed the presence of oligomeric urea in **CUB** (Fig. S20†).

More structural information on **CUG** and **CUB** was obtained by FT-IR spectroscopy (Fig. 5c). For **CUG**, the broad peaks between 2700 and 3600 cm^{-1} indicate the presence of OH and NH stretching vibrations. The strong signals at 1711 and 1597 or 1719 and 1622 cm^{-1} are assigned to C=O and C=N stretching modes, respectively, and the peak at 1378 cm^{-1} is assigned to C–N stretching modes. Notably, the peaks appear significantly broadened in comparison to, for example, **CUB** or typical nucleobases or purine bases. Such a peak broadening is typically observed for molecules that undergo significant H-bonding. The FT-IR spectrum of **CUB** shows a set of distinct absorption bands at 3474, 3463, and 3336 cm^{-1} , which are assigned to N–H stretching vibrations typically observed for primary amines (compared to urea, biuret, or melamine). The two sharp peaks at 1719 and 1622 cm^{-1} originate from C=O and C=N stretching modes, respectively. The peak at 1464 cm^{-1} derives from a C–N stretching vibration. In general, the spectrum resembles the FT-IR spectra of urea and its oligomers, as their dominant peaks occur in a similar fashion.

Thermogravimetric analysis provided information about the thermal stability of the isolated TAFs. **CUG** is stable up to a temperature of ~ 300 °C with a peak decomposition temperature of 364 °C (Fig. 5d). In this temperature regime, the main decomposition products are NH^+ , $\text{CH}_2\text{O}_2^{+*}$, CH_2O^{+*} , CHO_2^{+*} , CO_2^{+*} , CH_2NH_2^+ , $\text{CH}_3\text{CN}^{+*}$, and $\text{CH}_3\text{CN}^{+*}$ stemming from primary amines, CO_2 and N-containing heterocycles (Fig. S21†). The results, presented in Fig. 5e, clearly show the low thermal stability of **CUB**. At a peak temperature of 164 °C, the sample decomposes. A simultaneous mass analysis of the decomposition products reveals that the major decomposition products stem from primary amines and low-molecular-weight carbon species. The evaporation products are NH^+ , NH_2^+ , NH_3^{+*} , $\text{CH}_2\text{O}_2^{+*}$, CHO_2^{+*} , CO_2^{+*} , and CH_2NH_2^+ (Fig. S22†). Notably, the decomposition of **CUB** occurs at a significantly higher temperature of ~ 210 °C in combination with **CUG**. A TGA profile of a raw mixture prior to column chromatography is shown in Fig. S23.†

The elemental composition and the structural features of the proposed products, **CUG** and **CUB**, were confirmed by X-ray photoelectron spectroscopy (Fig. S24†). In **CUG**, the expected binding situation as for HPPT is observed, with contributions from C–N, C=N, C=O, and C–NH. Adsorbed H_2O causes a strong signal maximizing at 531 eV. The C–N or C=N features are the dominant X-ray absorption features in **CUB**. All peaks, the C_{1s} , N_{1s} and O_{1s} peaks, in **CUB** show a predominance of C=N, C–N, C–O, and C=O, as present in oligomeric ureas.

Particles. The insoluble fraction of the reaction product, **CUP**, was analyzed by means of a set of characterization methods. **CUP** was obtained by washing the centrifugate with water at 95 °C several times. About 10 wt% of the material removed during the washing process is composed of molecular compounds such as HPPT (Fig. S25†). The remaining material appears as a fine black powder without apparent fluorescence in dispersion. In alkaline solutions or basic solvents, such as DMSO or DMF, **CUP**

seemingly solubilizes with an apparent color change to brown. Upon re-dispersion of **CUP** into aqueous dispersion, slight yellow-brown coloring of the solvent is noted. This effect is even more pronounced in DMSO or dimethylformamide (DMF). A concentration dependent UV-vis and fluorescence analysis of **CUP** in H_2O , shown in Fig. S26†, reveals strong auto-quenching effects in solution. Moreover, the UV-vis absorption pattern shows a strong plasmonic background absorption trailing from the UV into the NIR. Two broad maxima at ~ 345 and 430 nm are observed in the UV-vis spectra (Fig. S26†). In principle, this absorption pattern resembles the one of **CUG**, however, with large red shifts of ~ 15 and 25 nm. The fluorescence intensity is rather low and maximizes at 463 nm upon excitation at 350 nm. Concentration dependent spectroscopic assays reveal a strong tendency towards aggregation-induced quenching at concentrations above 4 mg L^{-1} .

NMR experiments were performed in basic solution and DMSO but did not show any signals. Elemental analysis yields a composition of 46% C, 22% N, and 29% O. We examined the product by transmission electron microscopy (TEM). The TEM samples were prepared from diluted dispersions in DMSO. In Fig. 6a, a representative TEM image of **CUP** is shown. Throughout the investigated areas, particles with sizes of about 2–7 nm were observed. These are also seen in samples prepared from aqueous solutions, however, strongly aggregated. The X-ray powder diffraction pattern of **CUP** in Fig. 6b shows a peak at $27.2^\circ 2\theta$ (Cu K_α) indicating the presence of a graphitic (002) lattice spacing typically seen for graphitic or graphitic carbon nitride samples. The particle sizes observed in TEM match with the mean size of the graphitic domains as determined by the peak width using the Scherrer equation.

FT-IR spectroscopy reveals the presence of OH groups within the material (Fig. 6c). Furthermore, a large contribution to the IR absorption is coming from C=O stretching vibrations. Other peaks indicate the presence of C–N and C=N groups. Similar to the observation made for **CUG**, the IR-absorption peaks appear rather broad, which indicate strong H-bonding within the sample.

A more comprehensive picture about the composition and the type of bonding in the material was provided by X-ray photoelectron spectroscopy (XPS). The fitted spectra with focus on the C_{1s} , N_{1s} , and O_{1s} region are shown in Fig. 6d. Fitting of the C_{1s} signal suggests an abundance of sp^2 carbons.^{44,45} Other signals with lower intensity are assigned to C–C (sp^3), C=N and C–O. The C=N signals are also observed in the N_{1s} region at 398 eV. A set of three signals in the O_{1s} region is assigned to C–O, C=O, and O–C=O bonds. The thermal stability was determined with TGA in an inert atmosphere (Fig. 6e). Decomposition starts at ~ 324 °C and is accomplished at 610 °C.

Proposed reaction mechanism

Taking the results from the structural characterization into consideration, we propose a potential reaction mechanism. Citric acid and urea form a solid eutectic mixture at room temperature (Fig. 7). H-Bonds between the two species are



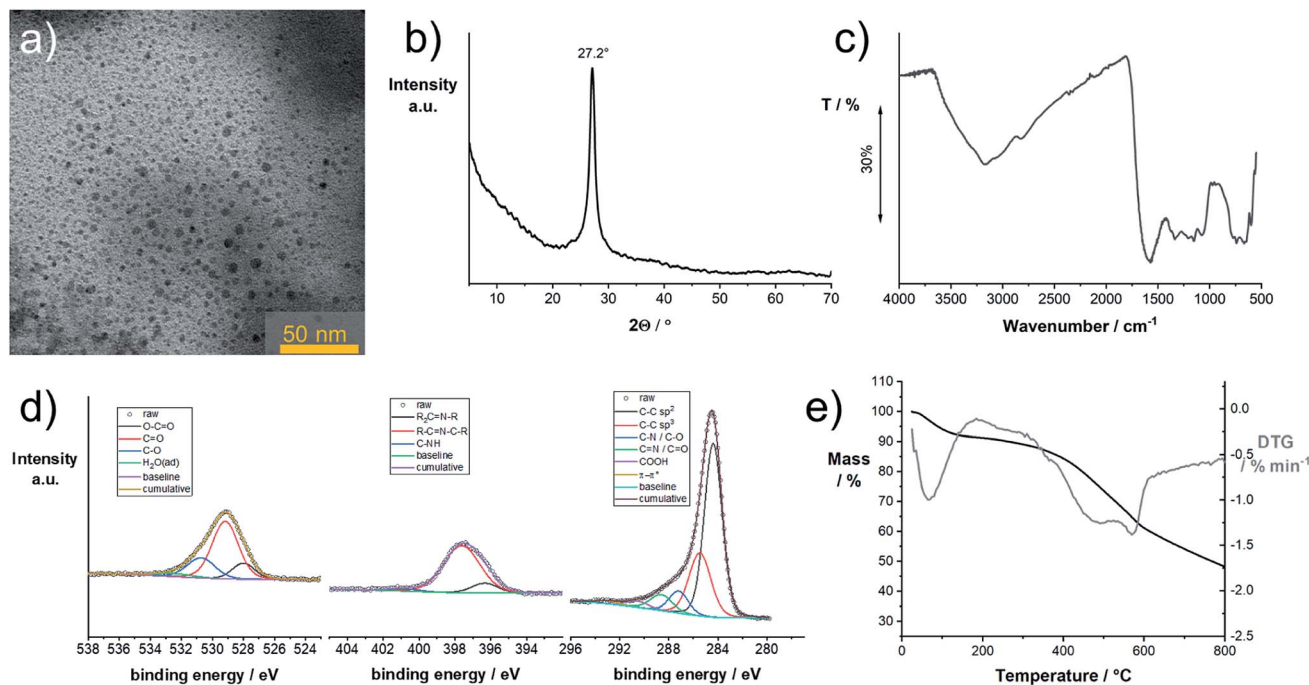


Fig. 6 Characterization of the insoluble reaction product, **CUp**, isolated from the reaction product of the thermal reaction product of citric acid and urea: (a) transmission electron micrograph of **CUp** deposited from a dispersion in DMSO; (b) powder X-ray pattern of **CUp**; (c) Fourier-transform infrared spectrum of **CUp**; (d) X-ray photoelectron spectra of **CUp** with emphasis on the C_{1s} , N_{1s} , and O_{1s} regions; (e) thermogravimetric analysis of **CUp** in an inert atmosphere.

responsible for a drastic reduction of the melting point to ~ 95 °C. The H-bond networks formed between citric acid and urea are expected to be rather complex due to the amphiphilic H-bond formation properties of both compounds. Upon heating to the reaction temperatures, urea dissociates into isocyanic acid and ammonia and condenses with citric acid to form citrazinic acid, which immediately reacts with isocyanic acid to form HPPT according to a mechanism provided in the literature.²⁵ Notably, as shown in the literature, the citric acid/urea reaction in H_2O yields different reaction products as the reaction from citrazinic acid to HPPT is suppressed by H_2O .²⁵ Simultaneously, excess urea condenses into oligomeric ureas, such as triuret or tetrauret, as well as small amounts of side products such as melamine or guanidine, the typical condensation products of urea.^{46,47} The unstable blue fluorescence likely originates from conjugated oligomeric ureas or isolated CN ring structures formed from urea which are stabilized by

their oligomers. These reaction intermediates form a strong H-bond network. Upon further heating, both **CUp** and **CUp** are consumed in a further condensation reaction to form **CUp**, which appears as insoluble particles. H-Bonding between all three components facilitates the stable dispersion of particles. Strong H-bonding is still observed in **CUp** and interactions between **CUp** and **CUp** are inferred from TGA measurements and shifts in the NMR spectra. In synergy with **CUp**, the thermal decomposition of **CUp** occurs at 210 °C instead of 164 °C (Fig. S23†). Significant shifts in the 1H -NMR spectra were observed in the mixture of both compounds (Fig. S27†), which strongly suggests that the H-bond networks formed between **CUp** and **CUp** increase their thermal stability. Considering the relative reaction yields of the three main compounds in the reaction at 180 °C and 230 °C, we assume a consumption of both **CUp** and **CUp** on account of **CUp**. These observations coincide with the results of other reports on the same reaction.²⁸

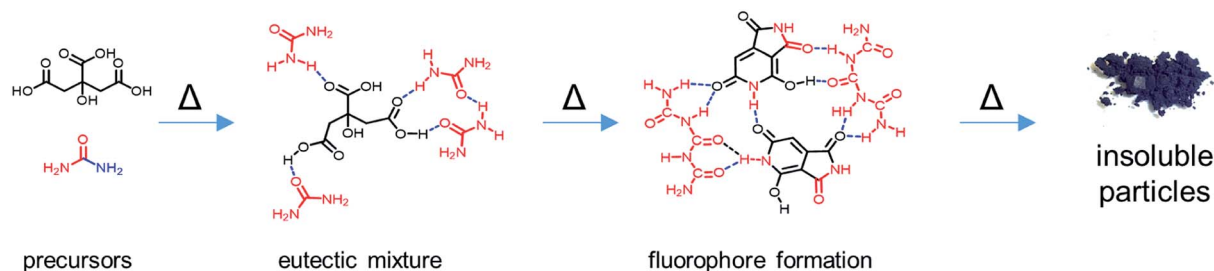


Fig. 7 Proposed reaction mechanism of citric acid and urea to produce solid organic nanoparticles via molecular intermediates.



This assumption is supported by the analysis of the elemental compositions. With respect to the determined compositions of the three components, **CUp** has the highest carbon content and a medium nitrogen content. On the one hand, XPS and FT-IR measurements show that large amounts of C–N and C=N bonds are present. The XRD peak at 2θ of 27.2° and the fact that the dominant carbon species is sp^2 -hybridized, as shown in XPS experiments, point to the presence of nitrogen-containing graphitic domains in **CUp**.

Notably, in our experiments, we focused on CA/U reaction mixtures with a molar ratio of 1 : 3. It is feasible that higher amounts of urea lead to the predominant formation of C_3N_4 clusters in the reaction product.^{23,34} Isocyanic acid, the initial reactive species formed, is known to react with cyanuric acid and carbon nitrides.⁴⁸ The covalent incorporation of **CUg** into such nitrogen-containing graphitic domains is feasible as absorption features resembling those of **CUg** are still observed in the solution phase of purified **CUp**.^{27,49} H-Bonding between excess TAFs and **CUp** may support the solubilization of the latter. In the crude mixture, molecular compounds such as **CUg** and **CUb** act as surfactants and prevent the aggregation of **CUp**.

Condensation products of only citric acid are largely suppressed by the excessive presence of urea. When heating only citric acid in neutral aqueous solution, typically a brown or orange product is obtained which is soluble in water. This brown product is most likely a polymer formed by the fusion of citric acid or aconitic acid molecules. Aconitic acid is formed at a temperature of $\sim 120^\circ\text{C}$ upon elimination of the hydroxyl group and a proton.⁵⁰ Upon addition of a base, the carboxylic acid groups are deprotonated and upon further heating, a decarboxylation reaction occurs which leads to the reduction and aromatization of the citric acid polymer.^{51,52} The product based on pure citric acid exhibits a single absorption maximum at $\sim 360\text{ nm}$ and the fluorescence quantum yields are reported to be rather low.⁵¹

Conclusions

The thermal reaction of citric acid and urea in the melt was thoroughly investigated. The composition of the reaction product is strongly dependent on the reaction parameters such as temperature, time, and composition. In this study, the reaction products were analyzed at a constant reaction time and different temperatures by means of absorption and fluorescence and NMR spectroscopies. Three main reaction products are formed during the reaction depending on the temperature, namely two molecular fluorophores and non-fluorescent carbonaceous particles. These products were isolated by a series of extractions and chromatography and thoroughly characterized in a comprehensive study. Based on the results, a potential reaction mechanism was proposed in which the nanoparticles are a product of the intermediately formed fluorophores.

The results presented herein demonstrate the complexity of the thermal citric acid/urea reaction. The raw reaction product should be seen as a complex mixture with symbiotic properties, similar to natural products such as litmus. Based on the results

presented and recent literature, a clear distinction between thermally accessed fluorophores and carbonaceous nanoparticles should be made and thorough separation may help to improve their performance in various applications.

These insights not only help to understand the origin of the fluorescence in pyrolyzed organic materials, in general, but also provide easy access to a new class of highly inexpensive, water-soluble fluorescent molecules, such as HPPT, which is an interesting candidate for biological or fluorescence imaging and sensing applications due to its excellent photophysical properties. Moreover, as demonstrated in earlier studies, non-fluorescent organic nanoparticles are excellent precursors for our recently developed laser-assisted carbonization process. The structural information from this study helps to understand the fundamental chemical requirements for a good carbon precursor for this laser-assisted carbonization process.

Experimental section

Synthesis: Two stock solutions of CA/U with molar ratios 1 : 3 and 1 : 5 were prepared with total concentrations of 100 or 84 g L^{-1} , respectively. 4 mL of the stock solutions were added to the microwave vessel and H_2O was evaporated under reduced pressure in a vacuum oven. The solid mixture was pre-stirred for 5 min at 90°C to ensure complete melting. Then the microwave power was increased to reach the reaction temperature. The reaction temperature was held for 20 min. The product was collected and analyzed or further purified. **Melting point analysis:** Homogeneous mixtures of Ca and U were produced by solubilizing both components (*ca.* 1 g in total) in 1 mL H_2O . H_2O was then slowly evaporated under reduced pressure at room temperature. The resulting homogeneous mixtures were then analyzed by differential scanning calorimetry. **Chromatographic separation:** The separated fractions were collected and condensed. The solution was filtered to remove any solid silica that was washed from the column. Each fraction was dried under reduced pressure. **Transmission electron microscopy** was performed using an EM 912 Omega from Zeiss operating at 120 kV. To prepare the TEM samples, the carbon material was dispersed in methanol by sonication for 10 min and 5 μL droplets of the dispersion were placed on a carbon-coated copper TEM grid and dried at room temperature. **Thermogravimetric analysis** was performed using a Thermo Microbalance TG 209 F1 Libra (Netzsch, Selb, Germany). A platinum crucible was used for measuring $10 \pm 1\text{ mg}$ of samples under a nitrogen flow of 20 mL min^{-1} and a purge flow of 20 mL min^{-1} at a heating rate of 10 K min^{-1} . **Elemental analysis** was performed with a vario MICRO cube CHNOS elemental analyzer (Elementar Analysensysteme GmbH). The elements were detected with a thermal conductivity detector (TCD) for C, H, N and O and an infrared (IR) detector for sulfur. **UV-vis-NIR absorption** measurements were performed with a Specord 210 plus from Analytik Jena using 10 mm quartz cuvettes. **Fluorescence** measurements were performed with a Fluoromax 4 from Horiba. The fluorescence decays were measured using a Single Photon Counting Controller Fluorohub (Horiba Jobin Yvon) operating in the time-correlated single-photon-counting



(TCSPC) mode. A nanosecond pulsed diode laser NanoLED-450 (Horiba Jobin Yvon) with a pulse width of 1.3 ns, $\lambda_{\text{ex}} = 447$ nm and a repetition rate of 1 MHz was used for excitation. *Fourier-transform infrared* measurements were performed using a Nicolet iS 5 FT-IR-spectrometer in conjunction with an iD5 ATR unit from Thermo Fisher Scientific. *X-ray diffraction* was performed on a Bruker D8 Advance diffractometer in the Bragg-Brentano mode at the Cu K α wavelength. *Nuclear-magnetic resonance spectroscopy* was performed on a 400 MHz Bruker Ascend 400 or a 700 MHz Bruker Ascend 700. *X-ray photoelectron spectroscopy* was performed on a Quantera II (Physical Electronics, Chanhassen, MN, USA). A monochromatic Al K α X-ray source (1486.6 eV) operating at 15 kV and 25 W was applied. Each measured spot was sputtered with Ar-ions (1 keV) for 30 seconds for surface cleaning. The C=C, sp² carbon peak was referenced to 284.4 eV according to the literature.^{53–56} Casa XPS was used for fitting. *Geometries* of tautomers A–C were pre-optimized using the MMFF94x⁵⁷ forcefield and the program MOE 2008.10.⁵⁸ Based on these geometries, DFT calculations were performed using the program package Gaussian 16 (ref. 59) with the hybrid functional M062X⁶⁰ and the basis set def2-TZVP.⁶¹ Dispersion correction was performed by using the empirical dispersion developed by Grimme.⁶² Moreover, calculations were performed in the presence of a solvent (MeOH, H₂O) using the PCM model developed by Tomasi.⁶³ For all obtained geometries, frequency analyses were performed to ensure that they are minima and to calculate the zero-point vibrational energy.

Conflicts of interest

There are no conflicts to declare.

Acknowledgements

We thankfully acknowledge the permanent educational and financial support from Prof. Markus Antonietti and the financial support from the Fonds der Chemischen Industrie. We thank Heike Runge, Rona Pitschke, and Antje Voelkel for assistance with materials characterization. M. L. acknowledges the Federal Ministry of Education and Research (BMBF) in the framework of NanoMatFutur (SynKat) for financial support (project number 03XP0265). We thank the Max Planck society for funding.

References

- 1 Y. Choi, Y. Choi, O.-H. Kwon and B.-S. Kim, Carbon Dots: Bottom-Up Syntheses, Properties, and Light-Harvesting Applications, *Chem.-Asian J.*, 2018, **13**(6), 586–598, DOI: 10.1002/asia.201701736.
- 2 R. Das, R. Bandyopadhyay and P. Pramanik, Carbon Quantum Dots from Natural Resource: A Review, *Mater. Today Chem.*, 2018, **8**, 96–109, DOI: 10.1016/j.mtchem.2018.03.003.
- 3 Z.-Y. Wu, S.-L. Xu, Q.-Q. Yan, Z.-Q. Chen, Y.-W. Ding, C. Li, H.-W. Liang and S.-H. Yu, Transition Metal-Assisted Carbonization of Small Organic Molecules toward Functional Carbon Materials, *Sci. Adv.*, 2018, **4**(7), eaat0788, DOI: 10.1126/sciadv.aat0788.
- 4 C. Xia, S. Zhu, T. Feng, M. Yang and B. Yang, Evolution and Synthesis of Carbon Dots: From Carbon Dots to Carbonized Polymer Dots, *Adv. Sci.*, 2019, **6**(23), 1901316, DOI: 10.1002/advs.201901316.
- 5 M.-M. Titirici, A. Thomas and M. Antonietti, Back in the Black: Hydrothermal Carbonization of Plant Material as an Efficient Chemical Process to Treat the CO₂ Problem?, *New J. Chem.*, 2007, **31**(6), 787, DOI: 10.1039/b616045j.
- 6 M. Antonietti and M. Oschatz, The Concept of “Noble, Heteroatom-Doped Carbons,” Their Directed Synthesis by Electronic Band Control of Carbonization, and Applications in Catalysis and Energy Materials, *Adv. Mater.*, 2018, **30**(21), 1706836, DOI: 10.1002/adma.201706836.
- 7 R. Demir-Cakan, N. Baccile, M. Antonietti and M.-M. Titirici, Carboxylate-Rich Carbonaceous Materials via One-Step Hydrothermal Carbonization of Glucose in the Presence of Acrylic Acid, *Chem. Mater.*, 2009, **21**(3), 484–490, DOI: 10.1021/cm802141h.
- 8 D. Yoo, Y. Park, B. Cheon and M.-H. Park, Carbon Dots as an Effective Fluorescent Sensing Platform for Metal Ion Detection, *Nanoscale Res. Lett.*, 2019, **14**(1), 272, DOI: 10.1186/s11671-019-3088-6.
- 9 J. T. Margraf, F. Lodermeier, V. Strauss, P. Haines, J. Walter, W. Peukert, R. D. Costa, T. Clark and D. M. Guldi, Using Carbon Nanodots as Inexpensive and Environmentally Friendly Sensitizers in Mesoscopic Solar Cells, *Nanoscale Horiz.*, 2016, **1**(3), 220–226, DOI: 10.1039/c6nh00010j.
- 10 S. H. Song, M.-H. Jang, J. Chung, S. H. Jin, B. H. Kim, S.-H. Hur, S. Yoo, Y.-H. Cho and S. Jeon, Highly Efficient Light-Emitting Diode of Graphene Quantum Dots Fabricated from Graphite Intercalation Compounds, *Adv. Opt. Mater.*, 2014, **2**(11), 1016–1023, DOI: 10.1002/adom.201400184.
- 11 D. H. Hasenöhr, A. Saha, V. Strauss, L. Wibmer, S. Klein, D. M. Guldi and A. Hirsch, Bulbous Gold–Carbon Nanodot Hybrid Nanoclusters for Cancer Therapy, *J. Mater. Chem. B*, 2017, **5**(43), 8591–8599, DOI: 10.1039/c7tb02039b.
- 12 J. Tang, B. Kong, H. Wu, M. Xu, Y. Wang, Y. Wang, D. Zhao and G. Zheng, Carbon Nanodots Featuring Efficient FRET for Real-Time Monitoring of Drug Delivery and Two-Photon Imaging, *Adv. Mater.*, 2013, **25**(45), 6569–6574, DOI: 10.1002/adma.201303124.
- 13 C. Wang, V. Strauss and R. B. Kaner, Carbon Nanodots for Capacitor Electrodes, *Trends Chem.*, 2019, **1**(9), 858–868, DOI: 10.1016/j.trechm.2019.05.009.
- 14 B. C. M. Martindale, G. A. M. Hutton, C. A. Caputo, S. Prantl, R. Godin, J. R. Durrant and E. Reisner, Enhancing Light Absorption and Charge Transfer Efficiency in Carbon Dots through Graphitization and Core Nitrogen Doping, *Angew. Chem., Int. Ed.*, 2017, **56**(23), 6459–6463, DOI: 10.1002/anie.201700949.
- 15 B. Yao, H. Huang, Y. Liu and Z. Kang, Carbon Dots: A Small Conundrum, *Trends Chem.*, 2019, **1**(2), 235–246, DOI: 10.1016/j.trechm.2019.02.003.



- 16 A. Sciortino, A. Cannizzo and F. Messina, Carbon Nanodots: A Review—From the Current Understanding of the Fundamental Photophysics to the Full Control of the Optical Response, *C*, 2018, **4**(4), 67, DOI: 10.3390/c4040067.
- 17 P. Tian, L. Tang, K. S. Teng and S. P. Lau, Graphene Quantum Dots from Chemistry to Applications, *Mater. Today Chem.*, 2018, **10**, 221–258, DOI: 10.1016/j.mtchem.2018.09.007.
- 18 S. Qu, X. Wang, Q. Lu, X. Liu and L. Wang, A Biocompatible Fluorescent Ink Based on Water-Soluble Luminescent Carbon Nanodots, *Angew. Chem., Int. Ed.*, 2012, **51**(49), 12215–12218, DOI: 10.1002/anie.201206791.
- 19 V. Strauss, A. Kahnt, E. M. Zolnhofer, K. Meyer, H. Maid, C. Placht, W. Bauer, T. J. Nacken, W. Peukert, S. H. Etschel, *et al.*, Assigning Electronic States in Carbon Nanodots, *Adv. Funct. Mater.*, 2016, **26**(44), 7975–7985, DOI: 10.1002/adfm.201602325.
- 20 V. Strauss, J. T. Margraf, C. Dolle, B. Butz, T. J. Nacken, J. Walter, W. Bauer, W. Peukert, E. Spiecker, T. Clark, *et al.*, Carbon Nanodots: Toward a Comprehensive Understanding of Their Photoluminescence, *J. Am. Chem. Soc.*, 2014, **136**(49), 17308–17316, DOI: 10.1021/ja510183c.
- 21 Y. Song, S. Zhu, S. Zhang, Y. Fu, L. Wang, X. Zhao and B. Yang, Investigation from Chemical Structure to Photoluminescent Mechanism: A Type of Carbon Dots from the Pyrolysis of Citric Acid and an Amine, *J. Mater. Chem. C*, 2015, **3**(23), 5976–5984, DOI: 10.1039/c5tc00813a.
- 22 J. Zhou, Y. Yang and C. Y. Zhang, A Low-Temperature Solid-Phase Method to Synthesize Highly Fluorescent Carbon Nitride Dots with Tunable Emission, *Chem. Commun.*, 2013, **49**(77), 8605, DOI: 10.1039/c3cc42266f.
- 23 F. Messina, L. Sciortino, R. Popescu, A. M. Venezia, A. Sciortino, G. Buscarino, S. Agnello, R. Schneider, D. Gerthsen, M. Cannas, *et al.*, Fluorescent Nitrogen-Rich Carbon Nanodots with an Unexpected β -C 3 N 4 Nanocrystalline Structure, *J. Mater. Chem. C*, 2016, **4**(13), 2598–2605, DOI: 10.1039/c5tc04096e.
- 24 S. A. Hill, D. Benito-Alifonso, S. A. Davis, D. J. Morgan, M. Berry and M. C. Galan, Practical Three-Minute Synthesis of Acid-Coated Fluorescent Carbon Dots with Tuneable Core Structure, *Sci. Rep.*, 2018, **8**(1), 12234, DOI: 10.1038/s41598-018-29674-2.
- 25 W. Kasprzyk, T. Świergosz, S. Bednarz, K. Walas, N. V. Bashmakova and D. Bogdał, Luminescence Phenomena of Carbon Dots Derived from Citric Acid and Urea – a Molecular Insight, *Nanoscale*, 2018, **10**(29), 13889–13894, DOI: 10.1039/c8nr03602k.
- 26 V. Hinterberger, C. Damm, P. Haines, D. M. Guldi and W. Peukert, Purification and Structural Elucidation of Carbon Dots by Column Chromatography, *Nanoscale*, 2019, **11**(17), 8464–8474, DOI: 10.1039/c9nr01029g.
- 27 J. Schneider, C. J. Reckmeier, Y. Xiong, M. von Seckendorff, A. S. Susha, P. Kasák and A. L. Rogach, Molecular Fluorescence in Citric Acid-Based Carbon Dots, *J. Phys. Chem. C*, 2017, **121**(3), 2014–2022, DOI: 10.1021/acs.jpcc.6b12519.
- 28 N. M. Zholobak, A. L. Popov, A. B. Shcherbakov, N. R. Popova, M. M. Guzyk, V. P. Antonovich, A. V. Yegorova, Y. V. Scrypnets, I. I. Leonenko, A. Y. Baranchikov, *et al.*, Facile Fabrication of Luminescent Organic Dots by Thermolysis of Citric Acid in Urea Melt, and Their Use for Cell Staining and Polyelectrolyte Microcapsule Labelling, *Beilstein J. Nanotechnol.*, 2016, **7**, 1905–1917, DOI: 10.3762/bjnano.7.182.
- 29 D. Qu and Z. Sun, The Formation Mechanism and Fluorophores of Carbon Dots Synthesized via a Bottom-up Route, *Mater. Chem. Front.*, 2020, **4**(2), 400–420, DOI: 10.1039/c9qm00552h.
- 30 S. Qu, D. Zhou, D. Li, W. Ji, P. Jing, D. Han, L. Liu, H. Zeng and D. Shen, Toward Efficient Orange Emissive Carbon Nanodots through Conjugated Sp²-Domain Controlling and Surface Charges Engineering, *Adv. Mater.*, 2016, **28**(18), 3516–3521, DOI: 10.1002/adma.201504891.
- 31 L. Sciortino, A. Sciortino, R. Popescu, R. Schneider, D. Gerthsen, S. Agnello, M. Cannas and F. Messina, Tailoring the Emission Color of Carbon Dots through Nitrogen-Induced Changes of Their Crystalline Structure, *J. Phys. Chem. C*, 2018, **122**(34), 19897–19903, DOI: 10.1021/acs.jpcc.8b04514.
- 32 W. J. Sell and T. H. Easterfield, LXXIII.—Studies on Citrazinic Acid. Part I, *J. Chem. Soc., Trans.*, 1893, **63**(I), 1035–1051, DOI: 10.1039/ct8936301035.
- 33 W. Wang, B. Wang, H. Embrechts, C. Damm, A. Cadranel, V. Strauss, M. Distaso, V. Hinterberger, D. M. Guldi and W. Peukert, Shedding Light on the Effective Fluorophore Structure of High Fluorescence Quantum Yield Carbon Nanodots, *RSC Adv.*, 2017, **7**(40), 24771–24780, DOI: 10.1039/c7ra04421f.
- 34 A. Sciortino, N. Mauro, G. Buscarino, L. Sciortino, R. Popescu, R. Schneider, G. Giammona, D. Gerthsen, M. Cannas and F. Messina, β -C 3 N 4 Nanocrystals: Carbon Dots with Extraordinary Morphological, Structural, and Optical Homogeneity, *Chem. Mater.*, 2018, **30**(5), 1695–1700, DOI: 10.1021/acs.chemmater.7b05178.
- 35 J. Zhou, Y. Yang and C. Zhang, A Low-Temperature Solid-Phase Method to Synthesize Highly Fluorescent Carbon Nitride Dots with Tunable Emission, *Chem. Commun.*, 2013, **49**(77), 8605, DOI: 10.1039/c3cc42266f.
- 36 A. Nandy, A. Kumar, S. Dwivedi, S. K. Pal and D. Panda, Connecting the Dots of Carbon Nanodots: Excitation (In) Dependency and White-Light Emission in One-Step, *J. Phys. Chem. C*, 2019, **123**(33), 20502–20511, DOI: 10.1021/acs.jpcc.9b02428.
- 37 Y. Wang, Y. Zhu, S. Yu and C. Jiang, Fluorescent Carbon Dots: Rational Synthesis, Tunable Optical Properties and Analytical Applications, *RSC Adv.*, 2017, **7**(65), 40973–40989, DOI: 10.1039/c7ra07573a.
- 38 Z. Li, J. R. Askim and K. S. Suslick, The Optoelectronic Nose: Colorimetric and Fluorometric Sensor Arrays, *Chem. Rev.*, 2019, **119**(1), 231–292, DOI: 10.1021/acs.chemrev.8b00226.
- 39 H. Blom and J. Widengren, Stimulated Emission Depletion Microscopy, *Chem. Rev.*, 2017, **117**(11), 7377–7427, DOI: 10.1021/acs.chemrev.6b00653.



- 40 J. W. Borst and A. J. W. G. Visser, Fluorescence Lifetime Imaging Microscopy in Life Sciences, *Meas. Sci. Technol.*, 2010, **21**(10), 102002, DOI: 10.1088/0957-0233/21/10/102002.
- 41 X. Miao, D. Qu, D. Yang, B. Nie, Y. Zhao, H. Fan and Z. Sun, Synthesis of Carbon Dots with Multiple Color Emission by Controlled Graphitization and Surface Functionalization, *Adv. Mater.*, 2018, **30**(1), 1704740, DOI: 10.1002/adma.201704740.
- 42 V. Strauss, K. Marsh, M. D. Kowal, M. F. El-Kady and R. B. Kaner, A Simple Route to Porous Graphene from Carbon Nanodots for Supercapacitor Applications, *Adv. Mater.*, 2018, **30**(8), 1704449, DOI: 10.1002/adma.201704449.
- 43 E. L. Smith, A. P. Abbott and K. S. Ryder, Deep Eutectic Solvents (DESS) and Their Applications, *Chem. Rev.*, 2014, **114**(21), 11060–11082, DOI: 10.1021/cr300162p.
- 44 A. Ganguly, S. Sharma, P. Papakonstantinou and J. Hamilton, Probing the Thermal Deoxygenation of Graphene Oxide Using High-Resolution In Situ X-Ray-Based Spectroscopies, *J. Phys. Chem. C*, 2011, **115**(34), 17009–17019, DOI: 10.1021/jp203741y.
- 45 D. Rosenthal, M. Ruta, R. Schlögl and L. Kiwi-Minsker, Combined XPS and TPD Study of Oxygen-Functionalized Carbon Nanofibers Grown on Sintered Metal Fibers, *Carbon*, 2010, **48**(6), 1835–1843, DOI: 10.1016/j.carbon.2010.01.029.
- 46 L. Stradella and M. Argentero, A Study of the Thermal Decomposition of Urea, of Related Compounds and Thiourea Using DSC and TG-EGA, *Thermochim. Acta*, 1993, **219**, 315–323, DOI: 10.1016/0040-6031(93)80508-8.
- 47 P. M. Schaber, J. Colson, S. Higgins, D. Thielen, B. Anspach and J. Brauer, Thermal Decomposition (Pyrolysis) of Urea in an Open Reaction Vessel, *Thermochim. Acta*, 2004, **424**(1–2), 131–142, DOI: 10.1016/j.tca.2004.05.018.
- 48 J. Liu, T. Zhang, Z. Wang, G. Dawson and W. Chen, Simple Pyrolysis of Urea into Graphitic Carbon Nitride with Recyclable Adsorption and Photocatalytic Activity, *J. Mater. Chem.*, 2011, **21**(38), 14398, DOI: 10.1039/c1jm12620b.
- 49 F. Ehrat, S. Bhattacharyya, J. Schneider, A. Löf, R. Wyrwich, A. L. Rogach, J. K. Stolarczyk, A. S. Urban and J. Feldmann, Tracking the Source of Carbon Dot Photoluminescence: Aromatic Domains versus Molecular Fluorophores, *Nano Lett.*, 2017, **17**(12), 7710–7716, DOI: 10.1021/acs.nanolett.7b03863.
- 50 M. M. Barbooti and D. A. Al-Sammerrai, Thermal Decomposition of Citric Acid, *Thermochim. Acta*, 1986, **98**, 119–126, DOI: 10.1016/0040-6031(86)87081-2.
- 51 R. Sun, Y. Wang, Y. Ni and S. Kokot, Graphene Quantum Dots and the Resonance Light Scattering Technique for Trace Analysis of Phenol in Different Water Samples, *Talanta*, 2014, **125**, 341–346, DOI: 10.1016/j.talanta.2014.03.007.
- 52 B. C. M. Martindale, G. A. M. Hutton, C. A. Caputo and E. Reisner, Solar Hydrogen Production Using Carbon Quantum Dots and a Molecular Nickel Catalyst, *J. Am. Chem. Soc.*, 2015, **137**(18), 6018–6025, DOI: 10.1021/jacs.5b01650.
- 53 S. Biniak, G. Szymański, J. Siedlewski and A. Świątkowski, The Characterization of Activated Carbons with Oxygen and Nitrogen Surface Groups, *Carbon*, 1997, **35**(12), 1799–1810, DOI: 10.1016/S0008-6223(97)00096-1.
- 54 H. Darmstadt, C. Roy and S. Kaliaguine, ESCA Characterization of Commercial Carbon Blacks and of Carbon Blacks from Vacuum Pyrolysis of Used Tires, *Carbon*, 1994, **32**(8), 1399–1406, DOI: 10.1016/0008-6223(94)90132-5.
- 55 J. L. Figueiredo and M. F. R. Pereira, The Role of Surface Chemistry in Catalysis with Carbons, *Catal. Today*, 2010, **150**(1–2), 2–7, DOI: 10.1016/j.cattod.2009.04.010.
- 56 M. E. Schuster, M. Hävecker, R. Arrigo, R. Blume, M. Knauer, N. P. Ileva, D. S. Su, R. Niessner and R. Schlögl, Surface Sensitive Study To Determine the Reactivity of Soot with the Focus on the European Emission Standards IV and VI, *J. Phys. Chem. A*, 2011, **115**(12), 2568–2580, DOI: 10.1021/jp1088417.
- 57 T. A. Halgren, Merck Molecular Force Field. I. Basis, Form, Scope, Parameterization, and Performance of MMFF94, *J. Comput. Chem.*, 1996, **17**(5–6), 490–519, DOI: 10.1002/(SICI)1096-987X(199604)17:5/6<490::AID-JCC1>3.0.CO;2-P.
- 58 *Molecular Operating Environment Version 2008.10*, Chem. Comput. Gr., 2008.
- 59 M. J. Frisch; G. W. Trucks, H. B. Schlegel, G. E. Scuseria, M. A. Robb, J. R. Cheeseman, G. Scalmani, V. Barone, G. A. Petersson, H. Nakatsuji, *et al.* *Gaussian 16, Revision C.01*, Gaussian, Inc., Wallingford CT, 2019.
- 60 Y. Zhao and D. G. Truhlar, Comparative DFT Study of van Der Waals Complexes: Rare-Gas Dimers, Alkaline-Earth Dimers, Zinc Dimer, and Zinc-Rare-Gas Dimers, *J. Phys. Chem. A*, 2006, **110**(15), 5121–5129, DOI: 10.1021/jp060231d.
- 61 F. Weigend, Accurate Coulomb-Fitting Basis Sets for H to Rn, *Phys. Chem. Chem. Phys.*, 2006, **8**(9), 1057, DOI: 10.1039/b515623h.
- 62 S. Grimme, J. Antony, S. Ehrlich and H. Krieg, A Consistent and Accurate Ab Initio Parametrization of Density Functional Dispersion Correction (DFT-D) for the 94 Elements H-Pu, *J. Chem. Phys.*, 2010, **132**(15), 154104, DOI: 10.1063/1.3382344.
- 63 J. Tomasi, B. Mennucci and R. Cammi, Quantum Mechanical Continuum Solvation Models, *Chem. Rev.*, 2005, **105**(8), 2999–3094, DOI: 10.1021/cr9904009.



Supporting Information to

Volker Strauss^{1*}, Huize Wang¹, Simon Delacroix¹, Marc Ledendecker², Pablo Wessig³

Synthesis	24
Nuclear Magnetic Resonance Spectroscopy of the Raw Products	24
UV-vis and Fluorescence Spectroscopy of the Raw Products.....	25
Nuclear Magnetic Resonance Spectroscopy of the Educts and References	26
Separation of the Raw Products.....	27
Extinction coefficients of CUg	27
Time-correlated Single-Photon Counting of CUg and CUB.....	28
Fluorescence Quantum Yields of CUg	28
Photostability of CUg	29
ESI - mass spectrometry of CUg and CUB.....	29
2D-Correlation NMR of CUg.....	30
DFT calculations of CUg (HPPT).....	31
2D-Correlation NMR of CUB.....	32
Nuclear Magnetic Resonance Spectroscopy of Biuret.....	33
Biuret test with CUB	33
Thermal Mass analysis of CUg and CUB	34
Thermogravimetric Analysis of the Raw Mixture	34
X-ray Photoelectron Spectroscopy of CUB and CUg	35
Nuclear Magnetic Resonance Spectroscopy during Washing of CUp	35
Optical Spectroscopy of dispersions of CUp in H ₂ O.....	36
Nuclear Magnetic Resonance Spectroscopy of a Non-Separated Mixture	36

Synthesis

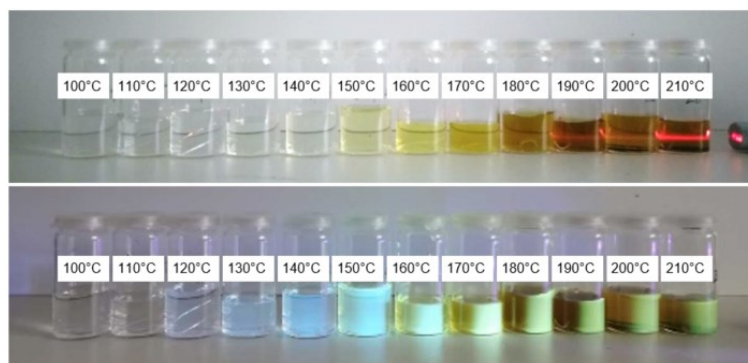


Figure S1. Photograph of aqueous sample solutions of the crude products (conc: 0.2 mg/mL) synthesized at temperatures between 100 – 220°C under illumination with a red laser (top) and under illumination with a UV-lamp (365 nm) (bottom).

Nuclear Magnetic Resonance Spectroscopy of the Raw Products

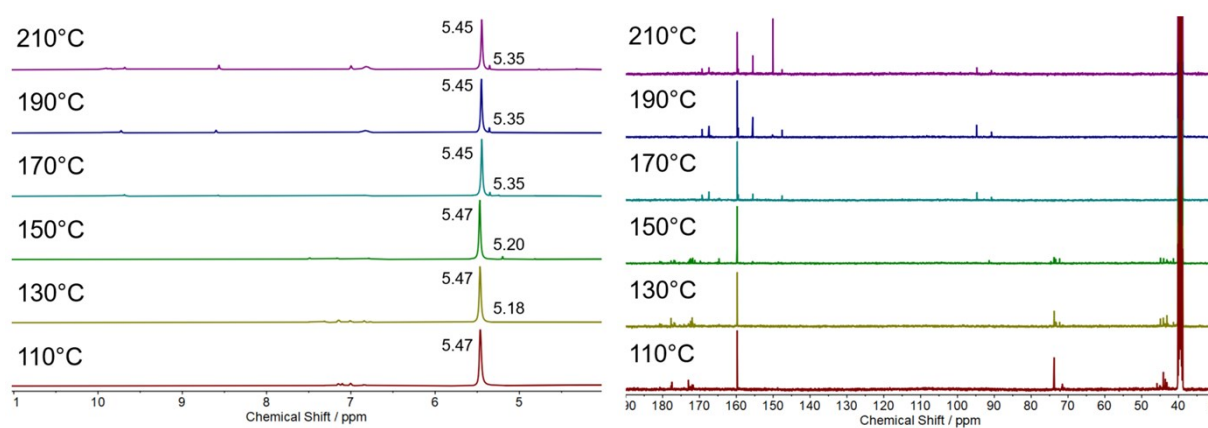


Figure S2. ¹H-NMR (left) and ¹³C-NMR (right) spectra of selected raw products of the CA/U reaction at different temperatures between 110-210°C.

UV-vis and Fluorescence Spectroscopy of the Raw Products

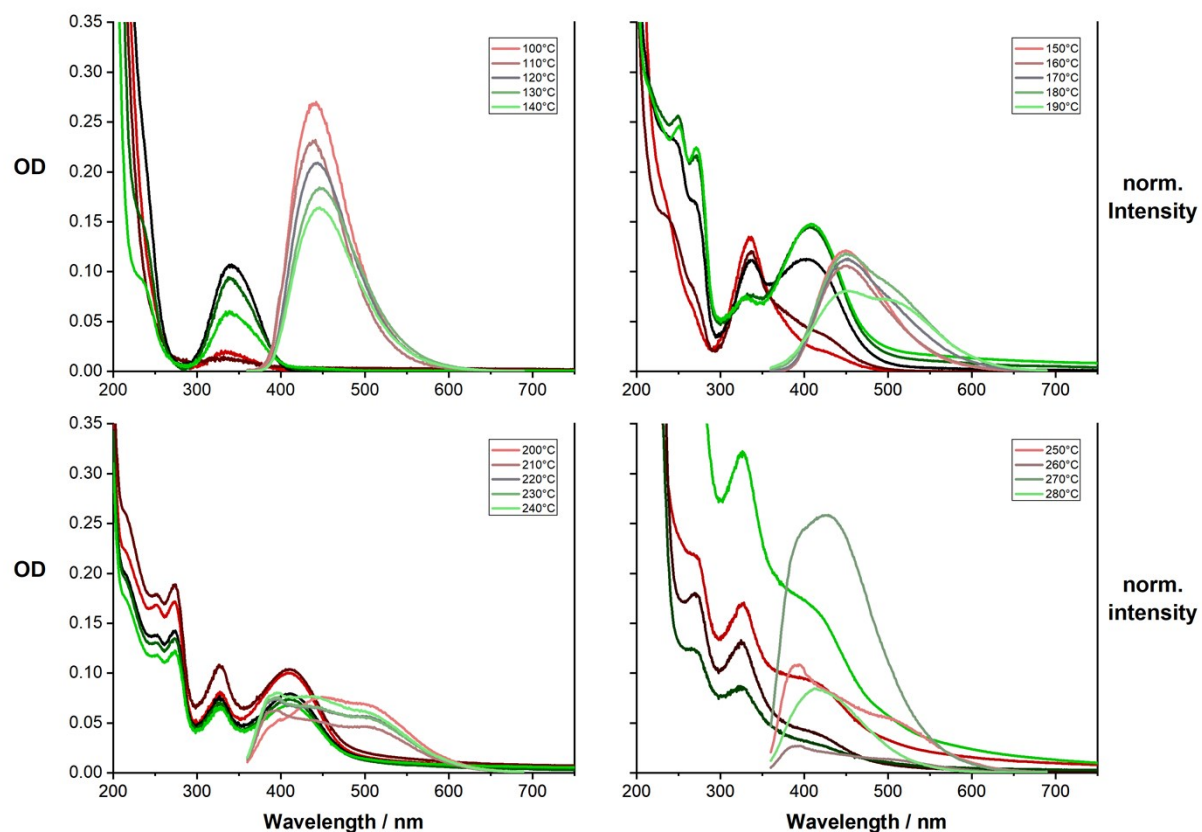


Figure S3. Combined electronic absorption (red to green) and excitation normalized ($\lambda_{\text{ex}} = 350 \text{ nm}$) emission (pale red to pale green) spectra of crude CA/U products (0.013 mg/mL) synthesized at different temperatures between 100 – 290°C; a) 100 – 140°C; b) 150 – 190°C; a) 200 – 240°C; a) 250 – 290°C.

Nuclear Magnetic Resonance Spectroscopy of the Educts and References

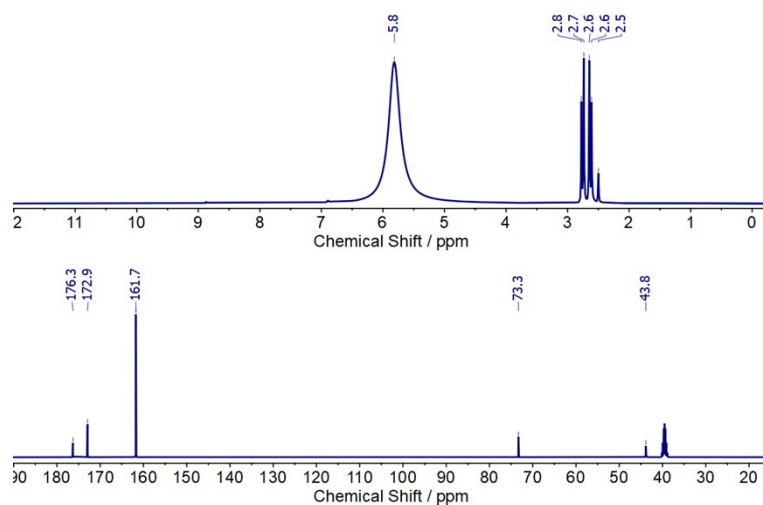


Figure S4. Top: ¹H-NMR (top) and ¹³C-NMR (bottom) spectra of *citric acid* and *urea* in DMSO-d₆.

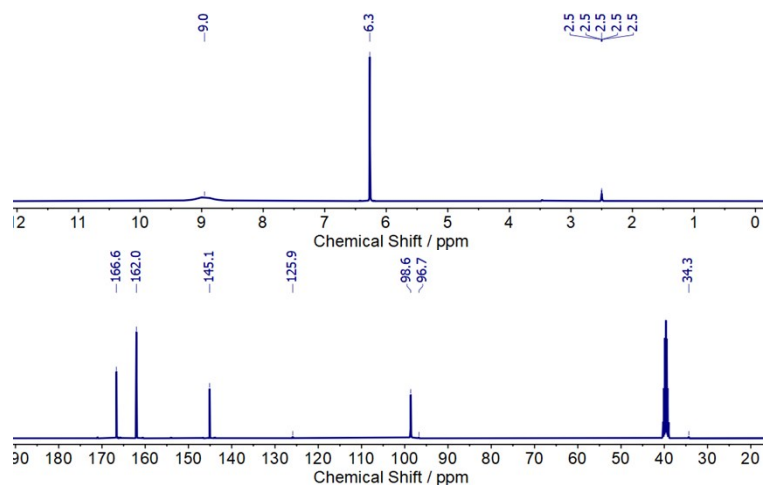


Figure S5. Top: ¹H-NMR (top) and ¹³C-NMR (bottom) spectra of *citrazinic acid* (commercial) in DMSO-d₆.

Separation of the Raw Products

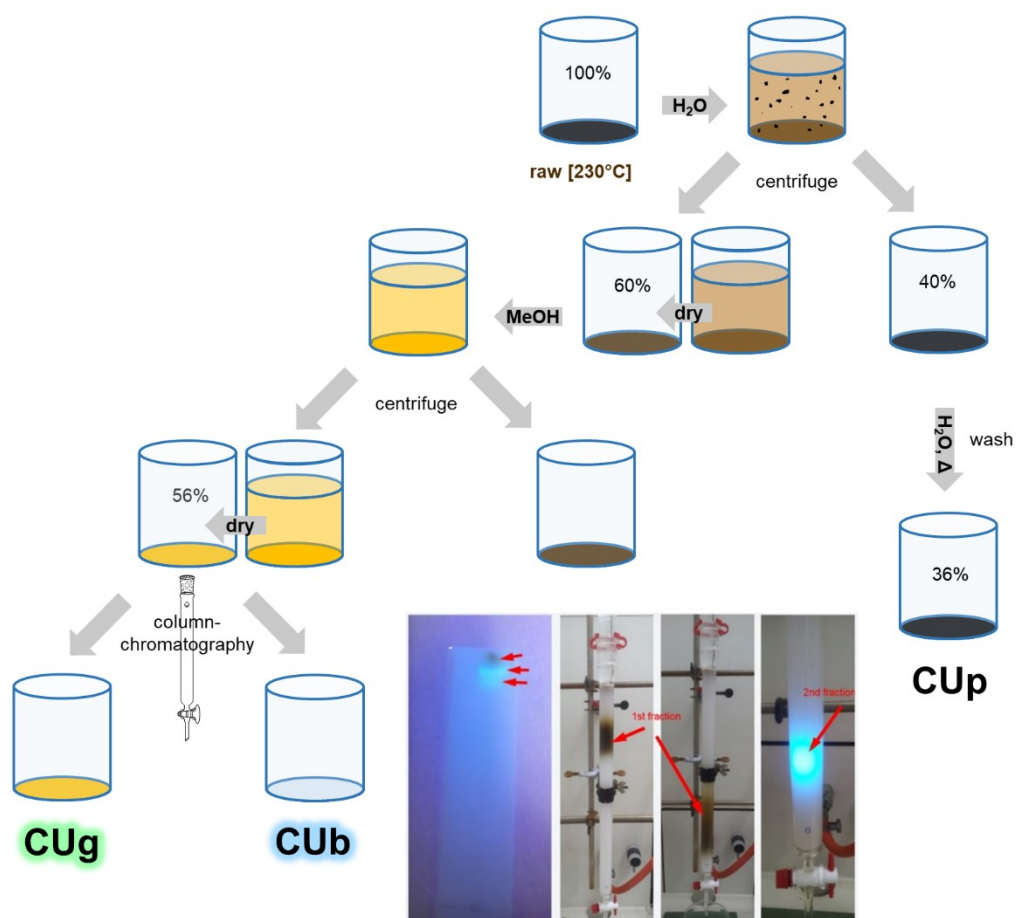


Figure S6. Illustration of the separation process of the raw products obtained from a thermal CA/U reaction.

Extinction coefficients of CUg

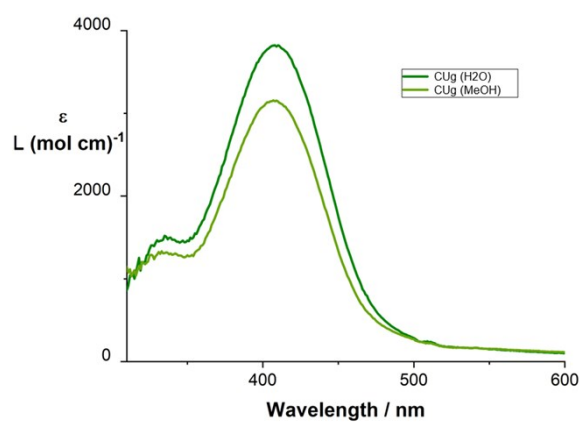


Figure S7. Molar extinction coefficients of CUg in H₂O and MeOH.

Time-correlated Single-Photon Counting of CUB and CUG

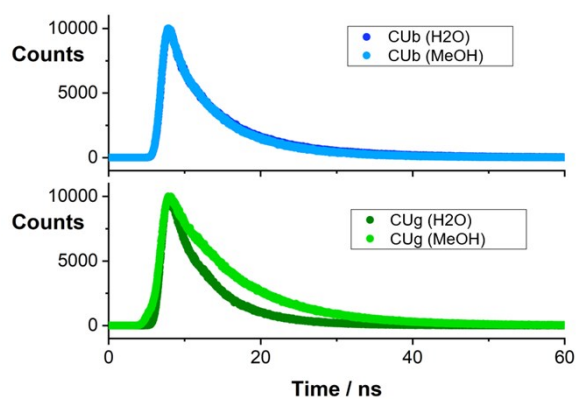


Figure S8. Fluorescence lifetime decay profiles obtained by TCSPC of **CUB** and **CUG** in H_2O and $MeOH$ at room temperature obtained upon excitation at 370 or 450 nm, respectively .

Table S1. Fluorescence lifetimes of **CUB** and **CUG** in $MeOH$ and H_2O .

		τ_1	A_1	τ_2	A_2
		ns	%	ns	%
CUB	$MeOH$	3.1	28	7.6	72
	H_2O	4.1	45	9.5	55
CUG	$MeOH$	9.0	100		
	H_2O	5.3	100		

Fluorescence Quantum Yields of CUG

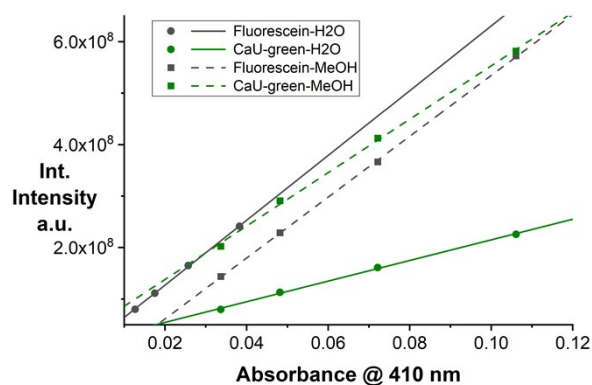


Figure S9. Determination of the fluorescence quantum yields of **CUG** in H_2O and $MeOH$ using Na -fluorescein as a standard.

Table S2. Fluorescence quantum yields of **CUg** determined by the gradient method using Na-fluorescein as a standard and in MeOH and H₂O.

	solvent	slope	Φ_{Fl} (%)
Na-Fluorescein	H ₂ O	6.30E+09	85 ⁶⁴
	MeOH	5.90E+09	79
CUg	H ₂ O	2.00E+09	27
	MeOH	5.20E+09	70

Photostability of CUg

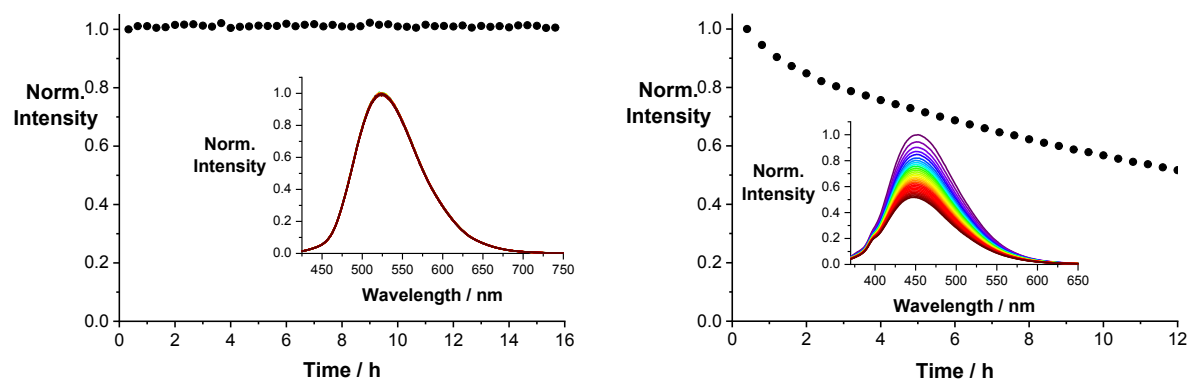


Figure S10. Left: photo-stability measurement of a 8.3×10^{-5} M solution of **CUg** in H₂O. The sample was constantly illuminated for 16h. The inset shows the fluorescence spectra in time intervals of 20 min; Right: Photo-stability measurement of **CUb** in H₂O. The inset shows the fluorescence spectra in time intervals of 24 min from purple to red.

ESI - mass spectrometry of CUg and CUb

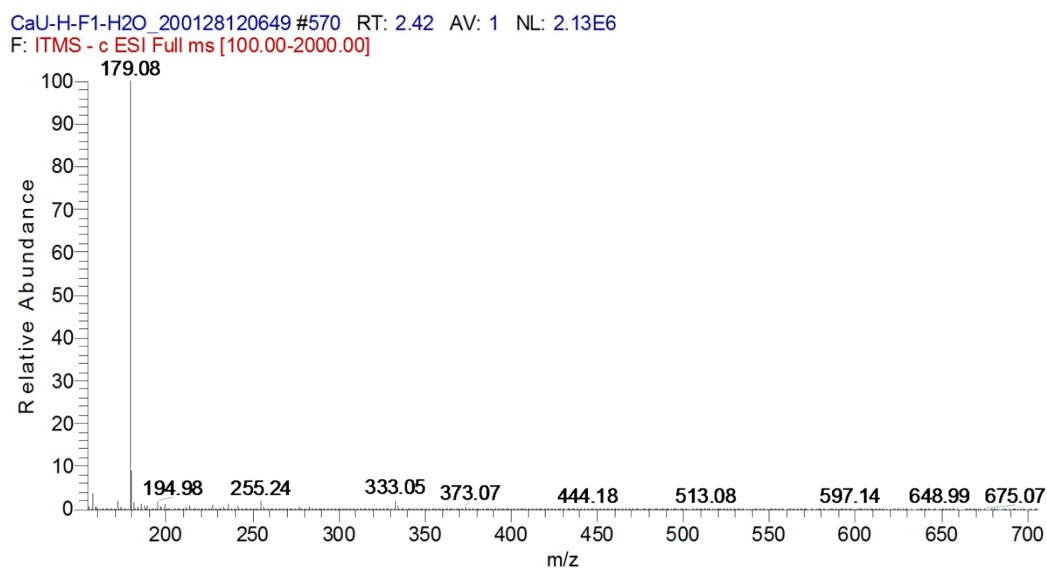


Figure S11. Liquid chromatography-electrospray ionization - mass spectrum of **CUg** obtained in negative ion mode.

CaU-H-F2-H2O_200128131350 #513 RT: 2.18 AV: 1 NL: 7.24E5
 F: ITMS + c ESI Full ms [100.00-2000.00]

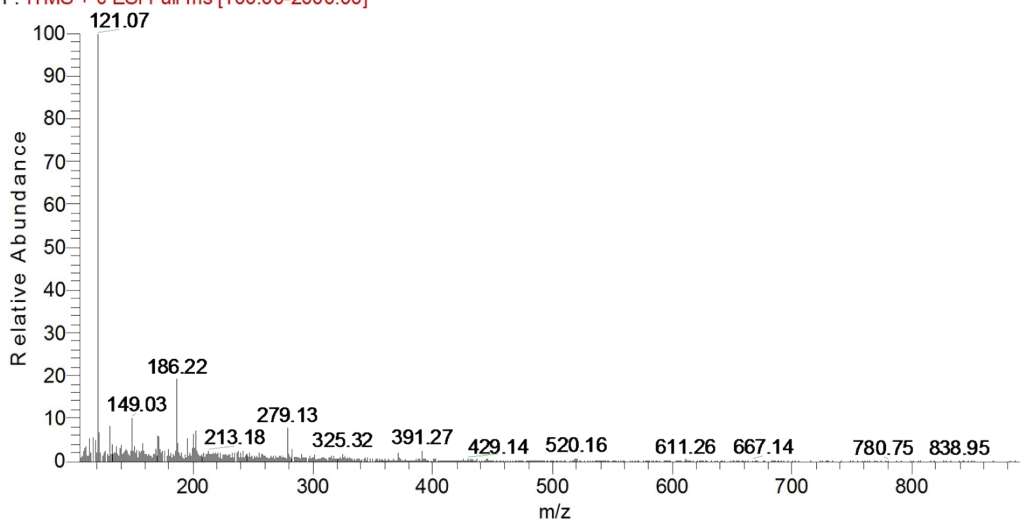


Figure S12. Liquid chromatography – electrospray ionization - mass spectrum of **CUb** obtained in positive ion mode.

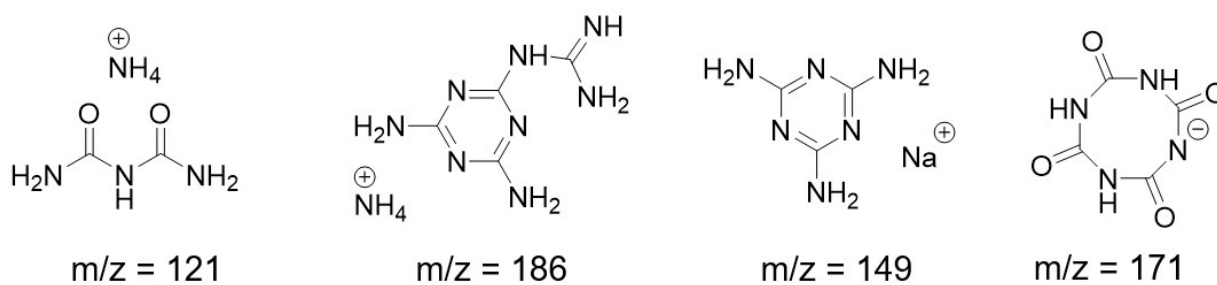


Figure S13. Potential compounds detected in the ESI-mass spectra of **CUb**.

2D-Correlation NMR of **CUg**

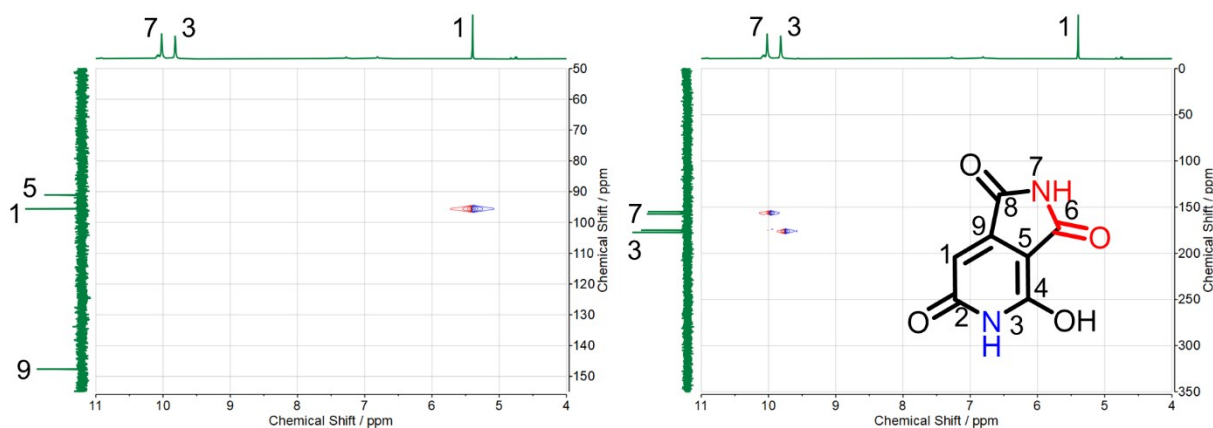


Figure S14. HSQC-C (left) and HSQC-N (right) of **CUg** in DMSO- d_6 showing the direct coupling of ^1H to ^{13}C or ^{15}N , respectively.

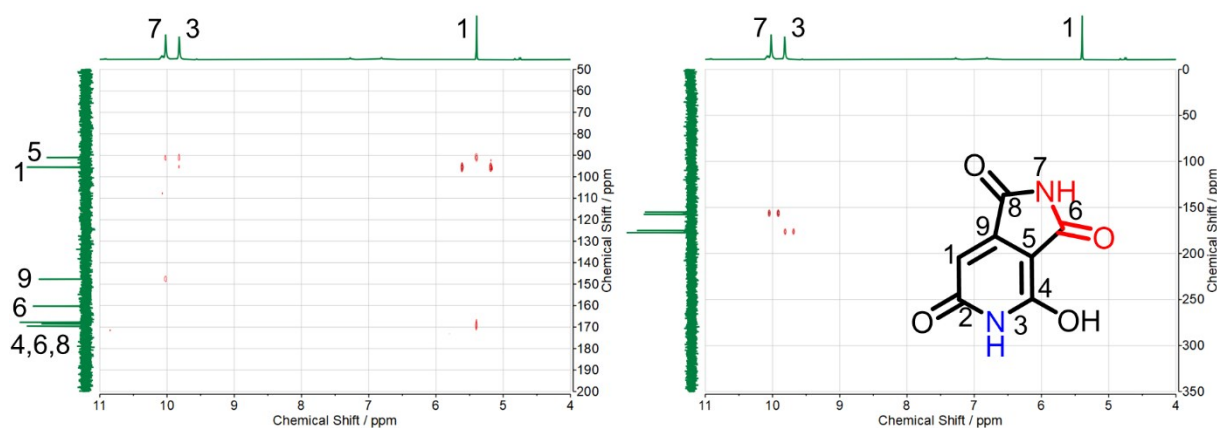


Figure S15. HMBC-C (left) and HMBC-N (right) **CUg** enriched with ^{15}N in DMSO-d_6 showing the three-bond coupling of ^1H to ^{13}C or ^{15}N , respectively.

DFT calculations of CUg (HPPT)

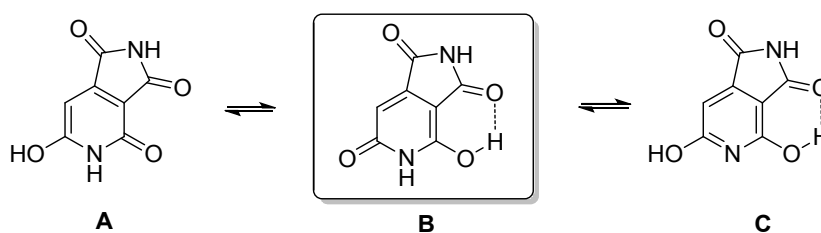
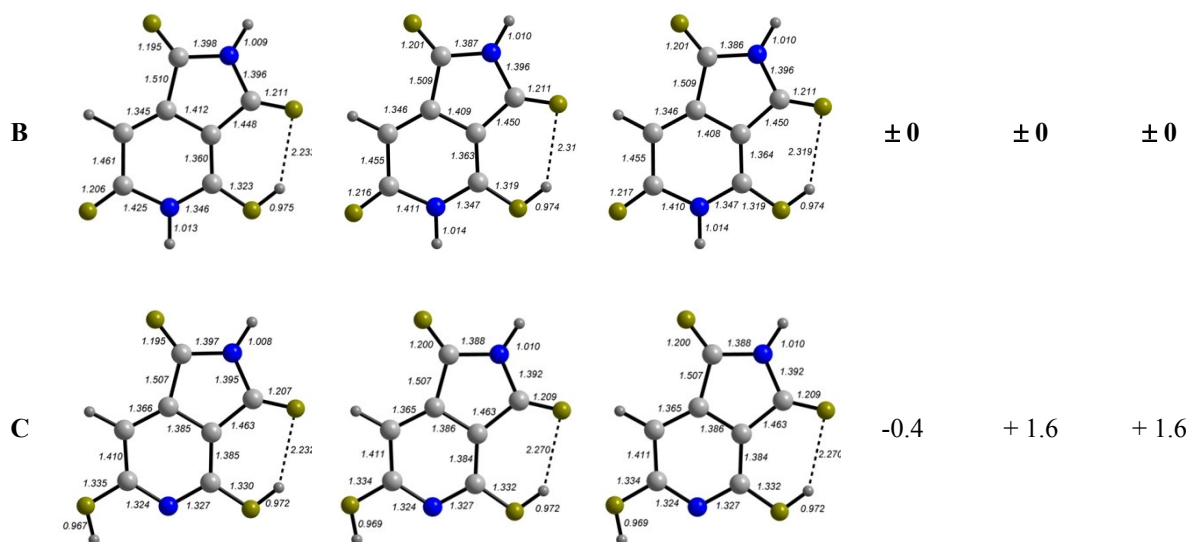


Figure S16. Molecular structures of the tautomeric forms of HPPT.

Table S3. DFT calculated tautomeric forms of HPPT with relative energy values in arbitrary units using M06-2X-D3/def2-TZVP, SCRF: PCM.

Geometry (vacuum)	Geometry (MeOH)	Geometry (H_2O)	E_{REL} (vac.)	E_{REL} (MeOH)	E_{REL} (H_2O)
			+10.9	+ 4.4	+ 4.2



2D-Correlation NMR of CUB

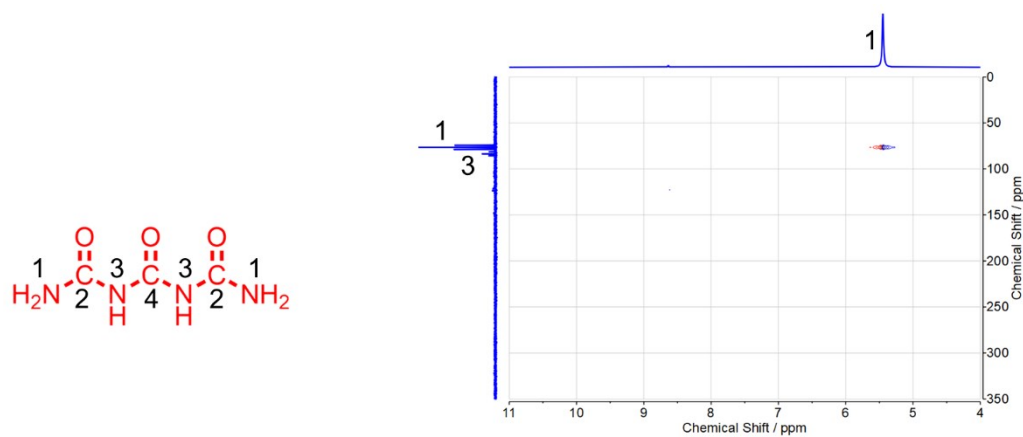


Figure S17. HSQC-N of CUB enriched with ^{15}N in DMSO- d_6 showing the direct coupling of ^1H to ^{13}C or ^{15}N , respectively.

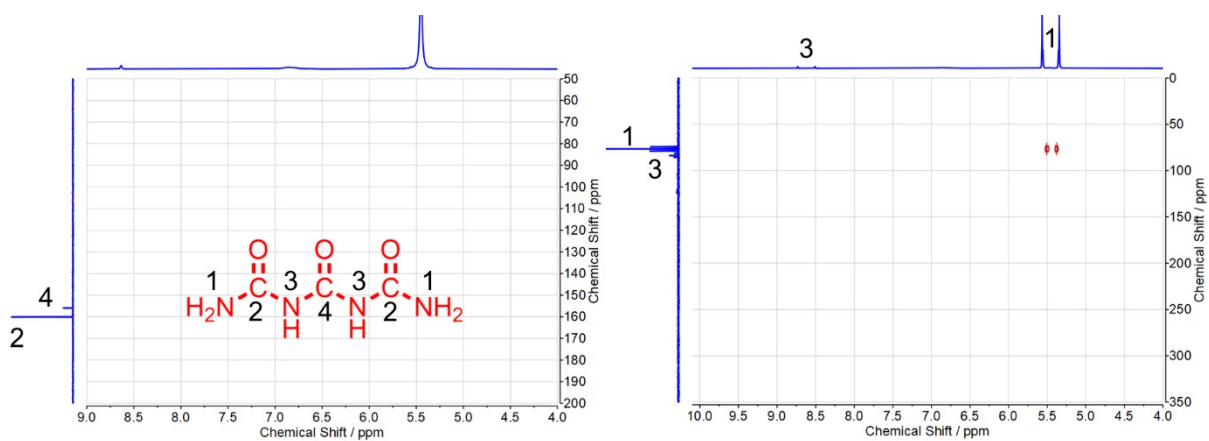


Figure S18. HMBC-C (left) and HMBC-N (right) of **CUB** enriched with ^{15}N in DMSO-d_6 showing the three-bond coupling of ^1H to ^{13}C or ^{15}N , respectively.

Nuclear Magnetic Resonance Spectroscopy of Biuret

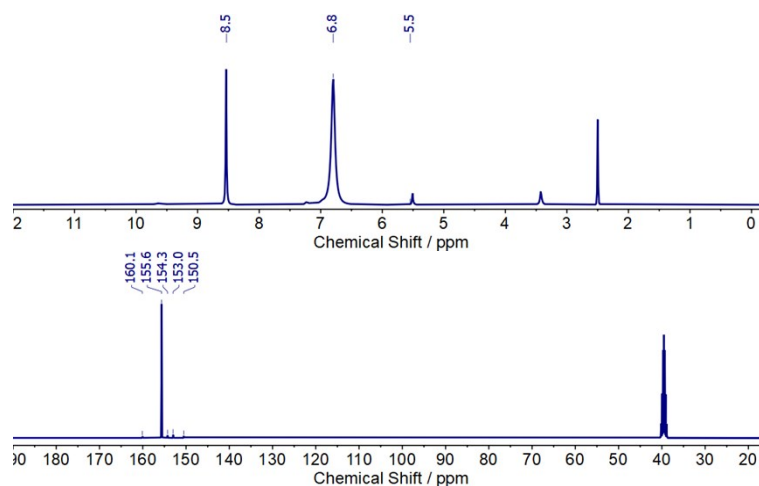


Figure S19. Top: ^1H -NMR (top) and ^{13}C -NMR (bottom) spectra of **biuret** (commercial) in DMSO-d_6 .

Biuret test with **CUB**

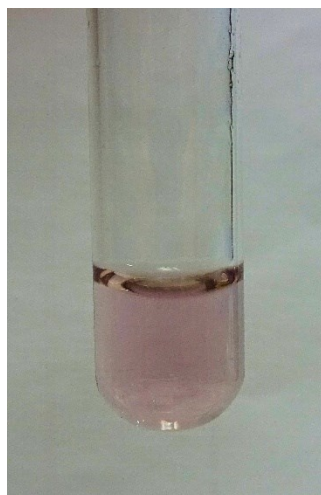


Figure S20. Photograph of a basic solution of **CUB** upon addition of a CuSO_4 solution.

Thermal Mass analysis of CUG and CUB

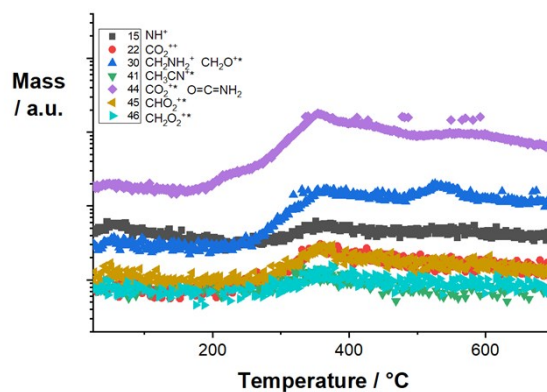


Figure S21. Temperature dependent mass spectrometric analysis of CUG.

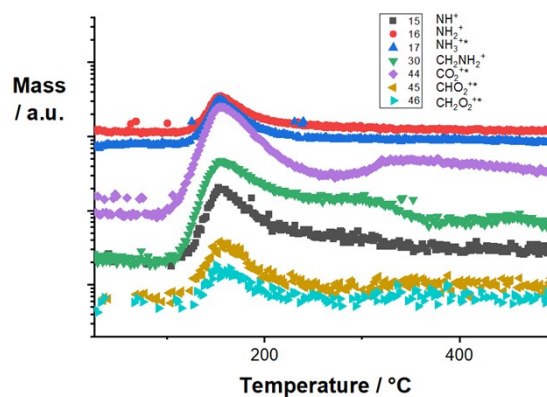


Figure S22. Temperature dependent mass spectrometric analysis of CUB.

Thermogravimetric Analysis of the Raw Mixture

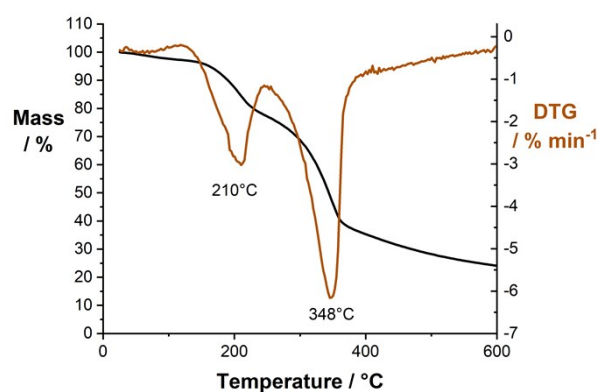


Figure S23. Thermogravimetric analysis of the supernatant of the raw product before column chromatography containing CUG and CUB.

X-ray Photoelectron Spectroscopy of CUB and CUG

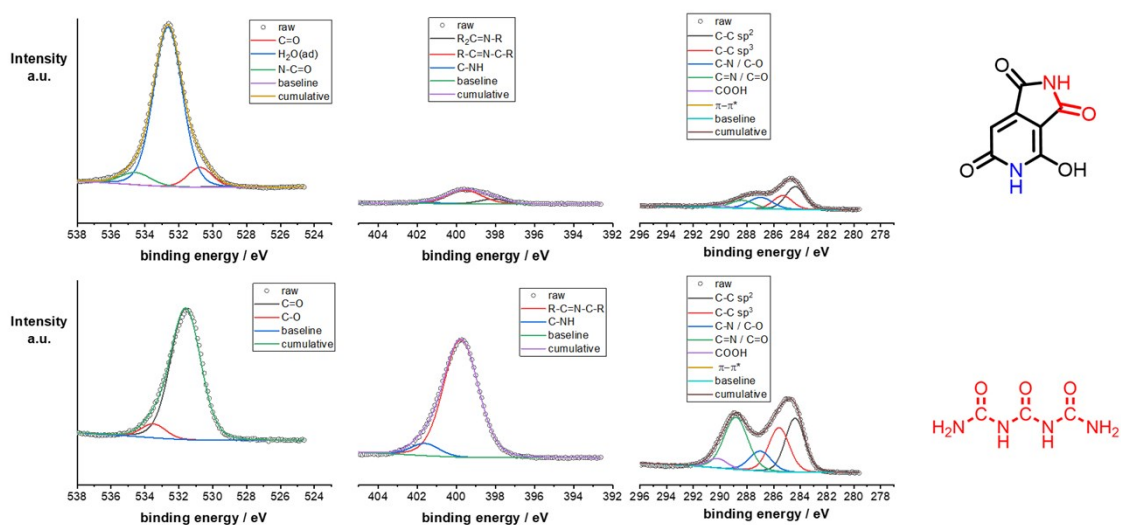


Figure S24. X-ray photoelectron spectra of CUG (top) and CUB (bottom) with emphasis on the C_{1s}, N_{1s}, and O_{1s} regions.

Nuclear Magnetic Resonance Spectroscopy during Washing of CUP

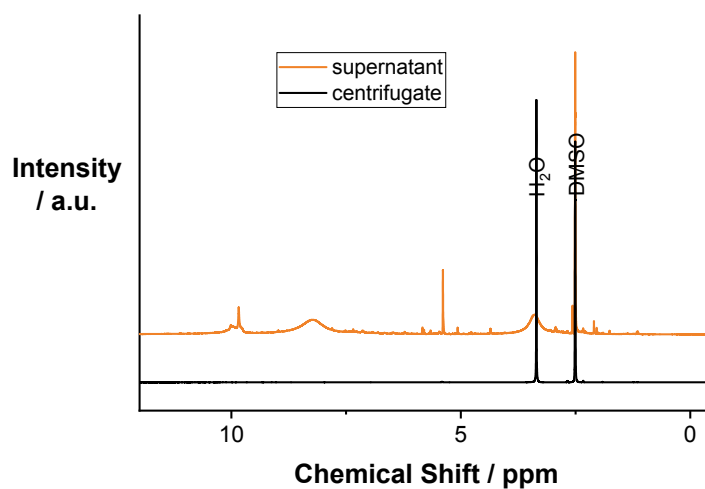


Figure S25. ¹H-NMR spectra of the supernatant and the redispersed centrifugate after washing CUP in H₂O at 95°C in DMSO-d₆.

Optical Spectroscopy of dispersions of CUp in H₂O.

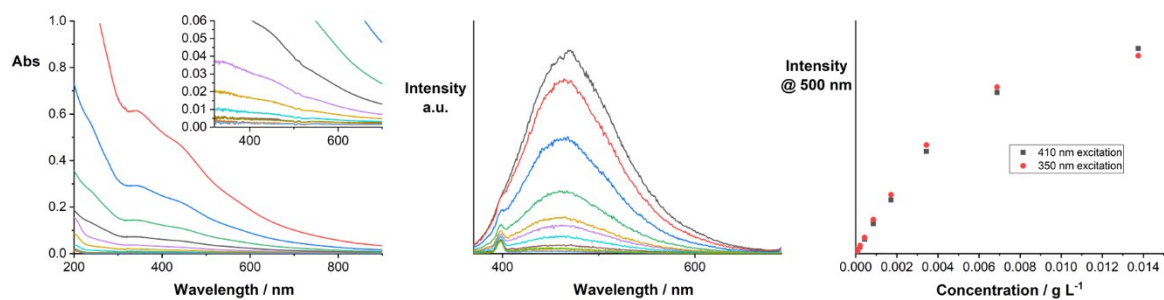


Figure S26. Absorption (left) and fluorescence (center) spectra of CUp in H₂O at room temperature at different concentrations. Right: Fluorescence intensity versus concentration of CUp in H₂O.

Nuclear Magnetic Resonance Spectroscopy of a Non-Separated Mixture

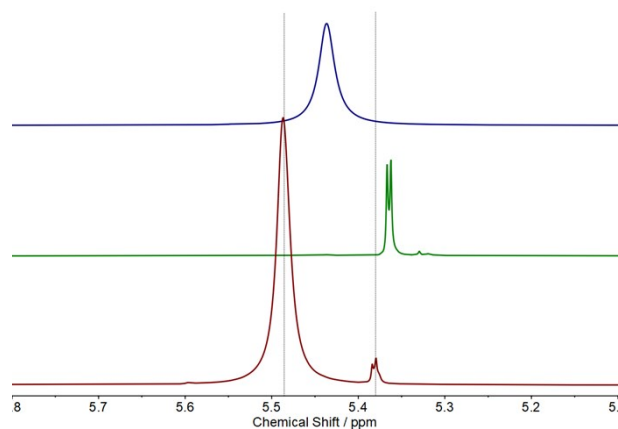


Figure S27. ¹H-NMR spectra of CUb (top), CUG (center) and the non-separated mixture of CUb and CUG (bottom) in DMSO-d₆.

References (continued from paper)

64. X.-F. Zhang, J. Zhang and L. Liu, Fluorescence Properties of Twenty Fluorescein Derivatives: Lifetime, Quantum Yield, Absorption and Emission Spectra, *J. Fluoresc.*, 2014, **24** (3), 819–826, 10.1007/s10895-014-1356-5



Laser-carbonization: Peering into the formation of micro-thermally produced (N-doped)carbons



Huize Wang^{a,1}, Simon Delacroix^{a,1}, Oliver Osswald^b, Mackenzie Anderson^c, Tobias Heil^a, Enrico Lepre^a, Nieves Lopez-Salas^a, Richard B. Kaner^{c,d}, Bernd Smarsly^b, Volker Strauss^{a,*}

^a Max Planck Institut für Kolloid- und Grenzflächenforschung Am Mühlenberg 1, 14476 Potsdam, Germany

^b Institute of Physical Chemistry, Justus-Liebig-University Giessen, Heinrich-Buff-Ring 17, 35392 Giessen, Germany

^c Department of Chemistry and Biochemistry and California NanoSystems Institute, University of California, Los Angeles (UCLA), Los Angeles, CA, USA

^d Department of Materials Science and Engineering, UCLA, Los Angeles, CA, USA

ARTICLE INFO

Article history:

Received 20 November 2020

Received in revised form

19 January 2021

Accepted 25 January 2021

Available online 31 January 2021

Keywords:

Carbonization

Laser-carbonization

N-doped carbon

Carbon laser patterning

WAXS

Wide-angle X-ray scattering

ABSTRACT

Even after centuries-old experience in carbonizing materials we can still learn new lessons and find new applications for carbonized materials. In the past decades, laser-assisted syntheses of materials have emerged as versatile tools for the fabrication of micro- and nanostructured functional devices. In this regard, laser-carbonization is of particular interest, as it provides a method for patterning eco-friendly and potentially biodegradable electronic materials for future applications in comparison to the state-of-the-art in flexible electronics. However, using molecular precursors for laser-carbonization has been a challenge for many years. We identified a set of three different precursors and conducted an in-depth morphological and compositional study to understand how molecular precursors must be prepared for the high-speed carbonization reactions used in laser-patterning. The resulting laser-patterned carbons (LP-C) or N-doped carbons (LP-NC) are different from their conventionally pyrolyzed reference products mostly in terms of morphology. A generally porous structure and a carbonization gradient induced by the top-to-bottom energy input are the most remarkable features. Additionally, the microstructure, the elemental composition and the resulting electronic properties are different as demonstrated by X-ray photoelectron spectroscopy (XPS) and wide-angle X-ray scattering (WAXS) analysis.

© 2021 Elsevier Ltd. All rights reserved.

1. Introduction

Carbonized materials have found widespread use as functional materials in many areas of both science, industry and even agriculture [1,2]. The most remarkable features of carbonized materials are their nanostructures like porosity and high surface area as well as their useful electronic properties with tunable conductivities or capacitances. Therefore, they are popular materials for sorbents [3], separators [4,5], catalyst supports [6], electrodes [7], and mechanical reinforcements [8]. Among all advantages of carbonized materials, the greatest is their simple production from biomass, biopolymers, natural organic compounds, or even waste products avoiding the exploitation of fossil carbon sources [9–13]. The

production and use of bio-based functional materials using simple methods instead of toxic or expensive materials can provide a great benefit for a resource and location independent industry.

However, gaining control over these materials properties during their synthesis is still subject to current research [14,15]. Today, carbonization is commonly achieved using either pyrolysis or hydrothermal methods [16]. The obtained products and their properties are a direct result of the precursors, the reaction conditions, such as temperature, pressure, time, or the presence of reactants in the synthesis environment. With both methods bulk quantities of carbonized materials for large-scale applications are produced. However, a big market for film-based or flexible electronic applications has been difficult to access for carbonized materials due to their

* Corresponding author.

E-mail address: volker.strauss@mpikg.mpg.de (V. Strauss).

¹ Huize Wang, Simon Delacroix contributed equally.

often impractical processability. In this field, progress has been made in applying carbon nano-allotropes, such as fullerenes [17], carbon nanotubes [18], or graphene [19,20] due to their defined electronic properties. However, a big drawback is their tedious and expensive production and the often low batch-to-batch reproducibility.

In this regard, the so-called laser-carbonization provides an opportunity to open the field of film-based electronics for carbonized materials. In general, laser-induced or -assisted synthesis, not only limited to carbon, has attracted a great deal of attention among materials scientists [21]. A major advantage of laser-synthesis is the possibility to fine-pattern films according to the requirements of the application and tunability with regard to laser-wavelengths and energy input. The precursors are directly carbonized on the substrate and their properties are adjusted by careful selection of the laser parameters [22]. The possibility of patterning enables new potential applications for carbons in e.g. micro charge-storage devices or electrical chemosensors [23–26]. The most famous precursors for laser-induced deposition of carbon films are graphene oxides (GO), which are particularly interesting due to their simple solution processability [27–29]. Upon laser irradiation GO is reduced to graphene or 3D-graphenes giving films with high surface areas and high electrical conductivities. Other well-known precursors are polyimides (PI) which form highly porous, disordered carbon films [30–32]. Here, commercial PI films have been the most widely used as objects of investigation. Both materials have been shown to offer enormous potential as electrode materials or sensor platforms [33–36].

Like conventional carbonization methods the precursors are decisive for the properties of the final products. Until now, the most widely used precursor systems are polymeric and the laser-carbonization of molecular precursors has been difficult to achieve. Typically, molecular precursors evaporate in the high energy flux of the laser beam. However, the use of molecular precursors provides sheer infinite possibilities for fine-tuning the properties of the final products.

Recently, we have identified and developed a method to obtain carbonized patterns from molecular precursors which involves the essential step of pre-condensation or pre-carbonization comparable to torrefaction [37,38]. After annealing the molecular precursors at 300 °C the carbon content increases and small graphitic domains form. These pre-carbonized intermediates are then processed to inks, which are applied on different substrates and finally carbonized in the laser beam. The heat of the laser induces the formation of a carbon-network, therefore, we refer to these intermediates as carbon network-forming agents (CNFA). In contrast to conventional pyrolysis, which occurs on a time scale of hours (several thousands of seconds), laser-pyrolysis occurs within just a few milliseconds. With respect to reorganization during crystallization and diffusion of gaseous decomposition products occurring during the carbonization reactions and laser-absorption effects, the final products are expected to be different to conventionally carbonized products.

In this work, we elaborate on the properties of the products of laser-carbonization and highlight differences to conventionally carbonized samples. The importance of several parameters and some general prerequisites for the selection of the molecular precursors are emphasized. In addition to our standard precursor system, citric acid and urea, two new precursors have been identified, namely cytosine and glucose. The composition of the pre-carbonized intermediates, and the final products have been characterized by energy-dispersive X-ray analysis (EDX) and combustion elemental analysis (CEA). A combinational study using wide-angle X-ray scattering (WAXS) and X-ray photoelectron spectroscopy (XPS) were performed to compare the laser- and conventionally carbonized products and obtain information about the composition and morphology of the final samples.

2. Results and discussion

2.1. Methods and materials

Laser-carbonization of molecular precursors is achieved in a two-step approach according to our recently developed method which involves the essential step of pre-condensation or pre-carbonization to avoid the evaporation of the molecular precursors – Fig. 1. First, the molecular precursors (citric acid/urea, glucose, cytosine) are pre-carbonized at 300 °C for 2 h in a muffle-furnace under inert atmosphere to obtain the carbon network-forming agents (CNFAs). The products are referred to as CA/U (300), glucose (300), or cytosine (300) indicating the precursors and the reaction temperature. The CNFAs are processed into inks by dispersing the CNFAs in ethylene glycol. The inks are then cast on the substrate (Si-wafers) and dried to obtain uniform films with a thickness of ~35 μm. The films are then irradiated with a CO₂-laser (μ_{ex} = 10.6 μm) with the desired pattern at ambient conditions and, finally, the unexposed material is rinsed off with water. The materials obtained are referred to as glucose (300)-ls, CA/U (300)-ls, or cytosine (300)-ls, indicating the laser-treatment of the CNFAs. For comparison, reference materials were produced. Glucose, CA/U, or cytosine were pyrolyzed at 950 °C for 2 h in a muffle-furnace under nitrogen atmosphere. These samples are referred to as glucose (950), CA/U (950), or cytosine (950). The reference carbonization temperature of 950 °C was primarily chosen as similar elemental compositions to the bulk laser-carbonized samples were found. A comparison with materials treated at 950 °C is reasonable, because at such temperatures the materials start to develop a non-graphitic structure and chemical transformations, such as decomposition, condensation etc., are widely completed [39].

First, the films of the CNFAs before and after laser-treatment were characterized in terms of morphology using scanning electron microscopy (SEM) (Fig. 2). Before laser-carbonization the films exhibited a granular appearance. The grain sizes are in a similar size range between ~100 nm and several microns. After laser-treatment all films show a highly disordered, porous morphology.

2.2. Laser parameters

Different materials, i.e. CNFAs, show different responses to laser-treatment. The laser parameters, such as incident power and scanning speed, play a crucial role in the carbonization process. We tested these settings for the three selected precursors. The product of laser power in W and scanning speed in s·m⁻¹ yields the energy fluence in J·m⁻¹. The fluence was quantified for a set of different

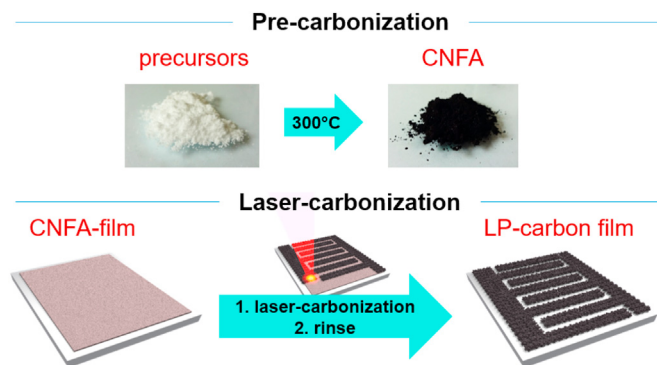


Fig. 1. Scheme summarizing the steps of molecular carbon laser-patterning; 1. Pre-carbonization of molecular precursors at 300 °C; 2. Laser-carbonization of CNFA-films to LP-carbon films.

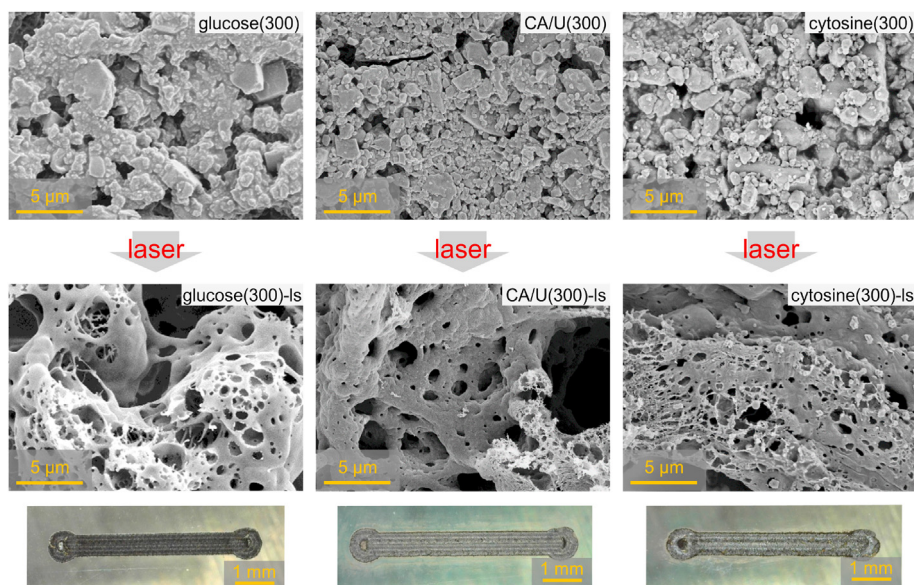


Fig. 2. Scanning electron micrographs of the CNFA-films of glucose (300), CA/U (300), and cytosine (300) before (upper) and after laser treatment (lower). Bottom: photographs of the laser-carbonized films on polyethyleneterephthalate (PET) substrates.

laser settings and plotted versus speed and power in the 2D-plot shown in Fig. 3a. In general, slower speeds and higher power yield higher fluence.

Each of the tested compounds gives a certain response pattern as shown in the 2D-plots in Fig. 3c–e. In these plots, the electrical conductivity of the final films is plotted versus laser power and scanning speed. Laser settings outside the range of the colored areas shown in Fig. 3c–e are either too strong or too weak. Too low fluence fails to complete the carbonization and too high fluence leads to complete evaporation of the film. We assume, that the carbonization yield improves when higher conductivities are achieved.

As shown in the 2D-plots, a strong dependence of the scanning-speed is observed. Glucose (300) shows the best response at a scanning-speed of $\sim 600 \text{ ms mm}^{-1}$, while both CA/U (300) and cytosine (300) show the best response at slower speeds of ~ 146 and $\sim 378 \text{ ms mm}^{-1}$. This indicates that the carbonization reaction for each precursor is dependent on the scanning speed, i.e. the irradiation time. The maximum conductivities achieved for glucose (300), CA/U (300) and cytosine (300) after laser-carbonization are 6500 , 2300 and 9500 S m^{-1} , respectively.

To explain this observation, we determined the laser material interaction. The excitation wavelength of the laser is $10.6 \mu\text{m}$ which corresponds to an energy of 943 cm^{-1} . We conducted transmission Fourier-transform infrared spectroscopy (FT-IR) measurements of the CNFAs and determined their extinction coefficients at the laser-excitation energy (Fig. 3f–h). All three CNFAs show weak absorption in this energy region. The extinction coefficient of CA/U (300) is significantly higher with $\epsilon = 0.56 \text{ L}\cdot(\text{g}\cdot\text{cm})^{-1}$, than those for cytosine (300) and glucose (300) with $\epsilon = 0.28$ or $0.21 \text{ L}\cdot(\text{g}\cdot\text{cm})^{-1}$, respectively. The laser excitation energy is located in the typical fingerprint region in the IR spectra where the transitions of C=C and C–H bending vibrations occur. However, the absorption spectra of particulate samples also exhibit a significant plasmon absorption trailing deep into the IR. Looking at the lack of distinct absorption bands in the IR-spectra of the three samples, we hypothesize that the plasmonic absorption of the aromatic domains within the pre-carbonized samples is responsible for the absorption and the dissipation of the laser energy across the film. The pre-

carbonization at $300 \text{ }^\circ\text{C}$ is essential to achieve crosslinking and prevent vaporization of the molecular precursors. A linear correlation between the scanning speed and the extinction coefficients indicates, that the carbonization reaction is dependent on the amount of energy absorbed by the material (Fig. 3b).

2.3. Proposed mechanism

Laser-carbonization is clearly a surface carbonization method. As shown previously for the CA/U precursor system, the penetration depth of the laser is limited to approximately $35 \mu\text{m}$ according to an estimation by the Beer-Lambert law [26,37]. Laser-carbonization is conducted with typical scanning speeds between 50 and 500 ms mm^{-1} . The reaction process is hypothesized to occur according to the scheme depicted in Fig. 4. The high energy impact of the laser causes the upper layer of the CNFA film to evaporate.¹ Then, the carbonization/C–C bond formation occurs, which causes the upper layer of the material to be carbonized. The laser radiation is then attenuated by the carbonized layers which dissipate the radiation in the form of heat across the film. After finishing the laser-patterning the unexposed films are removed by rinsing with water. A carbonized film with a gradient in the degree of carbonization results. The suggested mechanism is corroborated by our observation that thicker layers result in incompletely carbonized films resulting in delamination, while thinner films cause the substrate to become heated. PET as a flexible substrate melts, therefore a precise control of the film-thickness and the laser parameters is essential.

2.4. Micro/nanostructure analysis

First insights into the successful carbonization are obtained by the change of the Raman signals presented in Fig. S1. The presence of sharp D-, G-, and G'- bands in the spectra of all samples after laser-carbonization show a high degree of carbonization on top of the films. In terms of temperature-controlled carbonization the

¹ This is observed for all substances upon sudden laser irradiation.

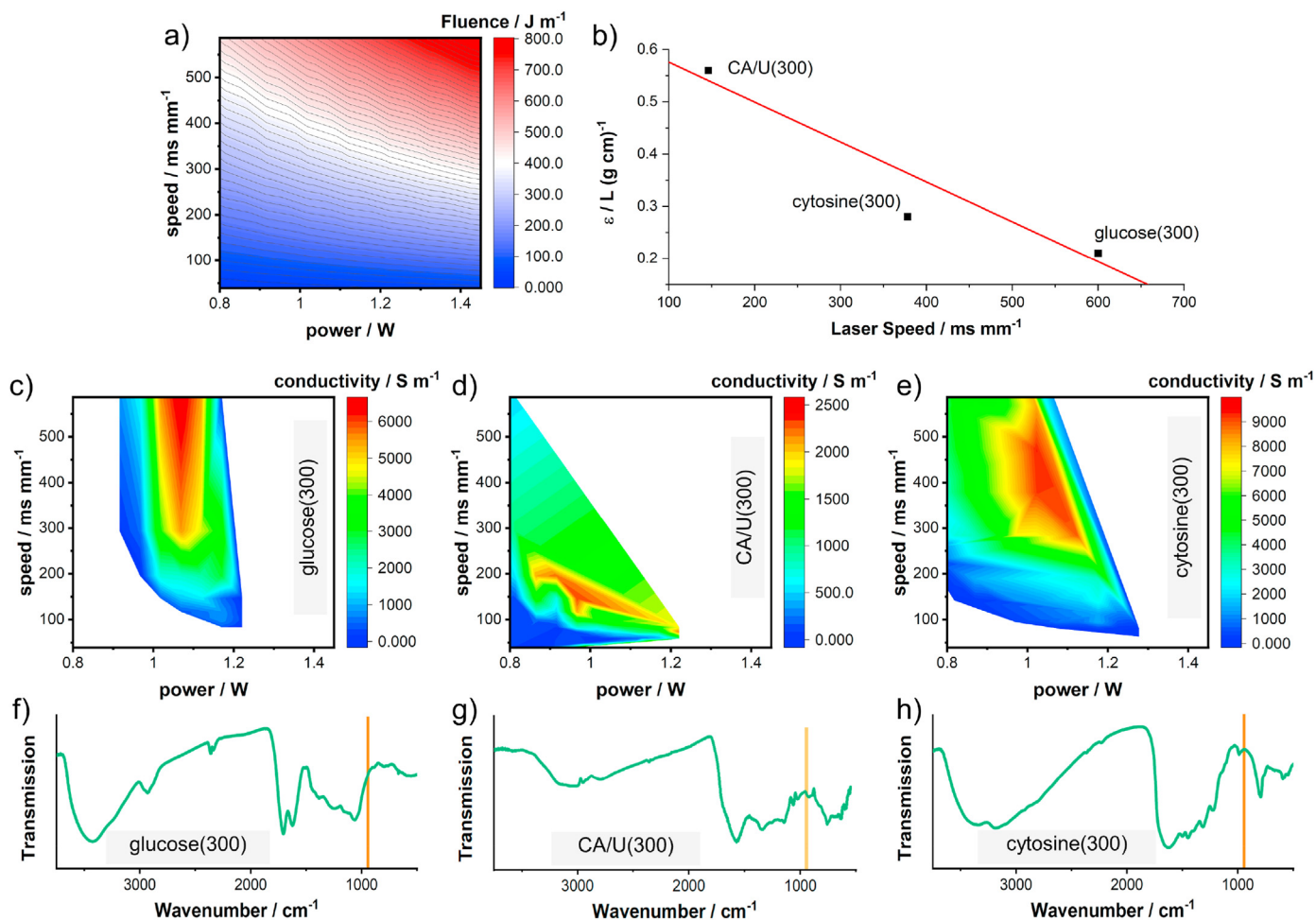


Fig. 3. Quantification of the laser parameters and the response of the CNFAs to different laser setting. a) Radiant fluence of the laser energy versus scanning speed and laser power; b) Correlation plot of versus extinction coefficient at the excitation wavelength versus laser speed; c), d), e) response of the CNFAs to scanning speed and laser power reflected in the electrical conductivity after laser treatment of glucose (300), CA/U (300), and cytosine (300); f), g), h) FT-IR spectra of glucose (300), CA/U (300), and cytosine (300) with the excitation energy of the laser indicated as an orange line.

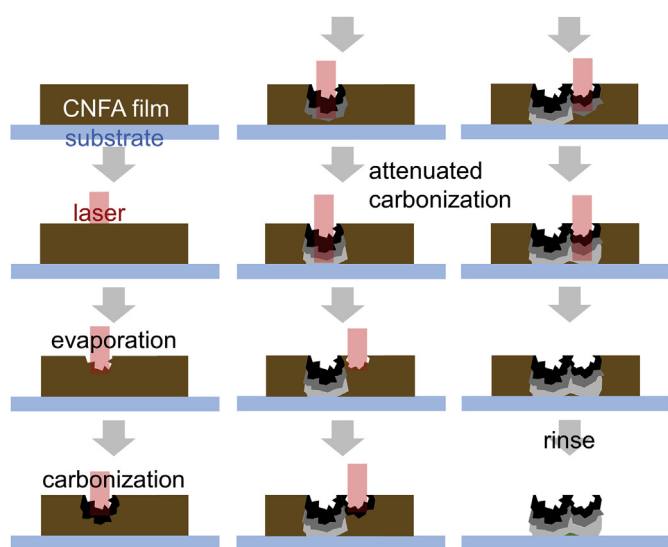


Fig. 4. Scheme illustrating the laser-carbonization process of a film of CNFA on a substrate: Laser impact causes evaporation, induces carbonization of the upper layer and a lower degree carbonization of the lower layers due to attenuation of the laser energy.

appearance of such sharp Raman signals with a relatively low D-band is remarkable as it indicates the formation of well-defined and extended graphene layers on top of the film which are typically observed for temperatures $>1800\text{ }^{\circ}\text{C}$ [40,41]. However, Raman spectroscopy is a surface sensitive technique. With respect to the porous surface structure of the laser-carbonized samples it is difficult to obtain an overall characterization of the bulk film by Raman spectroscopy.

The porous morphology is apparent when looking at the SEM images of the laser-carbonized samples in Fig. 2 and imply high surface areas. That is generally attractive for potential applications such as charge-storage electrodes or sensor platforms. To determine the active surface areas of laser-carbonized products, we employed the methylene blue (MB) adsorption method (Experimental Section) [27,38]. A set of six measurements per sample were conducted to give average values of 135 ± 29 , 165 ± 17 and $68 \pm 19\text{ m}^2\text{ g}^{-1}$ for glucose (300)-ls, CA/U (300)-ls, and cytosine (300)-ls, respectively. Please note, the MB adsorption method is used only for small amounts of material and may deviate from bulk sorption methods.

To obtain insights into the microscopic structure of the laser-carbonized films, we conducted a comparative study of the laser-carbonized materials and conventionally carbonized references, which were pyrolyzed in a chamber oven at $950\text{ }^{\circ}\text{C}$. Powders of the

laser-carbonized samples were obtained by laser-treating large-area CNFA films on Si-wafers and subsequently collecting and washing the powders to remove unreacted CNFA (Fig. S2 and Experimental Section).

The scanning electron micrographs in Fig. 5(-left) compare the laser-carbonized samples with the reference samples. More micrographs are presented in Fig. S3. In general, the laser-carbonized samples show a higher degree of disorder and a more porous morphology. The sheet-like structures of glucose (950) originate from the blowing process during heating [42]. Sheet-like features

are also observed for the glucose (300)-ls sample, however, the dimensions are much smaller (below 1 μm).

TEM analysis provides some insights into the microstructures of the samples (Fig. 5). However, only small fragments were analyzed and with respect to the intrinsic heterogeneity of the laser-treated samples the interpretation of their results must be considered carefully. For all samples except for cytosine (300)-ls, the fragments observed in TEM show predominantly amorphous character with small graphitic domains, which are clearly recognized in the high-resolution TEM images presented in Fig. S5. Their mainly

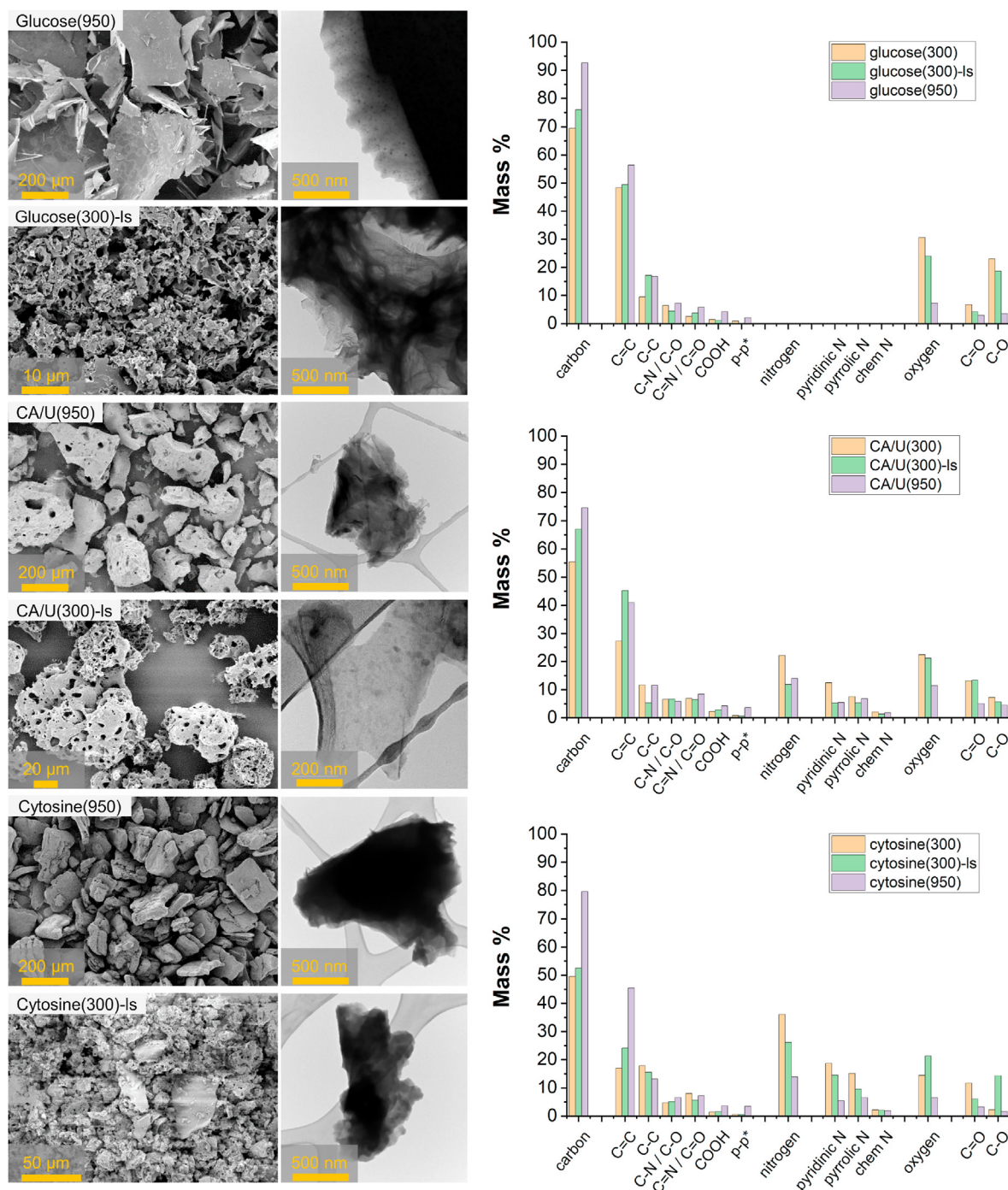


Fig. 5. Left: Scanning and transmission electron micrographs of the laser-carbonized samples and the references; Right: elemental composition diagrams of the CNFAs, the laser-carbonized samples and the references obtained by X-ray photoelectron spectroscopy.

amorphous character is also reflected in the typical diffuse diffraction patterns stemming from turbostratic graphitic carbon.

The three selected precursors contain different amounts of nitrogen. We tested the elemental compositions of their corresponding CNFAs and the final LP-carbons and compared these values with the reference samples annealed at 950 °C. In Table S1 the elemental compositions of all tested samples obtained by EDX of the as-prepared laser-treated films and elemental analysis (EA) of the collected powders are listed. For all tested compounds, the same general trends are observed. The carbon content increases after pre-carbonization, while the nitrogen content decreases. These trends continue upon increasing the temperatures to 950 °C.

The compositional gradient of the laser-carbonized films is expressed in the differences of the detected composition using surface sensitive EDX (~0.5 μm) and bulk sensitive EA. According to EDX, the carbon content on top of the films in glucose (300)-Is reaches 97 wt%. With respect to the gradual laser energy impact through the film, higher degrees of carbonization are achieved on top of the films in comparison to the average of the bulk films which is only 75 wt%. This state of carbonized glucose with disordered graphitic domains with a carbon content of ~77 wt% is commonly referred to as mesophase state carbon. This tendency is also observed for the nitrogen-containing samples. A significantly higher carbon content of 92 and 83 wt% is observed on top of the CA/U (300)-Is and cytosine (300)-Is films, respectively, while in the bulk the carbon content reaches only 68 or 50 wt%. Only CA/U (300)-Is shows a noticeable deviation from the reference product CA/U (950) in terms of bulk carbon content. This deviation is due to oxygen incorporated into the films. The thermogravimetric analysis of CA/U (300)-Is shows a gradual mass loss of ~16 wt% starting at ~400 °C for CA/U (300)-Is. This mass loss is not observed with CA/U (950) (Fig. S4).

X-ray photoelectron spectroscopy (XPS) was conducted to study the bonding and the chemical composition of all samples, i.e. the CNFAs, the laser-carbonized samples and the references. The full data sets for all samples are shown in Fig. S6–S8. The carbon, nitrogen, and oxygen contents of the samples obtained by XPS match fairly well with the values obtained from combustion elemental analysis. In general, the same trends in terms of carbonization or nitrogen mass loss at high temperatures are observed. Slight variations in the compositions are attributed to the surface sensitivity of XPS.

Interesting are the fine-structures in the carbon (C_{1s}), nitrogen (N_{1s}), and oxygen signals (O_{1s}). The C_{1s} area is composed of four main signals at 284.4, 285.7, 286.6, and 288.1 eV assigned to sp^2 and sp^3 carbon, C–N/C–O and C=N/C=O, respectively. The two main signals in the N_{1s} area at 398.8 and 400.3 eV originate from pyridinic and pyrrolic nitrogen, respectively [43,44]. In the O_{1s} region, two peaks at 531.7 and 533.8 eV assigned to C–O and C=O, respectively, appear. The areas of the fitted curves with respect to the sum of all signals yield the mass percentage of the detected species. These were plotted in diagrams to compare different samples (Fig. 5 right).

For glucose, both laser- and conventional carbonization lead to an increase in carbon and a decrease in oxygen. The trends for both methods are similar. Notably, the sp^2 carbon content in glucose (300) is already very high with ~69% of the overall sample mass. Laser-carbonization causes an increase of only ~7% carbon to the overall sample mass on account of the oxygen content. In the reference, glucose (950) the carbonization yield is much higher reaching a carbon content of 93%.

The CA/U system shows some different trends, in particular, with respect to their nitrogen content. In general, upon laser-carbonization the sp^2 carbon content increases more in comparison to the reference. The pyridinic nitrogen content in both CA/U

(300)-Is and CA/U (950) is reduced more in comparison to the pyrrolic nitrogen content. Again, the oxygen content in CA/U (300)-Is is significantly higher than in the reference.

Laser-treatment of cytosine (300) leads to a slight increase in the sp^2 carbon content on account of a decrease in the sp^3 -carbon content. At the same time a decrease in both pyridinic and pyrrolic nitrogen is noted. In the reference, cytosine (950), these trends are much more pronounced. Here, the oxygen content of cytosine (300)-Is is even higher than the precursor cytosine (300), which is again due to C–O species. In the reference sample, the oxygen content is lower.

The quantitative XPS analysis of the collected powder samples corroborates the proposed reaction mechanism. In general, laser-carbonization results in increased surface oxygenation compared to pyrolysis. While pyrolysis leads to a steady evaporation and transport of reactive side products, in laser-carbonization these reactive species are not removed fast enough. This leads to oxygenation of the reactive surface of the carbons. The sp^2 content is increased in all samples and especially in CA/U (300)-Is and cyt (950), but the trends are different for each precursor. In particular cyt (300)-Is deviates drastically from its reference cyt (950). We assume an interconnection/polymerization of the graphitic domains to be the main reaction occurring upon laser-carbonization.

To shed light on the graphitic domains and the crystallinity of the samples, we conducted a comparative WAXS analysis. In general, non-graphitic carbons (NGCs) as obtained in this study consist of stacks of sp^2 -hybridized graphene layers. Due to the rotational and translational disorder, e.g. a turbostratic arrangement [45], NGCs do not show any crystallographic (three-dimensional) long-range order and, therefore, the resulting diffraction patterns of these samples do not contain any (hkl) reflections like those of graphite [46]. Instead, their diffraction patterns show diffuse and, in many cases, overlapping (hk) and ($00l$) reflections [45,47], which are caused by the scattering within or between the individual layers (Fig. S10). Commonly, the most important and most interesting microstructural parameters of these NGCs are the layer size (L_a) and the stack size (L_c). In addition, the average graphene layer distance (a_3) and the disorder, e.g. the deviation of the C–C bond length (σ_1) and the variation in the layer distance (σ_3) are of interest (Fig. S9).

Due to the turbostratic structure of these NGCs, the resulting (hk) reflections are generally quite broad and also asymmetric [45,47], therefore a single-peak analysis such as applying the Scherrer equation [48] to obtain the layer dimension from the (hk) reflections using the full-width-at-half maxima (FWHM) approach is not suitable for evaluating this scattering data [49]. In addition, due to the lack of three-dimensional (hkl) reflections and the substantial degree of disorder, a classical Rietveld refinement cannot be performed. Instead an advanced approach for fitting the whole scattering vector range of the WAXS pattern by using a theoretical function according to the model of Ruland and Smarsly was used [50]. This advanced approach to fitting the scattering intensity obtained from a WAXS experiment was successfully tested in several studies using and preserving physically significant and meaningful parameters. A description of the model is given in the Experimental Section.

Glucose (950) shows a high average layer distance of $a_3 = 3.84 \text{ \AA}$ and a very high standard deviation of $\sigma_3 = 0.98 \text{ \AA}$. In addition, the minimal layer distance of $a_{3 \text{ min}} = 2.84 \text{ \AA}$ is small compared to the average distance, but results from the large variation in the layer distance. These parameters and the almost invisible (004) reflection (Fig. 6) suggest a small stack height ($L_c = 15.7 \text{ \AA}$) and disordered stacking. A possible reason for this observation might be the absence of an aromatic system and the high amount of oxygen in the precursor. This probably leads to the complete absence of a

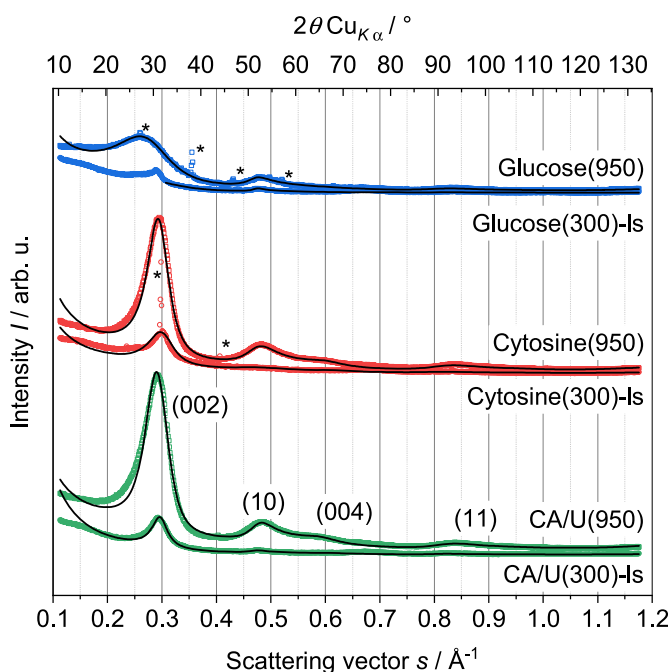


Fig. 6. Measured (dots) and fitted (line) WAXS patterns of the laser-carbonized samples – glucose (300)-ls, CA/U (300)-ls, and cytosine (300)-ls, in comparison to the reference samples pyrolyzed at 950 °C – glucose (950), CA/U (950), and cytosine (950).

stacking structure in glucose (300)-ls. The (002) reflection is asymmetric in the direction of the small scattering vectors and too small to be reasonably analyzed. Thus, the WAXS data of glucose (300)-ls were only fitted for $s > 0.3 \text{ \AA}^{-1}$, so the microstructural parameters for the stacking behavior could not be calculated.

In contrast, CA/U (950) and cytosine (950) show more pronounced WAXS patterns. A clear (002) and a small (004) reflection are visible for both samples (Fig. 6). The average layer distance of $a_3 = 3.4 \text{ \AA}$ is quite similar and (in the range of the fitting accuracy) comparable to the layer distance in graphite ($\sim 3.35 \text{ \AA}$) [51]. The comparison of these samples shows that the disorder of the stacking structure in CA/U (950) is higher than in cytosine (950), which is represented in the height and broadness of the (002) and (004) reflections. While the average stacking heights of $L_c = 20.0 \text{ \AA}$ for CA/U (950) and 23.2 \AA for cytosine (950) are similar, the minimal layer distance $a_{3 \text{ min}}$ is about 0.2 \AA smaller for CA/U (950). Also, the standard deviation of the layer distances σ_3 is $\sim 20\%$ higher for CA/U (950). This leads to the conclusion that the stacking structure in CA/U (950) is more disordered than in cytosine (950). One possible reason might be the amount of oxygen in CA/U (950) exerting an adverse effect on building up highly ordered graphite stacks [52].

The stacking in cytosine (300)-ls suffers from a significantly higher disorder compared to the reference cytosine (950), which is represented by the higher deviation from the graphitic layer distance (σ_3) of 0.50 \AA for cytosine (300)-ls compared to 0.35 \AA for cytosine (950). Furthermore, the average stack height (L_c) for cytosine (300)-ls was calculated to be slightly higher than for cytosine (950), but due to the high amount of oxygen in cytosine (300)-ls and the absence of a clear sp^2 structure, these values of cytosine (300)-ls suffer from a large error. For the same reason, the parameters for the stacking height L_c , homogeneity η , and the preferred orientation q could only be estimated for CA/U (300)-ls and also suffer from a large calculation error, especially with regard to the stacking height L_c . However, the deviation of the layer distance σ_3 , CA/U (300)-ls stands for a significantly higher disorder compared to the reference sample. Also, the average layer distance

a_3 is higher for the CA/U (300)-ls, which are both indications for the presence of a highly disordered stacking.

In terms of the layers, i.e. the sp^2 structure, the average layer size (L_a), the average C–C bond length (l_{cc}) and the standard deviation of the C–C bond length (σ_1) are the most relevant parameters, which were calculated from the refinement. Given the fitting accuracy and the resulting error, all calculated C–C bond lengths are in the range of pure graphene ($\sim 1.42 \text{ \AA}$) [51], only the calculated l_{cc} values for CA/U (950) and cytosine (950) are slightly smaller. However, considering the difficult determination of a precise mean value because of the large reflection width for these samples, the presence of a graphene-like sp^2 structure can be safely assumed. Only for cytosine (300)-ls, neither a (10) nor a (11) reflection is visible and, therefore, no clear sp^2 structure is present in this sample.

Glucose as a precursor also shows an interesting tendency regarding the layer structure. Glucose (950) consists of large graphene layers ($L_a = 80 \text{ \AA}$), but possessing a substantial disorder ($\sigma_1 = 0.221$), which is explained by the relatively high amount of oxygen and the absence of any aromatic system in the original precursor, i.e. glucose. In contrast, glucose (300)-ls consists of smaller layers ($L_a = 50 \text{ \AA}$) and a significantly lower disorder ($\sigma_1 = 0.1$). Because of the rather small and broad reflections in the WAXS pattern, these parameters suffer from a large calculation error.

Comparing CA/U (950) and CA/U (300)-ls, the latter shows significantly larger graphene domains ($L_a = 50 \text{ \AA}$ vs. 31 \AA), and a lower disorder ($\sigma_1 = 0.15$ vs. 0.18). Both parameters clearly indicate that for CA/U, the laser-carbonization leads to a more ordered sp^2 structure than oven pyrolysis. Higher disorder in the stacking and, at the same time, a higher degree of order in the individual layers can, with respect to the oxygen content, only be explained by surface-bound oxygen rather than incorporation into the sp^2 structure. The high amount of oxygen also rationalizes the absence of any (hk) reflections in the WAXS data of cytosine (300)-ls, which indicates that cytosine (300)-ls does not contain any ordered sp^2 structure. Oxygen prevents the condensation of ordered layers as well as ordered stacks as shown in the paragraph before and in Ref. [52]. Additionally, the oxygen or the relatively high amount of nitrogen in cytosine (300) also prevents the condensation of large and ordered sp^2 layers. For this reason, the layer dimension (L_a) is only $\sim 23 \text{ \AA}$ and the disorder, i.e. the deviation of the C–C bond length, is relatively high ($\sigma_1 = 0.18$).

Taking the results from the WAXS analysis into account, the choice of precursor has a major influence on the resulting product. The laser-carbonized samples consist of a significantly disordered stack structure, which is directly shown by the smaller and broader (002) and (004) reflections or their complete absence in comparison to the references. The disorder parameters for stacking ($a_{3 \text{ min}}$, σ_3) are generally higher than for the reference samples. The amount of oxygen inside the products (CA/U, cytosine) and in the precursor (glucose) seems to have a significant influence on the formation of the microstructure in the products. More precisely, oxygen prevents the condensation of perfect graphite-like stacking structures in glucose (300)-ls or even ordered sp^2 layers as in cytosine (300)-ls (high σ_1). For CA/U, on the other hand, laser-carbonization leads to significantly larger and higher ordered sp^2 layers. In general, laser-carbonization leads to larger non-graphitic carbon domains, i.e. a turbostratic arrangement of the layers. In principle, it is possible to produce large and ordered sp^2 layers, but with highly disordered stacks. Notably, the degree of disorder is expected to be a consequence of the gradient in the degree of the carbonization.

3. Conclusions

Laser-carbonization is an interesting new method opening possibilities to apply carbonized materials in 2D electronics and

high-surface area applications. In contrast to conventional pyrolysis in which chemical processes are allowed to occur on time scales of hours (thousands of seconds), these processes are confined to milliseconds in laser-carbonization. We conducted a comparative study with a set of three precursors – glucose, citric acid/urea, and cytosine – to investigate the mechanism of laser-carbonization. We found that pre-carbonization of the molecular precursors is a prerequisite for laser-carbonization. In this step condensation of the molecular precursors occurs which avoids evaporation of the precursors under the beam and supports the formation of a carbonized conductive foam. These pre-carbonized precursors are referred to as carbon network-forming agents (CNFA). The laser-parameters were systematically tested and found to be critical to the degree of carbonization and have to be selected for each CNFA. A correlation between the extinction coefficients of the CNFAs at the laser-wavelength and the degree of carbonization was found. Laser-treatment of the CNFA-films leads to a carbonized film with a gradient in terms of degree of carbonization due to the top-to-bottom energy input. The fast reactions in the laser, i.e. rapid heating and cooling, produces porous materials due laser-induced decomposition of functional groups and subsequent sudden release of gases. Laser-carbonized samples show generally greater disorder, larger turbostratic carbon domains, and a high degree of oxygenation on their surfaces throughout the films. This oxygenation has a significant influence on the formation, the size, and the layer structure of the graphitic domains.

The insights provided in this study are fundamental to understand laser-induced carbonization of molecular materials. Based on these results, new precursor systems can be explored and their laser reactions conditions can be rationalized and potentially predicted based on their extinction coefficients. Laser-carbonization offers a wide range of possibilities for the synthesis of selective materials requiring remarkable surface areas and multiple reaction sites in patterned 2D shapes. Their functionalities can be tuned by selection of the precursors and addends, which is subject to ongoing studies. Noteworthy, in contrast to other carbonization methods, such as hydrothermal or microwave-assisted laser-carbonization, only small amounts of materials are produced which narrows the areas of application to mainly 2D electronics.

4. Experimental Section

4.1. Chemicals

Citric acid (>99%, Sigma-Aldrich), urea (>99.3%, Alfa Aesar), D-glucose (anhydrous, Fisher Scientific GmbH), cytosine (99%, Merck), and ethylene glycol ($\geq 99.7\%$, AnalaR Normapur, VWR Chemicals) and polyvinylpyrrolidone (average mol wt. 10,000, Sigma Aldrich) were used as received.

4.2. Substrates

The PET substrate was Melinex sheets obtained from Plano GmbH. Silicon wafers were kindly provided by Siltronic AG.

4.3. Preparation of the CNFAs and the references

CA/U (300) was prepared according to a previously published procedure [37,58]. Glucose (300) and cytosine (300) were prepared by loading 10 g into a porcelain crucible and heating to 300 °C with a heating rate of 3.11 K min⁻¹. The hold-time at 300 °C was 120 min. The pre-carbonized products were used as obtained. CA/U (950), glucose (950), and cytosine (950) were prepared by loading 1 g into a porcelain crucible and heating to 950 °C with a heating rate of 3.11 K min⁻¹. The hold-time at 950 °C was 120 min. To obtain

samples for elemental analysis, large areas (10 × 10 cm) of the CNFA-films were laser-carbonized on Si-wafers. Subsequently, the laser-carbonized films were removed and the powders collected. The powders were thoroughly washed with 1.0 M NaOH by sequential sonication and centrifugation until the supernatant was clear, i.e. all unconverted precursors were washed out. The remaining black solid, was washed with H₂O and methanol to remove all NaOH and obtain the pure laser-carbonized product.

4.4. Preparation of the precursor films

Ethylene glycol was added to either CA/U (300), glucose (300), or cytosine (300) and stirred for 24 h to obtain a 1 g/L dispersion. A drop of the ink was applied onto the substrate and the ink was doctor bladed with a wet thicknesses of ~150 μm. Ethylene glycol was then evaporated at 80 °C on a precision hotplate (PZ2860-SR, Gestigkeit GmbH) to obtain the final films with thicknesses of ~35 μm, measured with a digital micrometer and confirmed by micro-computer tomography measurements as shown in Ref. [37].

4.5. Laser-carbonization

Laser-carbonization was conducted with a high-precision laser engraver setup (Speedy 100, Trotec) equipped with a 60 W CO₂ laser. Focusing was achieved with a 2.5 inch focus lens providing a focal depth of ~3 mm and a focus diameter of 170 μm. The center wavelengths of the laser is 10.6 ± 0.03 μm. Both power P and scanning speed v , generically given in %, were converted into transferrable units [W] and [$s \cdot m^{-1}$], respectively. The resulting energy input per distance (or fluence) in the cutting mode onto the film is given by

$$F = P \cdot v = P \cdot \frac{t}{d},$$

where P is the effective power in [W] and v is the speed in [$s \cdot m^{-1}$], which is determined by the time t required to irradiate the distance d . The laser settings (speed, power, and pulse frequency) were adjusted to meet the requirements of the precursor film and the substrate. The effective output power of the laser was measured with a Solo 2 (Gentec Electro-Optics) power meter.

4.6. WAXS fitting

Here, we provide a brief description of our used model [50] (Fig. S10). A more detailed description can be found in previous studies [53,54]. In principle, the obtained intensity of the scattering (I_{Obs}) is given by the normalized intensity distribution in electron units per carbon atom ($I_{e.u.}$), an absorption factor (A), a polarization factor (P), and a normalization constant (k):

$$I_{Obs} = k \cdot A \cdot P \cdot I_{e.u.} \quad (1)$$

$I_{e.u.}$ contains the intensity of the coherent scattering from the crystallographic structure (I_{coh}) and the incoherent Compton scattering (I_{incoh}):

$$I_{e.u.} = I_{coh} + I_{incoh} \quad (2)$$

The coherent scattering is in turn calculated by the interlayer scattering (I_{inter}), i.e. the interference of the stacking of the different graphene layers ((00 l) – reflections), the intralayer scattering (I_{intra}), i.e. the interference within a single graphene layer ((hk) – reflections), and the atomic form factor of carbon (f_c):

$$I_{\text{coh}} = f_c^2 (I_{\text{inter}} + I_{\text{intra}}) \quad (3)$$

I_{inter} and I_{intra} are defined by the stack size (L_c), the average (a_3) and minimal ($a_{3 \text{ min}}$) layer distance, the stack disorder (σ_3), the layer size (L_a), and the layer disorder (σ_1). Furthermore, the average number of layers per stack N can be calculated by:

$$N = L_c / a_3 \quad (4)$$

In addition to these physical meaningful parameters, the concentration of foreign atoms like hydrogen (c_H), nitrogen (c_N), oxygen (c_O) and sulfur (c_S) as well as a possible preferred orientation q during the WAXS measurement and the homogeneity of the stacks η is considered. Due to the small atomic form factor of hydrogen compared to carbon and the resulting low scattering intensity and the assumption that nitrogen is only present within the sp^2 layer structure and the complete absence of sulfur inside these samples, only c_O was considered in this study.

4.7. Surface area measurements

The active surface area of the sensor was determined by the methylene blue adsorption method [55–57]. Laser-patterned carbon films of size $2 \times 1 \text{ cm}^2$ were printed on aluminium sheets. The laser-patterned films were scratched off and collected, and their masses were determined with a microbalance ($\sim 0.3 \text{ mg}$). The powder was then dispersed in $9.5 \times 10^{-5} \text{ M}$ solutions of methylene blue in polypropylene vials and stirred for 24 h. The solutions were centrifuged, and the amount of adsorbed MB was determined by measuring the absorbance of the supernatant with respect to a reference solution. An area of 1.35 nm^2 per molecule MB is assumed. As a reference, the same mass of activated carbon was used ($1269 \text{ m}^2 \text{ g}^{-1}$). The standard error was determined by the standard deviation of six values obtained from six measurements.

4.8. Instrumental

Scanning electron microscopy was performed on a Zeiss LEO 1550-Gemini system (acceleration voltage: 3–10 kV). An Oxford Instruments X-MAX 80 mm^2 detector was used to collect the SEM-EDX data.

Transmission electron microscopy was performed using a double-Cs-corrected ARM200F, equipped with a cold field emission gun and operated at 80 kV. To prepare the TEM samples, the carbon material has been dispersed in methanol by sonication for 10 min and applying 5 μL droplets of the dispersion on a carbon-coated copper TEM grid and drying at room temperature.

Thermogravimetric analysis were performed using a Thermo Microbalance TG 209 F1 Libra (Netzsch, Selb, Germany). A platinum crucible was used for the measurement of $10 \pm 1 \text{ mg}$ of samples in a nitrogen flow of 20 mL min^{-1} and a purge flow of 20 mL min^{-1} at a heating rate of 10 K min^{-1} .

Elemental analysis was performed with a vario MICRO cube CHNOS elemental analyzer (Elementar Analysensysteme GmbH). The elements were detected with a thermal conductivity detector (TCD) for C, H, N and O and an infrared (IR) detector for sulfur.

Fourier-transform infrared measurements were performed using a Nicolet iS 5 FT-IR-spectrometer in conjunction with an iD5 ATR unit from ThermoFisher Scientific.

Extinction coefficients were determined by measuring a series of transmission infra-red absorption spectra with known concentrations in range between 1.6 and 7.8 g/L pressed into KBr pellets. The absorbance was plotted against the concentration and the extinction coefficients were determined from the slope of the fitting curve.

Raman spectra were obtained with a confocal Raman Microscope (alpha 300, WITec, Germany) equipped with a piezo-scanner (P-500, Physik Instrumente, Karlsruhe, Germany). The laser, $\lambda = 532 \text{ nm}$ was focused on the samples through a $50\times$ objective at a working distance of 1 mm. The laser power on the sample was set to 4–12 mW.

X-ray diffraction was performed on a Bruker D8 Advance diffractometer in the Bragg-Brentano mode at the Cu $K\alpha$ wavelength.

Conductivity measurements were performed on a Solartron 1287 potentiostat in combination with a SI 1260 impedance unit. For frequency measurements the current was kept constant at 0.1 mA and for current sweeps, a frequency of 100 Hz was used.

CRedit authorship contribution statement

Huize Wang: Investigation, Methodology, Validation, Writing - original draft. **Simon Delacroix:** Investigation, Methodology, Validation, Writing - original draft. **Oliver Osswald:** Investigation, Methodology, Validation, Writing - original draft. **Mackenzie Anderson:** Investigation. **Tobias Heil:** Investigation. **Enrico Lepre:** Resources, Investigation. **Nieves Lopez-Salas:** Resources, Supervision. **Richard B. Kaner:** Supervision, Writing - review & editing. **Bernd Smarsly:** Conceptualization, Supervision, Methodology, Writing - review & editing. **Volker Strauss:** Conceptualization, Methodology, Validation, Writing - original draft, Writing - review & editing, Supervision, Project administration.

Declaration of competing interest

The authors declare that they have no known competing financial interests or personal relationships that could have appeared to influence the work reported in this paper.

Acknowledgements

S.D. and H.W. contributed equally to this work. We are grateful for financial support from the Fonds der Chemischen Industrie and the Max Planck Society. The continuous educational support from Prof. Markus Antonietti is highly appreciated. Financial support for O.O. is provided by the DFG via the GRK (Research Training Group) 2204 “Substitute Materials for Sustainable Energy Technologies”. R.B.K. thanks the Dr. Myung Ki Hong Chair in Materials Innovation.

Appendix A. Supplementary data

Supplementary data to this article can be found online at <https://doi.org/10.1016/j.carbon.2021.01.145>.

References

- [1] S. Nizamuddin, M.T.H. Siddiqui, N.M. Mubarak, H.A. Baloch, S.A. Mazari, M.M. Tunio, G.J. Griffin, M.P. Srinivasan, A. Tanksale, S. Riaz, Advanced nanomaterials synthesis from pyrolysis and hydrothermal carbonization: a review, *Curr. Org. Chem.* 22 (2018) 446–461, <https://doi.org/10.2174/1385272821666171026153215>.
- [2] M.C. Rillig, M. Wagner, M. Salem, P.M. Antunes, C. George, H.-G. Ramke, M.-M. Titirici, M. Antonietti, Material derived from hydrothermal carbonization: effects on plant growth and arbuscular mycorrhiza, *Appl. Soil Ecol.* 45 (2010) 238–242, <https://doi.org/10.1016/j.apsoil.2010.04.011>.
- [3] G. Wei, Y.-E. Miao, C. Zhang, Z. Yang, Z. Liu, W.W. Tjiu, T. Liu, Ni-doped graphene/carbon cryogels and their applications as versatile sorbents for water purification, *ACS Appl. Mater. Interfaces* 5 (2013) 7584–7591, <https://doi.org/10.1021/am401887g>.
- [4] H.B. Park, H.W. Yoon, Y.H. Cho, Graphene oxide membrane for molecular separation. *Graphene Oxide*, John Wiley & Sons, Ltd, Chichester, UK, 2016, pp. 296–313, <https://doi.org/10.1002/9781119069447.ch9>.
- [5] Z. Cheng, H. Pan, J. Chen, X. Meng, R. Wang, Separator modified by cobalt-embedded carbon nanosheets enabling chemisorption and catalytic effects of

- polysulfides for high-energy-density lithium-sulfur batteries, *Adv. Energy Mater.* 9 (2019) 1901609, <https://doi.org/10.1002/aenm.201901609>.
- [6] M. Iwanow, T. Gärtner, V. Sieber, B. König, Activated carbon as catalyst support: precursors, preparation, modification and characterization, *Beilstein J. Org. Chem.* 16 (2020) 1188–1202, <https://doi.org/10.3762/bjoc.16.104>.
 - [7] R. Dubey, V. Guruviah, Review of carbon-based electrode materials for supercapacitor energy storage, *Ionics* 25 (2019) 1419–1445, <https://doi.org/10.1007/s11581-019-02874-0>.
 - [8] S.-S. Yao, F.-L. Jin, K.Y. Rhee, D. Hui, S.-J. Park, Recent advances in carbon-fiber-reinforced thermoplastic composites: a review, *Compos. B Eng.* 142 (2018) 241–250, <https://doi.org/10.1016/j.compositesb.2017.12.007>.
 - [9] S. Chen, Z. Liu, S. Jiang, H. Hou, Carbonization: a feasible route for reutilization of plastic wastes, *Sci. Total Environ.* 710 (2020) 136250, <https://doi.org/10.1016/j.scitotenv.2019.136250>.
 - [10] C.R. Lohri, H.M. Rajabu, D.J. Sweeney, C. Zurbrügg, Char fuel production in developing countries – a review of urban bio-waste carbonization, *Renew. Sustain. Energy Rev.* 59 (2016) 1514–1530, <https://doi.org/10.1016/j.rser.2016.01.088>.
 - [11] J. Gong, X. Chen, T. Tang, Recent progress in controlled carbonization of (waste) polymers, *Prog. Polym. Sci.* 94 (2019) 1–32, <https://doi.org/10.1016/j.progpolymsci.2019.04.001>.
 - [12] B. Hu, K. Wang, L. Wu, S.-H. Yu, M. Antonietti, M.-M. Titirici, Engineering carbon materials from the hydrothermal carbonization process of biomass, *Adv. Mater.* 22 (2010) 813–828, <https://doi.org/10.1002/adma.200902812>.
 - [13] H. Wang, Y. Shao, S. Mei, Y. Lu, M. Zhang, J. Sun, K. Matyjaszewski, M. Antonietti, J. Yuan, Polymer-Derived heteroatom-doped porous carbon materials, *Chem. Rev.* 120 (2020) 9363–9419, <https://doi.org/10.1021/acs.chemrev.0c00080>.
 - [14] M. Antonietti, N. Fechler, T.-P. Feller, Carbon aerogels and monoliths: control of porosity and nanoarchitecture via sol–gel routes, *Chem. Mater.* 26 (2014) 196–210, <https://doi.org/10.1021/cm402239e>.
 - [15] K. Sakaushi, M. Antonietti, Carbon- and nitrogen-based porous solids: a recently emerging class of materials, *Bull. Chem. Soc. Jpn.* 88 (2015) 386–398, <https://doi.org/10.1246/bcsj.20140317>.
 - [16] M.-M. Titirici, M. Antonietti, Chemistry and materials options of sustainable carbon materials made by hydrothermal carbonization, *Chem. Soc. Rev.* 39 (2010) 103–116, <https://doi.org/10.1039/B819318P>.
 - [17] C.J. Brabec, S. Gowrisanker, J.J.M. Halls, D. Laird, S. Jia, S.P. Williams, Polymer-fullerene bulk-heterojunction solar cells, *Adv. Mater.* 22 (2010) 3839–3856, <https://doi.org/10.1002/adma.200903697>.
 - [18] Y. Cao, S. Cong, X. Cao, F. Wu, Q. Liu, M.R. Amer, C. Zhou, Review of Electronics Based on Single-Walled Carbon Nanotubes, 2019, pp. 189–224, https://doi.org/10.1007/978-3-030-12700-8_7.
 - [19] T.-H. Han, H. Kim, S.-J. Kwon, T.-W. Lee, Graphene-based flexible electronic devices, *Mater. Sci. Eng. R Rep.* 118 (2017) 1–43, <https://doi.org/10.1016/j.mser.2017.05.001>.
 - [20] R. You, Y. Liu, Y. Hao, D. Han, Y. Zhang, Z. You, Laser fabrication of graphene-based flexible electronics, *Adv. Mater.* 32 (2020) 1901981, <https://doi.org/10.1002/adma.201901981>.
 - [21] J.D. Majumdar, I. Manna (Eds.), *Laser-Assisted Fabrication of Materials*, Springer Berlin Heidelberg, Berlin, Heidelberg, 2013, <https://doi.org/10.1007/978-3-642-28359-8>.
 - [22] D. Go, P. Lott, J. Stollenwerk, H. Thomas, M. Möller, A.J.C. Kuehne, Laser carbonization of PAN-nanofiber mats with enhanced surface area and porosity, *ACS Appl. Mater. Interfaces* 8 (2016) 28412–28417, <https://doi.org/10.1021/acsami.6b09358>.
 - [23] V. Strauss, M. Anderson, C.L. Turner, R.B. Kaner, Fast response electrochemical capacitor electrodes created by laser-reduction of carbon nanodots, *Mater. Today Energy.* 11 (2019) 114–119, <https://doi.org/10.1016/j.mtener.2018.10.018>.
 - [24] V. Strauss, M. Anderson, C. Wang, A. Borenstein, R.B. Kaner, Carbon nanodots as feedstock for a uniform hematite-graphene nanocomposite, *Small* 14 (2018) 1803656, <https://doi.org/10.1002/smll.201803656>.
 - [25] A. Borenstein, V. Strauss, M.D. Kowal, M. Yoonessi, M. Muni, M. Anderson, R.B. Kaner, Laser-reduced graphene-oxide/ferrocene: a 3-D redox-active composite for supercapacitor electrodes, *J. Mater. Chem. A.* 6 (2018) 20463–20472, <https://doi.org/10.1039/C8TA08249A>.
 - [26] S. Delacroix, A. Zieloniewska, A.J. Ferguson, J.L. Blackburn, S. Ronneberger, F.F. Loeffler, V. Strauss, Using carbon laser patterning to produce flexible, metal-free humidity sensors, *ACS Appl. Electron. Mater.* 2 (2020) 4146–4154, <https://doi.org/10.1021/acsaem.0c00942>.
 - [27] M.F. El-Kady, V. Strong, S. Dubin, R.B. Kaner, Laser scribing of high-performance and flexible graphene-based electrochemical capacitors, *Science* 335 (80) (2012) 1326–1330, <https://doi.org/10.1126/science.1216744>.
 - [28] Y. Zhang, L. Guo, S. Wei, Y. He, H. Xia, Q. Chen, H.-B. Sun, F.-S. Xiao, Direct imprinting of microcircuits on graphene oxides film by femtosecond laser reduction, *Nano Today* 5 (2010) 15–20, <https://doi.org/10.1016/j.nantod.2009.12.009>.
 - [29] Z. Wan, E.W. Streed, M. Lobino, S. Wang, R.T. Sang, I.S. Cole, D.V. Thiel, Q. Li, Laser-reduced graphene: synthesis, properties, and applications, *Adv. Mater. Technol.* 3 (2018) 1700315, <https://doi.org/10.1002/admt.201700315>.
 - [30] L. Huang, J. Su, Y. Song, R. Ye, Laser-induced graphene: en route to smart sensing, *Nano-Micro Lett.* 12 (2020) 157, <https://doi.org/10.1007/s40820-020-00496-0>.
 - [31] R. Ye, D.K. James, J.M. Tour, Laser-induced graphene: from discovery to translation, *Adv. Mater.* 31 (2019) 1803621, <https://doi.org/10.1002/adma.201803621>.
 - [32] J. Lin, Z. Peng, Y. Liu, F. Ruiz-Zepeda, R. Ye, E.L.G. Samuel, M.J. Yacaman, B.I. Yakobson, J.M. Tour, Laser-induced porous graphene films from commercial polymers, *Nat. Commun.* 5 (2014) 5714, <https://doi.org/10.1038/ncomms6714>.
 - [33] M.G. Stanford, K. Yang, Y. Chyan, C. Kittrell, J.M. Tour, Laser-induced graphene for flexible and embeddable gas sensors, *ACS Nano* 13 (2019) 3474–3482, <https://doi.org/10.1021/acsnano.8b09622>.
 - [34] Z. Wan, N.-T. Nguyen, Y. Gao, Q. Li, Laser induced graphene for biosensors, *Sustain. Mater. Technol.* 25 (2020), e00205, <https://doi.org/10.1016/j.susmat.2020.e00205>.
 - [35] R. Kazemzadeh, Woo Soo Kim, Flexible temperature sensor with laser scribed graphene oxide, 14th IEEE Int. Conf. Nanotechnol., IEEE, 2014, pp. 420–423, <https://doi.org/10.1109/NANO.2014.6967998>.
 - [36] V. Strong, S. Dubin, M.F. El-Kady, A. Lech, Y. Wang, B.H. Weiller, R.B. Kaner, Patterning and electronic tuning of laser scribed graphene for flexible all-carbon devices, *ACS Nano* 6 (2012) 1395–1403, <https://doi.org/10.1021/nn204200w>.
 - [37] S. Delacroix, H. Wang, T. Heil, V. Strauss, Laser-induced carbonization of natural organic precursors for flexible electronics, *Adv. Electron. Mater.* 27 (2020) 2000463, <https://doi.org/10.1002/aeml.202000463>.
 - [38] V. Strauss, K. Marsh, M.D. Kowal, M.F. El-Kady, R.B. Kaner, A simple route to porous graphene from carbon nanodots for supercapacitor applications, *Adv. Mater.* 30 (2018) 1704449, <https://doi.org/10.1002/adma.201704449>.
 - [39] M.O. Loeh, F. Badaczewski, K. Faber, S. Hintner, M.F. Bertino, P. Mueller, J. Metz, B.M. Smarsly, Analysis of thermally induced changes in the structure of coal tar pitches by an advanced evaluation method of X-ray scattering data, *Carbon N. Y.* 109 (2016) 823–835, <https://doi.org/10.1016/j.carbon.2016.08.031>.
 - [40] D.B. Schuepfer, F. Badaczewski, J.M. Guerra-Castro, D.M. Hofmann, C. Heiliger, B. Smarsly, P.J. Klar, Assessing the structural properties of graphitic and non-graphitic carbons by Raman spectroscopy, *Carbon N. Y.* 161 (2020) 359–372, <https://doi.org/10.1016/j.carbon.2019.12.094>.
 - [41] D.B. Schuepfer, F. Badaczewski, J. Peilstöcker, J.M. Guerra-Castro, H. Shim, S. Firoozabadi, A. Beyer, K. Volz, V. Presser, C. Heiliger, B. Smarsly, P.J. Klar, Monitoring the thermally induced transition from sp³-hybridized into sp²-hybridized carbons, *Carbon N. Y.* 172 (2021) 214–227, <https://doi.org/10.1016/j.carbon.2020.09.063>.
 - [42] C. He, Y. Jiang, X. Zhang, X. Cui, Y. Yang, A simple glucose-blowing approach to graphene-like foam/NiO composites for asymmetric supercapacitors, *Energy Technol.* 8 (2020) 1900923, <https://doi.org/10.1002/ente.201900923>.
 - [43] P. Lazar, R. Mach, M. Otyepka, Spectroscopic fingerprints of graphitic, pyrrolic, pyridinic, and chemisorbed nitrogen in N-doped graphene, *J. Phys. Chem. C* 123 (2019) 10695–10702, <https://doi.org/10.1021/acs.jpcc.9b02163>.
 - [44] Y. Yamada, J. Kim, S. Matsuo, S. Sato, Nitrogen-containing graphene analyzed by X-ray photoelectron spectroscopy, *Carbon N. Y.* 70 (2014) 59–74, <https://doi.org/10.1016/j.carbon.2013.12.061>.
 - [45] B.E. Warren, X-ray diffraction in random layer lattices, *Phys. Rev.* 59 (1941) 693–698, <https://doi.org/10.1103/PhysRev.59.693>.
 - [46] W. Ruland, B. Smarsly, X-ray scattering of non-graphitic carbon: an improved method of evaluation, *J. Appl. Crystallogr.* 35 (2002) 624–633, <https://doi.org/10.1107/S0021889802011007>.
 - [47] J. Biscoe, B.E. Warren, An X-ray study of carbon black, *J. Appl. Phys.* 13 (1942) 364–371, <https://doi.org/10.1063/1.1714879>.
 - [48] P. Scherrer, Bestimmung der inneren Struktur und der Größe von Kolloidteilchen mittels Röntgenstrahlen, in: *Kolloidchem. Ein Lehrb.*, Springer Berlin Heidelberg, Berlin, Heidelberg, 1912, pp. 387–409, https://doi.org/10.1007/978-3-662-33915-2_7.
 - [49] A. Sharma, T. Kyotani, A. Tomita, Comparison of structural parameters of PF carbon from XRD and HRTEM techniques, *Carbon N. Y.* 38 (2000) 1977–1984, [https://doi.org/10.1016/S0008-6223\(00\)00045-2](https://doi.org/10.1016/S0008-6223(00)00045-2).
 - [50] W. Ruland, B. Smarsly, X-ray scattering of non-graphitic carbon: an improved method of evaluation, *J. Appl. Crystallogr.* 35 (2002) 624–633, <https://doi.org/10.1107/S0021889802011007>.
 - [51] J.S. Lukesh, L. Pauling, The problem of the graphite structure, *Am. Mineral.* 35 (1950).
 - [52] F. Badaczewski, M.O. Loeh, T. Pfaff, S. Dobrotka, D. Wallacher, D. Clemens, J. Metz, B.M. Smarsly, Peering into the structural evolution of glass-like carbons derived from phenolic resin by combining small-angle neutron scattering with an advanced evaluation method for wide-angle X-ray scattering, *Carbon N. Y.* 141 (2019) 169–181, <https://doi.org/10.1016/j.carbon.2018.09.025>.
 - [53] K. Faber, F. Badaczewski, W. Ruland, B.M. Smarsly, Investigation of the microstructure of disordered, non-graphitic carbons by an advanced analysis method for wide-angle X-ray scattering, *Z. Anorg. Allg. Chem.* 640 (2014) 3107–3117, <https://doi.org/10.1002/zaac.201400210>.
 - [54] T. Pfaff, M. Simmermacher, B.M. Smarsly, CarbX: a program for the evaluation of wide-angle X-ray scattering data of non-graphitic carbons, *J. Appl. Crystallogr.* 51 (2018) 219–229, <https://doi.org/10.1107/S1600576718000195>.
 - [55] S. Naeem, V. Baheti, J. Wiener, J. Marek, Removal of methylene blue from aqueous media using activated carbon web, *J. Text. Inst.* 108 (2017) 803–811, <https://doi.org/10.1080/00405000.2016.1191745>.
 - [56] M. Rafatullah, O. Sulaiman, R. Hashim, A. Ahmad, Adsorption of methylene blue on low-cost adsorbents: a review, *J. Hazard Mater.* 177 (2010) 70–80,

<https://doi.org/10.1016/j.jhazmat.2009.12.047>.

[57] P.T. Hang, Methylene blue absorption by clay minerals. Determination of surface areas and cation exchange capacities (Clay-Organic studies XVIII), Clay Clay Miner. 18 (1970) 203–212, [https://doi.org/10.1346/](https://doi.org/10.1346/CCMN.1970.0180404)

[CCMN.1970.0180404](https://doi.org/10.1346/CCMN.1970.0180404).

[58] V. Strauss, H. Wang, S. Delacroix, M. Ledendecker, P. Wessig, Carbon nanodots revised: the thermal citric acid/urea reaction, Chem. Sci. 11 (2020) 8256–8266, <https://doi.org/10.1039/D0SC01605E>.

Supporting Information to

Laser-Carbonization: Peering into the Formation of Micro-thermally produced (N-doped)carbons

Huize Wang^{1,§}, Simon Delacroix^{1,§}, Oliver Osswald², Mackenzie Anderson³, Tobias Heil¹, Enrico Lepre¹, Nieves Lopez-Salas¹, Richard Kaner^{3,4}, Bernd Smarsly², Volker Strauss^{1,*}

Raman spectroscopy	25
Sample collection	25
Scanning electron microscopy	26
Elemental analysis	27
Thermogravimetric analysis.....	27
High-resolution transmission electron microscopy	28
X-ray photoelectron spectroscopy	29
Wide-angle X-ray scattering	32

Raman spectroscopy

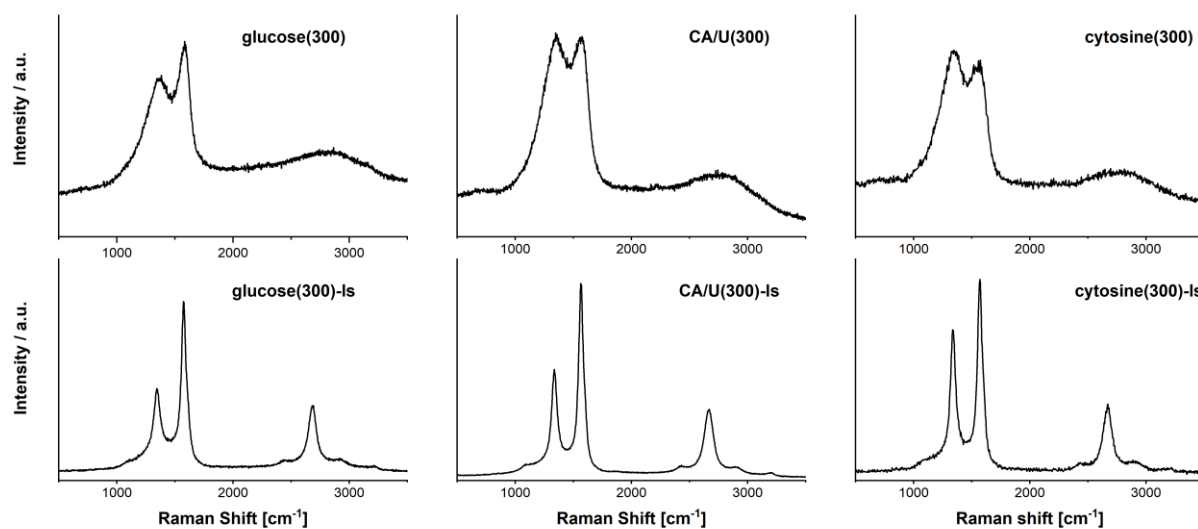


Figure S1. Raman spectra of glucose(300), glucose(300)-ls, glucose(950), CA/U(300), CA/U(300)-ls, CA/U(950), cytosine(300), cytosine(300)-ls, and cytosine(950) obtained upon excitation at 532 nm. The Raman spectra of the laser-treated samples were obtained on top of the films.

Sample collection

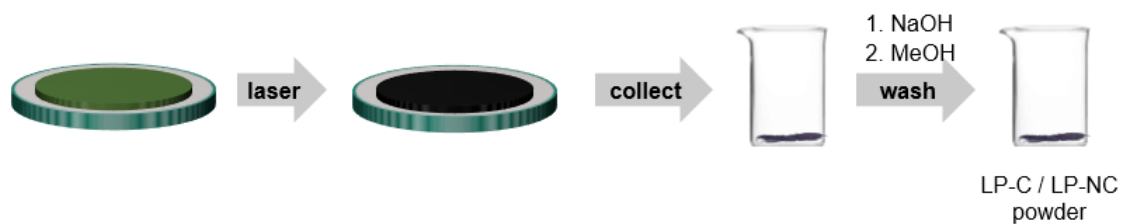


Figure S2. Scheme illustrating the sample preparation of the laser-carbonized powder samples.

Scanning electron microscopy

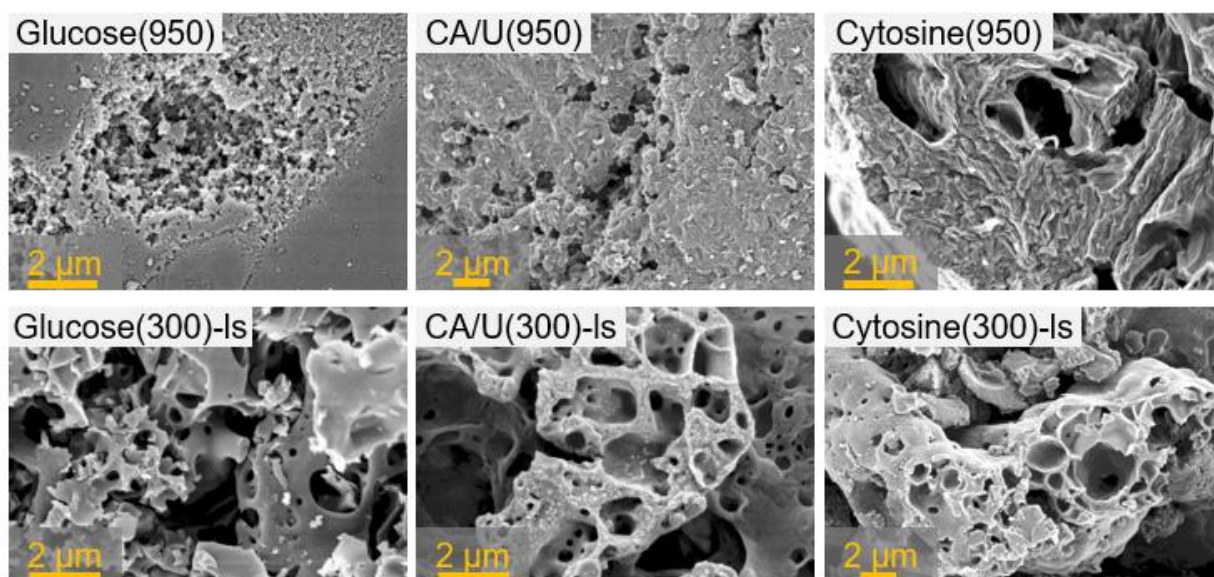


Figure S3. Scanning electron micrographs of glucose(950), glucose(300)-Is, CA/U(950), CA/U(300)-Is, and cytosine(950), and cytosine(300)-Is.

Elemental analysis

Table S1. Elemental mass percentage of the CNFAs, LP-carbon, and references obtained from combustion elemental analysis and energy dispersive X-ray analysis.

	<i>Elemental analysis of the collected powders</i>				<i>EDX of the as prepared films</i>			
	C	N	H	C/N	C	N	O	C/N
glucose (theor.)	40	-	7	-	40	-	53	-
glucose(300)	63	-	5	-	76	-	24	-
glucose(300)-ls	75	-	2	-	97	-	3	-
glucose(950)	77	-	1	-	81	-	19	-
CA/U (theor.)*	29	23	5		29	23	43	
CA/U(300)	47	19	3	2.4	54	27	19	2.0
CA/U(300)-ls	68	13	1	5.2	92	-	8	-
CA/U(950)	86	13	0	6.6	81	16	3	5.1
cytosine (theor.)	43	38	5		43	38	14	
cytosine(300)	50	33	3	1.5	55	34	11	1.6
cytosine(300)-ls	50	27		1.9	83	7	9	-
cytosine(950)	80	15	0	5.3	81	18	1	4.5

*The composition of 1:3 citric acid/urea was assumed as used in the starting reagent reacting via HPPT as an intermediate product of the citric acid/urea reaction. [58] The grey highlighted numbers were obtained from the as-prepared films. All other numbers were obtained from the collected powders.

Thermogravimetric analysis

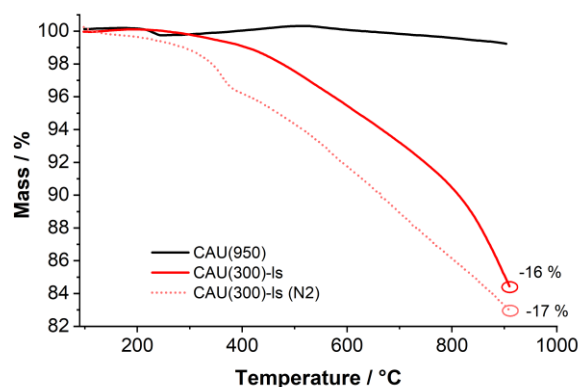


Figure S4. Comparative thermogravimetric analysis of CAU(950) (black line), and CAU(300)-ls obtained by laser-carbonization in air (red line) and N₂-atmosphere (dotted line).

High-resolution transmission electron microscopy

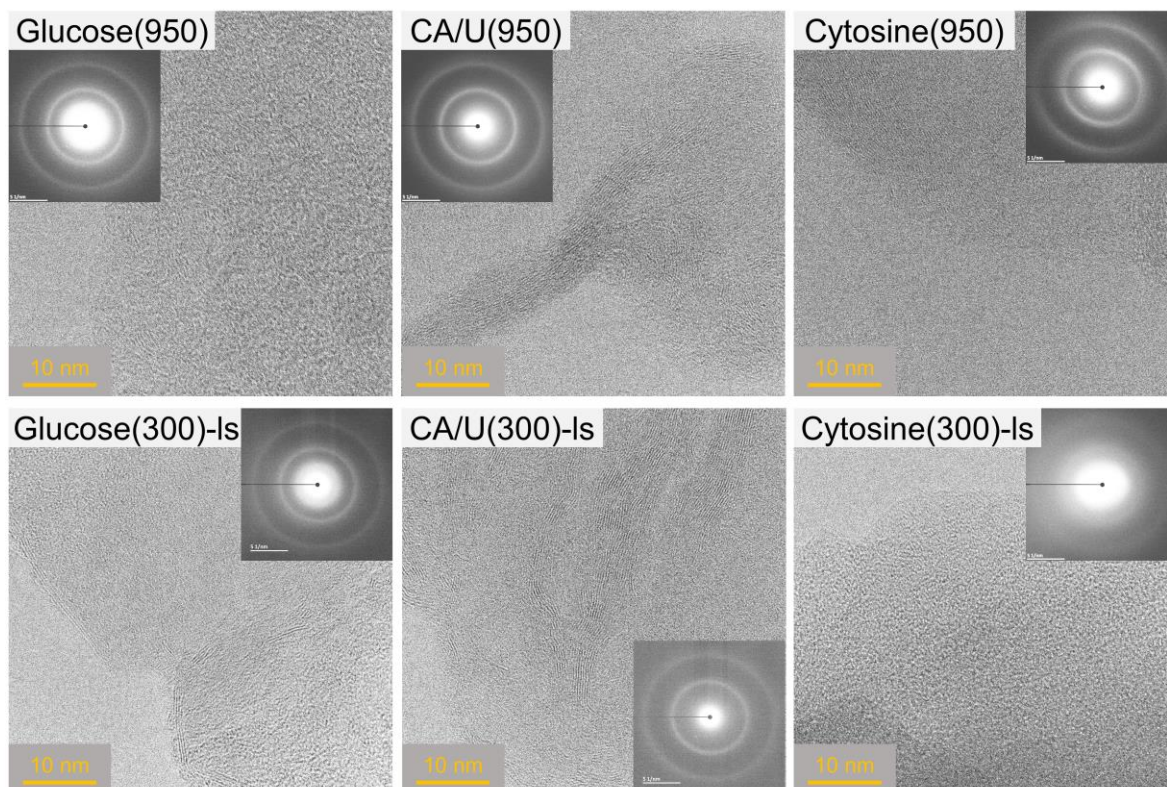


Figure S5. High-resolution transmission electron micrographs of fragments of glucose(950), glucose(300)-ls, CA/U(950), CA/U(300)-ls, and cytosine(950), and cytosine(300)-ls. The insets show the electron diffraction pattern of the selected areas.

X-ray photoelectron spectroscopy

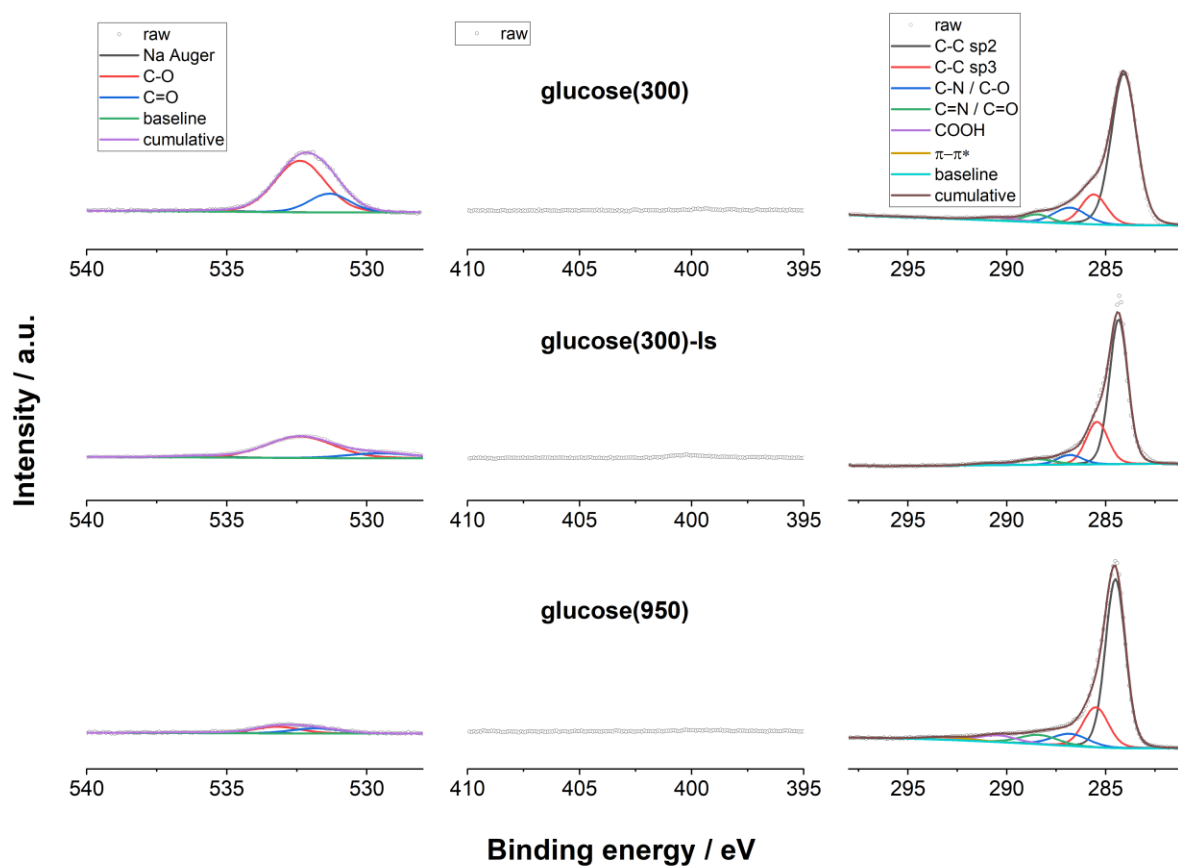


Figure S6. X-ray photoelectron spectrographs of the O_{1s}, N_{1s}, and C_{1s} regions (from left to right) of glucose(300), glucose(300)-ls, and glucose(950) (top to bottom).

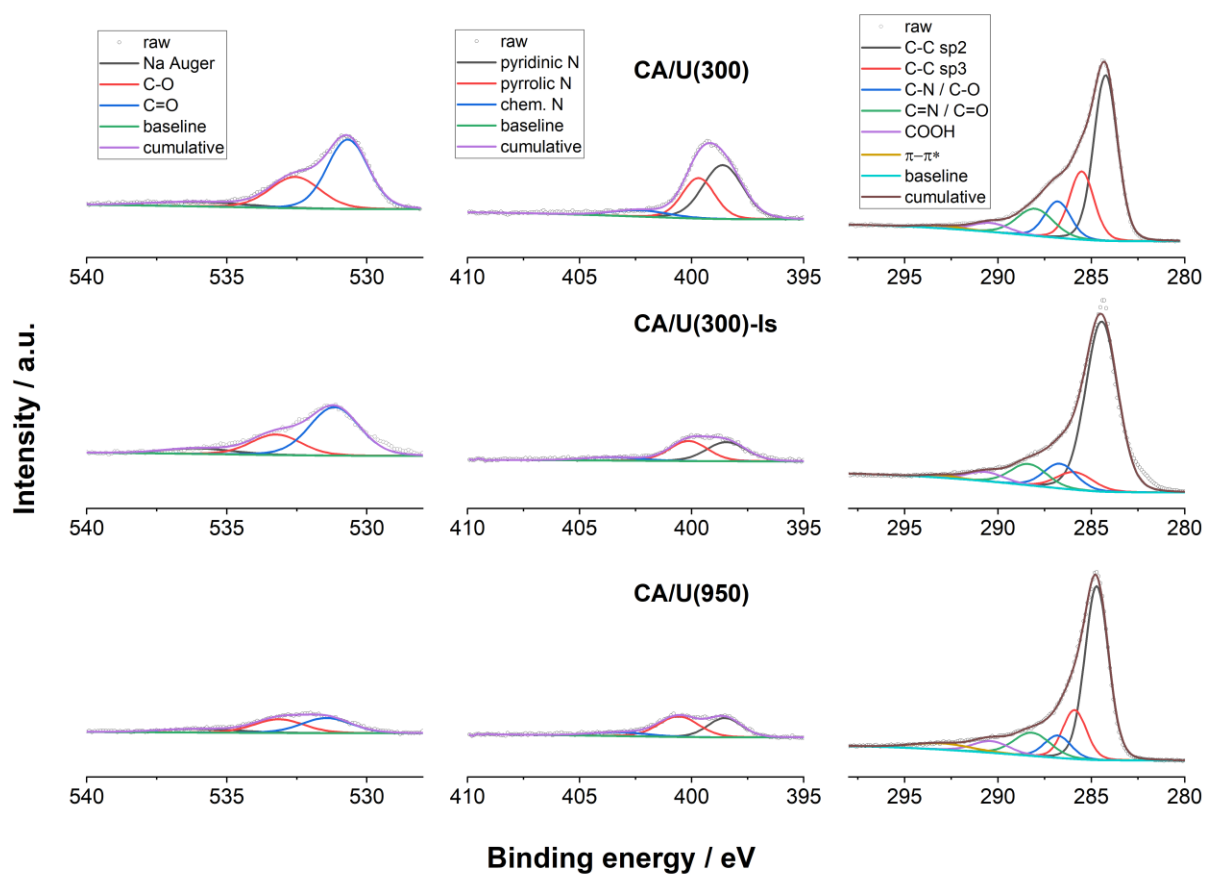


Figure S7. X-ray photoelectron spectrographs of the O_{1s}, N_{1s}, and C_{1s} regions (from left to right) of CA/U(300), CA/U(300)-ls, and CA/U(950) (top to bottom).

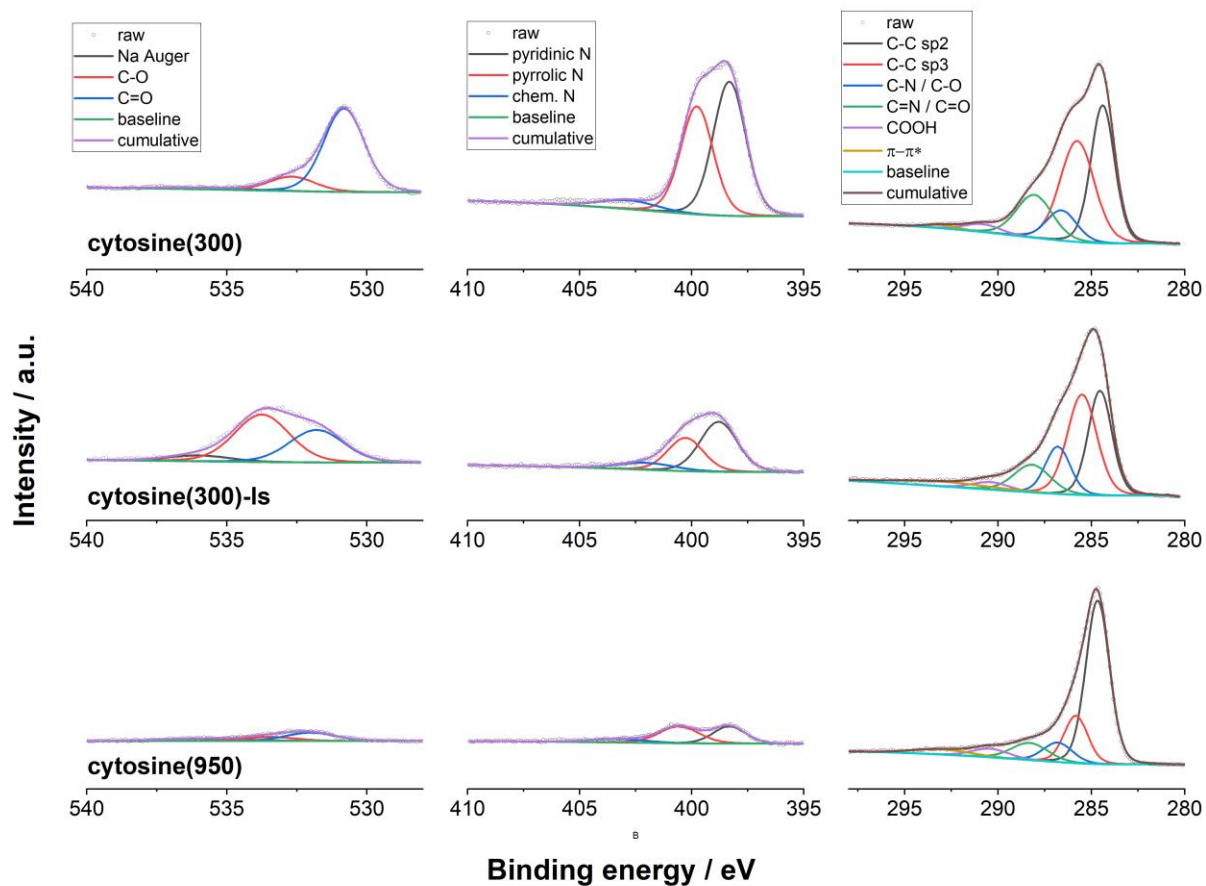


Figure S8. X-ray photoelectron spectrographs of the O_{1s} , N_{1s} , and C_{1s} regions (from left to right) of cytosine(300), cytosine(300)-ls, and cytosine(950) (top to bottom).

Wide-angle X-ray scattering

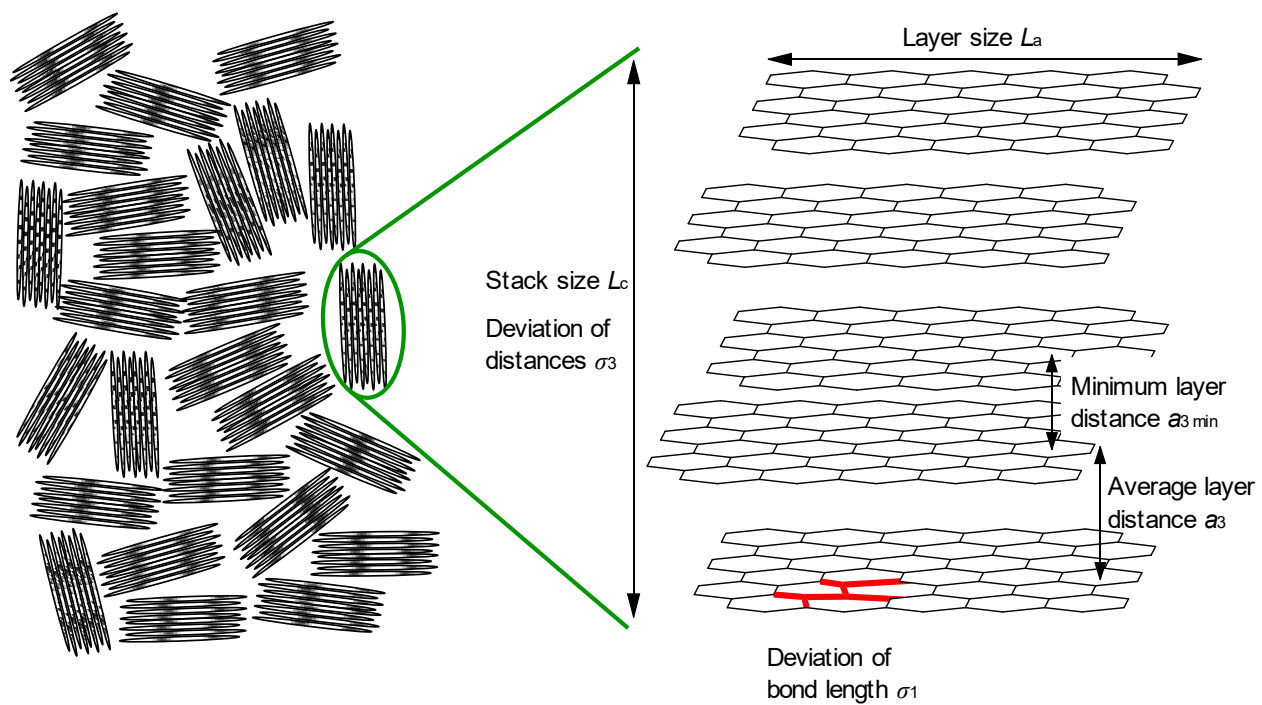


Figure S9. Principle structure of non-graphitic carbons (NGCs) containing a turbostratic stacking arrangement of single graphene layers.

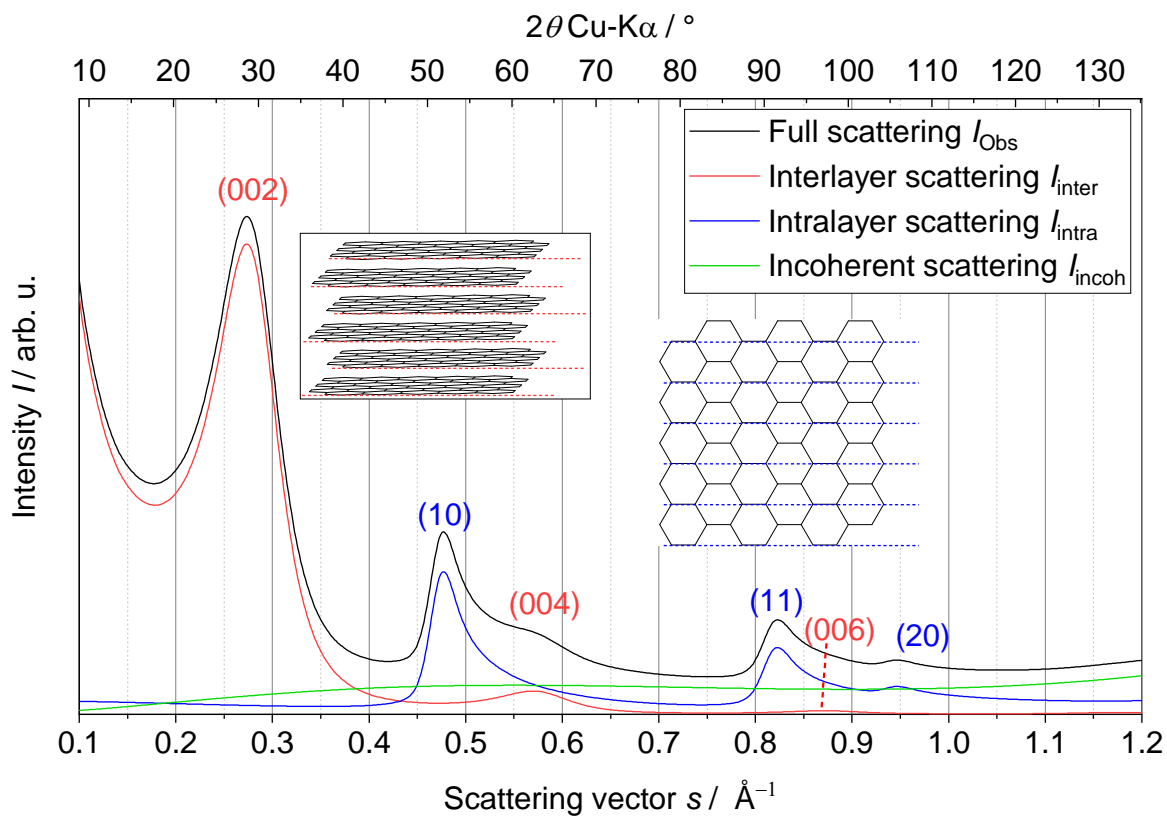


Figure S10. Representative example for an observed scattering intensity (I_{Obs}) of a NGC, which is given by a superposition of symmetric interlayer reflections (00l), asymmetric intralayer reflections (hk) and the incoherent scattering (I_{incoh}).

Table S2: Microstructure parameters of the resulting fits with assumed errors in brackets.*

	CA/U(950)	CA/U(300)-ls	cytosine(950)	cytosine(300)-ls	glucose(950)	glucose(300)-ls
$a_3 / \text{\AA}$	3.40 (0.03)	3.45 (0.09)	3.40 (0.03)	3.40 (0.09)	3.84 (0.10)	- -
$a_{3 \text{ min}} / \text{\AA}$	2.80 (0.06)	3.00 (0.15)	3.00 (0.06)	3.00 (0.15)	2.84 (0.14)	- -
$da_3 / \text{\AA}$	0.60 (0.01)	0.45 (0.01)	0.40 (< 0.01)	0.40 (< 0.01)	1.00 (0.03)	- -
$\sigma_3 / \text{\AA}$	0.30 (< 0.01)	0.50 (0.01)	0.35 (< 0.01)	0.50 (< 0.01)	0.98 (0.02)	- -
$L_c / \text{\AA}$	20.0 (8.7)	124.5 (78.6)	23.2 (11.5)	25.8 (14.2)	15.7 (5.5)	- -
N	5.9 (0.6)	36.1 (13.3)	6.8 (0.6)	7.6 (0.8)	4.1 (0.3)	- -
$l_{cc} / \text{\AA}$	1.401 (0.014)	1.421 (0.014)	1.406 (0.014)	-	1.416 (0.014)	1.411 (0.014)
σ_1	0.175 (0.004)	0.150 (0.008)	0.180 (0.004)	-	0.221 (0.004)	0.100 (0.005)
$L_a / \text{\AA}$	31.2 (9.7)	50.0 (10.0)	22.7 (1.0)	-	80.1 (64.1)	50.0 (20.0)
q	0.05 (0.03)	0.30 (0.15)	-	-	0.07 (0.03)	- -
η	0.95 (0.05)	0.55 (0.28)	0.93 (0.05)	-	1.00 (0.05)	- -
$c_O / \%$	0.11 (0.003)	0.15 (0.004)	0.06 (0.002)	0.30 (0.008)	0.04 (0.001)	0.00 (0)

* Some parameters could not be calculated due to the absence of a stacking or sp^2 structure. In addition to **Figure S9** da_3 describes the difference of the average layer distance to the minimal layer distance ($da_3 = a_3 - da_3$), N is the number of layers per stack, i.e. $N = L_c / a_3$, q is a parameter for the preferred orientation during the XRD measurements ($q = 0$ means no preferred orientation) and η is the homogeneity of the stacks ($\eta = 1$ means perfect homogeneity) and c_O describes the concentration of oxygen.

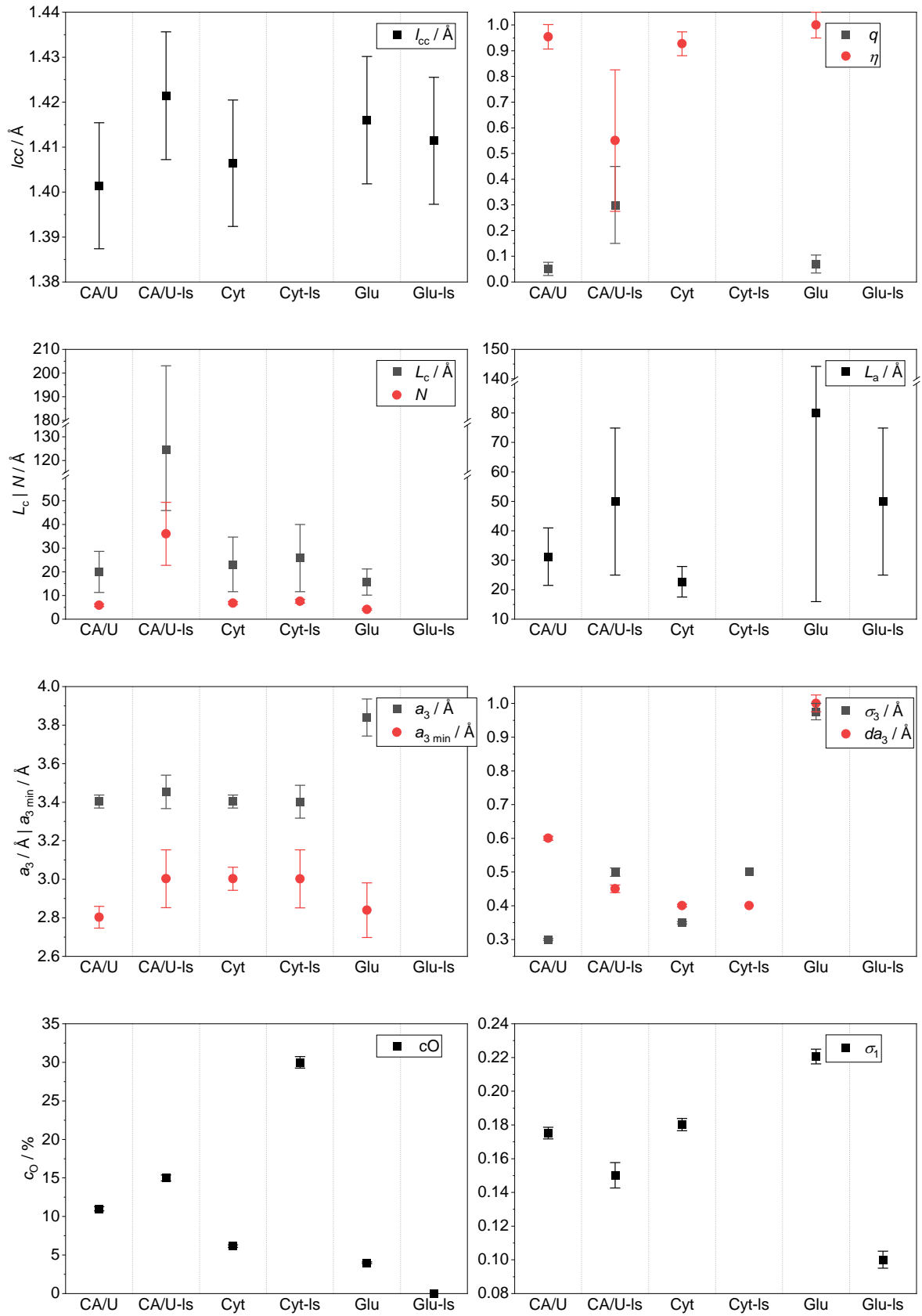


Figure S9. Microstructure parameters of the resulting fits. Additional parameters to **Figure S9** are described in **Table S2**.

Using Carbon Laser Patterning to Produce Flexible, Metal-Free Humidity Sensors

Simon Delacroix, Anna Zieleniewska, Andrew J. Ferguson, Jeffrey L. Blackburn, Sebastian Ronneberger, Felix F. Loeffler, and Volker Strauss*

Cite This: *ACS Appl. Electron. Mater.* 2020, 2, 4146–4154

Read Online

ACCESS |

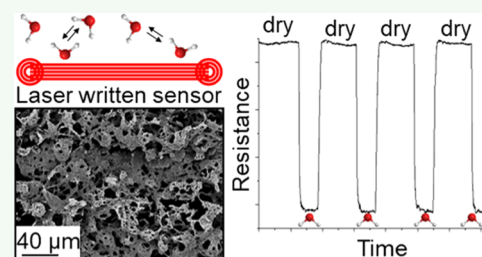
Metrics & More

Article Recommendations

Supporting Information

ABSTRACT: A relative humidity sensor was produced by carbon laser patterning of a carbon precursor ink on a flexible substrate. Citric acid and urea, both inexpensive and naturally abundant molecules, are used as initial precursors to obtain a porous carbon foam after CO₂ laser irradiation. The laser-patterned material is characterized by electron microscopy, Raman spectroscopy, and vertical scanning interferometry. An intrinsic p-type semiconducting behavior was confirmed by thermoelectric and Hall measurements. The resistance of this porous, metal-free material is sensitive to atmospheric variations, namely, temperature and relative humidity ($\approx 5 \Omega\%$). Under dry atmosphere, the sensor acts as a thermometer with a linear relationship between temperature and relative variation of resistance ($0.07\% \cdot K^{-1}$). The evolution of the sensor resistance at different relative humidities and temperatures is studied by electrical impedance measurements. The kinetic transitory regime of water desorption from the carbonaceous surface of the sensor is analyzed using Langmuir's model. The equilibrium constant of adsorption K_{ads} has been determined, and the standard enthalpy of adsorption of water on the sensor surface is estimated at $\Delta_{ads}H^\circ = -42.6 \text{ kJ} \cdot \text{mol}^{-1}$. The simple and inexpensive production and its high, stable sensitivity make laser-patterned carbon interesting for humidity sensing applications, and the method allows for the large-scale production of printed sensor arrays.

KEYWORDS: humidity sensor, carbon laser patterning, laser carbonization, carbon semiconductor, laser-induced graphene, sensing



INTRODUCTION

The development of new lab-on-a-chip sensors is essential to move toward miniaturization of devices, realization of sensor arrays, and their applications for on-site analysis.¹ Various fields could benefit from such progress, especially public health, with the sensing of volatile organic compounds or biomolecules for disease diagnosis.^{2–4} Such future sensors have to be inexpensive, easily producible, simple to integrate into a device, and based on ecologically sustainable precursors. The flexibility is another desired characteristic, which can assure a larger versatility of use of these lab-on-a-chip sensors.⁵

In terms of humidity sensing, the most common commercial materials used today are based on metal oxides or porous silicon.⁶ To reach the above-mentioned specifications of a sensor, however, metal-free materials and, in particular, conductive carbon materials are prime candidates.⁷ In recent years, carbon materials, such as graphene and carbon nanotubes, were subject to detailed investigations as active materials for humidity sensing.^{8,9} Their high electronic mobility at room temperature and small dimensions make graphenes, carbon nanotubes, and their derivatives extremely sensitive to molecules present in their environment.^{10,11} Advantages in terms of simple production, miniaturization, eco-friendliness, and economical fairness were targeted. The carbon nanoallotropes served as excellent test beds for

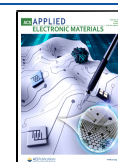
mechanistic studies; however, their real-world application is still impeded by the tedious production and resulting high costs. Here, use of bio-based carbon provides a significant advantage in terms of production costs.¹² Moreover, production techniques for realizing sensor array arrangements are in demand, as these help to reduce measurement errors, cross-interference, and the issue of normalization.^{13,14}

In the past years, printed carbon foams have been shown to be very promising as sensors due to their high specific surface area.^{15,16} A hurdle to the development of new devices is the difficulty to process and integrate such carbon foams into electronic circuits. High-temperature treatments in ovens and purification steps with hazardous solution are often used during their syntheses.¹⁷ Within the last decade, a simple processing technique for carbon foams has been developed: direct laser writing of carbons, also referred to as laser-induced carbons.^{18–20} In general, this strategy of laser fabrication has many advantages such as on-spot production, low energy

Received: October 23, 2020

Accepted: November 23, 2020

Published: December 9, 2020



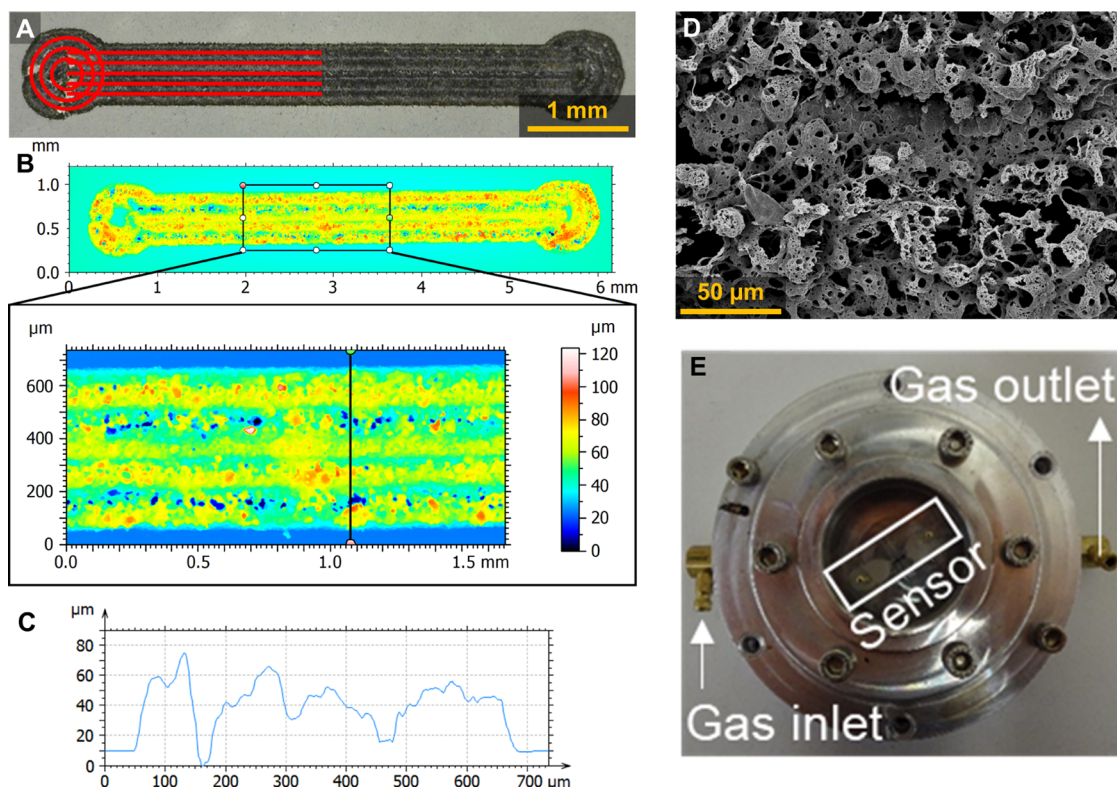


Figure 1. (A) Digital micrograph of the sensor platform obtained by laser patterning with the programmed laser pattern overlaid (red); (B) vertical scanning interferometry of the selected part of the digital micrograph; (C) height profile of the sensor platform on a line perpendicular to the laser pattern; (D) scanning electron micrograph of the sensor; and (E) sensor in the atmospheric chamber with gas inlet and outlet to control the relative humidity.

consumption, and high precision. Furthermore, laser patterning is compatible with roll-to-roll techniques, which allow a scalable production of such devices, and allows for the production of array patterns.^{20,21}

Typical precursors of laser-patterned carbon foams are graphene oxide (GO) or polyimide (PI)²² and also other precursors like phenolic resin,²³ paperboard,²⁴ wood,²⁵ coconut,²⁶ and lignin²⁷ have been studied. Recently, an alternative route to obtain laser-patterned carbon from molecule-based inks was introduced.^{28–31} Carbon-rich nanoparticles were synthesized via thermal treatment of organic molecules.³² These particles act as a carbon network forming agent (CNFA) in an ink, which is used to make films on various substrates. Laser patterning of the carbonaceous precursor film leads to a porous foam of carbon, while the unexposed film is simply rinsed off the substrate. A major advantage of this technique is the possibility to directly print carbon foams on any chosen substrate from rigid conductive silicon to flexible insulator plastic, which is fundamental for the production of future sensor arrays.³² Moreover, nitrogen functionalities are easily incorporated into porous carbon networks to provide additional binding sites for polar gases.

In this work, we used laser patterning of our in-house-developed carbon precursor ink to design a relative humidity sensor. Laser patterning of chemiresistors made of carbon foam is realized over a small area (2.5 mm²) on a flexible poly(ethylene terephthalate) (PET) substrate. First, the sensor platform is characterized by electron microscopy and Raman spectroscopy. Their intrinsic electronic properties, such as carrier density and mobility, are determined using thermoelectric and Hall measurements. The variation of sensor

resistance with temperature is thoroughly studied, followed by systematic testing of the change of resistance under different atmospheric conditions, namely, temperature and relative humidity. Finally, the interaction between water molecules and the sensor surface was characterized by calculating the thermodynamic constants of adsorption equilibrium and the standard enthalpy of adsorption of gaseous H₂O on the surface of the sensor. These results can be used to calibrate the sensor platform for quick quantitative on-spot measurements.

RESULTS AND DISCUSSION

Materials Characterization. The use of carbon-rich particles as precursors for laser-induced carbonization to obtain porous carbon foams was discussed in a previous study.³² Briefly, citric acid and urea are precarbonized in an oven at 300 °C for 2 h under an inert atmosphere. A black powder (CAU300) composed of carbon-rich particles and molecular side products was obtained. To eliminate the side products, the solid mixture was thoroughly washed in hot H₂O (see the [Experimental Section](#)). The dry product from the washing process, referred to as CAU300p, was used as the carbon network forming agent (CNFA).

The transmission electron microscopy image of CAU300p in [Figure S1B](#) shows aggregated carbonaceous particles of diameters between 50 and 200 nm. A peak at $2\theta = 27.4^\circ$ (Cu $K\alpha$) in the X-ray diffraction pattern is characteristic of the presence of graphitic layers ([Figure S1A](#)).

The ink used for laser patterning is composed of 48 wt % CAU300p (CNFA), 44 wt % ethylene glycol (solvent), and 8 wt % of polyvinylpyrrolidone (film forming agent (FFA)).

Films of thickness between 20 and 30 μm (manual digital micrometer measurement) were prepared by doctor blading on PET foil, and ethylene glycol was evaporated after 10 min at 80 $^{\circ}\text{C}$.

The sensor platform was laser-patterned into the film to obtain laser-patterned carbon (LPC). To maximize the contact area with the atmosphere, the pattern is composed of five parallel lines of 5 mm length distributed on 0.5 mm width. The sensor has a geometric area of 2.5 mm^2 (Figure 1A). At both ends of these line assemblies, three concentric circles were printed to ensure good electrical contact to the electrodes for impedance measurements. The nonprinted ink around the laser pattern was rinsed off with distilled water, and the sensor platform was dried under airflow.

After laser irradiation, the Raman spectrum of the LPC (Figure S2) shows a characteristic pattern of a turbostratic graphitic material: D and G vibration bands localized at 1337 and 1565 cm^{-1} and the G' band localized at 2665 cm^{-1} with a full width at half-maximum of 84 cm^{-1} .³³ This pattern, in particular, the pronounced D and D' bands, indicates the presence of large amounts of defects in the graphitic lattice. The appearance of a semicrystalline porous structure is confirmed by transmission electron microscopy (Figure S2B). The morphology of the LPC sensor platform, probed by vertical scanning interferometry (Figure 1B,C), shows high roughness with a mean height of approximately 30 μm (Figure S3). A more detailed overview image of the LPC sensor platform is given in the scanning electron micrograph in Figure 1D, which shows that the LPC has a foam-like porous morphology. The presence of micropores (Figure 1D) and mesopores (Figure S2B) indicates a high surface area. The methylene blue adsorption method (Experimental Section) is well suited to determine the surface area of small quantities (~ 0.1 mg) of carbonaceous samples. A surface area around 238 $\text{m}^2\cdot\text{g}^{-1}$ was determined for the sensor material with reference to activated carbon (1269 $\text{m}^2\cdot\text{g}^{-1}$), which is a prerequisite for good sensing properties. The elemental composition was analyzed by combustion analysis of the collected laser-patterned material. The composition of 68% C, 13% N, 2% H, and 16% O demonstrates the heterogeneity of the sensor material in the bulk. The same composition (72% carbon, 13% nitrogen, and 14% oxygen), is also reflected in the results of the powder XPS analysis shown in Figure S4. The fits of the XPS data reveal that the majority of the carbon in the LPC is sp^2 -hybridized (57%) and $\sim 18\%$ of the carbon is sp^3 -hybridized. Therefore, we describe the morphology of the LPC as rather amorphous or semicrystalline. The nitrogen is predominantly incorporated in the form of pyridinic/pyrrolic or graphitic nitrogen.^{34,35} Notably, the bulk composition shows a strong deviation from the surface composition of 97% C and 3% O measured by energy-dispersive X-ray analysis (EDX), which is due to the top-to-bottom energy input by the laser.

To obtain insights into the fundamental electronic properties of LPC films, thermoelectric and Hall effect measurements were carried out. Both experiments yielded positive values of Seebeck and Hall coefficients (Figure S5), indicating an intrinsic p-type character of the material. Notably, the values of both factors are relatively small, that is, $+2.3 \pm 0.5 \mu\text{V}\cdot\text{K}^{-1}$ and $+0.099 \pm 0.043 \text{ cm}^3\cdot\text{C}^{-1}$ for Seebeck and Hall coefficients, respectively. Such small positive Seebeck and Hall coefficients are not uncommon even for highly nitrogen-doped graphite or graphene materials due to unintentional doping with environmental water and oxygen molecules at room temperature.^{36,37}

Despite the high carrier density of $7.7 \times 10^{19} \text{ cm}^{-3}$, the material shows low mobilities of $0.12 \text{ cm}^2\cdot(\text{V}\cdot\text{s})^{-1}$. This is in line with the presence of a large number of defects and sp^3 carbon concluded from the Raman and XPS data. Similar observations have been noted for graphene where defects introduced during the nitrogen doping process are recognized to function as scattering centers that hinder the electron/hole transport.^{38,39} The reproducibility of these data was verified in several samples. For example, an average conductivity of $1.74 \pm 0.29 \text{ S cm}^{-1}$ was obtained for 30 sensor platforms.

To test the principle sensing properties of the laser-patterned carbon, the resistivity of the platform was measured upon variation of temperature and humidity. To this end, the platform was placed in a chamber (Figure 1E), where its resistance was monitored by measuring the electrical impedance. Two electrodes separated by 5 mm ensured the electrical contact through the windows of this chamber. The relative humidity inside this chamber was controlled by a humidity generator with a flow of 1.3 $\text{L}\cdot\text{min}^{-1}$. The volume of the chamber is ~ 0.1 L, ensuring that a complete change of the atmosphere is achieved in about 5 s. This system was contained and thermalized in an environmental chamber so that the relative humidity and the temperature of the sensor can be varied independently.

Resistance in Dependence of Temperature. Before changing the relative humidity inside the chamber, the resistance of the sensor was studied as a function of temperature at a constant humidity (Figure 2). To this end,

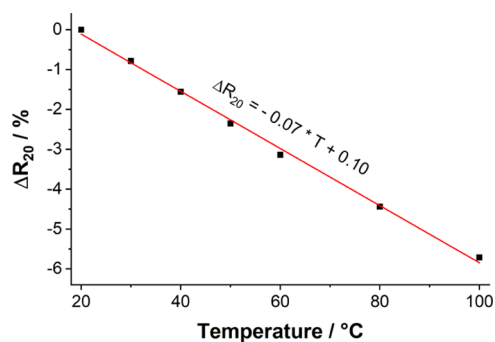


Figure 2. Relative variation of resistance in the temperature range between 20 and 100 $^{\circ}\text{C}$. The linear regression (red) is in good agreement ($r^2 = 0.9967$) with the experimental data.

a commercial humidity generator was used, in which dry and moisture-saturated airstreams are mixed via specifically designed humidity-resistant mass flow controllers. Dry air was flushed into the chamber, while the temperature inside the chamber was increased from 20 to 100 $^{\circ}\text{C}$ in steps of 10 $^{\circ}\text{C}$. After reaching thermal equilibrium, the resistance of the sensor was measured. The frequency and the current amplitude of the electrical impedance measurements were fixed at 1000 Hz and 0.05 mA, respectively, for every measurement. The relative variation of the resistance is defined by eq 1, where R_{20} and R_T are the resistance values at 20 $^{\circ}\text{C}$ and the tested temperature T , respectively

$$\Delta R_{20} = 100 \cdot \frac{R_T - R_{20}}{R_{20}} \quad (1)$$

The resistance–temperature relationship exhibits a decrease of resistance with increasing temperature. Although the commonly applied models follow an $\propto e^{1/T}$ dependence for

thermally activated transport in a semiconductor,^{40–42} the weak temperature dependence suggests that it would be difficult to distinguish between these models for this material system over the tested temperature regime. However, the observed linear trend allows simple calibration of the temperature-dependent resistance of our humidity sensor. The relative resistance decrease of 0.07% per Kelvin (K) corresponds to an absolute variation of approximately $2 \Omega \cdot K^{-1}$. Similar behavior is observed in other conductive organic materials such as single-walled carbon nanotubes or conducting polymers.⁴² The variation of resistance as a function of relative humidity in the following part is realized at constant temperatures.

Resistance in Dependence of Relative Humidity. As a first experiment to study the variation of resistance with changes in relative humidity (RH), the sensor temperature was fixed at 40 °C. The resistance was monitored during cycles between dry air and air with a relative humidity of 70% in the sensor chamber (Figure 3). The cycles of humid air were

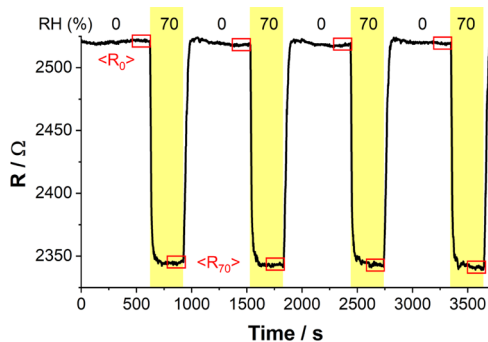


Figure 3. Variation of resistance during cycles between dry air and air with a relative humidity of 70% at 40 °C. The resistance values in the red squares (50 s intervals) are used to calculate the equilibrium average resistances $\langle R_0 \rangle$ and $\langle R_{70} \rangle$ under relative humidities of 0 and 70%, respectively.

chosen to be shorter (5 min) than those of dry air (10 min), because the equilibrium is reached slower for desorption than adsorption onto the sensing platform, suggesting a moderate hydrophilicity of the material. The resistance decreases in the presence of gaseous water in the chamber, consistent with previous observations of conductivity increase in the presence of water vapor in different carbonaceous materials like carbon nanotubes,⁴³ carbonized bamboo,⁴⁴ carbon quantum dots,⁴⁵ N-doped carbon sphere,⁴⁶ and graphene oxide.⁴⁷ Such an increase could be explained by two phenomena: charge transfer from the water molecules to the carbon materials, increasing the number of charge carriers,⁴³ or the occurrence of ionic conductivity in the water-filled pores of the materials for high humidity.⁴⁸ Here, we postulate the presence of nitrogen and oxygen functional groups in the sensor material (13 wt %) as polar binding sites for the adsorption of water molecules on the sensor surface even at a relatively low relative humidity.⁴⁹ Despite the lack of heteroatoms on top of the material, its porous nature allows for the penetration of gases in the environment to penetrate deep into the material and interact with functionalities. To ensure reproducible data treatment, an average of resistance values at the equilibrium was taken during the 50 s before a change in relative humidity for all of the cycles (red squares in Figure 3).

To study the environmental sensitivity of the sensor platform in depth, experiments were performed by varying the relative humidity and temperature (Figure 4). In a typical experiment, 10 min cycles between dry air and different relative humidities (RH = 30–100%) at fixed temperatures (10, 20, 30, and 40 °C) were run.⁵⁰ At 30 and 40 °C, 10 min of desorption was enough to reach equilibrium, but at 10 and 20 °C, 20 min of desorption is necessary. Adsorption was observed to be much faster than desorption on the sensor: the resistance reached its equilibrium value faster during the water adsorption, leading to quasi-squared shape curves.

At each temperature, the relative variation of resistance ΔR is calculated as a function of relative humidity (Figure 5) using eq 2, where $R(\%RH, T)$ is the sensor resistance in an atmosphere at temperature T containing a given percentage of relative humidity

$$\Delta R(\%RH, T) = \frac{R(0, T) - R(\%RH, T)}{R(0, T)} \quad (2)$$

For a given temperature, the variation of resistance with relative humidity has a classic shape of an isotherm curve. These calibration curves allow us to use the sensor as a hygrometer at a given temperature. The sensitivity S (in $\Omega \cdot \%$) of the sensor is defined as the variation of resistance for a 1% variation of the relative humidity. This sensitivity depends on the operating temperature of the sensor and on the relative humidity and is given by eq 3

$$S = \left| \frac{\Delta R(\%RH + 10, T) - \Delta R(\%RH, T)}{10} \right| \quad (3)$$

The different values of sensitivity are listed in Table 1. These sensitivity values are in the same range as other carbon-based materials, such as graphene, graphene oxide, etc., reported in the literature.⁵¹

Calculation of Thermodynamics Constants: Langmuir's Model. To access the thermodynamic constants, we decided to model the kinetic transitory regime using Langmuir's model to describe the interaction between water molecules and the sensor surface. The hypotheses of this model are the following: a simple monolayer of adsorbed molecules without interaction between each other is present at the sensor surface in equilibrium with gaseous molecules. Although multilayer adsorption or island formation cannot be ruled out, we did not see any indications for processes besides single-layer adsorption, and the fitting based on Langmuir's model yielded high accuracies. The equilibrium constant of adsorption K_{ads} is defined as the ratio between the rate constants of adsorption k_A and desorption k_D . At a given temperature, the fraction of occupied sites on the sensor surface is named θ . The variation of θ is given by eq 4, where P_{H_2O} is the partial pressure of water in the gas phase

$$\left(\frac{d\theta}{dt} \right)_T = k_A * P_{H_2O} * (1 - \theta) - k_D * \theta \quad (4)$$

The expression of θ is given by solving the preceding equation, with M as a constant

$$\theta(t) = M * e^{-(k_A * P_{H_2O} + k_D) * t} + k_A * P_{H_2O} \quad (5)$$

Furthermore, we observe a change in resistivity when water is adsorbed on the surface of the sensor. The last hypothesis consists of the proportionality between the resistance $R(t)$, or

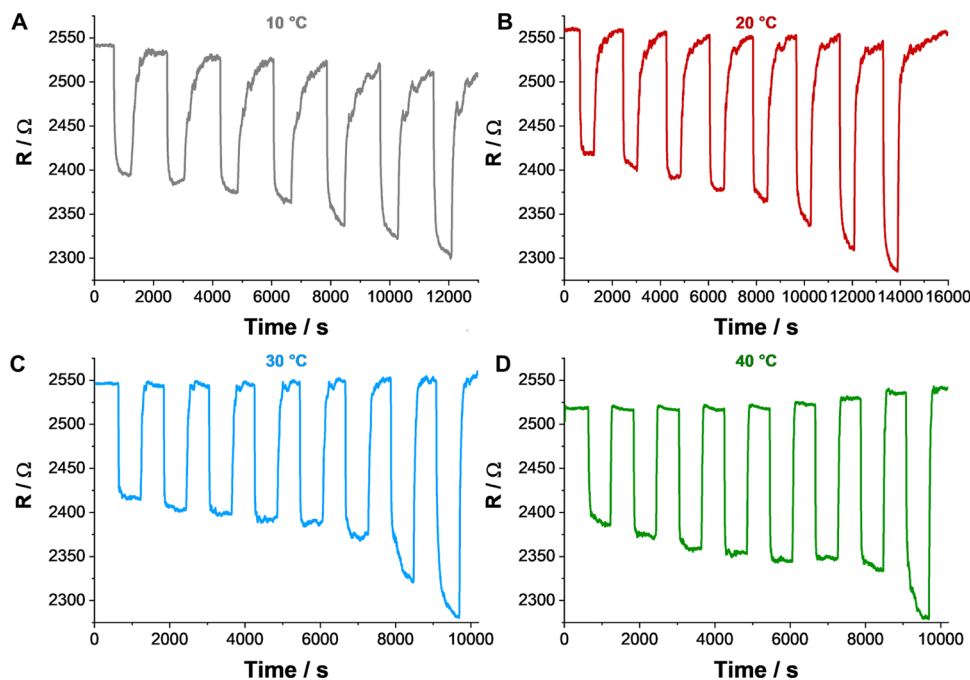


Figure 4. Variation of the sensor resistance during cycles of 10 min between dry air and different relative humidities at different temperatures. For each dataset, the relative humidity increases by 10% steps from 30 to 100% in steps of 10% (at 10 °C: from 40 to 100%). At 10 and 20 °C, the desorption cycles are 20 min long to completely reach the equilibrium.

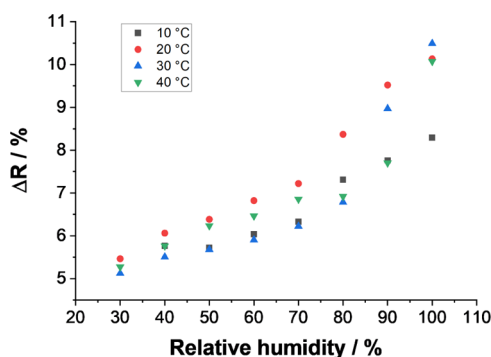


Figure 5. Relative variation of resistance ΔR with relative humidity at 10 (black squares), 20 (red circles), 30 (blue triangles), and 40 °C (green triangles).

Table 1. Sensitivity S (in $\Omega \cdot \%$) of the Sensor at Different Temperatures for Different Intervals of Relative Humidity (%RH)

%RH	10 °C	20 °C	30 °C	40 °C
30–40		6.00	3.81	4.89
40–50	0.39	3.23	1.75	4.72
50–60	3.15	4.37	2.24	2.30
60–70	2.91	3.98	3.18	3.90
70–80	9.84	11.50	5.63	0.66
80–90	4.51	11.51	21.86	7.81
90–100	5.29	6.11	15.22	23.75

more precisely, the corrected resistance $R'(t)$ defined in eq 6, and the fraction of occupied sites by water on the surface. The proportionality coefficient between R' and θ is named α (eq 7).

$$R'(t)_{\%RH,T} = R(t)_T - R(\%RH)_T \quad (6)$$

$$\theta(t) = \alpha * R'(t) \quad (7)$$

An example of the transitory regime of the corrected resistance R' during desorption is given in Figure 6 (black

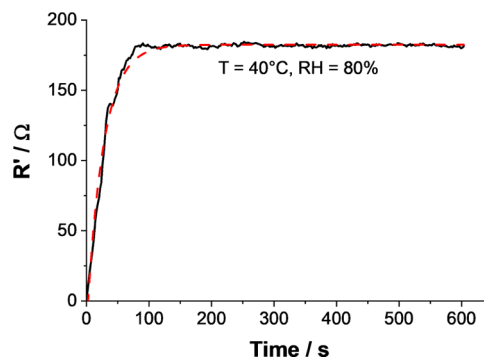


Figure 6. Kinetic transitory regime of the corrected resistance R' between two equilibrium states (black). At $t = 0$ s, the sensor is in equilibrium in an atmosphere with 80% relative humidity and the chamber is flushed with dry air. The temperature is fixed at 40 °C during the entire experiment. The black curve was fitted based on the Langmuir model (red).

curve). At the beginning of the experiment, the sensor is in equilibrium at an atmosphere of RH = 80% and $T = 40$ °C. At $t = 0$ s, the chamber is flushed with dry air, which causes the desorption of water molecules from the sensor surface. The resistance increases to reach a new equilibrium value in dry atmosphere. The corrected resistance R' is modeled (red curve) with an exponential law according to eq 5. The rate constants k_A and k_D were determined from the model parameters to calculate the equilibrium constant K_{ads} . All of the desorption curves at different relative humidities and different temperatures from Figure 4 were modeled by this approach. All values of fitted parameters and rate constants are

available in Tables S1–S8. Notably, the response time of ~ 100 s is on the order of typical carbon-based materials but still rather slow compared to other materials, such as, e.g., Mxenes.^{52–54}

The evolution of the equilibrium constant K_{ads} for different relative humidities at 10, 20, 30, and 40 °C is represented in Figure 7. For all of the tested atmospheric conditions, $K_{\text{ads}} < 1$,

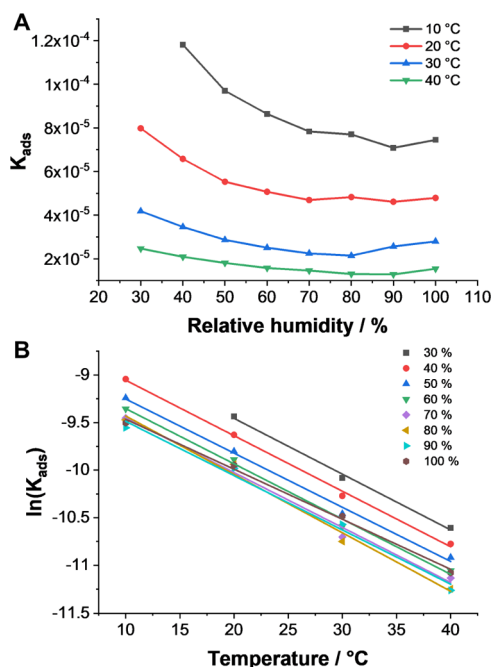


Figure 7. (A) Evolution of equilibrium constants K_{ads} with relative humidity at different temperatures. (B) Plot of the logarithm of K_{ads} as a function of temperature at different relative humidities to determine the standard enthalpy of adsorption $\Delta_{\text{ads}}H$.

explaining why desorption is slower than adsorption (Figure 4, in particular, for 10 and 20 °C). For atmospheres containing more than 70% of relative humidity, the equilibrium constant tends toward a constant value different for every temperature. This evolution suggests that the sensor surface begins to be saturated with H_2O and the adsorption is slowing down. At a constant relative humidity, K_{ads} decreases with temperature. This effect is well known and generally used to clean catalyst surfaces with high-temperature treatments.

Finally, it is possible to determine the standard enthalpy of water adsorption on the sensor surface according to the Van't Hoff equation (eq 8)

$$\frac{d(\ln K_{\text{ads}})}{dT} = \frac{\Delta_{\text{ads}}H^\circ}{RT^2} \quad (8)$$

Figure 7B shows the variation of the logarithm of K_{ads} with temperature at different RH values. In this temperature range, straight lines are observed with the same slope (see Table S9 for details of linear regressions). An average value of the slope is used to determine the standard enthalpy of adsorption $\Delta_{\text{ads}}H$ using eq 8. Thereby, $\Delta_{\text{ads}}H$ was estimated at $-42.6 \text{ kJ}\cdot\text{mol}^{-1}$. The sign of the standard enthalpy is negative because the water adsorption is favored on the sensor, explaining why 20 min of desorption is required at 10 and 20 °C compared to only 10 min of adsorption to reach the equilibrium. This value is in good agreement with those reported in the literature.^{55,56}

CONCLUSIONS

A resistive humidity sensor has been fabricated using carbon laser patterning on a flexible substrate (PET) of our in-house developed carbon precursor ink. After laser irradiation, electronic microscopy (SEM and TEM), vertical scanning interferometry, Raman spectroscopy, and X-ray photoelectron spectroscopy show a porous foam-like morphology consisting of heteroatom-rich turbostratic graphitic carbon. This metal-free porous structure is conductive and shows semiconductor-like behavior with low positive Hall and Seebeck coefficients typically observed for carbon materials. All of these features entail temperature- and environment-dependent resistivity, making laser-patterned carbon suitable as a sensor platform.

A significant change in relative resistance of this small-scale sensor upon changing the relative humidity was measured with a high sensitivity between 1 and $10 \text{ }\Omega\cdot\%\text{RH}^{-1}$ depending on temperature and relative humidity. The sensor is usable under classical atmospheric conditions between 10 and 40 °C and in a broad range of relative humidity from 30 to 100%. Finally, the kinetic transitory regime of water desorption has been studied at different temperatures and relative humidities. The equilibrium between gaseous and adsorbed water molecules is described with a simple Langmuir model, and equilibrium constants were calculated under different atmospheric conditions. The standard enthalpy of adsorption of water on the sensor carbonaceous surface is estimated at $42.6 \text{ kJ}\cdot\text{mol}^{-1}$. Selective incorporation of Schottky junctions into the materials to improve the charge transfer kinetics and reduce the sensor dimensions is currently under investigation.

EXPERIMENTAL SECTION

Chemicals and Substrate. Citric acid (99.5% for analysis) and urea (certified AR for analysis) were obtained from Fisher Scientific GmbH. Ethylene glycol ($\geq 99.7\%$, AnalaR Normapur) was obtained from VWR Chemicals. Polyvinylpyrrolidone (average mol. wt, 10 000) was obtained from Sigma-Aldrich. Melinex sheets (PET substrates, $d = 175 \text{ }\mu\text{m}$) were obtained from Plano GmbH and used as received.

Synthesis of the Carbon Network Forming Agent. Citric acid (2.5 g) and urea (2.5 g) were dissolved in 10 mL of distilled water in a crucible. The water was evaporated under vacuum to obtain a homogeneous mixture of solid citric acid and urea. The crucible was then heated to 300 °C under nitrogen for 2 h (1h30 ramp time to reach 300 °C) to obtain a black solid. This black solid was ground to a fine powder, dispersed in water, and stirred at 95 °C for 4 h. The supernatant was removed by centrifugation. The washing process was repeated four times to fully remove free molecular species. The remaining black solid was dried under vacuum.

Ink and Film Preparation. A 200 $\text{g}\cdot\text{L}^{-1}$ solution of PVP (wt 10 000) in ethylene glycol was prepared. This solution (200 μL) and CAU300 (200 mg) were mixed in a 4 mL vial and stirred for at least 1 h to obtain a homogeneous black slurry. A homogeneous film of this ink was prepared by doctor blading on PET, and the ethylene glycol was evaporated at 80 °C on a hot plate.

Laser Patterning of the Sensor. Laser irradiation was realized with a Trotec Speedy 100 printer equipped with a 60 W CO_2 laser (10.6 μm wavelength). The laser was operated at 1 W and 17.6 $\text{mm}\cdot\text{s}^{-1}$ in a pulsed mode at 1000 Hz. These settings correspond to a fluence of $0.567 \text{ J}\cdot\text{cm}^{-2}$. A typical resistive sensor platform was prepared as five 5 mm long lines separated by 0.1 mm and three concentric circles (0.3, 0.5, and 0.7 mm diameter) at both ends of the lines to ensure electric contact with silver ink (Figure 1A). Combustion analysis of the laser-patterned material was performed by removing the laser-patterned material from the substrate and subsequent washing in basic H_2O .

Surface Area Measurement. The active surface area of the sensor was determined by the methylene blue adsorption method.^{57–59} A laser-patterned carbon film of size $2 \times 1 \text{ cm}^2$ was printed on PET sheets. The laser-patterned films were scratched off and collected, and their masses were determined with a microbalance ($\sim 0.3 \text{ mg}$). The powder was then dispersed in $9.5 \times 10^{-5} \text{ M}$ solutions of methylene blue in polypropylene vials and stirred for 24 h. The solutions were centrifuged, and the amount of adsorbed MB was determined by measuring the absorbance of the supernatant with respect to a reference solution. An area of 1.35 nm^2 per molecule MB is assumed. As a reference, the same mass of activated carbon was used ($1269 \text{ m}^2 \cdot \text{g}^{-1}$).

Humidity Sensing. The sensor was placed in a custom-built chamber with a gas flow inlet (Figure 1E). This chamber was thermalized in an ESPEC SH-641 environmental chamber from ATEC. The humidity flow was controlled by a humidity generator HUMIgen-04 from Dr. Wernecke GmbH. The gas flux was $80 \text{ L} \cdot \text{h}^{-1}$, and the relative humidity was controlled with a precision of $\pm 3\%$.

Electrical characterizations were performed on a Solartron 1287 potentiostat in combination with an SI 1260 impedance unit. The frequency was fixed at 1000 Hz, and the current intensity is 0.05 mA for all measurements.

Instrumental Section. Scanning electron microscopy was performed on a Zeiss LEO 1550-Gemini system (acceleration voltage: 3–10 kV). Transmission electron microscopy was performed using an EM 912 Omega from Zeiss operating at 120 kV. Raman spectra were obtained with a confocal Raman microscope (alpha300, WITec, Germany). The laser ($\lambda = 532 \text{ nm}$) was focused on the samples through a 20x objective. The laser power on the sample was set at 1.0 mW. X-ray diffraction was performed on a Bruker D8 Advance diffractometer in the Bragg-Brentano mode at the Cu $K\alpha$ wavelength. Vertical scanning interferometry was performed with a vertical scanning interferometer smartWLI compact (GBS mbH, Germany) with the software smartVIS3D 2.28 Tango and visualized with MountainsMap 8. Hall measurements were carried out at room temperature in an Accent HL5500PC using a magnetic strength of 0.3 T. The samples were fabricated in a cloverleaf geometry, and the pins contacted the film via indium pads. After checking the ohmic response of the contacts, all of the measurements were done with the current source set for AC operation under vacuum. The entire Hall measurement was conducted five times, and the average value was sent to the result area. The whole procedure was repeated four times. The Seebeck coefficient was determined using a custom-built apparatus designed to implement the method of four coefficients.⁶⁰ The Seebeck voltage is measured at four different temperature gradients, all near $298 \pm 3 \text{ K}$. The thermopower is determined via linear fit on a plot of Seebeck voltage vs. temperature difference and is corrected for the built-in thermopower associated with the indium pads and copper blocks. The reported value is the average of four measurements. X-ray photoelectron spectra were recorded using a Kratos Axis Ultra DLD spectrometer equipped with a mono-spectra calibrated using carbon tape (Ted Pella) with a chromatic Al $K\alpha$ X-ray source ($h\nu 1/4 1486.6 \text{ eV}$). The high-resolution C_{1s} binding energy is 284.6 eV . Raw data were processed using CasaXPS software (version 2.3.23). C 1s spectra were fit using Gaussian–Lorentzian line shapes for all spectral components.

■ ASSOCIATED CONTENT

SI Supporting Information

The Supporting Information is available free of charge at <https://pubs.acs.org/doi/10.1021/acsaelm.0c00942>.

Materials characterization and data analysis (PDF)

■ AUTHOR INFORMATION

Corresponding Author

Volker Strauss – Department of Colloid Chemistry, Max-Planck-Institute of Colloids and Interfaces, 14476 Potsdam,

Germany; orcid.org/0000-0003-2619-6841;

Email: volker.strauss@mpikg.mpg.de

Authors

Simon Delacroix – Department of Colloid Chemistry, Max-Planck-Institute of Colloids and Interfaces, 14476 Potsdam, Germany

Anna Zieleniewska – National Renewable Energy Laboratory, Golden, Colorado 80401, United States; orcid.org/0000-0001-9987-7520

Andrew J. Ferguson – National Renewable Energy Laboratory, Golden, Colorado 80401, United States

Jeffrey L. Blackburn – National Renewable Energy Laboratory, Golden, Colorado 80401, United States; orcid.org/0000-0002-9237-5891

Sebastian Ronneberger – Department of Biomolecular Systems, Max-Planck-Institute of Colloids and Interfaces, 14476 Potsdam, Germany

Felix F. Loeffler – Department of Biomolecular Systems, Max-Planck-Institute of Colloids and Interfaces, 14476 Potsdam, Germany; orcid.org/0000-0002-8227-2522

Complete contact information is available at: <https://pubs.acs.org/doi/10.1021/acsaelm.0c00942>

Notes

The authors declare no competing financial interest.

■ ACKNOWLEDGMENTS

The authors are grateful for financial support from the Max Planck Society, the Fonds der Chemischen Industrie, the German Federal Ministry of Education and Research (13XP5050A), and the Max-Planck-Fraunhofer cooperation (Glyco3Display). They thank Klaus Bienert for the help provided for the use of the humidity generator, the technicians of the Colloid Chemistry department for their assistance with materials characterizations, and Markus Antonietti for continuous educational support. This work was authored, in part, by the National Renewable Energy Laboratory, operated by Alliance for Sustainable Energy, LLC, for the U.S. Department of Energy (DOE) under Contract No. DE-AC36-08GO28308. A.Z., A.J.F., and J.L.B. gratefully acknowledge funding provided by the Solar Photochemistry Program of the Chemical Sciences, Geosciences, & Biosciences (CSGB) Division at the U.S. DOE Office of Science: Basic Energy Sciences. The views expressed in the article do not necessarily represent the views of the DOE or the U.S. Government.

■ REFERENCES

- (1) Wongkaew, N.; Simsek, M.; Griesche, C.; Baeumner, A. J. Functional Nanomaterials and Nanostructures Enhancing Electrochemical Biosensors and Lab-on-a-Chip Performances: Recent Progress, Applications, and Future Perspective. *Chem. Rev.* **2019**, *119*, 120–194.
- (2) Tripathi, K. M.; Kim, T. Y.; Losic, D.; Tung, T. T. Recent Advances in Engineered Graphene and Composites for Detection of Volatile Organic Compounds (VOCs) and Non-Invasive Diseases Diagnosis. *Carbon* **2016**, *110*, 97–129.
- (3) Krishnan, S. K.; Singh, E.; Singh, P.; Meyyappan, M.; Nalwa, H. S. A Review on Graphene-Based Nanocomposites for Electrochemical and Fluorescent Biosensors. *RSC Adv.* **2019**, *9*, 8778–8781.
- (4) Li, H.; Shi, W.; Song, J.; Jang, H. J.; Dailey, J.; Yu, J.; Katz, H. E. Chemical and Biomolecule Sensing with Organic Field-Effect Transistors. *Chem. Rev.* **2019**, *119*, 3–35.

- (5) Nathan, A.; Ahnood, A.; Cole, M. T.; Lee, S.; Suzuki, Y.; Hiralal, P.; Bonaccorso, F.; Hasan, T.; Garcia-Gancedo, L.; Dyadyusha, A.; et al. Flexible Electronics: The next Ubiquitous Platform. *Proc. IEEE* **2012**, *100*, 1486–1517.
- (6) Rittersma, Z. M. Recent Achievements in Miniaturised Humidity Sensors—a Review of Transduction Techniques. *Sens. Actuators, A* **2002**, *96*, 196–210.
- (7) Tulliani, J.-M.; Inserra, B.; Ziegler, D. Carbon-Based Materials for Humidity Sensing: A Short Review. *Micromachines* **2019**, *10*, 232.
- (8) Lee, J.; Cho, D.; Jeong, Y. A Resistive-Type Sensor Based on Flexible Multi-Walled Carbon Nanotubes and Polyacrylic Acid Composite Films. *Solid-State Electron.* **2013**, *87*, 80–84.
- (9) Yu, Y.; Zhang, Y.; Jin, L.; Chen, Z.; Li, Y.; Li, Q.; Cao, M.; Che, Y.; Yang, J.; Yao, J. A Fast Response–Recovery 3D Graphene Foam Humidity Sensor for User Interaction. *Sensors* **2018**, *18*, 4337.
- (10) Schedin, F.; Geim, A. K.; Morozov, S. V.; Hill, E. W.; Blake, P.; Katsnelson, M. I.; Novoselov, K. S. Detection of Individual Gas Molecules Adsorbed on Graphene. *Nat. Mater.* **2007**, *6*, 652–655.
- (11) Meng, Z.; Stolz, R. M.; Mendecki, L.; Mirica, K. A. Electrically-Transduced Chemical Sensors Based on Two-Dimensional Nanomaterials. *Chem. Rev.* **2019**, *119*, 478–598.
- (12) Ziegler, D.; Palmero, P.; Giorcelli, M.; Tagliaferro, A.; Tulliani, J.-M. Biochars as Innovative Humidity Sensing Materials. *Chemosensors* **2017**, *5*, 35.
- (13) Moon, H. G.; Jung, Y.; Shin, B.; Song, Y. G.; Kim, J. H.; Lee, T.; Lee, S.; Jun, S. C.; Kaner, R. B.; Kang, C.; et al. On-Chip Chemiresistive Sensor Array for On-Road NO_x Monitoring with Quantification. *Adv. Sci.* **2020**, *7*, No. 2002014.
- (14) Wang, F.; Swager, T. M. Diverse Chemiresistors Based upon Covalently Modified Multiwalled Carbon Nanotubes. *J. Am. Chem. Soc.* **2011**, *133*, 11181–11193.
- (15) Ye, R.; James, D. K.; Tour, J. M. Laser-Induced Graphene: From Discovery to Translation. *Adv. Mater.* **2019**, *31*, No. 1803621.
- (16) Han, T.; Nag, A.; Afsarimaneh, N.; Mukhopadhyay, S. C.; Kundu, S.; Xu, Y. Laser-Assisted Printed Flexible Sensors: A Review. *Sensors* **2019**, *19*, 1462.
- (17) Inagaki, M.; Qiu, J.; Guo, Q. Carbon Foam: Preparation and Application. *Carbon* **2015**, *87*, 128–152.
- (18) Strong, V.; Dubin, S.; El-Kady, M. F.; Lech, A.; Wang, Y.; Weiller, B. H.; Kaner, R. B. Patterning and Electronic Tuning of Laser Scribed Graphene for Flexible All-Carbon Devices. *ACS Nano* **2012**, *6*, 1395–1403.
- (19) Lin, J.; Peng, Z.; Liu, Y.; Ruiz-Zepeda, F.; Ye, R.; Samuel, E. L. G.; Yacamán, M. J.; Yakobson, B. I.; Tour, J. M. Laser-Induced Porous Graphene Films from Commercial Polymers. *Nat. Commun.* **2014**, *5*, No. 5714.
- (20) Ye, R.; James, D. K.; Tour, J. M. Laser-Induced Graphene. *Acc. Chem. Res.* **2018**, *51*, 1609–1620.
- (21) Wang, Y.; Wang, Y.; Zhang, P.; Liu, F.; Luo, S. Laser-Induced Freestanding Graphene Papers: A New Route of Scalable Fabrication with Tunable Morphologies and Properties for Multifunctional Devices and Structures. *Small* **2018**, *14*, 1–9.
- (22) Wang, F.; Wang, K.; Zheng, B.; Dong, X.; Mei, X.; Lv, J.; Duan, W.; Wang, W. Laser-Induced Graphene: Preparation, Functionalization and Applications. *Mater. Technol.* **2018**, *33*, 340–356.
- (23) Sopronyi, M.; Sima, F.; Vault, C.; Delmotte, L.; Bahouka, A.; Ghimbeu, C. M. Direct Synthesis of Graphitic Mesoporous Carbon from Green Phenolic Resins Exposed to Subsequent UV and IR Laser Irradiations. *Sci. Rep.* **2016**, *6*, No. 39617.
- (24) de Araujo, W. R.; Frasson, C. M. R.; Ameku, W. A.; Silva, J. R.; Angnes, L.; Paixão, T. R. L. C. Single-Step Reagentless Laser Scribing Fabrication of Electrochemical Paper-Based Analytical Devices. *Angew. Chem., Int. Ed.* **2017**, *56*, 15113–15117.
- (25) Ye, R.; Chyan, Y.; Zhang, J.; Li, Y.; Han, X.; Kittrell, C.; Tour, J. M. Laser-Induced Graphene Formation on Wood. *Adv. Mater.* **2017**, *29*, No. 1702211.
- (26) Chyan, Y.; Ye, R.; Li, Y.; Singh, S. P.; Arnusch, C. J.; Tour, J. M. Laser-Induced Graphene by Multiple Lasing: Toward Electronics on Cloth, Paper, and Food. *ACS Nano* **2018**, *12*, 2176–2183.
- (27) Mahmood, F.; Zhang, C.; Xie, Y.; Stalla, D.; Lin, J.; Wan, C. Transforming Lignin into Porous Graphene via Direct Laser Writing for Solid-State Supercapacitors. *RSC Adv.* **2019**, *9*, 22713–22720.
- (28) Strauss, V.; Anderson, M.; Turner, C. L.; Kaner, R. B. Fast Response Electrochemical Capacitor Electrodes Created by Laser-Reduction of Carbon Nanodots. *Mater. Today Energy* **2019**, *11*, 114–119.
- (29) Strauss, V.; Marsh, K.; Kowal, M. D.; El-Kady, M.; Kaner, R. B. A Simple Route to Porous Graphene from Carbon Nanodots for Supercapacitor Applications. *Adv. Mater.* **2018**, *30*, No. 1704449.
- (30) Strauss, V.; Anderson, M.; Wang, C.; Borenstein, A.; Kaner, R. B. Carbon Nanodots as Feedstock for a Uniform Hematite-Graphene Nanocomposite. *Small* **2018**, *14*, No. 1803656.
- (31) Strauss, V.; Wang, H.; Delacroix, S.; Ledendecker, M.; Wessig, P. Carbon Nanodots Revised: The Thermal Citric Acid/Urea Reaction. *Chem. Sci.* **2020**, *11* (31), 8256–8266.
- (32) Delacroix, S.; Wang, H.; Heil, T.; Strauss, V. Laser-Induced Carbonization of Natural Organic Precursors for Flexible Electronics. *Adv. Electron. Mater.* **2020**, *6*, No. 2000463.
- (33) Malard, L. M.; Pimenta, M. A.; Dresselhaus, G.; Dresselhaus, M. S. Raman Spectroscopy in Graphene. *Phys. Rep.* **2009**, *473*, 51–87.
- (34) Lazar, P.; Mach, R.; Otyepka, M. Spectroscopic Fingerprints of Graphitic, Pyrrolic, Pyridinic, and Chemisorbed Nitrogen in N-Doped Graphene. *J. Phys. Chem. C* **2019**, *123*, 10695–10702.
- (35) Yamada, Y.; Kim, J.; Matsuo, S.; Sato, S. Nitrogen-Containing Graphene Analyzed by X-Ray Photoelectron Spectroscopy. *Carbon* **2014**, *70*, 59–74.
- (36) Esquinazi, P.; Krüger, J.; Barzola-Quiquia, J.; Schönemann, R.; Herrmannsdörfer, T.; García, N. On the Low-Field Hall Coefficient of Graphite. *AIP Adv.* **2014**, *4*, No. 117121.
- (37) Tu, N. D. K.; Lim, J. A.; Kim, H. A Mechanistic Study on the Carrier Properties of Nitrogen-Doped Graphene Derivatives Using Thermoelectric Effect. *Carbon* **2017**, *117*, 447–453.
- (38) Jin, Z.; Yao, J.; Kittrell, C.; Tour, J. M. Large-Scale Growth and Characterizations of Nitrogen-Doped Monolayer Graphene Sheets. *ACS Nano* **2011**, *5*, 4112–4117.
- (39) Ambrosi, A.; Chua, C. K.; Latiff, N. M.; Loo, A. H.; Wong, C. H. A.; Eng, A. Y. S.; Bonanni, A.; Pummer, M. Graphene and Its Electrochemistry – an Update. *Chem. Soc. Rev.* **2016**, *45*, 2458–2493.
- (40) Itkis, M. E.; Pekker, A.; Tian, X.; Bekyarova, E.; Haddon, R. C. Networks of Semiconducting SWNTs: Contribution of Midgap Electronic States to the Electrical Transport. *Acc. Chem. Res.* **2015**, *48*, 2270–2279.
- (41) Blackburn, J. L.; Kang, S. D.; Roos, M. J.; Norton-Baker, B.; Miller, E. M.; Ferguson, A. J. Intrinsic and Extrinsic Limited Thermoelectric Transport within Semiconducting Single-Walled Carbon Nanotube Networks. *Adv. Electron. Mater.* **2019**, *5*, No. 1800910.
- (42) Kaiser, A. B.; Skákalová, V. Electronic Conduction in Polymers, Carbon Nanotubes and Graphene. *Chem. Soc. Rev.* **2011**, *40*, 3786.
- (43) Zahab, A.; Spina, L.; Poncharal, P.; Marlière, C. Water-Vapor Effect on the Electrical Conductivity of a Single-Walled Carbon Nanotube Mat. *Phys. Rev. B* **2000**, *62*, 10000–10003.
- (44) Afify, A. S.; Ahmad, S.; Khushnood, R. A.; Jagdale, P.; Tulliani, J. M. Elaboration and Characterization of Novel Humidity Sensor Based on Micro-Carbonized Bamboo Particles. *Sens. Actuators, B* **2017**, *239*, 1251–1256.
- (45) Zhang, X.; Ming, H.; Liu, R.; Han, X.; Kang, Z.; Liu, Y.; Zhang, Y. Highly Sensitive Humidity Sensing Properties of Carbon Quantum Dots Films. *Mater. Res. Bull.* **2013**, *48*, 790–794.
- (46) Cunha, B. B.; Greenshields, M. W. C. C.; Mamo, M. A.; Coville, N. J.; Hümmelgen, I. A. A Surfactant Dispersed N-Doped Carbon Sphere-Poly(Vinyl Alcohol) Composite as Relative Humidity Sensor. *J. Mater. Sci. Mater. Electron.* **2015**, *26*, 4198–4201.
- (47) Guo, L.; Jiang, H. B.; Shao, R. Q.; Zhang, Y. L.; Xie, S. Y.; Wang, J. N.; Li, X.; Bin, J.; Jiang, F.; Chen, Q. D.; Zhang, T.; et al. Two-Beam-Laser Interference Mediated Reduction, Patterning and Nanostructuring of Graphene Oxide for the Production of a Flexible Humidity Sensing Device. *Carbon* **2012**, *50*, 1667–1673.

(48) Yao, Y.; Chen, X.; Zhu, J.; Zeng, B.; Wu, Z.; Li, X. The Effect of Ambient Humidity on the Electrical Properties of Graphene Oxide Films. *Nanoscale Res. Lett.* **2012**, *7*, No. 363.

(49) Liu, L.; Tan, S. J.; Horikawa, T.; Do, D. D.; Nicholson, D.; Liu, J. Water Adsorption on Carbon - A Review. *Adv. Colloid Interface Sci.* **2017**, *250*, 64–78.

(50) At 10 °C, 30% of Relative Humidity Is Not Accessible with the Environmental Chamber.

(51) Lv, C.; Hu, C.; Luo, J.; Liu, S.; Qiao, Y.; Zhang, Z.; Song, J.; Shi, Y.; Cai, J.; Watanabe, A. Recent Advances in Graphene-Based Humidity Sensors. *Nanomaterials* **2019**, *9*, No. 422.

(52) An, H.; Habib, T.; Shah, S.; Gao, H.; Patel, A.; Echols, I.; Zhao, X.; Radovic, M.; Green, M. J.; Lutkenhaus, J. L. Water Sorption in MXene/Polyelectrolyte Multilayers for Ultrafast Humidity Sensing. *ACS Appl. Nano Mater.* **2019**, *2*, 948–955.

(53) Pang, Y.; Jian, J.; Tu, T.; Yang, Z.; Ling, J.; Li, Y.; Wang, X.; Qiao, Y.; Tian, H.; Yang, Y.; et al. Wearable Humidity Sensor Based on Porous Graphene Network for Respiration Monitoring. *Biosens. Bioelectron.* **2018**, *116*, 123–129.

(54) Zhou, G.; Byun, J.-H.; Oh, Y.; Jung, B.-M.; Cha, H.-J.; Seong, D.-G.; Um, M.-K.; Hyun, S.; Chou, T.-W. Highly Sensitive Wearable Textile-Based Humidity Sensor Made of High-Strength, Single-Walled Carbon Nanotube/Poly(Vinyl Alcohol) Filaments. *ACS Appl. Mater. Interfaces* **2017**, *9*, 4788–4797.

(55) Picaud, S.; Collignon, B.; Hoang, P. N. M.; Rayez, J. C. Adsorption of Water Molecules on Partially Oxidized Graphite Surfaces: A Molecular Dynamics Study of the Competition between OH and COOH Sites. *Phys. Chem. Chem. Phys.* **2008**, *10*, 6998–7009.

(56) Tarasevich, Y. I.; Aksenenko, E. V. Interaction of Water, Methanol and Benzene Molecules with Hydrophilic Centres at a Partially Oxidized Model Graphite Surface. *Colloids Surf., A* **2003**, *215*, 285–291.

(57) Naeem, S.; Baheti, V.; Wiener, J.; Marek, J. Removal of Methylene Blue from Aqueous Media Using Activated Carbon Web. *J. Text. Inst.* **2017**, *108*, 803–811.

(58) Till, P.; Brindley, G. W. Methylene Blue Absorption by Clay Minerals. In *Determination of Surface Areas and Cation Exchange Capacities (Clay-Organic Studies XVIII)*; Pergamon Press: 1970; Vol. 18.

(59) Rafatullah, M.; Sulaiman, O.; Hashim, R.; Ahmad, A. Adsorption of Methylene Blue on Low-Cost Adsorbents: A Review. *J. Hazard. Mater.* **2010**, *177*, 70–80.

(60) Young, D. L.; Coutts, T. J.; Kaydanov, V. I.; Gilmore, A. S.; Mulligan, W. P. Direct Measurement of Density-of-States Effective Mass and Scattering Parameter in Transparent Conducting Oxides Using Second-Order Transport Phenomena. *J. Vac. Sci. Technol., A* **2000**, *18*, 2978–2985.

Supporting Information to

Using Carbon Laser-Patterning to Produce Flexible, Metal-Free Humidity Sensors

Simon Delacroix¹, Anna Zieleniewska², Andrew J. Ferguson², Jeffrey L. Blackburn²,
Sebastian Ronneberger³, Felix F. Loeffler³, Volker Strauss^{1,*}

¹ Department of Colloid Chemistry, Max-Planck-Institute of Colloids and Interfaces, Am Mühlenberg 1, 14476 Potsdam, Germany

² National Renewable Energy Laboratory, Golden Colorado, 80401, USA

³ Department of Biomolecular Systems, Max-Planck-Institute of Colloids and Interfaces, Am Mühlenberg 1, 14476 Potsdam, Germany

* volker.strauss@mpikg.mpg.de

X-ray diffraction of the precursor	S2
Raman spectroscopy of LP-carbon	S2
Vertical scanning interferometry of the sensor platform	S3
X-ray photoelectron spectroscopy	S3
Electronic characterization of the sensor platform	S4
Modeling of H ₂ O adsorption	S5

X-ray diffraction of the precursor

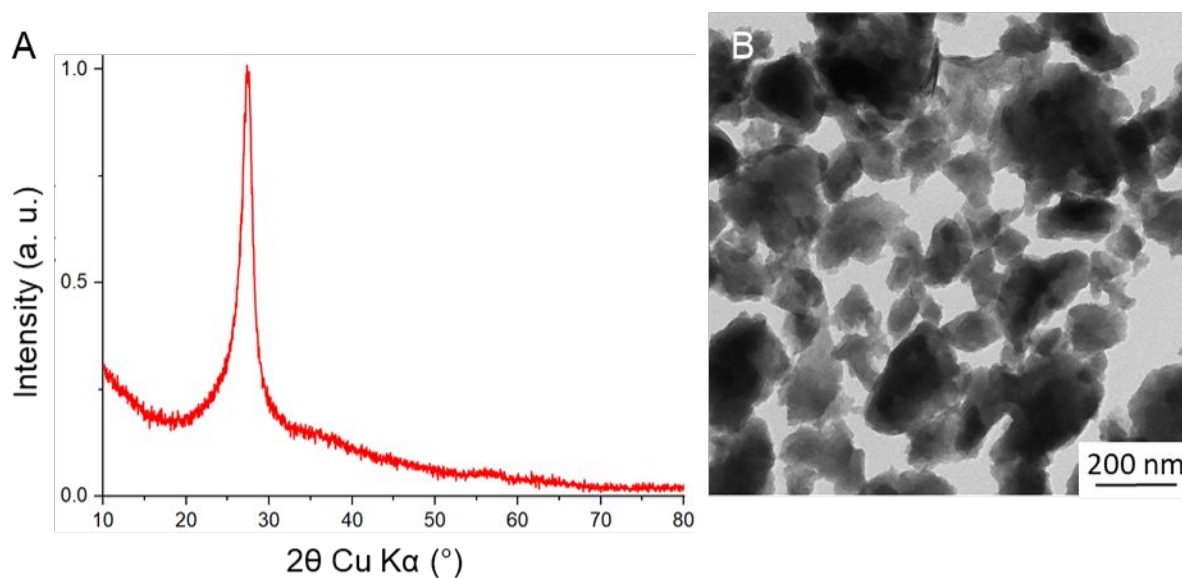


Figure S1. (A) X-ray diffraction pattern of CAU300; (B) Transmission electron micrograph of CAU300.

Raman spectroscopy of LP-carbon

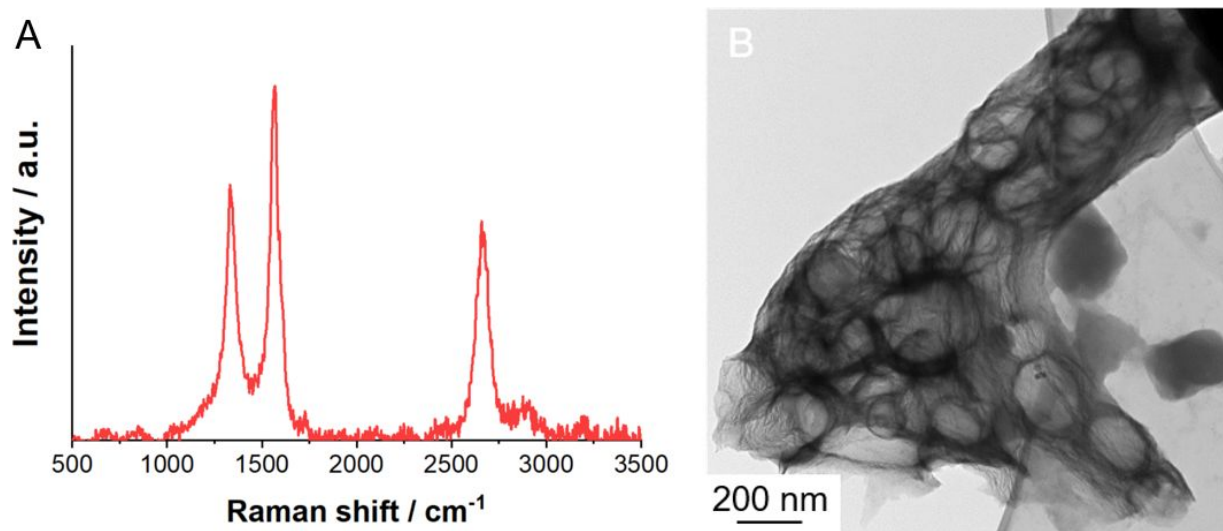


Figure S2. (A) Raman spectrum of the sensor material after laser treatment. (B) Transmission electron micrograph of a fragment of the sensor material.

Vertical scanning interferometry of the sensor platform

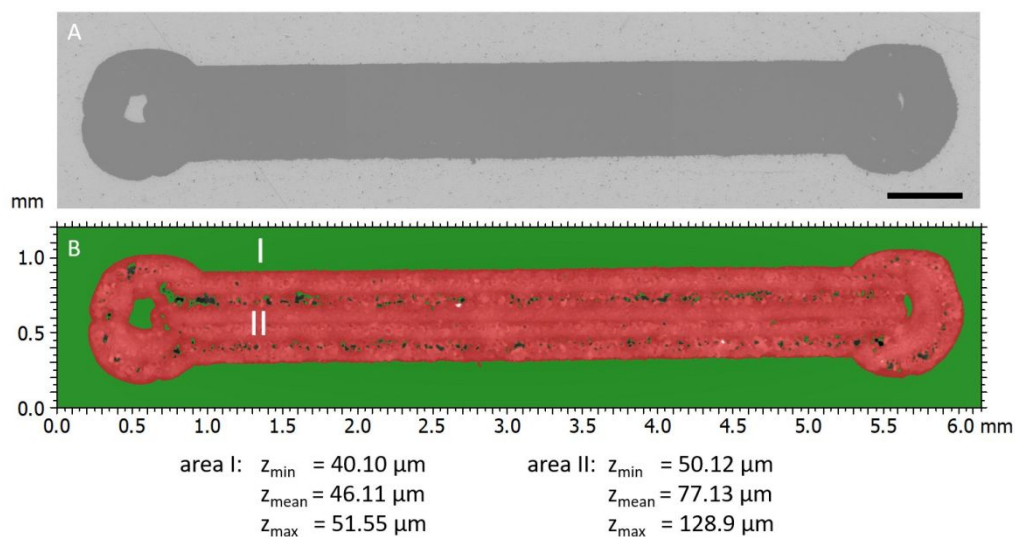


Figure S3. (A) Microscope image of the sensor platform. Scale bar: 500 μm . (B) Vertical scanning interferometry measurement of the sensor array resulting in a mean height of 31 μm .

X-ray photoelectron spectroscopy

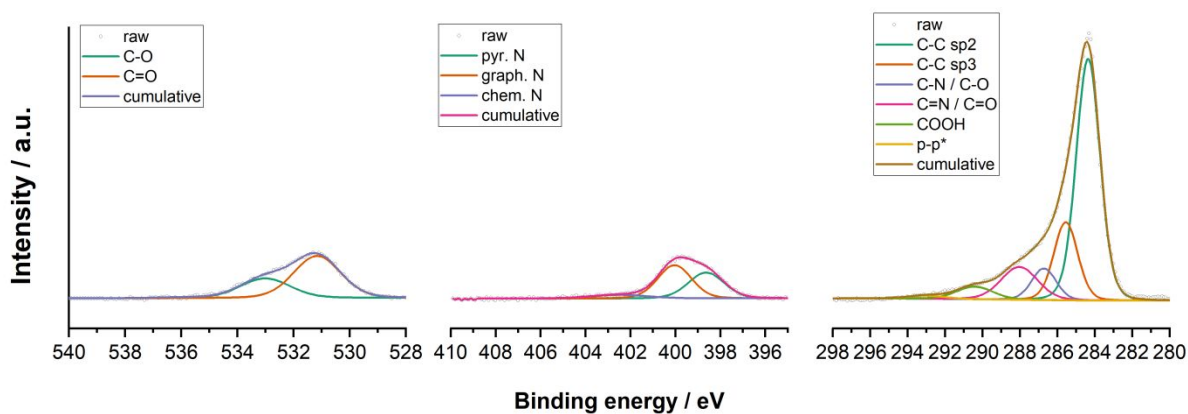


Figure S4. Powder X-ray photoelectron analysis of the laser-patterned carbon (LP-carbon) with focus on the C_{1s} , N_{1s} , and O_{1s} regions.

Electronic characterization of the sensor platform

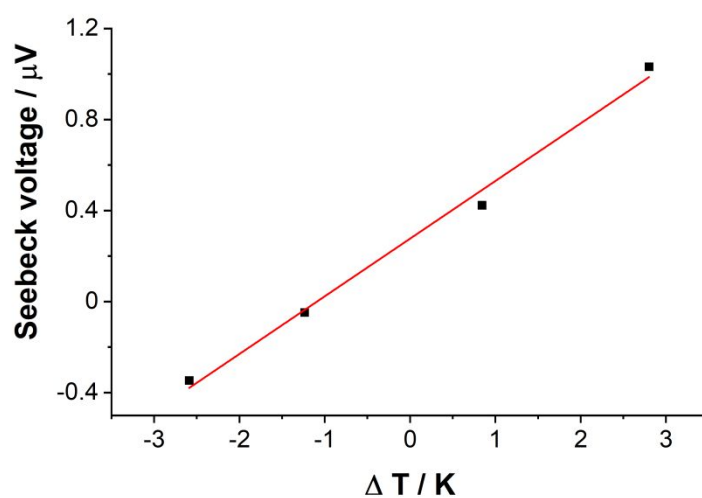


Figure S5. Seebeck voltage as a function of temperature difference of a laser-patterned carbon film.

Modeling of H₂O adsorption

Table S1. Parameters calculated from modeling R' during the transitory regime of desorption at 10 °C between different relative humidity and a dry atmosphere.

$R'(t) = A * e^{-B*t} + C$				
%RH	A	B	C	r ²
40	-148.34954	-0.00716	139.48763	0.99017
50	-123.74513	-0.00404	141.29264	0.98403
60	-125.96949	-0.0037	149.70898	0.97829
70	-124.18883	-0.00324	157.09075	0.97362
80	-120.29287	-0.00392	172.89428	0.93777
90	-141.01826	-0.00566	179.06018	0.91083
100	-148.87766	-0.00603	205.48543	0.89488

Table S2. Rates constants of adsorption desorption, proportionality constant α between θ and R' , constant M and equilibrium constant K calculated from the fit parameters at 10 °C.

%RH	k_A	k_D	α	M	K
40	-7.99458E-07	- 0.006767249	-2.81567E-06	0.0004177	0.000118136
50	-3.69939E-07	- 0.003812824	-1.60784E-06	0.000199	9.70248E-05
60	-3.00544E-07	- 0.003478527	-1.47936E-06	0.0001864	8.63998E-05
70	-2.37884E-07	- 0.003035485	-1.30189E-06	0.0001617	7.83678E-05
80	-2.80635E-07	- 0.003644264	-1.59482E-06	0.0001918	7.70073E-05
90	-3.71964E-07	- 0.005248845	-2.29618E-06	0.0003238	7.08659E-05
100	-4.11692E-07	- 0.005524369	-2.46067E-06	0.0003663	7.45228E-05

Table S3. Parameters calculated from modeling of the transitory regime of desorption at 20 °C between different relative humidity and a dry atmosphere.

$R'(t) = A * e^{-B*t} + C$				
%RH	A	B	C	r ²
30	-140.71304	-0.00781	139.81304	0.94573
40	-153.27996	-0.00636	154.80686	0.89869
50	-158.31436	-0.00659	161.74126	0.93044
60	-172.74945	-0.00732	173.15715	0.94953
70	-183.34934	-0.00781	184.54156	0.9457
80	-215.60001	-0.00909	216.28461	0.87776
90	-236.49388	-0.01155	234.98618	0.88832
100	-271.30556	-0.01111	269.77476	0.83638

Table S4. Rates constants of adsorption desorption, proportionality constant α between θ and R' , constant M and equilibrium constant K calculated from the fit parameters at 20 °C.

%RH	k_A	k_D	α	M	K
30	-6.07831E-07	- 0.007383447	-3.05088E-06	0.0004293	8.23235E-05
40	-4.11621E-07	- 0.005974853	-2.48792E-06	0.0003813	6.88922E-05
50	-3.57323E-07	- 0.006172073	-2.58392E-06	0.0004091	5.78935E-05
60	-3.5405E-07	- 0.006823082	-2.86975E-06	0.0004957	5.189E-05
70	-3.45211E-07	- 0.007244736	-3.06307E-06	0.0005616	4.76499E-05
80	-4.11491E-07	-0.00831995	-3.56036E-06	0.0007676	4.94583E-05
90	-5.06115E-07	- 0.010484482	-4.53439E-06	0.0010724	4.82728E-05
100	-5.01024E-07	-0.009938	-4.34436E-06	0.0011787	5.04149E-05

Table S5. Parameters calculated from modeling of the transitory regime of desorption at 30 °C between different relative humidity and a dry atmosphere.

$R'(t) = A * e^{-B*t} + C$				
%RH	A	B	C	r ²
30	-145.89515	-0.0296	129.61909	0.97421
40	-156.04606	-0.02288	142.22144	0.98291
50	-156.96848	-0.02139	146.71407	0.98713
60	-127.42247	-0.02176	151.51671	0.97869
70	-166.87886	-0.01919	160.03143	0.98468
80	-171.48205	-0.02009	173.03735	0.98769
90	-226.81205	-0.02455	227.83071	0.99513
100	-276.35348	-0.02612	271.67578	0.98879

Table S6. Rates constants of adsorption desorption, proportionality constant α between θ and R' , constant M and equilibrium constant K calculated from the fit parameters at 30 °C.

%RH	k _A	k _D	α	M	K
30	-1.17576E-06	- 0.028102073	-1.15564E-05	0.001686	4.18389E-05
40	-7.48433E-07	- 0.021608655	-8.93919E-06	0.0013949	3.46358E-05
50	-5.78374E-07	- 0.020161913	-8.37061E-06	0.0013139	2.86864E-05

60	-5.13116E-07	-	-8.62893E-06	0.0010995	2.50881E-05
70	-4.04335E-07	-	-7.51077E-06	0.0012534	2.2478E-05
80	-4.01668E-07	-	-7.88619E-06	0.0013523	2.14504E-05
90	-5.74098E-07	-	-9.63091E-06	0.0021844	2.56801E-05
100	-6.53186E-07	-0.02334612	-1.02103E-05	0.0028216	2.79784E-05

Table S7. Parameters calculated from modeling of the transitory regime of desorption at 40 °C between different relative humidity and a dry atmosphere.

$R'(t) = A * e^{-B*t} + C$				
%RH	A	B	C	r ²
30	-159.44449	-0.0624	132.10577	0.96302
40	-157.42228	-0.06446	147.09156	0.97256
50	-178.13286	-0.05076	159.10035	0.96972
60	-187.68674	-0.04635	166.09373	0.97577
70	-200.40185	-0.04151	178.82795	0.98003
80	-199.73627	-0.03771	182.48325	0.98758
90	-228.81662	-0.03688	201.83842	0.98563
100	-259.64438	-0.03724	260.07097	0.99623

Table S8. Rates constants of adsorption desorption, proportionality constant α between θ and R' , constant M and equilibrium constant K calculated from the fit parameters at 40 °C.

%RH	k_A	k_D	α	M	K
30	-1.46187E-06	- 0.059161484	-2.45146E-05	0.0039087	2.47098E-05
40	-1.26949E-06	- 0.060710213	-2.54929E-05	0.0040131	2.09107E-05
50	-8.62005E-07	- 0.047577291	-2.00044E-05	0.0035634	1.8118E-05
60	-6.83666E-07	- 0.043320908	-1.82372E-05	0.0034229	1.57814E-05
70	-5.64166E-07	- 0.038593769	-1.63075E-05	0.003268	1.46181E-05
80	-4.57291E-07	- 0.035008532	-1.48039E-05	0.0029569	1.30623E-05
90	-4.36917E-07	- 0.033976258	-1.43865E-05	0.0032919	1.28595E-05
100	-5.16366E-07	- 0.033426931	-1.46616E-05	0.0038068	1.54476E-05

Table S9. Slopes coefficient of determination of the linear regression of the straight lines from Figure 7B.

%RH	Slope	r²
30	-0.05863	0.99656
40	-0.05837	0.99795
50	-0.05691	0.99576
60	-0.05804	0.9943
70	-0.05773	0.99067
80	-0.06134	0.98845
90	-0.05706	0.98944
100	-0.05259	0.99577

Table S10. Standard enthalpy of adsorption of water on the surface sensor at different temperatures.

T (K)	$\Delta_{\text{ads}}H^\circ$ (J·mol⁻¹)
283.15	-38383.4
293.15	-41142.4
303.15	-43997.2
313.15	-46947.8

Table S11. Water pressure in the sensor chamber under different relative humidity and temperature conditions.

$P_{\text{H}_2\text{O}}$ (Pa)	10 °C	20 °C	30 °C	40 °C
10%RH	122.818	233.921	424.669	738.443
20%RH	245.636	467.842	849.338	1476.886
30%RH	368.454	701.763	1274.007	2215.329
40%RH	491.272	935.684	1698.676	2953.772
50%RH	614.09	1169.605	2123.345	3692.215
60%RH	736.908	1403.526	2548.014	4430.658
70%RH	859.726	1637.447	2972.683	5169.101
80%RH	982.544	1871.368	3397.352	5907.544
90%RH	1105.362	2105.289	3822.021	6645.987
100%RH	1228.18	2339.21	4246.69	7384.43

In Situ Synthesis of Molybdenum Carbide Nanoparticles Incorporated into Laser-Patterned Nitrogen-Doped Carbon for Room Temperature VOC Sensing

Huize Wang, Simon Delacroix, Anna Zieleniewska, Jing Hou, Nadezda V. Tarakina, Daniel Cruz, Iver Lauermann, Andrew J. Ferguson, Jeffrey L. Blackburn, and Volker Strauss*


Carbon laser-patterning (CLaP) is emerging as a new tool for the precise and selective synthesis of functional carbon-based materials for on-chip applications. The aim of this work is to demonstrate the applicability of laser-patterned nitrogen-doped carbon (LP-NC) for resistive gas-sensing applications. Films of pre-carbonized organic nanoparticles on polyethyleneterephthalate are carbonized with a CO₂-laser. Upon laser-irradiation a compositional and morphological gradient in the films is generated with a carbon content of 92% near the top surface. The specific surface areas of the LP-NC are increased by introducing sodium iodide (NaI) as a porogen. Electronic conductivity and surface area measurements corroborate the deeper penetration of the laser-energy into the film in the presence of NaI. Furthermore, impregnation of LP-NC with MoC_{1-x} (<10 nm) nanoparticles is achieved by addition of ammonium heptamolybdate into the precursor film. The resulting doping-sensitive nano-grain boundaries between p-type carbon and metallic MoC_{1-x} lead to an improvement of the volatile organic compounds sensing response of $\Delta R/R_0 = -3.7\%$ or -0.8% for 1250 ppm acetone or 900 ppm toluene at room temperature, respectively, which is competitive with carbon-based sensor materials. Further advances in sensitivity and in situ functionalization are expected to make CLaP a useful method for printing selective sensor arrays.

1. Introduction

Chemical sensors are gaining importance in everyday life for the detection and monitoring of pollutants, emissions, or sensing of biomarkers.^[1] But also in view of the advent of future technologies in bionics and robotics we observe a rising demand for sophisticated chemical sensing architectures.^[2] For practical applications and everyday use, ideal sensor materials are small, flexible, non-toxic, inexpensive, simple to produce, biodegradable, and operable at room temperature.^[3] However, producing efficient sensors for the selective recognition of gaseous or liquid analytes is often a challenge because existing technologies and materials are complex and expensive.^[4] Therefore, new production techniques and/or new materials and composites fulfilling all those requirements are needed.^[5] Chemical sensor arrays are one possible solution for achieving high selectivity in analyte mixtures,^[6] where the array selectivity is realized by pattern recognition using groups of individual sensors.^[7]

H. Wang, S. Delacroix, J. Hou, N. V. Tarakina, V. Strauss
Max Planck Institute of Colloids and Interfaces
Am Mühlenberg 1, 14476 Potsdam, Germany
E-mail: volker.strauss@mpikg.mpg.de

S. Delacroix
LPICM
CNRS UMR 7647
Ecole polytechnique
Institut Polytechnique de Paris
Palaiseau 91128, France

 The ORCID identification number(s) for the author(s) of this article can be found under <https://doi.org/10.1002/adfm.202104061>.

© 2021 The Authors. Advanced Functional Materials published by Wiley-VCH GmbH. This is an open access article under the terms of the Creative Commons Attribution License, which permits use, distribution and reproduction in any medium, provided the original work is properly cited.

DOI: 10.1002/adfm.202104061

A. Zieleniewska, A. J. Ferguson, J. L. Blackburn
National Renewable Energy Laboratory
Golden, CO 80401, USA

D. Cruz
Department of Inorganic Chemistry
Fritz-Haber-Institut der Max-Planck-Gesellschaft
Faradayweg 4-6, 14195 Berlin, Germany

D. Cruz
Department of Heterogeneous Reactions
Max Planck Institute for Chemical Energy Conversion
Stiftstraße 34-36, 45470 Mülheim an der Ruhr, Germany

I. Lauermann
PVcomB/Helmholtz-Zentrum Berlin für Materialien und Energie GmbH
Schwarzschildstraße 3, 12489 Berlin, Germany

This is a particularly good solution to tackle unwanted effects, such as cross-interference of analytes at ambient conditions.^[6] Simple and fast processing techniques with wide opportunities for chemical adjustments are required for the cost-effective realization of such chemical sensor arrays.

Laser-patterning of materials provides a solution for the direct synthesis of sensing materials for on-chip applications. In the past decade, laser-patterned carbons (LP-C) have emerged as versatile materials for sensor platforms with high surface areas and high binding affinities to a broad palette of compounds.^[8] Commonly, LP-Cs or specifically laser-induced graphenes (LIG), are obtained by laser-irradiation onto films of polymeric precursor materials, such as graphene oxide^[9,10] or polyimides.^[11,12] Thereby, precisely printed electronically conductive carbon electrodes with high specific surface areas (SSA) on flexible substrates are obtained. Recently, we investigated this laser-patterning technique and developed a method to utilize simple and naturally abundant molecular compounds as starting materials.^[13,14] These can be cast on flexible substrates and carbonized with a CO₂-laser to give 2D-patterns of electronically conductive nitrogen-doped carbons (NC), which show remarkable environmental stability.^[15] Such NCs are commonly obtained from direct pyrolysis of nitrogen-containing precursors and show superior sorption properties.^[16,17] In contrast, the so-called carbon laser-patterning (CLaP) process is an extremely cost-effective and fast method to produce NC-based platforms for chemical sensing.^[18] Furthermore, CLaP enables simple modification with different types of functionalities or nanoparticles that can be incorporated into the LP-NC network.^[13] The electronic and chemical modifications of these LP-NC networks facilitate the tuning toward higher sensitivity for certain analytes using, for example, metal carbides and inorganic salts.^[19]

Metal carbides are well known for their high electronic conductivity, thermal stability, and corrosion resistance.^[20] These attributes raise the interest in metal carbides as active materials in electronic and catalytic devices.^[21,22] Due to their similar band-structure to noble metals, metal carbides are often ascribed great potential to replace the former as catalysts.^[23,24] Their catalytic activity also makes metal carbides interesting for sensing applications.^[19,25,26] However, in pure form, metal carbides suffer from low SSA, which is a drawback for sensing applications. Moreover, due to high hardness their films tend to crack or delaminate from the substrates.^[27]

In particular, molybdenum carbides (Mo₂C or MoC) have been widely studied and are commonly used as electrocatalysts for biomass degradation or water splitting.^[23,28] Molybdenum carbides are usually synthesized during pyrolysis in presence of a carbon source.^[23] A great challenge is to increase their SSA by nano-structuring. For example, nanoparticles with sizes between 10 and 30 nm were achieved via the urea glass route.^[29] However, the formation of small, high surface-area molybdenum carbide nanoparticles is mostly achieved in conjunction with electronically active support materials, such as metallic or metal oxide supports but also conductive NCs or carbon nitrides.^[30,31] In synergy, NCs and nanocrystalline molybdenum carbides are expected to contribute their full performance toward improved interaction with adsorbates.^[32]

In this study, we use CLaP to synthesize high-surface area NC-network supported MoC_{1-x} nanoparticles as chemiresistors

for sensing volatile organic compounds (VOCs). The SSA of the LP-NC was increased by addition of sodium iodide (NaI) as an IR-laser transparent porogen. The final LP-NC films were characterized by X-ray powder diffraction, high-resolution scanning and transmission electron microscopy (TEM), energy dispersive X-ray spectroscopy (EDXS), and X-ray photoelectron spectroscopy (XPS) confirming the formation of the MoC_{1-x}-NC composite. Finally, defined resistive sensing platforms, printed on polyethyleneterephthalate (PET), and their performance to sensing VOCs such as acetone, toluene, and hexane at different atmospheric contents were tested. Pure carbon materials usually have no or a rather low room temperature response to non-redox VOCs, such as acetone or alcohols. In composites, positive effects of carbons, such as graphene or carbon nanotubes, added in low percentages are increased conductivity and surface areas.^[33–35] We show that carbon with only 13 wt% molybdenum is the active sensing material and outperforms other carbon materials in terms of resistive response. These results lay a foundation for examining sorption-sensitive and potentially selective LP-NC based composites for the use in printed sensor arrays.

2. Experimental Section

2.1. Chemicals

Citric acid (99%, Sigma Aldrich), urea (>99.3%, Alfa Aesar), ammonium heptamolybdate tetrahydrate (≥99% for analysis, Acros Organics), ethylene glycol (≥99.7%, AnalaR Normapur, VWR chemicals), polyvinylpyrrolidone (PVP; average mol wt. 10 000, Sigma Aldrich), acetone (≥99.8% HPLC grade, Thermo Fisher Scientific GmbH), hexane (AnalaR Normapur, VWR chemicals), and toluene (≥99.8% HPLC grade, Thermo Fisher Scientific GmbH) were used as received.

2.2. Substrates

Silicon wafers were obtained from MicroChemicals. Wafers used were either 4-inch boron doped FZ-Si wafer, orientation (100), with a thickness of 0.5 mm and a generic resistivity of 3–100 kΩcm or 4-inch FZ-Si wafer, orientation (100), with a thickness of 0.5 mm and a generic resistivity of 10–1000 kΩcm. Aluminum foil used was 35 μm thick. The PET substrates were Melinex sheets obtained from Plano GmbH.

2.3. Preparation of the CNFA

The CNFA was prepared according to a previously published protocol.^[15] In brief: citric acid and urea were annealed at 300 °C in a chamber oven for 2 h. After annealing, the black reaction product was dispersed in deionized H₂O and stirred at 95 °C for 24 h. The dispersion was centrifuged to obtain a black precipitate and a brown supernatant. The supernatant was removed and the washing process was repeated four times. After the last washing step, the precipitate was dried to obtain CA/U(300).

2.4. Preparation of the Precursor Films

PVP (film-forming agent; FFA) was dissolved in ethylene glycol (EtGly) to obtain a 0.2 g mL⁻¹ solution (PVP/EtGly). Ammonium heptamolybdate (AHM; (NH₄)₆Mo₇O₂₄; 0.1 g·mL⁻¹) and/or sodium iodide (NaI; 0.1–0.4 g·mL⁻¹) were added and carefully dissolved. CA/U(300) was then added and stirred for 24 h to obtain a 0.8 g·mL⁻¹ ink. All concentrations are given with respect to the volume of the solvent. A drop of the ink was applied onto the substrate and the ink was doctor bladed with a wet-thickness between 155 and 305 μm. Ethylene glycol was then evaporated at 80 °C on a precision hotplate (PZ2860-SR, Gestigkeit GmbH) to obtain the final films with thicknesses between 13 and 70 μm. The thickness was determined with a digital micrometer or cross-sectional SEM.

2.5. Laser-Carbonization

Laser-carbonization was conducted with a high-precision laser engraver setup (Speedy 100, Trotec) equipped with a 60 W CO₂ laser. Focusing was achieved with a 2.5 inch focus lens providing a focal depth of ≈3 mm and a focus diameter of 170 μm. The center wavelength of the laser was 10.6 ± 0.03 μm. The scanning speed v' , generically given in %, was converted into s·m⁻¹. The effective output power P of the laser was measured with a Solo 2 (Gentec Electro-Optics) power meter. The resulting energy input per distance (or fluence) F in J·m⁻¹ in the vector mode onto the film is given by

$$F = P \cdot v' \quad (1)$$

For the experiments, the laser settings were adjusted to meet the requirements of the films according to **Table 1**.

2.6. Determination of the Specific Surface Areas

The SSA of LP-NC were determined by the methylene blue (MB) adsorption method.^[36–38] LP-NC films in a size of 2 × 1 cm were printed on PET sheets and their masses were determined with a micro-balance. The PET-supported films were then immersed into 6 mL of a 9.5 × 10⁻⁵ M solution of MB in polypropylene vials and stirred for 24 h. The solutions were centrifuged and the amount of adsorbed MB was determined by measuring the absorbance of the supernatant with respect to a reference solution. An area of 1.35 nm² per molecule MB was assumed.

Table 1. Laser parameters used in the experiments to fit the film thickness.

Thickness [μm]	Power [%] (generic)	Power [W]	Speed [%] (generic)	Speed [s m ⁻¹]	Fluence [J m ⁻¹]
13	1.9	0.97	0.6	98	94.5
19	2.0	1.02	0.6	98	99.5
28	2.1	1.07	0.6	98	104.5
56	2.5	1.27	0.6	98	124.4
70	2.7	1.37	0.6	98	134.3

2.7. VOCs Sensing

The sensor platforms were placed in a gas-proof glass flow-cell ($V_{\text{cell}} \approx 0.1$ L) and their ends were connected to two electrode pins. The electrical characterization was performed with an impedance unit at a frequency of 1000 Hz and a current intensity at 0.05 mA for all measurements. The total flow of nitrogen was set to 1 L·min⁻¹. 30 min cycles between pure nitrogen and a flow containing different contents of acetone were performed. Either 1%, 5%, or 10% of the total flow were passed through a reservoir of the liquid VOCs with a temperature fixed at 30 °C. The final concentration of the analyte was approximated using the ideal gas law based on the vapor pressure of the VOC.^[39]

2.8. Characterization

Scanning electron microscopy was performed on a Zeiss LEO 1550-Gemini system (acceleration voltage: 3 to 10 kV). An Oxford Instruments X-MAX 80 mm² detector was used to collect the SEM-EDX data. TEM was performed using a double Cs corrected JEOL JEM-ARM200F (S)TEM operated at 80 kV, 10 μA, and equipped with a cold-field emission gun and a high-angle silicon drift EDX detector (solid angle up to 0.98 steradians with a detection area of 100 mm²). Annular dark field scanning TEM (ADF-STEM) images were collected at a probe convergence semi-angle of 25 mrad. The so-called “beam shower” procedure was performed with a defocused beam at a magnification of 8000× for 30 min. This procedure was necessary for reducing hydrocarbon contamination during subsequent imaging at high magnification. To prepare the TEM samples, the carbon material was dispersed in methanol, sonicated for 10 min, drop cast on a Lacey carbon TEM grid and dried at room temperature. Elemental combustion analysis was performed with a vario MICRO cube CHNOS elemental analyzer (Elementar Analysensysteme GmbH). The elements were detected with a thermal conductivity detector for C, H, N, and O and an IR detector for sulfur. Raman spectra were obtained with a confocal Raman Microscope (alpha300, WITec, Germany) equipped with a piezo-scanner (P-500, Physik Instrumente, Karlsruhe, Germany). The laser, $\lambda = 532$ or 785 nm was focused on the samples through a 20× objective. The laser power on the sample was set to 1.0 mW. X-ray diffraction was performed on a Bruker D8 Advance diffractometer in the Bragg-Brentano mode at the Cu K α wavelength. Impedance measurements were performed on a Solartron 1287 potentiostat in combination with a SI 1260 impedance unit. For frequency measurements, the current was kept constant at 0.1 mA and for current sweeps,

a frequency of 100 Hz was used. Hall measurements were carried out at room temperature in an Accent HL5500PC using a magnetic strength of 0.3 T. The samples were fabricated in a cloverleaf geometry and the pins contacted the film via indium pads. After checking the ohmic response of the contacts, the measurements for LP-NC(NaI40) were done with the current source set for AC operation under vacuum. The entire Hall measurement was cycled five times to obtain an average value. LP-MoC_{1-x}(10)@NC and LP-MoC_{1-x}(10)@NC(NaI40) measurements were done in the DC mode. Each measurement was repeated a minimum of four times. XPS was performed with a CISSY station (UHV) with a SPECS XR 50 X ray gun Mg K α radiation (1254.6 eV) and combined lens analyzer module. The Shirley background deletion was used in photoemission spectra analysis.

3. Results and Discussion

The process of CLaP using organic, molecular precursors has been described in detail in a previous study.^[15] First, so-called carbon network forming agents consisting of pre-carbonized molecular precursors were synthesized. To this end, mixtures of citric acid and urea were pyrolyzed in an oven at 300 °C for 2 h under a nitrogen flow to obtain a black powder. This powder is a mixture of carbon-rich nanoparticles and molecular side products.^[40] The insoluble carbon-rich nanoparticles particles were separated from the soluble side-products by washing in boiling H₂O. The insoluble particles appear agglomerated, with diameters between 50 and 500 nm according to TEM analysis (Figure S1A, Supporting Information). A peak at 27.4° 2 θ in the diffraction pattern (Figure S1B, Supporting Information) corresponds to the typical *d*-spacing for π -stacked hydrocarbons and is characteristic of the presence of polyaromatic domains within the CNFA. Their formation is confirmed by the presence of broad D- and G-bands at 1355 and 1568 cm⁻¹, respectively, in the Raman spectrum (Figure S1C, Supporting Information).

The CNFA was processed to highly viscous precursor inks (Figure 1A). The standard ink is composed of the CNFA, PVP as a FFA, and ethylene glycol (EtGly) as a solvent. Additional components, such as porogens (NaI) and functional additives (AHM) were added to tune the properties of the final LP-NC. The elemental compositions of these precursors are given in Table S1, Supporting Information. From these inks, films

with thicknesses between 15 and 70 μ m were prepared by doctor blading on a PET substrate and evaporating the solvent at 80 °C. Then, carbonization was achieved by irradiating the films with a mid-IR CO₂-laser with preset patterns (Figure 1B). After laser-treatment, the unexposed precursor film was removed by rinsing with deionized water. The resulting laser-carbonized structures are referred to as LP-NC films. Finally, the films were used as resistive sensor platforms to detect different VOCs in a gas-flow-cell (Figure 1C).

3.1. LP-NC

The SEM image in Figure S2A, Supporting Information shows the typical appearance of an LP-NC film with its foamy morphology composed of the conductive (nitrogen doped-) carbon network with macro and mesopores.^[18] These pores evolve during the laser-treatment upon sudden release of gases, such as CO or CO₂. The presence of smaller mesopores is also observed by TEM (Figure S2B, Supporting Information).

The original elemental composition of the CNFA is 47 wt% carbon (C), 19 wt% nitrogen (N), and 31 wt% oxygen (O) as determined by elemental combustion analysis. Upon laser-treatment, the overall composition changes to 68 wt% C, 13 wt% N, and 27 wt% O in the collected powders. Noteworthy, the degree of carbonization follows a gradient from the top to the bottom of the film as demonstrated in EDX elemental analysis maps of cross sections of the as-prepared LP-NC films (Figure 2A). Clearly, the top of the film is dominated by carbon while large amounts of nitrogen and oxygen are detected toward the bottom of the film. On top of the film, the carbon content reaches 92 wt% C (8 wt% O). In the XRD pattern of the as-prepared LP-NC a broad peak at 2 θ = 26.1° characteristic for graphitic layers is detected (Figure S2C, Supporting Information). The shift toward smaller angles in comparison to the CNFA is attributed to the reduction in nitrogen content and the higher degree of graphitization. The Raman spectrum shows common features of a turbostratic graphitic material showing D, G, and G' vibration bands localized at 1335, 1573, and 2664 cm⁻¹, respectively (Figure S2D, Supporting Information). The pronounced D band indicates the presence of significant amounts of graphitic defects, such as sp³-carbon, heteroatoms, or vacancies.

For electronic sorption applications, such as sensors, the electrical conductivity and the SSA are pivotal factors. To tune

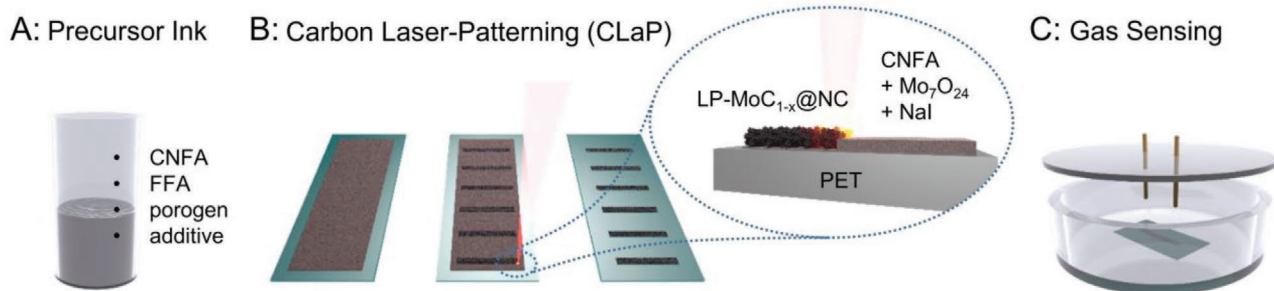


Figure 1. Scheme of the sensor production and measuring process; A) preparation of precursor inks with different compositions including CNFA, FFA, porogens, and additives; B) carbon laser-patterning of precursor films cast on PET and subsequent rinsing with H₂O to obtain LP-NC; C) electrochemical gas-sensing cell used to characterize the resistive response of the LP-NC sensor platforms in different environments.

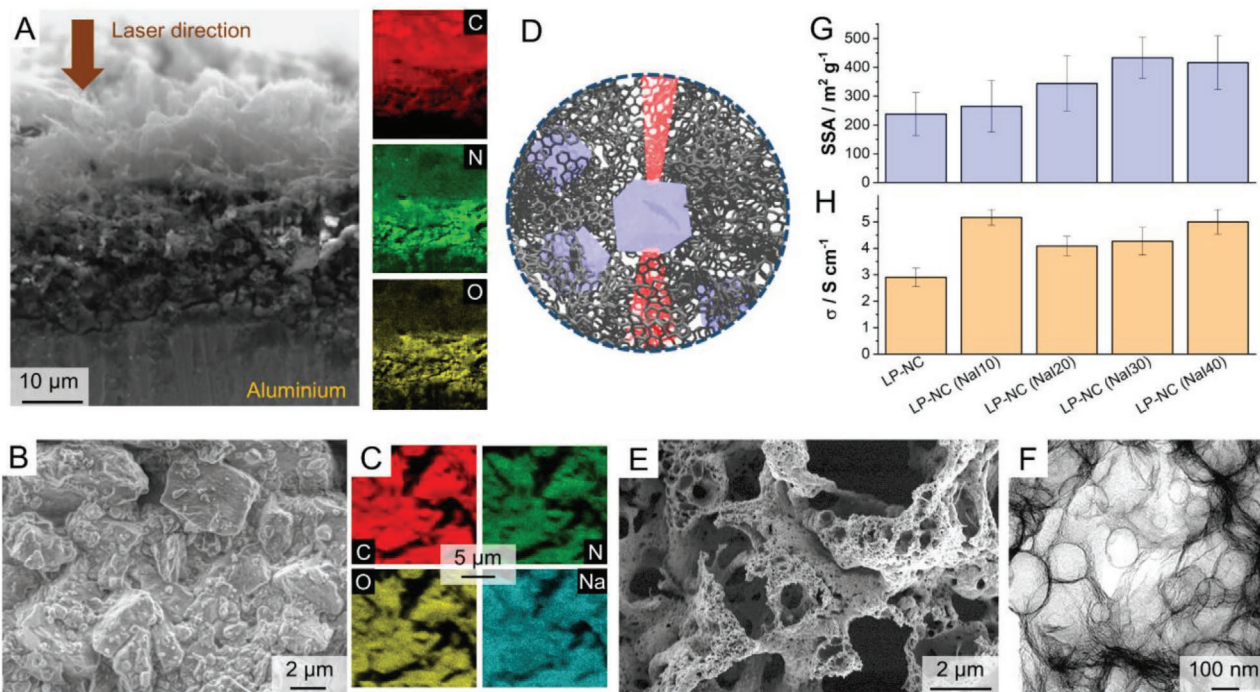


Figure 2. A) Scanning electron micrograph of a LP-NC film on an aluminium sheet and corresponding EDX maps showing the qualitative carbon, nitrogen, and oxygen distribution across the film; B) scanning electron micrograph of the CNFA film containing 40 wt% NaI and C) corresponding EDX maps; D) illustration of the alkali halide salt embedded in the CNFA film and their transmittance for IR-laser radiation; E) scanning electron micrograph of LP-NC(NaI40); F) transmission electron micrograph of LP-NC(NaI40). G) Dependence of specific surface area on the amount of NaI added to the CNFA film; H) dependence of sheet conductivity on the amount of NaI added to the CNFA film.

the SSA and, thus, the sorption-sensitivity of the sensor platforms, IR-transparent salts (alkali halides) were added as porogens. Among the typical IR-transparent salts, NaI shows the highest solubility in ethylene glycol, the solvent for the precursor ink. In this study, we focused on NaI only, because the solubility of other salts in ethylene glycol, such as NaCl, KCl, NaBr, and KBr is too low to reach porogenic activity. Its high solubility in water is also beneficial for the rinsing step after laser-treatment. Different amounts of NaI (10–50 wt% with respect to the CNFA) were added to the precursor inks and their impact on the formation and properties of the LP-NC films were tested. The products are named LP-NC(NaI10)–LP-NC(NaI40). Larger amounts of NaI (>40 wt%) result in delamination of the films. Upon drying, a homogeneous precursor film is formed (Figure 2B). As demonstrated by the EDX maps in Figure 2C, the NaI is uniformly blended into the CNFA film and does not separate or form micro-crystallites. The distributed IR-transparent salt within the film transmits the laser energy and allows effective carbonization of the surrounding CNFA (Figure 2D). After laser-treatment, the films show a uniform porous morphology and SEM analysis does not reveal major differences relative to the reference LP NC (Figure 2E). A representative TEM image in Figure 2F shows a strong resemblance to the reference LP-NC with bubble-like pores caused by the aforementioned laser-induced release of evaporating CNFA.

To quantify the SSAs of the LP-NC(NaI) films, the MB adsorption method was chosen, which is suitable for small quantities (<1 mg) of carbonaceous samples (see Experimental Section). The mass densities of the LP-NC films printed on PET

sheets were determined to be $\approx 10\text{--}50 \mu\text{g cm}^{-2}$. PET supported films with defined mass loadings were immersed into aqueous solutions of MB with defined concentrations and stirred for 24 h and the amount of MB adsorbed was determined by UV–vis absorption spectroscopy. Noteworthy, the MB adsorption method typically gives lower SSA values for nitrogen-doped carbons, meaning that the absolute values can be treated as a lower limit for the true SSA. For comparison, a list with other carbon and nitrogen-doped carbon materials is given in Table S2, Supporting Information. The SSAs of the LP-NC was increased from ≈ 238 to $\approx 433 \text{ m}^2 \cdot \text{g}^{-1}$ upon adding 30–40 wt% NaI to the precursor ink (Figure 2G). This range is similar to the range found for LIG from polyimides ($\approx 340 \text{ m}^2 \cdot \text{g}^{-1}$).^[41] The increased SSA by a factor of two and the largely unchanged morphological features of the LP-NC upon addition of NaI into the precursor ink confirms its hypothesized role as a porogen. After laser treatment, remaining NaI is removed by thorough rinsing of the film with H₂O, which is confirmed by EDX-analysis of the final films (Figure S3, Supporting Information). The Raman spectrum of LP-NC(NaI40) film (Figure S4, Supporting Information) shows a higher D-band compared to bare LP-NC, which indicates that NaI has an effect on the carbonization mechanism.

A statistical electronic analysis of 50 samples of the resulting LP-NC(NaI) films shows that the conductivity is generally higher when NaI was added (Figure 2H). Addition of 10 wt% NaI results in an increase from 2.8 to 5.2 S cm⁻¹. While higher amounts (20–40 wt%) cause a drop in conductivity, the conductivity remains above the reference sample without NaI. The

addition of a salt to the ink supports a better dispersion of the negatively charged CNFA particles due to the Debye–Hückel arrangement in a concentrated electrolyte solution. The Debye length is shortened resulting in an improved dispersion. At concentrations > 20 wt% the effect of NaI as a porogen from NaI crystallites sets in. LP-NC(NaI40) exhibits a positive Hall coefficient of $R_H = +0.19 \text{ cm}^3 \cdot \text{C}^{-1}$ indicating an intrinsic p-type semiconducting behavior that is commonly observed for carbonaceous samples carrying oxygen functionalities on their surface.^[42,43] Notably, the charge carrier mobility obtained from the Hall measurements of $0.23 \text{ cm}^2 \cdot (\text{V} \cdot \text{s})^{-1}$ for LP-NC(NaI40) is higher than the reference LP-NC ($0.12 \text{ cm}^2 \cdot (\text{V} \cdot \text{s})^{-1}$),^[18] which is in line with the increased SSA and thus a larger conjugated surface. The higher defect density in LP-NC(NaI40) measured by Raman spectroscopy (Figure S4, Supporting Information) contributes only little to lowering the charge carrier mobility.

As a general scheme, the presence of an IR-laser transparent salt in the precursor films supports the penetration of the laser energy into deeper layers of the precursor film. Subsequently, larger amounts of material are carbonized and contribute to the overall conductivity. The higher value for only 10% NaI may be attributed to a lower porogenic activity at such low concentrations and a better percolation of the carbon network. 40 wt% of NaI appears to be the best compromise to maximize the porosity, the electronic conductivity and to conserve a good mechanical stability, that is, avoiding delamination or cracking.

3.2. LP-MoC_{1-x}@NC

To increase the sensitivity toward different VOCs, the LP-NC was impregnated with MoC_{1-x} nanoparticles. To this end, a molecular molybdenum precursor was added to the ink in addition to the CNFA, the FFA, and the porogen. A negatively charged complex, AHM, was chosen to avoid flocculation in the precursor ink since the CNFA, CA/U(300), has a negative ζ -potential of -53 mV .^[15] Rapid heating in the laser spot initiates the AHM decomposition and the nucleation of molybdenum carbide (MoC_{1-x}) nanoparticles.

First, we tested the influence of the AHM content on the electronic properties of the final laser-patterned films, denoted as LP-MoC_{1-x}(wt%)@NC (Figure 3A). Addition of 1 wt% AHM with respect the mass of CNFA, results in a drop in conductivity from 2.9 to 1.0 S cm⁻¹. Higher amounts of AHM, 5 or 10 wt%, cause the conductivity to increase again to 2.2 or 3.2 S cm⁻¹. The films containing 20 wt% appear brittle and crack easily resulting in low conductivity and very high errors. The SSA remains largely unchanged (Figure S5, Supporting Information).

The MoC_{1-x} nanoparticle impregnated LP-NC produced with 10 wt% of AHM in the precursor ink, here referred to as LP-MoC_{1-x}(10)@NC was intensively characterized, as 10% of AHM appears to be the optimum content to preserve the mechanical stability and maximize the electronic conductivity. To determine the molybdenum content, the sample was

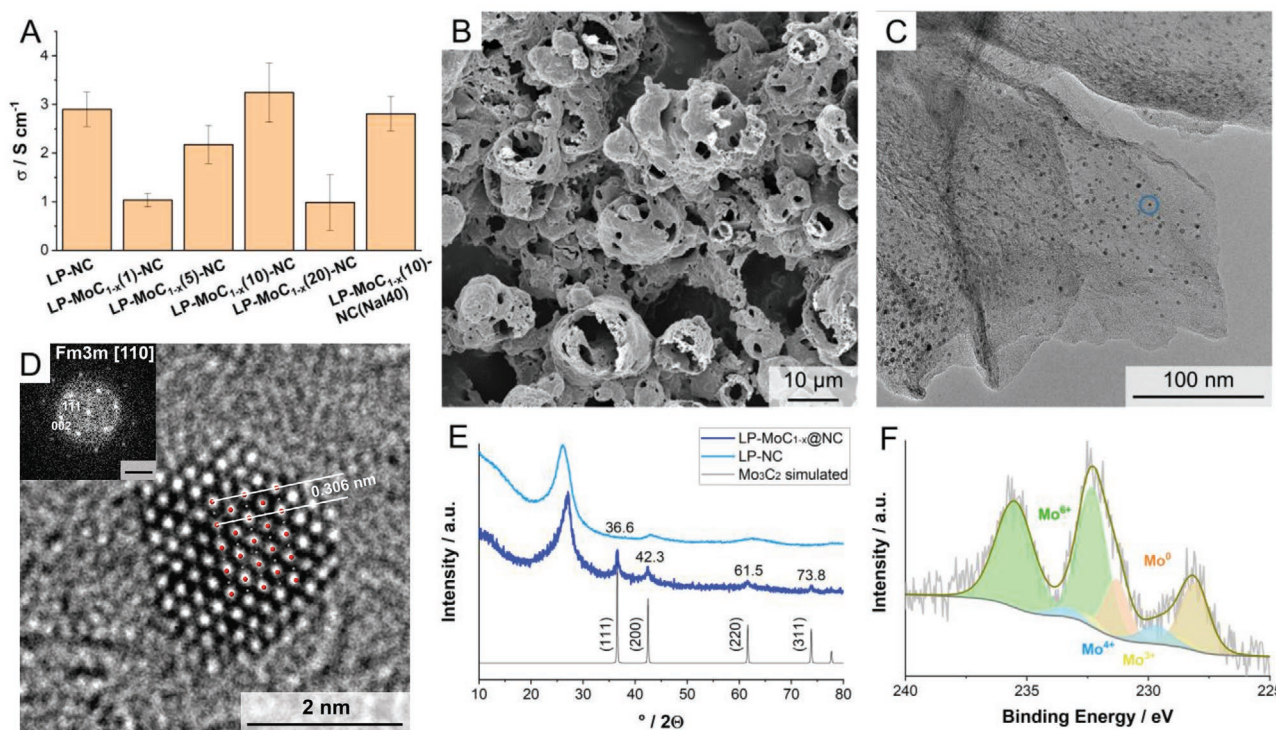


Figure 3. A) Electrical sheet conductivity of LP-MoC_{1-x}@NC with different amounts of AHM in the inks; B) scanning electron micrograph of LP-MoC_{1-x}(10)@NC showing a foam-like morphology; C) transmission electron microscopy image of LP-MoC_{1-x}(10)@NC. The overlapping atoms demonstrate the locations of Mo (red) and C (grey) in the crystal. The inset in (D) shows the corresponding fast Fourier transform indexed in a cubic unit cell, sp.gr. Fm $\bar{3}$ m. The scale bar is 5 nm⁻¹. E) X-ray powder diffraction patterns of LP-NC and LP-MoC_{1-x}(10)@NC, respectively, and the simulated pattern of Mo₃C₂; F) X-ray photoelectron spectrograph of the Mo_{3d} core level of LP-MoC_{1-x}(10)@NC.

analyzed by inductively coupled plasma mass spectrometry. After laser-treatment the overall Mo content is 12.9 wt% in LP-MoC_{1-x}(10)@NC. The higher Mo content in comparison to the precursor ink (4.28 wt%) shows that the CNFA evaporates more than the Mo precursor (AHM) during the laser-carbonization. The overall foamy morphology of the LP-MoC_{1-x}(10)@NC films is, in principle, the same as for LP-NC (Figure 3B) and macroscopic features, such as thickness and appearance, are not altered. The size range of the MoC_{1-x} nanoparticles as observed in the TEM images in Figure 3C is between 2 and 20 nanometers (Figure S6, Supporting Information).

Fast Fourier transformed HRTEM images of the particles can be indexed in the cubic lattice with the unit cell parameter $a = 4.15(4)$ Å, sp.gr. $Fm\bar{3}m$, and can be described with the NaCl-structure type typical for MoC_{1-x} solid solution (Figure 3C,D).^[44] Furthermore, the EDX spectra and the STEM-EDXS maps (Figure S7, Supporting Information) of the LP-MoC_{1-x}(10)@NC sample show the presence of Mo, C, N, and O, whereas the carbon network spectra only show N and O signals, confirming the formation of molybdenum carbide particles. The XRD pattern in Figure 3E shows the presence of a graphitic peak at $27^\circ 2\theta$, similar to that found for LP-NC, while all other peaks can be attributed to cubic MoC_{1-x} with the unit cell parameter $a = 4.253(5)$ Å.^[45] Discrepancies in the unit cell parameters obtained from either FFT or XRD can be explained by both, much lower accuracy of the lattice space determination of the HRTEM-FFT analysis and much lower statistics than in case of XRD.

The Mo_{3d} XPS core level spectrum in Figure 3F shows the presence of Mo in the oxidation states Mo⁰, Mo³⁺, Mo⁴⁺, and Mo⁶⁺. The most prominent are Mo⁰ at 228.1 (3d_{5/2}) and 231.3 eV (3d_{3/2}), and Mo⁶⁺ at 232.3 (3d_{5/2}) and 235.5 eV (3d_{3/2}). Minor signals at 228.8 (3d_{5/2}) and 232.4 eV (3d_{3/2}) and at 229.7 (3d_{5/2}) and 233.4 eV (3d_{3/2}) are attributed to Mo³⁺ and Mo⁴⁺, respectively. This oxidation pattern, especially the presence of Mo⁰ is typical for MoC_{1-x} or MoC.^[46] The fitting data of the C_{1s}, N_{1s}, and O_{1s} regions are presented in Figure S8, Supporting Information.

The Raman spectrum of LP-MoC_{1-x}(10)@NC shows sharp D- and G-bands, although the peaks appear much broader and the D-band significantly more intense, relative to LP NC (Figure S9, Supporting Information). The shape and intensity of the 2D band are correlated with the degree of stacking of graphitized domains within the material. Carbon in the amorphous state shows only a low intensity 2D band.^[47] At the same time, the D-band, which is correlated to the amount of sp²-defects is significantly increased. Therefore, we infer a lower degree of stacking due to the presence of MoC_{1-x} nanoparticles and a higher number of defects. From these observations, we deduce that the MoC_{1-x} nanoparticles are not only grown on the surface but also incorporated into the LP-NC network. The size distribution of the MoC_{1-x} nanoparticles is not affected by the presence of NaI during the laser-induced reaction (Figure S1, Supporting Information). As shown in the cross-sectional EDX maps of 70 μm thick LP-MoC_{1-x}(10)@NC(NaI40) films, the MoC_{1-x} nanoparticles are uniformly distributed across the film (Figure S11, Supporting Information).

The formation of MoC_{1-x} nanoparticles occurs in situ during the laser-induced carbonization. A commonly accepted mechanism is the reduction of transient molybdenum clusters to

molybdenum carbides by carbothermal reduction.^[48] High carbon content and high temperatures (>1500 °C) in the laser spot facilitate the formation of MoC_{1-x}.^[49] The presence of nanometer-sized graphitic domains surrounding the MoC_{1-x} nanoparticles are confirmed by high-resolution STEM images shown in Figure S12, Supporting Information. The meso/macroscopic morphology of the LP-MoC_{1-x}(10)@NC is not significantly affected by the presence of AHM in the precursor ink. However, the electronic properties (i.e., electrical conductivity) are impaired, with the drop in conductivity upon adding small amounts of AHM (<10 wt%) consistent with perturbation due to the increased number of defects in the LP-NC network. Larger amounts of AHM support the nucleation of metallic MoC_{1-x} nanoparticles, which contribute positively to the overall conductivity. Hall measurements yielded a positive coefficient also for LP-MoC_{1-x}(10)@NC of $R_H = +0.32$ cm³·C⁻¹. The charge carrier density is slightly lower with 1.96×10^{19} cm⁻³ than the LP-NC sample, while the charge carrier mobility is higher with 1.42 cm²·(V·s)⁻¹ (Table S3, Supporting Information). These electronic properties are affected by the addition of NaI. The Hall coefficient, $R_H = +2.67$ cm³·C⁻¹, is significantly higher than LP-MoC_{1-x}@NC, due to a threefold increase in charge carrier mobility to 4.35 cm²·(V·s)⁻¹ and lower charge carrier density of 2.34×10^{18} cm⁻³.

3.3. VOC Sensing

Finally, we tested films of the optimized materials, LP-NC(NaI40), LP-MoC_{1-x}(10)@NC, and LP-MoC_{1-x}(10)@NC(Na40), as sensor platforms for resistive sensing of VOCs. In every production step, several sensor platforms were printed consecutively into one film (Figure 4A). A standard sensor pattern is made of five parallel laser lines of 5 mm in length distributed across a width of ≈0.5 mm (Figure 4B). This simple geometry allows for the direct comparison of the materials properties, while geometric effects are neglected. For each measurement, a sensor platform was placed into a gas-flow-cell and the two ends of the sensor platform were connected by electrodes to measure the impedance in a four-probe arrangement. The gas composition inside the cell was controlled by two parallel connected mass-flow controllers to ensure a constant gas flow with compositions of 0.5–10% target gas in a carrier gas (N₂ or air) atmosphere. A prominent biomarker, namely acetone, was chosen as the primary target gas.^[50]

First, we tested the effect of film thickness on acetone sensitivity, using the LP-MoC_{1-x}(10)@NC sensor as a representative platform (Figure S13, Supporting Information). The best results for this sensor were achieved with a thickness of 70 μm, so we utilized this thickness range for additional tests. Thicker films tend to delaminate during the rinsing step. Notably, for films thinner than 19 μm a weak positive response, that is, an increase of resistivity upon exposure to acetone is detected, which is attributed to a lower degree of graphitization and higher defect density in the laser-patterned carbon.

The resistivity response of LP-NC(NaI40) upon exposure to 2.5% acetone is $\Delta R/R_0 = 2.7\%$ and a similar value of $\Delta R/R_0 = 3.0\%$ is detected for the non-porogen-containing

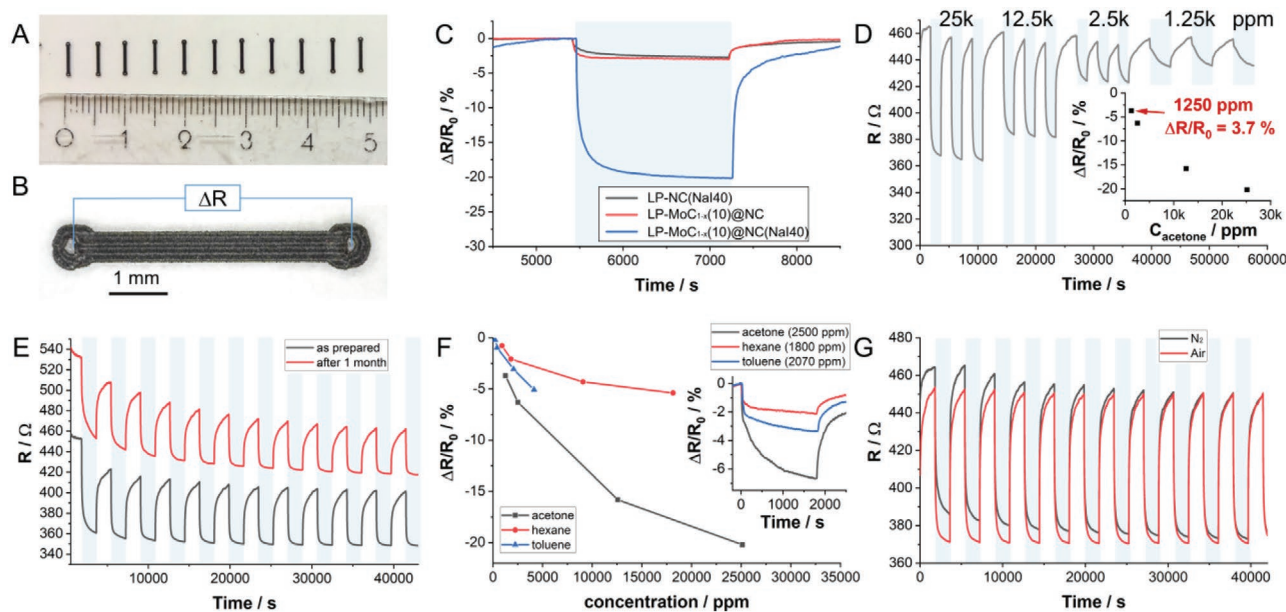


Figure 4. A) Photograph of a set of sensor platforms obtained by carbon laser-patterning on PET; B) optical micrograph showing the dimensions of the sensor-platform used for resistive gas-sensing experiments; C) response of the sensor materials LP-NC(NaI40), LP-MoC_{1-x}(10)@NC, and LP-MoC_{1-x}(10)@NC(NaI40) upon exposure to 2.5% acetone; D) resistive response of LP-MoC_{1-x}(10)@NC(NaI40) toward exposure to different concentrations of acetone; E) resistive response of LP-MoC_{1-x}(10)@NC(NaI40) after 1 month in comparison to a freshly prepared sensor platform; F) comparison of the resistive response of LP-MoC_{1-x}(10)@NC(NaI40) toward different concentrations of acetone (black), hexane (red), and toluene (blue); G) resistive response of LP-MoC_{1-x}(10)@NC(NaI40) toward 2.5% of acetone using N₂ (black) or dry air (red) as carrier gas.

LP-MoC_{1-x}(10)@NC (Figure 4C). In LP-MoC_{1-x}(10)@NC(NaI40) the response is drastically increased by more than a factor of six giving $\Delta R/R_0 = 20.2\%$ for 2.5% acetone. The response depends on the analyte concentration as shown in Figure 4D and a reasonable response of $\Delta R/R_0 = 3.7\%$ at relatively low analyte concentrations of 1250 ppm acetone is detected.

Next, we tested the long-term stability of the sensor platforms. To this end, the sensor platform was stored under ambient conditions for 1 month and tested under the same conditions for sensing acetone (2.5%). With respect to the freshly prepared sample, the aged sample shows a slightly lower response of $\Delta R/R_0 = 15.8\%$ (Figure 4E). The reduced overall conductivity is attributed to a partial oxidation/degradation of the surface groups on the LP-MoC_{1-x}@NC(NaI40).

As shown in the materials characterization section and previous studies, the surface of LP-NC and LP-MoC_{1-x}@NC(NaI40) is largely oxygenated.^[51] Such oxygen-containing functional groups cause the surface to be preferentially susceptible to polar analytes, which is supported by the data shown in Figure 4F. The response toward polar acetone is significantly higher than to non-polar analytes such as hexane or toluene. The higher response to toluene in contrast to hexane is likely due to their attractive π - π interactions with π -conjugated domains on the surface of LP-MoC_{1-x}@NC(NaI40).

The typical sensing mechanism for acetone with semiconductor materials like metal oxides or graphene composites is proposed to stem from the interaction with ionosorbed oxygen.^[52] Before any sensor experiments, in the initial state, oxygen from the atmosphere is adsorbed and reduced to oxygen anions like O₂⁻, O⁻, or O²⁻ on the semiconductor surface resulting in a decrease of the electron density in the composite

material. In presence of acetone, these oxygen anions react to form CO₂ resulting in an increase of the electronic density of the semiconductor.^[6,53,54] However, this mechanism requires the supply of oxygen during operation and high operating temperatures. In our experiments we used either nitrogen or dry air as carrier gases (Figure 4G). The response in terms of resistivity change in both media is the same. Moreover, the response time and the recovery time during acetone cycling are similar in both carrier gases. This indicates that the presence of O₂ does not influence the sensing behavior, as the effect on the electronic properties during acetone exposure is negligible. Therefore, we conclude that the change in resistance is dominated by electronic sensitization effects rather than chemical, that is, physisorption of gaseous acetone onto the surface of the LP-MoC_{1-x}(10)@NC(NaI40) and the subsequent modulation of the depletion regions.^[55]

Considering these observations, our laser-patterned composite material shows intriguing performance in room temperature sensing of VOCs. Reliable room temperature sensing of VOCs using simple resistive architectures based on carbon is a challenge due to difficulties in processing and stability. Although many conventional sensing materials like metal oxides show a higher sensitivity at room temperature, their production and processing is rather tedious requiring deposition on interdigitated gold electrodes.^[56,57] In comparison to other carbon and graphene based materials the performance of LP-MoC_{1-x}(10)@NC(NaI40) is competitive.^[58-60] For example, multi-walled carbon nanotubes as p-type semiconductor show a response of $\approx 0.4\%$ to 15 ppm acetone at room temperature.^[33] Reduced graphene oxide is often used as a conductive sensing platform showing $\Delta R/R_0$ values of $\approx 1\%$

upon exposure to ≈ 500 – 1000 ppm of different alcohols at room temperature.^[34,35]

Generally, in carbonaceous materials, the active sites involved in the sensing mechanisms are presumed to be defects in the graphitic structure, such as vacancies or oxygen functional groups.^[61] According to elemental analysis, Raman, and XRD, the conductive carbonized part of the LP-NC is composed of highly defective, porous, and oxygenated turbostratic carbon. Its defective nature makes the surface rather polar with a high intrinsic binding affinity to polar analytes. In contrast to graphene with a largely unperturbed π -surface, the surface of LP-NC is not expected to be more sensitive with chemisorbed oxygen.

Taking these aspects into consideration the LP-NC sensor material differs from graphene. Due to its intrinsically oxygenated surface, LP-NC acts as a p-type semiconductor,^[18] which is confirmed by positive Hall coefficients mentioned above. Upon interaction of the surface defects or functional groups with the analytes, the charge carrier density within the LP-NC increases which is reflected in an increase in conductivity.^[53]

A common approach to increase the sensitivity of carbon materials is the integration of Schottky or heterojunctions,^[62] e.g., between carbon nanotubes and Au nanoparticles. These show response of $\Delta R/R_0 = 4.6\%$ to 800 ppm acetone.^[63]

By introduction of MoC_{1-x} nanoparticles into the LP-NC, nanoscale grain boundaries are created between the metallic MoC_{1-x} and the semiconducting LP-NC. These cause the formation of Schottky junctions and thus depletion zones around the nanoparticles (Figure 5). According to the Mott-theory, p-type semiconductors form rectifying contacts to metals of work function lower than that of the semiconductor, that is, $\Phi_M < \Phi_S$ and ohmic contacts for $\Phi_M > \Phi_S$. The work function of MoC_{1-x} solid solution is difficult to determine experimentally. The work functions of metal carbides are highly dependent on the phase, the crystal facet, and the type of termination. For example, the theoretically determined work functions of MoC or Mo_2C range between 3.4 and 7.5 eV.^[64–66] Given the polydisperse nature of MoC_{1-x} incorporated into LP-NC, different facets and compositions are exposed to the surrounding carbon. LP-NC is best compared with amorphous or poly-crystalline carbons, such as MWCNTs or carbon black. Their work functions are typically $\approx 4.5 \pm 0.3$ eV.^[67–69]

In the present case, the MoC_{1-x} nanoparticles accumulate charge carriers and create doping-sensitive zones. Acetone as a closed shell molecule is expected to interact with the LP-NC surface by formation or enhancement of dipoles on the surface which induce a charge modulation within the doping-sensitive grain boundaries.^[70,71] Therefore, the higher sensing response in LP- $\text{MoC}_{1-x}(10)\text{@NC}(\text{NaI40})$ is explained by the lower charge carrier density in the overall material and the increased SSA.

This is the first example of a molecule-based laser-patterned resistive carbon sensor based on direct interactions with the target gas and the in situ incorporation of metal nanoparticles. Synthetically and environmentally, this method displays an advantage over LIG from polyimides, which have shown great promise as sensing platforms after post-functionalization with nanoparticles.^[72–76] Conceptually, they are different in terms of morphology and detection mechanisms. For

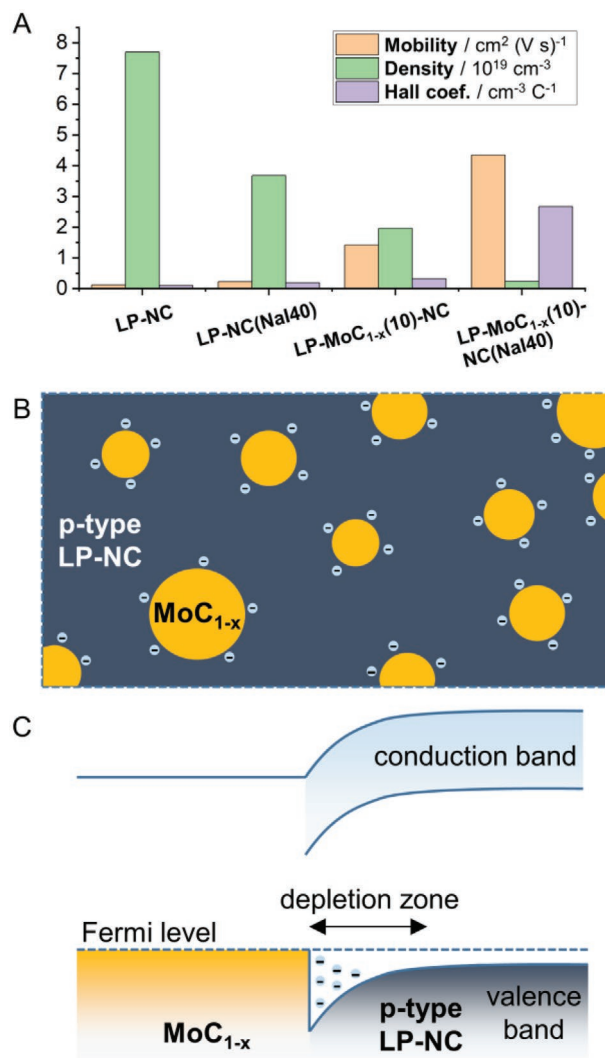


Figure 5. A) Comparison of the charge carrier mobilities, densities, and Hall coefficients of the four tested samples obtained by Hall measurements. B) Illustration of the charge accumulation by MoC_{1-x} nanoparticles embedded into a conductive p-type LP-NC network; C) corresponding band-diagram illustrating the depletion zones created around the MoC_{1-x} nanoparticles (1 column).

example, LIGs have shown a high response to different gases versus vacuum as a response to the different thermal conductivities of the respective gases.^[12] In other concepts, laser-patterned resistive carbons are used as transducer platforms for functionalization with selective bio-receptors.^[8] In our LP-NC and their nano-composites, we observe several effects simultaneously. On the one hand, we have a highly defective carbon, which allows an intrinsic room-temperature sensitivity toward different target gases. On the other hand, the uniform impregnation of MoC_{1-x} nanoparticles forms overlapping doping sensitive Schottky-junctions. Indeed, it has been shown, for example, that the particle size of certain materials and the subsequent generation of converging Schottky barriers lead to drastic increases in sensitivity.^[77–79] Their exact synergetic effects are yet to be explored in future studies on the detailed sensing mechanism.

4. Conclusions

In this study, we demonstrated the applicability of CLaP for resistive sensing of VOCs. CLaP is an interesting new tool for the fast and precise large-scale production of patterned carbonized films with different compositions for sensor arrays. The use of molecular starting materials enables wide possibilities for tuning the compositional and electronic properties of the obtained films. This study presents first insights into how the materials properties can be tuned to increase the sensitivity toward different analytes.

The specific surface area of the LP-NC was increased by addition of an IR-laser-transparent alkali halide salt—sodium iodide—into the precursor inks. Moreover, the fast speed of the laser-induced reaction allows for the in situ synthesis of small and uniform MoC_{1-x} nanoparticles with sizes < 10 nm achieved by the simple selective addition of soluble precursors to the precursor ink. The thus created Schottky junctions at the nanoscale grain boundaries between MoC_{1-x} and the conductive carbon network further decrease the charge carrier density whereby the sensitivity of the LP-NC films toward acetone was drastically increased.

The room-temperature sensing operation of the MoC_{1-x} nanoparticle impregnated LP-NCs is stable and reproducible and shows a remarkable long-term stability. However, to detect concentrations of analytes on the order of parts per billion improvements in the materials structure are necessary. Alternative porogens to further increase the surface area or tune the pore properties to facilitate bulk interactions with target gases rather than outer surface only may be a possible solution. Moreover, for mobile application under ambient conditions and different relative humidities, concepts for the selectivity toward different analytes, for example, tuning the graphitization degree, have to be studied. Further targets of future studies will be miniaturization and optimization of the platform geometries as the sizes of the obtained sensor platforms are limited by the resolution of the laser and the grain size of the agglomerated precursor particles. The CLaP method, in principle, allows for the simple incorporation of different kinds of nanoparticles of tunable sizes, which is a good foundation for systematic studies on the interplay between nanoparticles and their impact on their sensing properties toward different analytes.

Supporting Information

Supporting Information is available from the Wiley Online Library or from the author.

Acknowledgements

H.W. and S.D. contributed equally to this work. The authors are grateful for financial support from the Fonds der Chemischen Industrie and the Max Planck Society. The continuous educational support from Prof. Markus Antonietti is highly appreciated. The authors thank Heike Runge for assistance with electron microscopy and characterization and Klaus Bienert for help with the gas sensing setup. This work was authored, in part, by the National Renewable Energy Laboratory, operated by Alliance for Sustainable Energy, LLC, for the US Department of Energy (DOE) under Contract No. DE-AC36-08GO28308. A.Z., A.J.F., and J.L.B.

gratefully acknowledge funding provided by the Solar Photochemistry Program of the Chemical Sciences, Geosciences, and Biosciences (CSGB) Division at the US DOE Office of Science: Basic Energy Sciences. The views expressed in the article do not necessarily represent the views of the DOE or the US Government.

Open access funding enabled and organized by Projekt DEAL.

Conflict of Interest

The authors declare no conflict of interest.

Data Availability Statement

Research data are not shared.

Keywords

carbon laser-patterning, molybdenum carbide, porogens, room temperature sensors, volatile organic compounds sensors

Received: April 30, 2021

Revised: July 17, 2021

Published online: August 11, 2021

- [1] T. M. Swager, K. A. Mirica, *Chem. Rev.* **2019**, *119*, 1.
- [2] B. Ciui, A. Martin, R. K. Mishra, T. Nakagawa, T. J. Dawkins, M. Lyu, C. Cristea, R. Sandulescu, J. Wang, *ACS Sens.* **2018**, *3*, 2375.
- [3] N. Wongkaew, M. Simsek, C. Griesche, A. J. Baeumner, *Chem. Rev.* **2019**, *119*, 120.
- [4] C. Mackin, A. Fasoli, M. Xue, Y. Lin, A. Adebisi, L. Bozano, T. Palacios, *2D Mater.* **2020**, *7*, 022002.
- [5] M. E. Franke, T. J. Koplín, U. Simon, *Small* **2006**, *2*, 36.
- [6] H. G. Moon, Y. Jung, B. Shin, Y. G. Song, J. H. Kim, T. Lee, S. Lee, S. C. Jun, R. B. Kaner, C. Kang, C. Kim, *Adv. Sci.* **2020**, *7*, 2002014.
- [7] M. G. Campbell, S. F. Liu, T. M. Swager, M. Dincă, *J. Am. Chem. Soc.* **2015**, *137*, 13780.
- [8] L. Huang, J. Su, Y. Song, R. Ye, *Nano-Micro Lett.* **2020**, *12*, 157.
- [9] C. Zhu, L.-Q. Tao, Y. Wang, K. Zheng, J. Yu, X. L. X. Chen, Y. Huang, *Sens. Actuators, B* **2020**, *325*, 128790.
- [10] A. Watanabe, J. Cai, S. Ogawa, E. Aoyagi, S. Ito, in *Laser-Based Micro- and Nanoprocessing XIII* (Eds: U. Klotzbach, R. Kling, A. Watanabe), SPIE, Bellingham **2019**, p. 38.
- [11] S. Sharma, S. K. Ganeshan, P. K. Pattnaik, S. Kanungo, K. N. Chappanda, *Mater. Lett.* **2020**, *262*, 127150.
- [12] M. G. Stanford, K. Yang, Y. Chyan, C. Kittrell, J. M. Tour, *ACS Nano* **2019**, *13*, 3474.
- [13] V. Strauss, M. Anderson, C. Wang, A. Borenstein, R. B. Kaner, *Small* **2018**, *14*, 1803656.
- [14] V. Strauss, M. Anderson, C. L. Turner, R. B. Kaner, *Mater. Today Energy* **2019**, *11*, 114.
- [15] S. Delacroix, H. Wang, T. Heil, V. Strauss, *Adv. Electron. Mater.* **2020**, *6*, 2000463.
- [16] J. P. Paraknowitsch, J. Zhang, D. Su, A. Thomas, M. Antonietti, *Adv. Mater.* **2010**, *22*, 87.
- [17] J. Pampel, A. Mehmood, M. Antonietti, T.-P. Fellingner, *Mater. Horiz.* **2017**, *4*, 493.
- [18] S. Delacroix, A. Zieleniewska, A. Ferguson, J. L. Blackburn, S. Ronneberger, F. Löffler, V. Strauss, *ACS Appl. Electron. Mater.* **2020**, *2*, 4146.

- [19] S. A. Shafiee, S. C. Perry, H. H. Hamzah, M. M. Mahat, F. A. Al-lolage, M. Z. Ramli, *Electrochem. Commun.* **2020**, *120*, 106828.
- [20] S. A. Rasaki, B. Zhang, K. Anbalgam, T. Thomas, M. Yang, *Prog. Solid State Chem.* **2018**, *50*, 1.
- [21] W.-F. Chen, J. T. Muckerman, E. Fujita, *Chem. Commun.* **2013**, *49*, 8896.
- [22] T. Niu, *Nano Today* **2018**, *18*, 12.
- [23] Y. Deng, Y. Ge, M. Xu, Q. Yu, D. Xiao, S. Yao, D. Ma, *Acc. Chem. Res.* **2019**, *52*, 3372.
- [24] Y. Ma, G. Guan, X. Hao, J. Cao, A. Abudula, *Renewable Sustainable Energy Rev.* **2017**, *75*, 1101.
- [25] D. Geng, M. Li, X. Bo, L. Guo, *Sens. Actuators, B* **2016**, *237*, 581.
- [26] K. Hantanasirisakul, Y. Gogotsi, *Adv. Mater.* **2018**, *30*, 1804779.
- [27] C. Giordano, C. Erpen, W. Yao, M. Antonietti, *Nano Lett.* **2008**, *8*, 4659.
- [28] J. G. Howalt, T. Vegge, *Phys. Chem. Chem. Phys.* **2013**, *15*, 20957.
- [29] L. Ma, L. R. L. Ting, V. Molinari, C. Giordano, B. S. Yeo, *J. Mater. Chem. A* **2015**, *3*, 8361.
- [30] X. Zang, C. Shen, Y. Chu, B. Li, M. Wei, J. Zhong, M. Sanghadasa, L. Lin, *Adv. Mater.* **2018**, *30*, 1800062.
- [31] M. Abou Hamdan, A. Nassereddine, R. Checa, M. Jahjah, C. Pinel, L. Piccolo, N. Perret, *Front. Chem.* **2020**, *8*, 452.
- [32] Y. Liu, G. Yu, G.-D. Li, Y. Sun, T. Asefa, W. Chen, X. Zou, *Angew. Chem., Int. Ed.* **2015**, *54*, 10752.
- [33] I. Hafaiedh, W. Elleuch, P. Clement, E. Llobet, A. Abdelghani, *Sens. Actuators, B* **2013**, *182*, 344.
- [34] A. Lipatov, A. Varezchnikov, P. Wilson, V. Sysoev, A. Kolmakov, A. Sinitskii, *Nanoscale* **2013**, *5*, 5426.
- [35] R. Kumar, R. Ghosh, *Sens. Bio-Sens. Res.* **2020**, *28*, 100336.
- [36] S. Naeem, V. Baheti, J. Wiener, J. Marek, *J. Text. Inst.* **2017**, *108*, 803.
- [37] M. Rafatullah, O. Sulaiman, R. Hashim, A. Ahmad, *J. Hazard. Mater.* **2010**, *177*, 70.
- [38] P. T. Hang, *Clays Clay Miner.* **1970**, *18*, 203.
- [39] Y. Li, T. Täffner, M. Bischoff, B. Niemeyer, *Int. J. Chem. Eng.* **2012**, *2012*, 417029.
- [40] V. Strauss, H. Wang, S. Delacroix, M. Ledendecker, P. Wessig, *Chem. Sci.* **2020**, *11*, 8256.
- [41] J. Lin, Z. Peng, Y. Liu, F. Ruiz-Zepeda, R. Ye, E. L. G. Samuel, M. J. Yacaman, B. I. Yakobson, J. M. Tour, *Nat. Commun.* **2014**, *5*, 5714.
- [42] P. Esquinazi, J. Krüger, J. Barzola-Quiquia, R. Schönemann, T. Herrmannsdörfer, N. García, *AIP Adv.* **2014**, *4*, 117121.
- [43] N. D. K. Tu, J. A. Lim, H. Kim, *Carbon* **2017**, *117*, 447.
- [44] B. Granier, J.-M. Badie, F. Almeida Costa Oliveira, T. Magalhães, N. Shohoji, L. Guerra Rosa, J. Cruz Fernandes, *Mater. Trans.* **2008**, *49*, 2673.
- [45] K. Oshikawa, M. Nagai, S. Omi, *J. Phys. Chem. B* **2001**, *105*, 9124.
- [46] [42]
- [47] D. B. Schuepfer, F. Badaczewski, J. M. Guerra-Castro, D. M. Hofmann, C. Heiliger, B. Smarsly, P. J. Klar, *Carbon* **2020**, *161*, 359.
- [48] C.-M. Song, W.-C. Cao, C.-Y. Bu, K. He, G.-H. Zhang, *J. Aust. Ceram. Soc.* **2020**, *56*, 1333.
- [49] B. Predel, in *B-Ba-C-Zr*, Springer-Verlag, Berlin/Heidelberg **1992**, p. 1.
- [50] K. M. Tripathi, T. Y. Kim, D. Losic, T. T. Tung, *Carbon* **2016**, *110*, 97.
- [51] H. Wang, S. Delacroix, O. Osswald, M. Anderson, T. Heil, E. Lepre, N. Lopez-Salas, R. B. Kaner, B. Smarsly, V. Strauss, *Carbon* **2021**, *176*, 500.
- [52] D. Zhang, A. Liu, H. Chang, B. Xia, *RSC Adv.* **2015**, *5*, 3016.
- [53] P. Sun, Y. Cai, S. Du, X. Xu, L. You, J. Ma, F. Liu, X. Liang, Y. Sun, G. Lu, *Sens. Actuators, B* **2013**, *182*, 336.
- [54] F. Liu, X. Chu, Y. Dong, W. Zhang, W. Sun, L. Shen, *Sens. Actuators, B* **2013**, *188*, 469.
- [55] T. Hussain, M. Sajjad, D. Singh, H. Bae, H. Lee, J. A. Larsson, R. Ahuja, A. Karton, *Carbon* **2020**, *163*, 213.
- [56] S. Shao, H. Wu, S. Wang, Q. Hong, R. Koehn, T. Wu, W.-F. Rao, *J. Mater. Chem. C* **2015**, *3*, 10819.
- [57] H. Liu, Y. Guo, R. Xie, T. Peng, G. Ma, Y. Tang, *Sens. Actuators, B* **2017**, *246*, 164.
- [58] B. Liu, Y. Huang, K. W. Kam, W.-F. Cheung, N. Zhao, B. Zheng, *Biosens. Bioelectron.: X* **2019**, *1*, 100016.
- [59] M. Rodner, D. Puglisi, S. Ekeroth, U. Helmersson, I. Shteplyuk, R. Yakimova, A. Skallberg, K. Uvdal, A. Schütze, J. Eriksson, *Sensors* **2019**, *9*, 918.
- [60] C.-M. Yang, T.-C. Chen, Y.-C. Yang, M. Meyyappan, C.-S. Lai, *Sens. Actuators, B* **2017**, *253*, 77.
- [61] D. J. Buckley, N. C. G. Black, E. G. Castanon, C. Melios, M. Hardman, O. Kazakova, *2D Mater.* **2020**, *7*, 032002.
- [62] A. Di Bartolomeo, *Phys. Rep.* **2016**, *606*, 1.
- [63] S. J. Young, Z. D. Lin, *Microsyst. Technol.* **2018**, *24*, 3973.
- [64] H. W. Hugosson, O. Eriksson, U. Jansson, A. V. Ruban, P. Souvatzis, I. A. Abrikosov, *Surf. Sci.* **2004**, *557*, 243.
- [65] J. R. dos Santos Politi, F. Viñes, J. A. Rodriguez, F. Illas, *Phys. Chem. Chem. Phys.* **2013**, *15*, 12617.
- [66] A. A. Rouse, J. B. Bernhard, E. D. Sosa, D. E. Golden, *Appl. Phys. Lett.* **2000**, *76*, 2583.
- [67] W. S. Su, T. C. Leung, C. T. Chan, *Phys. Rev. B* **2007**, *76*, 235413.
- [68] T. Fabish, M. Hair, *J. Colloid Interface Sci.* **1977**, *62*, 16.
- [69] H. F. Ivey, *Phys. Rev.* **1949**, *76*, 567.
- [70] A. V. Singhal, H. Charaya, I. Lahiri, *Crit. Rev. Solid State Mater. Sci.* **2017**, *42*, 499.
- [71] T. O. Wehling, M. I. Katsnelson, A. I. Lichtenstein, *Chem. Phys. Lett.* **2009**, *476*, 125.
- [72] J. Zhu, M. Cho, Y. Li, I. Cho, J.-H. Suh, D. Del Orbe, Y. Jeong, T.-L. Ren, I. Park, *ACS Appl. Mater. Interfaces* **2019**, *11*, 24386.
- [73] R. Ye, Z. Peng, T. Wang, Y. Xu, J. Zhang, Y. Li, L. G. Nilewski, J. Lin, J. M. Tour, *ACS Nano* **2015**, *9*, 9244.
- [74] J. Zhang, M. Ren, Y. Li, J. M. Tour, *ACS Energy Lett.* **2018**, *3*, 677.
- [75] M. Ren, J. Zhang, J. M. Tour, *ACS Appl. Energy Mater.* **2019**, *2*, 1460.
- [76] J. Zhang, C. Zhang, J. Sha, H. Fei, Y. Li, J. M. Tour, *ACS Appl. Mater. Interfaces* **2017**, *9*, 26840.
- [77] Z. Ansari, S. Ansari, T. Ko, J.-H. Oh, *Sens. Actuators, B* **2002**, *87*, 105.
- [78] F. Lu, Y. Liu, M. Dong, X. Wang, *Sens. Actuators, B* **2000**, *66*, 225.
- [79] C. Xu, J. Tamaki, N. Miura, N. Yamazoe, *Sens. Actuators, B* **1991**, *3*, 147.

ADVANCED FUNCTIONAL MATERIALS

Supporting Information

for *Adv. Funct. Mater.*, DOI: 10.1002/adfm.202104061

In Situ Synthesis of Molybdenum Carbide Nanoparticles
Incorporated into Laser-Patterned Nitrogen-Doped
Carbon for Room Temperature VOC Sensing

*Huize Wang, Simon Delacroix, Anna Zieleniewska, Jing
Hou, Nadezda V. Tarakina, Daniel Cruz, Iver Lauermann,
Andrew J. Ferguson, Jeffrey L. Blackburn, and Volker
Strauss**

Supporting Information to

**In Situ Synthesis of Molybdenum Carbide Nanoparticles Incorporated
into Laser-Patterned Nitrogen-doped Carbon for Room Temperature
VOC Sensing**

Huize Wang^{1,§}, Simon Delacroix^{1,§}, Anna Zieleniewska³, Jing Hou¹, Nadezda V. Tarakina¹, Daniel Cruz^{4,5}, Iver Lauer mann⁶, Andrew J. Ferguson³, Jeffrey L. Blackburn³, Volker Strauss^{1,*}

Carbon Network-Forming Agents (CNFA)	24
Laser-patterned nitrogen-doped carbon (LP-NC)	25
LP-NC + sodium iodide	26
Molybdenum carbide impregnated LP-NC (LP-MoC_{1-x}@NC)	27

Carbon Network-Forming Agents (CNFA)

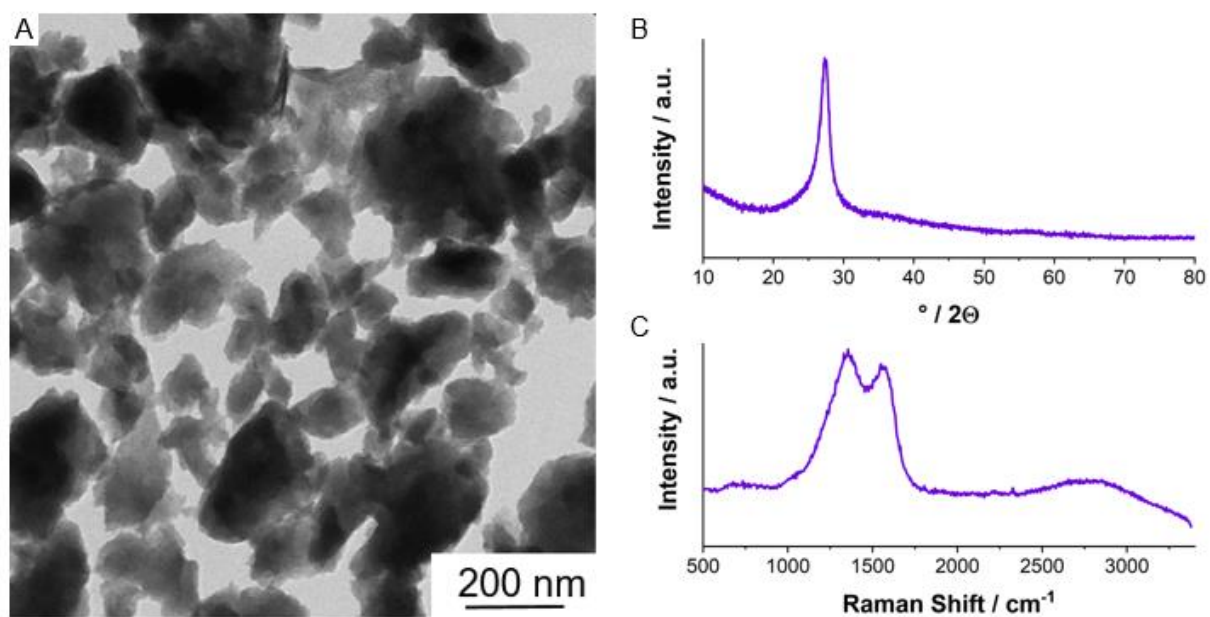


Figure S1. A) Transmission electron micrograph of CA/U(300) deposited from a dispersion in H₂O; B) X-ray diffraction pattern of CA/U(300); C) Raman pattern of CA/U(300) upon excitation at 532 nm.

Table S1. Elemental compositions of the precursors obtained by elemental combustion analysis and inductively coupled plasma mass spectrometry

	C (wt%)	N (wt%)	H (wt%)	O (wt%)	Mo (wt%)
LP-NC (precursor)	47	19	3.1	31	
LP-MoC _{1-x} @NC (precursor)	49	16	3.5	27	4.3

Laser-patterned nitrogen-doped carbon (LP-NC)

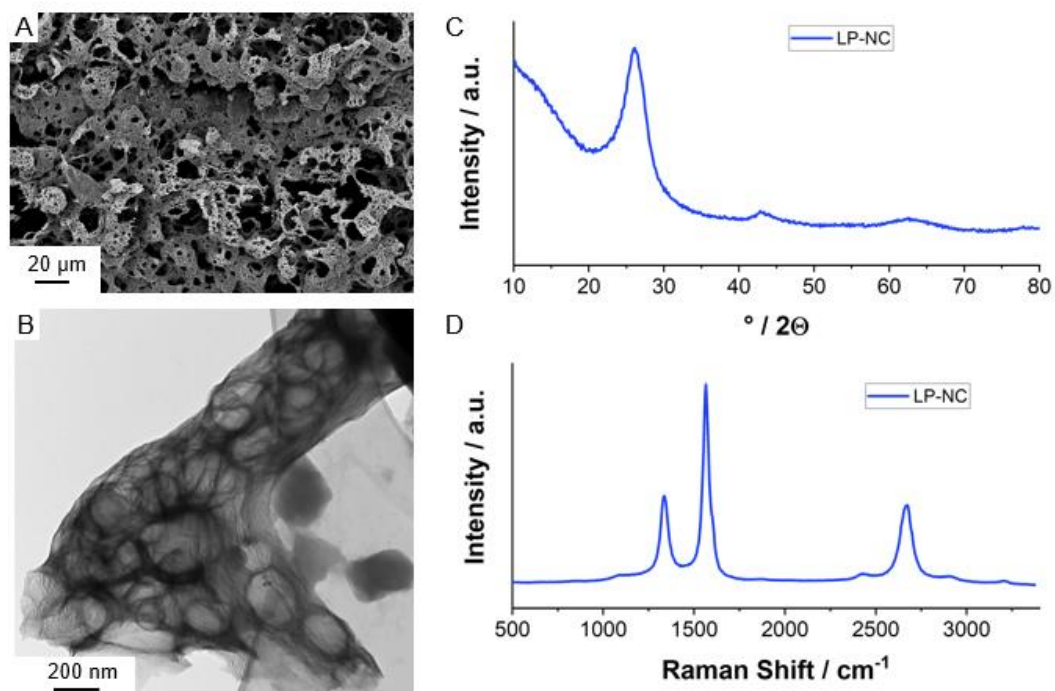


Figure S2. A) Top-view scanning electron micrograph of LP-NC; B) Transmission electron micrograph of a fragment of LP-NC. C) X-ray powder diffraction patterns of LP-NC; D) Raman spectrum of LP-NC obtained upon excitation at 532 nm.

LP-NC + sodium iodide

Table S2. Comparative list of the specific surface areas of different N-doped carbons* obtained by BET sorption measurements and the MB adsorption method.**

	C/N ratio	BET surface area	MB surface area
activated carbon	∞	1672	1269
C8NZ	3.1	1834	497
C8LZ	5.7	1701	358
A8LK	2.1	389	71
LP-NC	5.2		238

* Bulk samples of the listed N-doped carbons were obtained from pyrolysis of nitrogen-rich precursors (internal compounds, not yet published).

** In contrast to the BET sorption method, the MB adsorption method is a liquid based method for the determination of the specific surface areas of small amounts of carbonaceous materials (< 1 mg) and allows only limited conclusions on absolute values, but good estimations on relative values. The accessibility of micropores is generally different in the gas and the liquid phase.

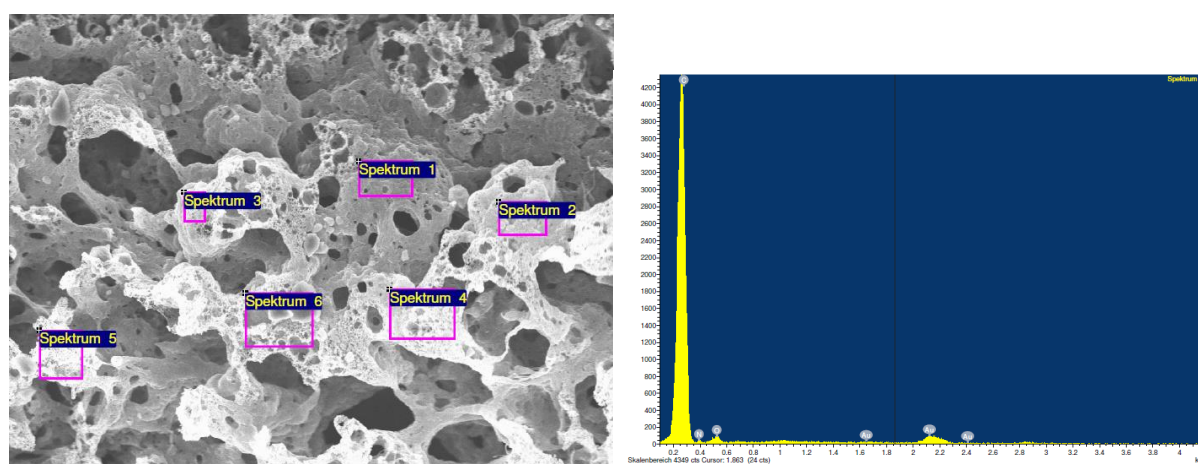


Figure S3. Energy-dispersive X-ray analysis of LP-NC film produced with 40 wt% NaI. Au-impurities originate from the substrate. No sodium was detected ($K\alpha$ of sodium has an energy of 1.041 keV)

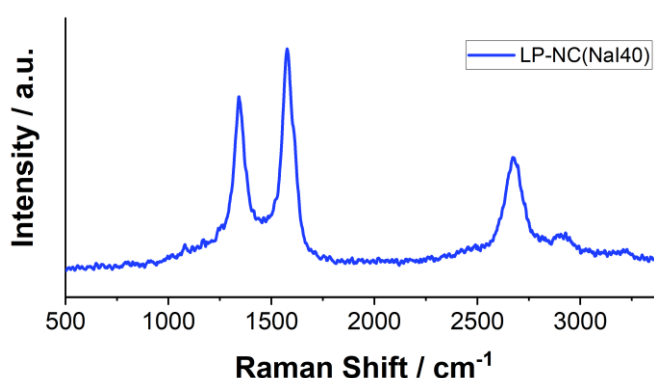


Figure S4. Raman spectrum of LP-NC film produced with 40 wt% NaI obtained upon excitation at 532 nm.

Molybdenum carbide impregnated LP-NC ($\text{LP-MoC}_{1-x}\text{@NC}$)

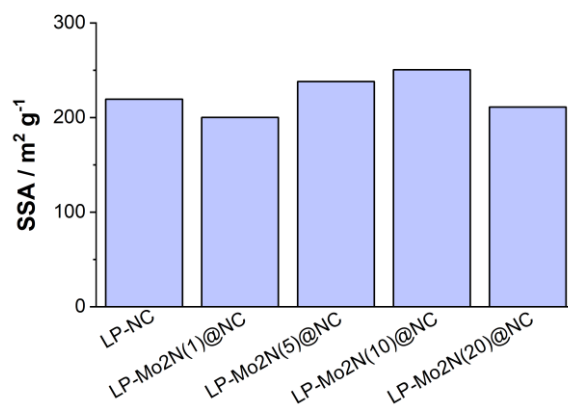


Figure S5. Specific surface areas of $\text{LP-MoC}_{1-x}\text{@NC}$ s obtained with different amounts of AHM in the precursor ink.

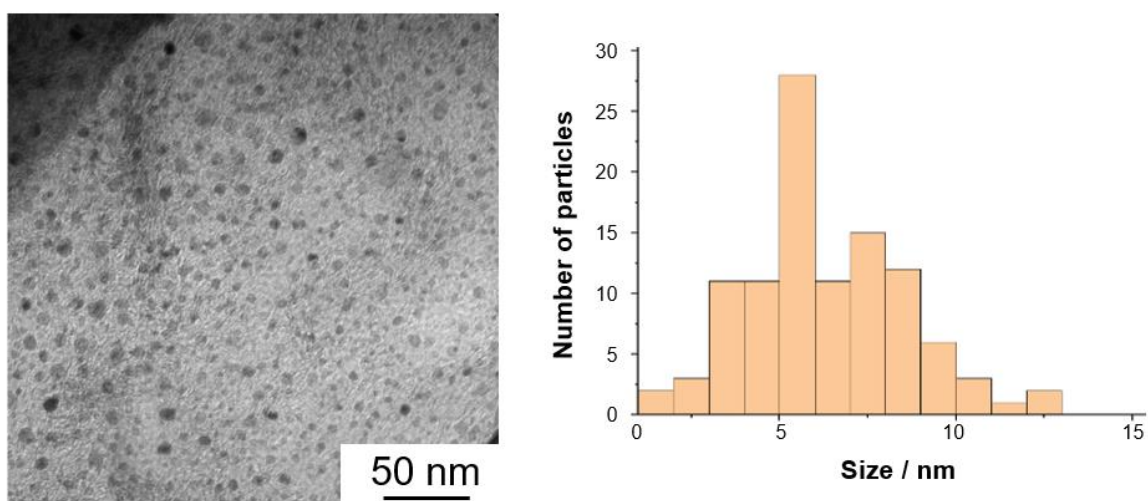


Figure S6. A) Transmission electron micrograph of $\text{LP-MoC}_{1-x}\text{@NC}$; B) Size distribution histogram of the diameters of the MoC_{1-x} nanoparticles (100 particles).

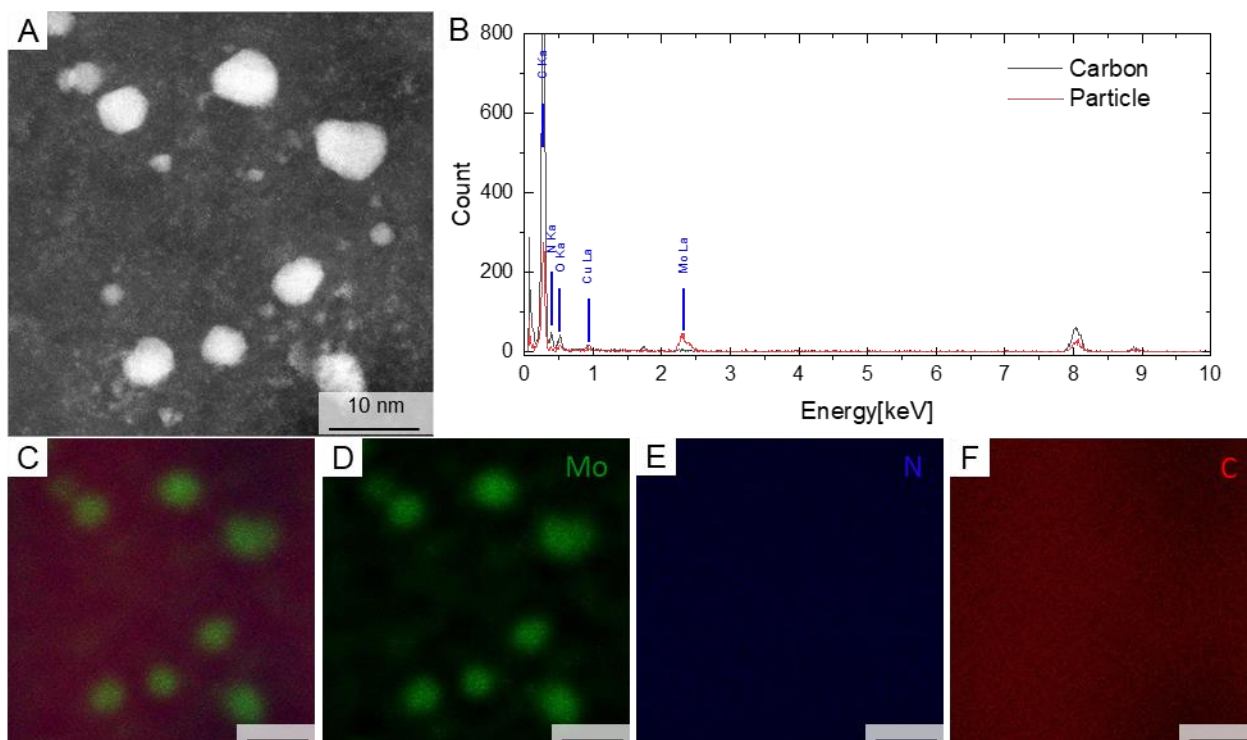


Figure S7. A) ADF-STEM image of $LP-MoC_{1-x}@NC(NaI40)$. B) EDX spectrum of the carbon substrate (grey) and the particle (red) regions in (A). C) The overlap of elemental mapping over region (A). Elemental mapping of (D) Mo (green), (E) N (blue) and (F) C (red). The scale bar is 10 nm.

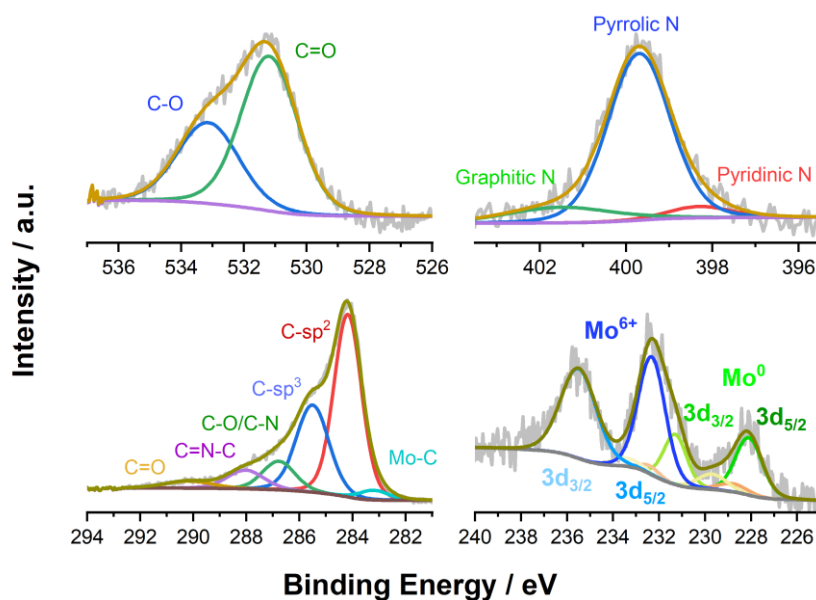


Figure S8. X-ray photoelectron spectra of the O_{1s} , N_{1s} , C_{1s} , and Mo_{3d} regions (from top left to bottom right) of $LP-MoC_{1-x}(10)@NC$. The strong $C-sp^3$ and $C-O/C-N$ signals are attributed to adventitious carbon.

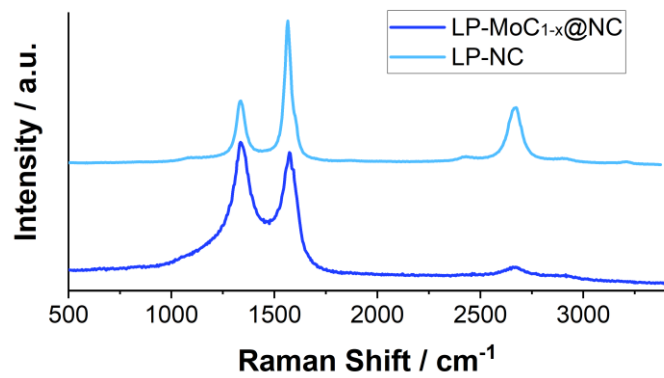


Figure S9. Raman spectra of LP-NC and LP-MoC_{1-x}(10)@NC upon excitation at 532 nm.

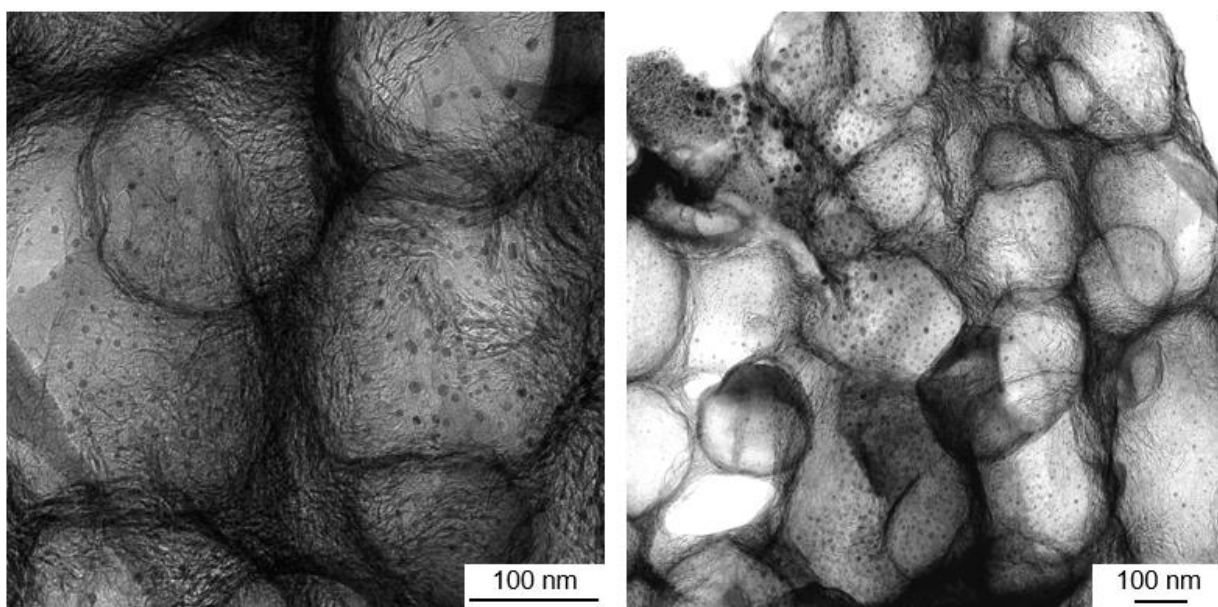


Figure S10. Transmission electron micrographs of LP-MoC_{1-x}@NC(Na140).

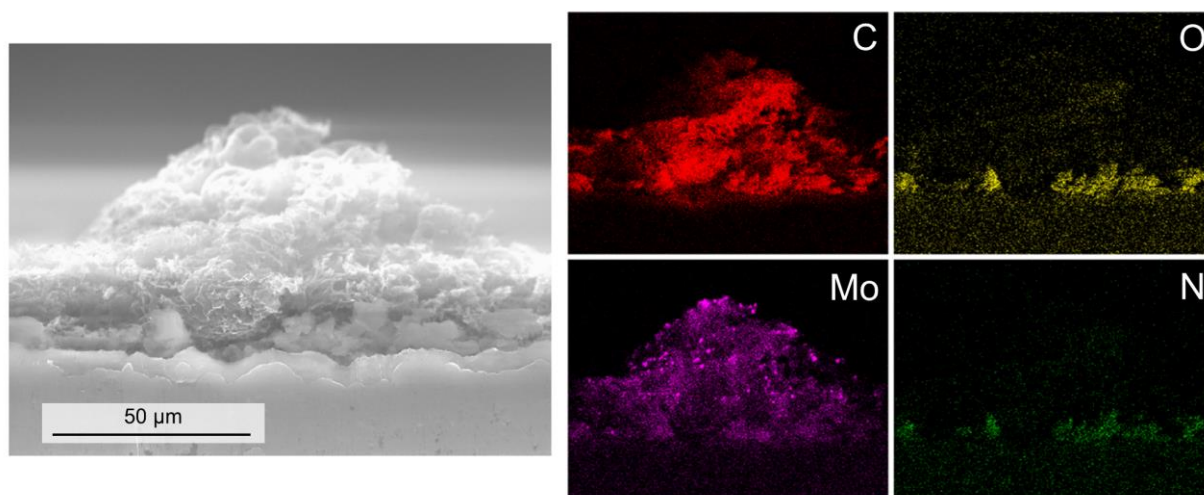


Figure S11. Cross-sectional SEM and EDX analysis of $LP-MoC_{1-x}@NC(NaI40)$ on an aluminium sheet.

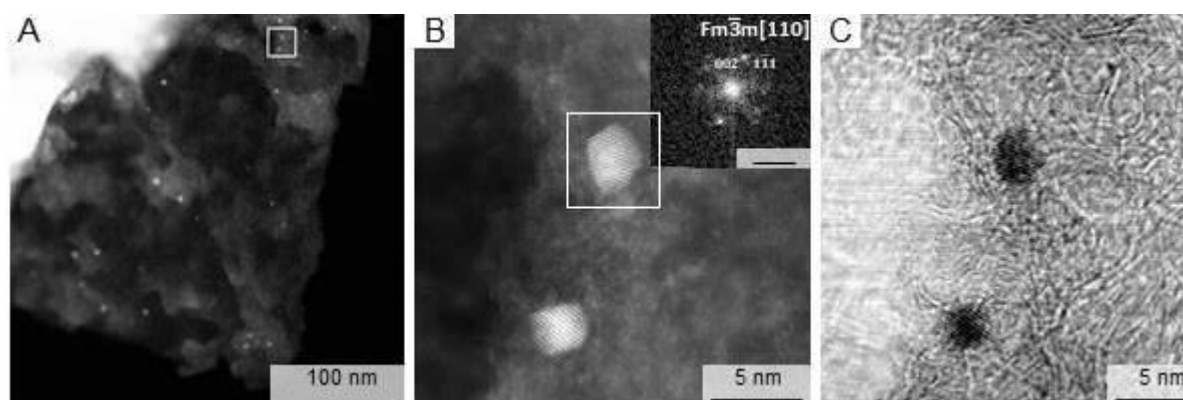


Figure S12. (a) ADF-STEM image of $LP-MoC_{1-x}@NC(NaI40)$. (b-c) ADF and BF STEM images of the region indicated by the grey square in (a). The inserted FFT from the selected particle in (b) is indexed in a cubic unit cell, $a = 4.15(4)\text{\AA}$. The scale bar is 5 nm-1.

Table S3. Comparative list of the electronic features obtained by Hall measurements.

Sample	Mobility / $\text{cm}^2 \cdot (\text{V} \cdot \text{s})^{-1}$	Charge carrier density / cm^{-3}	Hall coefficient / $\text{cm}^3 \cdot \text{C}^{-1}$
LP-NC	0.12	7.70×10^{19}	+0.099
LP-NC(NaI40)	0.23	3.68×10^{19}	+0.19
LP- $MoC_{1-x}(10)@NC$	1.42	1.96×10^{19}	+0.32
LP- $MoC_{1-x}(10)@NC(NaI40)$	4.35	2.34×10^{18}	+2.67

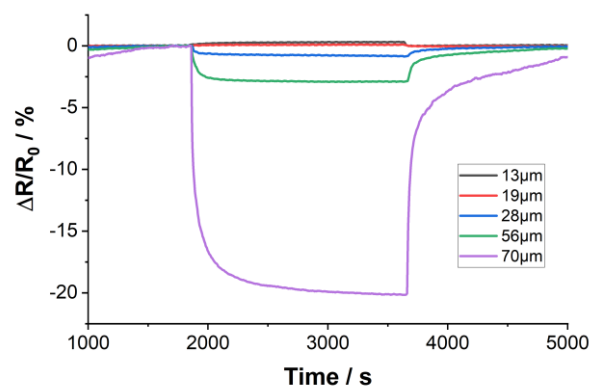


Figure S12. Resistive response of $LP\text{-}MoC_{1-x}@NC(NaI40)$ films of different thickness ranging between 13 and 70 μm .

Laser-Patterned Porous Carbon/ZnO Nanostructure Composites for Selective Room-Temperature Sensing of Volatile Organic Compounds

Huize Wang, Pablo Jiménez-Calvo, Marco Hepp, Mark Andrew Isaacs, Charles Otieno Ogolla, Ines Below-Lutz, Benjamin Butz, and Volker Strauss*



Cite This: *ACS Appl. Nano Mater.* 2023, 6, 966–975



Read Online

ACCESS |



Metrics & More



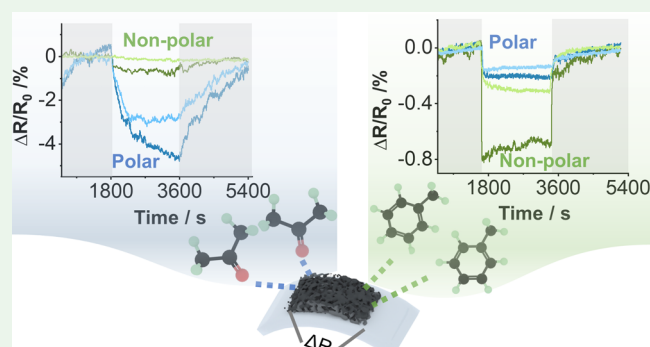
Article Recommendations



Supporting Information

ABSTRACT: The development of mobile, noninvasive, and portable sensor technologies for diagnostics and emission control is highly demanded. For that purpose, laser carbonization is studied as a tool to produce responsive carbon materials from inexpensive organic precursors for the room-temperature selective detection of volatile organic compounds (VOCs) applicable in future sensor array-based devices. To increase the response of intrinsically low-responsive laser-patterned carbons (LP-C) to analytes in the gas phase, we tested carbonization in the presence of nanoscale ZnO precursors in primary inks. Following the addition of a zinc salt, $\text{Zn}(\text{NO}_3)_2$, a noticeable 43-fold increase in the sensor response ($\Delta R/R_0 = -21.5\%$ toward 2.5% acetone) was achieved. This effect is explained by a significant increase in the measurable surface area up to $\sim 700 \text{ m}^2 \cdot \text{g}^{-1}$ due to the carbothermic reduction supported by the in situ formation of ZnO nanoparticles. Varying Zn concentrations or the addition of as-prepared ZnO nanorods lead to different surface properties like the surface area, porosity, and polarity of LP-C. A predominant effect of the surface polarity on the selectivity toward different analytes of the sensors during physisorption, e.g., acetone vs toluene, was identified and tested. The best-performing LP-C sensors were finely characterized by transmission/scanning electron microscopies and X-ray photoelectron/energy-dispersive X-ray/Raman spectroscopies.

KEYWORDS: carbon laser patterning, laser carbonization, carbon/zinc oxide nanocomposites, VOC sensing, carbonization, chemiresistor, chemisensor



INTRODUCTION

Volatile organic compounds (VOCs) are human-made contaminants in indoor environments as well as indicators for diseases.¹ Instruments for precise VOC concentration monitoring are in high demand, first for identification and second for preventing diseases.^{2,3} For example, diabetes can be prevented in time by detecting acetone in exhaled breath.^{4,5} Among the conventional methods for gastrointestinal disease diagnosis are colonoscopies, tissue biopsies, or antimicrobial swab cultures.⁶ All of these techniques present the same drawbacks of being (semi-)invasive, time-consuming, expensive, and not scalable and requiring sophisticated chemical analysis instruments. On the other hand, indoor air quality control (hospitals) is an important analysis, typically conducted by certified large-scale chamber testing facilities (EN 16516). General physical analysis methods that can perform indoor gas detection include gas-chromatography, mass spectrometry, quartz-crystal microbalance, or Fourier transform infrared spectroscopy (FT-IR) spectroscopy, while

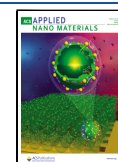
physicochemical methods include mainly the use of electrochemical cells.⁷

For these reasons, mobile noninvasive chemical detection methods toward VOCs are promising for substituting the conventional complicated methods.⁸ With the rapid development of artificial intelligence (AI) and machine learning algorithms, small-scale sensor array technologies have again moved into the focus of attention as a tool for the realization of electronic noses.^{9,10} First mobile commercial products based on sophisticated nanotechnology are currently in the final phase of development.¹¹ Typical materials used for the selective detection of VOCs are metal oxide-based semiconductors,¹² nonviable for long term due to their low

Received: October 4, 2022

Accepted: December 28, 2022

Published: January 17, 2023



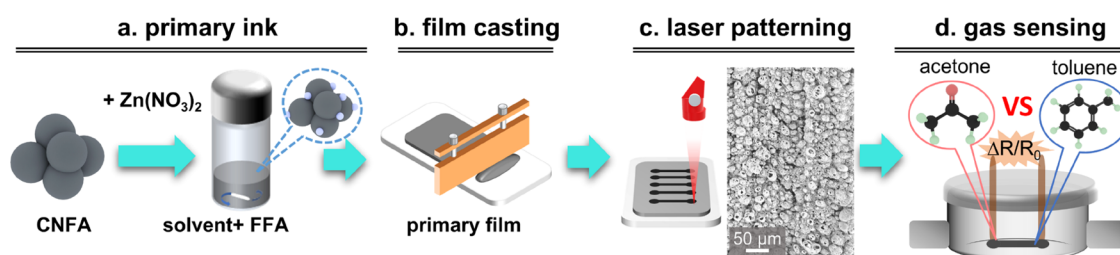


Figure 1. Illustration of the preparation process of the LP-C/Zn films and their characterization in a resistive gas sensing setup: (a) preparation of the primary ink; (b) film casting on the flexible PET substrate; (c) carbon laser patterning of the primary film and a representative SEM image of the resulting LP-C film; (d) electrochemical gas sensing cell used to characterize the resistive response of the LP-C sensor platforms in different gases inside the chamber.

abundancy, high cost of the raw material, and stability issues over time.¹³ Operation temperatures of 200–400 °C make these materials highly sensitive; also, the associated devices are high energy-consuming and expensive. Alternative materials, such as carbon nanotubes and nanoparticle composites, are promising for room-temperature detection of VOCs; however, those typically come along with high production costs.¹⁴

New functional materials, such as hierarchical porous carbons, constitute interesting alternatives for utilization in everyday use or disposable sensor arrays.^{15–17} Such porous carbon materials are usually prepared by the templated pyrolysis of organic precursors, incorporating functional active sites for enhancing selective analytes' interactions.¹⁸ Major challenges that need to be tackled to prepare efficient porous carbon materials applicable for sensors are sensitivity, selectivity, stability, scalability, and flexibility.^{19,20}

With modern laser pyrolysis, non-crude oil-based molecular precursors can be converted into conductive carbonized materials in the form of patterns on different substrates.^{21–24} The resulting porous structures and their tunable conductivity makes these laser-patterned carbons (LP-C) interesting as active materials in resistive gas sensors.^{25–33} This process avoids the inherent difficulties of processing carbonized materials into flexible conductive films and provides a scalable method for the production of stable resistive sensors. In particular, the possibility of tuning the properties of the carbons by simple modification of the primary ink formulas has demonstrated a significant enhancement of the sensitivity of LP-C.³⁴ That makes this process generally interesting for commercial applications.

Here, we report a simple method to incorporate selectivity elements into LP-Cs for tuning the surface properties of the LP-C sensing material, thereby for the selective detection of VOCs. Upon the addition of minor amounts of zinc nitrate ($\text{Zn}(\text{NO}_3)_2$) as a precursor, small ZnO nanoparticles are formed in situ during laser carbonization. The role of zinc oxide (ZnO) as an intermediary nanoscale porogen and graphitization agent has already been reported and successfully proven to increase the active surface area of porous carbon.^{35–37} The high process temperatures in the upper layers support the direct evaporation of Zn formed during $\text{Zn}^+ \rightarrow \text{ZnO} \rightarrow \text{Zn}$ driven by the carbothermic reduction. In addition, we observe a variation in the surface relative to the Zn concentration. The concentration-dependent distribution of these graphitized domains and the increased surface area support the selectivity toward different VOCs. Moreover, the direct addition of readily prepared ZnO nanorods as a precursor leads to the formation of larger graphitic domains, supported by Raman spectroscopy, facilitating the preferential

detection of VOCs that presumably adsorb to extended π -surfaces.

RESULTS AND DISCUSSION

Carbon laser patterning was performed according to a previously described protocol with several modifications.³⁴ A citric acid/urea-based carbon network-forming agent (CNFA) was thoroughly mixed with a film-forming agent (FFA) containing the solvent (ethylene glycol) and different amounts of $\text{Zn}(\text{NO}_3)_2$ were added (Figure 1a). The resulting viscous inks were doctor-bladed on PET substrates and dried to obtain films with a mean thickness of ca. 40 μm (Figure 1b). The films containing different amounts of $\text{Zn}(\text{NO}_3)_2$ are referred to as LP-C/Zn(1–8), with the number indicating the mass percentage of Zn with respect to the mass of CNFA (Table 1). The energy-dispersive X-ray analysis of the top-view primary films shows a homogeneous distribution of the zinc salt (Figure S1).

Table 1. Composition of the Investigated Samples

sample	CA/ U(300) (mg)	$\text{Zn}(\text{NO}_3)_2 \cdot 6$ H_2O (mg)	ZnO nanorods (mg)	effective m_{Zn} (wt %)
LP-C/Zn(0)	200	0		0%
LP-C/Zn(1)	200	10		1%
LP-C/Zn(2)	200	20		2%
LP-C/Zn(4)	200	40		4%
LP-C/Zn(5)	200	60		5%
LP-C/Zn(6)	200	80		6%
LP-C/Zn(7)	200	100		7%
LP-C/Zn(8)	200	120		8%
LP-C/ZnO(2)	200		5	2%
LP-C/ZnO(7)	200		20	7%

Resistive patterns with dimensions of 5 × 0.5 mm were imprinted onto the films with a high-precision CO₂-laser engraver (see the Experimental Section). The laser parameters, i.e., scanning speed and power, were optimized to achieve a high degree of carbonization and high reproducibility in terms of conductivity. After laser patterning, the unexposed precursor film was rinsed off with H₂O. Subsequently, the sensor strips LP-C/Zn were tested as resistive sensor platforms to detect acetone and toluene at room temperature in a gas-flow cell (Figure 1d).

The topographical scanning electron microscopy (SEM) analyses of the LP-C/Zn films show a spore-like morphology for all zinc-containing samples (Figure S2). In contrast, the reference LP-C/Zn(0) is characterized by open hierarchical

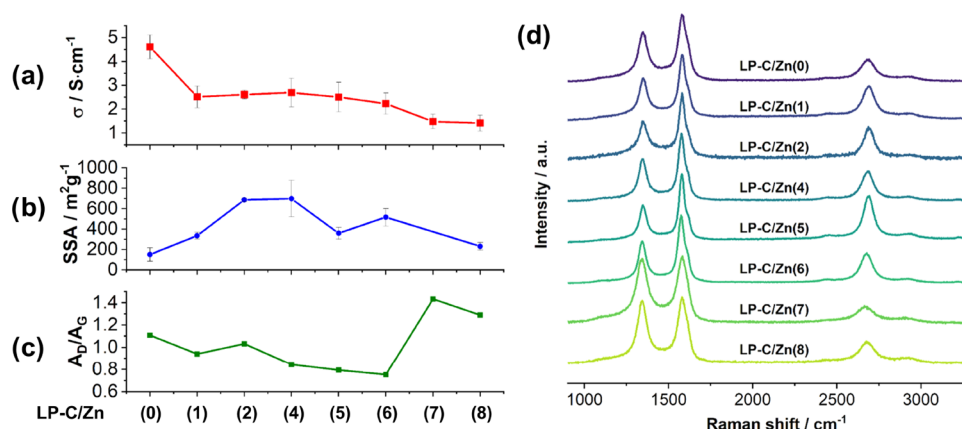


Figure 2. (a) Plot of sheet conductivity and (b) specific surface areas determined by the methylene blue adsorption method of the LP-C/Zn films; (c) A_D/A_G (area of the peak) ratio of LP-C/Zn films in the Raman spectra; (d) top-view Raman spectra of the LP-C/Zn films obtained with an excitation wavelength of 532 nm.

porous morphology (Figure S2). Notably, the spore-like character of the LP-C/Zn films is more pronounced for higher Zn concentrations (Figure S3).

A crucial property of resistive sensors is their conductivity. First, we tested the impact of the addition of zinc salt on the conductivity of the LP-C/Zn films by measuring the resistances of 30 sensor films of each as-prepared composite. A mean thickness of 40 μm was assumed for the determination of the sheet conductivity.³⁸ As shown in Figure 2a, the conductivity drops from 4.6 in reference to 2.5 $S \cdot cm^{-1}$ at 1 wt % Zn (LP-C/Zn(1)). Up to a concentration of 6 wt % Zn (LP-C/Zn(6)), the conductivity is on the same order, while another drop in conductivity to 1.4 $S \cdot cm^{-1}$ is observed at concentrations >7 wt % of Zn. Notably, at concentrations >8 wt %, the films tend to crack upon drying and eventually delaminate during the laser process. This quasilinear conductivity trend may be explained by the different factors that influence porous carbon materials: grain boundaries, particle sizes, atomic arrangement, and wettability, among others.³⁹

The zinc salt is added with the intention of increasing the specific surface area (SSA) of LP-C by exploiting the carbothermic reduction of in situ-generated ZnO nanoparticles.³⁷ Due to the low mass density of the films, the characterization of the SSA using quantitative gas sorption techniques is intricate. Therefore, we utilized the methylene blue (MB) adsorption method to obtain insights into the evolution of the SSAs. It is noteworthy that the MB adsorption method is a liquid-based method and gives only indications about trends as it typically gives lower SSA values for nitrogen-containing carbons.³⁴ Moreover, potentially existing micropores are not accessible with this measurement method. However, the trend shows unambiguously higher SSAs upon the addition of zinc salt to the precursor films. The highest value is reached for a concentration of 4 wt % of Zn (LP-C/Zn(4)) with $\sim 700 m^2 \cdot g^{-1}$ (Figure 2b). For higher zinc concentrations, the SSAs decrease steadily.

Raman spectra of the LP-C/Zn and LP-C/ZnO series (Figures 2c,d and S4) exhibited an interesting top-layer analysis, complementing structural observations and correlated trends. All samples show features of a highly carbonized material with pronounced D- and G-bands at 1348 and 1578 cm^{-1} , respectively. Minor contributions from disordered and amorphous carbon at 1200 and 1470 cm^{-1} , designated as D4

and D3, were also observed and considered in the fittings.^{40,41}

A clear trend toward high graphitization with lower defect density is observed as the A_D/A_G ratio reduces from 1.1 to 0.75 between LP-C/Zn(0) and LP-C/Zn(6) (Figure 2c). This is concomitant with a decrease in the peak width of the 2D band at 2670 cm^{-1} , which indicates a higher stacking order of the graphite planes.⁴² It is noteworthy that the Raman spectra were recorded at the surface of the films and are not ideally representative of the entire material. Due to the porous surface structure of laser-carbonized samples, the overall Raman spectroscopy characterization of PET film samples is challenging.

The general occurrence of a structural and chemical gradient in laser-carbonized materials prompted us to perform a cross-sectional transmission electron microscopy (TEM) analysis of the best-performing sensor films, LP-C/Zn(5). To this end, the porous LP-C/Zn(5) sensor films were infiltrated and embedded in an epoxy resin and cut with a microtome into thin slices of ~ 50 nm thickness.³⁸ An optical micrograph of the block face is presented in Figure 3a. Across the entire section, the films show a distinct porosity with visible pore sizes on the order of 5–10 μm represented in the scanning electron micrograph in Figure 3b.

The area in Figure 3b was further analyzed by energy-dispersive X-ray (EDX) analysis to obtain an overview of the chemical composition across the film. As demonstrated in previous studies, due to the direct exposure to the laser beam, the upper layer consists of porous turbostratic graphite with a highly crystalline structure (Figure 3c–e) and it is free of Zn.³⁸ In the lower layers, significant amounts of Zn were detected (Figure 3b). Scanning transmission electron microscopy–electron energy-loss spectroscopy (STEM-EELS) further confirmed the clear chemical and structural delineation between the highly graphitized top layer and the Zn/N-containing bottom layer (Figure 3c, right).

Depth-dependent laser thermal material conversion was evident based on the presence of highly ordered graphitic structures in the upper layer and ZnO in the lower part of the sensor, as detailed by the high-resolution TEM (HRTEM) images and the corresponding selected-area electron diffraction (SAED) patterns (Figure 3d–f).

These observations were corroborated by X-ray photoelectron spectroscopy (XPS) (Figure S5 and S6). In the C_{1s} energy region, the main peak at 284.4 eV is attributed to sp^2 -

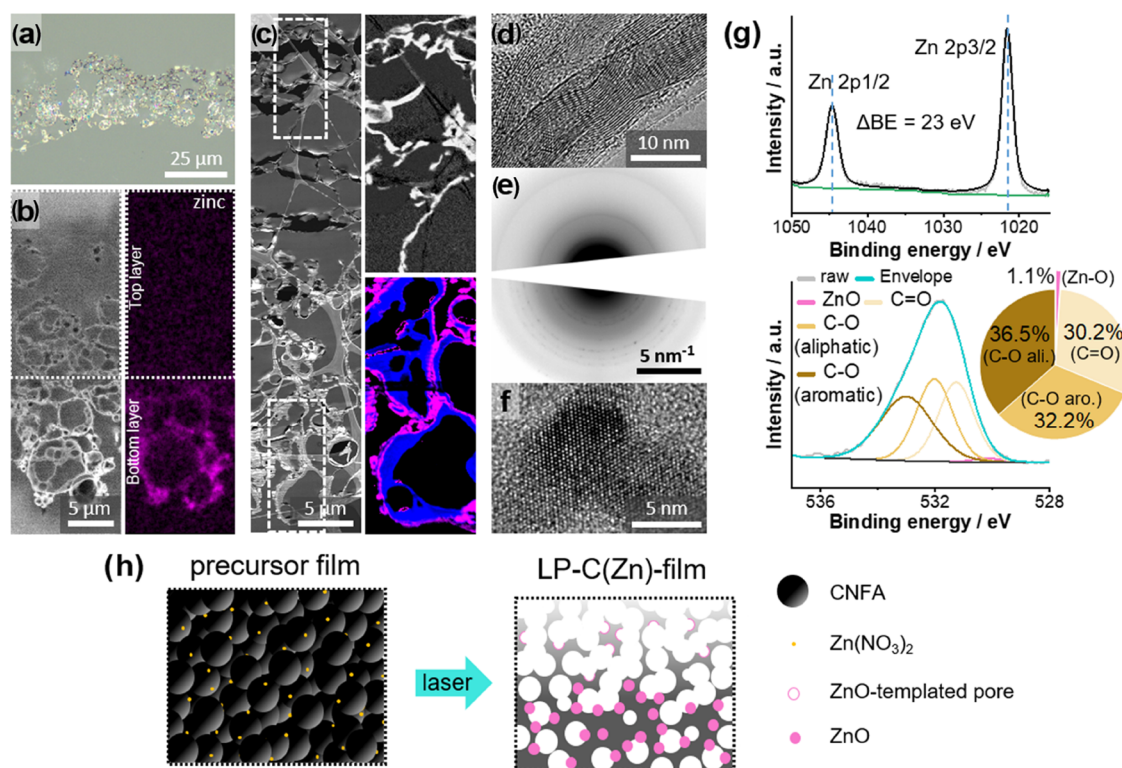


Figure 3. (a) Cross-sectional optical micrograph of LP-C/Zn(5); (b) cross-sectional backscatter SEM micrograph with a correlated qualitative EDX element map of zinc (net intensities displayed); (c) cross-sectional TEM analyses of the sensor film: (left) the representative high-angle annular dark-field (HAADF)-STEM micrograph with unfiltered regions (black), epoxy resin (dark gray), and lacey TEM support film (light gray), (top right) graphitized carbon component in the upper layer identified by principle component analysis (PCA), (bottom right) N (blue) and Zn (purple) distribution in the bottom layer of the sensor; (d) exemplary HRTEM image of graphitized carbon in the upper layer; (e) combined SAED pattern of graphitic domains in the top layer and ZnO in the bottom layer (logarithmic display); (f) exemplary HRTEM image of the ZnO nanoparticle in the lower layer; (g) XPS analysis of the LP-C/Zn(5) film surface: the XPS Zn 2p region (upper panel) and O 1s region with percentual peak distribution (lower panel); (h) proposed formation mechanism of the LP-C/Zn composite structure. Zn(NO₃)₂ is distributed among the CNFA particles in the precursor films. After laser carbonization, the in situ-generated ZnO nanoparticles catalyze the pore formation in the upper layer and remain in the lower layer.

carbon; the other minor peaks at 285.2, 286.0, 287.5, and 289.1 eV correspond to sp³-carbon, C–N/C–O, C=N/C=O, and COOH, respectively. The N_{1s} region of the laser-carbonized films (LP-C/Zn(*x*)) was deconvoluted into three individual peaks maximizing at 399.0, 400.0, and 401.4 eV corresponding to pyridinic, pyrrolic, and graphitic nitrogen, respectively. For the primary films C/Zn(*x*), two additional peaks at 402.8 and 406.4 eV originate from NO₃[−] and NO₂[−],⁴³ which are attributed to the addition of Zn(NO₃)₂ into the primary inks. The vanishing of these peaks confirms the decomposition of Zn(NO₃)₂ after laser patterning.

In the Zn_{2p} region (Figure 3g), the two intense peaks centered at binding energies of 1021.5 and 1044.5 eV are attributed to Zn 2p_{3/2} and Zn 2p_{1/2}. The Zn 2p spectra of Zn oxide suffers from an overlap of Zn metal peaks, which makes it difficult to unambiguously determine the chemical state of Zn.^{44,45} Nonetheless, the different binding energy of oxygen in metal oxides compared to organic compounds are reflected in the O_{1s} region⁴⁵ and can be used to identify the variety of ZnO surfaces.⁴⁶ The O_{1s} signal is deconvoluted into four peaks (Figure 3g), three major peaks centered at 531.2, 532.1, and 533.0 eV assigned to C=O, C–O (aliphatic), and C–O (aromatic),⁴⁷ respectively, along with a 0.8% peak contribution at 530.2 eV assigned to Zn–O.⁴⁶

These results demonstrate the function of nanosized ZnO as a pore templating agent in the upper layers of the film during

laser carbonization. The ZnO hard-templating effect based on the carbothermic reduction at different temperature stages occurs in situ within the time frame of milliseconds in a one-step process. As Figure 3h shows, the homogeneously distributed zinc salt (Zn(NO₃)₂) in the primary films forms ZnO nanoparticles upon elevating the reaction temperature during laser carbonization. When the laser-induced temperature reaches ~670 °C, ZnO is reduced to Zn according to the carbothermic reduction mechanism, during which carbon is oxidized to gaseous monoxide carbon (CO_g).³⁵ Remaining carbon is rearranged and recrystallized and thus forms highly graphitized domains (Figure 3c–e).⁴⁸ At temperatures above the boiling point of zinc (907 °C), liquid zinc evaporates. The high degree of graphitization and the absence of ZnO nanoparticles in the upper layers of the LP-C/Zn film indicate that the reaction temperatures are significantly higher than 907 °C. On the other hand, the presence of considerable amounts of ZnO nanoparticles and the rather amorphous character of carbon in the lower layers indicates lower reaction temperatures below 670 °C. Due to continuous evaporation of the carbaceous matrix in the lower layer under those conditions, surface enrichment as well as the ripening of ZnO occurs (Figure 3c).

The increased SSA and the potential occurrence of ZnO-templated micropores is a great advantage for sensitivity toward the detection of gaseous analytes. We tested the

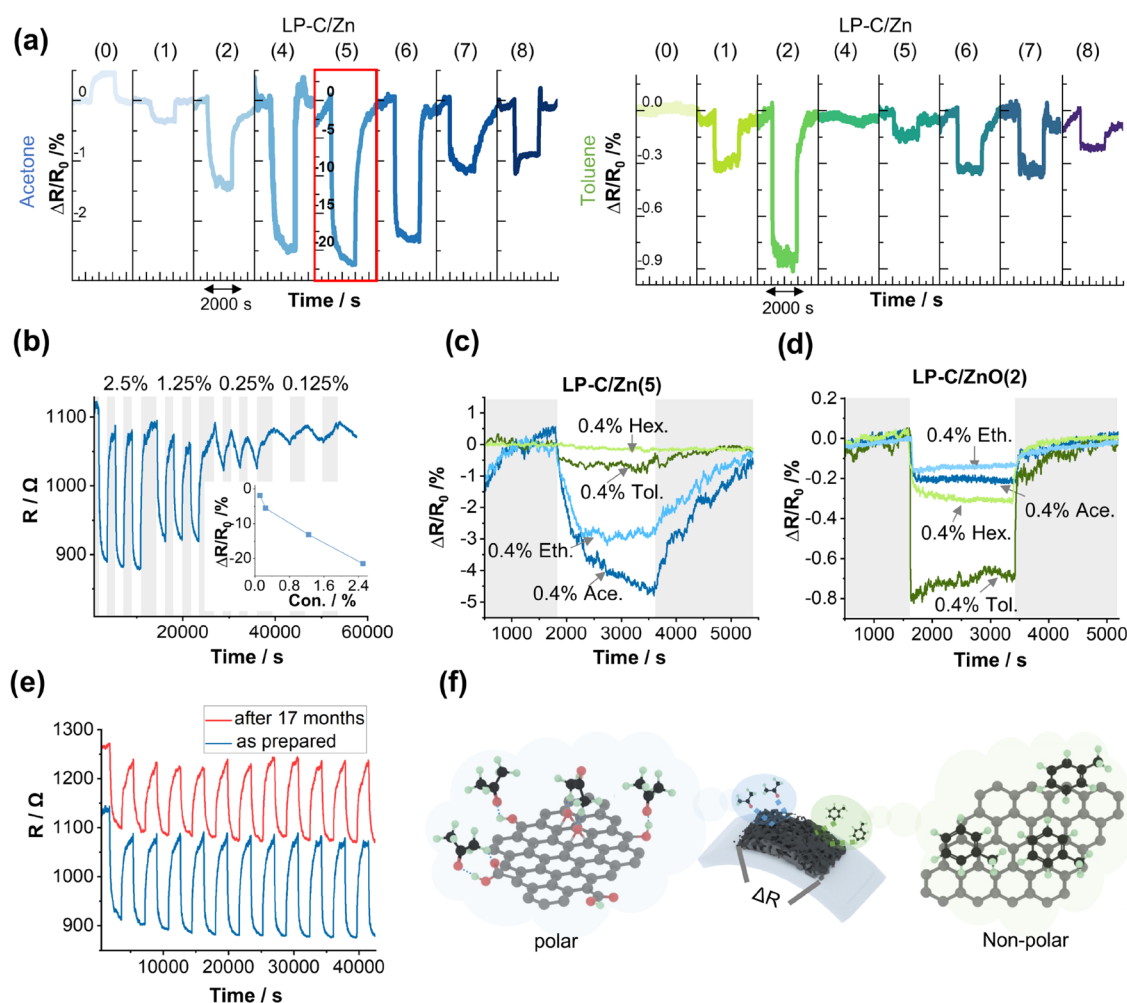


Figure 4. (a) Sensing response of the LP-C/Zn films toward 2.5% acetone (left) and 0.4% toluene (right); (b) resistive response of the LP-C/Zn(5) film toward 2.5, 1.25, 0.25, and 0.125% acetone (inserted is a plot of the sensitivity response $\Delta R/R_0$ vs CO_2 concentration) (gray area: 100% nitrogen sparged, nongray area: contains different concentrations of analytes); (c) resistive response of the LP-C/Zn(5) film toward 0.4% acetone, 0.4% ethanol, 0.4% toluene, and 0.4% hexane; (d) resistive response of the LP-C/ZnO(2) film toward 0.4% acetone, 0.4% ethanol, 0.4% toluene, and 0.4% hexane; (e) resistive response of LP-C/Zn(5) after 17 months toward 2.5% acetone in comparison to a freshly prepared sensor platform; (f) illustration of the adsorption mechanism of polar (acetone) and nonpolar (toluene) analytes to polar (oxygenated) or nonpolar (π -conjugated) surfaces.

resistive response of each sensor composite film toward the exposure of representative polar and nonpolar VOCs, namely, acetone and toluene.⁴⁹ Figure 4a,b shows the response of each sensor film with different Zn content toward the test analytes. All samples, except for the reference without Zn, show a clear negative response upon exposure to acetone. The response to acetone rises with the Zn content and reaches a peak for the sample with 5 wt % of Zn (LP-C/Zn(5), e.g., $\Delta R/R_0 = -21.5\%$ at 2.5% acetone). In comparison to the samples with slightly less or more Zn, LP-C/Zn(4) and LP-C/Zn(6), the response is drastically low by one order of magnitude. Also, the response toward the nonpolar analyte, toluene, is enhanced in the zinc-containing films, although the trends are not as clear in this case. In fact, the reference film free of zinc shows no response toward toluene whatsoever. The highest response of $\Delta R/R_0 = -0.9\%$ to the exposure of 0.4% toluene is observed for LP-C/Zn(2). Samples LP-C/Zn(4) and (5) give lower specific responses for toluene and again LP-C/Zn(6) gives a decent response. The drastic increase in the response at LP-C/Zn(5) is likely due to the formation of high amounts of micropores in this concentration regime.

The response depends on the analyte concentration, as shown in Figure 4b. A reasonable response of $\Delta R/R_0 = -1.9\%$ at relatively low analyte concentrations of 0.125% (1250 ppm) acetone is detected. With regard to selectivity, the sample LP-C/Zn(5) shows the highest affinity and selectivity to polar VOCs, e.g., $\Delta R/R_0 = -4.7\%$ at 0.4% acetone and $\Delta R/R_0 = -3.0\%$ at 0.4% ethanol (Figure 4c), while it shows little response to nonpolar toluene and hexane at the same concentration. This response pattern indicates physisorption based on different binding mechanisms of polar and nonpolar analytes. In addition, in stability testing of up to 24 h, we observed that sensitivity remained nearly constant over time (Figure S13).

In previous works, we demonstrated the polar character of the LP-C surface due to an abundance of oxygen functional groups.²⁵ For polar analytes such as acetone, two physisorption scenarios with polar sites on the surface need to be considered: hydrogen-bonding and van der Waals interactions. Considering that the latter consist of contributions from dipole, induction, and dispersion forces, the adsorption of acetone to the LP-C surface is mostly attributed to dipole–dipole interactions.^{50–52}

For toluene, on the other hand, dispersion forces or π - π stacking are implicit (Figure 4f).^{53,54} Taking these fundamental molecular interactions into consideration, the sorption selectivity in the different samples is attributed to the surface properties of LP-C. Generally, the surface of LP-C is polar and, therefore, sensitive to polar analytes. On the one hand, the hard-templating effect of ZnO nanoparticles promotes the formation of small pores and eventually micropores, which enhances the response toward acetone. On the other hand, the graphitization-catalyzing effect of ZnO during carbothermic reduction promotes the formation of an extended π -surface, which enhances the sensitivity toward toluene.

To demonstrate the feasibility of the suggested mechanism, we also tested the sensing performance of films prepared with presynthesized ZnO nanorods with average sizes of $\sim 2 \mu\text{m}$ as precursors. These sensor films are named LP-C/ZnO(x), with x indicating the mass percentage of Zn in the precursor inks. The rhombus-like ZnO nanorods were randomly distributed in the primary film and underwent the same in situ carbothermic reduction process during laser patterning (Figure S7). Due to their significantly larger size, the ZnO nanorods are expected to support the formation of larger graphitic domains in the upper layers of the LP-C films. Indeed, the SEM images show an open porous but nonsporulated morphology (Figure S8). After the laser patterning process, it can be seen from the EDX mapping analysis (Figure S9) that some of the ZnO nanorods or their debris are still distributed on the surface of the sensor films, but their shapes are enlarged or even broken due to the expansion effect. Regarding the characteristics in terms of graphitization (Figure S10) and electrical conductivity, the two representative samples, LP-C/ZnO(2) and LP-C/ZnO(7), show the same trends as the samples from the LP-C/Zn(x) series. In comparison to the reference LP-C, the conductivity of the LP-C/Zn(x) series decreased (Figure S11). However, we observe a slight increase in conductivity with the amount of ZnO nanorods added. We assume that the enhanced formation of graphitized domains supports electrical conductivity.

In general, for the samples prepared with presynthesized ZnO nanorods, upon laser patterning, the ZnO nanorods in the upper layer are partially reduced to Zn to catalyze the graphitization of surrounding carbon and then evaporate. Parts of the ZnO nanorods accumulate in the intermediate region of the bottom and top layer, whereas particle ripening is hindered in the lowest region due to preoxidation and lower temperatures (Figure S12).

In fact, the sample containing 2 wt % Zn, i.e., LP-C/ZnO(2), shows a significantly higher selectivity toward 0.4% toluene and hexane with a response of $\Delta R/R_0 = -0.8$ and 0.3%, respectively, than to acetone ($\Delta R/R_0 = -0.2\%$ at 0.4% acetone) and ethanol ($\Delta R/R_0 = -0.13\%$ at 0.4% ethanol) (Figure 4d). Furthermore, as shown in Figure S14, LP-C/ZnO(2) shows good stability over time. A reasonable response of $\Delta R/R_0 = 0.14\%$ at a relatively low analyte concentration of 0.4% (400 ppm) toluene is detected.

At last, we tested the long-term stability of the sensor platforms. We stored the sensor film LP-C/Zn(5) under ambient conditions for 17 months and tested it under the same 2.5% acetone. Comparing the freshly prepared sample, the aged sample shows a slightly lower response of $\Delta R/R_0 = -12.7\%$ (Figure 4e). The reduced sensitivity is attributed to the increased base resistance, which may be due to a partial oxidation/degradation of the surface groups on the sensor films.³⁴ Moreover, we tested the sensor films at different

ambient temperatures (Figure S15) and at room temperature (25 °C), which shows the highest resistance response. On the other hand, a stable and fast response, even at an ambient temperature of 60 °C, is observed.

CONCLUSIONS

The carbothermic reduction initiated by the presence of ZnO nanoparticles during laser carbonization was studied. ZnO nanoparticles were generated in situ from $\text{Zn}(\text{NO}_3)_2$ that was added to the primary films. A comprehensive investigation of the chemical composition and microscopic morphology by XPS and cross-sectional HRTEM reveals a heterogeneous gradient profile due to the induced temperature gradient during laser carbonization. Two positive effects were observed: (1) A significant increase in the active surface area due to the hard-templating effect of the ZnO and (2) the catalysis of graphitization around the ZnO nanoparticles. By careful selection of the initial $\text{Zn}(\text{NO}_3)_2$ concentration, the surface structure of LP-C can be tuned in terms of surface properties, predominantly porosity and polarity. Thereby, a drastically enhanced response toward different VOCs was achieved in resistive sensing experiments. Notably, electronic effects on the sensitivity were not specifically tested. At a concentration of 5 wt % Zn, the response toward acetone was increased by 43 \times with respect to the reference ($\Delta R/R_0 = -21.5\%$ at 2.5% acetone), which is attributed to a significantly higher porosity. The surface polarity was considered an important factor. Using presynthesized ZnO nanorods as additives, large graphitic domains were obtained after laser carbonization, which present extended nonpolar π -surfaces as active sites. Thereby, a response with a high selectivity toward toluene ($\Delta R/R_0 = -0.8\%$ at 0.4% toluene) was achieved. The herein-presented advancements in laser carbonization may inspire the development of smart sensor arrays based on a simple materials processing technology. Yet, the increase of the sensitivity to the low ppm level and the decrease in the response times still remain a challenge.

EXPERIMENTAL SECTION

Chemicals. Citric acid (99%, Sigma-Aldrich), urea (>99.3%, Alfa Aesar), zinc nitrate hexahydrate ($\text{Zn}(\text{NO}_3)_2 \cdot 6\text{H}_2\text{O}$, standard grade, Thermo Fisher Scientific GmbH), ethylene glycol ($\geq 99.7\%$, AnalaR Normapur, VWR chemicals), poly(vinylpyrrolidone) (average mol wt. 10,000, Sigma-Aldrich), acetone ($\geq 99.8\%$ HPLC grade, Thermo Fisher Scientific GmbH), and toluene ($\geq 99.8\%$ HPLC grade, Thermo Fisher Scientific GmbH) were used as received.

Substrate. Melinex sheets (PET substrates) with a thickness of 170 μm were obtained from Plano GmbH.

Preparation of the CNFA. The CNFA was prepared following a protocol described elsewhere.²¹ Briefly, citric acid and urea were mixed in equivalent weight proportions in a quartz crucible. The mixture was annealed at 300 °C in a tube furnace (RHTC 80/450/15, Nabertherm) for 2 h with a heating rate of 3.11 $\text{K}\cdot\text{min}^{-1}$. After annealing, the reaction products were ground by ball milling (PM 100, Retsch) for 1 h at 600 rpm. The resulting black powder is named CA/U(300).

Preparation of the ZnO Nanorods. $\text{Zn}(\text{NO}_3)_2$ (3g) and NaOH (0.8 g) were added to 500 ml of H_2O . The resulting white suspension was partially added to the microwave vessel. Then, using a microwave power of 200 W to reach the reaction temperature of 150 °C held for 5 min. The reaction product mixture was centrifuged to remove the soluble part. The precipitate was washed with ethanol and centrifuged; the washing process was repeated 2 times. The obtained white solid ZnO nanorods were dried overnight at 70 °C in the oven.

Preparation of the Primary Films. Poly(vinylpyrrolidone) (PVP) (film-forming agent) was dissolved in ethylene glycol (EtGly) to obtain a 0.2 g·mL⁻¹ solution (PVP/EtGly). Solutions with eight different concentrations of zinc nitrate (Zn(NO₃)₂) ranging from 0 to 0.6 mg·mL⁻¹ were prepared, referred to as LP-C/Zn(1–8), where the number represents the amount of Zn in wt % (Table 1). CA/U(300) was then added and stirred for 24 h to obtain a viscous suspension with a concentration of 0.8 g·mL⁻¹. All concentrations are given with respect to the volume of the solvent. A drop of the ink was applied onto the substrate and the ink was doctor bladed with a blade distance of 300 μm. Ethylene glycol was then evaporated at 80 °C on a precision hotplate (PZ2860-SR, Gestigkeit GmbH) overnight to obtain films with a thickness of 40 μm. The thickness was determined with a digital micrometer or cross-sectional SEM.

Laser Carbonization. A high-precision laser engraver setup (Speedy 100, Trotec) equipped with a 60 W CO₂-laser ($\lambda = 10.6 \pm 0.03 \mu\text{m}$) was used for laser carbonization. Focusing was achieved with a 2.5 in. focus lens providing a focal depth of ~ 3 mm and a focus diameter of 170 μm. The scanning speed v' , generically given in percentage, was converted into $\text{s}\cdot\text{m}^{-1}$. The effective output power P of the laser was measured with a Solo 2 (Gentec Electro-Optics) power meter. The resulting energy input per distance (or fluence) F in $\text{J}\cdot\text{m}^{-1}$ in the vector mode onto the film is given by

$$F = P \cdot v'$$

For the experiments, the laser settings were adjusted to meet the requirements of the films according to Table 2. Each laser pattern consists of five parallel laser lines with a length of 5 mm and a line separation of 0.1 mm to obtain a sensor film.

Table 2. Laser Parameters Used in the Experiments to Fit the Film Thickness

thickness(μm)	power%(generic)	power(W)	speed%(generic)	speed(s·m ⁻¹)	fluence(J·m ⁻¹)
20	2.0	1.02	0.6	98	99.5

VOCs Sensing. The sensor experiments were performed in a gas-flow cell ($V_{\text{cell}} \approx 0.1$ L). The ends of the sensor films were connected to two electrode pins and electrically characterized with an impedance unit (Solartron 1287 potentiostat in combination with a SI 1260 impedance unit) at a frequency of 1000 Hz and in AC conditions applying a current of 0.05 mA. The gas flow was controlled with a set of three mass-flow controllers (GF040 from Brooks instruments). The total gas flow was set to 1 L·min⁻¹. Cycles of 30 min between pure nitrogen and the analyte (acetone or toluene) were performed. To this end, a defined volume of the total flow was passed through a reservoir of the respective liquid VOCs. The final concentration of the analyte was approximated using the ideal gas law based on the vapor pressure of the VOC.

Characterization. Conductivity measurements were carried out by connecting the ends of each sensor film with silver ink and measuring the resistance with a four-point geometry using an RS PRO2 RSDM3055A digital multimeter.

Specific surface area measurements were performed using the methylene blue adsorption method.^{55–57} LP-C films of size $2 \times 4 \text{ cm}^2$ were printed on PET sheets. Pieces of $\sim 0.5 \times 1 \text{ cm}^2$ with the laser-patterned films on top were balanced and then immersed into defined solutions of methylene blue (9.5×10^{-5} M) to disperse the LP-C film in the solution. To determine the mass of the film, the PET substrate was removed and weighted. The LP-C dispersion in the MB solution was stirred for 24 h and then centrifuged. The amount of adsorbed MB was determined by measuring the absorbance of the supernatant with respect to a reference solution. An area of 1.35 nm² per molecule MB is assumed. As a reference, the same mass of activated carbon was used (1269 m²·g⁻¹). The standard error was determined by the standard deviation of six values obtained from six measurements.

Raman spectra were obtained with a confocal Raman microscope (alpha300, WITec, Germany) equipped with a piezo-scanner (P-500, Physik Instrumente, Karlsruhe, Germany). The laser, $\lambda = 532$ nm, was focused on the samples through a 50× objective. The laser power on the sample was set to 5.0 mW.

Cross-sectional preparation of LP-C for electron microscopic analyses was performed using a Leica EM UC7 ultramicrotome. Therefore, sensor strips were embedded in epoxy resin (Araldite 502, Science Services, Germany) to enable sectioning by infiltrating the highly porous heterostructures. Curing of the epoxy resin was carried out overnight at 60 °C. A diamond knife (DiATOME 45° trim knife) was utilized to trim a trapezoid-shaped block face which subsequently was cut with a DiATOME 45° ultrasonic diamond knife to obtain cross-sectional TEM samples with minimal compression. The floating sections (deionized water) were transferred onto lacey carbon TEM grids (Plano AG) to provide sufficient support. Analysis by optical microscopy (OM) and environmental SEM was conducted with the resulting block face.

Top-view scanning electron microscopy was performed on a Zeiss LEO 1550-Gemini system (acceleration voltage: 3 to 10 kV). An Oxford Instruments X-MAX 80 mm² detector was used to collect the SEM-EDX data. Cross-sectional imaging with back-scattered electrons and EDXS elemental mapping of the epoxy-embedded samples (microtomy block surface) were performed using an environmental FEI Quanta 250 FEG-SEM. An Apollo XL SDD detector was used to obtain EDXS elemental maps at 5 keV primary electron energy as a compromise between count rate and lateral resolution. To reduce sample charging, the instrument was operated at a N₂ pressure of 70–90 Pa.

Transmission electron microscopy was performed using a Thermo Fisher FEI Talos F200X operated at 200 kV. Besides an XFEG high-brightness gun and a large-area Super-X EDXS detector, the instrument is equipped with a Gatan Continuum ER spectrometer for electron energy-loss spectroscopy. Bright-field imaging, selected-area electron diffraction, high-resolution TEM, and high-angle annular dark-field scanning TEM were utilized to analyze the structure and morphology of the LP-C microtomic cross-sections. Dual EELS mappings with an energy range of the core-loss spectra of 200–800 eV (dispersion 0.3 eV/channel) for the upper region and 200–1800 eV (dispersion 0.75 eV/channel) for the lower region were acquired to include the ionization edges of C, N, O, and Zn at around 285, 400, 532, and 1020 eV, respectively.

To visualize the distribution of graphitized carbon in the top layer as well as the N and Zn distributions of the bottom layer, principal component analysis (PCA) was employed to analyze the STEM-EELS data. PCA was used as implemented in the Gatan Microscopy Suite (GMS) version 3.4.⁵⁸ (The details of the data evaluation are described in our previous study).

X-ray photoelectron spectroscopy was acquired using a Kratos Axis SUPRA using monochromated Al $K\alpha$ (1486.69 eV) X-rays at 15 mA emission and 12 kV HT (180W) and a spot size/analysis area of $700 \times 300 \mu\text{m}^2$. The instrument was calibrated to gold metal Au 4f (83.95 eV) and dispersion was adjusted to give a BE of 932.6 eV for the Cu 2p_{3/2} line of metallic copper. The Ag 3d_{5/2} line FWHM at 10 eV pass energy was 0.544 eV. The source resolution for monochromatic Al $K\alpha$ X-rays is ~ 0.3 eV. The instrumental resolution was determined to be 0.29 eV at 10 eV pass energy using the Fermi edge of the valence band for metallic silver. Resolution with the charge compensation system on <1.33 eV FWHM on PTFE. High-resolution spectra were obtained using a pass energy of 20 eV, step size of 0.1 eV, and sweep time of 60 s, resulting in a line width of 0.696 eV for Au 4f_{7/2}. Survey spectra were obtained using a pass energy of 160 eV. Charge neutralization was achieved using an electron flood gun with the filament current = 0.4 A, charge balance = 2 V, and filament bias = 4.2 V. Successful neutralization was adjudged by analyzing the C 1s region wherein a sharp peak with no lower BE structure was obtained. Spectra have been charge corrected to the main line of the carbon 1s spectrum (adventitious carbon) set to 284.8 eV. All data was recorded at a base pressure of below 9×10^{-9} Torr and a room temperature of

294 K. Data was analyzed using CasaXPS v2.3.19PR1.0. Peaks were fit with a Shirley background prior to component analysis.

■ ASSOCIATED CONTENT

Data Availability Statement

The datasets generated during and/or analyzed during the current study are available from the corresponding author upon reasonable request.

SI Supporting Information

The Supporting Information is available free of charge at <https://pubs.acs.org/doi/10.1021/acsanm.2c04348>.

Energy-dispersive X-ray analysis; scanning electron microscopy; Raman spectroscopic analysis; X-ray photoelectron spectroscopic analysis; X-ray photoelectron spectroscopic analysis; electrical conductivity measurements; cross-sectional microscopic analysis; and sensor performance (PDF)

■ AUTHOR INFORMATION

Corresponding Author

Volker Strauss – Max Planck Institut für Kolloid- und Grenzflächenforschung, 14476 Potsdam, Germany; orcid.org/0000-0003-2619-6841; Email: volker.strauss@mpikg.mpg.de

Authors

Huize Wang – Max Planck Institut für Kolloid- und Grenzflächenforschung, 14476 Potsdam, Germany
Pablo Jiménez-Calvo – Max Planck Institut für Kolloid- und Grenzflächenforschung, 14476 Potsdam, Germany; orcid.org/0000-0002-9826-6995
Marco Hepp – Micro- and Nanoanalytics Group, University of Siegen, 57076 Siegen, Germany; orcid.org/0000-0002-5811-8672
Mark Andrew Isaacs – Harwell XPS, Research Complex at Harwell, Rutherford Appleton Laboratories, Didcot OX11 0FA, U.K.; orcid.org/0000-0002-0335-4272
Charles Otieno Ogolla – Micro- and Nanoanalytics Group, University of Siegen, 57076 Siegen, Germany
Ines Below-Lutz – Max Planck Institut für Kolloid- und Grenzflächenforschung, 14476 Potsdam, Germany
Benjamin Butz – Micro- and Nanoanalytics Group, University of Siegen, 57076 Siegen, Germany; orcid.org/0000-0002-9744-3419

Complete contact information is available at: <https://pubs.acs.org/doi/10.1021/acsanm.2c04348>

Author Contributions

H.W.: investigation, methodology, validation, formal analysis, and writing—original draft; P.J.-C.: investigation, methodology, validation, formal analysis, and writing—original draft; M.H.: investigation, methodology, validation, formal analysis, and writing—original draft; M.I.: investigation, methodology, validation, and writing—original draft; I.B.-L.: investigation; B.B.: supervision, methodology, validation, and writing—review & editing; and V.S.: conceptualization, methodology, validation, writing—original draft, writing—review & editing, supervision, and project administration.

Funding

Open access funded by Max Planck Society.

Notes

The authors declare no competing financial interest.

The authors declare that they have no known competing financial interests or personal relationships that could have appeared to influence the work reported in this paper.

■ ACKNOWLEDGMENTS

The authors are grateful for financial support from the Fonds der Chemischen Industrie and the Max Planck Society. The authors thank Klaus Bienert for help with the gas sensing setup. Open access funding was enabled and organized by the German Projekt DEAL. The X-ray photoelectron (XPS) data collection was performed at the EPSRC National Facility for XPS (“HarwellXPS”), operated by Cardiff University and UCL, under Contract No. PR16195. Part of this work was performed at the DFG-funded Micro- and Nanoanalytics Facility (MNaF) of the University of Siegen (INST 221/131-1) utilizing its major TEM instrument FEI Talos F200X (DFG INST 221/93-1, DFG INST 221/126-1) and sample preparation equipment.

■ REFERENCES

- (1) Environmental Protection Agency. *Technical Overview of Volatile Organic Compounds*, 2017.
- (2) Szulczyński, B.; Gębicki, J. Currently Commercially Available Chemical Sensors Employed for Detection of Volatile Organic Compounds in Outdoor and Indoor Air. *Environments* **2017**, *4*, No. 21.
- (3) Spinelle, L.; Gerboles, M.; Kok, G.; Persijn, S.; Sauerwald, T. Review of Portable and Low-Cost Sensors for the Ambient Air Monitoring of Benzene and Other Volatile Organic Compounds. *Sensors* **2017**, *17*, No. 1520.
- (4) Saasa, V.; Malwela, T.; Beukes, M.; Mokgotho, M.; Liu, C.-P.; Mwakikunga, B. Sensing Technologies for Detection of Acetone in Human Breath for Diabetes Diagnosis and Monitoring. *Diagnostics* **2018**, *8*, No. 12.
- (5) Meng, F.; Shi, X.; Yuan, Z.; Ji, H.; Qin, W.; Shen, Y.; Xing, C. Detection of Four Alcohol Homologue Gases by ZnO Gas Sensor in Dynamic Interval Temperature Modulation Mode. *Sens. Actuators, B* **2022**, *350*, No. 130867.
- (6) Probert, C.; Ahmed, I.; Khalid, T.; Smith, S.; Ratcliffe, N. Volatile Organic Compounds as Diagnostic Biomarkers in Gastrointestinal and Liver Diseases. *J. Gastrointest. Liver Dis.* **2009**, *18*, 337–343.
- (7) Das, S.; Pal, M. Review—Non-Invasive Monitoring of Human Health by Exhaled Breath Analysis: A Comprehensive Review. *J. Electrochem. Soc.* **2020**, *167*, No. 037562.
- (8) Wilson, A. D. Application of Electronic-Nose Technologies and VOC-Biomarkers for the Noninvasive Early Diagnosis of Gastrointestinal Diseases. *Sensors* **2018**, *18*, No. 2613.
- (9) Hayasaka, T.; Lin, A.; Copa, V. C.; Lopez, L. P.; Loberternos, R. A.; Ballesteros, L. I. M.; Kubota, Y.; Liu, Y.; Salvador, A. A.; Lin, L. An Electronic Nose Using a Single Graphene FET and Machine Learning for Water, Methanol, and Ethanol. *Microsyst. Nanoeng.* **2020**, *6*, No. 50.
- (10) Guo, L.; Wang, T.; Wu, Z.; Wang, J.; Wang, M.; Cui, Z.; Ji, S.; Cai, J.; Xu, C.; Chen, X. Portable Food-Freshness Prediction Platform Based on Colorimetric Barcode Combinatorics and Deep Convolutional Neural Networks. *Adv. Mater.* **2020**, *32*, No. 2004805.
- (11) <https://smart-nanotubes.com/>; date of access: December 06, 2022.
- (12) Ji, H.; Mi, C.; Yuan, Z.; Liu, Y.; Zhu, H.; Meng, F. Multi-Component Gas Detection Method via Dynamic Temperature Modulation Measurements Based on Semiconductor Gas Sensor. *IEEE Trans. Ind. Electron.* **2022**, 1–10.
- (13) Wang, C.; Yin, L.; Zhang, L.; Xiang, D.; Gao, R. Metal Oxide Gas Sensors: Sensitivity and Influencing Factors. *Sensors* **2010**, *10*, 2088–2106.

- (14) Andre, R. S.; Sanfelice, R. C.; Pavinatto, A.; Mattoso, L. H. C.; Correa, D. S. Hybrid Nanomaterials Designed for Volatile Organic Compounds Sensors: A Review. *Mater. Des.* **2018**, *156*, 154–166.
- (15) Zhang, W.; Li, G.; Yin, H.; Zhao, K.; Zhao, H.; An, T. Adsorption and Desorption Mechanism of Aromatic VOCs onto Porous Carbon Adsorbents for Emission Control and Resource Recovery: Recent Progress and Challenges. *Environ. Sci.: Nano* **2022**, *9*, 81–104.
- (16) Kante, K.; Florent, M.; Temirgaliyeva, A.; Lesbayev, B.; Bandosz, T. J. Exploring Resistance Changes of Porous Carbon upon Physical Adsorption of VOCs. *Carbon* **2019**, *146*, 568–571.
- (17) Jiao, Y.; Cho, S. W.; Lee, S.; Kim, S. H.; Jeon, S.-Y.; Hur, K.; Yoon, S. M.; Moon, M.-W.; Wang, A. A Hierarchically Porous Carbon Fabric for Highly Sensitive Electrochemical Sensors. *Adv. Eng. Mater.* **2018**, *20*, No. 1700608.
- (18) Zhang, X.; Gao, B.; Creamer, A. E.; Cao, C.; Li, Y. Adsorption of VOCs onto Engineered Carbon Materials: A Review. *J. Hazard. Mater.* **2017**, *338*, 102–123.
- (19) Mulmi, S.; Thangadurai, V. Editors' Choice—Review—Solid-State Electrochemical Carbon Dioxide Sensors: Fundamentals, Materials and Applications. *J. Electrochem. Soc.* **2020**, *167*, No. 037567.
- (20) Zhao, X.-H.; Ma, S.-N.; Long, H.; Yuan, H.; Tang, C. Y.; Cheng, P. K.; Tsang, Y. H. Multifunctional Sensor Based on Porous Carbon Derived from Metal–Organic Frameworks for Real Time Health Monitoring. *ACS Appl. Mater. Interfaces* **2018**, *10*, 3986–3993.
- (21) Delacroix, S.; Wang, H.; Heil, T.; Strauss, V. Laser-Induced Carbonization of Natural Organic Precursors for Flexible Electronics. *Adv. Electron. Mater.* **2020**, *6*, No. 2000463.
- (22) Edberg, J.; Brooke, R.; Hosseinaei, O.; Fall, A.; Wijeratne, K.; Sandberg, M. Laser-Induced Graphitization of a Forest-Based Ink for Use in Flexible and Printed Electronics. *npj Flexible Electron.* **2020**, *4*, No. 17.
- (23) Mohazzab, B. F.; Jaleh, B.; Nasrollahzadeh, M.; Khazalpour, S.; Sajjadi, M.; Varma, R. S. Upgraded Valorization of Biowaste: Laser-Assisted Synthesis of Pd/Calcium Lignosulfonate Nanocomposite for Hydrogen Storage and Environmental Remediation. *ACS Omega* **2020**, *5*, 5888–5899.
- (24) Yuan, M.; Luo, F.; Rao, Y.; Wang, Y.; Yu, J.; Li, H.; Chen, X. Laser Synthesis of Superhydrophilic O/S Co-Doped Porous Graphene Derived from Sodium Lignosulfonate for Enhanced Microsupercapacitors. *J. Power Sources* **2021**, *513*, No. 230558.
- (25) Delacroix, S.; Zieleniewska, A.; Ferguson, A. J.; Blackburn, J. L.; Ronneberger, S.; Loeffler, F. F.; Strauss, V. Using Carbon Laser Patterning to Produce Flexible, Metal-Free Humidity Sensors. *ACS Appl. Electron. Mater.* **2020**, *2*, 4146–4154.
- (26) Sharma, S.; Ganeshan, S. K.; Pattnaik, P. K.; Kanungo, S.; Chappanda, K. N. Laser Induced Flexible Graphene Electrodes for Electrochemical Sensing of Hydrazine. *Mater. Lett.* **2020**, *262*, No. 127150.
- (27) Wan, Z.; Nguyen, N.-T.; Gao, Y.; Li, Q. Laser Induced Graphene for Biosensors. *Sustainable Mater. Technol.* **2020**, *25*, No. e00205.
- (28) Watanabe, A.; Cai, J.; Ogawa, S.; Aoyagi, E.; Ito, S. Laser Reduced Graphene Oxide-Based Interdigitated Electrode for Sensor Applications. In *Laser-based Micro- and Nanoprocessing XIII*; Klotzbach, U.; Kling, R.; Watanabe, A., Eds.; SPIE, 2019; p 38.
- (29) Luo, J.; Yao, Y.; Duan, X.; Liu, T. Force and Humidity Dual Sensors Fabricated by Laser Writing on Polyimide/Paper Bilayer Structure for Pulse and Respiration Monitoring. *J. Mater. Chem. C* **2018**, *6*, 4727–4736.
- (30) Zhu, C.; Tao, L.-Q.; Wang, Y.; Zheng, K.; Yu, J.; L, X.; Chen, X.; Huang, Y. Graphene Oxide Humidity Sensor with Laser-Induced Graphene Porous Electrodes. *Sens. Actuators, B* **2020**, *325*, No. 128790.
- (31) Rahimi, R.; Ochoa, M.; Ziaie, B. Direct Laser Writing of Porous-Carbon/Silver Nanocomposite for Flexible Electronics. *ACS Appl. Mater. Interfaces* **2016**, *8*, 16907–16913.
- (32) Nam, K.-H.; Abdulhafez, M.; Castagnola, E.; Tomaraei, G. N.; Cui, X. T.; Bedewy, M. Laser Direct Write of Heteroatom-Doped Graphene on Molarly Controlled Polyimides for Electrochemical Biosensors with Nanomolar Sensitivity. *Carbon* **2022**, *188*, 209–219.
- (33) Stanford, M. G.; Yang, K.; Chyan, Y.; Kittrell, C.; Tour, J. M. Laser-Induced Graphene for Flexible and Embeddable Gas Sensors. *ACS Nano* **2019**, *13*, 3474–3482.
- (34) Wang, H.; Delacroix, S.; Zieleniewska, A.; Hou, J.; Tarakina, N. V.; Cruz, D.; Lauermaun, I.; Ferguson, A. J.; Blackburn, J. L.; Strauss, V. In Situ Synthesis of Molybdenum Carbide Nanoparticles Incorporated into Laser-Patterned Nitrogen-Doped Carbon for Room Temperature VOC Sensing. *Adv. Funct. Mater.* **2021**, *31*, No. 2104061.
- (35) Yan, B.; Zheng, J.; Wang, F.; Zhao, L.; Zhang, Q.; Xu, W.; He, S. Review on Porous Carbon Materials Engineered by ZnO Templates: Design, Synthesis and Capacitance Performance. *Mater. Des.* **2021**, *201*, No. 109518.
- (36) Yan, R.; Leus, K.; Hofmann, J. P.; Antonietti, M.; Oschatz, M. Porous Nitrogen-Doped Carbon/Carbon Nanocomposite Electrodes Enable Sodium Ion Capacitors with High Capacity and Rate Capability. *Nano Energy* **2020**, *67*, No. 104240.
- (37) Strubel, P.; Thieme, S.; Biemelt, T.; Helmer, A.; Oschatz, M.; Brückner, J.; Althues, H.; Kaskel, S. ZnO Hard Templating for Synthesis of Hierarchical Porous Carbons with Tailored Porosity and High Performance in Lithium-Sulfur Battery. *Adv. Funct. Mater.* **2015**, *25*, 287–297.
- (38) Hepp, M.; Wang, H.; Derr, K.; Delacroix, S.; Ronneberger, S.; Loeffler, F. F.; Butz, B.; Strauss, V. Trained Laser-Patterned Carbon as High-Performance Mechanical Sensors. *npj Flexible Electron.* **2022**, *6*, No. 3.
- (39) Kossmann, J.; Sánchez-Manjavacas, M. L. O.; Zschiesche, H.; Tarakina, N. V.; Antonietti, M.; Alberio, J.; López-Salas, N. Cu II /Cu I Decorated N-Doped Carbonaceous Electrocatalysts for the Oxygen Reduction Reaction. *J. Mater. Chem. A* **2022**, *10*, 6107–6114.
- (40) Sadezky, A.; Muckenhuber, H.; Grothe, H.; Niessner, R.; Pöschl, U. Raman Microspectroscopy of Soot and Related Carbonaceous Materials: Spectral Analysis and Structural Information. *Carbon* **2005**, *43*, 1731–1742.
- (41) Pawlyta, M.; Rouzaud, J.-N.; Duber, S. Raman Microspectroscopy Characterization of Carbon Blacks: Spectral Analysis and Structural Information. *Carbon* **2015**, *84*, 479–490.
- (42) Schuepfer, D. B.; Badaczewski, F.; Guerra-Castro, J. M.; Hofmann, D. M.; Heiliger, C.; Smarsly, B.; Klar, P. J. Assessing the Structural Properties of Graphitic and Non-Graphitic Carbons by Raman Spectroscopy. *Carbon* **2020**, *161*, 359–372.
- (43) Bandis, C.; Scudiero, L.; Langford, S. C.; Dickinson, J. T. Photoelectron Emission Studies of Cleaved and Excimer Laser Irradiated Single-Crystal Surfaces of NaNO₃ and NaNO₂. *Surf. Sci.* **1999**, *442*, 413–419.
- (44) Kazansky, L. P.; Pronin, Y. E.; Arkhipushkin, I. A. XPS Study of Adsorption of 2-Mercaptobenzothiazole on a Brass Surface. *Corros. Sci.* **2014**, *89*, 21–29.
- (45) Biesinger, M. C.; Lau, L. W. M.; Gerson, A. R.; Smart, R. S. C. Resolving Surface Chemical States in XPS Analysis of First Row Transition Metals, Oxides and Hydroxides: Sc, Ti, V, Cu and Zn. *Appl. Surf. Sci.* **2010**, *257*, 887–898.
- (46) Wöll, C. The Chemistry and Physics of Zinc Oxide Surfaces. *Prog. Surf. Sci.* **2007**, *82*, 55–120.
- (47) Smith, M.; Scudiero, L.; Espinal, J.; McEwen, J. S.; Garcia-Perez, M. Improving the Deconvolution and Interpretation of XPS Spectra from Chars by Ab Initio Calculations. *Carbon* **2016**, *110*, 155–171.
- (48) Wang, H.; Ogolla, C. O.; Panchal, G.; Hepp, M.; Delacroix, S.; Cruz, D.; Kojda, D.; Ciston, J.; Ophus, C.; Knop-Gericke, A.; Habicht, K.; Butz, B.; Strauss, V. Flexible CO₂ Sensor Architecture with Selective Nitrogen Functionalities by One-Step Laser-Induced Conversion of Versatile Organic Ink. *Adv. Funct. Mater.* **2022**, No. 2207406.

(49) Lee, M.-G.; Lee, S.-W.; Lee, S.-H. Comparison of Vapor Adsorption Characteristics of Acetone and Toluene Based on Polarity in Activated Carbon Fixed-Bed Reactor. *Korean J. Chem. Eng.* **2006**, *23*, 773–778.

(50) Kwon, S.; Vidic, R.; Borguet, E. The Effect of Surface Chemical Functional Groups on the Adsorption and Desorption of a Polar Molecule, Acetone, from a Model Carbonaceous Surface, Graphite. *Surf. Sci.* **2003**, *522*, 17–26.

(51) Su, C.; Guo, Y.; Yu, L.; Zou, J.; Zeng, Z.; Li, L. Insight into Specific Surface Area, Microporosity and N, P Co-Doping of Porous Carbon Materials in the Acetone Adsorption. *Mater. Chem. Phys.* **2021**, *258*, No. 123930.

(52) Chen, R.; Han, N.; Li, L.; Wang, S.; Ma, X.; Wang, C.; Li, H.; Li, H.; Zeng, L. Fundamental Understanding of Oxygen Content in Activated Carbon on Acetone Adsorption Desorption. *Appl. Surf. Sci.* **2020**, *508*, No. 145211.

(53) Tang, M.; Huang, X.; Peng, Y.; Lu, S. Hierarchical Porous Carbon as a Highly Efficient Adsorbent for Toluene and Benzene. *Fuel* **2020**, *270*, No. 117478.

(54) Lu, S.; Huang, X.; Tang, M.; Peng, Y.; Wang, S.; Makwarimba, C. P. Synthesis of N-Doped Hierarchical Porous Carbon with Excellent Toluene Adsorption Properties and Its Activation Mechanism. *Environ. Pollut.* **2021**, *284*, No. 117113.

(55) Naeem, S.; Baheti, V.; Wiener, J.; Marek, J. Removal of Methylene Blue from Aqueous Media Using Activated Carbon. *Web. J. Text. Inst.* **2017**, *108*, 803–811.

(56) Rafatullah, M.; Sulaiman, O.; Hashim, R.; Ahmad, A. Adsorption of Methylene Blue on Low-Cost Adsorbents: A Review. *J. Hazard. Mater.* **2010**, *177*, 70–80.

(57) Hang, P. T. Methylene Blue Adsorption by Clay Minerals. Determination of Surface Areas and Cation Exchange Capacities (Clay-Organic Studies XVIII). *Clays Clay Miner.* **1970**, *18*, 203–212.

(58) Lucas, G.; Burdet, P.; Cantoni, M.; Hébert, C. Multivariate Statistical Analysis as a Tool for the Segmentation of 3D Spectral Data. *Micron* **2013**, *52–53*, 49–56.

Recommended by ACS

Arrays of Functionalized Graphene Chemiresistors for Selective Sensing of Volatile Organic Compounds

Natalia Alzate-Carvajal, Adina Luican-Mayer, *et al.*

FEBRUARY 15, 2023
ACS APPLIED ELECTRONIC MATERIALS

READ 

Plasma-Polymerized and Iodine-Doped Polyvinyl Acetate for Volatile Organic Compound Gas Sensing Applications

Baliram Nadekar, Pravin More, *et al.*

FEBRUARY 28, 2023
ACS APPLIED POLYMER MATERIALS

READ 

Carbon Nanostructure Embedded Novel Sensor Implementation for Detection of Aromatic Volatile Organic Compounds: An Organized Review

Nibedita Nath, Fernando Gomes de Souza Jr., *et al.*

JANUARY 23, 2023
ACS OMEGA

READ 

Fully Inkjet-Printed Chemiresistive Sensor Array Based on Molecularly Imprinted Sol–Gel Active Materials

Xiao Ye, Kenshi Hayashi, *et al.*

JUNE 22, 2022
ACS SENSORS

READ 

Get More Suggestions >

Supporting Information

Laser-Patterned Porous Carbon/ZnO Nanostructure Composites for Selective Room Temperature Sensing of Volatile Organic Compounds

Huize Wang¹, Pablo Jiménez-Calvo¹, Marco Hepp², Mark Andrew Isaacs³, Charles Otieno Ogolla², Ines Below-Lutz¹, Benjamin Butz², Volker Strauss^{1*}

Affiliations

¹ Max Planck Institut für Kolloid- und Grenzflächenforschung Am Mühlenberg 1, 14476 Potsdam, Germany

² Micro- and Nanoanalytics Group, University of Siegen, 57076, Siegen, Germany

³ Harwell XPS, Research Complex at Harwell, Rutherford Appleton Laboratories, Didcot OX11 0FA, UK

* volker.strauss@mpikg.mpg.de

Table of Contents

Energy dispersive X-ray analysis of Zn(NO ₃) ₂ -enriched primary films	S2
Scanning electron microscopy of Zn(NO ₃) ₂ -based sensors.....	S2
Energy dispersive X-ray analysis of Zn(NO ₃) ₂ -based sensors	S2
Raman spectroscopic analysis of Zn(NO ₃) ₂ -based sensors	S3
X-ray photoelectron spectroscopic analysis of Zn(NO ₃) ₂ -based sensors	S4
X-ray photoelectron spectroscopic analysis of Zn(NO ₃) ₂ -enriched primary films	S5
Scanning electron microscopy of ZnO-nanorods-based sensors.....	S6
Energy dispersive X-ray analysis of ZnO-nanorods-based sensors	S6
Raman spectrum of ZnO nanorods-based sensors.....	S7
Electrical conductivity of ZnO nanorods-based sensors	S7
Cross-sectional microscopic analysis	S8
Sensor performance	S9

Energy dispersive X-ray analysis of $\text{Zn}(\text{NO}_3)_2$ -enriched primary films

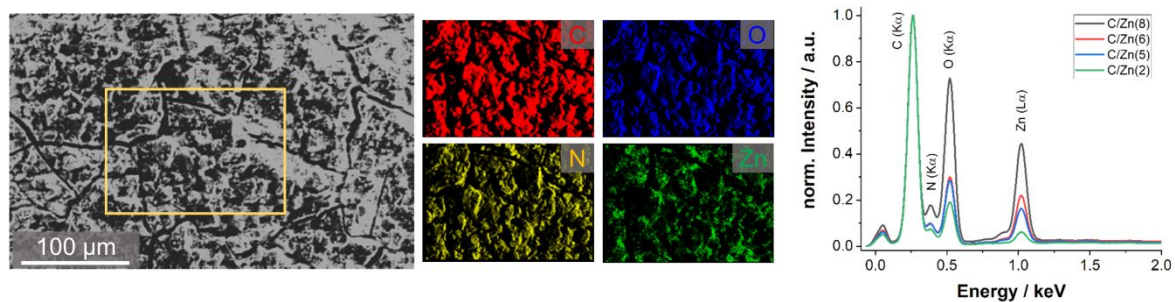


Figure S1. Exemplary top-view EDX map of the precursor film C/Zn(8), EDX spectra of C/Zn(2), (5), (6), and (8).

Scanning electron microscopy of $\text{Zn}(\text{NO}_3)_2$ -based sensors

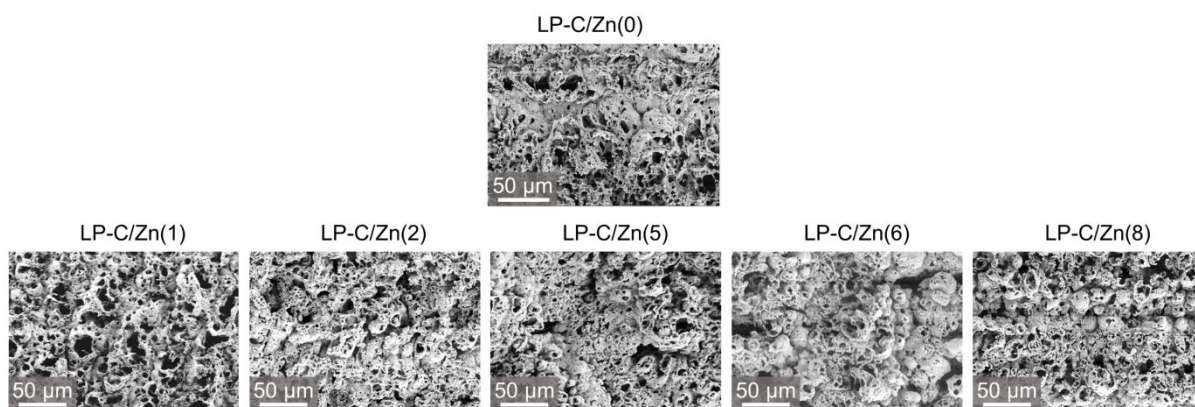


Figure S2. Top-view scanning electron micrographs of LP-C/Zn (0),(1),(2), (5), (6), and (8).

Energy dispersive X-ray analysis of $\text{Zn}(\text{NO}_3)_2$ -based sensors

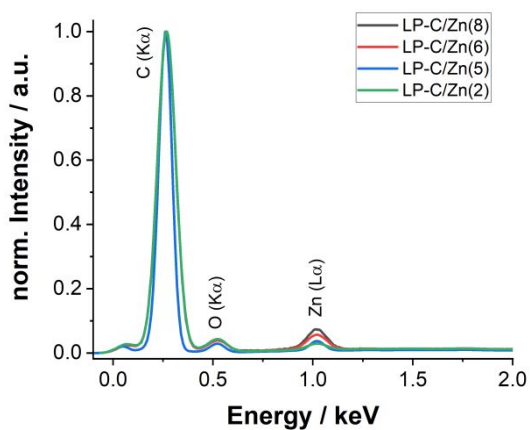


Figure S3. EDX spectra of LP-C/Zn(2), (5), (6), and (8).

Raman spectroscopic analysis of $\text{Zn}(\text{NO}_3)_2$ -based sensors

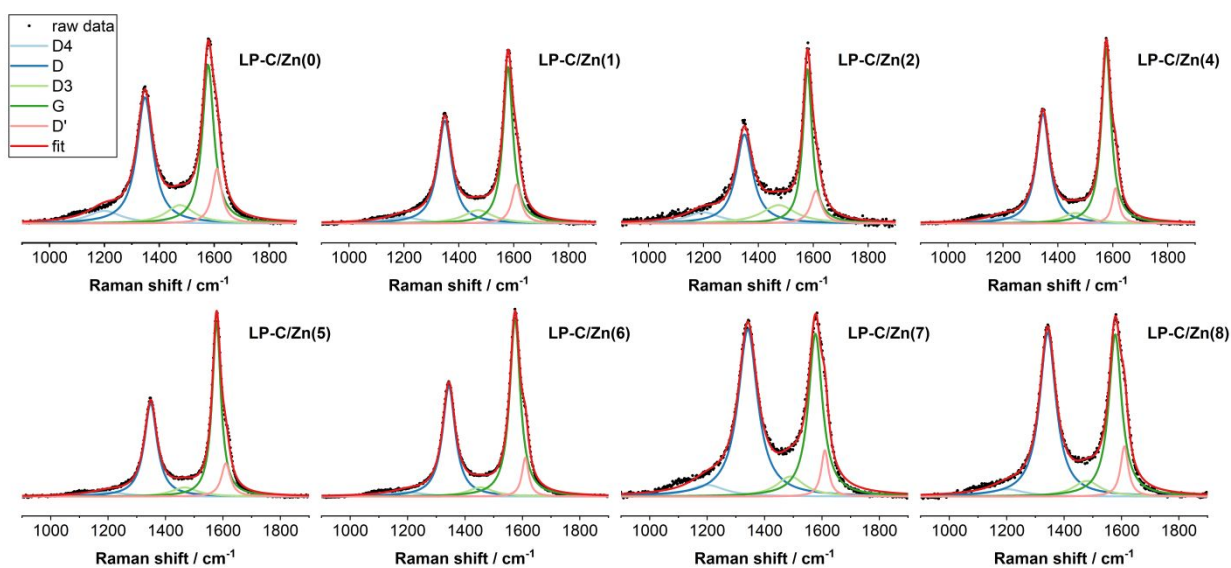


Figure S4. Multi-peak fittings of the Raman modes in the region between 900 and 1900 cm^{-1} .

X-ray photoelectron spectroscopic analysis of $\text{Zn}(\text{NO}_3)_2$ -based sensors

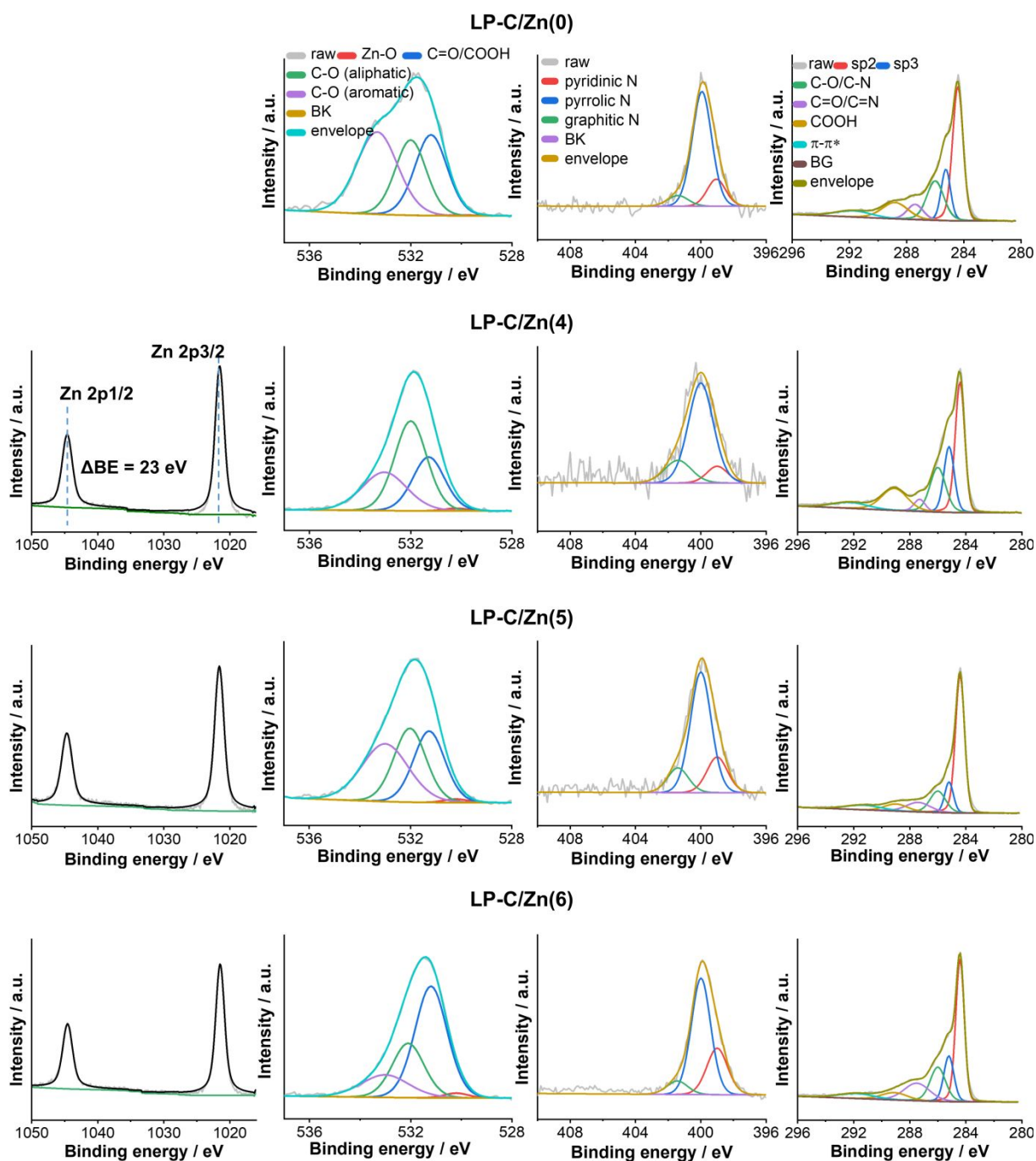


Figure S5. X-ray photoelectron spectroscopic analysis of LP-C/Zn(0),(4),(5) and (6)

X-ray photoelectron spectroscopic analysis of Zn(NO₃)₂-enriched primary films

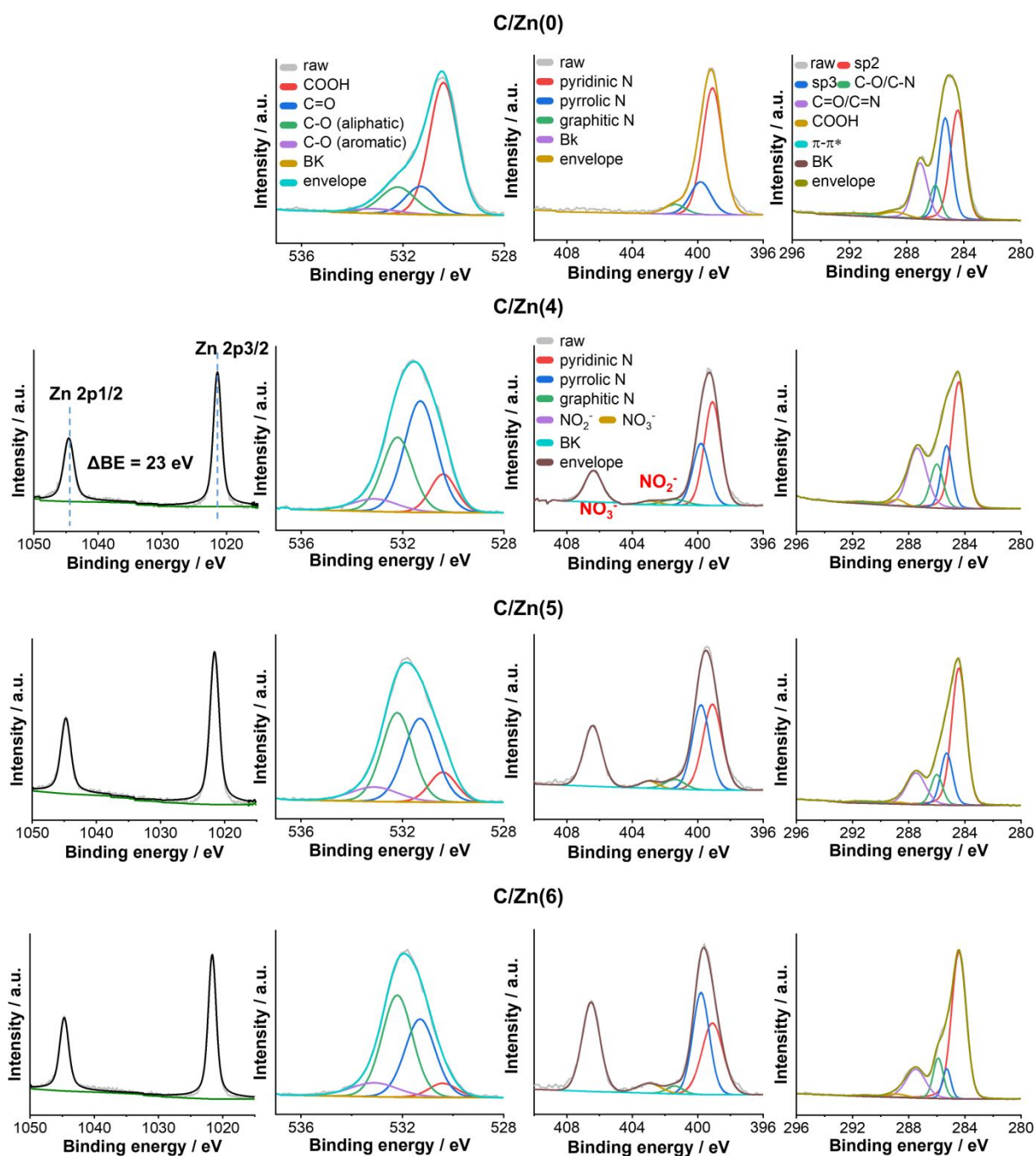


Figure S6. X-ray photoelectron spectroscopic analysis of primary films C/Zn(0),(4),(5) and (6)

Scanning electron microscopy of ZnO-nanorods-based sensors

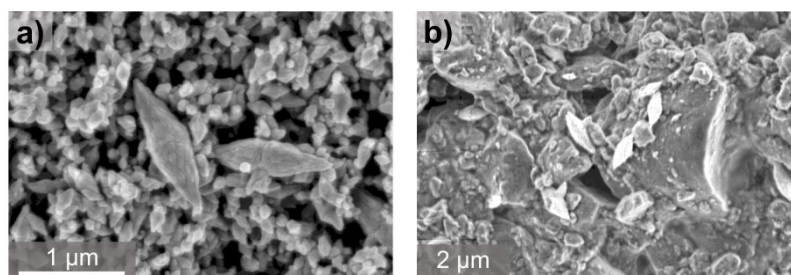


Figure S7. Scanning electron micrographs of a) ZnO nanorods and b) primary film of LP-C/ZnO(2)

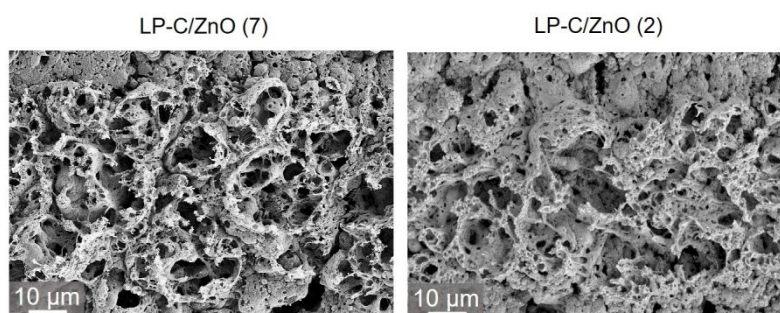


Figure S8. Top-view scanning electron micrographs of LP-C/ZnO(7) (left) and LP-C/ZnO(2) (right).

Energy dispersive X-ray analysis of ZnO-nanorods-based sensors

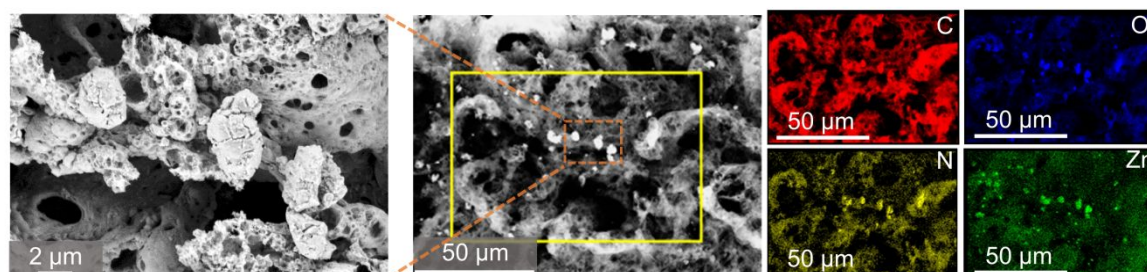


Figure S9. Exemplary top-view EDX map of sensor film LP-C/ZnO(2).

Raman spectrum of ZnO nanorods-based sensors

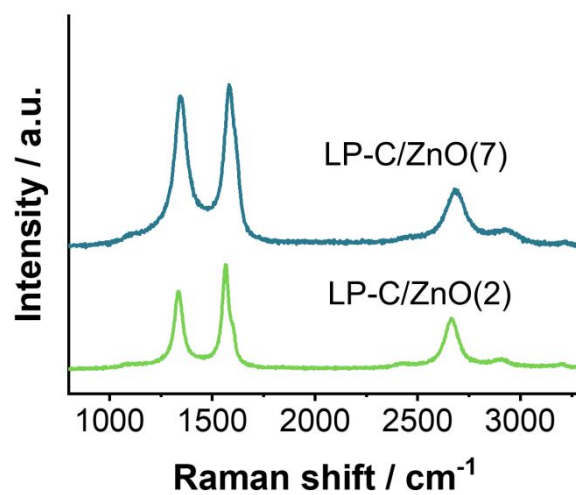


Figure S10. Top-view Raman spectra of sensor films LP-C/ZnO(2) and LP-C/ZnO(7).

Electrical conductivity of ZnO nanorods-based sensors

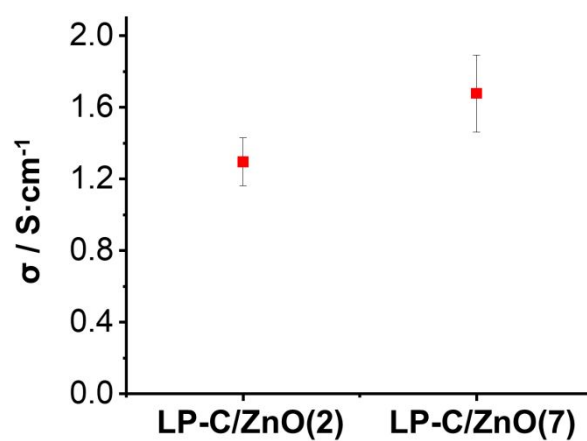


Figure S11. Electrical conductivity of sensor films LP-C/ZnO(2) and LP-C/ZnO(7).

Cross-sectional microscopic analysis

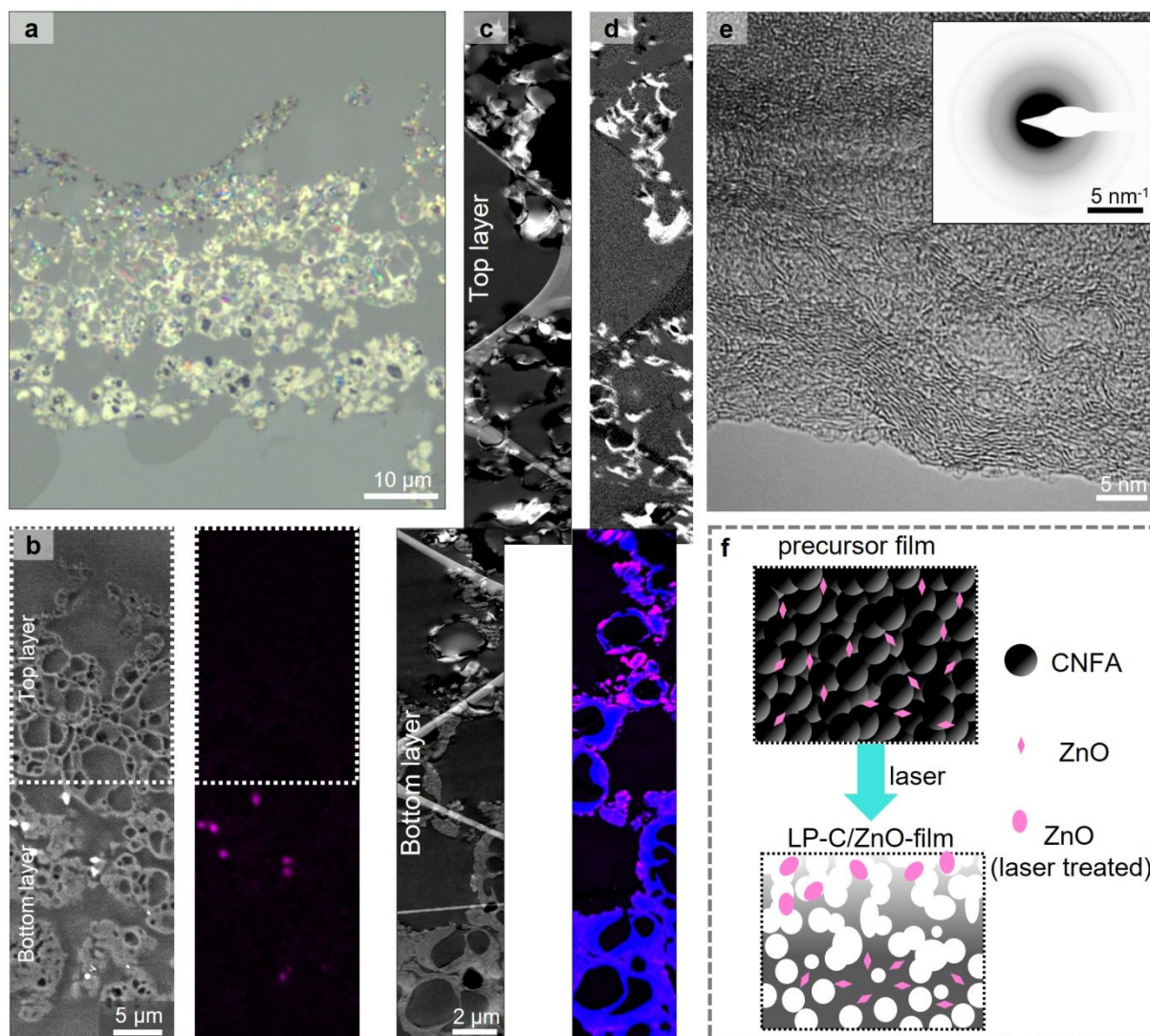


Figure S12. a) Cross-sectional optical micrograph of the sensor film; b) Cross-sectional backscatter SEM micrograph with correlated qualitative EDX element map of zinc (net intensities displayed); Cross-sectional TEM analyses of the sensor film: c) Representative high-angle annular dark-field (HAADF)-STEM micrograph with uninfiltrated regions (black), epoxy resin (dark grey), and lacey TEM support film (light grey) d) (top) Graphitized carbon component in upper layer identified by PCA, (bottom) N (blue) and Zn (purple) distribution in bottom layer of sensor; e) HRTEM image of graphitized C of top layer with corresponding SAED pattern (inset); f) Proposed formation mechanism of the LP-C/ZnO composite structure.

Sensor performance

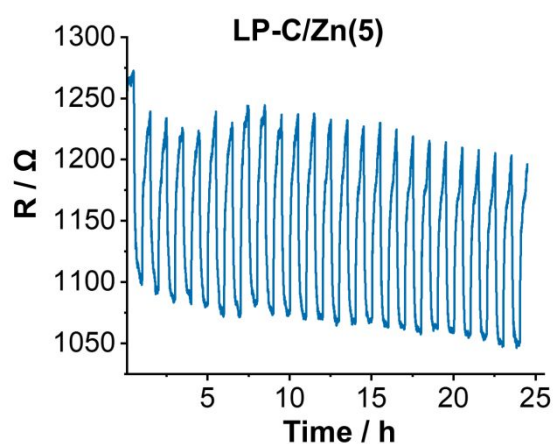


Figure S13. Stability test over time of LP-C/Zn(5) film towards 2.5% acetone.

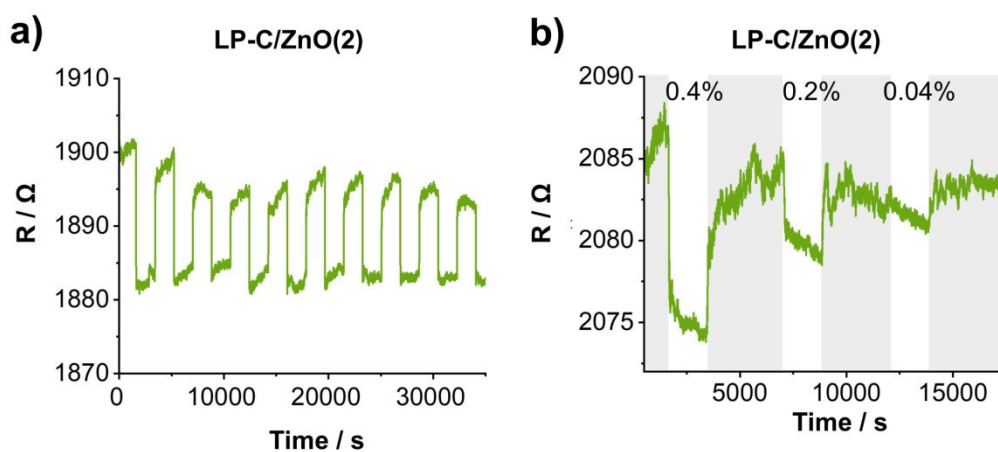


Figure S14. a) Stability test over time of LP-C/ZnO(2) film. b) Resistive response of LP-C/ZnO(2) film towards 0.4%, 0.2% and 0.04% toluene.

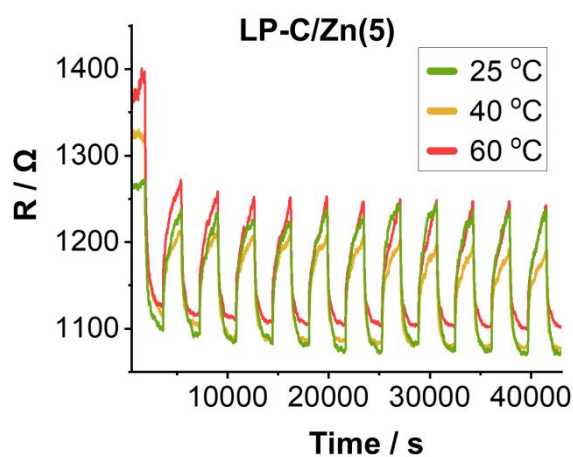


Figure S15. Resistive response of LP-C/Zn(5) film towards 2.5% acetone at 25, 40 and 60 °C

ARTICLE OPEN



Trained laser-patterned carbon as high-performance mechanical sensors

Marco Hepp¹, Huize Wang², Katharina Derr¹, Simon Delacroix³, Sebastian Ronneberger², Felix F. Loeffler², Benjamin Butz¹ and Volker Strauss¹✉

We describe the mechanical properties of turbostratically graphitized carbon films obtained by carbon laser-patterning (CLaP) and their application as bending or mechanical pressure sensors. Stable conductive carbonized films were imprinted on a flexible polyethylene terephthalate (PET) substrate by laser-induced carbonization. After initial gentle bending, i.e. training, these sponge-like porous films show a quantitative and reversible change in resistance upon bending or application of pressure in normal loading direction. Maximum response values of $\Delta R/R_0 = 388\%$ upon positive bending (tensile stress) and -22.9% upon negative bending (compression) are implicit for their high sensitivity towards mechanical deformation. Normal mechanical loading in a range between 0 and 500 kPa causes a response between $\Delta R/R_0 = 0$ and -15% . The reversible increase or decrease in resistance is attributed to compression or tension of the turbostratically graphitized domains, respectively. This mechanism is supported by a detailed microstructural and chemical high-resolution transmission electron microscopic analysis of the cross-section of the laser-patterned carbon.

npj Flexible Electronics (2022)6:3; <https://doi.org/10.1038/s41528-022-00136-0>

INTRODUCTION

With the advent of future applications in robotics, bionics, and smart textiles, flexible electronic devices are receiving an enormous scientific interest^{1–3}. Besides charge storage, energy conversion, or light-emitting devices, flexible responsive materials—sensors—are being explored for health monitoring or human-machine interfaces^{4–6}.

Typical functional (semi)conductive materials for flexible electronics include metal or semiconductor nanowires or nanoparticles (e.g., silver, gold, metal oxides)^{7–10}. Their nanoscale morphologies and properties are decisive for their flexible performance and advantageous for their utilization in thin skin-like devices¹. For the fabrication of reliable devices, methods such as chemical vapor deposition, photolithography, screen printing, polydimethylsiloxane (PDMS) transfer techniques, or transfer printing are commonly used². In most cases, these nanomaterials are coupled with or processed into flexible and stretchable polymers such as PDMS matrices^{11,12}. For film thicknesses on the micrometer scale inner material shear forces typically cause cracking or delamination¹³.

A great potential is attributed to organic electronic materials based on conductive polymers, such as poly(3,4-ethylenedioxythiophene) polystyrene sulfonate (PEDOT:PSS), polyaniline, or polyacetylene due to their easy processability, structural tunability, and light-weight^{14–16}. However, several drawbacks, such as poor environmental stability, poor repeatability, or low mechanical stability, arise with their utilization¹⁷. Great achievements in developing flexible electronic devices have been made with nanocarbons such as carbon nanotubes or graphene^{18–21}. These materials are generally well-suited for thin-film flexible electronic devices due to their intrinsically low dimensions and tunable electronic properties, which have been demonstrated in a plethora of studies^{22,23}. A broad overview of carbon-based

materials used in flexible electronics is covered in a recent book on ‘flexible carbon-based electronics’¹⁷. Among the greatest challenges for the production of flexible devices are long-term stability and large-scale production.

In general, carbonized natural materials with high-surface areas and high conductivities have the potential to replace currently used standards due to their abundance and environmental sustainability²⁴. In fact, a trend towards using carbon-based semiconductor materials is observed in the past few years, due to undeniable advantages like tunable electronic properties or flexible morphology and above all: biodegradability and resource independence²⁵. However, reproducible processing of carbonized materials into functional devices is often a challenge. Modern processing methods, such as 3D-printing or laser-processing have recently emerged as simple fabrication techniques^{26,27}. The latter is particularly interesting as it allows for the variable printing of film-based electronics in various structures²⁸. Laser patterning of electrically conductive carbon is investigated mostly in terms of laser-assisted reduction of graphene oxide (GO) into 3D-graphene films, which have been used for energy storage and sensing applications^{28–34}. Major drawbacks are the high costs of GO production and the difficulties in tuning the properties of the resulting reduced GO films as it requires a multitude of synthesis steps. Another high potential material is laser-induced graphene (LIG) from polyimides (PI) which can be understood as a type of laser-induced carbonization^{35–41}. Even more advantageous is the use of organic nanoparticle inks based on naturally abundant molecules as precursors. It provides transferability to different flexible substrates and a high degree of tunability of the properties of the final carbons^{42,43}. These inks can be produced from a variety of molecular precursors⁴⁴. Moreover, the porous, semi-crystalline structures are environmentally stable and their

¹Micro- and Nanoanalytics Group, University of Siegen, Paul-Bonatz Str. 9–11, Siegen 57076, Germany. ²Max Planck Institut für Kolloid- und Grenzflächenforschung, Am Mühlenberg 1, 14476 Potsdam, Germany. ³LPICM, CNRS UMR 7647, Ecole polytechnique, Institut Polytechnique de Paris, Palaiseau 91128, France.

✉email: volker.strauss@mpikg.mpg.de

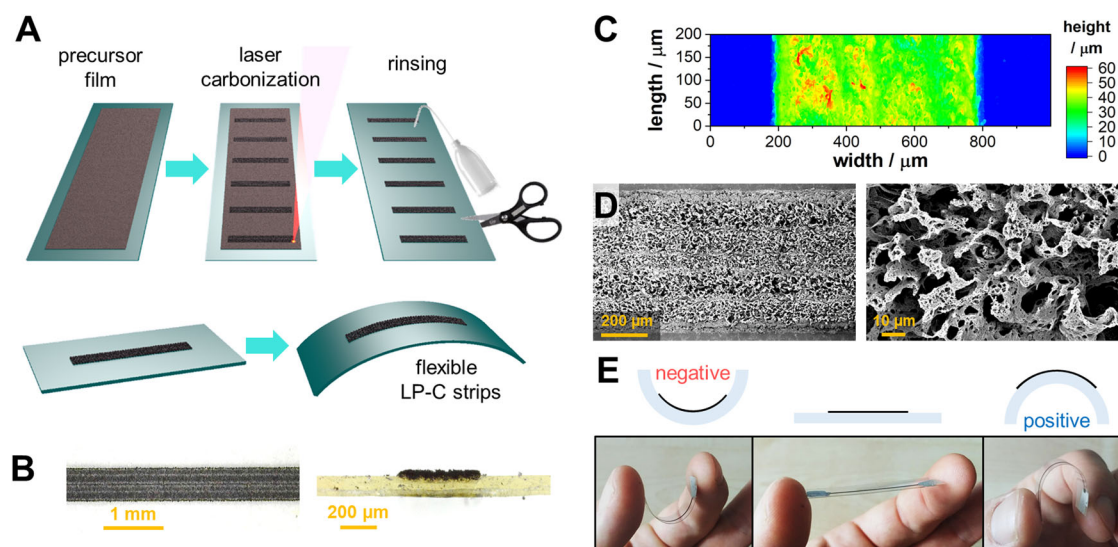


Fig. 1 Fabrication and initial characterization of flexible LP-C sensor strips. **A** Scheme of the fabrication process of laser-patterned carbon structures. **B** Digital optical micrographs of a laser-patterned carbon strip on transparent PET, top view on the left and cross-section on the right. **C** 2D height profile of a LP-C sensor strip obtained by vertical scanning interferometry. **D** Scanning electron micrographs of a LP-C film on PET shown in **(B)**. **E** Photographs of the LP-C strip on flexible PET upon positive and negative bending.

electrical properties are responsive to temperature and chemical environment^{45,46}.

In this study, we utilize carbon laser-patterning (CLaP) to produce functional carbon-based films with an intrinsically flexible morphology as a transferable and inexpensive method to produce reliable mechano-sensor platforms. The laser-patterned carbon (LP-C) was obtained from simple molecular precursors, namely citric acid and urea, and forms a composite with the flexible substrate, namely polyethylene terephthalate (PET) or polyurethane (PU). Based on a comprehensive cross-sectional investigation by high-resolution transmission electron microscopy (HRTEM), scanning transmission electron microscopy (STEM), and electron energy loss spectroscopy (EELS) a mechanism for the change in resistance of the LP-C films is proposed. After gentle training, the mechano-sensor strips show reliable and stable performance for several hundred cycles. The impact on the electronic properties during quantitative bending and compression experiments was analyzed in depth. Reversible changes in resistance on the order of $\Delta R/R_0 = 388\%$ upon positive bending and -22.9% upon negative bending are characteristic. Furthermore, quantitative reversible responses between $\Delta R/R_0 = 0$ and -15% were measured for mechanical pressure in the normal loading direction.

RESULTS

Fabrication of the sensor strips

Laser-patterned carbon (LP-C) was fabricated according to a recently published protocol with small modifications⁴³. In brief, a mixture of citric acid and urea was pre-carbonized at 300 °C. The thus obtained carbon network-forming agent (CNFA) was processed to an ink using ethylene glycol as a solvent, polyvinylpyrrolidone (PVP) as a film forming agent (FFA), and sodium iodide as a porogen. The mixture was gently stirred for 24 h to obtain a homogeneous viscous ink, which was applied on polyethylene terephthalate substrates (PET), polyurethane (PU), or nitrile gloves by doctor blading. The ink was patterned with a CO₂-laser engraver using the vector mode according to Fig. 1A (see “Experimental” section for details). Finally, the unexposed precursor film was rinsed off the substrate with H₂O. The presence of an infrared-laser transparent porogen (NaI) supports the penetration of the laser energy into deeper layers and increases the carbonization yield. However, no residues were found after

laser patterning by spectroscopic electron microscopy within the limitations of the applied techniques.

Characterization

Typical dimensions of LP-C patterns are 10 × 0.5 mm or 2 × 0.5 mm serving as a standard for the flexibility or compression tests, respectively. An optical micrograph of a representative printed pattern is presented in Fig. 1B. The thickness of the resulting laser-carbonized patterns was varied between 34 and 53 μm by adjusting the distance of the doctor blade during precursor film application (Supplementary Fig. 1). The films generally show a high roughness due to the hierarchical porous structure generated during the laser carbonization as shown in the height profiles obtained by vertical interference topography measurements (Fig. 1C). The roughness arises with the formation of the foamy structure due to evaporating products during the carbonization process (Fig. 1D). The laser treatment imposes a rapid heating, through which carbonization is achieved⁴². The energy input takes place from top to bottom of the film resulting in gradual carbonization across the film. This foamy morphology provides a high degree of mechanical flexibility compared to purely crystalline materials.

As we have shown in previous studies, the penetration depth of the laser is dependent on the extinction coefficient of the precursor material⁴⁴. A thickness of 15–50 μm allows for penetration throughout the precursor film. The electrical conductivities across the films were determined to be $7.2 \pm 0.8 \text{ S cm}^{-1}$. The LP-C film appears to be resistant against bending and touching as shown in the photographs in Fig. 1E. After manual fast bending, however, the films showed an infinitely high resistance although upon inspection by eye the LP-C strip seems intact. Upon slow bending, only minor changes in resistivity were detected as in detail discussed in the following.

Bending sensor

To study the stress-strain characteristics of the LP-C strips, we monitored the resistance R upon quantitative bending using a specially designed movable electrode stage suited for periodic fatigue testing. In the photographs in Fig. 2A an LP-C strip on PET is mounted between two electrodes. One of the electrodes was moved with a defined speed to bend the LP-C strip in positive

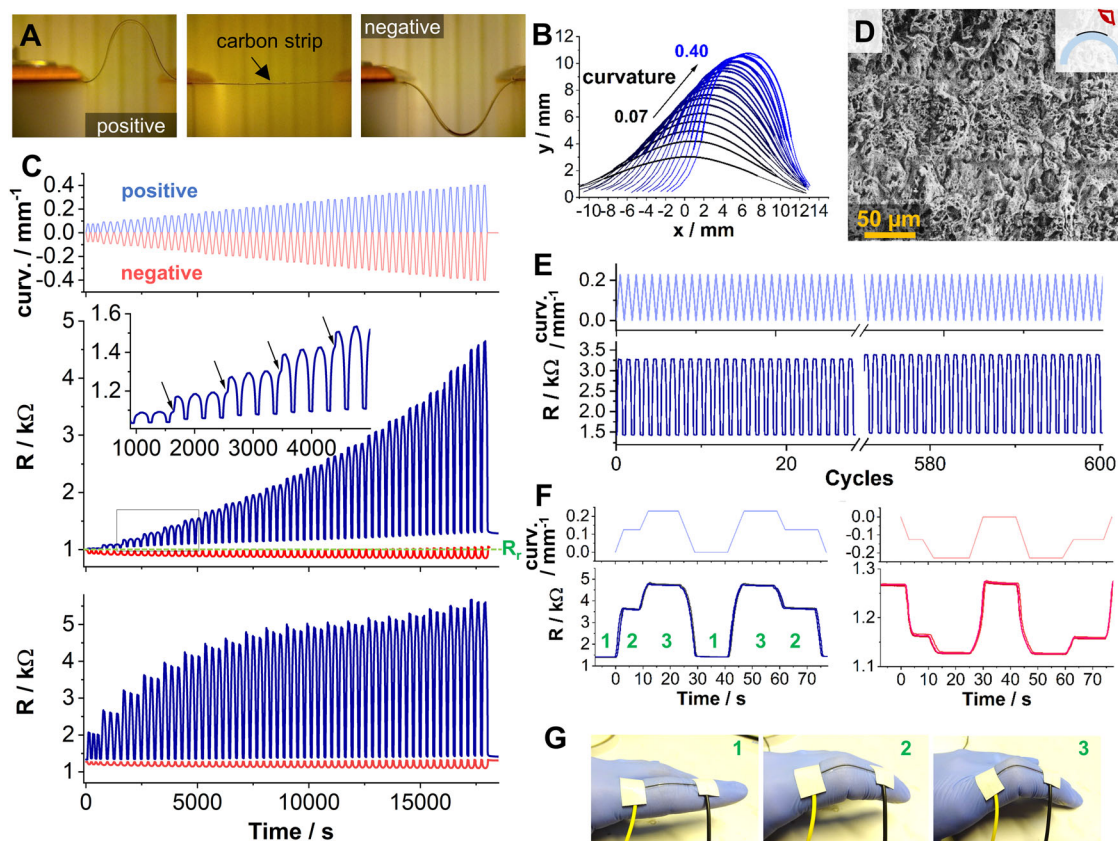


Fig. 2 Performance of flexible LP-C strips as bending sensors. **A** Photographs of a LP-C strip on flexible PET showing maximum bending in positive and negative direction. **B** Curvature analysis of the LP-C strip in dependence of the distance between the two electrodes in the movable stage. **C** Training the LP-C strip: Upper panel: applied change in curvature of the LP-C strip (blue: positive bending; red: negative bending). Center panel: Corresponding resistance response in the first run (training mode). Lower panel: Corresponding resistance response after the first cycle (operation mode). **D** SEM image of the LP-C strip at maximum bending after training. **E, F** Performance of the trained LP-C strip in operation mode. Upper panel: change in curvature of the LP-C strip in the movable stage. Lower panel: Corresponding resistance response of three cycles. **G** Photographs of a LP-C sensor strip fixed onto a nitrile glove for detection of finger motions.

(upward) or negative (downward) direction. The maximum curvature of the bending is dependent on the distance between the two electrodes as shown in Fig. 2B and was quantified in a range between a minimum value of 0.07 and a maximum value of 0.4 mm^{-1} (see Supplementary Fig. 2 and “Experimental” section). The LP-C strip was placed in the center between the moveable electrode stage and the electronic response towards quantitative bending was recorded with a four-probe resistance measurement setup.

Initially, the LP-C strips were bent with a speed of 1 mm s^{-1} to reach the maximum curvature of 0.4 mm^{-1} within 10 s. After this first test, the electrical integrity of the LP-C strip is irreversibly destroyed, i.e. the resistance of the LP-C strip responds indistinctly to a quantitative change in curvature (Supplementary Fig. 3). This is attributed to fractures of the material upon fast bending. A closer inspection by scanning electron microscopy (SEM) (Supplementary Fig. 4) shows the emergence of cracks when looking at the LP-C pattern in a bent state. To avoid fracture, fresh LP-C strips were bent at a slow speed of only $10 \mu\text{m s}^{-1}$ starting at low curvatures of 0.07 mm^{-1} and slowly increasing to the maximum curvature of 0.4 mm^{-1} (three times for each curvature/amplitude) (Fig. 2C). Thereby, the electrical integrity of such LP-C strips was retained. This systematic training procedure was applied for both bending directions, positive and negative in a subsequent manner to each LP-C strip. The upper panel in Fig. 2C shows the applied curvature as a function of time (blue = positive bending, red = negative bending), while the center panel shows the corresponding response of R upon bending in the first

run (training). The lower panel depicts the resulting response of R for operation. In the training of the positive bending, at low curvatures, the change in R is rather small but becomes larger with increasing curvatures. After the training, the response has changed in terms of ΔR and stabilizes for all subsequent cycles—in the operation mode. A closer look at the resistance curves during the first cycle in the inset of Fig. 2C shows two interesting aspects: (1) ΔR behaves non-linear to the change in curvature and (2) each time the curvature is increased, a step in the ΔR curve is observed. This response is attributed to a slowly induced structural change in the material. This sustainable change is finally reflected in a subtle increase of the resistance at rest (R_r)—in the flat state—in the particular case from 1.02 before to 1.29Ω after the bending experiment. Nevertheless, the structural integrity of the LP-C film in the bent state is largely retained and only minor cracks in the material are observed (Fig. 2D and Supplementary Fig. 4).

The asymmetric top-to-bottom geometry of the LP-C sensor strips, i.e. the placement of the active layer on one side of the substrate, is an advantage for the differentiation between positive and negative bending. As shown in the red curves in Fig. 2C, a decrease in resistance is observed upon negative bending. Although, the extent of ΔR is significantly smaller ($\Delta R_{\text{max}} \approx -183 \Omega$) than for positive bending, a quantitative and reversible signal is obtained.

After finishing the training, the LP-C strips can be cycled at any speed (max: 400 mm s^{-1}) to any indicated curvature giving a stable response (lower panel in Fig. 2C). For example, 600 bending cycles to a fixed curvature show a stable quantitative response

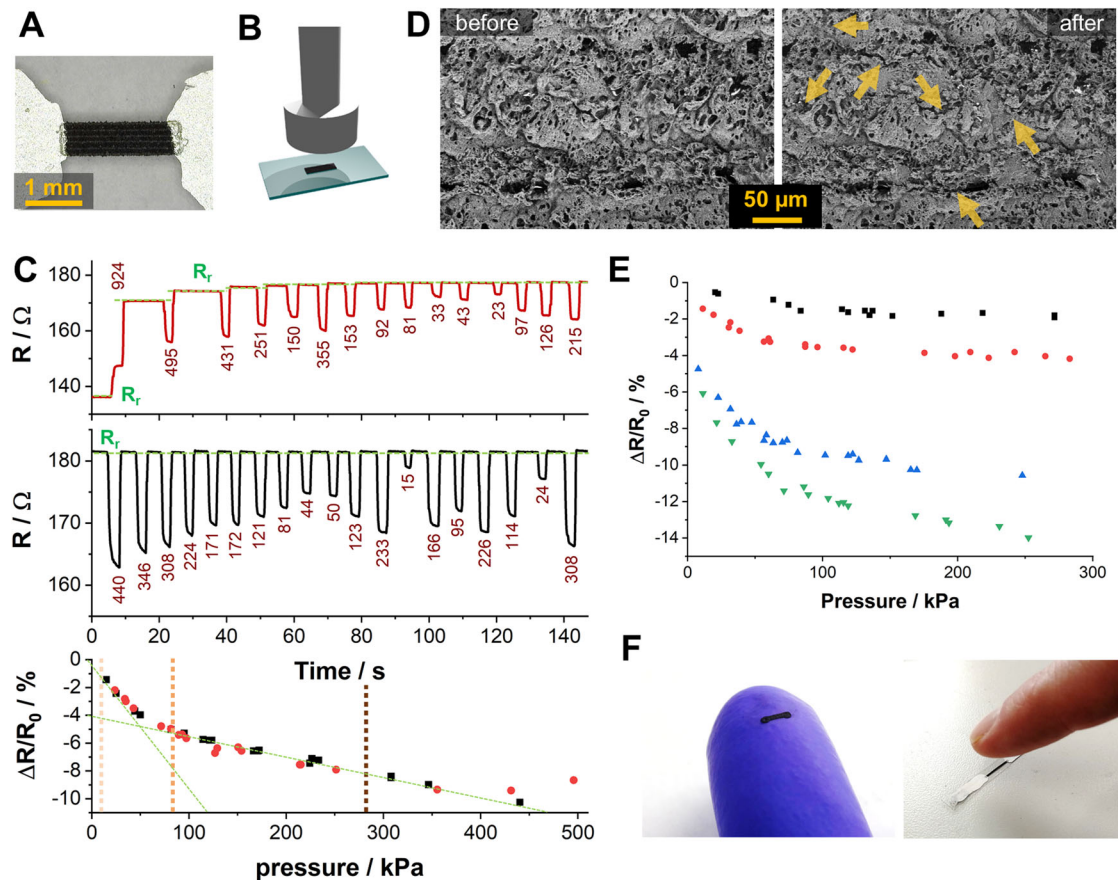


Fig. 3 Performance of flexible LP-C strips as pressure sensors. **A** Photograph of an LP-C pressure sensor on flexible PET used for quantitative experiments. **B** Experimental setup for the pressure sensing experiments. **C** Training and performance of the LP-C. Upper panel: Initial response of the resistance upon application of different pressures (Training). Center panel: Response of the resistance upon application of different pressures after training/stabilization (Operation). Lower panel: Change in resistance in dependence of the applied pressure, the dashed lines indicate a quantification of finger pressure (smart phone touch (light), pressing door bell (medium), maximum finger pressure (dark)). **D** Scanning electron micrographs of the LP-C pressure sensor before and after applying a maximum pressure of 500 kPa. **E** Quantitative response of LP-C sensors with different thickness or laser settings. **F** Photographs of LP-C pressure sensors directly printed onto nitrile gloves or PET.

(Fig. 2E). Two further exemplary bending patterns are given in Fig. 2F. The two bending directions and the extent of bending can be clearly differentiated. Such patterns represent, for instance, finger motions in the positive mode as shown in Fig. 2G.

The response is systematically dependent on the film thickness. In Supplementary Fig. 5 the resistance response of four samples with different thicknesses—34, 41, 48, and 53 μm —is shown. Notably, the general response behavior is the same for all tested samples. In the low curvature regime ($<0.10 \text{ mm}^{-1}$), the response of thicker films is weaker, while in the high curvature regime ($>0.15 \text{ mm}^{-1}$), the response of thicker films is significantly higher. For example, at maximum curvature we find $\Delta R/R = 451\%$ for a 48 μm thick film in the positive training cycle, whereas for 41 and 34 μm thick films we measure $\Delta R/R$ values of 302% and 259%. A mean film thickness of 53 μm leads to a non-quantitative response at high curvatures (Supplementary Fig. 5B). Therefore, we consider the mean thickness of 48 μm to be the upper threshold for producing stable quantitative sensors. These films are characterized by maximum operating $\Delta R/R$ values of 388% and -22.9% for maximum curvature in the positive and negative bending mode, respectively. (Supplementary Fig. 5C, D).

Strain sensor

To test the flexibility with regard to stretching and their applicability as strain sensors, LP-C films were printed on

stretchable polyurethane (PU) substrates. The printing pattern was slightly adopted to provide a better integrity upon substrate deformation (Supplementary Fig. 6). Quantitative response was observed upon stretching the LP-C film to 1.1 or 2.2% giving $\Delta R/R$ values of 13 or 73%, respectively. Up to a strain of 3.3%, a reversible behavior was measured giving $\Delta R/R$ values of around 425%, but the signal is indistinct quantitative. Strain higher than 3.3% results in irreversible rupture of the LP-C film.

Mechanical pressure sensors

The flexibility of the electrically conductive LP-C on PET and, in particular, the porous foamy morphology induced by the laser carbonization also facilitates the application as mechanical pressure sensors (normal loading direction). A force gauge with a flat tip (diameter 1.5 mm, mounted on a manual test bench) was employed to quantitatively apply pressure on an LP-C strip ($0.5 \times 2 \text{ mm}$) to test the electrical response upon normal mechanical loading (Fig. 3A, B). As in the previous bending experiments an initial training step was applied to bring the sensor into a reversible state, i.e. stabilizing the resistance at rest (R_r). The training is visualized in the upper panel of Fig. 3C. First, a maximum pressure of 924 kPa was applied which caused an increase in R_r from 136 to 171 Ω . This procedure was repeated with different pressure until the R_r after application of pressure was stabilized. After each pressure exertion a temporary decrease

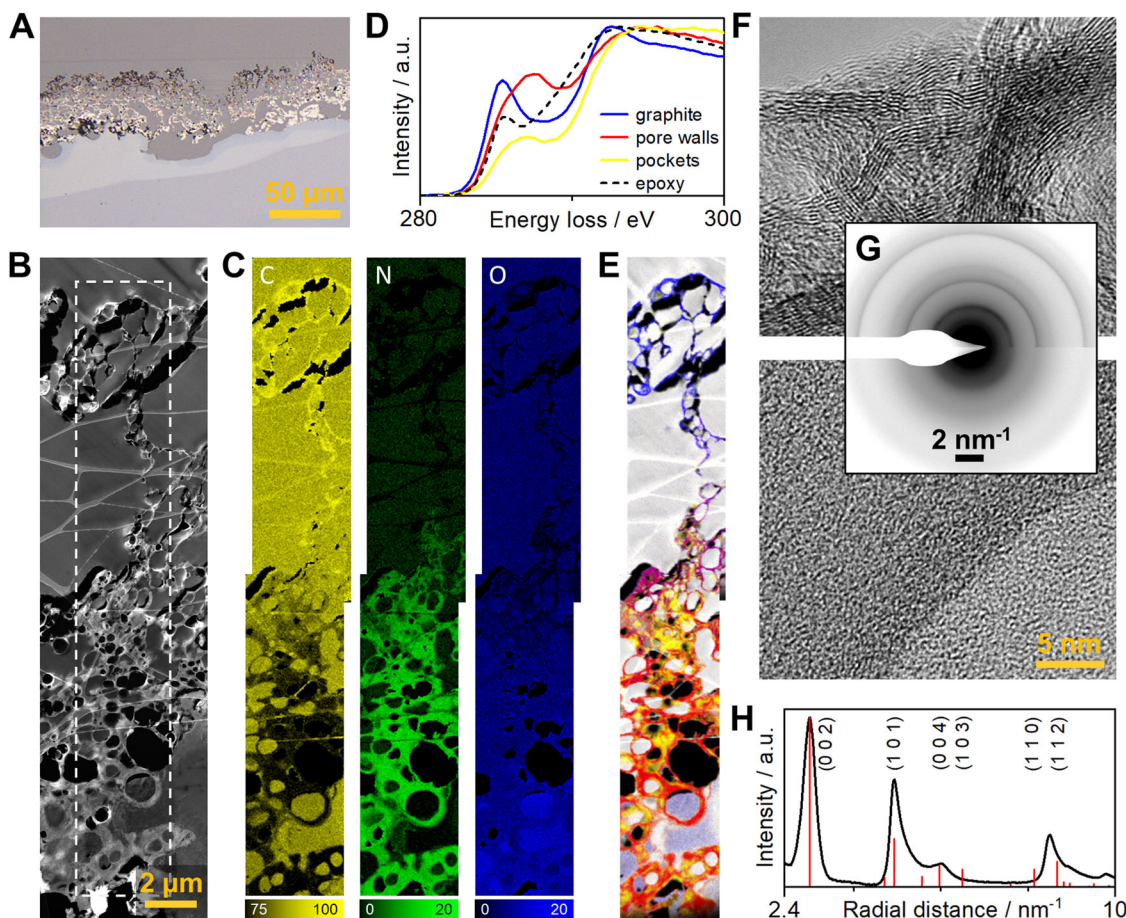


Fig. 4 Cross-sectional chemical and structural analysis of flexible LP-C sensor strips. **A** Optical micrograph of the resin infiltrated LP-C film. **B** Cross-sectional high-angle annular dark-field (HAADF)-STEM overview of LP-C film (PET substrate on bottom cropped, some pores appear black due to insufficient infiltration, web of Lacey TEM support film superimposed, epoxy at constant gray value). **C** EELS elemental maps of C, N, and O taken from the dashed area in **(A)** (concentrations given in at% without hydrogen). **D** Bonding analysis of the same region (blue: pure graphitic carbon, red: amorphous pore walls, yellow: pockets, white/black: resin). **E** EELS fitting parameters visualizing the distributions of the four components. **F** Representative HRTEM images from the upper and lower film regions. **G** Representative selected-area electron diffraction (SAED) patterns from the upper and lower regions of the LP-C film where the atomic-resolution micrographs were recorded. **H** Radial intensity scan from SAED pattern of the upper region of the LP-C film as shown in **(F)** (black) and simulated graphitic carbon (red).

in resistance is noted, however, the R_t increases slightly until it stabilizes at 181 Ω .

Once the R_t is stable, the sensor strip was tested for different pressure settings. Every subsequent pressure exertion quantitatively translates to a decrease in resistance. The center panel of Fig. 3C shows the resistance of an LP-C sensor strip upon subsequent application of different pressures as indicated in the graph. Notably, during operation the R_t is stable. In the lower panel of the graph, the quantitative response in terms of $\Delta R/R_0$ is shown. The change in resistance scales in a bi-linear fashion with the applied pressure as shown in the lower panel of Fig. 3C. In the low-pressure regime <60 kPa, a steeper slope is observed with $\Delta R/R_0$ values of up to -5% . The high-pressure regime >60 kPa is characterized by a resistance response of $\Delta R/R_0$ in the range of -5 to -10% . The overall morphology of the LP-C strip after the application of pressure appears still porous. However, obvious compression effects are noted. The SEM images in Fig. 3D show the same spot of the LP-C strip before and after exertion of pressure. Apparently, the porous structure is plastically compressed, which leads to a temporary increase in conductivity, as additional connections within the conductive material are established. Upon release of the mechanical pressure, these temporarily established connections are disconnected.

Like with the bending sensors, the response of LP-C as pressure sensors changes with the thickness of the LP-C. As demonstrated in Fig. 3E, four different mean film thicknesses of 34, 41, 48, and 53 μm were tested and a higher response was found for thicker LP-C films. The 53 μm thick film gives a response with maximum values of $\Delta R/R_0 = -15\%$. A lower mean thickness of 34 μm results in $\Delta R/R_0$ of only -5% . One intriguing aspect about the employed laser carbonization technique is its versatility regarding the choice of substrates. For example, the LP-C sensors can be printed directly onto nitrile gloves (Fig. 3F).

Cross-sectional characterization

To obtain a deeper understanding of the functional principle of the electronically responsive LP-C sensors, we conducted a detailed cross-sectional analysis. To preserve the film morphology and to generate cross-sectional samples for optical microscopy (OM) and TEM by ultramicrotomy, the LP-C films were infiltrated and thus completely embedded in a resin (see “Experimental” section).

The optical micrograph in Fig. 4A shows that the LP-C film is literally imprinted into the PET substrate. Under the applied laser illumination, the upper layer of approximately 40 μm of the PET

substrate appears lighter with respect to the rest of the substrate. In this region, the LP-C penetrates into the PET and vice versa providing the overall stability of the LP-C films against delamination. This effect stems from the heat induced by the laser, which causes the PET to melt ($m_p = 260^\circ\text{C}$) and merge with the LP-C. The molten PET becomes visible after removing the LP-C film with the aid of ultrasonication in 0.1 M KOH/H₂O (Supplementary Fig. 7). Furthermore, the optical micrograph shows a color/reflectance gradient from dark gray to shiny from the top to bottom of the film. This is correlated to chemical and structural variations across the film, which were analyzed in detail by (S)TEM.

Throughout the whole film, the LP-C patterns appear highly porous with a sponge-like structure as demonstrated by the STEM micrograph of a representative thin section Fig. 4B. The analysis corroborates a high degree of open porosity as almost all pores are well infiltrated with the resin throughout the films with a few local exceptions mostly on the substrate side (also confirmed by OM). Those residual voids appear black in the detailed analysis and do not show any signals (Fig. 4B, C, E). The pore diameters typically range from a few tens of nanometers up to a few micrometers throughout the functional film (Fig. 4A, B). The thickness of the pore walls varies from only a few nanometers at the top of the film and up to a few 100 nm towards the PET substrate (cf. STEM overview image in Fig. 4B and corresponding chemical-bond mapping in Fig. 4E). Moreover, at the substrate side, pockets between the pores are found, which are more evident in the chemical-bond mapping in Fig. 4E. Those pockets appear to be filled with less converted precursor material.

The cross-sectional TEM investigation allows for a detailed chemical and structural analysis across the whole LP-C film. A clear gradient with respect to the local chemical composition and consequently the bonding of carbon was found and confirms our previous interpretations⁴⁴. The EELS elemental distributions in Fig. 4C show the compositional gradients of carbon, nitrogen, and oxygen across the film. As expected from the laser treatment with the highest process temperature at the upper half of the film, the top part appears to be converted to mostly graphitic carbon explaining the thin pore walls. In contrast, high nitrogen and oxygen contents close to the composition of the reactants are determined in the lower half of the film. Unfortunately, the local concentration of hydrogen is not directly accessible by the employed techniques. The chemical-bond analysis (Fig. 4D, E, details in Experimental Section) clearly confirms the almost exclusive presence of graphitic carbon in the upper part (cf. obtained reference spectrum of graphite in Fig. 4D), while two components, i.e. amorphous pore walls and the less affected pocket regions in-between are clearly distinguished in the lower part of the film. Although the pockets between the pores – towards the substrate side – and the adjacent pore walls show similar compositions and are thus hardly separable in the elemental distributions (Fig. 4C), they clearly show different bonding character (Fig. 4E). Representative HRTEM images of the upper and the lower part of the films are presented in Fig. 4F. These images in conjunction with corresponding selected-area electron diffraction (SAED) patterns in Fig. 4G confirm a high degree of crystallinity of turbostratic graphitic carbon in the upper LP-C film regions while the lower regions still consist of predominantly amorphous pore walls and pockets. The crystal structure of graphite is clearly confirmed by comparing the radial SAED intensity distribution from the upper film region with a kinetic simulation presented in Fig. 4H; the differences in intensities, in particular the lower intensities of the (002), (004) and related reflections are attributed to the geometry of the cross-sectional TEM sample with presumably less basal planes of the graphite in diffraction condition.

DISCUSSION

Taking all information from the cross-sectional analysis into consideration, we draw the following conclusions. The overall mechanical stability against delamination is provided by penetration of molten PET into the LP-C film. Furthermore, we observe systematic chemical and structural gradients across the films due to the depth-dependent energy input during the laser-induced carbonization, resulting in a gradual graphitization. Around 10–15 μm below the film surface a clear and considerably abrupt transition region from crystalline turbostratic graphite to amorphous oxygen and nitrogen containing carbon is found.

This observation supports previous results⁴⁴. During laser carbonization, heat induced by the laser causes the decomposition of the precursor. The subsequent rapid release of gases causes the formation of pores, while the remaining material (pore walls) carbonizes and partly graphitizes. A lower degree of graphitization in the lower regions results in thicker pore walls. The expansion of the material during the laser-induced evaporation of the precursors causes some of the unreacted precursor material to be trapped in pockets between the pores.

It seems likely, that the turbostratically graphitized material is responsible for the electronic conductivity, however, morphological variations throughout the film impede a detailed micro-electrical analysis. As the overall porous morphology stays intact after mechanical training as well as during operation, the origin of the change in resistivity is attributed to nanoscopic changes of the local microstructure while preserving the mechanical integrity. The conductive part, i.e. the pore walls, is of turbostratic graphitic nature, i.e. nanocrystalline carbon and is best compared to activated carbons⁴⁴. According to the electric contact theory⁴⁷, the conductivity of activated carbons depends on the distance between conductive particles and their average size⁴⁸. Application of mechanical stress such as positive bending of the LP-C sensor effectively results in the release of mechanical pressure from the carbon network while application of mechanical pressure (negative bending) compresses the graphitized domains in the carbon network. In the same manner, the conductivity in activated carbons changes upon variation of the pressure^{49,50}. In LP-C, maximum bending results in a response of $\Delta R/R_0 \approx 400\%$ or -15% for positive or negative bending, respectively. Most stand-alone (binder-free) flexible carbon materials are based on graphene, carbon nanotubes, or carbon fibers. These carbon materials are genuinely advantageous due to their extremely high conductivities and their chemical inertness. However, their high conductivities limit their response for resistive sensing. For example, a graphene/carbon nanotube composite gives a $\Delta R/R_0 = 2\%$ at maximum bending. Pure carbon nanotube (CNT) networks give an even lower response⁵¹. Motion sensors based on carbon blacks are typically composited with conductive metallic nanoparticles to form conductive networks. Such motion sensors give a reasonable response of up to $\Delta R/R_0 \approx 80\%$ ⁵². However, in these scenarios, the response is not sensitive to the bending direction. In comparison, the herein discussed conductive foamy turbostratic carbon networks produced by CLaP are an extremely simple and cost-effective method and show excellent performance as mechanical sensors. Yet, the main drawback is the limited performance when applied as strain sensors.

We presented a comprehensive study on the mechanical properties of turbostratically graphitized carbon films obtained by CLaP. After slow training, the porous films show a stable and reproducible change in resistance of $\Delta R/R_0 = 388\%$ and -22.9% upon bending in positive or negative direction, respectively, with a quantitative response to any curvature. The films are environmentally stable and can be operated for several thousand cycles. A quantitative response is also obtained upon compression at normal loading. These properties make laser-patterned carbon films applicable as mechanical motion and pressure sensors

envisioning their utilization in robotics and bionics. An in-depth microscopic and spectroscopic cross-sectional analysis provides unprecedented insights into the microstructure and local chemistry of laser-patterned carbon. A compositional and structural gradient across the film due to the unidirectional laser impact was visualized by HRSTEM and EELS analyses. The sponge-like morphology of the turbostratic crystalline carbon provides a high degree of flexibility for reversible resistance changes. These properties make laser-patterned carbon interesting as a novel sustainable material for mechanical sensors with excellent mechanical properties and durability.

METHODS

Raw materials

Citric acid (99.5% for analysis, Fisher Scientific GmbH), urea (Certified AR for analysis, Fisher Scientific GmbH), ethylene glycol ($\geq 99.7\%$, AnalaR Normapur, VWR), polyvinylpyrrolidone (average mol wt. 10,000, Sigma Aldrich), sodium iodide (99.5% min, Alfa Aesar) were used without further purification. PET substrates (Melinex sheets, Dupont) with a thickness of 170 μm were used as obtained from Plano GmbH. PU substrate was Desmopan 9370 AU from Covestro Deutschland AG.

Preparation of carbon network-forming agent (CNFA) and the precursor films

Citric acid and urea were thoroughly mixed in a quartz crucible. The vessel was covered with a lid to avoid spilling of the foaming reaction product and to allow evaporation of evolving gases a small opening was placed under the lid. The mixtures were annealed at 300 $^{\circ}\text{C}$ in a tube furnace for 2 h under constant flux of N_2 (0.1 L min^{-1}). After annealing, the black reaction product was retained and grinded in a ball mill to obtain a fine black powder (CNFA).

Polyvinylpyrrolidone (200 mg mL^{-1}) was dissolved in ethylene glycol (EtGly) to obtain a 0.2 g mL^{-1} solution (PVP/EtGly). Sodium iodide was dissolved in the mixture at a concentration of 0.4 mg mL^{-1} . The CNFA was then added and stirred for 24 h to obtain a 1 g mL^{-1} dispersion. The resulting ink was doctor bladed on the PET substrates to obtain uniform films. Ethylene glycol was then evaporated at 80 $^{\circ}\text{C}$ on a precision hotplate (PZ2860-SR, Gestigkeit GmbH) to obtain the precursor films.

Laser-assisted carbonization

Laser carbonization was conducted with a high-precision laser engraver setup (Speedy 100, Trotec) equipped with a 60 W CO_2 laser. Focusing was achieved with a 2.5 inch focus lens providing a focal depth of ~ 3 mm and a focus diameter of 170 μm . The center wavelength of the laser is 10.6 ± 0.03 μm . The scanning speed v' , generically given in %, was converted into s m^{-1} . The effective output power P of the laser was measured with a Solo 2 (Gentec Electro-Optics) power meter. The resulting energy input per distance (or fluence) F in J m^{-1} in the vector mode onto the film is given by

$$F = P \cdot v'$$

For the experiments, the laser settings were adjusted to meet the requirements of the films. After laser carbonization the unexposed zones of the precursor films were rinsed off the substrate with H_2O .

Mechano-resistance measurements

Bending experiments were performed with a home-made force table. The sample strip was clamped by two opposing copper electrode clips at a distance of 25 mm, of which one was connected to a movable table. To provide a better electrical contact both ends of the carbon strip were connected with silver paint to the copper electrodes. The curvature of the bending was determined by translating the shapes from photographs into x - y data using the freeware Engauge Digitizer⁵³. The curvature is defined as the inverse radius at the maximum point of bending.

Compression experiments were conducted with a digital force gauge with a flat tip with a diameter of 1.5 cm mounted on a manual test bench. Sensor strips with dimensions 0.5 \times 2 mm were patterned on PET substrates. At the two ends of the pattern silver ink was applied to provide proper contact to the electrodes. Reference measurements were

conducted to ensure that the silver ink did not affect the performance of the sensor.

In all experiments, the resistance was monitored in four-point geometry using a RS PRO RSDM3055A digital multimeter controlled by Matlab-based software.

Preparation of resin infiltrated films for cross-sectional TEM analysis

Cross-sectional preparation of electron transparent TEM samples was conducted by ultramicrotomy using a Leica EM UC7 microtome. To conserve the film morphology, individual patterned samples on PET were extracted by doctor-blade cutting and embedded in epoxy (Epofix, Struers, Germany). A self-built vacuum tool was employed to infiltrate the highly open-porous samples. Curing of the epoxy was achieved by annealing at 60 $^{\circ}\text{C}$ for 4 h. The sample regions, potentially damaged by blade cutting, were removed by trimming (DiATOME 45 $^{\circ}$ trim knife) a truncated pyramid with a trapezoid-shaped block face. Cross-sectional TEM samples were cut with a DiATOME 45 $^{\circ}$ histo diamond knife and were subsequently transferred onto Lacey carbon TEM grids (TedPella/Plano) for enhanced support.

Characterization

Scanning electron microscopy was performed on a Zeiss LEO 1550 Gemini microscope at acceleration voltages in the range of 3–10 kV.

Vertical scanning interferometry was performed with a vertical scanning interferometer smartWLI compact (GBS mbH, Germany) with the software smartVIS3D 2.28 Tango and visualized with MountainsMap 8.

Transmission electron microscopy was performed utilizing a Thermo Fisher FEI Talos F200X operated at 200 kV. The instrument is equipped with a XFEI high-brightness gun, a large-area Super-X EDXS detector and a Gatan Continuum ER spectrometer (with high-speed DualEELS, dispersion 0.3 eV/channel, DigiScan, EDXS integration, GMS 3.4x) for electron energy-loss spectroscopy. For morphological and structural analyses, bright-/dark-field (BF/DF) imaging, selected-area electron diffraction (respective selected-area diameter on sample corresponding to almost 1 μm), high-resolution TEM and high-angle annular dark-field scanning TEM were conducted, while advanced electron energy-loss spectroscopy was employed for detailed compositional and chemical-bond analyses. Owing the relative thickness of the prepared cross-sections (around 0.4–1.2 mean-free paths for inelastic scattering depending on the local material), Dual EELS was used to simultaneously record core-loss as well as corresponding low-loss spectra for systematic energy-loss recalibration and the removal of multiple scattering from the element-specific core-loss spectra by deconvolution. The core-loss spectra in the energy-loss range of 200–800 eV covered all interested ionization edges of C, N, and O at around 285 eV, 400 eV and 532 eV, respectively. The elemental distributions of C, N, and O were quantified using the theoretical ionization cross-sections as implemented in the Gatan software suite because the results from the used epoxy as internal reference closely correspond to its given composition. The presented atomic concentrations exclude hydrogen because it is not measurable by EELS, thus $c_{\text{C}} + c_{\text{N}} + c_{\text{O}}$ in Fig. 4B equals 100 at%. For detailed chemical-bond analyses, four major components, namely the epoxy, graphitic carbon (upper sample regions), pore walls in the lower regions and less reacted pockets, were identified and reference spectra were obtained from the mapping itself. Therefore, individual spectra from such well characterized regions (match with STEM/HRTEM data) were thoroughly selected, summarized and finally normalized. To distinguish between the different components, each individual spectrum of a mapping was evaluated by fitting (multiple least-squares minimization) those references to the carbon ionization edge (energy-loss range 280–310 eV). The evaluation implied the thorough verification of the corresponding intensities of the N and O ionization edges.

DATA AVAILABILITY

All data needed to evaluate the conclusions in the paper are present in the paper and/or the Supplementary Materials. Additional datasets generated during and/or analysed during the current study are available from the corresponding author on reasonable request.

Received: 11 August 2021; Accepted: 17 December 2021;
Published online: 21 January 2022

REFERENCES

- Corzo, D., Tostado-Blázquez, G. & Baran, D. Flexible electronics: status, challenges and opportunities. *Front. Electron.* **1**, 594003 (2020).
- Zou, M. et al. Flexible devices: from materials, architectures to applications. *J. Semicond.* **39**, 011010 (2018).
- Wang, P. et al. The evolution of flexible electronics: from nature, beyond nature, and to nature. *Adv. Sci.* **7**, 2001116 (2020).
- Nag, A., Mukhopadhyay, S. C. & Kosel, J. Wearable flexible sensors: a review. *IEEE Sens. J.* **17**, 3949–3960 (2017).
- Chortos, A. & Bao, Z. Skin-inspired electronic devices. *Mater. Today* **17**, 321–331 (2014).
- Wang, X., Liu, Z. & Zhang, T. Flexible sensing electronics for wearable/attachable health monitoring. *Small* **13**, 1602790 (2017).
- Gong, S. et al. A wearable and highly sensitive pressure sensor with ultrathin gold nanowires. *Nat. Commun.* **5**, 3132 (2014).
- Amjadi, M., Pichitpajongkit, A., Lee, S., Ryu, S. & Park, I. Highly stretchable and sensitive strain sensor based on silver nanowire–elastomer nanocomposite. *ACS Nano* **8**, 5154–5163 (2014).
- Wang, B. et al. Flexible and stretchable metal oxide nanofiber networks for multimodal and monolithically integrated wearable electronics. *Nat. Commun.* **11**, 2405 (2020).
- Yao, S. & Zhu, Y. Wearable multifunctional sensors using printed stretchable conductors made of silver nanowires. *Nanoscale* **6**, 2345 (2014).
- Wang, X., Gu, Y., Xiong, Z., Cui, Z. & Zhang, T. Silk-molded flexible, ultrasensitive, and highly stable electronic skin for monitoring human physiological signals. *Adv. Mater.* **26**, 1336–1342 (2014).
- Lipomi, D. J. et al. Skin-like pressure and strain sensors based on transparent elastic films of carbon nanotubes. *Nat. Nanotechnol.* **6**, 788–792 (2011).
- Wang, X. et al. Self-cross-linked arrays enabled flexible mechanical sensors for monitoring the body tremor. *npj Flex. Electron.* **4**, 8 (2020).
- Liao, C. et al. Flexible organic electronics in biology: materials and devices. *Adv. Mater.* **27**, 7493–7527 (2015).
- Zhang, F., Zang, Y., Huang, D., Di, C. & Zhu, D. Flexible and self-powered temperature–pressure dual-parameter sensors using microstructure-frame-supported organic thermoelectric materials. *Nat. Commun.* **6**, 8356 (2015).
- Ge, G. et al. Muscle-inspired self-healing hydrogels for strain and temperature sensor. *ACS Nano* **14**, 218–228 (2020).
- Samori, P. & Palermo, V. *Flexible Carbon-based Electronics* (Wiley-VCH Verlag GmbH & Co. KGaA, 2018).
- Rakitin, A., Papadopoulos, C. & Xu, J. M. Carbon nanotube self-doping: calculation of the hole carrier concentration. *Phys. Rev. B* **67**, 33411 (2003).
- Kuzmany, H. et al. Determination of SWCNT diameters from the Raman response of the radial breathing mode. *Eur. Phys. J. B—Condens. Matter Complex Syst.* **22**, 307–320 (2001).
- Wang, F., Dukovic, G., Brus, L. & Heinz, T. Time-resolved fluorescence of carbon nanotubes and its implication for radiative lifetimes. *Phys. Rev. Lett.* **92**, 17–20 (2004).
- Tan, P. H. et al. Photoluminescence spectroscopy of carbon nanotube bundles: evidence for exciton energy transfer. *Phys. Rev. Lett.* **99**, 137402 (2007).
- Gu, Y. et al. Flexible electronic eardrum. *Nano Res.* **10**, 2683–2691 (2017).
- Yamamoto, Y. et al. Printed multifunctional flexible device with an integrated motion sensor for health care monitoring. *Sci. Adv.* **2**, e1601473 (2016).
- Yuan, J., Giordano, C. & Antonietti, M. Ionic liquid monomers and polymers as precursors of highly conductive, mesoporous, graphitic carbon nanostructures. *Chem. Mater.* **22**, 5003–5012 (2010).
- Van Noorden, R. Chemistry: the trials of new carbon. *Nature* **469**, 14–16 (2011).
- Ambrosi, A. & Pumera, M. 3D-printing technologies for electrochemical applications. *Chem. Soc. Rev.* **45**, 2740–2755 (2016).
- Majumdar, J. D. & Manna, I. *Laser-Assisted Fabrication of Materials. Springer Series in Materials Science* Vol. 161, (Springer, 2013).
- Strong, V. et al. Patterning and electronic tuning of laser scribed graphene for flexible all-carbon devices. *ACS Nano* **6**, 1395–1403 (2012).
- Kumar, R. et al. Laser-assisted synthesis, reduction and micro-patterning of graphene: Recent progress and applications. *Coord. Chem. Rev.* **342**, 34–79 (2017).
- Gao, W. et al. Direct laser writing of micro-supercapacitors on hydrated graphite oxide films. *Nat. Nanotechnol.* **6**, 496–500 (2011).
- Sokolov, D. A., Rouleau, C. M., Geohagan, D. B. & Orlando, T. M. Excimer laser reduction and patterning of graphite oxide. *Carbon* **53**, 81–89 (2013).
- Sokolov, D. A., Shepperd, K. R. & Orlando, T. M. Formation of graphene features from direct laser-induced reduction of graphite oxide. *J. Phys. Chem. Lett.* **1**, 2633–2636 (2010).
- Ghoniem, E., Mori, S. & Abdel-Moniem, A. Low-cost flexible supercapacitors based on laser reduced graphene oxide supported on polyethylene terephthalate substrate. *J. Power Sources* **324**, 272–281 (2016).
- Trusovas, R. et al. Reduction of graphite oxide to graphene with laser irradiation. *Carbon* **52**, 574–582 (2013).
- Bürger, A., Fitzer, E., Heym, M. & Terwiesch, B. Polyimides as precursors for artificial carbon. *Carbon* **13**, 149–157 (1975).
- Inagaki, M. et al. Carbonization of polyimide film “Kapton”. *Carbon* **27**, 253–257 (1989).
- Stanford, M. G., Yang, K., Chyan, Y., Kittrell, C. & Tour, J. M. Laser-induced graphene for flexible and embeddable gas sensors. *ACS Nano* **13**, 3474–3482 (2019).
- Huang, L., Su, J., Song, Y. & Ye, R. Laser-induced graphene: en route to smart sensing. *Nano-Micro Lett.* **12**, 157 (2020).
- Ye, R., James, D. K. & Tour, J. M. Laser-induced graphene: from discovery to translation. *Adv. Mater.* **31**, 1803621 (2019).
- Mamleyev, E. R. et al. Laser-induced hierarchical carbon patterns on polyimide substrates for flexible urea sensors. *npj Flex. Electron.* **3**, 2 (2019).
- Lin, J. et al. Laser-induced porous graphene films from commercial polymers. *Nat. Commun.* **5**, 5714 (2014).
- Strauss, V., Marsh, K., Kowal, M. D., El-Kady, M. F. & Kaner, R. B. A simple route to porous graphene from carbon nanodots for supercapacitor applications. *Adv. Mater.* **30**, 1704449 (2018).
- Delacroix, S., Wang, H., Heil, T. & Strauss, V. Laser-induced carbonization of natural organic precursors for flexible electronics. *Adv. Electron. Mater.* **6**, 2000463 (2020).
- Wang, H. et al. Laser-carbonization: peering into the formation of micro-thermally produced (N-doped)carbons. *Carbon* **176**, 500–510 (2021).
- Delacroix, S. et al. Using carbon laser patterning to produce flexible, metal-free humidity sensors. *ACS Appl. Electron. Mater.* **2**, 4146–4154 (2020).
- Wang, H. et al. In situ synthesis of molybdenum carbide nanoparticles incorporated into laser-patterned nitrogen-doped carbon for room temperature VOC sensing. *Adv. Funct. Mater.* **31**, 2104061 (2021).
- Holm, R. *Electric Contacts* (Springer, 1967).
- Pantea, D., Darmstadt, H., Kaliaguine, S. & Roy, C. Electrical conductivity of conductive carbon blacks: influence of surface chemistry and topology. *Appl. Surf. Sci.* **217**, 181–193 (2003).
- Adinaveen, T., Vijaya, J. J. & Kennedy, L. J. Comparative study of electrical conductivity on activated carbons prepared from various cellulose materials. *Arab. J. Sci. Eng.* **41**, 55–65 (2016).
- Sánchez-González, J., Macías-García, A., Alexandre-Franco, M. F. & Gómez-Serrano, V. Electrical conductivity of carbon blacks under compression. *Carbon* **43**, 741–747 (2005).
- Shi, J. et al. Graphene reinforced carbon nanotube networks for wearable strain sensors. *Adv. Funct. Mater.* **26**, 2078–2084 (2016).
- Zhang, W., Liu, Q. & Chen, P. Flexible strain sensor based on carbon black/silver nanoparticles composite for human motion detection. *Materials* **11**, 1836 (2018).
- Mitchell, M., Muftakhidinov, B. & Winchen, T. Engauge Digitizer Software. Available at: <http://markummitchell.github.io/engauge-digitizer> (2021).

ACKNOWLEDGEMENTS

The authors are grateful for financial support from the Fonds der Chemischen Industrie and the Max Planck Society. The continuous educational support from Prof. Markus Antonietti is highly appreciated. Part of this work was performed at the DFG-funded Micro-and Nanoanalytics Facility (MNAF) of the University of Siegen (INST 221/131-1) utilizing its major TEM instrumentation (DFG INST 221/93-1, DFG INST 221/126-1) and sample preparation equipment. We thank Klaus Bienert for helping in designing and setting up the force table. We thank Covestro Deutschland AG for providing substrates.

AUTHOR CONTRIBUTIONS

M.H.: Investigation, Methodology, Validation, Writing—Original Draft; H.W.: Investigation, Methodology; K.D.: Investigation, Validation; S.D.: Investigation, Methodology, Validation; S.R.: Resources, Investigation; F.F.L.: Resources, Supervision; B.B.: Conceptualization, Supervision, Methodology, Validation, Writing—Original Draft, Writing—Review & Editing; V.S.: Conceptualization, Methodology, Validation, Writing—Original Draft, Writing—Review & Editing, Supervision, Project administration.

FUNDING

Open Access funding enabled and organized by Projekt DEAL.

COMPETING INTERESTS

The authors declare no competing interests.

ADDITIONAL INFORMATION

Supplementary information The online version contains supplementary material available at <https://doi.org/10.1038/s41528-022-00136-0>.

Correspondence and requests for materials should be addressed to Volker Strauss.

Reprints and permission information is available at <http://www.nature.com/reprints>

Publisher's note Springer Nature remains neutral with regard to jurisdictional claims in published maps and institutional affiliations.



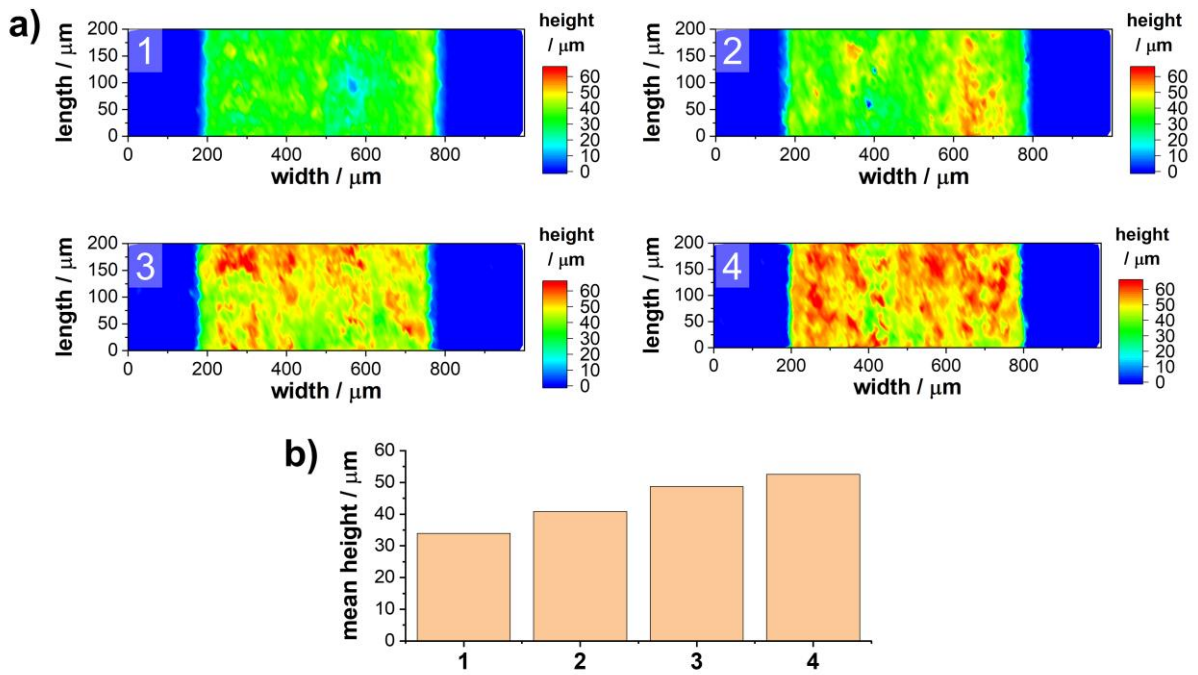
Open Access This article is licensed under a Creative Commons Attribution 4.0 International License, which permits use, sharing, adaptation, distribution and reproduction in any medium or format, as long as you give appropriate credit to the original author(s) and the source, provide a link to the Creative Commons license, and indicate if changes were made. The images or other third party material in this article are included in the article's Creative Commons license, unless indicated otherwise in a credit line to the material. If material is not included in the article's Creative Commons license and your intended use is not permitted by statutory regulation or exceeds the permitted use, you will need to obtain permission directly from the copyright holder. To view a copy of this license, visit <http://creativecommons.org/licenses/by/4.0/>.

© The Author(s) 2022

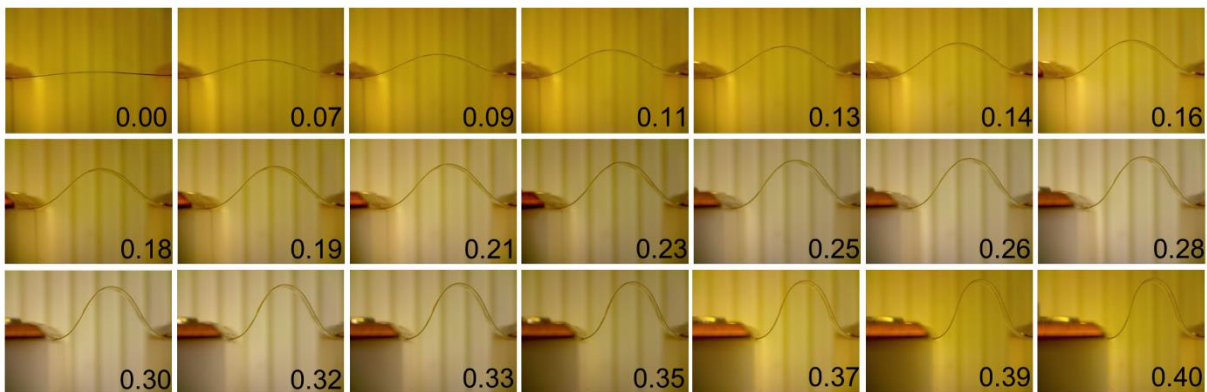
Supplementary Information to
Trained Laser-Patterned Carbon as High-Performance
Mechanical Sensors

Marco Hepp, Huize Wang, Katharina Derr, Simon Delacroix, Sebastian Ronneberger, Felix Loeffler, Benjamin Butz, Volker Strauss*

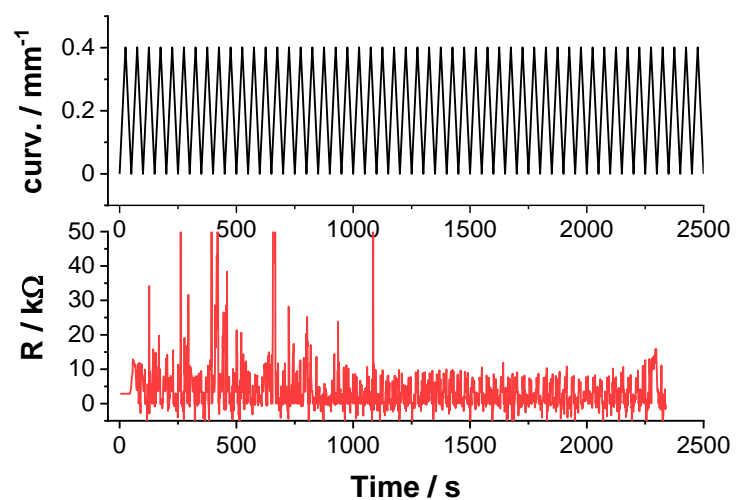
Supplementary Figures



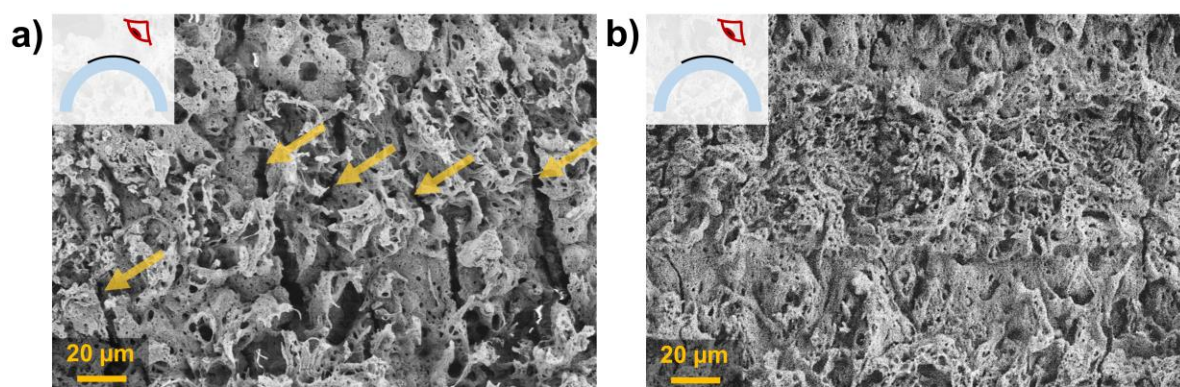
Supplementary Figure 1. Thickness analysis of LP-C sensor strips. a) 2D height profiles of the LP-sensor strips measured by vertical scanning interferometry; b) Mean height of the LP-sensor strips obtained from the 2D height profiles above.



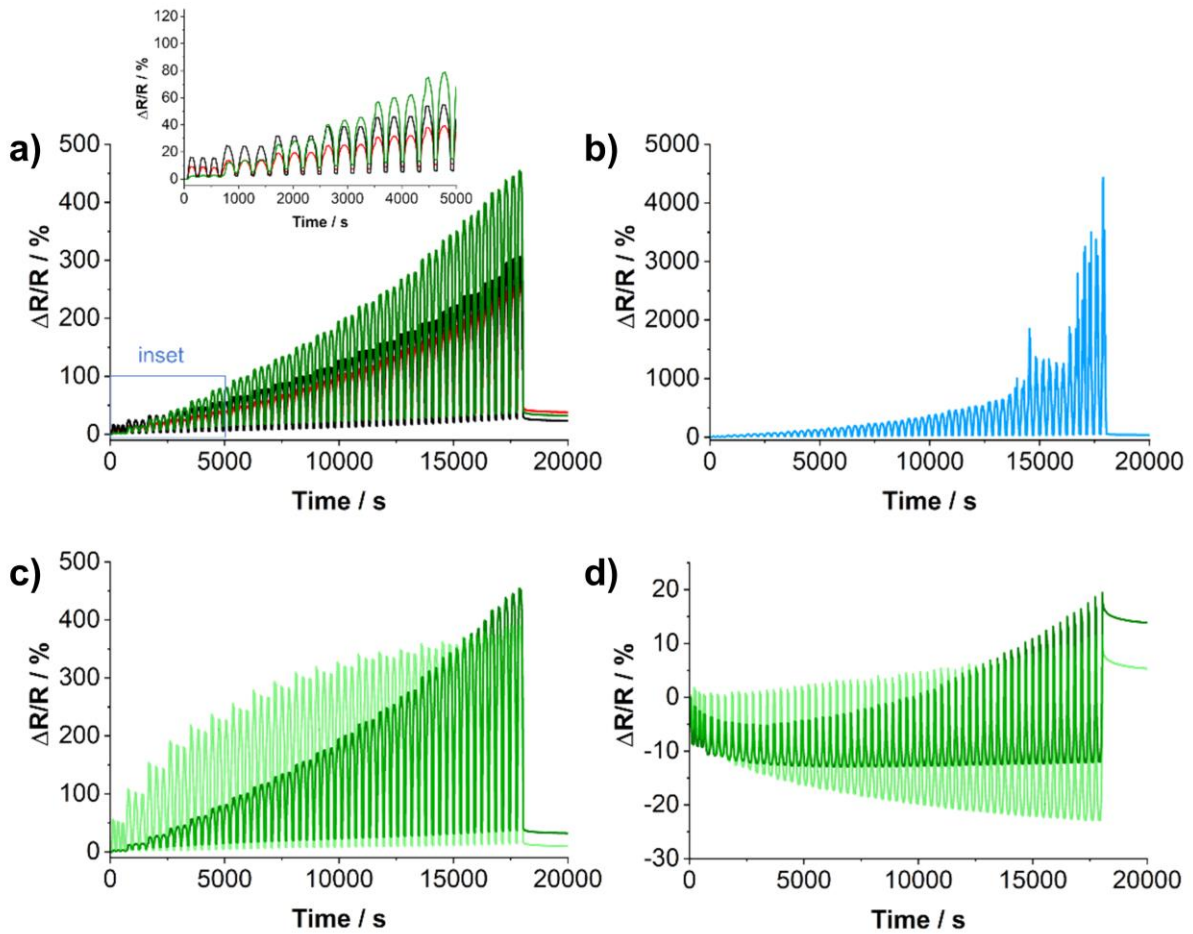
Supplementary Figure 2. Bending experiments. Photographs of the LP-C strip on PET mounted between two movable electrodes. The number indicates the curvature.



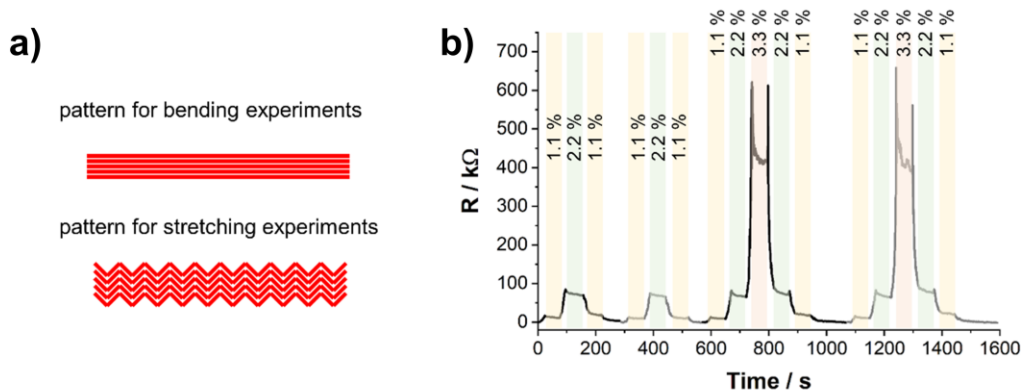
Supplementary Figure 3. Bending experiments. a) change in curvature of the LP-C strip in the movable stage at a speed of 0.4 mm s^{-1} . b) Corresponding change in resistance.



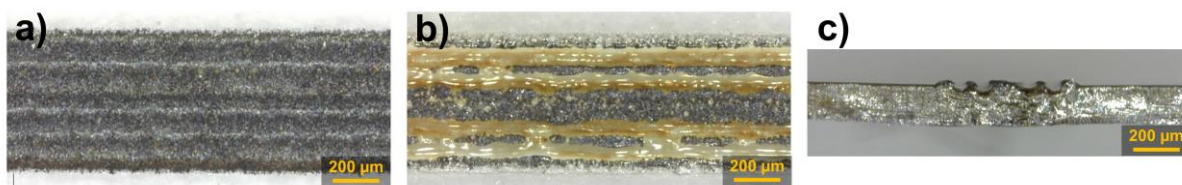
Supplementary Figure 4. Scanning electron micrographs of LP-C strips in a bent state (positive = upwards) a) without and b) after training.



Supplementary Figure 5. Performance of LP-C sensor strips with different thickness. a) Resistance response in the training cycles (positive curvature) of LP-C strips with different mean thickness – 34 μm (red), 41 μm (black), 48 μm (green); b) Resistance response in the training cycles of an LP-C strip with a thickness of 53 μm (blue). c) Resistance response in the positive bending training (dark green) and operating cycle (light green) of LP-C strip with a mean thickness of 48 μm (green); d) Resistance response in the negative bending training (dark green) and operating cycle (light green) of LP-C strip with a mean thickness of 48 μm (green).



Supplementary Figure 6. Stretching experiments. a) Printing pattern used for stretching experiments. Sensor strips were printed on PU substrates; b) Response of R upon stretching the sensor strip to 1.1, 2.2, or 3.3%.



Supplementary Figure 7. PET substrate after removing the LP-C film. a) Digital micrograph of a LP-C strip on PET; b) The same region after removing the LP-C film by ultrasonication in 0.1 M KOH/H₂O; c) Cross-sectional view on the PET substrate after removing the LP-C film by ultrasonication in 0.1 M KOH/H₂O. The two images in the center and on the right show the molten regions in the PET substrate. It can be seen that besides the laser keyholes the PET elevates above the flat upper substrate surface.

Flexible CO₂ Sensor Architecture with Selective Nitrogen Functionalities by One-Step Laser-Induced Conversion of Versatile Organic Ink

Huize Wang, Charles Otieno Ogolla, Gyanendra Panchal, Marco Hepp, Simon Delacroix, Daniel Cruz, Danny Kojda, Jim Ciston, Colin Ophus, Axel Knop-Gericke, Klaus Habicht, Benjamin Butz,* and Volker Strauss*

Nitrogen-containing carbons (NC) are a class of sustainable materials for selective CO₂ adsorption. A versatile concept is introduced to fabricate flexible NC-based sensor architectures for room-temperature sensing of CO₂ in a one-step laser conversion of primary films cast from abundant precursors. By the unidirectional energy impact in conjunction with depth-dependent attenuation of the laser beam, a layered sensor heterostructure with a porous transducer and active sensor layer is formed. Comprehensive microscopic and spectroscopic cross-sectional analyses confirm the preservation of the high content of imidazole nitrogen in the sensor. The performance is optimized in terms of material morphology, chemical composition, and surface chemistry to achieve a linear relative resistive response of up to $\Delta R/R_0 = -14.3\%$ (10% of CO₂). Thermodynamic analysis yields $\Delta_{\text{ads}}H$ values of -35.6 and 34.1 kJ·mol⁻¹ for H₂O and CO₂, respectively. The sensor is operable even in humid environments (e.g., $\Delta R/R_{0,\text{RH}} = 80\% = 0.53\%$) and shows good performance upon strong mechanical deformation.

need for comprehensive CO₂ monitoring on local and global scales.^[1,2] To fight global warming, a deeper awareness of the public of the impact of greenhouse gases like CO₂ may be required. In industrial and work environments, high concentrations of CO₂ (in)directly pose health risks due to acidosis or the enrichment of undesired species like viruses, or may cause performance loss even during office work.^[3] Capable smart mobile devices and flexible wearables to collect exhaled breath may support decentralized healthcare as well as professional and amateur sport.^[4]

Handheld or stationary infrared absorption sensors represent state-of-the-art device technology but exhibit limitations regarding versatility, compactness, and integrability.^[5] Integrated micro-sensors,

with a superior property portfolio including small size, flexibility, and low cost would facilitate comprehensive spatial and temporal analyses of CO₂ in a wide range of applications.^[6]

Thus, the development of simple miniaturized sensors with a rapid response for a wide range of CO₂ concentrations has

1. Introduction

Monitoring CO₂ is imperative to understand its origin and impact. Both, the global climate crisis and the current COVID-19 pandemic have shifted attention and created awareness of the

H. Wang, V. Strauss
Max-Planck-Institut für Kolloid- und Grenzflächenforschung
Am Mühlenberg 1, 14476 Potsdam, Germany
E-mail: volker.strauss@mpikg.mpg.de

C. O. Ogolla, M. Hepp, B. Butz
Micro-and Nanoanalytics Group
University of Siegen
Paul-Bonatz Str. 9–11, 57076 Siegen, Germany
E-mail: benjamin.butz@uni-siegen.de

G. Panchal, D. Kojda, K. Habicht
Dept. Dynamics and Transport in Quantum Materials
Helmholtz-Zentrum Berlin für Materialien und Energie GmbH
Hahn-Meitner-Platz 1, 14109 Berlin, Germany

 The ORCID identification number(s) for the author(s) of this article can be found under <https://doi.org/10.1002/adfm.202207406>.

© 2022 The Authors. Advanced Functional Materials published by Wiley-VCH GmbH. This is an open access article under the terms of the Creative Commons Attribution License, which permits use, distribution and reproduction in any medium, provided the original work is properly cited.

DOI: 10.1002/adfm.202207406

S. Delacroix
LPICM
CNRS UMR 7647
Ecole polytechnique
Institut Polytechnique de Paris
91128 Palaiseau, France

D. Cruz, A. Knop-Gericke
Department of Inorganic Chemistry
Fritz-Haber-Institut der Max-Planck-Gesellschaft
Faradayweg 4–6, 14195 Berlin, Germany

D. Cruz, A. Knop-Gericke
Department of Heterogeneous Reactions
Max Planck Institute for Chemical Energy Conversion
Stiftstraße 34–36, 45470 Mülheim an der Ruhr, Germany

J. Ciston, C. Ophus
National Center for Electron Microscopy
Molecular Foundry
Lawrence Berkeley National Laboratory
1 Cyclotron Road, Berkeley, California, USA

K. Habicht
Institut für Physik und Astronomie
Universität Potsdam
Karl-Liebknecht-Str. 24-25, 14476 Potsdam, Germany

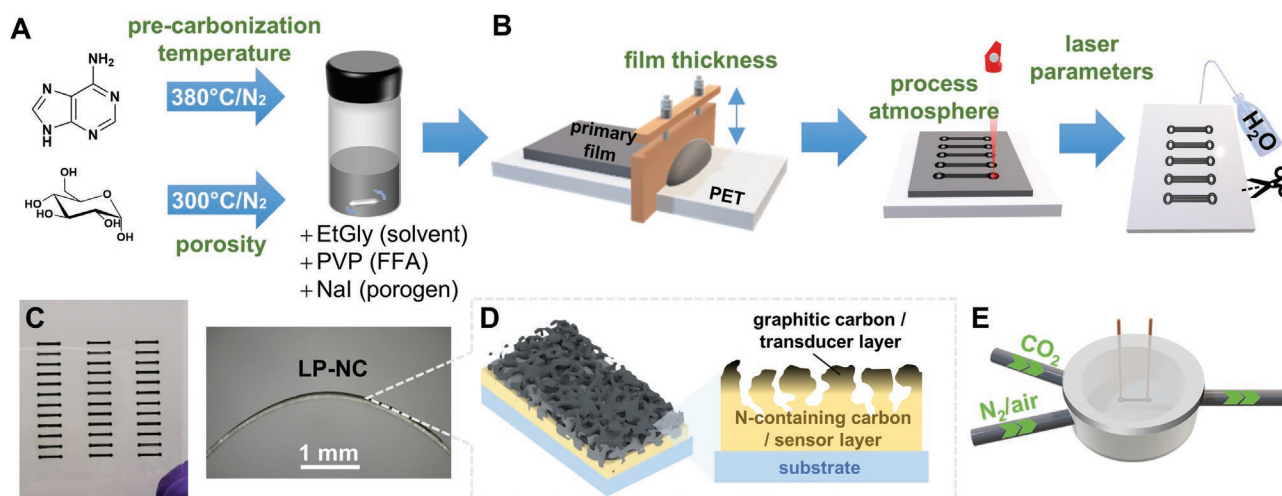


Figure 1. Scheme of sensor fabrication, optimization, and testing: A) Pyrolysis of adenine/glucose, mixing with porogen, film-forming agent, and solvent to obtain a viscous ink; B) Coating by doctor-blading and subsequent laser-patterning in different atmospheres; C) Photographs of a 20 cm² PET substrate with 36 LP-NC sensor strips (left) and a single sensor strip on flexible PET bent in positive direction (right); D) Schematic of the “inverted” sensor architecture of an LP-NC sensor with the graphitized carbon transducer layer and the N-containing carbon sensor layer; E) Illustration of the gas-sensing cell used to characterize the resistive response of the LP-NC sensors in different environments.

attracted the attention of materials scientists.^[7] Device concepts are typically based on synthetically functionalized or hybridized (with metals or metal oxides) carbon nanomaterials (CNM) to provide specific active sites on their surface or to tune their electronic properties, respectively.^[8,9] However, relatively high costs, associated with the sophisticated materials and fabrication processes, are still a challenge for commercialization.^[10]

A promising inexpensive alternative is tailored nitrogen-containing carbons (NCs). Such NCs, obtained from pyrolysis, are a class of materials, which has been proposed for selective CO₂ capture or conversion as they intrinsically provide selective binding sites for CO₂.^[11–15] In particular, polypyrrole or imidazole-based NCs demonstrate a remarkable CO₂ sorption capacity as well as excellent environmental stability and electrical conductivity.^[16–18] Like CNMs, those particulate NCs require additional processing steps to generate complex sensor architectures.

Considering that simple, fast, and cost-effective processing makes a difference in applicability, printing technologies are a favored solution as they minimize fabrication costs and personal training procedures.^[19] In the past decade, laser processing has become popular for the fabrication of flexible miniaturized chemical^[20–23] and mechanical^[24–26] sensors^[27] but also other flexible d. Commonly, porous laser-patterned carbon (LP-C) films with tailored properties are obtained by laser treatment of, for example, graphene oxide,^[28] polyimides,^[29] or lignins.^[30] Typical strategies for sensor improvements for gaseous or liquid analytes include detection by a change of the thermal conductivity, by incorporation of heterojunctions, or post-functionalization.^[20–27] In contrast to using polymeric precursors, naturally abundant, molecular compounds as starting materials provide enhanced versatility to engineer materials by implementing specific functional groups during their fabrication.^[31]

This study demonstrates that the proposed concept of single-step laser-patterning of optimized organic precursor coatings

enables the fabrication of tailored sensor heterostructures even on flexible substrates. Here, we present a complete architecture for CO₂ sensing on polyethyleneterephthalate (PET).^[32] The flexible nitrogen-containing LP-C (LP-NC) sensors exhibit high sensitivity to CO₂ and a decent degree of selectivity even in humid environments in conjunction with good cycling stability and excellent mechanical properties. Adenine was used as the major precursor due to its rich nitrogen functionalities; glucose and sodium iodide were employed as foaming agents and porogen, respectively. The fabrication process was optimized in terms of precursor synthesis, primary film composition/thickness, laser parameters, and reaction atmosphere to enhance the sensor response. The performance for CO₂ sensing was proven in dry as well as humid environments. Structure formation and operating principle of the complex sensor were elucidated by comprehensive micro- and nanoanalyses.

2. Results and Discussion

2.1. Design of CO₂ Gas Sensor and Processing

Laser-patterned LP-NC sensors (0.5 × 5 mm with enlarged end electrodes) were realized in a resistive sensor design. The integrated approach includes ink optimization/preparation, film-casting, and laser-carbonization (Figure 1A,B). The precursor ink combines functionalities of pre-carbonized adenine (C₅N₅H₅) as nitrogen-rich precursor, pre-carbonized glucose as foaming agent^[33] (and additional carbon source), sodium iodide (NaI) as porogen,^[34] and polyvinylpyrrolidone (PVP) as film-forming agent (FFA).^[35] Those were dissolved in ethylene glycol (EtGly) and the resulting ink was cast onto flexible polyethyleneterephthalate (PET) substrates of 20 cm² by doctor-blade coating.

The primary films were irradiated with a mid-infrared CO₂-laser under different atmospheres (air, N₂, or O₂) to create

the LP-NC sensor strips. The unexposed precursor material was rinsed off the substrates with deionized water. By laser treatment, we produce an “inverted” sensor architecture with a graphitized carbon transducer layer (upper layer) and N-containing carbon sensor layer (lower layer) inside each sensor film (Figure 1D). A typical electrical or electrochemical sensor architecture is composed of 1) a high-surface area sensor material with specific binding sites and 2) a conductive transducer material that transmits the signal to a 3) read-out unit. In the present case, the conductive transducer material evolves as a porous graphitic carbon network on top of the sensor layer.

In each batch, 36 gas sensor strips were produced in only 144 s (Figure 1C). Subsequently, the LP-NC strips were tested as resistive sensor platforms to detect CO₂ at room temperature in a gas-flow cell (Figure 1E). To enhance the sensor response toward CO₂, the pre-carbonization parameters, laser parameters, process atmosphere, ink composition, and coating thickness were optimized.

2.2. Materials and Process Optimization

2.2.1. Screening CNFA Reaction Temperature

Pre-carbonization of molecular precursors is a requirement for laser-carbonization, as it condenses the precursors and supports the formation of a conductive LP-C film (Figure 2A).^[31] In a temperature range of 300–400 °C, adenine undergoes condensation, which is revealed by a color change and a reduction of the N-content (formation of carbon-network forming agent: CNFA) (p. S2, Figure S1, Supporting Information).

To be applicable as chemiresistive sensors, the electric conductivity (σ) of LP-NC and the change of resistance upon exposure to 10% CO₂ (response: $\Delta R/R_0$) are essential factors. We tested the influence of the pre-carbonization temperature on σ of the LP-NC (produced under air) and their response to exposure to 10% CO₂. The LP-NC films produced from the different CNFAs are named LP_{air}-Ade300 – LP_{air}-Ade400. In Figure 2A, the conductivity and response to exposure of 10%

CO₂ of these films are plotted. LP_{air}-Ade300 and LP_{air}-Ade320, and LP_{air}-Ade400 are not conductive while the highest conductivity of 30.6 S cm⁻¹ is observed for LP_{air}-Ade340. In initial sensing experiments, we found that LP_{air}-Ade380 shows the highest $\Delta R/R_0$ values in comparison to the precursors annealed at lower or higher temperatures (Figure 2A). For all subsequent sensing experiments, we used the Ade380 as the standard CNFA. Glucose was pre-carbonized at 300 °C according to the previous optimization.^[31]

2.2.2. Laser Parameters

As recently demonstrated, each CNFA shows a characteristic response to the laser processing parameters, i.e., the incident power and scanning speed.^[31] Optimal scan speeds of 189 cm s⁻¹ and laser power of 1.1 W (pp. S2–S3, Figure S2, Supporting Information) were obtained by optimizing the conductivity and performance of reference LP-NCs (pure adenine-CNFA).

2.2.3. Process Atmosphere

Moreover, the reaction atmosphere is a critical factor for the resulting properties (Figure 2B), as laser-patterning involves pyrolysis and combustion processes, and the surface polarity induced by oxygenation was found to improve the sorption of CO₂. When changing from N₂ or air to a pure O₂ atmosphere, the resistive response was increased by more than one order of magnitude from $\Delta R/R_0 = -0.22\%$ to -3.2% for LP_{O₂}-Ade380 at 10% CO₂ exposure, while the LP-NC morphology is only marginally influenced by the reaction atmosphere (p. S3, Figure S3, Supporting Information).

2.2.4. Porosity – Foaming Agent

Increasing porosity leads to improving the accessibility of CO₂ to active sites in the film. Glucose is a well-known precursor for

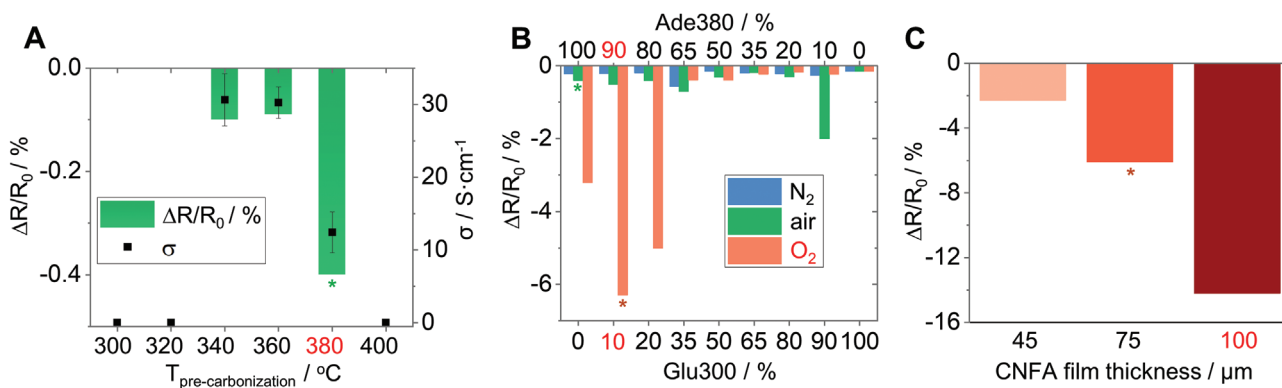


Figure 2. Materials and process optimization: A) Dependency of electric sheet conductivity (black dots) and resistive response (green) on pre-carbonization temperature of adenine (LP_{air}-Ade300–400) upon exposure to 10% CO₂:90% N₂ (starting coating thickness 75 μm, optimized pre-carbonization temperature highlighted in red; green star symbol referring to the same sample in B); B) Resistive response (10% CO₂:90% N₂) of pure and mixed LP-NC heterostructures upon laser-treatment in different environments (N₂, O₂, air) (optimized composition highlighted in red; orange star symbol referring to the same sample in C); C) Resistive response of LP_{O₂}-Ade380₉₀/Glu300₁₀ sensors, laser-treated in oxygen, with different thickness of 45, 75, and 100 μm upon exposure to 10% CO₂:90% N₂.

carbonized materials that generate high surfaces by foaming. In this study, we use pre-carbonized glucose (Glu300) as a CNFA in laser patterning, and a carbon foam is obtained. Bubbles in a size range between tens of nanometers up to several microns are observed (Figure S4, Supporting Information). This foaming effect of Glu300 during laser-carbonization is used to increase the porosity of the LP-NC. To test this hypothesis nine compositions with different mixing ratios of Ade380 (N-source) and Glu300 (foaming agent) were tested for the response toward 10% CO₂ (Figure 2B; p. S4, Figure S4, Supporting Information). As both, high concentrations of active N-sites and good access to those sites by sufficient porosity are required, LP-NC films with a significant fraction of glucose-CNFA yield the highest responses., i.e., the best response is obtained for adding 10 wt% of Glu300 to the Ade380 precursor film (LP_{O₂}-Ade380₉₀/Glu300₁₀) produced under O₂ reaching $\Delta R/R_0 = -6.3\%$. Therefore, for the optimized sensor, comprehensively investigated in this study, a CNFA ratio of 90:10 wt% (adenine-CNFA:glucose-CNFA) was used.

2.2.5. Film thickness

The response of LP_{O₂}-Ade380₉₀/Glu300₁₀ was finally enhanced to $\Delta R/R_0 = -14.3\%$ by increasing the thickness of the initial precursor coating from 75 to 100 μm (Figure 2C), while the response of the 45 μm film was much reduced (Figure 2C). This is owing to a reduced number of active sites in the lower layers. In fact, a balance between the severely graphitized upper layer and the preservation of active N-sites in the lower layers is required to form an efficient two-layer sensor heterostructure. However, further increase of the thickness leads to delamination (e.g., materials loss upon rinsing).

2.3. Microstructure and chemistry of sensor architecture

To unravel the structure formation and functionality of the LP_{O₂}-Ade380₉₀/Glu300₁₀ sensor with its N and O functionalities, a comprehensive investigation of the film morphology, local composition/bonding, and structure was carried out (Figure 3). Throughout the entire laser-irradiated area the films show a typical open-porous morphology^[35] (Figure 3A,C,D; Figure S5, Supporting Information) facilitated by the synergistic foaming effects of Glu300 and NaI. The depth-dependent attenuation of the irradiation was successfully utilized in one-step laser treatment to create the lateral heterostructure with transducer and sensor sub-layers (Figure 3C,D). Strongly different morphologies of the two layers in terms of composition and structure (Figure 3C–F; Figure S5, Supporting Information) afford their different functions. The excellent mechanical integrity and good interconnection are reflected in the cross-sectional data as well as in the sensing tests upon repeated elastic bending (Figure 4F).

The granular starting morphology with μm-sized glucose/adenine-CNFA particles is proven by cross-sectional SEM-EDXS (Figure 3C). To distinguish between device regions from the glucose-CNFA and the embedding resin, the local presence of the porogen NaI is considered. The homogeneous

Na distribution within the sensor layer in contrast to the patchy N-distribution confirms a few μm-sized regions, which are attributed to the globular glucose-based CNFA within the N-containing matrix.

Extensive pore formation occurs during laser treatment. In the upper transducer layer, open, interconnected macropores are generated as indicated by the complete infiltration by epoxy resin (Figure 3C,D). That pore network ensures excellent accessibility to the active N-sites of the sensor layer by the analyte and carrier gas. Only a sparse network of graphitized carbon remains, which is laterally interconnected and ensures a sufficient charge transport capability. The sensor layer exhibits a generally lower degree of porosity as expected from the reduced laser impact at larger depths. Only a minor volume fraction of enclosed meso- and macropores was observed (e.g., unfilled pores in Figure 3C,D (left), Figure S5C, Supporting Information). A quite narrow transition zone between the sensor and transducer layer is corroborated by the cross-sectional analyses (Figure 3B,C). The foaming agent becomes pyrolyzed or partially transformed into graphitized carbon, whereas the porogen NaI (partially) evaporates, with NaI still being present in the sensor layer (Figure 3C, Na map).

In conjunction with the depth-dependent pore morphology, severe compositional and chemical bond gradients are revealed (Figure 3C,D). The gradient conversion of the precursors, both, from the sensor to the transducer layer as well as within the sensor layer from the core regions to the surfaces, is evident. The global preferential loss of nitrogen during carbonization^[36] is depicted in Figure 3C,D (cf. N/C maps). The graphitized carbon skeleton of the central transducer layer did not show any nitrogen signals in EELS/EDXS. Occasionally, residual N-rich particles are found (Figure 3C,D, N map), which are explained by severe enthalpic cooling upon evaporation of the adjacent material.

Within the sensor layer, an abrupt depletion of the local nitrogen content in the shell regions is observed, while the composition of the core regions is rather constant (Figure 3D, N/C maps of sensor layer). Comparing that core composition after laser treatment, i.e., a concentration ratio of nitrogen:carbon ≈35:55 (at%), with the composition of the adenine-CNFA (Figure S1, Supporting Information) indicates a slight preferential loss of nitrogen. Substantial concentrations of oxygen of the order of 5 at% are present, both, in the transducer layer as well as the shell of the sensor layer due to the conversion in an oxygen environment (Figure 3D; Figure S5B, Supporting Information).

The strong thermal impact in the hot zone during laser treatment, which is the upper half of the device, yields the highly graphitized transducer layer as concluded from HRTEM, electron diffraction, 4D-STEM, EELS, and Raman microscopy (Figure 3F–H; Figures S5D and S7, Supporting Information).^[37] Independent of the reaction atmosphere the surface Raman spectra show common features of a turbostratic graphitic material, i.e., the presence of pronounced D-, G-, and D'-bands, indicating a high degree of graphitization.^[38] Notably, the LP_{O₂}-Ade380₉₀/Glu300₁₀ sensor, processed in an oxygen atmosphere, shows a significantly higher degree of graphitization as only negligible contributions of sp³ and disorder-related D4 and D3 bands at 1200 and 1460 cm⁻¹, respectively, and a lower defect-attributed D-band are

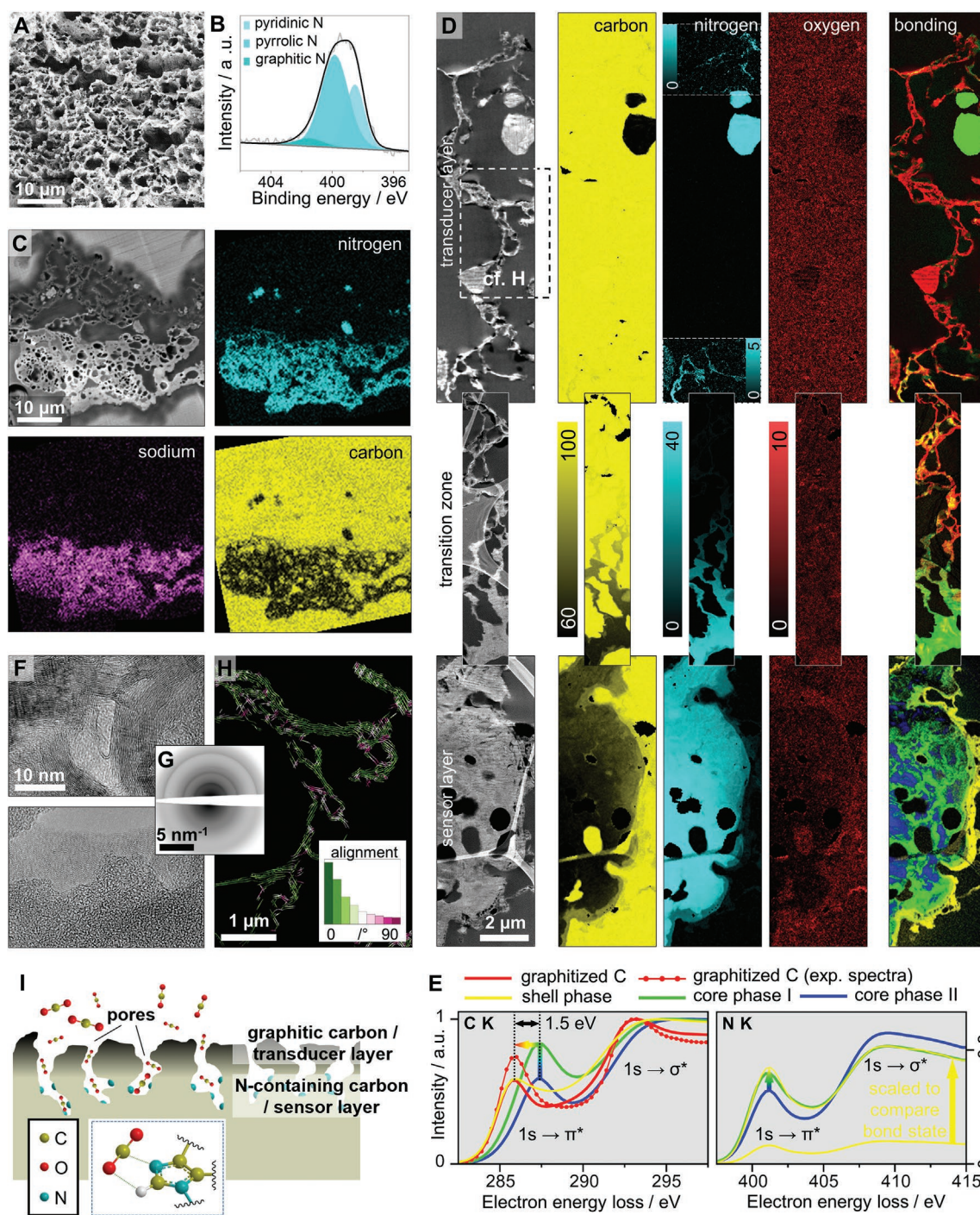


Figure 3. Scale-bridging characterization of $\text{LP}_{\text{O}_2}\text{-Ade380}_{90}/\text{Glu300}_{10}$ sensor: A) Top-view SEM micrograph; B) X-ray photoelectron spectrum with emphasis of the $\text{N}/1s$ region; C) Cross-sectional backscatter SEM micrograph with correlated EDX element maps (composition in at% with sum of C, N, O, Na being considered 100 at%); D) Cross-sectional TEM analyses (microtome, epoxy-embedded cross-section) of representative regions (not necessarily adjacent) of the transducer and sensor layers as well as the transition zone: (left) HAADF-STEM micrographs with a few unfiltered pores (black), embedding epoxy resin (homogeneous dark gray), and superimposed lacey TEM support film (wavy horizontal contrast features in the STEM image of the sensor layer indicate slight thickness variations due to microtomic sectioning), (center) corresponding EELS element maps with color codes in at% (sum of C, N, O being considered 100 at%) with locally enhanced contrast in upper N map (0–5 at%) where nitrogen is present, (right) bond mapping showing distributions (weightings) of major phases identified by PCA (red: graphitized carbon, yellow: shell phase, green/blue: core phases I/II); E) Respective PCA spectra of those phases (details in Figure S6, Supporting Information) with selected energy-loss ranges of C and N ionization edges (background corrected, C edge normalized, N relative to C); F) Exemplary HRTEM images (overview images in Figure S5, Supporting Information) and G) SAED patterns of graphitized carbon and shell regions; H) Flowline visualization of local basal-plane orientation with respect to respective pore surface (ROI marked in D, details in Figure S5, Supporting Information): local misalignment angle between basal-plane normal and pore-surface normal according to color code in histogram (distribution of misalignment angles in inset); I) Schematic function of sensor.

observed.^[39,40] In more detail, 4D-STEM revealed a strong interplay of local morphology and local crystal structure within the transducer layer. The systematic alignment of the surface-near graphite basal planes parallel to the local pore surfaces, indicated in individual HRTEM micrographs (e.g., Figure S5D, Supporting Information), is depicted on a global scale in Figure 3H and Figure S5E (Supporting Information) (cf. Figure 3D, explanation in Figure S5E, Supporting Information). The representative region of the transducer layer yielded more than 50% of the graphitic material (with (001) excited for evaluation) within only $\pm 20^\circ$ misalignment (inset in Figure 3H).

The sensor layer is amorphous and shows several “phases” of different chemical compositions identified by principal component analysis of the EELS maps (blue/green/yellow in Figure 3D). Although the material is not in thermodynamic equilibrium, the term “phase” is used to describe regions of similar composition and structure. These phases show indications for evolving ordering with ongoing conversion (Figure 3F,G; Figure S6A in Supporting Information, the multi-scattering resonance of C ionization edge of shell phase).

Two major aspects, which are CO₂-specific binding sites (nitrogen)^[41–43] in conjunction with increased surface polarity by ionic groups (oxygen),^[43] have been described in the literature that facilitates the adsorption of CO₂ in porous carbon materials. DFT calculations confirm a strong energetic interaction between CO₂ and N-containing functional groups, in particular to multi-N-containing species like imidazole units.^[44] The laser treatment of LP_{O₂}-Ade380₉₀/Glu300₁₀ under high O₂ concentration enhances its surface polarity by introducing oxygen-containing groups such as C–O and C=O (Figure 3D; Figure S6, Supporting Information) and strongly enhances the response (Figure 2B). The specific binding of CO₂ is explained by the presence of pyrrolic N species (Figure 3B).^[43]

For a correlation to the chemical bonding within the optimized sensor, surface X-ray photoelectron spectroscopy (XPS), global IR spectroscopy, and EELS bond analyses were performed. XPS confirms a high degree of carbonization and the presence of oxygen and nitrogen-containing functional groups by the prominent sp²-carbon peak at 284.6 and in the C_{1s} region and signals at 285.4, 286.1, and 287.5 eV assigned to sp³-carbon, C–N/C–O, and C=N/C=O, respectively (Figures S8–S10, Supporting Information). Oxygen is bound in the form of C=O, C–O (aliphatic), and C–O (aromatic) as evidenced by a set of three peaks at 531.3, 532.4, and 533.6 eV.^[45] Most importantly, the N_{1s} area shows a prominent signal at 399.8 eV stemming from pyrrolic/imidazolic N and two minor peaks at 398.5 and 401.5 eV typical for pyridinic and graphitic N, respectively (Figure 3B).^[46,47] Among the nitrogen functionalities, the pyrrolic/imidazolic species amount to 61%. This composition is independent of the addition of the foaming agent as it is also observed for the pure LP_{O₂}-Ade380 (Figure S8, Supporting Information). In accordance with the EELS bonding analysis, the XPS results support the interpretation of having imidazolic N groups as active sites but should not be interpreted as direct evidence.

Upon laser treatment of the pure adenine-CNFA as well as the optimized sensor, a variety of N functional groups is preserved in the N-containing phases of the lower layer. These functional groups are detected in the low-energy region of the FT-IR spectrum at 1064, 1241, and 1390 cm^{–1} (Figure S11,

Supporting Information). The latter two most likely originate from C–N stretching vibrations, either graphitic or pyrrolic/imidazolic N.^[46,48] The XPS analysis shows a major content of pyrrolic/imidazolic N in the LP-NC films. It has been shown, that pyrrolic N decomposes at temperatures >600–800 °C.^[49] The cross-sectional analyses of the sensor indicate that the laser-induced reaction temperatures in the sensor layer are lower, and thus a major part of the pyrrolic/imidazolic N is preserved after laser treatment.

Four major phases were identified throughout the device cross-sections by EELS bond analyses (Figure 3D(right),E; Figure S6, Supporting Information). Highly graphitized carbon (red, no N) constitutes the transducer layer^[37] whereas the sensor layer consists of three N-containing phases, which are a shell phase (yellow) and two less transformed core phases I/II (green/blue) of the same composition but in different bond states.^[36,50] The detailed discussion is given in the supporting information (Supporting Information, pp. S5–S8). In conclusion, very high degrees of sp² hybridization of both elements in all phases are confirmed with an increase in the early stage of the transformation from core phase II to I (Figure 3E, blue \rightarrow green).^[37] While the spectral data is governed by C=C bonds in the graphitized carbon and predominantly C=N bonds in both core phases with high N content, the dilution of N renders the shell phase a transition state (spectral superposition) between both extremes with both, C=C and C=N bonds present (Figure 3E).^[36,51] Partial electron transfer from C to N causes the spectral shift by 1.5 eV.^[51]

The sensor functionality is particularly attributed to those sp²-bound N species observed within the shell phase.^[52,53] To distinguish between different pyrrolic/imidazolic/graphitic nitrogen functionalities on the nanometer or even atomic scale is, however, challenging due to the bulk characteristics of the spectra with manifold contributions from different atomic configurations.

As a reference, an LP-NC film from cytosine without pyrrolic nitrogen was prepared, which did not show any sensing response (Figure S12, Supporting Information). Although laser-treatment of cytosine produces LP-NC films with a high nitrogen content and similar resistivity and morphology,^[31] the inherent absence of pyrrolic N in the precursor only generates non-active N-sites. As an additional reference experiment, we prepared laser-carbonized polyimide (well-known as laser-induced graphene (LIG)). Again, no sensing response toward CO₂ was observed (Figure S13, Supporting Information). Noteworthy, the influence of the charge carrier properties of the LP-NC on the sensor performance, tested by Hall measurements, is negligible (Figure S14, Supporting Information). Only the charge carrier mobility is slightly increased in the sensors produced under oxygen. We assume that the combustion supported by O₂ increases the effective reaction temperature, which leads to a higher degree of graphitization and thus a higher charge carrier mobility.

2.4. Sensor Performance

A comprehensive performance test of LP_{O₂}-Ade380₉₀/Glu300₁₀ (thickness 100 μ m), was conducted (Figure 4). The maximum

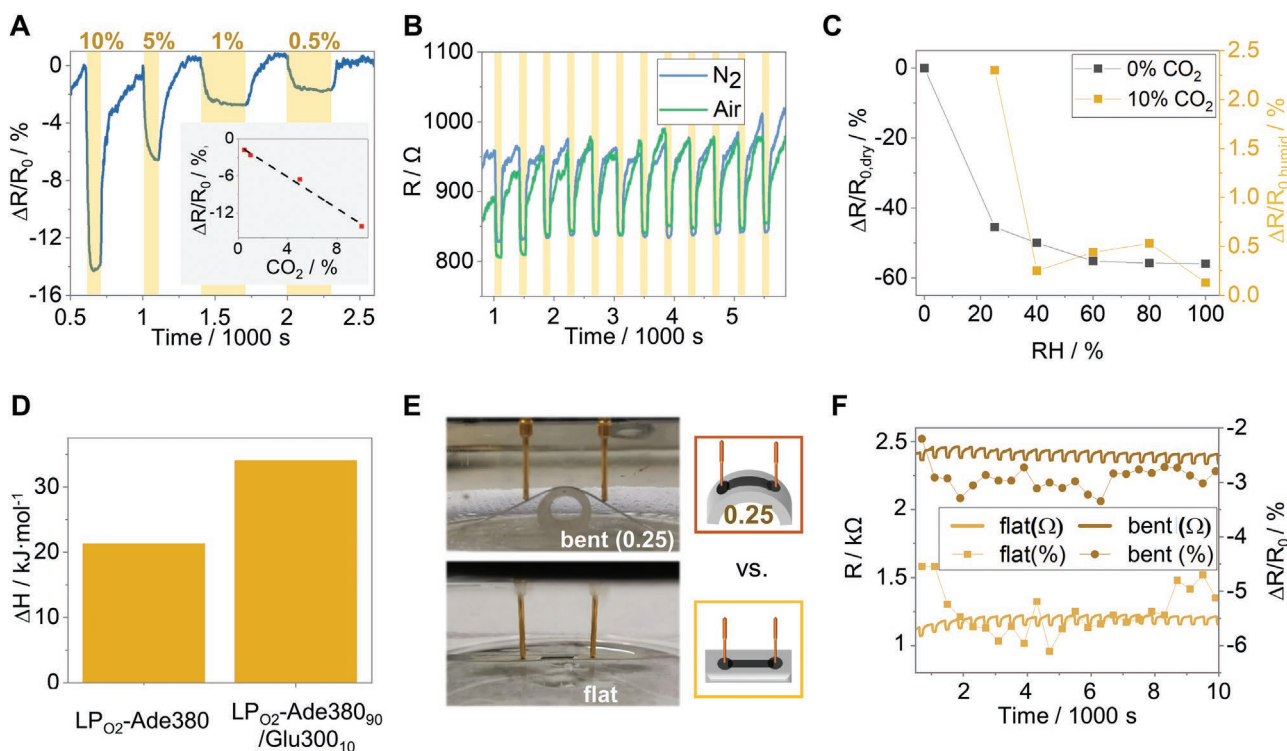


Figure 4. Performance of LP_{O₂}-Ade380₉₀/Glu300₁₀ sensor: A) Resistance response toward exposure to different CO₂ concentrations in N₂ as carrier gas; B) Resistance response toward 10% of CO₂ using N₂ (blue) or dry air (green) as carrier gas; C) Resistance response toward different relative humidities in the N₂ carrier gas (black) and to 10% CO₂ (90% N₂) at different humidities (orange); D) Values of $\Delta_{\text{ads}}H$ for CO₂ on the LP_{O₂}-Ade380₉₀/Glu300₁₀ sensor in comparison to the reference LP_{O₂}-Ade380; E) and F) Resistance response of a sensor with a thickness of 75 μm toward 10% of CO₂ upon bending (curvature: 0.25 mm⁻¹) (brown) compared to the flat state (orange) (N₂ carrier gas).

response values $\Delta R/R_0$ of that sensor to different concentrations of CO₂ follow a linear trend (Figure 4A) indicating that no saturation is reached at the maximum tested analyte concentrations. Even at 0.5% CO₂ a reasonable response of $\Delta R/R_0 = -1.8\%$ is achieved. Fitting of the data in Figure 4 yields a sensitivity of $S = -1.28 \times 10^{-6} \text{ ppm}^{-1}$. The response is stable upon cycling and is identical in air and N₂ as carrier gases (Figure 4B). The response and recovery times during cycling are the same in both environments with $t_{\text{res}} = 25 \text{ s}$ and $t_{\text{rec}} = 60 \text{ s}$. Consequently, the presence of O₂ does not influence the detection mechanism. In addition, the optimized film LP_{O₂}-Ade380₉₀/Glu300₁₀ shows a rather low sensing response to the volatile organic compounds (VOCs) acetone and ethanol as interference analytes (Figure S15, Supporting Information).

The sensing performance was further characterized at different relative humidities (RH) (Figure 4C). Naturally, polar LP-NC surfaces show a high affinity to adsorption of H₂O which is usually orders of magnitude higher than CO₂ due to its electron-accepting character.^[43] Although LP_{O₂}-Ade380₉₀/Glu300₁₀ shows a very strong and fast response to H₂O (up to $\Delta R/R_0 = 50\%$ in RH = 100%, Figure S16, Supporting Information), stable selective response to CO₂ even at such high relative humidity levels is detectable (Figure S17, Supporting Information). For example, in the range of RH of 40–80%, the response increases from $\Delta R/R_0 = 0.25$ to 0.53% (Figure 4C). This supports the hypothesis of selective binding sites for CO₂. In

comparison, also nanocarbon-based gas sensors show a strong relative response to H₂O. Typical strategies for achieving selectivity are compositing with selective moieties such as polypyrrole or nitrogen doping.^[7–9]

To understand the interaction between the LP-NCs and water/CO₂ the standard enthalpy of adsorption $\Delta_{\text{ads}}H^0$ was determined using a simple Langmuir's model: a monolayer of adsorbed analyte (CO₂ or H₂O) without interaction between each other is present at the sensor surface in equilibrium with gaseous analyte molecules. Assuming that the change of the sensor resistance is proportional to the quantity of adsorbed analyte, the transitory regime of the sensing curves is fitted to determine the adsorption equilibrium constants at different temperatures (Figures S18–S21 and Tables S2–S3, Supporting Information). Finally, the standard enthalpy of analyte adsorption $\Delta_{\text{ads}}H$ on the sensor surface is determined according to the Van't Hoff equation. The optimized sensor shows very large $\Delta_{\text{ads}}H^0$ values of 34.1 kJ·mol⁻¹ for CO₂ in comparison to only 21.3 kJ·mol⁻¹ for the reference LP_{O₂}-Ade380 (Figure 4D). Similar values for $\Delta_{\text{ads}}H^0$ for CO₂ adsorption in porous N-containing carbons are reported for CO₂.^[43] The increase upon glucose addition is attributed to the foaming effect in LP_{O₂}-Ade380₉₀/Glu300₁₀, resulting in a higher amount of exposed pyrrolic/imidazolic N and a larger interaction with the CO₂ molecules for a given quantity of sensor material. Notably, the method is not suitable for the determination of $\Delta_{\text{ads}}H^0$ values for water (Figures S18–S21, Supporting Information).

The sensing properties are retained upon mechanical deformation for a sensor strip with a thickness of 75 μm . The change in resistance ΔR upon defined bending was quantified using a movable electrode stage connected to a four-probe multimeter (Figure S22, Supporting Information). It is reversible and comparable to previously analyzed LP-Cs.^[32] In order to simulate the bending of the sensor film on the finger (Figure S23, Supporting Information), we placed a flexible hose with a diameter of ≈ 6 mm under the sensor film resulting in a curvature of 0.25 mm^{-1} determined by translating the shapes from photographs into x - y data using the freeware Engauge Digitizer. Then the sensor performance in the bent state was analyzed in the gas-sensing cell (Figure 4E,F) (1000 s, 24 cycles). Details of the experiment are given in the Supporting Information (pp S16). For comparison, the same sensor strip was analyzed in a flat state. Independent of the curvature, a stable response is observed. Figure 4F demonstrates that the absolute change in resistance ΔR , the feedback upon CO_2 loading, is retained upon bending, whereas the resistance baseline shifts toward higher values with increasing deformation. Consequently, the relative response in the bent state is just about half of that in a flat configuration ($\Delta R/R = -2.9$ vs -5.7%). The observed baseline change by a factor of around two for the curvature of 0.25 mm^{-1} is in agreement with previous results about mechanical LP-(N)C sensors.^[32] Moreover, the response and recovery times, t_{res} and t_{rec} , are the same. From the proposed functions of the transducer and sensor layers, such behavior has to be expected because both, the efficiency/density of the chemical binding sites for CO_2 as well as their accessibility through the still highly porous transducer layer, are hardly altered by such a degree of deformation.

To demonstrate its applicability, the $\text{LP}_{\text{O}_2}\text{-Ade380}_{90}/\text{Glu300}_{10}$ sensor was used to repeatedly measure the CO_2 level in exhaled breath (Figure S23, Supporting Information). Therefore, the flexible sensor was directly placed under ambient conditions without the need for a mask. In view of their rapid response, high sensitivity, and good selectivity under ambient conditions as well as their mechanical properties, the developed LP-NC sensors may prospectively be employed as real-time wearable breath detection sensors.

3. Conclusions

The depth-dependent laser-induced conversion of organic precursor coatings has successfully been utilized to fabricate a complete flexible sensor architecture for selective CO_2 sensing at room temperature. The method exhibits decisive advantages for producing N-containing carbons from adenine as a precursor: the gradual carbonization induces the formation of a graphitized transducer layer but retains the active binding sites in the less impacted, buried sensor layer. By introducing glucose as an efficient foaming agent, the sensitivity is enhanced, as it systematically opens pore channels to access those active species. In turn, the active sites, i.e., imidazolic nitrogen, are preserved in the lower sensor layer. Systematic optimization of the sensor morphology and surface chemistry resulted in a drastic performance increase of almost two orders of magnitude.

The introduced fabrication route, based on mostly abundant organic precursors, is highly versatile as it facilitates the utilization of chemical functionalities of the primary ink by a simple one-step laser writing process. The well-defined morphology and chemical functionality of those sensor architectures may be tailored for other applications by changing/optimizing the vast process parameters including the selected precursor materials with their specific functionalities, the ink composition, the primary coating thickness, the substrate, the laser-treatment parameters, and the conversion environment. The proposed concept provides a materials synthesis strategy for chemical sensors integratable into sensor array technologies which may lead to application in wearable, easy-to-operate, and real-time sensing devices. The conceptual development for the simultaneous read-out during flexible operation is the subject of future feasibility studies.

4. Experimental Section

Chemicals and Materials: Adenine (>99%, TCI Europe N.V.), D-glucose (anhydrous, Fisher Scientific GmbH), ethylene glycol (>99.7%, AnalaR Normapur, VWR Chemicals), polyvinyl-pyrrolidone (average mol wt. 10000, Sigma Aldrich), sodium iodide (99.5%, Alfa Aesar) were used as received. The PET substrates with a thickness of 170 μm were Melinex sheets obtained from Plano GmbH.

Preparation of the CNFAs: Glu300 and Ade300-400 were prepared by loading 1 g of D-glucose or 2 g of adenine into an alumina crucible or a quartz glass boat with a lid and heating at different temperatures between 300 $^{\circ}\text{C}$ and 400 $^{\circ}\text{C}$ in a tube furnace with a heating rate of 3 K min^{-1} . A gentle stream of N_2 (0.1 L min^{-1}) was ensured during the reaction. The hold-time was 2 h. The reaction products were retained and grinded in a ball mill (diameter of the ball: 1 cm) for 1 h with a speed of 600 rpm to obtain finely powdered products Glu300 or Ade300-380 (Figure S1, Supporting Information).

Preparation of the Primary Coatings: Polyvinylpyrrolidone (PVP) (Film-forming agent) was dissolved in EtGly to obtain a 0.2 g mL^{-1} solution (PVP/EtGly).^[35] Sodium iodide (0.4 g mL^{-1}) was added and dissolved.^[34] The solution was added to the CNFA and gently stirred for 24 h to obtain homogeneous inks. The samples are labeled according to: $\text{CNFA}_{1,\text{content}}/(\text{CNFA}_{2,\text{content}})$, e.g., Ade380 and Glu300 as CNFAs synthesized from adenine and glucose by pre-carbonization at 380 $^{\circ}\text{C}$ and 300 $^{\circ}\text{C}$, respectively. All concentrations of the different samples with respect to the volume of the solvent are given in **Table 1**. A drop of the ink was applied onto the substrate and the ink was doctor bladed with a blade distance between 300 and 500 μm . Ethylene glycol was then evaporated at 80 $^{\circ}\text{C}$ on a precision hotplate (PZ2860-SR, Gestigkeit GmbH) to obtain the final films with thicknesses between 30–100 μm . The thickness was determined with a digital micrometer or vertical scanning interferometry.

Laser-Carbonization: Laser-carbonization was conducted with a high-precision laser engraver setup (Speedy 100, Trotec) equipped with a 60 W CO_2 laser. Focusing was achieved with a 2.5-inch focus lens providing a focal depth of ≈ 3 mm and a focus diameter of $d = 170$ μm . The center wavelength of the laser is 10.6 ± 0.03 μm . The scanning speed v , generically given in %,

Table 1. The concentrations of components in the inks.

Inks	Ade300-400 [g mL ⁻¹]	Glu300 [g mL ⁻¹]	EtGly/PVP [μL]
Ink_Ade300-Ade400	0.57	0	350
Ink_Glu300	0	0.47	430
Inks	Ade380 [g mL ⁻¹]	Glu300 [g mL ⁻¹]	EtGly/PVP [μL]
Ink_Ade380 ₁₀ /Glu300 ₉₀	0.06	0.51	350
Ink_Ade380 ₂₀ /Glu300 ₈₀	0.11	0.46	350
Ink_Ade380 ₃₅ /Glu300 ₆₅	0.2	0.37	350
Ink_Ade380 ₅₀ /Glu300 ₅₀	0.29	0.29	350
Ink_Ade380 ₆₅ /Glu300 ₃₅	0.37	0.2	350
Ink_Ade380 ₈₀ /Glu300 ₂₀	0.51	0.06	350
Ink_Ade380 ₉₀ /Glu300 ₁₀	0.51	0.06	350

was converted into cm²·s⁻¹. The effective output power P in watts of the laser was measured with a Solo 2 (Gentec Electro-Optics) power meter. The resulting energy input per area (or fluence) F in J·cm⁻² in the vector mode onto the film is given by

$$F = \frac{P}{v \cdot d} \quad (1)$$

For the experiments, the laser settings were adjusted to meet the requirements of the films according to **Table 2**. A standard sensor strip is made of five parallel lines of 5 mm in length distributed across a width of 0.5 mm. An open-top atmospheric chamber was designed to generate a continuous flow of a selected gas (O₂ or N₂) for the fabrication of LP-NC under controlled gas atmospheres (Figure S3, Supporting Information). The laser-patterned (LP) samples are labeled according to: LP_{atmosphere}-CNFA1_{content}/CNFA2_{content}, e.g., LP_{O₂}-Ade380₉₀/Glu300₁₀ for a laser-patterned film of a mixture of Ade380:Glu300 (90:10 wt.%) as CNFAs under O₂ reaction atmosphere.

CO₂ Sensing: The sensor platforms were placed in a gas-proof glass flow cell ($V_{\text{cell}} \approx 0.1$ L) and their ends were connected to two electrode bins. The electrical characterization was performed with an impedance unit at a frequency of 80 Hz and an alternating current (AC) of 0.05 mA for all measurements.

The total flow of gas mixtures was set to 1 L min⁻¹. Concentrations of 0.5%, 1%, 5%, and 10% CO₂ with respect to the total flow were controlled by mass flow controllers (GF040, Brooks Instrument GmbH). Humidity was controlled by a humidity generator (HUMIgen-04, Dr. Wernecke Feuchtemesstechnik). The sensitivity of the sensor was calculated according to

$$S = \frac{\Delta R}{R_0 \cdot \Delta C} \quad (2)$$

Table 2. Laser parameters used in the experiments to fit the coating thickness.

Samples	Thickness [μm]	Power % [generic]	Power W	Speed % [generic]	Speed cm s ⁻¹	Fluence [J cm ⁻²]
LP_Glu300	75	2.20	1.12	0.30	0.53	125
LP_Ade380	75	2.10	1.07	0.30	0.53	119
LP _{O₂/N₂/air} -Ade380 ₉₀ /Glu300 ₁₀	45	1.90	0.97	0.30	0.53	108
	75	2.10	1.07	0.30	0.53	119
	100	2.20	1.12	0.30	0.53	125

Langmuir's model was used to describe the interaction between the gas molecules and the sensor surface. At a given temperature, the fraction of occupied sites on the sensor surface is θ . The equilibrium constant of adsorption K is defined as the ratio between the rate constants of adsorption k_A and desorption k_D . The variation of θ is given by Equation 3, where P_A is the partial pressure of the analyte in the gas phase:

$$\theta = \frac{K * P_A}{1 + K * P_A} \quad (3)$$

When molecules are adsorbed on the surface of the LP-NC, the resistivity decreases. Then θ is given by:

$$\theta = \alpha * (R_0 - R_{eq}) \quad (4)$$

where R_0 is the initial resistance, R_{eq} is the resistance at equilibrium, α is the proportionality coefficient.

The heat of adsorption of CO₂ or H₂O was determined according to the van 't Hoff equation.

$$\frac{d(\ln K)}{dT} = \frac{\Delta H_{\text{ads}}}{RT^2} \quad (5)$$

Bending Experiments: The experiments were performed with a homemade movable stage. The PET-supported sample strip was mounted between two electrodes (one movable) at a distance of 25 mm and bent in a positive (upwards) direction (Figure S20, Supporting Information). To provide a better electrical contact both ends of the carbon strip were connected with silver paint. The curvature of the bending was determined by translating the shapes from photographs into x - y data using the freeware Engauge Digitizer. The curvature is defined as the inverse radius at the maximum point of bending.

Sample Preparation for Electron Microscopy: Cross-sectional preparation of the sensors was conducted by ultramicrotomy utilizing a Leica EM UC7 microtome. Individual sensor strips were separated by doctor-blade cutting and embedded in epoxy resin (Araldite 502, Science Services, Germany) to facilitate the sectioning of the highly porous sensor heterostructures. Impregnation of the pores was supported by evacuation and subsequent pressurization of the uncured resin using a dedicated pressure vessel (miniclave steel, Büchi AG, Switzerland). Curing was carried out overnight at 60 °C. To create a trapezoid-shaped block face and to remove potentially damaged sample regions from cutting, trimming with a diamond knife (DiATOME 45° trim knife) was performed. A DiATOME 45° ultrasonic diamond knife was employed to obtain cross-sectional

TEM samples with minimal compression. The floating sections (deionized water) were transferred onto lacey carbon TEM grids (Plano AG) to provide sufficient support at reduced impact during EELS measurements. The resulting block face was used for complementary analysis by optical microscopy (OM) and environmental SEM.

5. Instrumental

5.1. Scanning Electron Microscopy

Top-view scanning electron microscopy with secondary electrons was performed on a Zeiss LEO 1550-Gemini field-emission microscopes (acceleration voltage: 3–10 kV). Cross-sectional EDXS element mapping and related imaging with back-scattered electrons of the embedded sensors (microtomy block surface) were performed using an environmental FEI Quanta 250 FEG-SEM. The instrument is equipped with an Apollo XL SSD detector for energy-dispersive X-ray spectroscopy and a differential pumping system to allow operation at low-vacuum levels for minimal charging. EDXS element maps were obtained at 5 keV primary electron energy to obtain sufficient count rates at the best achievable lateral resolution under low-vacuum conditions (≈ 100 Pa).

5.2. Transmission Electron Microscopy

For bright-field transmission electron microscopy (bright-field TEM, BFTEM), selected-area electron diffraction (SAED), selected area diameter 150 nm), and high-resolution TEM (HRTEM), a FEI TitanX 60–300 TEM (NCEM/LBNL) (Schottky emitter, super twin objective lens, no aberration corrector, operated at 200 kV acceleration voltage) with Gatan 2k Ultrascan CCD camera was utilized. A gold particle sample was used to calibrate microscope magnification and camera length.

High-angle annular dark-field Scanning TEM (HAADF-STEM) in conjunction with electron energy-loss spectroscopy (EELS) were carried out using an FEI Talos F200X S/TEM (MNAF/Univ. Siegen) at 200 kV acceleration voltage. The microscope is equipped with an XFEG high-brightness gun and a Gatan Continuum ER spectrometer (with high-speed DualEELS, DigiScan, EDXS integration, GMS 3.5x). The acceleration voltage of 200 kV was chosen as a compromise between the mean-free path for inelastic scattering (EELS) and electron-beam induced damaging, the latter being minimized by sub-pixel scanning during EELS mapping acquisition.

EELS mappings were acquired from representative areas of the microtomic sensor cross-sections, which exhibit excellent and homogeneous relative thicknesses of $t/\lambda \approx 0.35 - 0.5$ depending on the local sensor density (≈ 0.25 for the adjacent embedding epoxy due to the lower density). Dual EELS mappings (step size ≈ 20 nm) with core loss spectra in the energy-loss range of 200–800 eV (dispersion 0.3 eV/channel, ratio convergence/acceptance angle ≈ 2) were recorded to cover the essential ionization of C, N, and O at ≈ 285 , 400, and 532 eV, respectively. Energy calibration was employed utilizing the respective low-loss datasets.

EELS element distributions for C, N, and O were derived by quantification with theoretical cross-sections as implemented in the Gatan software. For background correction, a power law function for C, O but a 1st-order log-polynomial function for N were employed (pre-edge fit range for all elements: 50 eV, post-edge fit ranges: 50 eV (C) and 25 eV (N, O)). As hydrogen as well as Na, I are not accessible in the recorded spectra range, the presented atomic concentrations refer to $c_C + c_N + c_O = 100$ at%.

To unravel variations of the local bond states within the sensor cross-sections without a priori knowledge of the resultant reaction products, principal component analysis (PCA), as implemented in GMS 3.40 (with Varimax orthogonal matrix rotation)^[54] was applied to the recorded EELS datasets. As a result, PCA components were obtained, which describe individual phases, meaning, which include all three ionization edges, rather than individual element-specific signals. The spatial distributions in the main manuscript depict the lateral weighting factors of those identified components/phases. Due to better statistics, however, the phase-specific PCA components were separated into their C, N, and O contributions (independent background correction for each ionization edge), normalized with respect to the maximal intensity of the C K ionization edge, and presented throughout the manuscript. To verify the validity of those obtained spectral PCA distributions, 50 experimental spectra were selected from the respective mapping datasets, summed, normalized, and compared to the corresponding spectral PCA components (Figure S6, Supporting Information). The major challenges and limitations of PCA in this study are in detail discussed in the supporting material (pp. S5–S7, Supporting Information).

Experimental 4D-STEM datasets were acquired using the TEAM I instrument (NCEM/LBNL), a double aberration-corrected Thermo Fisher Titan fitted with a Gatan Continuum energy filter and K3 direct electron detector (operated in electron counting mode, 4x binning).^[55] The energy-filtered diffraction patterns (15 eV slit width, central beam covered by 2.5 mrad beam stop) were acquired at an accelerating voltage of 300 kV in microprobe mode with a beam convergence semi-angle of 0.7 mrad (beam diameter ≈ 2 nm, beam current 70 pA) and a covered spectrometer semi-angle of maximum 21 mrad. A shadow image of the sample (i.e., a strongly defocused image of the STEM probe) was recorded to align the rotation between the scan field and recorded diffraction patterns. The datasets were evaluated employing the py4DSTEM software package.^[56] Details are provided in the supporting information. Fourier-transform infrared spectroscopy

FT-IR spectroscopy was performed using a Nicolet iS 5 FT-IR-spectrometer in conjunction with an iD7 ATR unit from ThermoFisher Scientific. The LP-NC powder was scratched off the PET substrate and directly analyzed.

5.3. Raman Spectroscopy

Raman spectra were obtained with a confocal Raman Microscope (alpha300, WITec, Germany) equipped with a piezo-scanner (P-500, Physik Instrumente, Karlsruhe, Germany). The laser, $\lambda = 532$ nm was focused on the samples through a 50x objective. The laser power on the sample was set to 5.0 mW.

5.4. Hall Measurements

The electrical conductivity σ of carbonized films was determined at room temperature by the van der Pauw method^[57] in a Hall effect measurement system 8404 (Lake Shore Cryotronics, Inc.). The samples, all shaped in precise cloverleaf geometry with a 10 mm diameter, were placed on a commercial 10 mm prober pin sample card of the 8404 Hall effect measurement system. Excitation currents from -5 to $+5$ mA have been used for the I - V measurements. All the I - V curves for all four different four-probe contact configurations show the expected linear behavior.

Both, the DC and the Double AC Hall method^[58,59] employing two MFLI lock-in amplifiers (Zurich Instruments AG) and a CS580 voltage-driven current source (Stanford Research Systems) have been applied in the same setup to determine the charge carrier concentration. Different sets of oscillating excitation current ($I = 2$ to 6 mA with frequency $f_I = 88$ Hz) and magnetic field (0.08, 0.16, and 0.23 T with frequency $f_B = 0.8$ Hz) have been used to measure the Hall voltage $V_H = V(f_I + f_B) + V(f_I - f_B)$, automated by a home made LabVIEW program. The linear relationship between V_H and $I \times B$ (Equation 6) is used to calculate the charge carrier density

$$p = \frac{1}{et} \frac{\partial(I \times B)}{\partial V_H} \quad (6)$$

where e is the elementary charge and t is the thickness of the sample. The charge carrier mobility μ was calculated by the formula $\mu = \frac{\sigma}{pe}$.

5.5. X-Ray Photoelectron Spectroscopy

XPS measurements were performed at the ISSS beamline of the synchrotron radiation facility BESSY II of Helmholtz-Zentrum Berlin, Germany. The used endstation consisted of a bending magnet (D41) and a plane grating monochromator (PGM) in the soft X-ray range 80–2000 eV with an 80–200 μ m beam spot. The photoelectron analyzer is provided by SPECS GmbH (Phoibos 150) hemispherical analyzer. In order to minimize losses of photons and electrons, a 50 nm thick SiNx X-ray membrane close to the sample was used. Each sample was fixed on the sapphire sample holder. XPS spectra were analyzed through CasaXPS and Igor Pro. The spectra were deconvoluted with a combined Gaussian and Lorentzian function after a Shirley + linear background subtraction.

Supporting Information

Supporting Information is available from the Wiley Online Library or from the author.

Acknowledgements

The authors gratefully acknowledge funding from the Fonds der Chemischen Industrie and the Max Planck Society and the support from Prof. Markus Antonietti. Part of this work was performed at the

DFG-funded Micro-and Nanoanalytics Facility (MNAF) of the University of Siegen (INST 221/131-1) utilizing its major TEM instrument FEI Talos F200X (DFG INST 221/93-1, DFG INST 221/126-1) and sample preparation equipment. Work at the Molecular Foundry (MF) at Lawrence Berkeley National Laboratory (LBNL) was supported by the Office of Science, Office of Basic Energy Sciences, of the U.S. Department of Energy under Contract No. DE-AC02-05CH11231. The authors thank Klaus Bienert for help with the humidity generator and Heinrich Horstmann for fruitful discussions about the optimization of the cross-sectional TEM preparation. The authors thank the Helmholtz-Zentrum Berlin (HZB) and Fritz Haber Institute - Max-Planck-Gesellschaft (FHI-MPG) for the provision of beamtime.

Open access funding enabled and organized by Projekt DEAL.

Conflict of Interest

The authors declare no conflict of interest.

Author Contributions

H.W.: Investigation, Conceptualization, Methodology, Validation, Writing – Original Draft; C.O.O.: Investigation, Methodology, Validation, Writing – Original Draft; G.P.: Investigation, Methodology, Validation, M.H.: Investigation, Methodology, Validation; S.D.: Investigation, Methodology, Validation; D.C.: Investigation, Methodology, Validation; J.C.: Investigation, Methodology, Validation; C.O.: Investigation, Methodology, Validation; A.K.-G.: Supervision; K.H.: Writing – Review & Editing, Supervision; B.B.: Conceptualization, Supervision, Methodology, Validation, Writing – Original Draft, Writing – Review & Editing; V.S.: Conceptualization, Methodology, Validation, Writing – Original Draft, Writing – Review & Editing, Supervision, Project administration.

Data Availability Statement

The data that support the findings of this study are available from the corresponding author upon reasonable request.

Keywords

carbon films, carbon laser-patterning, carbonization, CO₂-sensors, flexible gas sensors, graphitization, nitrogen-doped carbons, pyrolysis

Received: June 29, 2022
Revised: August 11, 2022
Published online: October 9, 2022

- [1] N. Oreskes, *Science* **2004**, 306, 1686.
- [2] W. Ripple, *Bioscience* **2019**, 70, 8.
- [3] K. Permentier, S. Vercaemmen, S. Soetaert, C. Schellekens, *Int. J. Emerg. Med.* **2017**, 10, 17.
- [4] R. D. Manzanedo, P. Manning, *Sci. Total Environ.* **2020**, 742, 140563.
- [5] S. Mulmi, V. Thangadurai, *J. Electrochem. Soc.* **2020**, 167, 037567.
- [6] T. M. Swager, K. A. Mirica, *Chem. Rev.* **2019**, 119, 1.
- [7] Y. Lin, Z. Fan, *Mater. Sci. Semicond. Process.* **2020**, 107, 104820.
- [8] E. Llobet, *Sensors Actuators, B Chem* **2013**, 179, 32.
- [9] K. R. Ratinac, W. Yang, S. P. Ringer, F. Braet, *Environ. Sci. Technol.* **2010**, 44, 1167.
- [10] C. Wang, *Adv. Mater.* **2019**, 31, 1903491.

- [11] D. Yu, *Energy & Fuels* **2018**, *32*, 3726.
- [12] J. W. F. To, *J. Am. Chem. Soc.* **2015**, *138*, 1001.
- [13] J. Wei, *Adv. Funct. Mater.* **2013**, *23*, 2322.
- [14] J. Gong, M. Antonietti, J. Yuan, *Angew. Chemie* **2017**, *129*, 7665.
- [15] W. Ju, *Nat. Commun.* **2017**, *8*, 944.
- [16] M. Sevilla, P. Valle-Vigón, A. B. Fuertes, *Adv. Funct. Mater.* **2011**, *21*, 2781.
- [17] V. Chandra, *Chem. Commun.* **2012**, *48*, 735.
- [18] S. R. Venna, M. A. Carreon, *J. Am. Chem. Soc.* **2010**, *132*, 76.
- [19] Y. Yang, *Nat. Biotechnol.* **2020**, *38*, 217.
- [20] M. G. Stanford, K. Yang, Y. Chyan, C. Kittrell, J. M. Tour, *ACS Nano* **2019**, *13*, 3474.
- [21] A. R. Cardoso, *Biosens. Bioelectron.* **2019**, *124–125*, 167.
- [22] G. Xu, Z. A. Jarjes, V. Desprez, P. A. Kilmartin, J. Travas-Sejdic, *Biosens. Bioelectron.* **2018**, *107*, 184.
- [23] C. Fenzl, *ACS Sens.* **2017**, *2*, 616.
- [24] W. Yang, *ACS Appl. Mater. Interfaces* **2020**, *12*, 3928.
- [25] L. Q. Tao, *Nat. Commun.* **2017**, *8*, 14579.
- [26] Y. Wang, Y. Wang, P. Zhang, F. Liu, S. Luo, *Small* **2018**, *14*, 1802350.
- [27] L. Huang, J. Su, Y. Song, R. Ye, *Nano-Micro Lett.* **2020**, *12*, 157.
- [28] M. F. El-Kady, V. Strong, S. Dubin, B. K. R., *Science* **2012**, *335*, 1326.
- [29] J. Lin, *Nat. Commun* **2014**, *5*, 5.
- [30] R. Ye, *Adv. Mater.* **2017**, *29*, 1702211.
- [31] H. Wang, *Carbon N. Y.* **2021**, *176*, 500.
- [32] M. Hepp, et al., *npj Flex. Electron.* **2022**, *6*, 3.
- [33] X. X. Wang, et al., *Nat. Commun.* **2013**, *4*, 2905.
- [34] H. Wang, *Adv. Funct. Mater.* **2021**, *31*, 2104061.
- [35] S. Delacroix, H. Wang, T. Heil, V. Strauss, *Adv. Electron. Mater.* **2020**, *6*, 2000463.
- [36] F. Ramos, TEM, in *Electron Microscopy and Analysis*, U.K. Institute of Physics Publishing, Bristol **1999**. 381–384.
- [37] H. Daniels, R. Brydson, B. Rand, A. Brown, *Philos. Mag.* **2007**, *87*, 4073.
- [38] D. B. Schuepfer, *Carbon N. Y.* **2020**, *161*, 359.
- [39] A. Sadezky, H. Muckenhuber, H. Grothe, R. Niessner, U. Pöschl, *Carbon N. Y.* **2005**, *43*, 1731.
- [40] M. Pawlyta, J. - N. Rouzaud, S. Duber, *Carbon N. Y.* **2015**, *84*, 479.
- [41] Y. Zhao, X. Liu, Y. Han, *RSC Adv.* **2015**, *5*, 30310.
- [42] Y. Zhao, X. Liu, K. X. Yao, L. Zhao, Y. Han, *Chem. Mater.* **2012**, *24*, 4725.
- [43] M. Oschatz, M. Antonietti, *Energy Environ. Sci.* **2018**, *11*, 57.
- [44] H. M. Lee, I. S. Youn, M. Saleh, J. W. Lee, K. S. Kim, *Phys. Chem. Chem. Phys.* **2015**, *17*, 10925.
- [45] M. Smith, L. Scudiero, J. Espinal, J. S. McEwen, M. Garcia-Perez, *Carbon N. Y.* **2016**, *110*, 155.
- [46] P. Lazar, R. Mach, M. Otyepka, *J. Phys. Chem. C* **2019**, *123*, 10695.
- [47] R. C. Dante, *Carbon N. Y.* **2017**, *121*, 368.
- [48] A. Misra, P. K. Tyagi, M. K. Singh, D. S. Misra, *Diam. Relat. Mater.* **2006**, *15*, 385.
- [49] J. R. Pels, F. Kapteijn, J. A. Moulijn, Q. Zhu, K. M. Thomas, *Carbon N. Y.* **1995**, *33*, 1641.
- [50] A. Jaleel, et al., *Chem. Eng. J.* **2022**, *433*, 133571.
- [51] A. Fernández, et al., *Appl. Phys. Lett.* **1996**, *69*, 764.
- [52] M. Demir, et al., *Int. J. Energy Res.* **2018**, *42*, 2686.
- [53] F. Alvarez, M. C. dos Santos, *J. Non. Cryst. Solids* **2000**, *266–269*, 808.
- [54] G. Lucas, P. Burdet, M. Cantoni, C. Hébert, *Micron* **2013**, *52–53*, 49.
- [55] C. Ophus, *Microsc. Microanal.* **2019**, *25*, 563.
- [56] B. H. Savitzky, *Microsc. Microanal.* **2021**, *27*, 712.
- [57] L. J. v. d. Pauw, *Philips Res. Reports* **1958**, *13*, 1.
- [58] P. Chu, S. Niki, J. W. Roach, H. H. Wieder, *Rev. Sci Instrum.* **1987**, *58*, 1764.
- [59] A. Kasai, A. Abdulla, T. Watanabe, M. Takenaga, *Jpn. J. Appl. Phys.* **1994**, *33*, 4137.

Supporting Information

for *Adv. Funct. Mater.*, DOI: 10.1002/adfm.202207406

Flexible CO₂ Sensor Architecture with Selective Nitrogen Functionalities by One-Step Laser-Induced Conversion of Versatile Organic Ink

Huize Wang, Charles Otieno Ogolla, Gyanendra Panchal, Marco Hepp, Simon Delacroix, Daniel Cruz, Danny Kojda, Jim Ciston, Colin Ophus, Axel Knop-Gericke, Klaus Habicht, Benjamin Butz, and Volker Strauss**

Supporting Information to

Flexible CO₂ sensor architecture with selective nitrogen functionalities by one-step laser-induced conversion of versatile organic ink

Huize Wang, Charles Otieno Ogolla, Gyanendra Panchal, Marco Hepp, Simon Delacroix, Daniel Cruz, Danny Kojda, Jim Ciston, Colin Ophus, Axel Knop-Gericke, Klaus Habicht, Benjamin Butz, and Volker Strauss

Material Optimization	S2
CNFA reaction temperature	S2
Laser parameters	S2
Process atmosphere	S3
Porosity – foaming agent.....	S3
Characterization and discussion	S5
Cross-sectional characterization.....	S5
EELS chemical-bond analysis.....	S6
Raman spectroscopy	S8
X-ray photoelectron spectroscopy.....	S9
Fourier-transform infrared spectroscopy	S11
Reference material testing	S11
Hall measurements	S12
Sensor performance	S12
Interference test	S12
Thermodynamic analysis.....	S13
Bending experiments	S16
Operation mode	S17
References	S17

Material Optimization

CNFA reaction temperature

The selection of the pyrolysis temperature during pre-carbonization is critical to the electronic properties of final LP-NC. To identify the optimal pyrolysis temperature, adenine was pyrolyzed at temperatures between 300-400 °C and their products were tested as CNFAs. The samples are denoted with respect to the annealing temperature, for example, Ade380 represents adenine annealed at 380 °C. Notably, as the pre-carbonization temperature increases, the color of the products becomes darker from light brown over dark brown to black (Figure S1). The elemental compositions of all CNFAs obtained by elemental combustion analysis show a trend towards an increase of the C/N ratio with increasing temperature. Only minor changes for pyrolysis temperatures above 320 °C were observed. It seems likely that at 320 °C crosslinking/polymerization of adenine starts to occur.

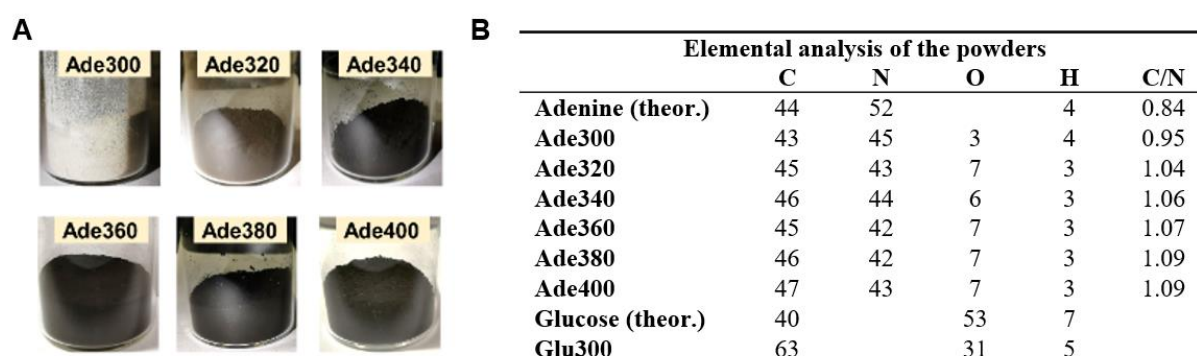


Figure S1. A) Photographs of as-synthesized CNFA powders; B) Elemental mass percentage of the CNFAs and reference obtained from combustion elemental analysis.

Laser parameters

We optimized the laser processing parameters, i.e. the incident power and scanning speed, as they are critical for the carbonization process of the selected CNFA – Ade380. A quantification of the energy fluence based on the relationship of power and scanning speed is given in the plot in Figure S2. In general, slower speed and higher power give higher energy fluence. Each CNFA gives a characteristic response pattern in terms of resulting conductivity.¹ Ade380 shows the highest conductivities of up to 24 S·cm⁻¹ in the speed range between 150-450 ms·mm⁻¹ (0.67-0.22 cm·s⁻¹) and the power range 0.95-1.15 W.

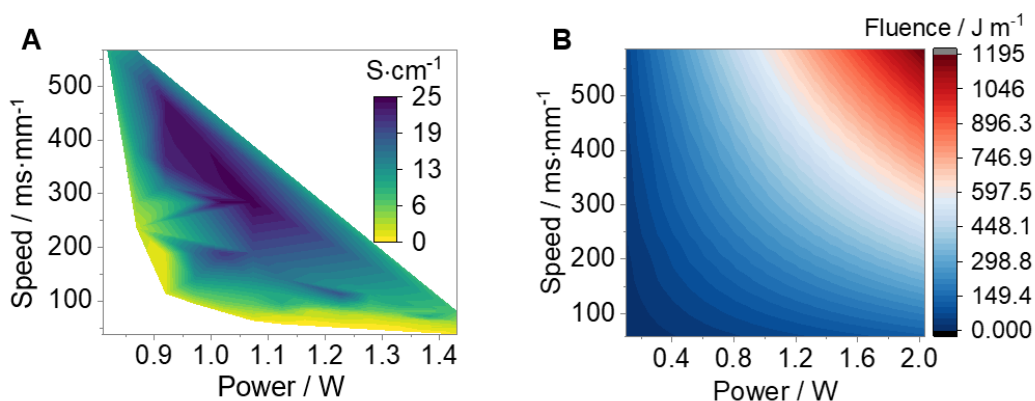


Figure S2. 2D plot of the electrical conductivities of LP_{air}-Ade380 in dependence of laser power and scanning speed; B) Radiant energy fluence of the laser energy versus scanning speed and laser power.

Process atmosphere

We employed an open-top atmospheric chamber to fabricate LP-NC under controlled reaction atmospheres while keeping the pressure constant (Figure S3). The resulting LP-NC films are denoted accordingly, for example, LP_{N₂}-Ade(380) represents laser-patterned Ade380 under N₂ atmosphere.

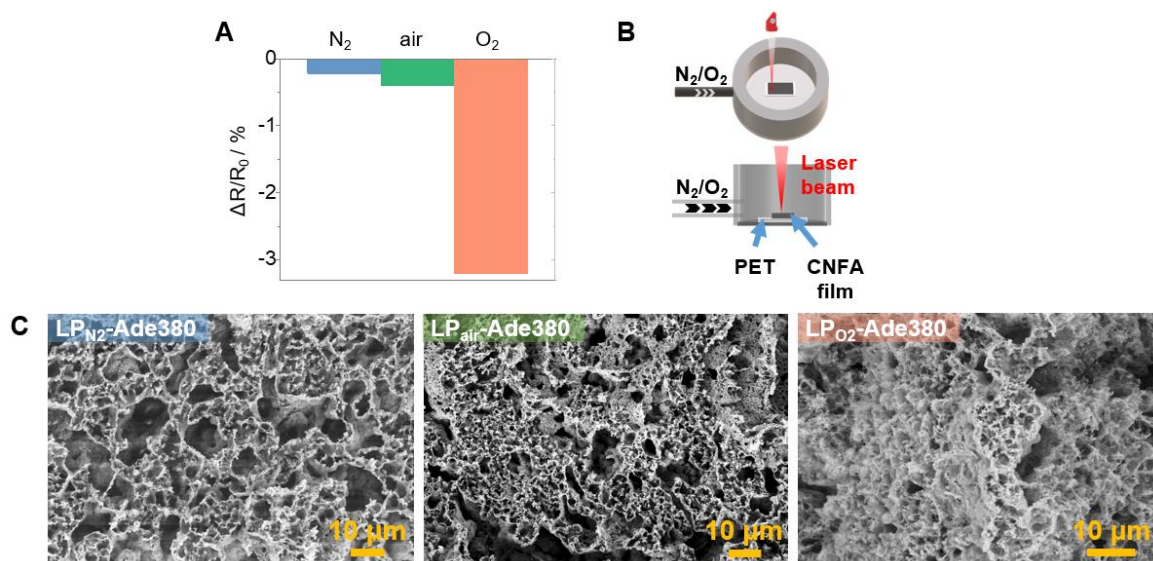


Figure S3. A) Influence of the synthesis atmosphere on the response of LP-Ade(380) to exposure of 10 % CO₂; B) Illustration of the fabrication of laser-carbonized films inside a controlled atmosphere chamber: top view and side view; C) Top view SEM images with lower magnification of laser-carbonized films with different CNFAs under N₂/O₂ gas atmospheres.

Porosity – foaming agent

Foaming, i.e. formation of bubbles, is commonly observed in thermally treated carbohydrates.² When using pre-carbonized glucose (Glu300) as a CNFA in laser-patterning, a carbon foam with bubbles in a size range between tens of nanometers up to several microns are observed (**Figure S4A**). Prior to laser-treatment the primary coatings of Glu300 and Ade380 consist of micron sized

particles. The foaming of Glu300 during laser-carbonization is used to increase the porosity of the LP-NC. The best response is obtained for adding 10 wt% of Glu300 to the Ade380 primary coating (LP_{O_2} - Ade380₉₀/Glu300₁₀) produced under O₂ reaching $\Delta R/R_0 = -6.3\%$. As a reference, the pure glucose derived LP-Cs were tested, but all samples regardless of the atmosphere ($LP_{N_2/air/O_2}$ -Glu300) show a low response of only $\Delta R/R_0 \approx -0.15\%$ to exposure of 10% CO₂ (**Figure 2B**).

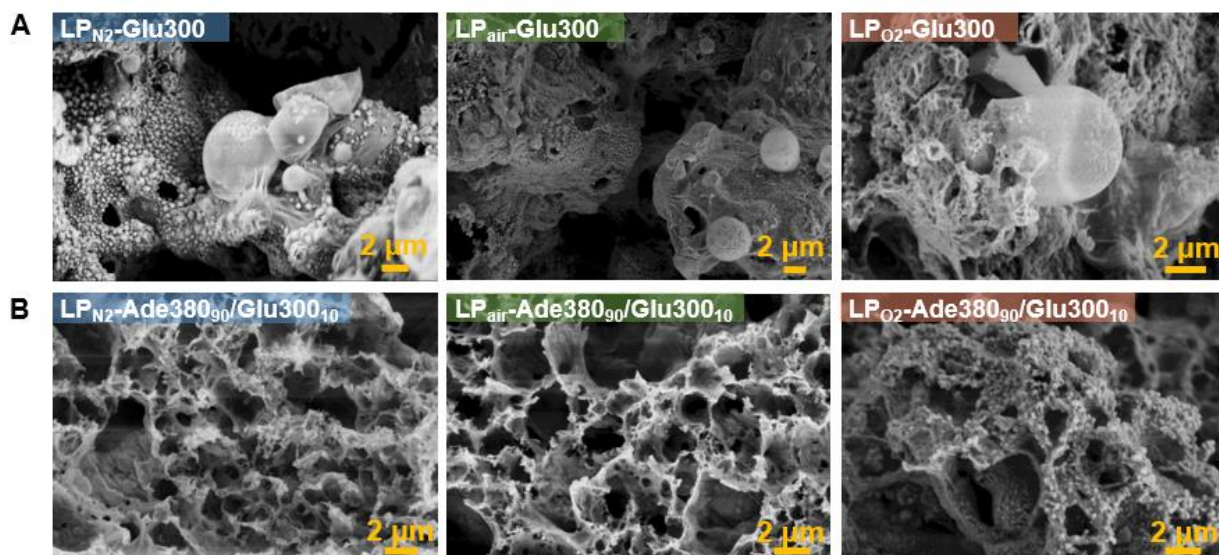


Figure S4. A) Top view SEM images of the LP-C films obtained from Glu300 as a CNFA in different process atmospheres; B) Top view SEM images of LP_{N₂}-Ade380₉₀/Glu300₁₀, LP_{air}-Ade380₉₀/Glu300₁₀, and LP_{O₂}-Ade380₉₀/Glu300₁₀.

Characterization and discussion

Cross-sectional characterization

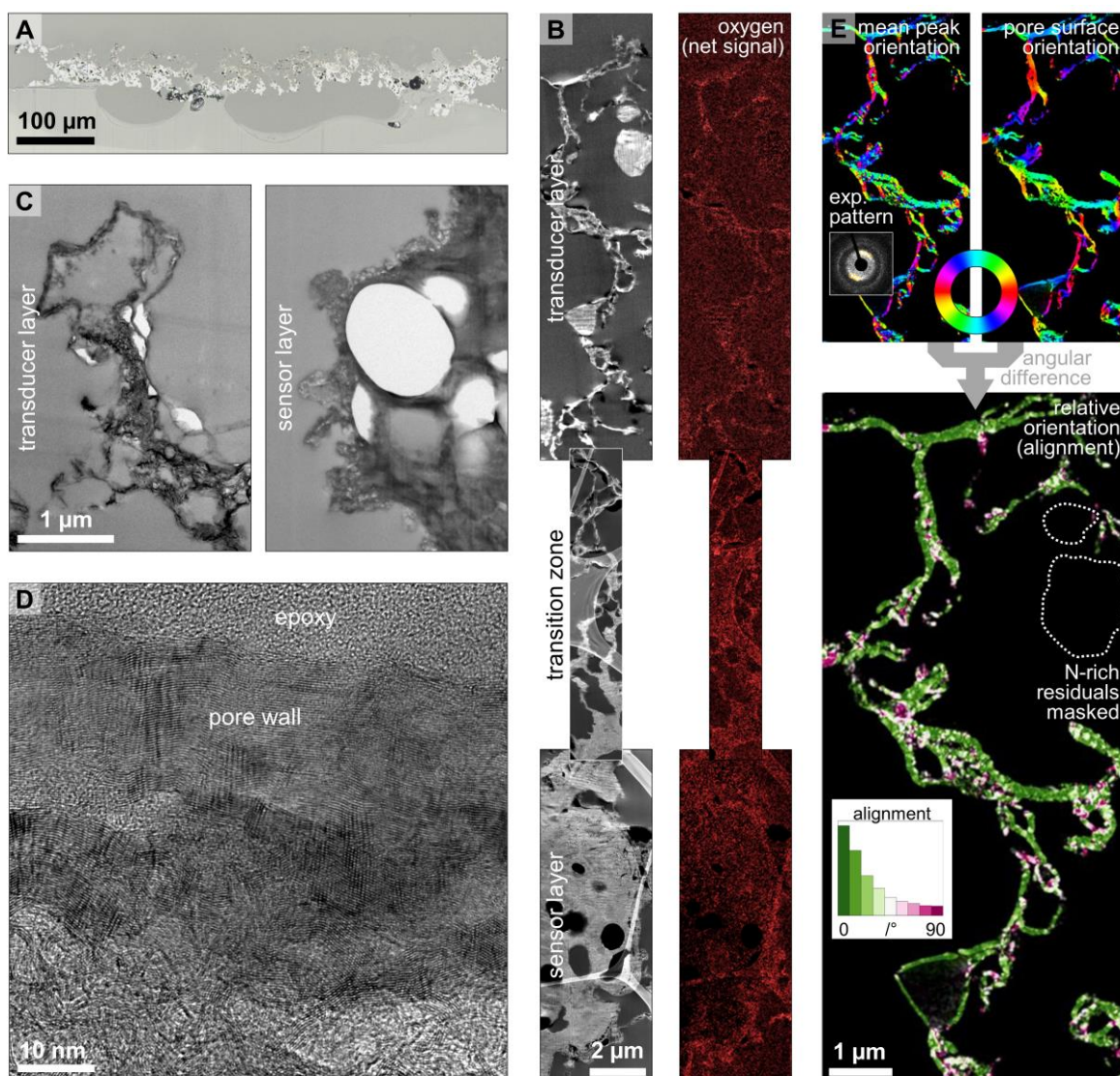


Figure S5. Supplementary cross-sectional data of LP₀₂-Ade380₉₀/Glu300₁₀ sensor: A) optical bright-field micrograph of embedded sensor (microtomy block surface) in reflection, B) EELS oxygen net signal (red) visualizing higher oxygen content in the graphitized carbon phase and the shell phase: this information is lost upon quantification as epoxy exhibits similar O content but lower density, C) overview bright-field TEM micrographs depicting the regions, where the presented HRTEM images were recorded, D) supplementary HRTEM image of the graphitized carbon phase; E) Determination of local basal-plane alignment³ with respect to the respective pore surface (similar region as in B) by comparing the mean peak orientations of (001) Bragg peaks of graphitic carbon for all probed positions (2-fold rotational symmetry applied, exemplary microprobe diffraction pattern depicted) and local orientation of the pore surface calculated from two independent derivatives using a Gaussian kernel with a standard deviation of 8 probe positions (2-fold rotational symmetry applied). Details about the utilized flowline visualization (Figure 3H) are found in Ref. ⁴.

EELS chemical-bond analysis

Chemical bond analyses by principal component analysis (PCA)⁵ of the EELS datasets were conducted (methods section). The spectral PCA components with significant Eigen values (Figure 3E), well describing the experimental datasets in the whole spectroscopic range (with C, N, and O ionization edges), were extracted to derive their spatial distributions (Figure 3D). Various boundary conditions due to the complex samples, however, caused minor inevitable residual intensities between the experimental and the joint PCA data considering only the selected components. Those are

- the sample thickness of $t/\lambda \approx 0.4\text{--}0.5$ (a few 10 nm). Although a probe size of only a few Å was used, many EELS spectra will not have originated from pure material due to the sample morphology (projection through different phases, including the epoxy). Although that thickness already caused slight spectral shifts to higher energy losses, multiple scattering was not corrected for (prior to PCA) because of unresolved artifacts from common deconvolution techniques.
- slight thickness and density variations within the ultra-microtomic cross-sections.
- the anisotropic ionization of the randomly aligned graphitized carbon^{6,7} causing local orientation-dependent variations of the $1s \rightarrow \pi^*$ to $1s \rightarrow \sigma^*$ intensity ratio (not exactly at magic angle). Hence, the average intensity ratio, determined by PCA may locally underestimate (or even overestimate) the measured experimental signals (Figure S6).
- minor spectral artifacts due to the very large fields of view of the recorded mappings at the upper microscope limit in regular STEM mode (no de-scan coils available).

Nonetheless, four major phases were clearly identified throughout the device cross-section (Figure 3D (right)). Those are the graphitized carbon phase (red), the shell phase (yellow) and the two core phases I/II (green/blue) of the same composition but in significantly different bond states. The EELS PCA spectra of those phases and their spatial distributions are shown in Figure 3D, E and Figure S6. Those PCA components were validated by comparing to 50 (summed and normalized) representative experimental spectra (marked by lines with symbols in Figure S6). Most fit very well; only the intensity ratio of $1s \rightarrow \pi^*$ and $1s \rightarrow \sigma^*$ (pre-peak intensity) of the graphitized carbon is not well reproduced in all regions as discussed before.

Those spectra exhibit characteristic but significantly different shapes of the C K and N K edges with distinct peaks at energy losses due to ionization from $1s$ into the respective π^*/σ^* anti-bonding states (dipole-allowed transitions), representing π -/ σ -bonds and thus the local hybridization state of the involved species^{8,9}, pronounced $1s \rightarrow \pi^*$ pre-peaks (relative to the normalized ($1s \rightarrow \sigma^*$ peaks) and thus high degrees of sp^2 hybridization were found for both, carbon and nitrogen, in all identified phases. Dependent on the phase and its predominant atomic nearest-neighbor environment of the major element carbon, the peak positions of the C K ionization edge

(exemplarily marked for the $1s \rightarrow \pi^*$ peak in Figure 3E, left) distinctly shift. Those shifts are explained by the partial electron transfer from carbon to the more electronegative nitrogen (or oxygen).¹⁰

As the spectral data is a superposition of independent ionization events at hundreds of carbon atoms in different environments per probed sample volume, the local composition must be considered. The most probable next-neighbor possibilities for sp^2 hybridized carbon in those phases are C=N versus C=C, with a minor fraction of C=O due to the relatively low oxygen concentrations.¹¹ As a consequence, the observed pronounced C K pre-peak of the N-rich core phases I/II is attributed to predominantly C=N bonding within those phases, yielding a shift of 1.5 eV. This is in agreement with literature.¹⁰ The typical energies of the pre-peak as well as the narrow $1s \rightarrow \sigma^*$ peak in the spectrum of the graphitized sp^2 carbon resemble the C=C bonding in that crystalline phase; C=O bonds as well contribute to that measured signal to a minor extent (not resolved), with similar intensity distributions ($1s \rightarrow \pi^*$ and $1s \rightarrow \sigma^*$ transitions) expected at even higher energy losses. Due to the consecutive loss of nitrogen, a systematic transition from the N-rich core phases I/II through the N-poor shell phase to the final graphitized carbon (no nitrogen) is seen in Figure 3E (left). In accordance to the composition of the shell phase with significant fractions of, both, C=C and C=N environments, the spectrum of the C ionization edge of that phase is considered a superposition of the measured extremes with $(1s \rightarrow \pi^*)_{C=C \text{ or } C=N \text{ or } (C=O)}$, $(1s \rightarrow \sigma^*)_{C=C \text{ or } C=N \text{ or } (C=O)}$ and $(1s \rightarrow \sigma^*)$ signal contributions with $(1s \rightarrow \pi^*)_{C=C}$ dominating. This particularly explains the shallow valley observed.⁹

In contrast, there is generally no shift of the N K ionization edge (cf. energy loss at $1s \rightarrow \pi^*$) because the bond partners of any nitrogen atom are most probably carbon atoms independent of the N content of the respective phase (Figure 3E, right). The same integral N K intensities of the two core phases I/II reflect the similar composition of the core regions, whereas the reduced N content of the rim phase is evident from the reduced N K signal (with respect to the corresponding C signals of the different phases). However, a systematic change of the shapes of the N as well as C ionization edges from the core phases II to I is observed, i.e., increasing $1s \rightarrow \pi^*:1s \rightarrow \sigma^*$ ratios, indicating the increase of sp^2 -bound nitrogen as well as carbon in core phase I.¹² The shell phase exhibits a very similar shape of the N ionization edge and thus similar nitrogen bonding as core phase I (for comparison the intensities of the shell phase are scaled in Figure 3E (right)).

The phase distributions in Figure 3D (right) confirm that the transducer layer consists of the most converted phase (graphitized C) with a minor fraction of less converted material, while the less converted shell and core phases are mostly found in the sensor layer. The transition zone in between consists of core phase I, shell phase and graphitized carbon with a narrow gradient as shown.

The high degree of crystallinity of the transducer layer is corroborated by the evolving extended fine structures of the C ionization edge (Figure S6A, left) with a pronounced feature around $\Delta E = 329$ eV (typical multiple elastic scattering resonance (MSR) for graphite).⁹ The core and shell

phases of the sensor layer are amorphous with indications of local ordering within the shell layer by the faint but broad MSR at around $\Delta E = 328$ eV.

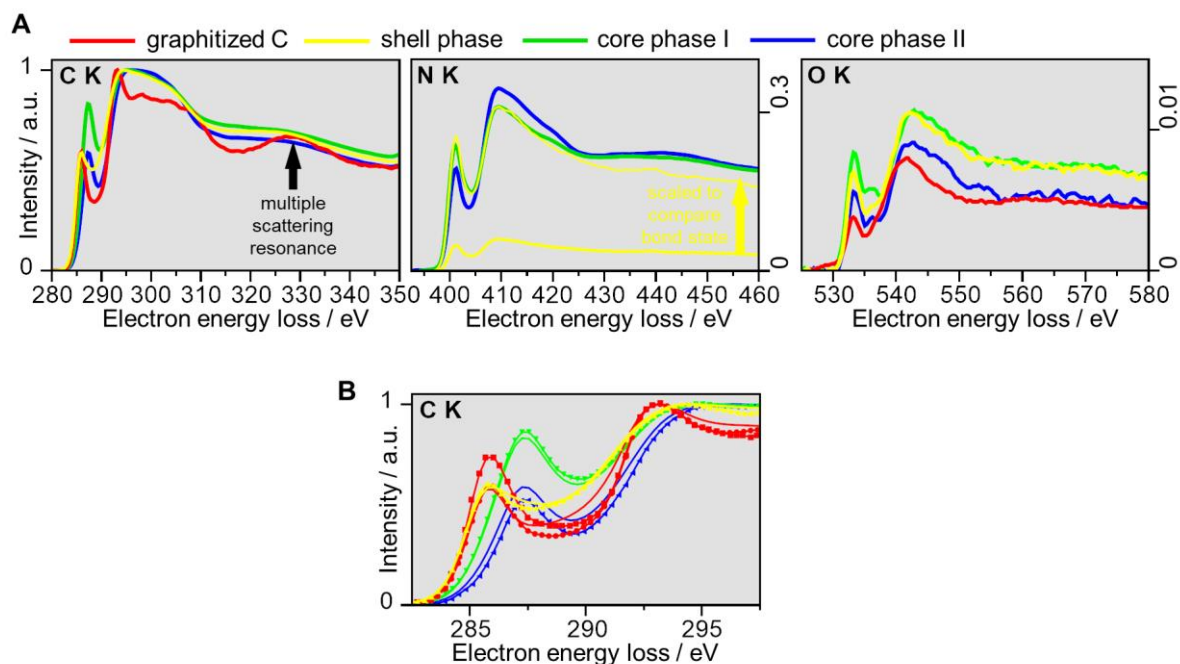


Figure S6. Supplementary data to EELS chemical-bond analyses: A) PCA components of the C K, N K, and O K ionization edges (same as in Figure 3E but with different energy-loss ranges (for each phase, the N, O edges are in scale with the respective C K edge): C K edge of graphitized carbon with pronounced MSR close to 330 eV (evolving in shell phase), B) validation of PCA components (continuous lines) by comparison to 50 summed and normalized experimental spectra from selected regions (marked by lines with symbols): two experimental curves are shown for the graphitized carbon, which are obtained from thin pore walls (squares) and an extended graphitized region (circles)

Raman spectroscopy

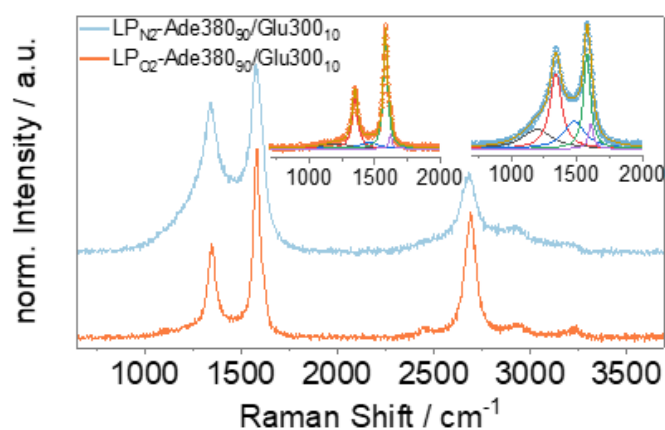


Figure S7. Raman spectrum of LP_{N2}-Ade380₉₀/Glu300₁₀ and LP_{O2}-Ade380₉₀/Glu300₁₀ obtained upon excitation at 532 nm. The insets show a deconvolution of the D and G region.

X-ray photoelectron spectroscopy

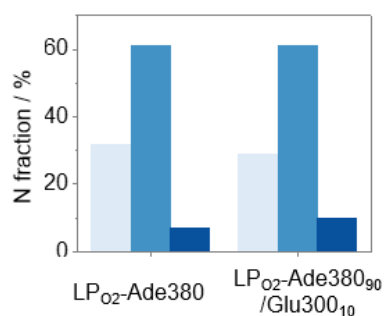


Figure S8. Composition of nitrogen of LP_{O2}-Ade380₉₀/Glu300₁₀ in comparison to LP_{O2}-Ade380 obtained by XPS.

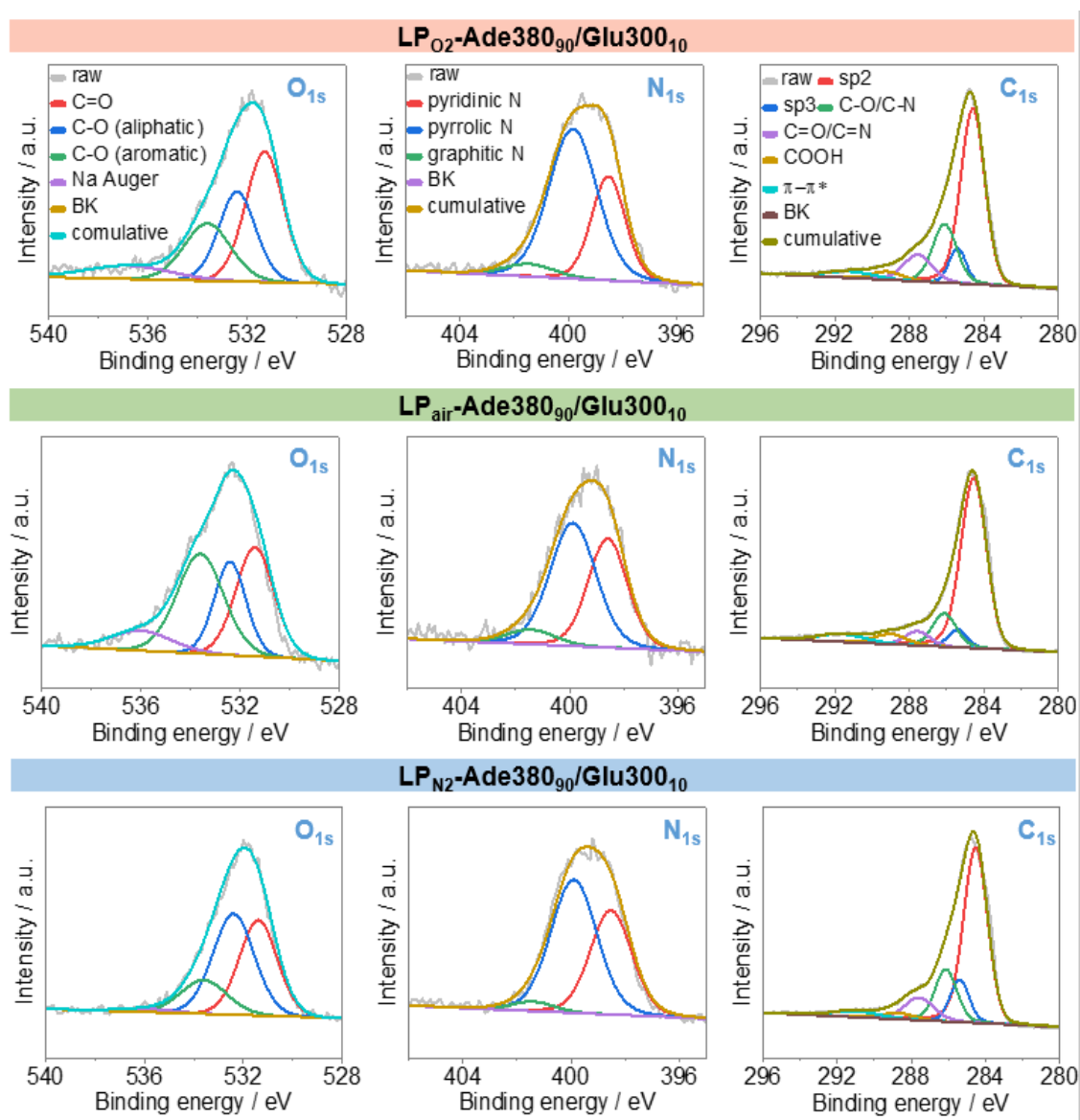


Figure S9. X-ray photoelectron spectrographs of the O_{1s}, N_{1s}, and C_{1s} regions (from left to right) of LP_{O2}-Ade380₉₀/Glu300₁₀, LP_{air}-Ade380₉₀/Glu300₁₀ and LP_{N2}-Ade380₉₀/Glu300₁₀ (top to bottom).

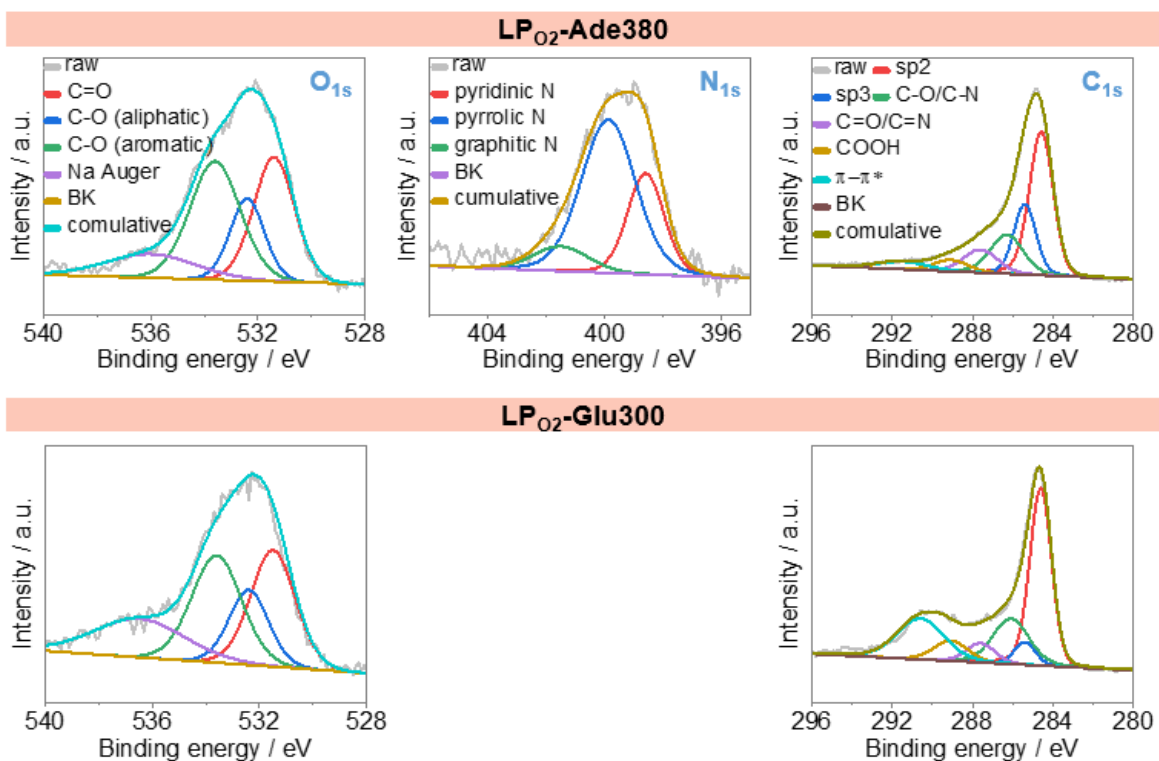


Figure S10. X-ray photoelectron spectrographs of the O_{1s}, N_{1s}, and C_{1s} regions (from left to right) of LP_{O2}-Ade380 and LP_{O2}-Glu300 (top to bottom).

Table S1. Composition of carbon of sensor obtained by deconvolution of the C_{1s} and O_{1s} peaks of the XPS spectra.

Sample	C _{1s} peaks (% of total peak area)						O _{1s} peaks (% of total peak area)		
	C-Sp ²	C-Sp ³	C-N/ C-O	C=N/ C=O	COOH	π- π*	C=O	C-O (aliph)	C-O (arom)
LP _{O2} -Ade ₉₀ /Glu ₁₀	55.1	7.9	19.2	10.3	3.4	4.1	45.4	30.2	24.4
LP _{air} -Ade ₉₀ /Glu ₁₀	66.1	5.2	12.4	5.5	5.0	5.8	35.4	25.1	39.5
LP _{N2} -Ade ₉₀ /Glu ₁₀	56.8	11.1	16.0	9.4	2.7	4.0	38.7	44.6	16.7
LP _{O2} -Ade380	42.9	19.9	16.7	10.3	5.1	5.1	36.8	20.3	42.9
LP _{O2} -Glu300	41.4	5.2	18.2	6.2	7.7	21.3	38.5	21.9	39.5

Fourier-transform infrared spectroscopy

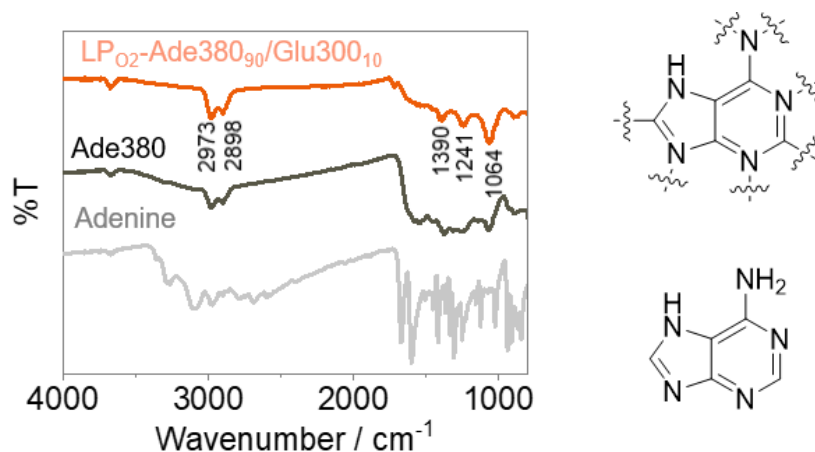


Figure S11. Fourier-transform infrared spectrum of adenine, Ade380 and LP_{O2}-Ade380₉₀/Glu300₁₀.

Reference material testing

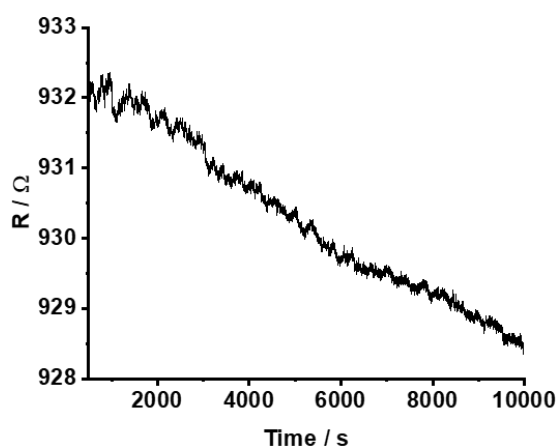


Figure S12. Resistive response of the laser-patterning sensor using an optimized cytosine based LP-NC towards 10% of CO₂.¹

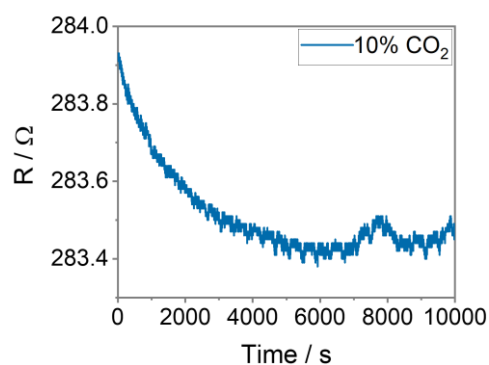


Figure S13. Resistance response of laser-patterned polyimide (LP-PI) towards 10% CO₂ using N₂ as carrier gas

Hall measurements

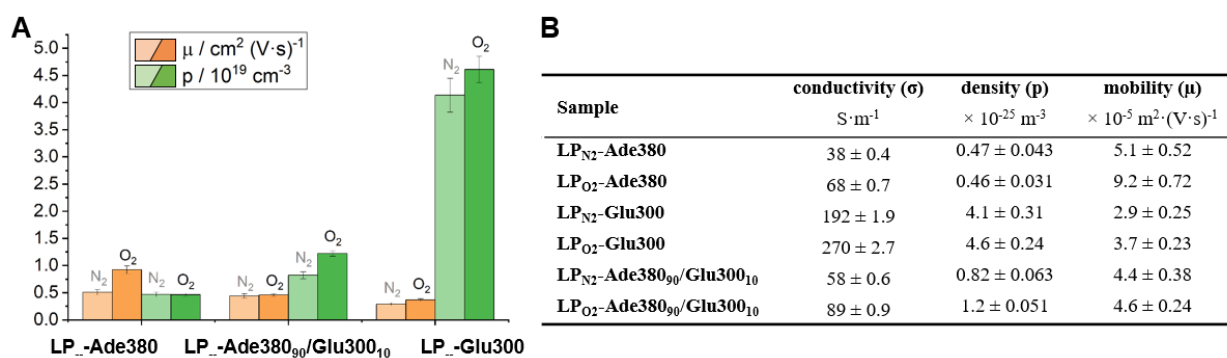


Figure S14. A) Charge carrier mobilities (μ) and charge carrier densities (p) of all laser-carbonized films obtained by Hall measurements; B) Charge carrier properties of all laser-carbonized films obtained by Hall measurements.

Figure S13 presents the charge carrier mobilities (μ) (orange) and densities (p) (green) of LP-Ade380, LP-Glu300, and LP-Ade380₉₀/Glu300₁₀ produced in either N₂ or O₂ atmosphere. Obviously, LP-Glu300 exhibits generally high p with values up to 10 x higher than in LP-Ade380. Throughout all tested samples, O₂ in the reaction atmosphere promotes an increase in both μ and p . Upon addition of Glu300 to Ade380, p is increased by a factor of ~ 2 . In view of the band-structure and the influence of the charge density, for sensor applications, low p is favorable to achieve higher sensitivity.¹³ However, the effect of Glu300 on the overall sensor performance is positive. We assume that the porogenic activity of Glu300 outweighs the detriment of the increased p .

Sensor performance

Interference test

We performed some selectivity sensing experiments using volatile organic compounds (VOCs) acetone and ethanol as interference analytes. In Figure S15, the optimized sensor film LP_{O₂}-Ade380₉₀/Glu300₁₀ shows a resistance response $\Delta R/R_0 = 0.06\%$ to 2.5 % acetone and almost no response to 0.8% ethanol.

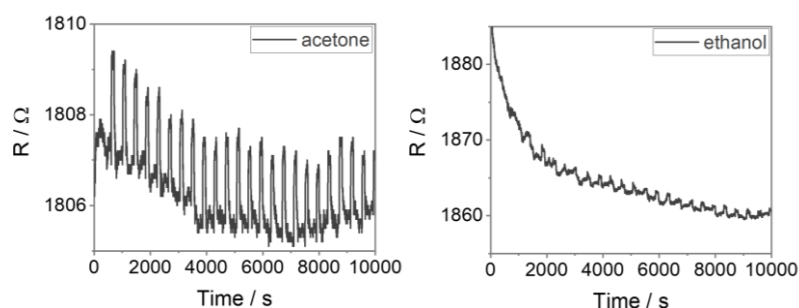


Figure S15. Resistance response of sensor films LP_{O₂}-Ade380₉₀/Glu300₁₀ sensor towards 2.5% acetone (left) and 0.8% ethanol (right) using N₂ as carrier gas.

Thermodynamic analysis

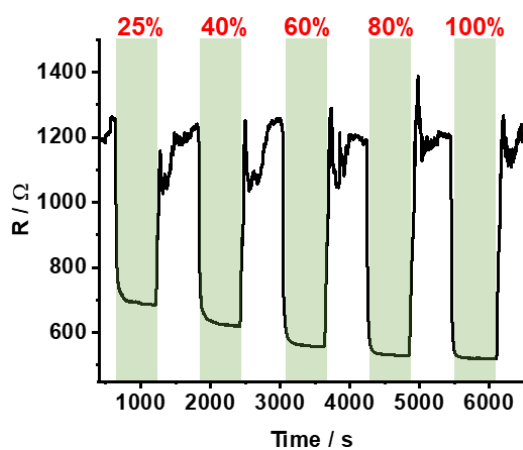


Figure S16. Resistance response of LP₀₂_Ade380₉₀/Glu300₁₀ to different relative humidities in a 100% N₂ environment.

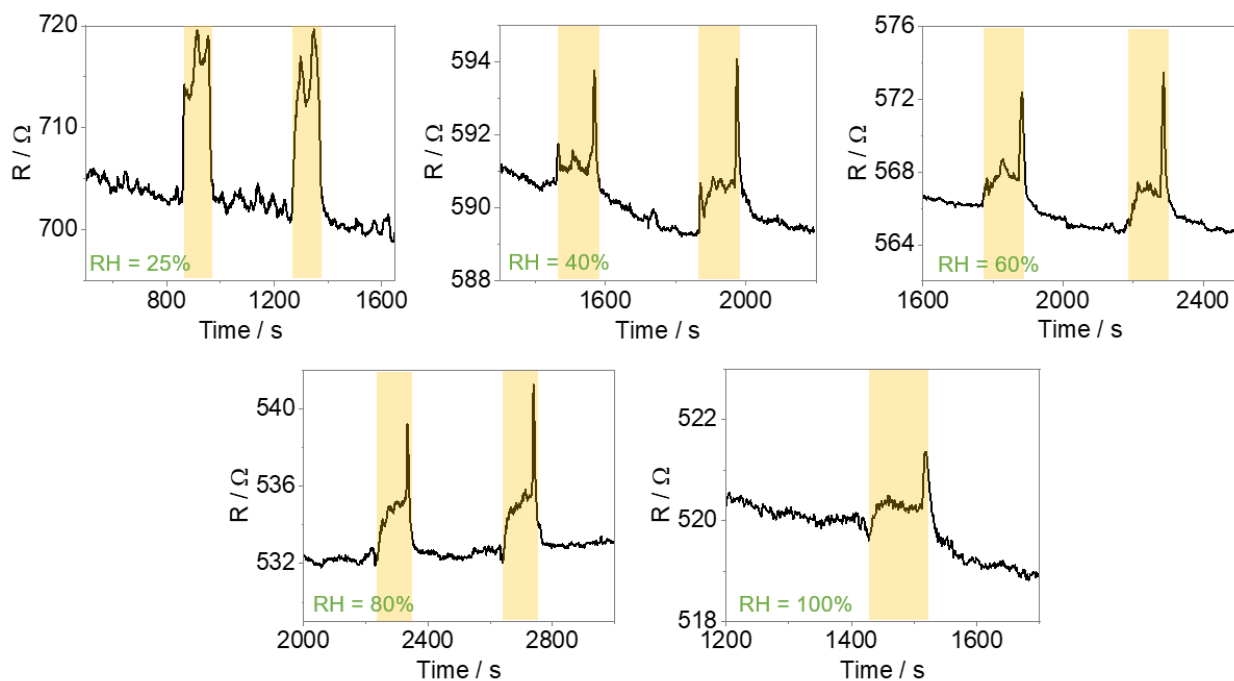


Figure S17. Resistance response of LP₀₂_Ade380₉₀/Glu300₁₀ to 10% CO₂ (90%N₂) at different relative humidities. The sharp peak at the end of the cycles originates from a sudden pressure release from the valve.

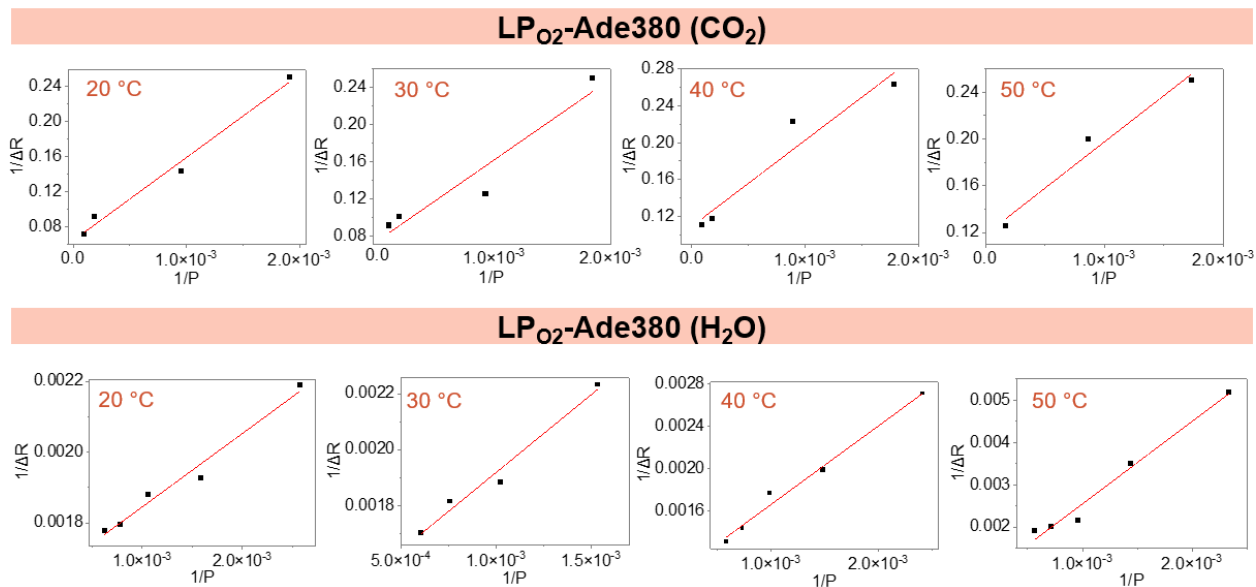


Figure S18. Plots of $1/\Delta R$ as a function of $1/P$ at 20°C , 30°C , 40°C and 50°C for the determination of the equilibrium constants K of LP_{O₂_Ade380 to CO₂ (upper panel) or H₂O (lower panel).}

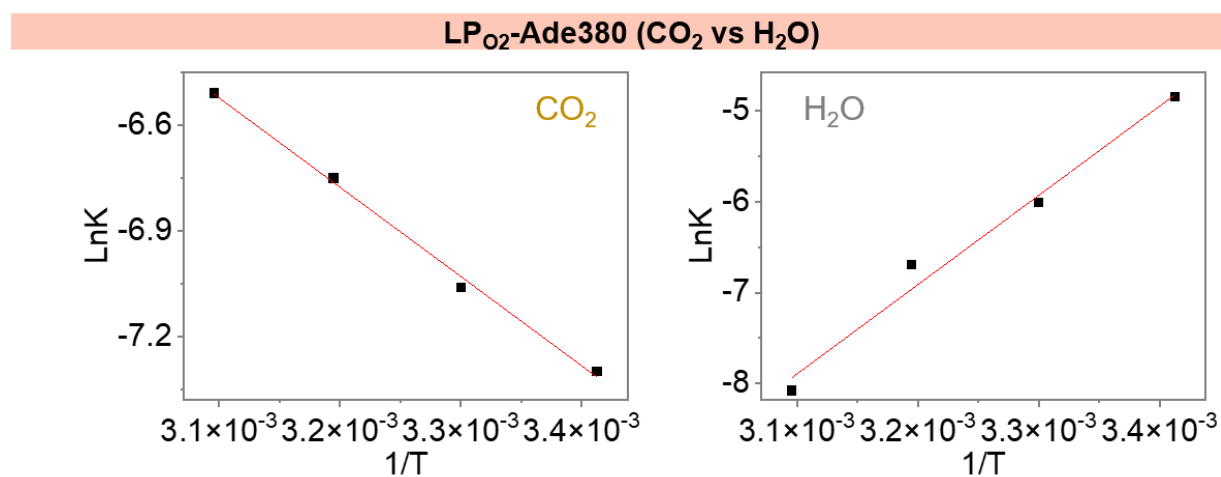


Figure S19. Plots of $\ln K$ as a function of $1/T$ for the determination of $\Delta_{\text{ads}}H$ of CO₂ and H₂O to LP_{O₂_Ade380.}

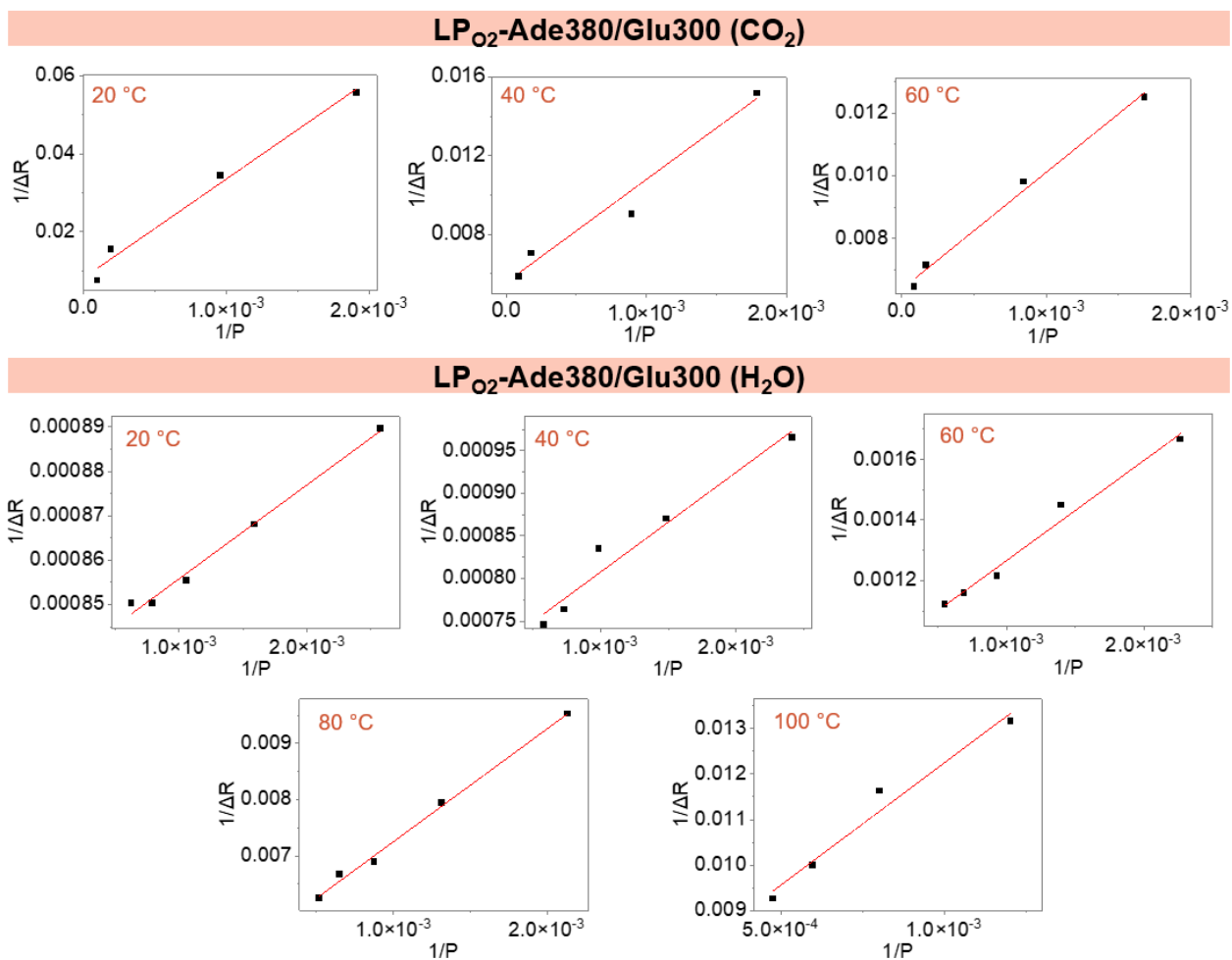


Figure S20. Plots of $1/\Delta R$ as a function of $1/P$ at 20 °C, 40 °C and 60 °C for the determination of the equilibrium constants K of LP_{O2}-Ade380₉₀/Glu300₁₀ to CO₂ (upper panel) and H₂O (lower panel):

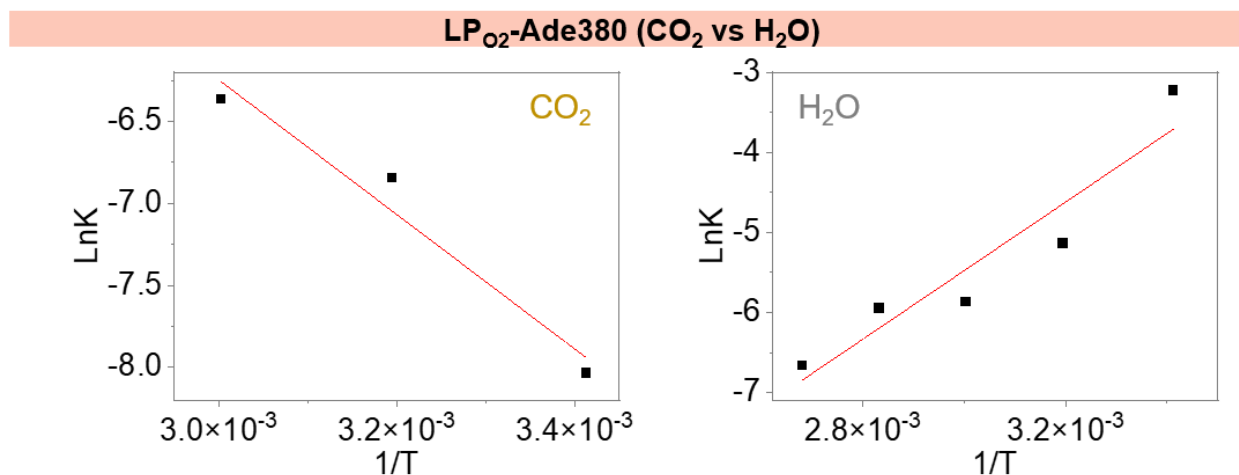


Figure S21. Plots of $\ln K$ as a function of $1/T$ for the determination of $\Delta_{\text{ads}}H$ of CO₂ and H₂O to LP_{O2}-Ade380₉₀/Glu300₁₀.

Table S2. Equilibrium constants K , parameter α , and heat of adsorption $\Delta_{\text{ads}}H$ of $LP_{O_2_Ade380}$.

$LP_{O_2_Ade380}$				
	CO_2		H_2O	
	K	α	K	α
20 °C	6.76×10^{-4}	0.06	7.88×10^{-3}	1.64×10^{-3}
30 °C	8.58×10^{-4}	0.07	2.45×10^{-3}	1.36×10^{-3}
40 °C	1.17×10^{-3}	0.11	1.23×10^{-3}	9.19×10^{-4}
50 °C	1.49×10^{-3}	0.12	3.08×10^{-4}	6.01×10^{-4}
$\Delta_{\text{ads}}H$	21.3 kJ·mol ⁻¹		-81.7 kJ·mol ⁻¹	

Table S3. Equilibrium constants K , parameter α , and heat of adsorption $\Delta_{\text{ads}}H$ of $LP_{O_2_Ade380_{90}/Glu300_{10}}$.

$LP_{O_2_Ade380_{90}/Glu300_{10}}$				
	CO_2		H_2O	
	K	α	K	α
20 °C	6.23×10^{-4}	8.00×10^{-3}	4.00×10^{-2}	8.35×10^{-4}
40 °C	1.07×10^{-4}	5.57×10^{-3}	5.86×10^{-3}	6.90×10^{-3}
60 °C	1.72×10^{-3}	6.39×10^{-3}	2.83×10^{-3}	9.35×10^{-4}
80 °C			2.62×10^{-3}	5.25×10^{-4}
100 °C			1.28×10^{-4}	6.88×10^{-3}
$\Delta_{\text{ads}}H$	34.1 kJ·mol ⁻¹		-35.6 kJ·mol ⁻¹	

Bending experiments

The curvature of the bending is dependent on the distance between the two electrodes and was determined in a range between a minimum value of 0.09 and a maximum value of 0.41 mm⁻¹.¹⁴ The response changes gradually with the curvature. During the first (initial) bending sequence, the sensor strip was bent at a slow speed of only 10 $\mu\text{m s}^{-1}$ starting at low curvatures of 0.09 mm⁻¹ and slowly increasing to the maximum curvature of 0.4 mm⁻¹ (three times for each curvature/amplitude). **Figure S20** shows the corresponding response of increasing R: small change at low curvatures, becomes larger at increasing curvatures. After the first run, the response remains stable in all subsequent runs and exhibit a quantitative response to any curvature.

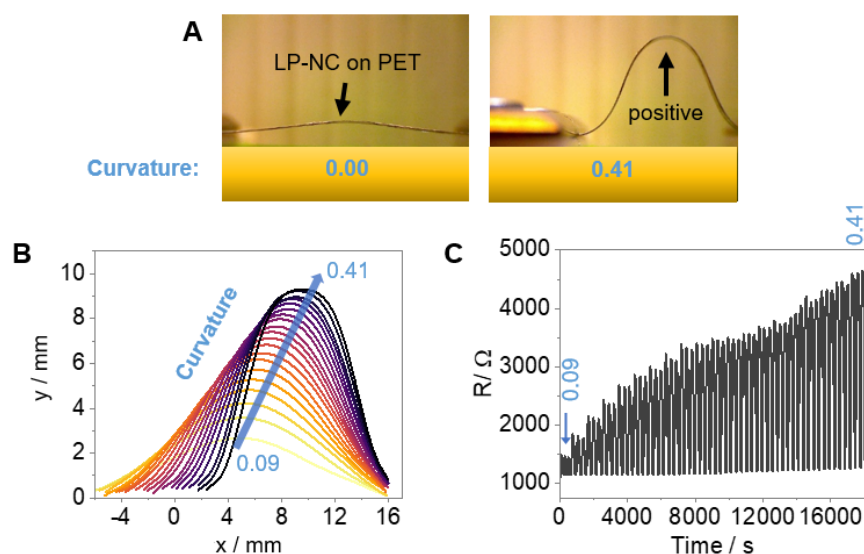


Figure S22. A) Photographs of the $LP_{O_2_Ade380_{90}/Glu300_{10}}$ sensor strip on PET mounted between two electrodes (one movable). B) Curvature analysis of the LP-NC strip in dependence of the distance between the two electrodes in the movable stage; C) Change in resistance upon steadily increasing the curvature in the first run (training mode); D) Change in resistance upon steadily increasing the curvature in all subsequent runs (operation mode).

Operation mode

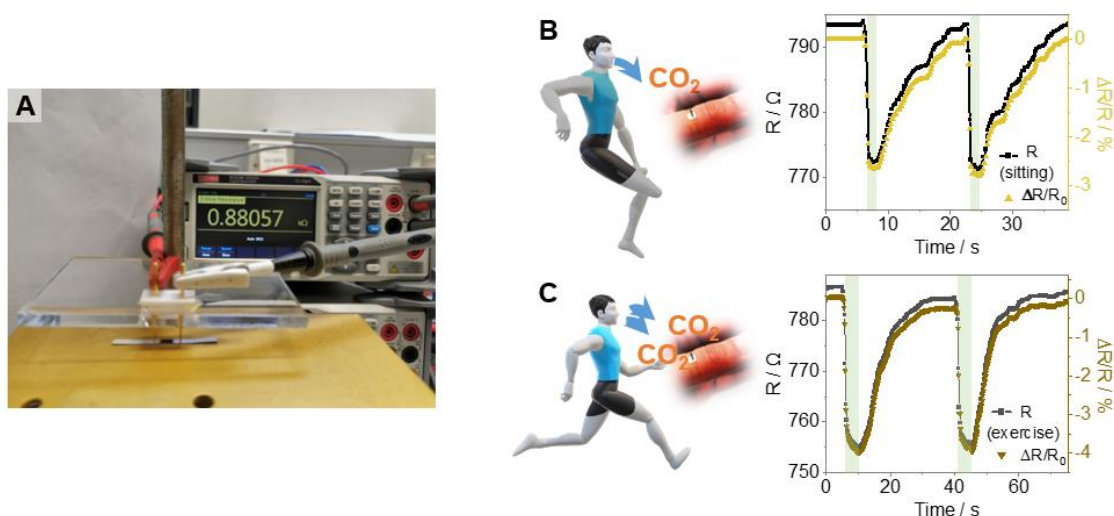


Figure S23. A) Photograph of breath monitoring test in an open environment; B) resistive and kinetic response of $LP_{O_2-Ade38090}/Glu30010$ to exhaled breath of a human at rest; C) Resistive and kinetic response to exhaled breath of a human at exercise.

References

1. Wang, H. *et al.* Laser-carbonization: Peering into the formation of micro-thermally produced (N-doped)carbons. *Carbon N. Y.* **176**, 500–510 (2021).
2. Wang, X. X. *et al.* Three-dimensional strutted graphene grown by substrate-free sugar blowing for high-power-density supercapacitors. *Nat. Commun.* **4**, (2013).
3. Ophus, C. *et al.* Automated Crystal Orientation Mapping in py4DSTEM using Sparse Correlation Matching. *Microsc. Microanal.* **28**, 390–403 (2022).
4. Panova, O. *et al.* Diffraction imaging of nanocrystalline structures in organic semiconductor molecular thin films. *Nat. Mater.* **18**, 860–865 (2019).
5. Lucas, G., Burdet, P., Cantoni, M. & Hébert, C. Multivariate statistical analysis as a tool for the segmentation of 3D spectral data. *Micron* **52–53**, 49–56 (2013).
6. Daniels, H. *et al.* Experimental and theoretical evidence for the magic angle in transmission electron energy loss spectroscopy. *Ultramicroscopy* **96**, 523–534 (2003).
7. Ferrari, A. C. & Robertson, J. Interpretation of Raman spectra of disordered and amorphous carbon. *Phys. Rev. B* **61**, 14095–14107 (2000).
8. Fernández, A. *et al.* Characterization of carbon nitride thin films prepared by dual ion beam sputtering. *Appl. Phys. Lett.* **69**, 764–766 (1996).
9. Daniels, H., Brydson, R., Rand, B. & Brown, A. Investigating carbonization and graphitization using electron energy loss spectroscopy (EELS) in the transmission electron microscope (TEM). *Philos. Mag.* **87**, 4073–4092 (2007).
10. Ramos, F. *et al.* TEM, Edx and EELS Study of Cnx and Si Doped Cnx Thin Films. in *Electron Microscopy and Analysis* 381–384 (Bristol, U.K. Institute of Physics Publishing, 1999).
11. Pels, J. R., Kapteijn, F., Moulijn, J. A., Zhu, Q. & Thomas, K. M. Evolution of nitrogen functionalities in carbonaceous materials during pyrolysis. *Carbon N. Y.* **33**, 1641–1653 (1995).
12. Wan, L. & Egerton, R. F. Preparation and characterization of carbon nitride thin films. *Thin Solid Films* **279**, 34–42 (1996).
13. Wang, H. *et al.* In Situ Synthesis of Molybdenum Carbide Nanoparticles Incorporated into Laser-Patterned Nitrogen-Doped Carbon for Room Temperature VOC Sensing. *Adv. Funct. Mater.* **31**, 2104061 (2021).
14. Hepp, M. *et al.* Trained Laser-Patterned Carbon for High-Performance Mechanical Sensors. *npj Flex. Electron.* DOI: 10.1038/s41528-022-00136-0 (2021). doi:10.1038/s41528-022-00136-0

Cite this: *J. Mater. Chem. A*, 2022, 10, 24156

Modulating between $2e^-$ and $4e^-$ pathways in the oxygen reduction reaction with laser-synthesized iron oxide-grafted nitrogen-doped carbon[†]

Huize Wang,[‡] Maria Jerigova,[‡] Jing Hou,[‡] Nadezda V. Tarakina,[‡] Simon Delacroix,[‡] Nieves López-Salas^{‡*} and Volker Strauss^{‡*}

In this study, we demonstrate the tuning of the oxygen reduction reaction (ORR) using iron/iron oxide nanoparticle grafted laser-patterned nitrogen-doped carbon (LP-NC) electrodes. Depending on the preparation route, *i.e.* addition of a molecular $\text{Fe}(\text{NO}_3)_2$ precursor before (route 1) or after pre-carbonization (route 2) of the citric acid/urea precursors, either the $4e^-$ or the $2e^-$ pathway in the ORR is facilitated leading to either H_2O or H_2O_2 as a reaction product, respectively. The kinetic reaction conditions afford mixed valence metal oxide nanoparticles embedded in LP-NC in the form of either $\text{Fe}_2\text{O}_3/\text{Fe}$ or $\text{Fe}_2\text{O}_3/\text{FeO}/\text{Fe}$, respectively, facilitated by an *in situ* carbothermal reduction during the laser-induced carbonization. In HR(S)TEM analysis we found evidence for the occurrence of Fe_2O_3 in the η - or α -phase, depending on the preparation route. Reciprocally, the graphitization is also affected by the preparation route leading to either homogeneous graphitization or a locally graphitized shell structures around the nanoparticles. In the $4e^-$ mediated ORR facilitated by η - $\text{Fe}_2\text{O}_3/\text{Fe}@$ LP-NC onset potentials as low as 0.70 V (vs. RHE) with a H_2O_2 production efficiency of 4% and 10% in alkaline and neutral electrolyte, respectively, were determined. On the other hand, α - $\text{Fe}_2\text{O}_3/\text{FeO}/\text{Fe}@$ LP-NC presents an onset potential for the $2e^-$ mediated ORR as low as 0.77 V with a H_2O_2 production efficiency of nearly 80%. The changes in selectivity and physicochemical properties of the electrocatalysts by applying simple modifications in the synthetic route point to laser-patterning as a very promising route to scale up designer electrodes for electrochemical conversion.

Received 24th July 2022
Accepted 2nd October 2022

DOI: 10.1039/d2ta05838c

rsc.li/materials-a

Introduction

In the face of current global energy and environmental challenges, the development of alternative energy conversion systems has become increasingly critical. In this regard, electrochemical energy conversion facilitated by sustainable electrocatalysts is expected to be a frontrunner in future energy supply.¹ An essential reaction in a number of electrocatalytic applications is the oxygen reduction reaction (ORR), in which molecular oxygen (O_2) is electrochemically reduced to either H_2O or H_2O_2 following the $4e^-$ or $2e^-$ pathway, respectively.² In the ORR process, the common intermediate adsorbate on the catalyst interface is $*\text{-OOH}$ ($*$ denotes an active site). Depending on the active sites and the catalyst design either the dissociation

at the active site ($*\text{-OOH}$) or the O–O bond ($*\text{O-OH}$) is favoured, resulting in the formation of H_2O_2 or $2\text{H}_2\text{O}$, respectively. According to the standard potentials the $4e^-$ pathway is thermodynamically preferred.³

The latter is applied in state-of-the-art proton-exchange membrane (PEM) fuel cells to convert chemical energy into electric energy.⁴ Today, carbon-supported platinum (Pt) is the preferred choice of a catalyst system in commercial devices to achieve the best economic ORR performance.⁵ Such systems provide excellent reaction kinetics and flexibility.^{6,7} However, high costs due to limited natural reserves and rapid deactivation due to the inevitable phenomenon of methanol crossover are still limiting factors for the widespread practical application of PEM fuel cells.⁸ Furthermore, the $4e^-$ ORR is used in metal-air batteries.⁹ On the other hand, H_2O_2 formed in the $2e^-$ reduction pathway is a valuable chemical used in many applications such as paper production, chemical synthesis, or water treatment,¹⁰ and is currently produced by a highly energy-consuming process of anthraquinone oxidation.¹¹ However, the production of cheap and stable catalysts showing high selectivity towards the $2e^-$ reduction pathway is still a topic of research.¹²

[‡]Department of Colloid Chemistry, Max Planck Institute of Colloids and Interfaces, Am Mühlenberg 1, 14476 Potsdam, Germany. E-mail: Nieves.LopezSalas@mpikg.mpg.de; volker.strauss@mpikg.mpg.de

[§]LPICM, CNRS UMR 7647, Ecole polytechnique, Institut Polytechnique de Paris, Palaiseau 91128, France

[†] Electronic supplementary information (ESI) available. See <https://doi.org/10.1039/d2ta05838c>

[‡] Contributed equally.



To avoid the use of expensive noble metals, abundant transition metals on carbon supports with competitive catalytic activity and selectivity for the ORR are a promising alternative.¹³ For instance, iron oxides (α -Fe₂O₃,¹⁴ γ -Fe₂O₃ (ref. 15 or Fe₃O₄ (ref. 16) or iron carbides^{17,18} have been shown to catalyze the 4e⁻ pathway reduction of O₂ and exhibit long-cycle durability. Furthermore, recent research shows that the adsorption and desorption of adsorbates on the catalyst surface in iron-nitrogen co-doped carbon-based catalysts is enhanced due to the unique electronic Fe–N–C bond structures. It has a favourable impact on surface stability and catalyst activity, and exhibits an anti-poisoning effect in fuel cells.^{19,20} On the other hand, some reports show iron oxides embedded in carbon matrices that selectively catalyze the 2e⁻ pathway of the ORR.^{21–23} Additionally, Fe single-atom coordinated oxidized carbon nanotubes have shown high activity (>90%) in the selective 2e⁻ ORR in neutral electrolytes.²⁴ Understanding the mechanisms behind selectivity is still a central issue in designing catalysts.²⁵

An essential aspect for commercial application in electrocatalytic systems are the fabrication costs of the electrodes. In the past few years, laser-assisted processing methods of low-cost starting materials have been widely investigated for applied electrocatalytic systems. For instance, in 2017, a laser-carbonized membrane was demonstrated as an efficient electrode for water-splitting to produce both H₂ and O₂.²⁶ In 2018, O₂-plasma treatment of the surface of such laser-carbonized membranes was proven to increase the density of oxygen functional groups as active sites, which reduces the activation energy by facilitating adsorption of OER intermediates.²⁷ Therefore, in addition to high electrocatalytic activity, the simple and low-energy-consumption preparation method of the electrode has attracted extensive attention.

Here, we report the laser-assisted synthesis of a carbon-supported mixed valence iron oxide-based ORR catalyst. We use citric acid and urea as molecular precursors to create a carbon network-forming agent (CNFA) for laser-assisted carbonization and iron(III) nitrate as a precursor for the *in situ* formation of iron-containing nanoparticles in a laser-patterned nitrogen-doped carbon (LP-NC) matrix. By selection of the synthesis route, the structure of the composite is varied and the ORR selectivity is tuned between the 2e⁻ and 4e⁻ pathways. Comprehensive complementary analysis by X-ray photoelectron spectroscopy (XPS) and high-resolution transmission electron microscopy (HRTEM) suggests the kinetic formation of catalytically active mixed valence iron oxide nanoparticles of different compositions depending on the synthesis route. Their formation mechanism *via* laser-induced carbothermal reduction also influences the local graphitization of the LP-NC matrix surrounding the mixed valence iron oxide nanoparticles.

Results and discussion

Sample preparation and characterization

Laser-patterned catalyst electrodes were fabricated by a two-step approach including ink preparation and laser-carbonization. The inks were prepared by two different routes as illustrated in

Fig. 1. In route 1, all molecular precursors, namely citric acid, urea, and Fe(NO₃)₃ were thoroughly mixed and then pre-carbonized at 300 °C for 2 h (see the Experimental section). The resulting iron-containing carbon network-forming agents (CNFA(Fe)) with different iron contents were then processed into inks. In route 2, different amounts of Fe(NO₃)₃ were added to the readily prepared iron-free CNFA and further processed to inks. As a standard solvent for all inks, ethylene glycol was used. The inks were doctor-bladed on the substrates (PET, Si wafer, or carbon cloth) and dried to obtain films with mean thicknesses of ~30 μm. Then the dry films were irradiated with a mid-infrared CO₂-laser ($\lambda = 10.6 \mu\text{m}$) to create homogeneous electrode films in the desired dimensions. The resulting iron-containing LP-NC electrodes are named LP-NC(Fe)_n(*x*) with *n* indicating the preparation route (1 or 2) and *x* indicating the mass percentage of Fe after laser-carbonization. The mass percentages of iron in the laser-patterned films were determined by inductively coupled plasma mass spectrometry (ICP-MS) and are listed in Table 1.

In accordance with previous observations, laser-induced carbonization causes a drastic increase in the carbon content at the expense of nitrogen and oxygen (Table S1†). The quantitative iron content is slightly increased after laser treatment. For example, the carbon and iron contents of 48 wt% and 2.3 wt% in CNFA(Fe)₁(2.3) increased to 78 wt% and 3 wt% in LP-NC(Fe)₁(3.0) after laser carbonization (Table S1†), respectively. The addition of iron nitrate seems to have no significant influence on the formation of the typical disordered, porous morphology of the films with a relatively low iron content. Only in route 1 at higher concentrations of Fe, *e.g.* 12.1 wt%, the morphology of LP-NC(Fe)₁(12.1) is considerably different compared to that of the films with lower Fe concentrations in terms of forming a somewhat crumpled structure. In comparison, no such impact on the morphology upon addition of iron nitrate is observed for the films prepared by route 2.

The Raman spectra of the films prepared by following route 1, *i.e.* LP-NC(Fe)₁(*x*), show relatively sharp D-, G-, and G'-bands at 1340, 1574, and 2676 cm⁻¹, respectively, and negligible contributions from disorder-induced carbon and sp³-carbon (D3 at 1460 cm⁻¹ and D4 at 1200 cm⁻¹), indicating the formation of a turbostratic graphitic material with a high degree of carbonization.^{28,29} With the increasing iron content an increase in the defect related D-band is observed. The same principal observation is also made in the films prepared by following route 2. However, all LP-NC(Fe)₂(*x*) films show large contributions of D3 and D4 peaks as well as a low and broad G' band. This is generally attributed to samples with a lower degree of graphitization. Iron-based compounds are well-known as catalysts for graphitization of carbon.³⁰ The mechanism of graphitization is often not clear; however, in this case we observe an obvious difference between the two preparation routes. During pre-carbonization at 300 °C partial decomposition and cross-linking of the molecular precursors occur. Adding Fe(NO₃)₃ to the molecular precursors prior to pre-carbonization supports the formation of an iron-containing CNFA(Fe), in which Fe³⁺ is present during the cross-linking, and is thus homogeneously incorporated by coordination (Fig. S1†). On the other hand, the



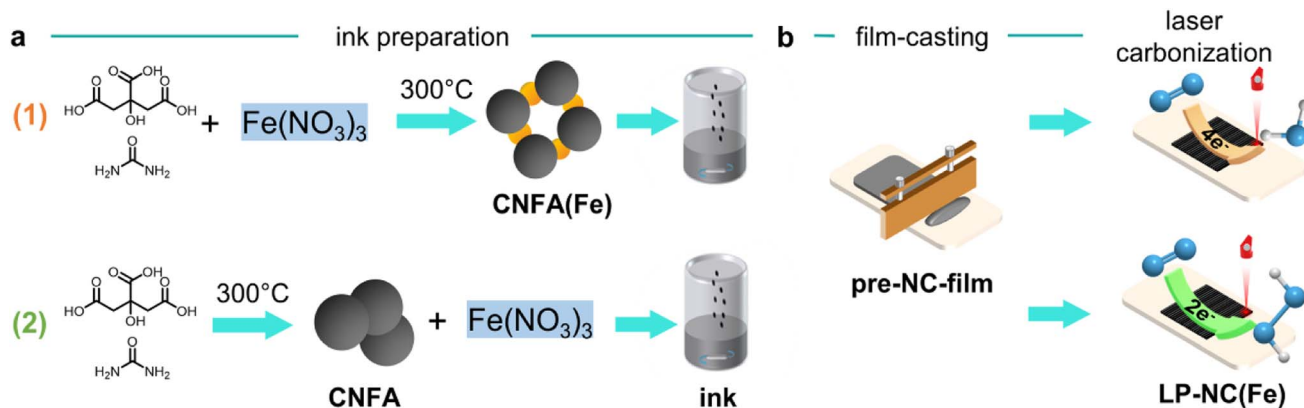


Fig. 1 Illustration of the sample preparation via two routes. (a) Route 1: mixtures of citric acid, urea, and $\text{Fe}(\text{NO}_3)_3$ are pre-carbonized at 300°C and the resulting CNFA(Fe) is processed to an ink; Route 2: citric acid and urea are pre-carbonized at 300°C and $\text{Fe}(\text{NO}_3)_3$ is added to the CNFA and processed to an ink; (b) casting of the CNFA films on substrates and laser-patterning of the films.

Table 1 Overview of the samples. The upper half was prepared according to route 1 and the lower half was prepared according to route 2

	Sample, LP-NC(Fe) _n (x)	Citric acid, g	Urea, g	$\text{Fe}(\text{NO}_3)_3 \cdot 9\text{H}_2\text{O}$, g	Fe content (ICP), %
Route 1	LP-NC(Fe) ₁ (3.0)	5	5	0.2	3.0
	LP-NC(Fe) ₁ (4.6)	5	5	0.3	4.6
	LP-NC(Fe) ₁ (12.1)	5	5	1	12.1
		CNFA, g		$\text{Fe}(\text{NO}_3)_3 \cdot 9\text{H}_2\text{O}$, g	Fe content (ICP), %
Route 2	LP-NC(Fe) ₂ (3.3)		0.2	0.02	3.3
	LP-NC(Fe) ₂ (3.8)		0.2	0.04	3.8
	LP-NC(Fe) ₂ (14.5)		0.2	0.1	14.5

iron-free CNFA used in route 2 is cross-linked before $\text{Fe}(\text{NO}_3)_3$ is added. As a result, the *in situ* decomposition of the iron-precursors is affected, which is demonstrated in the different Raman patterns, on the one hand, and different electrical conductivities, on the other. In route 1, LP-NC(Fe)₁(3.0) exhibits the highest electrical conductivity with 7.8 S cm^{-1} and decreases with the higher iron content (Fig. S2†), whereas for route 2 the opposite trend is observed, namely LP-NC(Fe)₂(3.3) with a lower iron content has a lower electrical conductivity of 3.5 S cm^{-1} , which increases to 8.7 S cm^{-1} for higher iron contents LP-NC(Fe)₂(14.5).

Further support for this interpretation is found in the XRD patterns of the films, as we observe narrower graphitic (200) and (10) reflections at 26 and $44^\circ 2\theta$ for samples prepared by route 1 (Fig. 2e–f). Interestingly, the (10) reflection increases in intensity with the increasing iron concentration, indicating an increase in defects and a change in the lateral size of the graphitic domains.³¹ This suggests that an optimal amount of iron is necessary to achieve a high degree of graphitization. Additional peaks at 30.0 , 35.4 , 43.0 , 53.4 , 56.9 and 62.5° that appear in the film with the highest iron concentration LP-NC(Fe)₁(12.1) are assigned to the (220), (311), (400), (422), (511), and (440) crystal planes of Fe_3O_4 [ICDD 19-629],

respectively. These peaks are not detected in the samples with lower iron concentrations, most likely due to a too small size and too low concentrations of iron-containing nanoparticles.

As a reference, for the primary films of route 1, only graphitic reflection with no signals of iron oxides is observed (Fig. S4†). This indicates that iron oxide is formed during laser-carbonization and not during pre-carbonization. This is also reflected in reference measurements using TEM/EDX analysis, where no iron oxide particles are found in the primary films (Fig. S4†).

In the XRD patterns of the samples prepared by route 2 (Fig. 2f), e.g. LP-NC(Fe)₂(14.5), the diffraction peaks at 35.6 and 49.5° correspond to the (110) and (024) lattice planes of Fe_2O_3 (ICDD 33-664) and those at 35.4 and 43.0° are assigned to the (311) and (400) crystal planes of Fe_3O_4 . Again, for LP-NC(Fe)₂(3.3) with a lower Fe content, only the graphitic reflection (002) and the carbon (111) symmetric Bragg reflection are observed. Therefore, we conclude that the addition of iron nitrate in different routes not only affects the final oxidation form of iron but also the degree of graphitization and the local crystal structure of the LP-NC.

To study the bonding structure of the materials, X-ray photoelectron spectra (XPS) of all LP-NCs as well as the primary



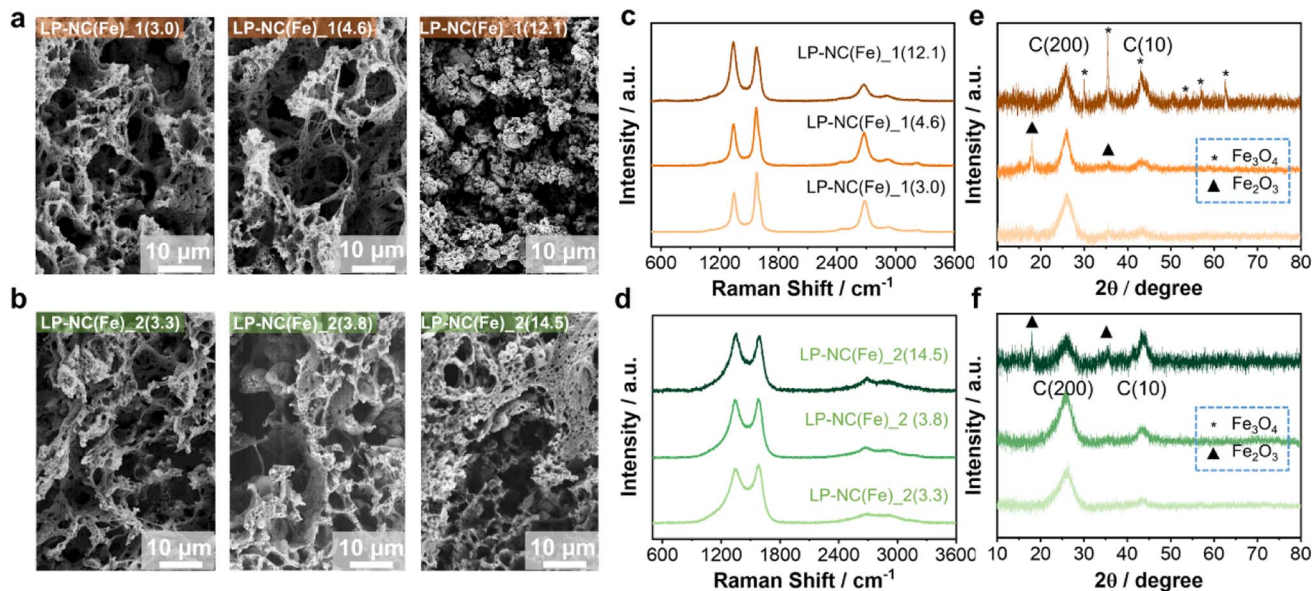


Fig. 2 (a) SEM images of films of LP-NC(Fe)₁(*x*) prepared on a flexible PET substrate by following route 1 and (b) LP-NC(Fe)₂(*x*) prepared by following route 2; (c) corresponding Raman spectra of LP-NC(Fe)₁(*x*) samples prepared by following route 1 and (d) route 2; (e) corresponding X-ray powder diffraction (XRD) patterns of the LP-NC(Fe)₁(*x*) films prepared by following route 1 and (f) route 2.

films with a focus on the C_{1s}, N_{1s}, O_{1s}, and Fe_{2p} regions were collected (Fig. S5–S9[†]). The C_{1s} region of all LP-NCs reveals a high degree of carbonization reflected by the prominent sp²-carbon peak at 284.4 eV and the presence of oxygen and nitrogen-containing functional groups indicated by the peaks at 285.3, 286.2 and 287.9 eV which are assigned to sp³-carbon, C–N/C–O, and C=N/C=O, respectively. The N_{1s} areas of LP-NCs from both route 1 and route 2 show a prominent signal at 399.8 eV stemming from pyrrolic N and two minor peaks at 398.5 and 401.5 eV from pyridinic and graphitic N, respectively. In the primary films, pyridinic N is the major peak (Fig. S7[†]).

An important difference between the primary films of route 1 and route 2 (pre-NC(Fe)₁(*x*) and pre-NC(Fe)₂(*x*)) is found in the N_{1s} region. The pre-NC(Fe)₂(*x*) films (route 2) show an additional peak at 406.5 eV corresponding to NO₃[−] (Fig. S9[†]), while it is not present in pre-NC(Fe)₁(*x*) (route 1). This indicates that in route 1, iron nitrate is decomposed after pre-carbonization. The O_{1s} regions of the samples show peaks originating in oxygen functional groups from the carbon matrix, as well as an iron oxide related peak at 530.1 eV (Fig. S6 and S9[†]). The intensity of this peak increases with an increase in the iron content coming from the formation of iron oxide.

For the Fe_{2p} region of route 2, in the primary film pre-NC(Fe)₂(3.3), the peaks at 710.3 eV and 723.4 eV constitute the characteristic doublet of Fe 2P_{3/2} and 2P_{1/2} core-level spectra of Fe³⁺ are observed due to the addition of iron nitrate (Fig. 3a). After laser-carbonization, the spectra of LP-NC(Fe)₂(3.3) shows an additional Fe(0) peak at 706.8 and the peaks shift to high binding energy and broaden, which is typically assigned to the co-presence of Fe³⁺ and Fe²⁺ species.^{32,33} In contrast, for LP-NC(Fe)₁(3.0), in addition to the Fe(0) peak, the levels Fe³⁺(2P_{3/2}) and Fe³⁺(2P_{1/2}) and their satellite peak at around 719.5 eV are characteristic of Fe₂O₃. However, the peaks

observed in the primary film pre-NC(Fe)₁(3.0) shift to low binding energy and the peaks appearing at 709.5 eV and 722.6 eV are assigned to Fe²⁺(2P_{3/2}) and Fe²⁺(2P_{1/2}), respectively. Interestingly, from the elemental composition quantified by using the XPS spectra (Table S2[†]), the iron content on the surface of the LP-NC(Fe)₂(*x*) films of route 2 is significantly higher than that of route 1.

The two samples with low iron contents, LP-NC(Fe)₁(3.0) and LP-NC(Fe)₂(3.3), were investigated using (scanning) transmission electron microscopy ((S)TEM) and energy-dispersive X-ray (EDX) microanalysis (Fig. 3b). In both samples iron-containing nanoparticles are embedded in a carbonized matrix; however, the type of the crystalline phase formed during the synthesis and the overall distributions of the particles in the matrix are found to be different. In the LP-NC(Fe)₂(3.3) sample we observed a local increase in the degree of graphitization of the carbonized matrix around the iron-containing particles, forming a “graphitic” shell. In contrast, in LP-NC(Fe)₁(3.0) the carbon film displayed uniform graphitization throughout all analyzed areas (Fig. 3c). This observation is in good agreement with the Raman data presented above, showing that LP-NC(Fe)₁(3.0) exhibits a higher degree of graphitization. Analysis of fast Fourier transforms (FFTs) obtained from the HRTEM images of iron-containing nanoparticles suggests that these two samples contain different forms of iron oxides. LP-NC(Fe)₁(3.0) has η-Fe₂O₃ particles (orthorhombic unit cell, sp.gr. *Cmcm*), while in LP-NC(Fe)₂(3.3) α-Fe₂O₃ particles (trigonal unit cell, sp.gr. *R3c*) and FeO particles (cubic unit cell, *Fm3m*) were observed. In general, the LP-NC(Fe)₂(3.3) sample was found to be less homogeneous, showing, in addition to nanoparticles, large Fe–O-containing flakes as well as very small Fe-containing clusters (Fig. S11[†]). Local EDX analysis performed on both samples



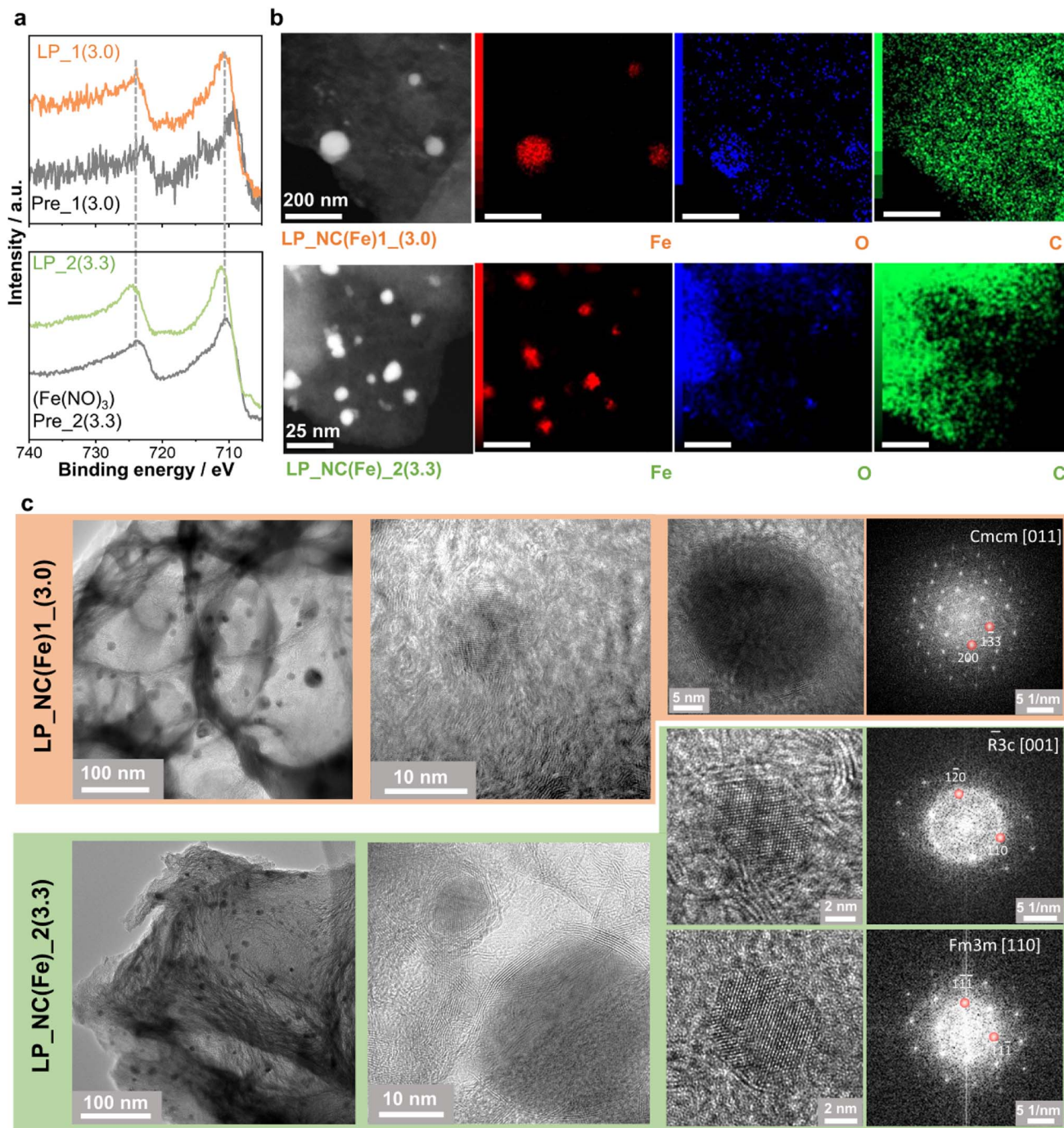


Fig. 3 (a) Fe_{2p} regions of the XPS spectra of LP_NC(Fe)_1(3.0)/pre_NC(Fe)_1(3.0) (top) and LP_NC(Fe)_2(3.3)/pre_NC(Fe)_2(3.3) (bottom); (b) ADF-STEM images and the corresponding EDX maps of Fe-K α , O-K, and C-K signals in LP_NC(Fe)_1(3.0) (top) and LP_NC(Fe)_2(3.3) (bottom) samples. The corresponding EDX spectra are shown in Fig. S10;† (c) overview TEM images and HRTEM images of Fe-containing nanoparticles in LP_NC(Fe)_1(3.0) (orange) and LP_NC(Fe)_2(3.3) (green). Fast Fourier transforms obtained from HRTEM images of the particles are shown on the right.

confirms that nanoparticles contain Fe and O; however, since oxygen is partially present in the carbonized matrix, direct determination of the phase composition from EDX maps is not always possible. Moreover, one can see variations of the contrast in annular-dark field STEM (ADF-STEM) images (Fig. 3a) and in the oxygen distribution in the O-K maps,

suggesting that the oxygen content can vary even within the same particle. Overall, the TEM and EDX data are in line with XPS measurements, suggesting that *via* route 1 Fe₂O₃ oxide is predominantly formed, while route 2 leads to the formation of both Fe₂O₃ and FeO.³⁴ The intrinsic inhomogeneity among the



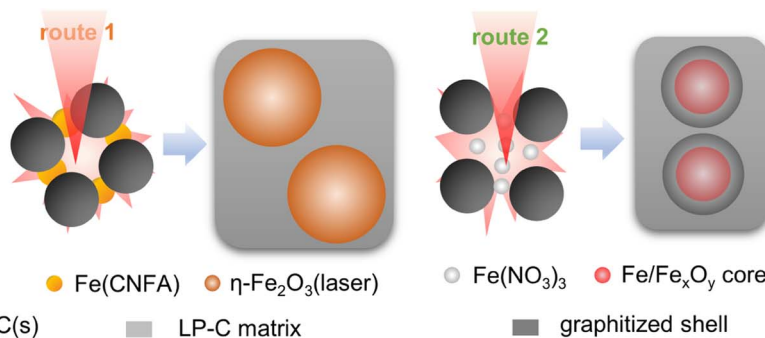
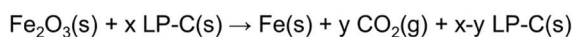
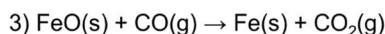
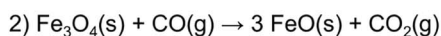
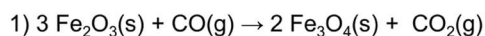
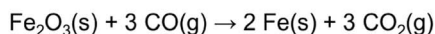
Carbothermal reduction:

Fig. 4 Carbothermal reduction mechanisms and illustration of the formation of iron containing particles embedded into the LP-NC matrix in route 1 and route 2.

particles found by EDX can be the reason for the small but distinct signal of Fe(0) observed in the XPS spectra (Fig. S11†).

Proposed formation mechanism

Taking the results of the previous characterization investigations into consideration, we propose the formation mechanism based on carbonization of the CNFA and simultaneous carbothermal reduction of the iron precursors (Fig. 4). Typically, during such carbothermal reductions, which occur in the temperature range of up to 1000 °C, the carbon is oxidized and cleaves off CO or CO₂, which subsequently supports the graphitization of the remaining carbon.^{35,36} Notably, the reaction temperature cannot be measured directly. However, by the degree of graphitization a reaction temperature gradient of <500 °C and >1500 °C between the lower and the upper layer of the LP-NC film is assumed.³⁷ The difference between the two routes lies in the prearrangement and the nature of the iron precursors in the primary inks.

For route 1, at temperatures >80 °C urea decomposes into isocyanate and ammonia which reacts with iron nitrate to generate coordinated Fe³⁺ species (see XPS) and potentially FeO(OH).³⁸ These Fe³⁺ species are expected to be incorporated homogeneously into the cross-linked CNFA. In a previous study, we demonstrate that upon annealing a mixture of citric acid and urea, two main intermediate products are formed, namely HPPT and oligomeric urea.³⁹ These two components form strong hydrogen-bond networks which eventually cross-link at elevated temperatures to form aggregated particles. The Fe³⁺ species are found homogeneously inside these particles (Fig. S4†). A recrystallization into α-Fe₂O₃, as it has been observed in other studies at ~300 °C, cannot be confirmed.^{40–42} Although, the decomposition of iron nitrate during pre-carbonization (Fig. S7†) is confirmed, no iron oxide nanoparticles were identified in XRD (Fig. S3†) or TEM (Fig. S4†) analysis. The involvement of Fe³⁺ species in the process of cross-linking during pre-carbonization may enhance thermal stability and electrical conductivity of the resulting LP-NC network, which is observed from the XPS spectra (Fig. 3) of pre-NC(Fe)₁(x) where the peaks shift to a lower binding energy. During laser-carbonization the cross-linked pre-NC(Fe)₁(x) form a homogeneous graphitized carbon matrix with predominantly η-Fe₂O₃ particles incorporated.

On the other hand, in route 2, Fe(NO₃)₃ is added after cross-linking and does not influence the cross-linking of the CNFA. The transformation from Fe(NO₃)₃ into iron-containing nanoparticles occurs during laser-treatment on a short kinetic time-scale. The effect of the carbothermal reduction is apparent by the formation of the graphitic shells around the iron-containing particles (Fig. 3c). This shift of thermal energy during the laser treatment leads to the localized graphitic domains while larger fractions of the carbon network are still amorphous, which explains the presence of D3 and D4 bands in the Raman spectra (Fig. 2d). In general, higher concentrations of iron precursors foster the formation of larger iron oxide particles which are detected in XRD, while the small particle sizes of <20 nm at low concentrations do not afford sharp peaks.

Electrocatalytic ORR performance

The performance of the LP-NC(Fe)₁(x) and LP-NC(Fe)₂(x) composite materials was evaluated as ORR electrocatalysts in alkaline media (0.1 M KOH) using a rotating ring disk electrode (RRDE) set up. The analysis was performed using a glassy carbon RRDE tip with a platinum ring (see the Experimental section). A slurry prepared using ground materials with Nafion as a binder was drop cast on the tip. The larger current densities reached with LP-NC(Fe)₁(x) samples compared to that with LP-NC(Fe)₂(x) in the linear sweep voltammetry curves (Fig. 5) are indicative for higher activity and local conductivity of the samples (Fig. S2†) and could be explained by the higher graphitization of the catalyst. The number of electrons transferred during the reduction reaction was calculated based on the amount of H₂O₂ detected at the Pt ring. LP-NC(Fe)₁(x) samples clearly promote the reduction of oxygen mainly through a 4e⁻ transfer mechanism but, at lower iron loadings a certain contribution of the 2e⁻ transfer mechanism is observed. On the other hand, O₂ is reduced through a 2e⁻ transfer by LP-NC(Fe)₂(3.3) and through a 4e⁻ transfer mechanism by sample LP-NC(Fe)₂(14.5).

There are many properties which influence the performance and mechanism of a sample as a catalyst in the ORR, such as conductivity, structure and functional groups of the carbon matrix as well as the presence of metallic particles. Due to this fact, it is not easy to pinpoint the exact catalytic site and clearly state a cause for the main difference between samples. Samples



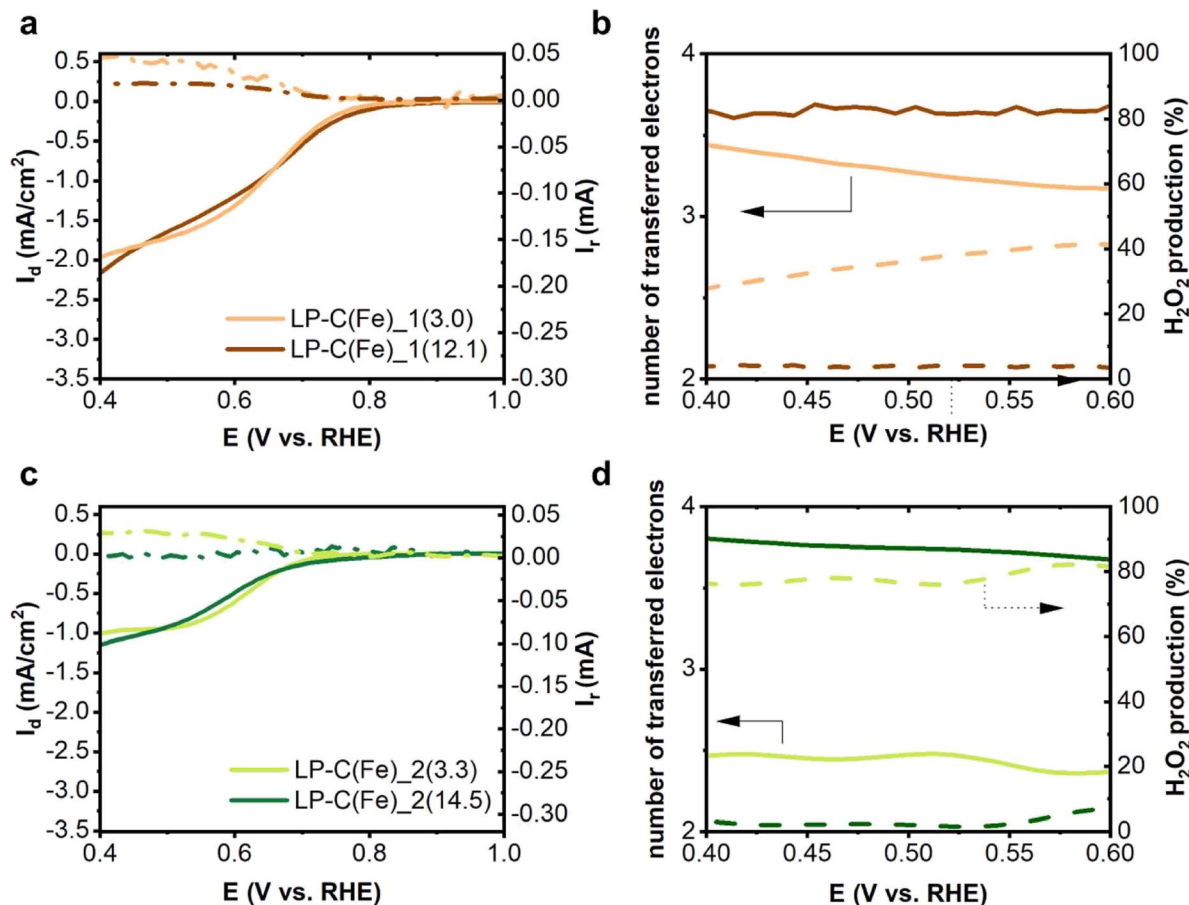


Fig. 5 ORR performance in oxygen saturated 0.1 M KOH evaluated using an RRDE setup. (a) Linear sweep voltammetry and (b) calculated number of transferred electrons and H₂O₂ production efficiency of LP-NC(Fe)₁(3.0), LP-NC(Fe)₁(4.6), and LP-NC(Fe)₁(12.1); (c) linear sweep voltammetry and (d) calculated number of transferred electrons and H₂O₂ production efficiency of LP-NC(Fe)₁(3.3), and LP-NC(Fe)₁(14.5). H₂O₂ ring current and selectivity (%) are in dashed lines.

prepared by route 1 are more conductive which enhances the current densities. The difference in conductivity may facilitate the electron transfer and favour the 4e⁻ transfer mechanism.

Another property that needs to be addressed is the nitrogen species. Importantly, the samples LP-C(Fe)₁(3.0) and LP-C(Fe)₂(3.3) contain mainly pyrrolic nitrogen and show relatively high H₂O₂ production efficiency (Table S3[†]). The role of pyrrolic nitrogen in selective H₂O₂ production was well demonstrated by Yang *et al.* in a report on low-cost N-doped carbon catalysts fabricated in a one-step carbonization of pomelo peel biomass waste.⁴³ Furthermore, Li *et al.* have shown that an increase in the content of pyrrolic nitrogen leads to a higher production of H₂O₂, which they further supported by X-ray absorption near-edge structure spectroscopy (XANES) analysis.⁴⁴ When looking at our XPS analysis, it was found that the content of pyrrolic nitrogen compared to that of other nitrogen types is higher for samples from route 2, which supports the 2e⁻ mechanism. Pyrrolic nitrogen is dominant in both sets of samples, and might have a larger influence as a catalytic site at lower iron loadings. This goes along with the certain contribution of the 2e⁻ mechanism observed for samples LP-NC(Fe)₁(3.0) and LP-NC(Fe)₂(3.3).

The studies on carbon-based materials that contain iron oxide do not show a clear correlation between the type of iron oxide and the resulting mechanism and a through literature survey is presented in Table S4.[†] We observed a clear difference in the nature of the iron oxides present in our materials as summarized in Table 2. In the case of LP-NC(Fe)₁(*x*), the iron oxide is distributed on an evenly carbonised matrix, meaning that the iron oxide will be directly in contact with the electrolyte. In the case of LP-NC(Fe)₂(*x*), the iron oxide nanoparticles are surrounded by a graphitic layer, which prevents direct exposure to the electrolyte. This will change the active site and will have an effect on the desorption of the -OOH intermediate, which might lead to a different mechanism. We observed that for both sets of samples the performance of the electrocatalysts towards the 4e⁻ mechanism is enhanced at larger iron loadings. At larger loadings, the formation of larger carbon graphitic domains is more favourable which might facilitate the electron transfer. The iron catalytic sites from route 1 are exposed to the electrolyte and the support conductivity favours that, even at low iron loadings, the contribution of the 4e⁻ transfer mechanism predominates. On the other hand, in samples from route 2 the sites are not directly exposed to the electrolyte and the



Table 2 Summary of the results obtained using the materials as oxygen reduction reaction electrocatalysts

Sample	Onset E^b , V	n^a			Fe type
		pH = 14 ^b	pH = 14 ^b	pH = 7.2 ^c	
LP-NC(Fe)_1(3.0)	0.77	3.5	40%	10%	η -Fe ₂ O ₃ and Fe(0)
LP-NC(Fe)_1(12.1)	0.80	4	2%	—	Fe ₃ O ₄
LP-NC(Fe)_2(3.3)	0.70	2.5	80%	3%	α -Fe ₂ O ₃ , FeO, and Fe(0)
LP-NC(Fe)_2(14.5)	0.72	3.5	8%	—	α -Fe ₂ O ₃

^a Number of transferred electrons. ^b 0.1 M KOH as an electrolyte. ^c Phosphate buffer as an electrolyte.

carbon support is not as conductive. Thus, at a low iron content, the 2e⁻ mechanism predominates due to the contribution of the pyrrolic functional groups and the poorer conductivity. When the loading of iron increases, the contribution of the 4e⁻ transfer mechanism also does. We also analysed the behaviour of samples LP-C(Fe)_2(3.8) in order to further corroborate this hypothesis (Fig. S12[†]). The results show that when the iron content is between that of samples LP-C(Fe)_2(3.3) and LP-C(Fe)_2(14.5), the contribution of both mechanisms is also in between. For instance, the average number of electrons transferred is 3 and the average percentage of H₂O₂ produced is 50%.

Samples LP-C(Fe)_1(3.0) and LP-C(Fe)_2(3.3) were also evaluated in O₂-saturated neutral media (500 mM phosphate buffer with pH 7.2). In this electrolyte, the onset of the ORR is at 0.5 V vs. RHE in both cases. Both samples yield very little H₂O₂ and the number of transferred electrons is above 3 (Fig. S13[†]). The limiting current obtained was much larger than that found in basic media.

Conclusions

In summary, we introduced a concept to fabricate ORR catalyst electrodes by a simple and cost-effective laser-assisted carbonization method affording mixed valence iron oxide nanoparticles embedded in a nitrogen-doped carbon matrix. The electrodes are based on earth-abundant and recyclable materials and are processed by an efficient, fast and low-energy synthesis method. By simply changing the preparation sequence we were able to modulate the catalyst performance between the 2e⁻ and 4e⁻ pathways and thereby create product selectivity in the ORR. Our experimental results demonstrate how different iron contents and the sequence of the film preparation influence the chemical and structural composition of the active catalysts, namely the type of iron oxide, the degree of graphitization, and the local structure of the final laser-carbonized electrodes. The effect of the type of nitrogen functionality, degree of graphitization and iron type was used to rationalize the ORR performance of the samples. The obtained mixed valence iron oxide structures, namely 3 wt% α -Fe₂O₃/FeO/Fe embedded into N-pyrrolic doped carbons were identified as highly active and selective for O₂ reduction to H₂O₂. Well graphitized LP-NC with predominant η -Fe₂O₃/Fe species embedded preferably supports the 4e⁻ pathway to generate H₂O with 4% and 10% efficiency in alkaline or neutral electrolyte,

respectively. Future efforts can be focused on the electrode design for pure H₂O generation and the utilization of alternative carbon-network forming agents or precursors for the selective formation of catalytically active interfaces. Such electrodes may find application as environmentally friendly and sustainable alternatives in, for example, energy storage, water treatment, and H₂O₂ generation.

Experimental section

Materials

Citric acid (>99%, Sigman-Aldrich), urea (>99.3%, Alfa Aesar), iron(III) nitrate nonahydrate (>98%, Alfa Aesar), ethylene glycol (\geq 99.7%, AnalaR Normapur, VWR chemicals), polyvinylpyrrolidone (average mol wt. 10 000, Sigma-Aldrich), 0.1 M Titripur® potassium hydroxide solution (Aldrich), Nafion 117 5% solution (Aldrich) and pH 7 phosphate buffer solution (500 mM, Aldrich) were used.

Preparation of LP-NC(Fe)_n(x)

Route 1. 5 g citric acid, 5 g urea and 0.2, 0.3, or 1.0 g iron(III) nitrate nonahydrate (Fe(NO₃)₃·9H₂O) were dissolved in 10 mL methanol and thoroughly mixed. The solvent was evaporated and the solid mixture was annealed at 300 °C for 2 h in a tube furnace at a heating rate of 3.11 K min⁻¹. The resulting black powders were ground by ball milling (PM 100, Retsch) for 1 h at 650 rpm to obtain the iron doped carbon network-forming agents (CNFA(Fe)). 0.2 g of each CNFA(Fe) were then dispersed in 2 mL of ethylene glycol and stirred for 24 h to obtain viscous inks.

Route 2. The CNFA (CA/U(300)) was prepared according to route 1 without the addition of Fe(NO₃)₃·9H₂O.⁴⁵ Fe(NO₃)₃·9H₂O was dissolved in 0.2 mL ethylene glycol to obtain solutions with different concentrations between 0.1 and 0.5 g mL⁻¹. 0.2 g of CA/U(300) was then added and the mixture was stirred for 24 h to obtain a viscous ink.

A drop of the ink was applied onto the substrate (PET) and the ink was doctor bladed with a blade distance of 130 μ m. Ethylene glycol was then evaporated at 80 °C on a precision hotplate (PZ2860-SR, Gestigkeit GmbH) to obtain the final films with mean thicknesses of 30 μ m.

The powder collection of the sample. A drop of the ink was applied onto a Si wafer and then doctor bladed with a blade distance of 700 μ m. Ethylene glycol was evaporated at 80 °C on a hotplate. After laser-carbonization, the powder of LP-NC(Fe)



was scraped off the silicon wafer. The powders were thoroughly washed with 1.0 M NaOH by sequential sonication and centrifugation until the supernatant was clear, *i.e.* all unconverted precursors were washed out. The remaining black solid was washed with H₂O and methanol to remove all NaOH and obtain a pure laser-carbonized product.

A high-precision laser engraver setup (Trotec Speedy 100, 60 W CO₂-laser, 2.5 inch focus lens, and a spot size of 170 μm) was used for laser-carbonization. The resulting energy fluence ($F = 72 \text{ J m}^{-1}$) was calculated from the product of the laser power ($P = 1.02 \text{ W}$) and the scanning speed (71 s m^{-1}). Each laser pattern consists of 100 parallel laser lines with a length of 10 mm and a line separation of 0.1 mm to obtain a homogeneous electrode film of $10 \times 10 \text{ mm}$.

Characterization

Raman spectra were obtained with a confocal Raman microscope (alpha300, WITec, Germany) equipped with a piezo-scanner (P-500, Physik Instrumente, Karlsruhe, Germany). The laser, $\lambda = 532 \text{ nm}$, was focused on the samples through a $50\times$ objective. The laser power on the sample was set to 5.0 mW. Scanning electron microscopy was performed on a Zeiss LEO 1550-Gemini system (acceleration voltage: 3 to 10 kV). An Oxford Instruments X-MAX 80 mm² detector was used to collect the SEM-EDX data. Transmission electron microscopy (TEM) was performed using a double Cs corrected JEOL JEM-ARM200F (S)TEM operated at 80 kV, 10 μA and equipped with a cold-field emission gun and a high-angle silicon drift energy dispersive X-ray (EDX) detector (solid angle up to 0.98 steradians with a detection area of 100 mm²). Annular dark field scanning transmission electron microscopy (ADF-STEM) images were collected at a probe convergence semi-angle of 25 mrad. The so-called “beam shower” procedure was performed with a defocused beam at a magnification of $8000\times$ for 30 minutes; it was necessary for reducing hydrocarbon contamination during subsequent imaging at high magnification. To prepare the TEM samples, the carbon material has been dispersed in methanol, sonicated for 10 min, drop cast on a lacey carbon TEM grid and dried at room temperature. Elemental combustion analysis was performed with a vario MICRO cube CHNOS elemental analyzer (Elementar Analysensysteme GmbH). The elements were detected with a thermal conductivity detector (TCD) for C, H, N and O and an infrared (IR) detector for sulphur. Inductively coupled plasma mass spectrometry (ICP-MS) was performed with a PerkinElmer ICP-OES Optima 8000. The sample preparation: 10 mg powder of the sample was added into the ICP tube, followed by 167 μL conc. HNO₃ and 333 μL conc. HCl. X-ray diffraction was performed on a Bruker D8 Advance diffractometer in the Bragg–Brentano mode at the Cu K α wavelength. XPS measurements were performed on a ThermoScientific Escalab 250 Xi. A micro-focused, monochromated AlK α X-ray source (1486.68 eV) and a 400 μm spot size were used in the analysis. Samples were prepared using carbon tape. Calibration was performed according to the sp² peak in each sample. CasaXPS software was used to analyze the resulting spectra. Electrochemical tests were performed using a rotating ring disk electrode (RRDE) purchased from PINE and Interface 1000 and Interface 1010

(Gamry) potentiostats. The three-electrode cell setup consisted of an Ag/AgCl electrode as a reference, a Pt wire as a counter electrode and 5 mm glassy carbon (disk)/platinum (ring) RRDE tips modified with the materials as working electrodes. It is important to consider that by using Pt rings the number of transferred electrons might be overestimated.⁴⁶ To prepare the RRDE tips for measurements, 10 μL of catalyst ink was deposited on the glassy carbon tip and dried at room temperature overnight. The ink is prepared by mixing 50 μL of Nafion 117 solution (5 wt%, purchased by Aldrich), 500 μL of distilled water, 250 μL of isopropanol, and 5 mg powder of laser-carbonized samples as catalysts. Linear sweep voltammetry (LSV) was performed in O₂ saturated 0.1 M KOH solution, or pH 7, 500 mM phosphate buffer, with a scan rate of 10 mV s^{-1} at 1000 rpm rotation speed. The ring was set at a potential of 1.2 V *vs.* RHE to ensure fast oxidation of H₂O₂. The collection efficiency of the ring was calibrated before the measurements following the indication of the RRDE setup provider. The electron transfer number, n , and hydrogen peroxide yield, % H₂O₂, are calculated using eqn (1) and (2).w

$$n = 4 \times \frac{I_d \times N}{I_d \times N + I_r} \quad (1)$$

$$\% \text{H}_2\text{O}_2 = 100 \times \frac{2 \times I_r}{I_d \times N + I_r} \quad (2)$$

here I_r stands for ring current, I_d for disk current and N for the collection efficiency of the electrodes. The collection efficiency was empirically measured using a ferrocyanide/ferricyanide half-reaction as a single-electron, reversible half-reaction. The rotating ring disc electrodes were placed in 10 mM of potassium ferricyanide (K₃Fe(CN)₆) 0.1 M KOH solution and were operated at rotation rates between 500 and 2000 rpm. The potential of the disk electrode was swept from cathodic potentials at 50 mV s^{-1} towards more negative potentials (potential range 0.3 V to $-0.75 \text{ V vs. Ag/AgCl}$). The potential of the ring electrode was biased at 0.5 V *vs.* Ag/AgCl. The current obtained from the ring when the disk was disconnected was subtracted from I_r . The measured ratio of the ring (anodic) limiting current to the disk (cathodic) limiting current is the empirical collection efficiency. We checked that this number was independent of the rotation rate. We obtained a collection efficiency of 0.21 ± 0.01 for the bare GC, and a collection efficiency of 0.26 ± 0.03 for all electrodes except for electrode LP-C(Fe)₁(3.0) for which the collection efficiency was 0.45 ± 0.05 .

Data availability statement

All data needed to evaluate the conclusions in the paper are present in the paper and/or the ESI.† Additional datasets generated during and/or analysed during the current study are available from the corresponding author on reasonable request.

Conflicts of interest

The authors declare that they have no known competing financial interests or personal relationships that could have appeared to influence the work reported in this paper.



Author contributions

Huize Wang: investigation, conceptualization, methodology, validation, writing – original draft; Maria Jerigova: investigation, conceptualization, methodology, validation, writing – original draft; Jing Hou: investigation, conceptualization, methodology, validation, writing – original draft; Nadezda V. Tarakina: conceptualization, methodology, validation, writing – original draft, writing – review & editing, supervision; Nieves López-Salas: conceptualization, methodology, validation, writing – original draft, writing – review & editing, supervision, project administration; Volker Strauss: conceptualization, methodology, validation, writing – original draft, writing – review & editing, supervision, project administration.

Acknowledgements

We gratefully acknowledge funding from the Fonds der Chemischen Industrie and the Max Planck Society and the support from Prof. Markus Antonietti. Open Access funding was provided by the Max Planck Society.

References

- 1 J. Masa, C. Andronesco and W. Schuhmann, Electrocatalysis as the Nexus for Sustainable Renewable Energy: The Gordian Knot of Activity, Stability, and Selectivity, *Angew. Chem., Int. Ed.*, 2020, **59**, 15298–15312.
- 2 S. Chu, Y. Cui and N. Liu, The path towards sustainable energy, *Nat. Mater.*, 2016, **16**, 16–22.
- 3 X. Zhao and Y. Liu, Origin of Selective Production of Hydrogen Peroxide by Electrochemical Oxygen Reduction, *J. Am. Chem. Soc.*, 2021, **143**, 9423–9428.
- 4 M. Shao, Q. Chang, J. P. Dodelet and R. Chenitz, Recent Advances in Electrocatalysts for Oxygen Reduction Reaction, *Chem. Rev.*, 2016, **116**, 3594–3657.
- 5 Y.-J. Wang, N. Zhao, B. Fang, H. Li, X. T. Bi and H. Wang, Carbon-Supported Pt-Based Alloy Electrocatalysts for the Oxygen Reduction Reaction in Polymer Electrolyte Membrane Fuel Cells: Particle Size, Shape, and Composition Manipulation and Their Impact to Activity, *Chem. Rev.*, 2015, **115**, 3433–3467.
- 6 L. Zhang, P. Lu, Y. Luo, J. Y. Zheng, W. Ma, L. X. Ding and H. Wang, Graphene-quantum-dot-composited platinum nanotube arrays as a dual efficient electrocatalyst for the oxygen reduction reaction and methanol electro-oxidation, *J. Mater. Chem. A*, 2021, **9**, 9609–9615.
- 7 L. Zhang, S. Jiang, W. Ma and Z. Zhou, Oxygen reduction reaction on Pt-based electrocatalysts: four-electron vs. two-electron pathway, *Chin. J. Catal.*, 2022, **43**, 1433–1443.
- 8 Y. Li, W. Zhou, H. Wang, L. Xie, Y. Liang, F. Wei, J.-C. Idrobo, S. J. Pennycook and H. Dai, An oxygen reduction electrocatalyst based on carbon nanotube–graphene complexes, *Nat. Nanotechnol.*, 2012, **7**, 394–400.
- 9 Y. L. Zhang, K. Goh, L. Zhao, X. L. Sui, X. F. Gong, J. J. Cai, Q. Y. Zhou, H. Da Zhang, L. Li, F. R. Kong, D. M. Gu and Z. B. Wang, Advanced non-noble materials in bifunctional catalysts for ORR and OER toward aqueous metal–air batteries, *Nanoscale*, 2020, **12**, 21534–21559.
- 10 Q. Chang, P. Zhang, A. H. B. Mostaghimi, X. Zhao, S. R. Denny, J. H. Lee, H. Gao, Y. Zhang, H. L. Xin, S. Siahrostami, J. G. Chen and Z. Chen, Promoting H₂O₂ production via 2-electron oxygen reduction by coordinating partially oxidized Pd with defect carbon, *Nat. Commun.*, 2020, **11**, 1–9.
- 11 G. Gao, Y. Tian, X. Gong, Z. Pan, K. Yang and B. Zong, Advances in the production technology of hydrogen peroxide, *Chin. J. Catal.*, 2020, **41**, 1039–1047.
- 12 N. Wang, S. Ma, P. Zuo, J. Duan and B. Hou, Recent Progress of Electrochemical Production of Hydrogen Peroxide by Two-Electron Oxygen Reduction Reaction, *Adv. Sci.*, 2021, **8**, 1–26.
- 13 K. Chen, K. Liu, P. An, H. Li, Y. Lin, J. Hu, C. Jia, J. Fu, H. Li, H. Liu, Z. Lin, W. Li, J. Li, Y.-R. Lu, T.-S. Chan, N. Zhang and M. Liu, Iron phthalocyanine with coordination induced electronic localization to boost oxygen reduction reaction, *Nat. Commun.*, 2020, **11**, 4173.
- 14 Y. Xue, W. Jin, H. Du, S. Wang, S. Zheng and Y. Zhang, Tuning α -Fe₂O₃ nanotube arrays for the oxygen reduction reaction in alkaline media, *RSC Adv.*, 2016, **6**, 41878–41884.
- 15 Z. Xiao, G. Shen, F. Hou, R. Zhang, Y. Li, G. Yuan, L. Pan, J. J. Zou, L. Wang, X. Zhang and G. Li, Highly dispersed γ -Fe₂O₃ embedded in nitrogen doped carbon for the efficient oxygen reduction reaction, *Catal. Sci. Technol.*, 2019, **9**, 4581–4587.
- 16 Y. Wang, R. Gan, H. Liu, M. Dirican, C. Wei, C. Ma, J. Shi and X. Zhang, Fe₃O₄/Fe₂O₃/Fe nanoparticles anchored on N-doped hierarchically porous carbon nanospheres as a high-efficiency ORR electrocatalyst for rechargeable Zn-air batteries, *J. Mater. Chem. A*, 2021, **9**, 2764–2774.
- 17 J. Zhu, Z. Xiong, J. Zheng, Z. Luo, G. Zhu, C. Xiao, Z. Meng, Y. Li and K. Luo, Nitrogen-doped graphite encapsulated Fe/Fe₃C nanoparticles and carbon black for enhanced performance towards oxygen reduction, *J. Mater. Sci. Technol.*, 2019, **35**, 2543–2551.
- 18 Z. Schnepf, Y. Zhang, M. J. Hollamby, B. R. Pauw, M. Tanaka, Y. Matsushita and Y. Sakka, Doped-carbon electrocatalysts with trimodal porosity from a homogeneous polypeptide gel, *J. Mater. Chem. A*, 2013, **1**, 13576–13581.
- 19 Y. Yan, H. Cheng, Z. Qu, R. Yu, F. Liu, Q. Ma, S. Zhao, H. Hu, Y. Cheng, C. Yang, Z. Li, X. Wang, S. Hao, Y. Chen and M. Liu, Recent progress on the synthesis and oxygen reduction applications of Fe-based single-atom and double-atom catalysts, *J. Mater. Chem. A*, 2021, **9**, 19489–19507.
- 20 H. Shen, T. Thomas, S. A. Rasaki, A. Saad, C. Hu, J. Wang and M. Yang, Oxygen Reduction Reactions of Fe-N-C Catalysts: Current Status and the Way Forward, *Electrochem. Energy Rev.*, 2019, **2**, 252–276.
- 21 W. R. P. Barros, Q. Wei, G. Zhang, S. Sun, M. R. V Lanza and A. C. Tavares, Oxygen reduction to hydrogen peroxide on Fe₃O₄ nanoparticles supported on Printex carbon and Graphene, *Electrochim. Acta*, 2015, **162**, 263–270.



- 22 X. Xu, C. Shi, Q. Li, R. Chen and T. Chen, Fe–N-Doped carbon foam nanosheets with embedded Fe₂O₃ nanoparticles for highly efficient oxygen reduction in both alkaline and acidic media, *RSC Adv.*, 2017, 7, 14382–14388.
- 23 X. Cheng, S. Dou, G. Qin, B. Wang, P. Yan, T. T. Isimjan and X. Yang, Rational design of highly selective nitrogen-doped Fe₂O₃-CNTs catalyst towards H₂O₂ generation in alkaline media, *Int. J. Hydrogen Energy*, 2020, 45, 6128–6137.
- 24 K. Jiang, S. Back, A. J. Akey, C. Xia, Y. Hu, W. Liang, D. Schaak, E. Stavitski, J. K. Nørskov, S. Siahrostami and H. Wang, Highly selective oxygen reduction to hydrogen peroxide on transition metal single atom coordination, *Nat. Commun.*, 2019, 10, 3997.
- 25 B. Wu, H. Meng, D. M. Morales, F. Zeng, J. Zhu, B. Wang, M. Risch, Z. J. Xu and T. Petit, Nitrogen-Rich Carbonaceous Materials for Advanced Oxygen Electrocatalysis: Synthesis, Characterization, and Activity of Nitrogen Sites, *Adv. Funct. Mater.*, 2022, 2204137.
- 26 J. Zhang, C. Zhang, J. Sha, H. Fei, Y. Li and J. M. Tour, Efficient Water-Splitting Electrodes Based on Laser-Induced Graphene, *ACS Appl. Mater. Interfaces*, 2017, 9, 26840–26847.
- 27 J. Zhang, M. Ren, L. Wang, Y. Li, B. I. Yakobson and J. M. Tour, Oxidized Laser-Induced Graphene for Efficient Oxygen Electrocatalysis, *Adv. Mater.*, 2018, 30(21), 1707319.
- 28 D. B. Schüpfer, F. Badaczewski, J. Peilstöcker, J. M. Guerra-Castro, H. Shim, S. Firoozabadi, A. Beyer, K. Volz, V. Presser, C. Heilliger, B. Smarsly and P. J. Klar, Monitoring the thermally induced transition from sp³-hybridized into sp²-hybridized carbons, *Carbon N Y*, 2021, 172, 214–227.
- 29 M. Pawlyta, J.-N. Rouzaud and S. Duber, Raman microspectroscopy characterization of carbon blacks: Spectral analysis and structural information, *Carbon N Y*, 2015, 84, 479–490.
- 30 R. D. Hunter, J. Ramírezramírez-Rico and Z. Schnepp, Iron-catalyzed graphitization for the synthesis of nanostructured graphitic carbons, *J. Mater. Chem. A*, 2022, 10, 4489–4516.
- 31 O. Paris, C. Zollfrank and G. A. Zickler, Decomposition and carbonisation of wood biopolymers—a microstructural study of softwood pyrolysis, *Carbon N Y*, 2005, 43, 53–66.
- 32 G. Sun, B. Dong, M. Cao, B. Wei and C. Hu, Hierarchical dendrite-like magnetic materials of Fe₃O₄, γ-Fe₂O₃, and Fe with high performance of microwave absorption, *Chem. Mater.*, 2011, 23, 1587–1593.
- 33 X. Teng, D. Black, N. J. Watkins, Y. Gao and H. Yang, Platinum-maghemite core-shell nanoparticles using a sequential synthesis, *Nano Lett.*, 2003, 3, 261–264.
- 34 E. Bykova, L. Dubrovinsky, N. Dubrovinskaja, M. Bykov, C. McCammon, S. V. Ovsyannikov, H.-P. Liermann, I. Kuppenko, A. I. Chumakov, R. Rüffer, M. Hanfland and V. Prakapenka, Structural complexity of simple Fe₂O₃ at high pressures and temperatures, *Nat. Commun.*, 2016, 7, 10661.
- 35 T. Murakami, T. Takahashi, S. Fuji, D. Maruoka and E. Kasai, Development of Manufacturing Principle of Porous Iron by Carbothermic Reduction of Composite of Hematite and Biomass Char, *Mater. Trans.*, 2017, 58, 1742–1748.
- 36 B. V. L'vov, Mechanism of carbothermal reduction of iron, cobalt, nickel and copper oxides, *Thermochim. Acta*, 2000, 360, 109–120.
- 37 H. Wang, C. O. Ogolla, G. Panchal, M. Hepp, S. Delacroix, D. Cruz, D. Kojda, A. Knop-Gericke, K. Habicht, B. Butz and V. Strauss, Flexible CO₂ sensor architecture with selective nitrogen functionalities by one-step laser-induced conversion of versatile organic ink, *Adv. Funct. Mater.*, 2022, 2207406.
- 38 M. Koebel and E. O. Strutz, Thermal and hydrolytic decomposition of urea for automotive selective catalytic reduction systems: Thermochemical and practical aspects, *Ind. Eng. Chem. Res.*, 2003, 42, 2093–2100.
- 39 V. Strauss, H. Wang, S. Delacroix, M. Ledendecker and P. Wessig, Carbon nanodots revised: The thermal citric acid/urea reaction, *Chem. Sci.*, 2020, 11, 8256–8266.
- 40 J. Morales and J. L. Tirado, Changes in Crystallite Size and Microstrains from the Thermal Decomposition of Synthetic of Hematite Akaganeite, *J. Solid State Chem.*, 1984, 312, 303–312.
- 41 D. G. Chambaere and E. De Grave, The β-FeOOH to α-Fe₂O₃ phase transformation: structural and magnetic phenomena, *Phys. Chem. Miner.*, 1985, 12, 176–184.
- 42 S. Musić, S. Krehula and S. Popović, Thermal decomposition of β-FeOOH, *Mater. Lett.*, 2004, 58, 444–448.
- 43 Y. Yang, F. He, Y. Shen, X. Chen, H. Mei, S. Liu and Y. Zhang, A biomass derived N/C-catalyst for the electrochemical production of hydrogen peroxide, *Chem. Commun.*, 2017, 53, 9994–9997.
- 44 L. Li, C. Tang, Y. Zheng, B. Xia, X. Zhou, H. Xu and S. Z. Qiao, Tailoring Selectivity of Electrochemical Hydrogen Peroxide Generation by Tunable Pyrrolic-Nitrogen-Carbon, *Adv. Energy Mater.*, 2020, 10, 1–10.
- 45 H. Wang, S. Delacroix, O. Osswald, M. Anderson, T. Heil, E. Lepre, N. Lopez-Salas, R. B. Kaner, B. Smarsly and V. Strauss, Laser-carbonization: Peering into the formation of micro-thermally produced (N-doped)carbons, *Carbon N Y*, 2021, 176, 500–510.
- 46 R. Zhou, Y. Zheng, M. Jaroniec and S. Z. Qiao, Determination of the Electron Transfer Number for the Oxygen Reduction Reaction: From Theory to Experiment, *ACS Catal.*, 2016, 6, 4720–4728.



Supporting Information to
**Modulating between 2e⁻ and 4e⁻ pathway in the oxygen
reduction reaction with laser-synthesized iron oxide-grafted
nitrogen-doped carbon**

Huize Wang, Maria Jerigova, Jing Hou, Nadezda V. Tarakina, Simon Delacroix, Nieves Lopez-Salas, Volker Strauss

Chemical composition	S2
Electrical properties	S3
Pre-Carbonization	S3
X-ray photoelectron spectroscopy.....	S5
STEM and EDX analysis	S11
Oxygen reduction reaction performance.....	S12
Comparison with published studies	S14
References.....	S15

Chemical composition

Table S1. Elemental mass percentage of *pre-NC(Fe)_1(x)* and *LP-NC(Fe)_n(x)* obtained from combustion elemental analysis (N,C,H) and ICP-MS (Fe).*

sample	N	C	H	Fe
CNFA (CA/U300)	13	68	1	-
pre-NC(Fe)_1(2.3)	21	48	3	2.3
pre-NC(Fe)_1(2.7)	19	42	3	2.7
pre-NC(Fe)_1(8.6)	21	42	3	8.6
LP-NC(Fe)_1(3.0)	10	72	1	3.0
LP-NC(Fe)_1(4.6)	7	72	1	4.6
LP-NC(Fe)_1(12.1)	6	60	1	12.1
LP-NC(Fe)_2(3.3)	13	60	2	3.3
LP-NC(Fe)_2(3.8)	11	67	2	3.8
LP-NC(Fe)_2(14.5)	8	60	1	14.5

* The remaining mass is due oxygen.

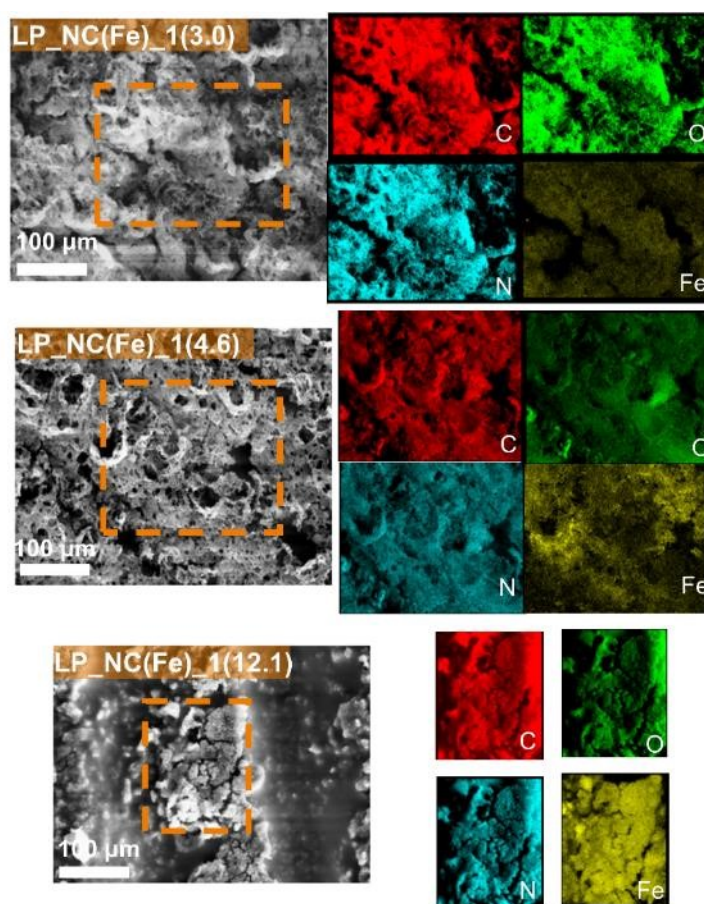


Figure S1. EDX mapping of *LP_NC(Fe)_1(3.0)*, *LP_NC(Fe)_1(4.6)* and *LP_NC(Fe)_1(12.1)*.

Electrical properties

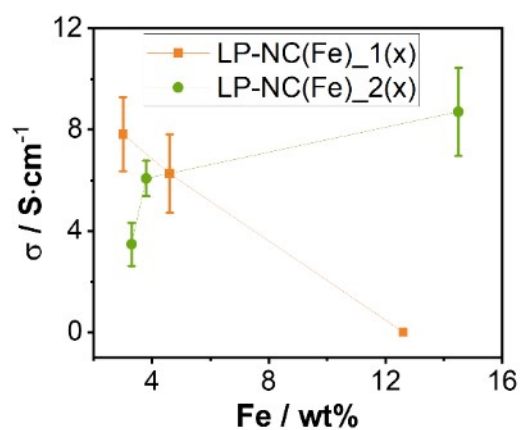


Figure S2. Electrical conductivity of films LP-NC(Fe)_1(x) and LP-NC(Fe)_2(x) obtained by averaging 30 sample films.

Pre-Carbonization

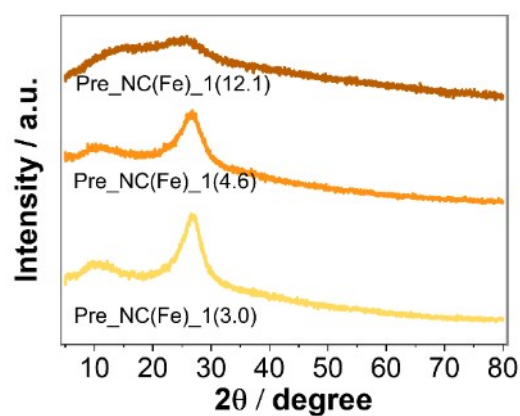


Figure S3. X-ray powder diffraction patterns of the primary films to route 1 (pre-NC(Fe)_1(y)), pre-carbonized at 300 °C.

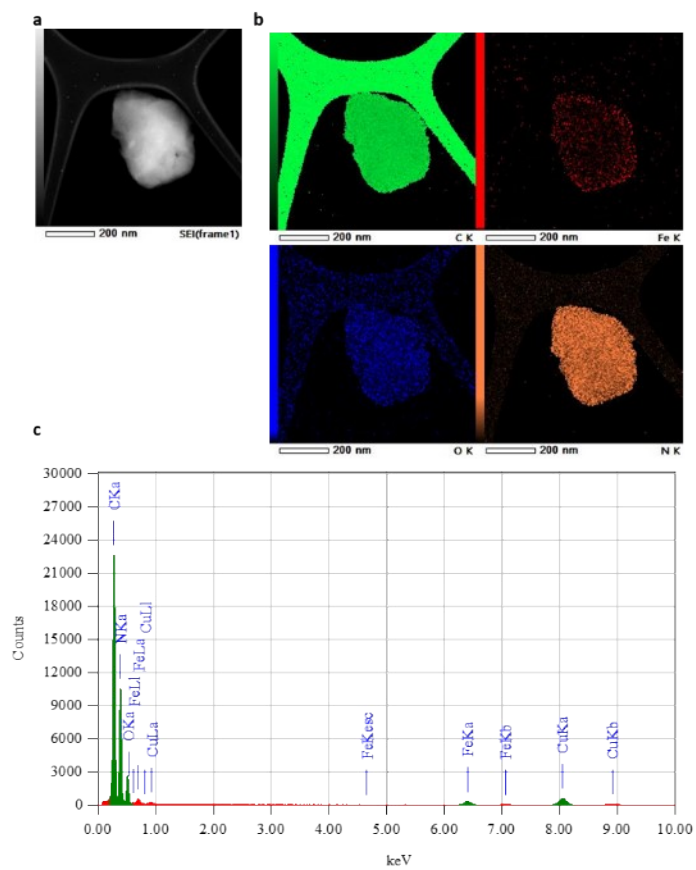


Figure S4. (a) STEM-ADF images of *pre_NC(Fe)_1(3.0)*; (b) corresponding EDX elemental mappings and spectrum from (a).

X-ray photoelectron spectroscopy

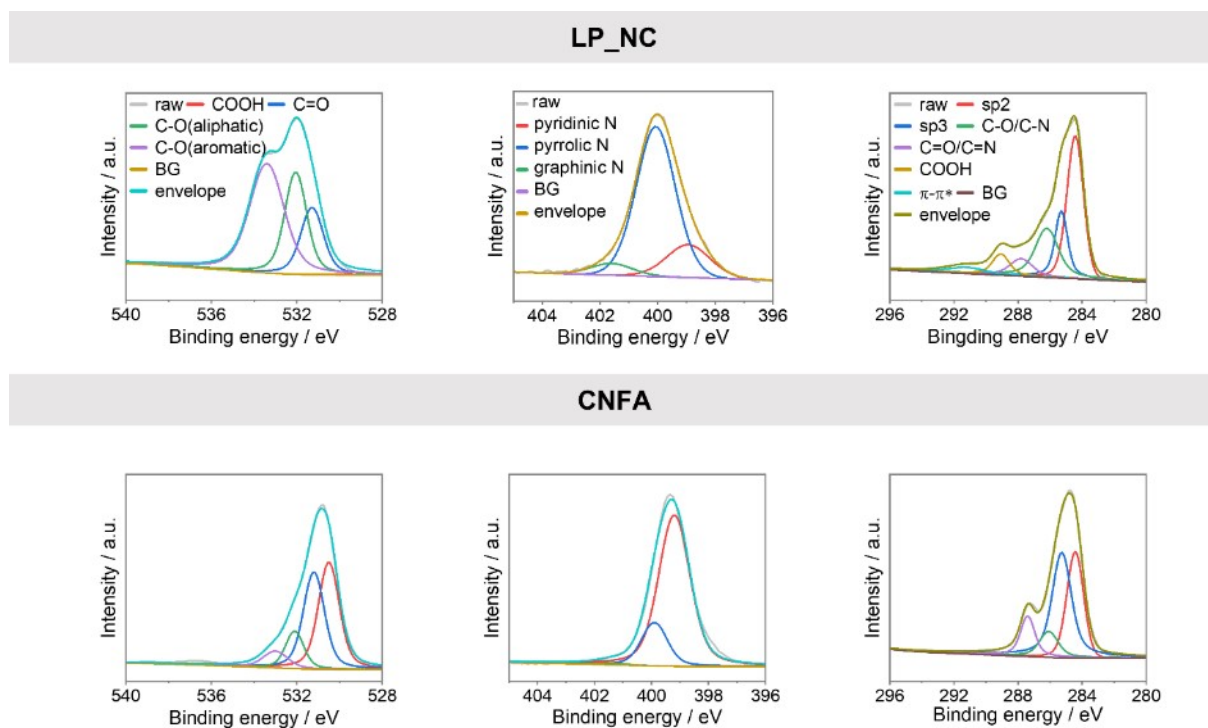


Figure S5. XPS spectra of *LP_NC* (reference) and the *CNFA* (CA/U(300)) with emphasis on the O_{1s} (left), N_{1s} (middle), and C_{1s} regions (right).

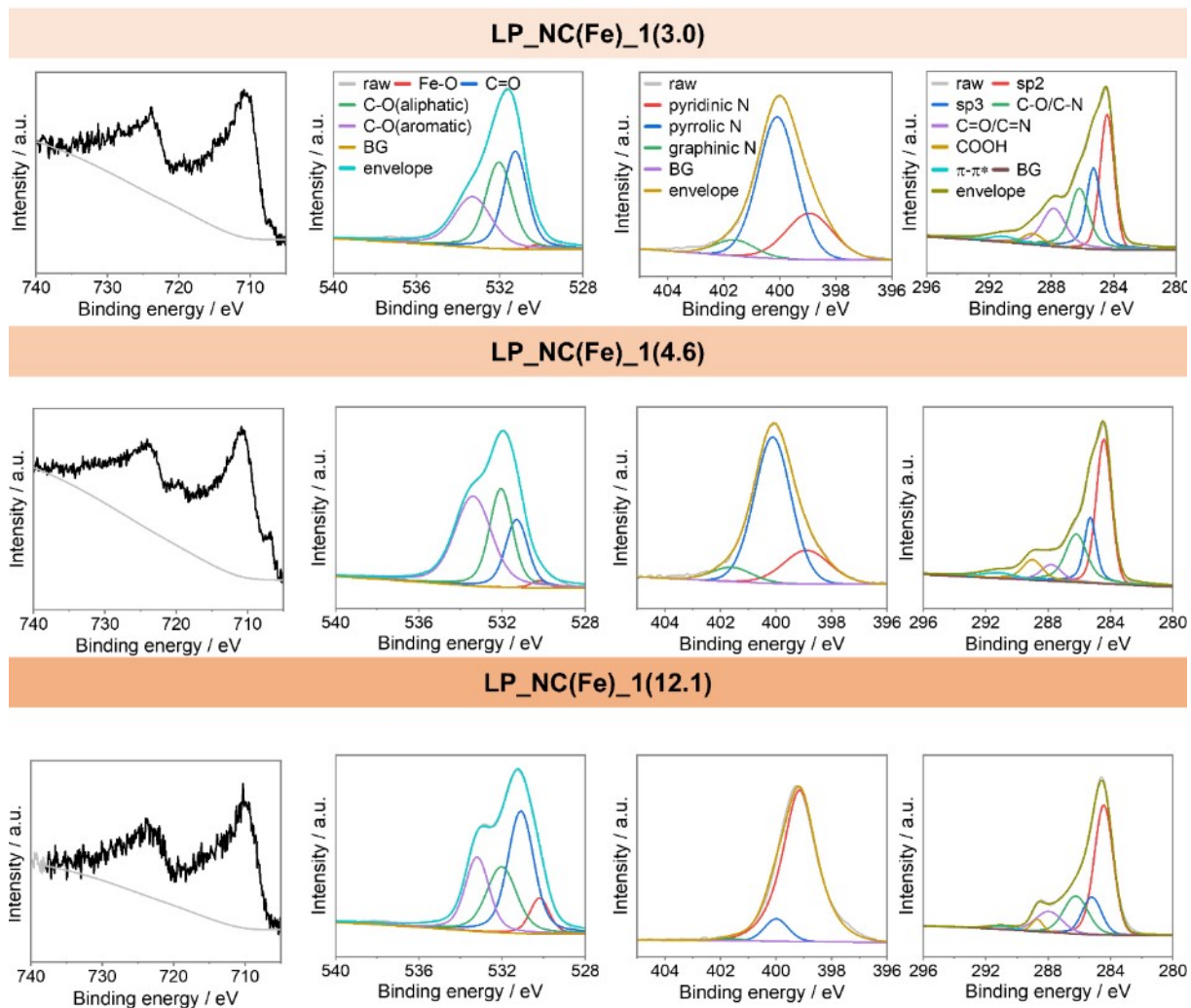
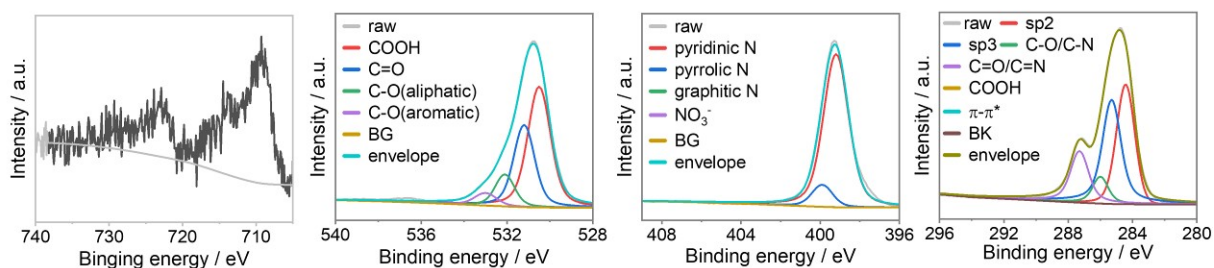
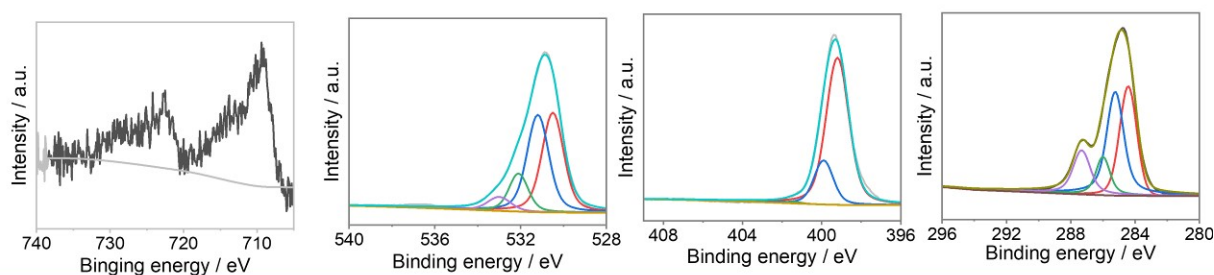


Figure S6. XPS spectra of the samples prepared by route 1: **LP_NC(Fe)_1(3.0)**, **LP_NC(Fe)_1(4.6)** and **LP_NC(Fe)_1(12.1)** with emphasis on the F_{2p} , O_{1s} , N_{1s} , and C_{1s} (from left to right) regions.

Pre_NC(Fe)_1(3.0)



Pre_NC(Fe)_1(4.6)



Pre_NC(Fe)_1(12.1)

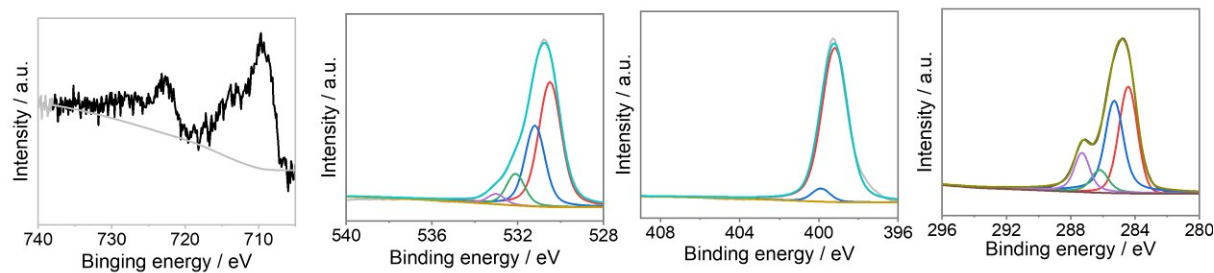


Figure S7. XPS spectra of the primary films of route 1: *pre_NC(Fe)_1(3.0)*, *pre_NC(Fe)_1(4.6)* and *pre_NC(Fe)_1(12.1)* with emphasis on the F_{2p}, O_{1s}, N_{1s}, and C_{1s} (from left to right) regions.

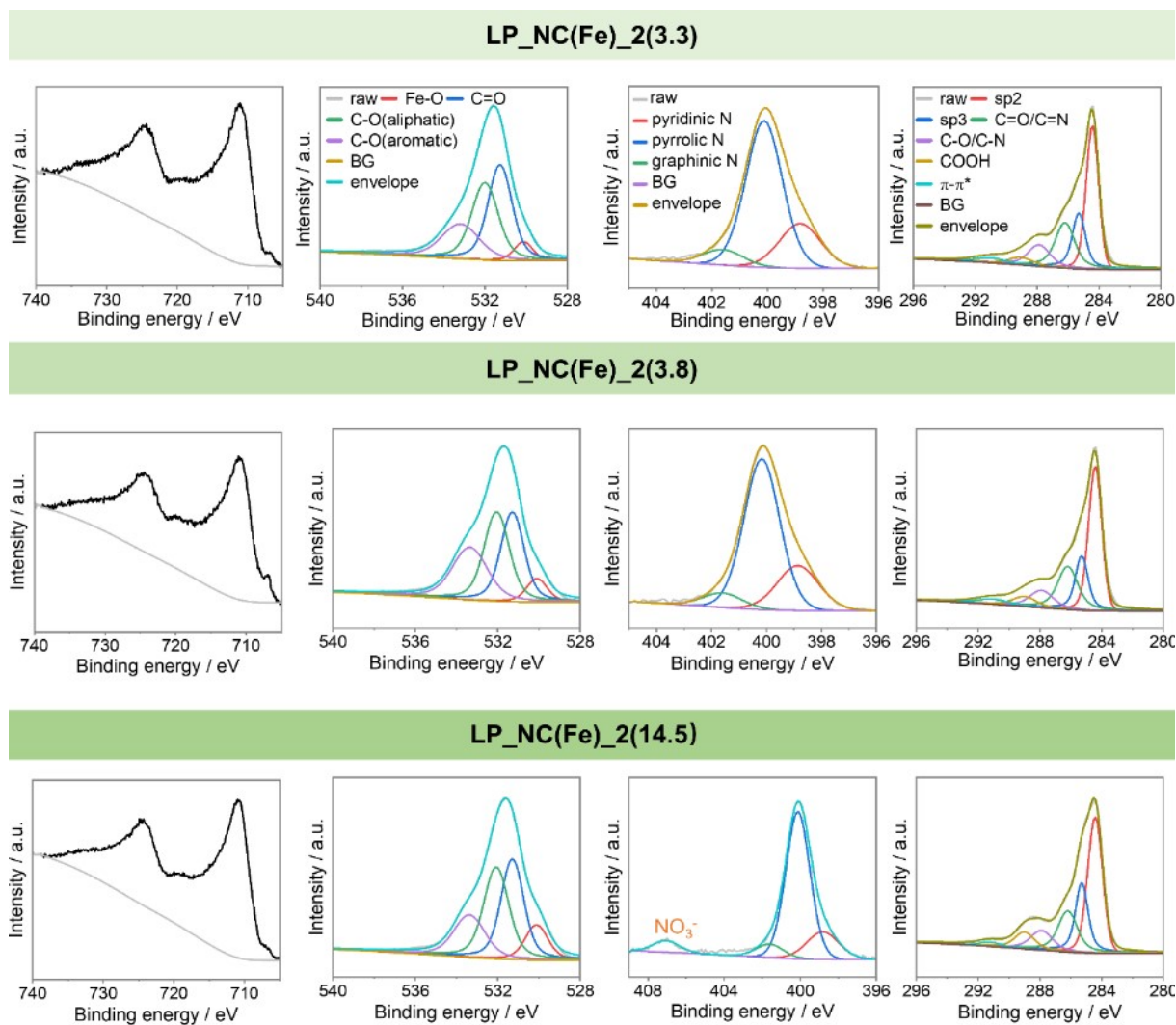


Figure S8. XPS spectra of the samples prepared by route 2: **LP_NC(Fe)_2(3.3)**, **LP_NC(Fe)_2(3.8)** and **LP_NC(Fe)_2(14.5)** with emphasis on the F_{2p} , O_{1s} , N_{1s} , and C_{1s} (from left to right) regions.

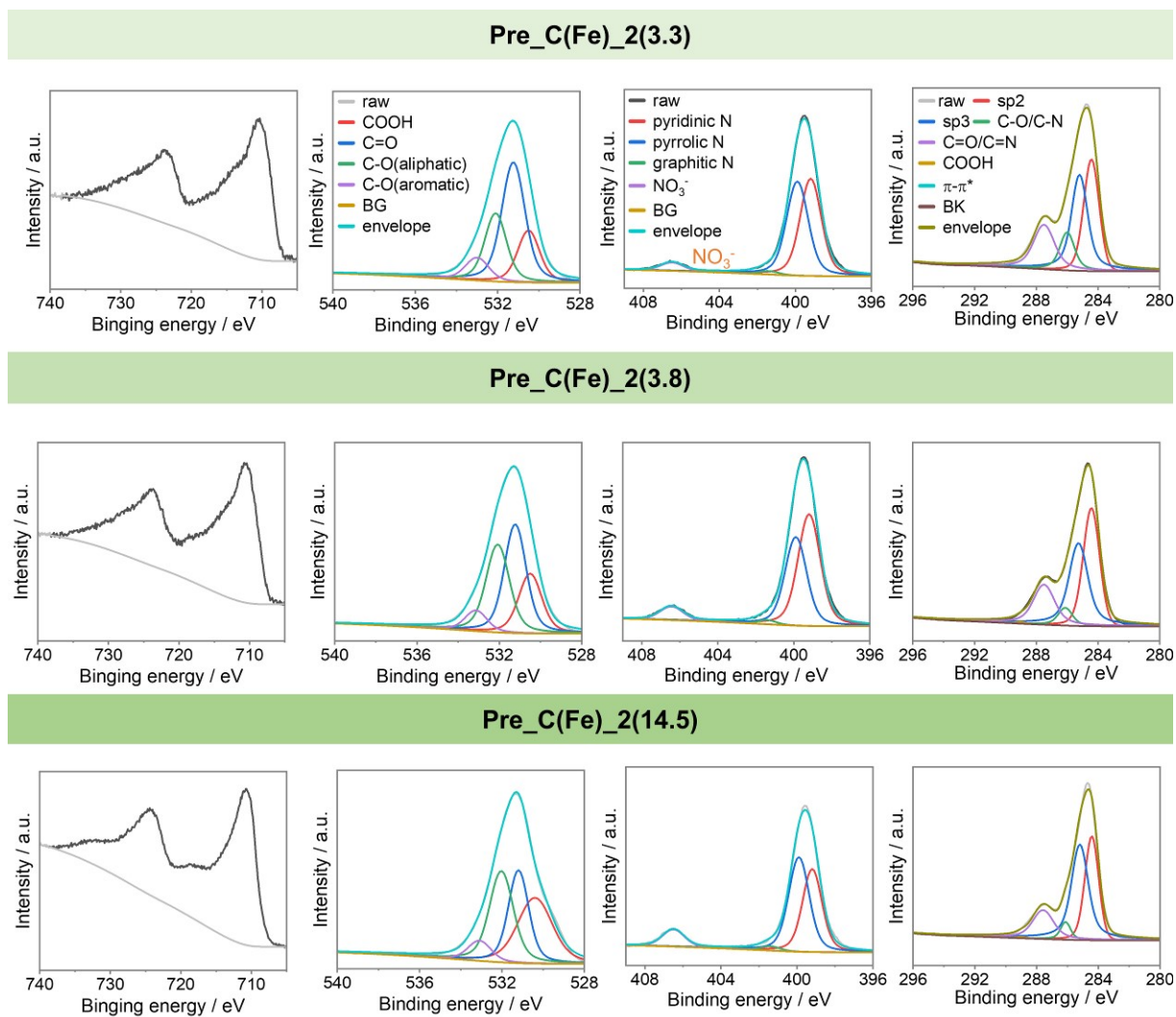


Figure S9. XPS spectra of the primary films of route 2: *pre_NC(Fe)_2(3.3)*, *pre_NC(Fe)_2(3.8)* and *pre_NC(Fe)_2(14.5)* with emphasis on the F_{2p}, O_{1s}, N_{1s}, and C_{1s} (from left to right) regions.

Table S2. Elemental mass percentage of pre-NC(Fe)_1(x) and LP-NC(Fe)_n(x) obtained from XPS survey spectra quantification

Sample	N	C	O	Fe
LP-NC	5.05	77.54	17.41	-
pre-NC(Fe)_1(2.3)	13.63	69.21	17.08	0.09
pre-NC(Fe)_1(2.7)	12.06	71.03	16.78	0.13
pre-NC(Fe)_1(8.6)	12.92	70.63	16.10	0.35
LP-NC(Fe)_1(3.0)	9.77	77.24	12.82	0.74
LP-NC(Fe)_1(4.6)	4.11	75.42	15.53	0.96
LP-NC(Fe)_1(12.1)	6.33	74.58	18.96	0.56
LP-NC(Fe)_2(3.3)	7.05	72.43	14.74	5.78
LP-NC(Fe)_2(3.8)	5.25	73.02	16.48	5.25
LP-NC(Fe)_2(14.5)	3.02	61.29	23.92	11.77

Table S3. Composition of nitrogen of laser-carbon obtained by deconvolution of the N_{1s} peaks of the XPS spectra

Sample	N_{1s} peaks (% of total peak area)				H_2O_2 production
	Pyridinic N	Pyrrolic N	Graphitic N	NO_3^-	
LP-NC	18.36	75.34	6.29	-	60
LP-NC(Fe)_1(3.0)	26.21	65.98	7.80	-	40
LP-NC(Fe)_1(4.6)	20.71	71.61	7.68	-	
LP-NC(Fe)_1(12.1)	90.83	8.44	0.73	-	2
LP-NC(Fe)_2(3.3)	25.37	67.50	6.93	-	80
LP-NC(Fe)_2(3.8)	21.22	68.09	10.70	-	
LP-NC(Fe)_2(14.5)	42.01	50.49	2.12	5.37	8

STEM and EDX analysis

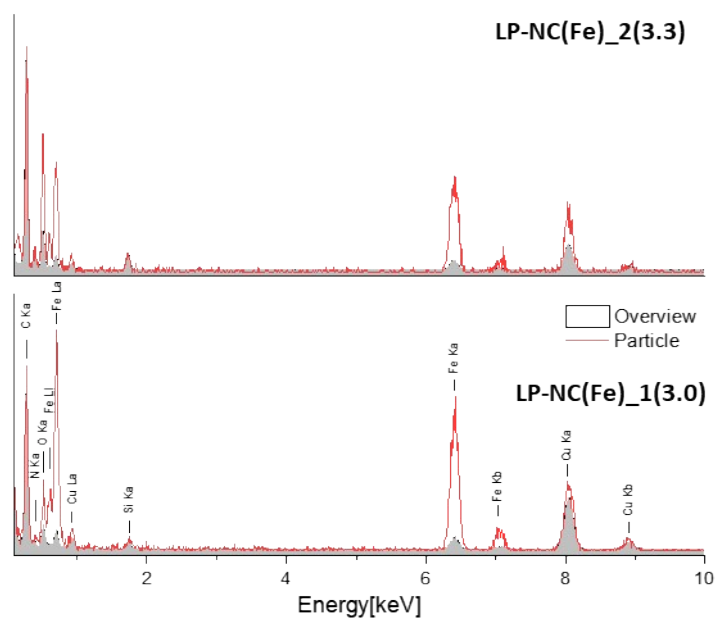


Figure S10. EDX spectrum on overview (grey filling) and particle (red line) regions of LP_NC(Fe)₁(3.0) (bottom) and LP_NC(Fe)₂(3.3) (top).

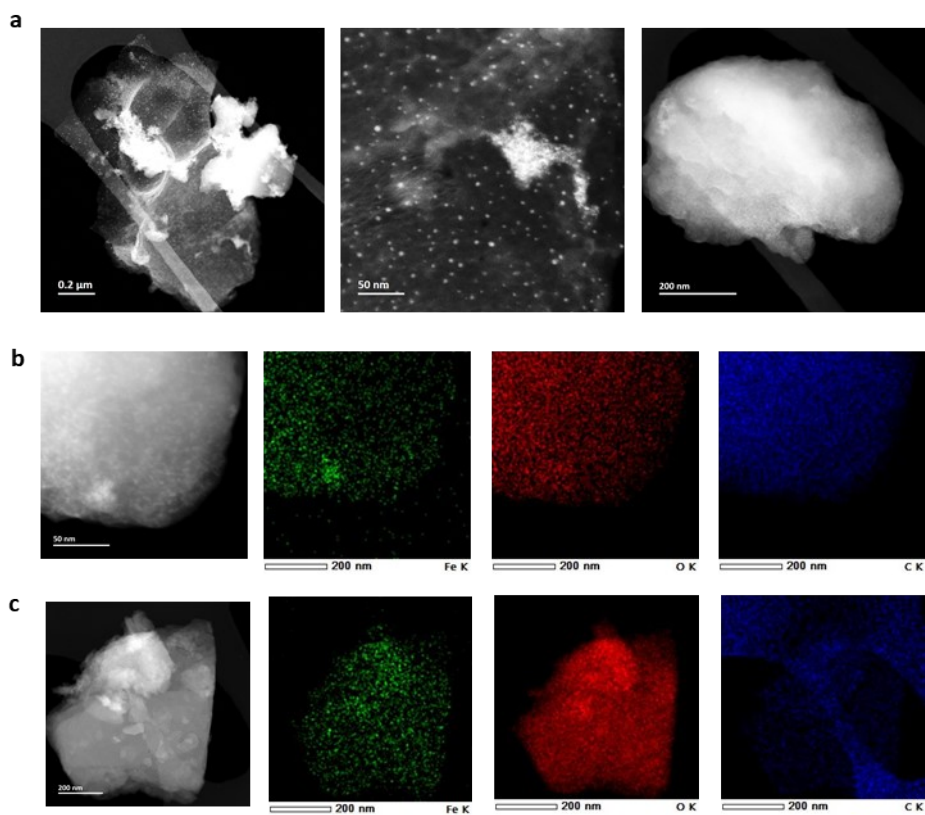


Figure S11. (a) STEM image of thin film, clusters, and dense substrate (from left to right) from LP_NC(Fe)₂(3.3); (b) EDX of dense carbon substrate grafted with iron clusters; (c) EDX with solid flake containing iron and oxide.

Oxygen reduction reaction performance

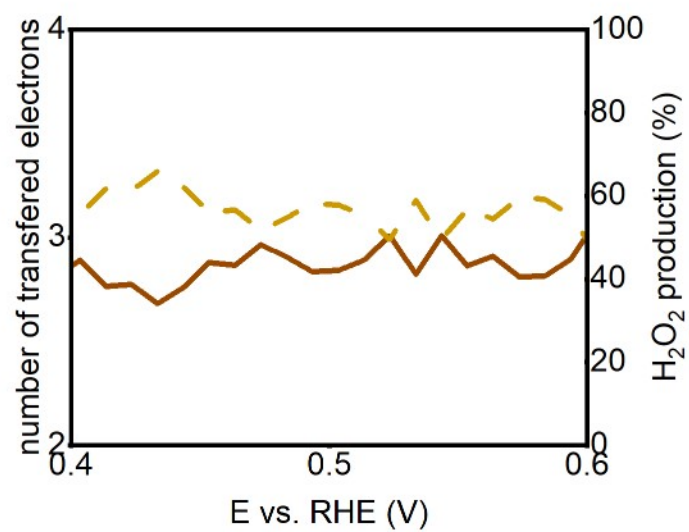


Figure S12. Calculated number of transferred electrons and H₂O₂ production efficiency of LP-C(Fe)₂(3.8) in KOH 0.1M. H₂O₂ production (%) in dashed lines.

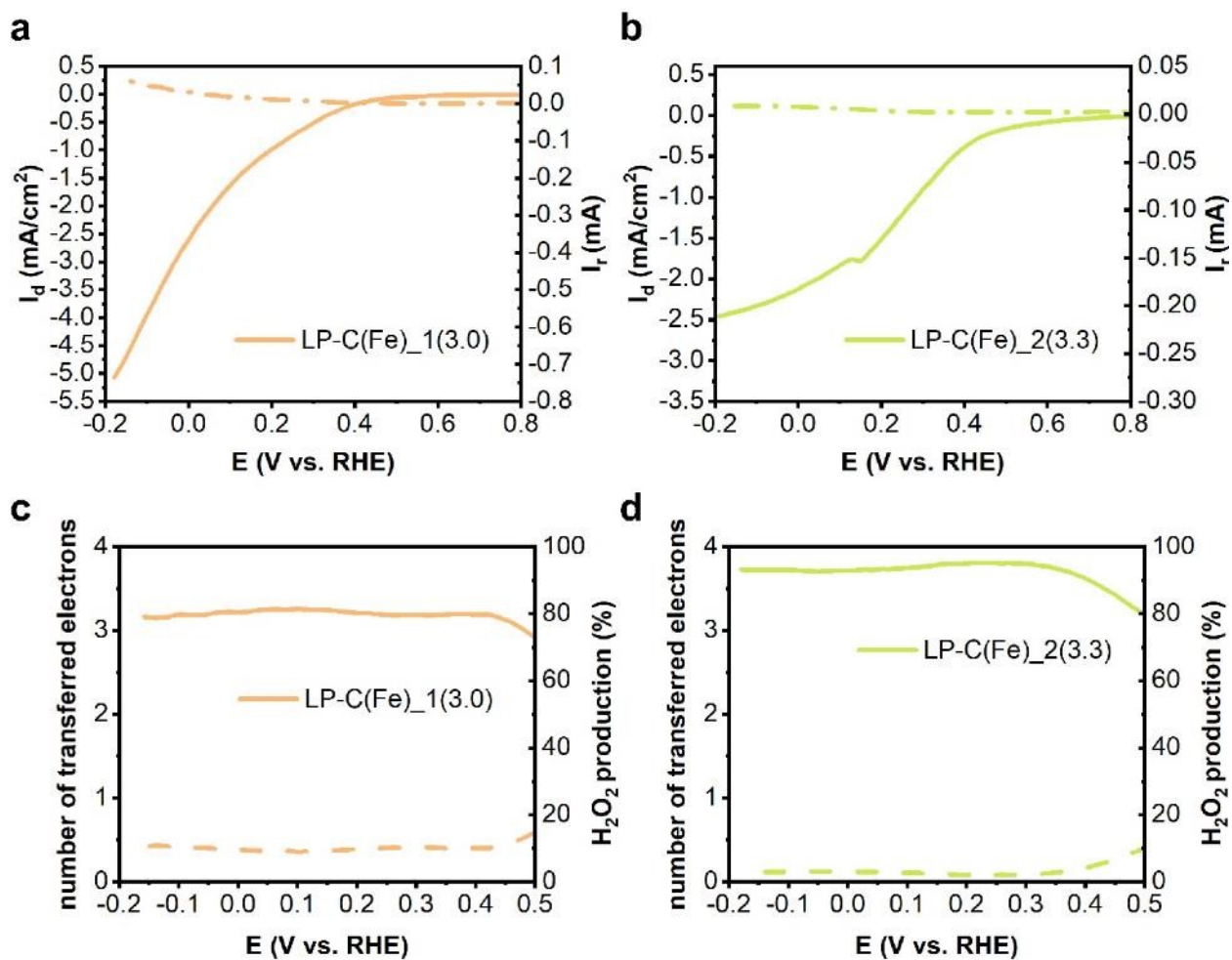


Figure S13. ORR performance in oxygen saturated 0.5M phosphate buffer (pH 7.2) evaluated using an RRDE setup. (a) and (b) Linear sweep voltammetry of LP-C(Fe)₁(3.0) and LP-C(Fe)₂(3.3), (c) and (d) Calculated number of transferred electrons and H₂O₂ production efficiency of LP-C(Fe)₁(3.0) and LP-C(Fe)₂(3.3). H₂O₂ ring current and selectivity (%) in dashed lines

Comparison with published studies

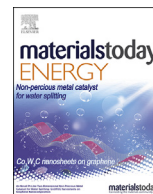
Table S4. Overview of onset potentials and H_2O_2 production efficiencies of previously published and our materials in alkaline electrolyte. The onset potential was calculated by the intercept with X-axes of the tangent to the LSV curve at E1/2. The values in Table S4 are either given in the text or estimated from the data given in each manuscript.

Sample	Fe type	Onset potential (V vs. RHE)	Mechanism	max. H_2O_2 prod	Ref.
CA/U300	-	0.73	2 e ⁻	60	this work
LP-C(Fe)_2(3.3)	α -Fe ₂ O ₃ /FeO/Fe(0)@LP_C	0.77	2 e ⁻	80	this work
LP-C(Fe)_2(14.5)	α -Fe ₂ O ₃ /FeO/Fe(0)@LP_C	0.72	4 e ⁻	8	this work
Fe-CNT	Fe-C-O	0.82	2 e ⁻	95	1
CG400	-	0.72	2 e ⁻	93	2
O-CNT	-	0.73	2 e ⁻	93	3
Fe ₃ O ₄ -graphene	Fe ₃ O ₄ nanoparticles	0.74	2 e ⁻	80	4
CeO ₂ /C	-	0.75	2 e ⁻	44	5
SnNi/C	-	0.70	2 e ⁻	88	6
Fe ₃ O ₄ @NT	Fe ₃ O ₄		2 e ⁻		7
NC@Fe ₂ O ₃ -CNT	γ -Fe ₂ O ₃ , Fe-N _x , and Fe ₅ C ₂	0.96	2 e ⁻	97.3	8
Fe ₂ O ₃	(001) Fe ₂ O _{3-x}	0.73	2 e ⁻	100	9
Fe ₂ O ₃	(012) Fe ₂ O _{3-x}	0.84	-	10	
α -Fe ₂ O ₃ /g-C ₃ N ₄	α -Fe ₂ O ₃		2 e ⁻ and 4 e ⁻	20	10
Fe ₃ O ₄ NP	Fe ₃ O ₄	-0.6 V vs. SCE (pH 8.5)	2 e ⁻ and 4e ⁻	50	11
γ -Fe ₂ O ₃ /rGO	γ -Fe ₂ O ₃	0.78	2+2 e ⁻	-	12
LP-C(Fe)_1(3.0)	η -Fe ₂ O ₃ /Fe(0)	0.77	2 e ⁻ and 4 e ⁻	40	this work
LP-C(Fe)_1(12.1)	Fe ₃ O ₄	0.80	4 e ⁻	2	this work
Fe ₂ O ₃ /P-S-GC	Fe ₂ O ₃	0.97	4 e ⁻	-	13
α -Fe ₂ O ₃ @NT	α -Fe ₂ O ₃		4 e ⁻		7
γ -Fe ₂ O ₃ @CNF	γ -Fe ₂ O ₃	0.92	4 e ⁻	-	14
Fe _{Sx} /FeO _{Nx} /NSC	Fe-N ₄ and Fe ₂ O ₃	0.99	4 e ⁻	15	15
Fe ₂ O ₃ /N-PCs-850	Fe ₂ O ₃	0.936	4 e ⁻	5	16
Fe ₂ O ₃ /FeN _x @CNF	Fe ₂ O ₃ and Fe-N	1.10	4 e ⁻	3	17
Fe ₂ O ₃ @CNF	Fe ₂ O ₃	1.06	4 e ⁻	20	
Fe-Fe ₂ O ₃ @NGr	Fe(0), Fe ₂ O ₃ , and Fe-N	0.075 V vs. Hg/HgO		13	18
Fe-Fe ₂ O ₃ @RGO	Fe(0) and Fe ₂ O ₃	-0.07 V vs. Hg/HgO		51.2	
Fe ₂ O ₃ @Fe-N-C-800	Fe ₂ O ₃ and Fe-N	1.02	4 e ⁻	-	19
Fe/Fe ₂ O ₃ /Fe ₃ C@N-CNT	Hollow particles Fe/Fe ₂ O ₃ /Fe ₃ C	0.90	4 e ⁻	2	20
Fe-CNSs-N	α -Fe ₂ O ₃ and Fe ₃ O ₄	0.90	4 e ⁻	-	21
FeN _x /Fe ₂ O ₃ -CNF	γ -Fe ₂ O ₃ and Fe-N	0.87	4 e ⁻	6	22
Fe ₂ O ₃ /N-bio-C	Fe ₂ O ₃	0.90	hybrid	-	23
Fe and N co-doped C	Fe-N-C	0.51 (neutral pH)	4 e ⁻	-	24
OMCS-Fe ₂ O ₃		0.804	4 e ⁻	-	25
Fe ₂ O ₃ @NC-800	γ -Fe ₂ O ₃	0.97	4 e ⁻	1.20	26
Fe ₃ O ₄ - GO	Fe ₃ O ₄		4 e ⁻	-	27
Fe ₂ O ₃ /GO	Fe ₂ O ₃	0.85	2+2e ⁻	-	28
Fe/N-CNTs	Fe-N	0.862	4 e ⁻		29
P-Fe-C-900	P-Fe-C	0.825	4 e ⁻	15	30
Hemin/NPC-900	Fe-N-C	0.99	4 e ⁻	-	31
Fe@N/HCS	Fe ₃ O ₄	0.90	4 e ⁻	15	32
Fe ₃ O ₄ @NHCS	Fe ₃ O ₄	0.9	4 e ⁻	-	33
Fe ₃ O ₄ /Fe ₃ C@NC-1	Fe ₃ O ₄ and Fe ₃ C	0.97	4 e ⁻	10	34
Fe ₃ O ₄ NPs/NGC	Fe ₃ O ₄	1.015	4 e ⁻	9	35
COP@K10-Fe-900	Fe ₃ O ₄ and Fe-N-C	0.97	4 e ⁻	10	36
Fe ₃ O ₄ @NGA	Fe ₃ O ₄	0.92	4 e ⁻	-	37
Fe ₃ O ₄ /FeNSG-3	Fe-N-C and Fe ₃ O ₄	0.951	4 e ⁻	6	38
C-FePPDA-900	Fe ₃ O ₄ with o-vacancies on n-doped carbon	0.87	4 e ⁻	7.5	39
Fe ₃ O ₄ @FeNC	Fe ₃ O ₄ and Fe-N		4 e ⁻	2	40
Fe ₃ O ₄ /NCMTs-800(IL)	Fe ₃ O ₄	0.794	4 e ⁻	-	41

References

- 1 K. Jiang, S. Back, A. J. Akey, C. Xia, Y. Hu, W. Liang, D. Schaak, E. Stavitski, J. K. Nørskov, S. Siahrostami and H. Wang, *Nat. Commun.*, 2019, **10**, 3997.
- 2 Y.-H. Lee, F. Li, K.-H. Chang, C.-C. Hu and T. Ohsaka, *Appl. Catal. B Environ.*, 2012, **126**, 208–214.
- 3 Z. Lu, G. Chen, S. Siahrostami, Z. Chen, K. Liu, J. Xie, L. Liao, T. Wu, Di. Lin, Y. Liu, T. F. Jaramillo, J. K. Nørskov and Y. Cui, *Nat. Catal.*, 2018, **1**, 156–162.
- 4 W. R. P. Barros, Q. Wei, G. Zhang, S. Sun, M. R. V Lanza and A. C. Tavares, *Electrochim. Acta*, 2015, **162**, 263–270.
- 5 M. H. M. T. Assumpção, A. Moraes, R. F. B. De Souza, I. Gaubeur, R. T. S. Oliveira, V. S. Antonin, G. R. P. Malpass, R. S. Rocha, M. L. Calegari, M. R. V Lanza and M. C. Santos, *Appl. Catal. A Gen.*, 2012, **411–412**, 1–6.
- 6 V. S. Antonin, M. H. M. T. Assumpção, J. C. M. Silva, L. S. Parreira, M. R. V Lanza and M. C. Santos, *Electrochim. Acta*, 2013, **109**, 245–251.
- 7 Y. Xue, W. Jin, H. Du, S. Wang, S. Zheng and Y. Zhang, *RSC Adv.*, 2016, **6**, 41878–41884.
- 8 X. Cheng, S. Dou, G. Qin, B. Wang, P. Yan, T. T. Isimjan and X. Yang, *Int. J. Hydrogen Energy*, 2020, **45**, 6128–6137.
- 9 R. Gao, L. Pan, Z. Li, C. Shi, Y. Yao, X. Zhang and J.-J. Zou, *Adv. Funct. Mater.*, 2020, **30**, 1910539.
- 10 S. Dutta, T. K. Jana, R. Maiti, K. De and K. Chatterjee, *ChemistrySelect*, 2021, **6**, 11759–11767.
- 11 Y. Xiao, J. Hong, X. Wang, T. Chen, T. Hyeon and W. Xu, *J. Am. Chem. Soc.*, 2020, **142**, 13201–13209.
- 12 Q. Feng, Z. Chen, K. Zhou, M. Sun, X. Ji, H. Zheng and Y. Zhang, *ChemistrySelect*, 2021, **6**, 8177–8181.
- 13 H. Zhao, J. Wang, C. Chen, D. Chen, Y. Gao, M. Saccoccio and F. Ciucci, *RSC Adv.*, 2016, **6**, 64258–64265.
- 14 Z. Yao, Y. Li, D. Chen, Y. Zhang, X. Bao, J. Wang and Q. Zhong, *Chem. Eng. J.*, 2021, **415**, 129033.
- 15 Y. Lei, F. Yang, H. Xie, Y. Lei, X. Liu, Y. Si and H. Wang, *J. Mater. Chem. A*, 2020, **8**, 20629–20636.
- 16 T. Zhang, L. Guan, C. Li, J. Zhao, M. Wang, L. Peng, J. Wang and Y. Lin, *Catalysts*, 2018, **8**, 101.
- 17 M. Wang, T. Liao, X. Zhang, J. Cao, S. Xu, H. Tang and Y. Wang, *Adv. Mater. Interfaces*, 2022, **9**, 2101904.
- 18 V. M. Dhavale, S. K. Singh, A. Nadeema, S. S. Gaikwad and S. Kurungot, *Nanoscale*, 2015, **7**, 20117–20125.
- 19 X. Xu, C. Shi, Q. Li, R. Chen and T. Chen, *RSC Adv.*, 2017, **7**, 14382–14388.
- 20 B. Zhang, T. Li, L. Huang, Y. Ren, D. Sun, H. Pang, J. Yang, L. Xu and Y. Tang, *Nanoscale*, 2021, **13**, 5400–5409.
- 21 Y. Wang, R. Gan, H. Liu, M. Dirican, C. Wei, C. Ma, J. Shi and X. Zhang, *J. Mater. Chem. A*, 2021, **9**, 2764–2774.
- 22 Q. Yu, S. Lian, J. Li, R. Yu, S. Xi, J. Wu, D. Zhao, L. Mai and L. Zhou, *J. Mater. Chem. A*, 2020, **8**, 6076–6082.
- 23 Y. Wu, H. Jiao, M. Hou and P. Zhang, *J. Phys. Conf. Ser.*, 2021, **2079**, 12002.
- 24 Y. Su, H. Jiang, Y. Zhu, W. Zou, X. Yang, J. Chen and C. Li, *J. Power Sources*, 2014, **265**, 246–253.
- 25 J. He, B. Li, J. Mao, Y. Liang, X. Yang, Z. Cui, S. Zhu and Z. Li, *J. Mater. Sci.*, 2017, **52**, 10938–10947.
- 26 Z. Xiao, G. Shen, F. Hou, R. Zhang, Y. Li, G. Yuan, L. Pan, J. J. Zou, L. Wang, X. Zhang and G. Li, *Catal. Sci. Technol.*, 2019, **9**, 4581–4587.
- 27 K. Lellala, *Energy & Fuels*, 2021, **35**, 8263–8274.
- 28 S. Arya Gopal, A. Edathiparambil Poullose, C. Sudakar and A. Muthukrishnan, *ACS Appl. Mater. Interfaces*, 2021, **13**, 44195–44206.
- 29 W. Liu, K. Yuan, Q. Ru, S. Zuo, L. Wang, S. Yang, J. Han and C. Yao, *Arab. J. Chem.*, 2020, **13**, 4954–4965.
- 30 Z. Yang, J. Wu, X. Zheng, Z. Wang and R. Yang, *J. Power Sources*, 2015, **277**, 161–168.
- 31 Z. Lu, J. Chen, W. Wang, W. Li, M. Sun, Y. Wang, X. Wang, J. Ye and H. Rao, *Small*, 2021, **17**, 2007326.

- 32 B. Wang, Y. Ye, L. Xu, Y. Quan, W. Wei, W. Zhu, H. Li and J. Xia, *Adv. Funct. Mater.*, 2020, **30**, 2005834.
- 33 Y. Li, H. Huang, S. Chen, X. Yu, C. Wang and T. Ma, *Nano Res.*, 2019, **12**, 2774–2780.
- 34 M. Liu, X. Guo, L. Hu, H. Yuan, G. Wang, B. Dai, L. Zhang and F. Yu, *ChemNanoMat*, 2019, **5**, 187–193.
- 35 Y. Chen, L. Li, X. Liu, W. Wan and J. Luo, *Mater. Res. Express*, 2019, **6**, 65019.
- 36 J. Guo, Y. Cheng and Z. Xiang, *ACS Sustain. Chem. Eng.*, 2017, **5**, 7871–7877.
- 37 Z. Liang, W. Xia, C. Qu, B. Qiu, H. Tabassum, S. Gao and R. Zou, *ChemElectroChem*, 2017, **4**, 2442–2447.
- 38 Y. Li, Y. Zhou, C. Zhu, Y. H. Hu, S. Gao, Q. Liu, X. Cheng, L. Zhang, J. Yang and Y. Lin, *Catal. Sci. Technol.*, 2018, **8**, 5325–5333.
- 39 Y. Deng, X. Tian, G. Shen, Y. Gao, C. Lin, L. Ling, F. Cheng, S. Liao and S. Zhang, *J. Colloid Interface Sci.*, 2020, **567**, 410–418.
- 40 S. Hu, W. Ni, D. Yang, C. Ma, J. Zhang, J. Duan, Y. Gao and S. Zhang, *Carbon N. Y.*, 2020, **162**, 245–255.
- 41 G. Liu, B. Wang, P. Ding, Y. Ye, W. Wei, W. Zhu, L. Xu, J. Xia and H. Li, *J. Alloys Compd.*, 2019, **797**, 849–858.



Fast response electrochemical capacitor electrodes created by laser-reduction of carbon nanodots

Volker Strauss^{a, c}, Mackenzie Anderson^a, Christopher L. Turner^a, Richard B. Kaner^{a, b, *}

^a Department of Chemistry and Biochemistry and California NanoSystems Institute, University of California, Los Angeles (UCLA), Los Angeles, CA, USA

^b Department of Materials Science and Engineering, UCLA, Los Angeles, CA, USA

^c Max Planck Institut für Kolloid- und Grenzflächenforschung Am Mühlenberg 1, 14476 Potsdam, Germany

ARTICLE INFO

Article history:

Received 17 September 2018

Received in revised form

28 October 2018

Accepted 30 October 2018

Available online 23 November 2018

Keywords:

AC-line filtering

Carbon nanodots

Laser conversion

3D-graphene

3D-carbon

ABSTRACT

The conversion of small bio-based molecules into electro-active functional carbon nanomaterials such as carbon nanodots or graphene is attracting increasing interest. In this communication we demonstrate the use of laser-reduced carbon nanodots (lrcND) as electrodes for electrochemical capacitors. A CO₂-laser-assisted process is utilized to convert CNDs into highly conductive 3D-carbon monoliths. Exclusion of molecular oxygen from the reaction environment has a positive effect on device parameters and particularly on the frequency response. Using this simple and inexpensive method, an extremely fast RC time constant of 0.29 ms and a capacitance of 0.259 mF cm⁻² at 120 Hz were obtained. This can be attributed to an effective conversion of CNDs into graphitic carbon in an oxygen-free environment and the presence of unconverted CNDs in the 3D-carbon network acting as doping agents.

© 2018 Elsevier Ltd. All rights reserved.

1. Introduction

During the past few years, carbon-based electrodes, in particular, graphene and carbon nanotubes, have been extensively investigated as active materials in high-frequency electric double layer capacitors (HF-EDLCs) [1]. Due to the wide variety of carbon materials and their high electronic conductivity, flexibility, and tunable porosity, they are considered promising materials for high-speed capacitor applications, such as AC-line filtering [2]. Fine-tuning the architecture of graphene-based electrodes can lead to remarkably short RC time constants for the electrodes, on the order of a few milliseconds [3–5].

The RC time constants (τ_{RC}), i.e. the product of resistance (R) and the capacitance (C) at a given frequency, are a characteristic parameter of EDLCs and relate to the frequency at which the electric response of a device switches from resistive to capacitive [6,7]. In general, a fast τ_{RC} is preferable since this allows for very fast charging and discharging, but more than this, a fast frequency

response can enable applications for AC-line filtering. Decisive factors to achieve low τ_{RC} are low electronic and ionic series resistance throughout the device. This can be enabled by a) low charge transport resistance in the active material, b) low electrolyte/electrode and electrode/current collector interface resistance, c) absence of micropores in the active materials to avoid ionic resistance, and d) avoiding slow-kinetic pseudocapacitive reaction sites. A perspective on important device parameters for HF-EDLCs is given in a recent review article [7].

A range of examples demonstrate that by proper alignment of carbon materials, low τ_{RC} can be achieved. Carbon materials applicable for HF-EDLCs include onion-like carbon (26 ms) [8], chemical vapor deposited carbon nanotubes (0.19 ms) [9], and electrochemically reduced graphene oxide (1.35 ms) [10]. Additionally, composite materials consisting of graphene oxide/carbon nanotubes (4.8 ms) [11] or printable graphene/conducting polymer hybrids (0.47 ms) [12] were found to have extraordinarily short frequency response times. Another material developed for HF-EDLC applications is porous conducting poly(3,4-ethylenedioxythiophene) with a τ_{RC} of 0.8 ms [13]. Also highly porous materials like electrochemically reduced graphene oxide and carbon black have been shown to possess low τ_{RC} of only 0.35 ms [10,14]. Among the most promising materials are vertically aligned graphene sheets or nitrogen-doped holey graphene, offering high capacitance, yet very low τ_{RC} of only 0.2 ms [15,16]. Among the more abundant and thus

* Corresponding author. Department of Chemistry and Biochemistry and California NanoSystems Institute, University of California, Los Angeles (UCLA), Los Angeles, CA, USA.

E-mail addresses: volker.strauss@mpikg.mpg.de (V. Strauss), kaner@chem.ucla.edu (R.B. Kaner).

economic materials is carbon black with RC time constants as low as 0.35 and remarkably high areal capacitance of 0.56 mF cm^{-2} [14]. A comprehensive overview of active materials for HF EDLCs has been reviewed recently [7].

Most of these examples utilize rather elaborate or costly fabrication techniques. In contrast, our standard laser-assisted reduction process represents a simple template-free, and fast one-step conversion process [17,18]. Using this method we have demonstrated that films of graphene oxide, carbon nanodots (CND) and composites thereof can be converted into functional 3D-carbon electrodes for HF-EDLCs [19–23]. We found that the laser-reduction of CND into 3D-turbostratic graphene yields electrodes with remarkably low τ_{RC} [19]. Notably, CNDs are made of natural small molecules and, therefore, represent a way to convert renewable carbon sources into functional electronic materials [3,24]. Previously, they have mainly been investigated as photoactive compounds for a range of optical and charge-transfer applications, but they are increasingly being used as feedstock for charge storage materials [25,26]. For example, their relatives, graphene quantum dots (GQD), have been successfully integrated as active material in interdigitated Au electrodes exhibiting τ_{RC} of $<0.1 \text{ ms}$ in aqueous electrolytes [27].

In this paper we show that a change of the reaction environment and the laser power for the laser-assisted reduction of annealed carbon nanodots (CND300, annealed at $300 \text{ }^\circ\text{C}$) leads to improvements of the frequency response of the resulting 3D-carbon electrodes. The electrochemical properties of this 3D-carbon in EDLC electrodes were examined focusing on the frequency response. The main factors for improvement of τ_{RC} are the absence of molecular O_2 in the reaction environment and the presence of unconverted material in the carbon network. By improvement of these parameters, RC time constants as low as 0.29 ms were obtained.

2. Results and discussion

CNDs are a few nanometers in size and feature an sp^2 -hybridized π -conjugated carbon core and a variety of functional groups on their surfaces [19,25]. Typical functional groups in annealed CNDs (CND300) are hydroxyls and carboxylates and the C:O atomic ratio is $\sim 2:1$. In the CO_2 -laser-assisted reduction process, CNDs are converted into electronically conductive, porous 3D-graphene networks [19]. The CO_2 -laser irradiation causes the material to heat up to several hundred degrees Celsius and then rapidly cool down to room temperature. Upon laser impact, the functional groups are cleaved and turned into gases leading to rapid expansion, reduction and vaporization of the CND300. Subsequently, the reduced CND300 reacts in the gas phase upon rapid cooling to form extended graphitic sheets. This process is illustrated in the schematic diagram presented in Fig. 1.

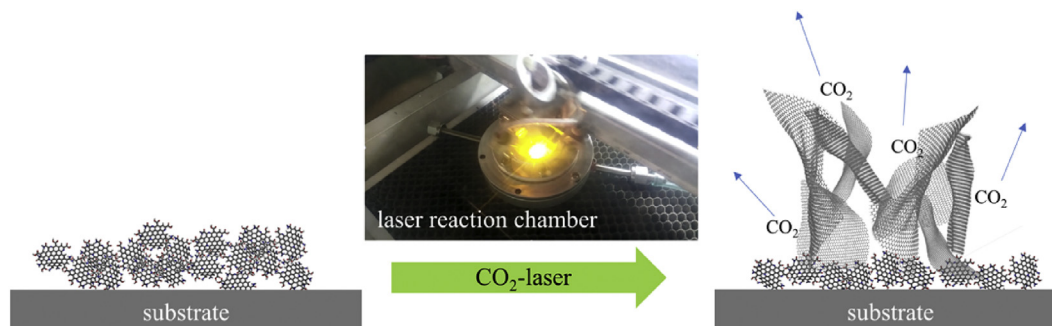


Fig. 1. Illustration of the CO_2 -laser conversion process for CND300; Inset image: photograph of the gas reaction chamber using a benchtop CO_2 -laser.

Li et al. reported a significant influence of the reaction environment during laser reduction on the resulting material [28]. We used a similar laser reaction chamber in our experiments (see Experimental Section) to test the influence of the reaction medium during the laser reduction of CND300.

First, the materials properties of IrCND300 reduced under O_2 or Ar were analyzed in terms of mass loss, accessible surface areas, and sheet conductivities. The mass loss during the laser-reduction process is $\sim 60\%$ in both reaction environments (Fig. 2e). Laser-reduction under O_2 leads to a slightly increased specific surface area of $351 \text{ m}^2 \text{ g}^{-1}$ compared to $333 \text{ m}^2 \text{ g}^{-1}$ under Ar. In the absence of O_2 a higher sheet conductivity of 295 S m^{-1} compared to with 248 S m^{-1} under O_2 is achieved.

In the SEM images in Fig. 2, the same elementary structural features are observed independent of the reaction medium. A closer look reveals some small differences. During laser-conversion in an O_2 atmosphere, a greater occurrence of open pores was found on the surface of the IrCND300. Exclusion of O_2 from the reaction atmosphere prevents the opening of the pores. IrCND300(Ar) exhibits a porous structure with graphitic surface features.

To elucidate the chemical structure, the products of the laser reduction in both Ar and O_2 atmospheres were characterized by XPS and Raman spectroscopy. The XPS spectra of IrCND300 reduced under Ar and O_2 with an emphasis on the C_{1s} region are shown in Fig. 2c. All products show a dominant peak at 284.6 eV indicating that the majority of carbon in the samples is sp^2 -hybridized. The two IrCND300 samples have a similar composition with a carbon content of 84% for reduction in both argon and oxygen environments. The final sp^2 -carbon content is higher under Ar with 78% sp^2 -carbon compared to 74% under O_2 .

The Raman spectra of both samples show the same set of peaks, namely the D-, the G-, D', and G'-peak at ~ 1329 , ~ 1578 , ~ 1609 , and $\sim 2652 \text{ cm}^{-1}$, respectively (Fig. 2f). The intensities of the D and D'-bands relate to defects in the graphitic lattice. Notably, the film reduced under O_2 shows a significantly enhanced D-band, indicating a higher number of defects. The $I_{\text{D}}/I_{\text{G}}$ ratio is 1.47 under O_2 and 0.97 under Ar. When taking a closer look at the G-band, a bathochromic shift of the G-band of 3 cm^{-1} from $1584 \text{ (O}_2)$ to 1581 cm^{-1} (Ar) is noted, indicating an increase in electron density when turning from O_2 to Ar as the reaction medium. The G-band is sensitive to both electron doping and the size of the crystalline domains. A downshift of the G-band originates either from a shift of electron density into the conduction band of graphene/graphite or a higher degree of crystallinity of the sp^2 -phases in the graphitic sample [29,30]. Presumably, the oxygen containing functional groups provide electron trap states and withdraw electron density from the conjugated sp^2 -network.

We tested the electrochemical performance of IrCND300 reduced under O_2 or Ar in EDLCs using 0.1 M TBAPF_6 in acetonitrile

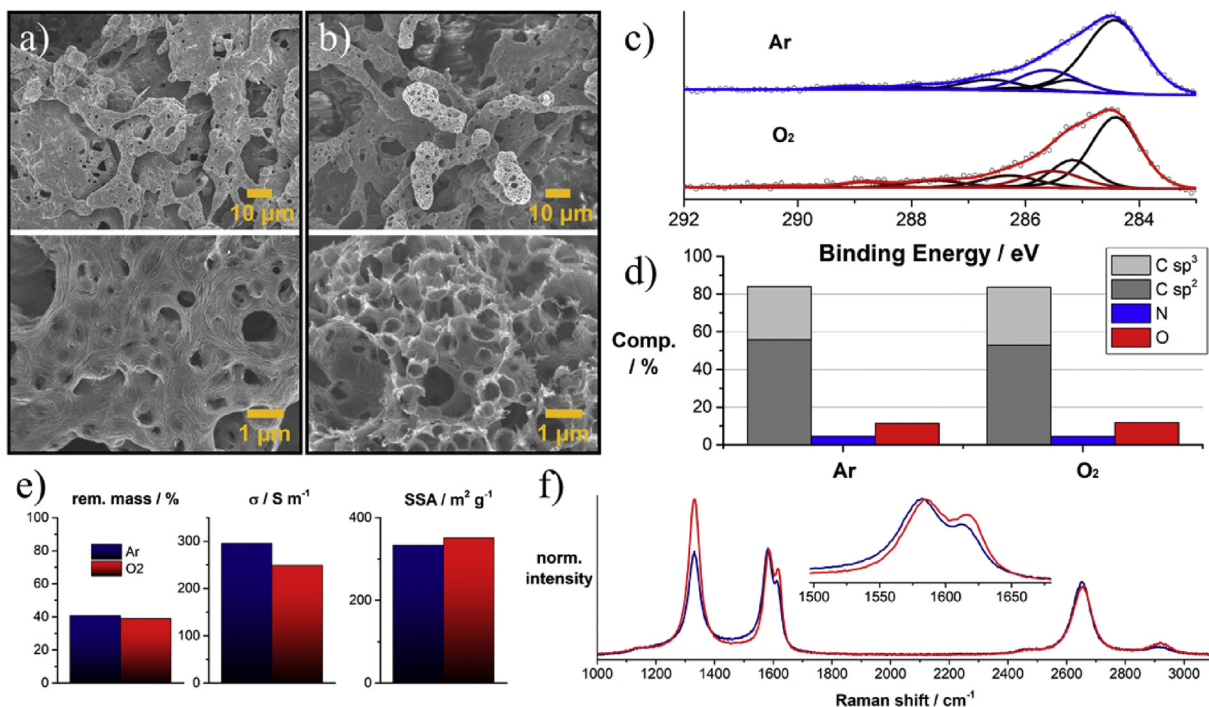


Fig. 2. Characterization of the IrCND300 film; a) Scanning electron micrographs of IrCND300(Ar); b) Scanning electron micrographs of IrCND300(O₂); c) XPS spectra of the C_{1s} region of IrCND300 reduced in Ar and O₂ atmosphere, respectively; d) Elemental composition of IrCND300 reduced in Ar and O₂ atmosphere, respectively; e) remaining mass after laser reduction of CND300 under argon (blue) and oxygen (red) using the same laser parameters, sheet conductivity of IrCND300 reduced under argon (blue) and oxygen (red), and specific surface area of IrCND300 reduced under argon (blue) and oxygen (red); f) Raman spectra of IrCND300 reduced in Ar (blue) and O₂ (red) atmosphere obtained upon excitation at 633 nm.

(MeCN) as the electrolyte. In the following paragraphs we discuss the results obtained from cyclic voltammetry (CV) and electrochemical impedance spectroscopy (EIS).

Two representative cyclic voltammograms of mass normalized symmetric IrCND300 cells using 0.1 M TBAPF₆/MeCN as the electrolyte solution at 100 mV s⁻¹ are shown in Fig. 3a. Both cells show a capacitive curve shape without redox peaks. The shape of the CV curve is more rectangular for IrCND300(Ar) than for IrCND300(O₂) as a result of lower series resistance. The capacitance increases by a factor of 1.5 in an oxygen environment. The rectangular line shape for IrCND300(Ar) is retained even at high scan rates up to 100 V s⁻¹ (Fig. 3b). Both cells show excellent cycling stability (Fig. 3c). Over 20,000 cycles, only 2% of the initial capacitance of IrCND300(Ar) is lost. Interestingly, in the O₂ reduced cell, the capacitance increases by 3% after 20,000 cycles. This can be attributed to atmospherically adsorbed O₂ onto the electrode before immersion into the electrolyte solution. Upon application of the voltage the O₂ desorbs or decomposes and exposes the new sites to the electrolyte.

The Nyquist plots in Fig. 3d shows the corresponding frequency response of the IrCND300 HF-EDLCs under O₂ and Ar. A positive polarization effect is reflected in the impedance plot where a lower maximum phase angle of -84° is observed for IrCND300(Ar) and only -79° for IrCND300(O₂). The abnormal behavior in the high frequency region is due to instrumental artifacts [31]. Moreover, the phase angle plot in Fig. 3e shows that a wider capacitive frequency window ranging from ~0.1–100 Hz is available in the Ar reduced cells. The yellow shaded area indicates the frequency window typically used for the characterization of EDLCs using CV scan rates between 10 and 500 mV s⁻¹. At frequencies of <0.1 Hz, the phase angle drops towards lower values as leakage resistance becomes dominant, rendering this frequency region impractical for EDLC applications. For the CND300 based EDLCs, the frequency range showing capacitive characteristics is 1000–100,000 mV s⁻¹. The

frequency at which the phase angle is 45°, i.e. where the device transitions from resistive to capacitive behavior, is 955 or 495 Hz corresponding to relaxation times (τ₀) of 1.05 or 2.02 ms. At 120 Hz, areal capacitances of 0.259 and 0.342 mF cm⁻² and RC-time constants (τ_{RC}) of 0.29 ms and 0.77 ms were obtained for IrCND300(Ar) and IrCND300(O₂), respectively (Fig. 3f). The phase angles at 120 Hz are 78° in IrCND300(Ar) and only ~60° in IrCND300(O₂).

Based on the presented results we conclude that the absence of O₂ during the laser reduction process has a positive effect on the frequency response of IrCND300-based HF-EDLCs. In the absence of oxygen the formation of micropores is prevented, which facilitates fast ion transport and a higher electrical conductivity due to lower defect density in the active material.

The electrochemical parameters, in particular the frequency response, are also affected by unconverted CND300 remaining within the porous 3D-carbon network during the laser conversion (Fig. 1). These were removed from the graphitized 3D-carbon network by washing the electrodes with either *N*-methyl-2-pyrrolidone (NMP) or aqueous KOH solution. A scanning electron micrograph of the top-side and the bottom-side of the carbon film after washing is presented in Fig. 4a. From the cyclic voltammograms of these electrodes, a 2.25 times higher capacitance compared to unwashed electrodes was determined (Fig. 4b). However, the less ideal curve shape indicates a higher series resistance; this was confirmed with impedance measurements that show a dramatically increased minimum phase angle of -57° and a frequency at -45° of 48 Hz compared to 955 Hz in the unwashed IrCND300(Ar) electrodes (Fig. 4c). CND300 is composed of charged particles attached to the surface of the electrode, likely via π-π-stacking (Fig. 4d). Thus, the charges are located on the electrode/electrolyte interface and are accessed by applying bias. The π-π interactions prevent CND300 from diffusing, which reduces diffusion resistance. The unconverted parts of CND300 can act as doping

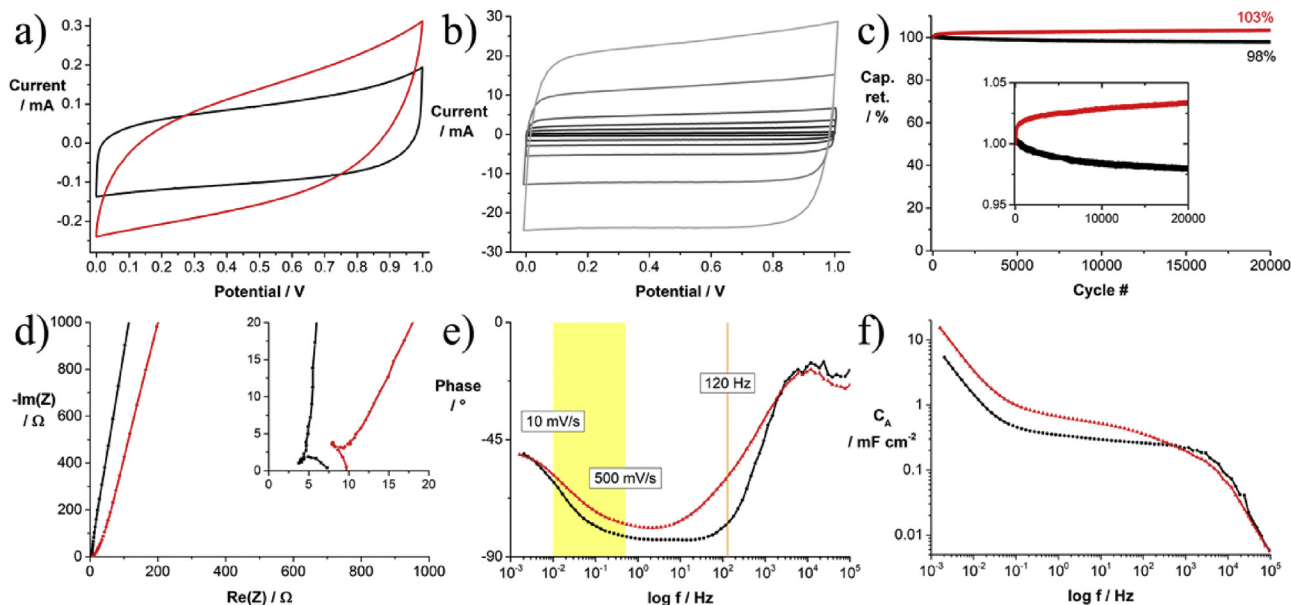


Fig. 3. a) Cyclic voltammograms of two EDLCs assembled with IrCND300(Ar) (black) and IrCND300(O₂) (red) electrodes in 0.1 M TBAPF₆/MeCN as electrolyte at a scan rate of 100 mV s⁻¹; b) Cyclic voltammograms of a IrCND300(Ar) EDLC in 0.1 M TBAPF₆/MeCN as the electrolyte at different scan rates between 1 and 100 V s⁻¹; c) Cycling stability of IrCND300(Ar) (black) and IrCND300(O₂) (red) over 20,000 cycles at a current density of 8 A g⁻¹ or 750 mA cm⁻², i.e. 60 Hz; d) Nyquist impedance plots of two EDLCs assembled with IrCND300(Ar) (black) or IrCND300(O₂) (red) in 0.1 M TBAPF₆/MeCN as the electrolyte; e) Phase angle plots of two EDLCs assembled with IrCND300(Ar) (black) or IrCND300(O₂) (red) in 0.1 M TBAPF₆/MeCN as the electrolyte; f) Specific areal capacitance at different scan rates obtained from electrochemical impedance measurements.

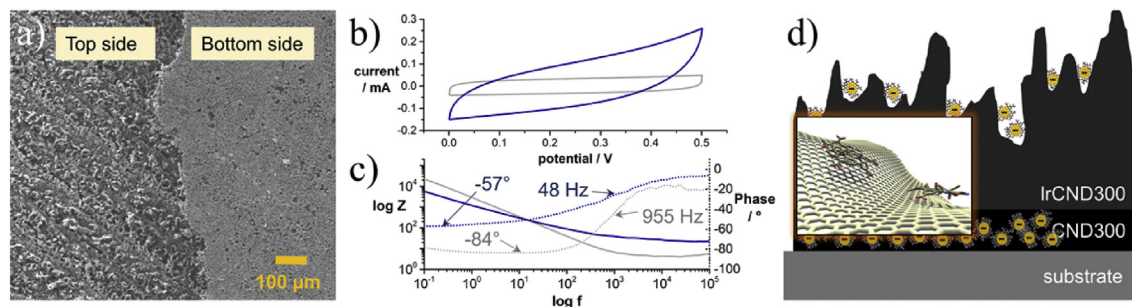


Fig. 4. a) Scanning electron micrograph comparing the top and the bottom sides of a IrCND300 film after removing from the substrate by KOH washing; b) Cyclic voltammograms of EDLCs with washed (blue) and unwashed (gray) IrCND300(Ar) in 0.1 M TBAPF₆/MeCN as electrolyte at a scan rate of 100 mV s⁻¹; c) Bode impedance plot of EDLCs with washed (blue) and unwashed (gray) IrCND300(Ar) in 0.1 M TBAPF₆/MeCN as electrolyte; d) Illustration of the structure of IrCND300 film; Inset: Illustration of CND300 interacting with IrCND300.

agents or solid-state electrolytes keeping the charges immediately at the electrode/electrolyte interface and thus reducing the τ_{RC} of the overall device. Removal of these unreacted particles makes the electrode surfaces and micropores accessible to the electrolyte, which increases the capacitance, but also the series resistance. Therefore, the use of organic electrolyte systems in which CND300 is entirely insoluble are essential for the high frequency response of the devices.

Different concepts to achieve HF-EDLCs based on carbon materials have been introduced in the literature. Typical procedures for the fabrication of HF-EDLCs include several steps such as photolithography, chemical vapor deposition, and electrodeposition. The most common substrates are noble metals such as gold. A list of carbon-based materials and device architectures with significantly low τ_{RC} is given in Table 1. Interestingly, most of the concepts introduced include fabrication by electrodeposition which generally provides a better contact between the substrate and the active material. To decrease the internal series resistance, graphene buffer layers in vertically grown CNT carpets have been grown to support conduction between the active CNT layer and the substrate

[9]. Usually EDLCs optimized for low τ_{RC} feature comparatively small active layer thicknesses of only a few hundred nanometers. As the thickness of the active material increases, the τ_{RC} increases as a result of the longer ion diffusion length [9,12,32]. For example, it was found that the series resistance in carbon nanotube/carbon black based HF-EDLCs was significantly lower when the stainless steel substrate was roughened, which improves the contact between the active material and the substrate [32]. A decisive advantage of our IrCND300 electrodes is the simple fabrication procedure and the eco-friendly nature of the starting material. In comparison to carbon black based HF-EDLCs [14], the laser-assisted method provides the possibility of micropatterning.

3. Conclusions

We have described the influence of the reaction medium on the final product of the laser-assisted reduction process of carbon nanodot films. In the presence of oxygen, changes in the morphology of the pores in the 3D-carbon monolith are observed. These are associated with higher defect densities in the material as

Table 1
Summary of carbon-based EDLCs featuring fast τ_{RC} .

Active material	Substrate	Electrolyte	Method	Design	τ_{RC} [ms]	ESR [Ω]	C_A [mF cm ⁻²] (120 Hz)	ϕ_{120Hz} [$^\circ$]	Year
Onion-like carbon	Au	TBAPF ₄ /PC	Electro-deposition	Inter-digitated	26		0.9 (100 V s ⁻¹)		2010 [8]
Vertically aligned graphene	Ni	25% KOH	PECVD	Disks	<0.2	1.1	131	-82	2010 [16]
Carbon black	Cellulose or polypropylene	25% KOH	Adhesive coating	Sandwich	0.354	0.44	0.559	-75	2011 [14]
rGO/CNT	Ti/Au	3 M KCl	Electro-deposition	Inter-digitated	4.8		2.8 (50 V s ⁻¹)	-60	2012 [11]
ErGO	Au	25% KOH	Electro-deposition	Inter-digitated	1.35	3.4 (120 Hz)	0.283	-84	2012 [10]
Graphene quantum dots	Au	EMIMBF ₄ /MeCN	Electro-deposition	Inter-digitated	0.054		0.468	-74	2013 [27]
Grown CNT carpets	Ni	1 M Na ₂ SO ₄	CVD	Inter-digitated	0.195	21.3	0.230	-81.5	2013 [9]
SWCNT	Stainless steel	0.5 M H ₂ SO ₄	Cold pressing	Disks	0.199	0.25	0.601	-81	2015 [32]
Poly(3,4-ethylene-dioxythiophene)	Ti/Au	1 M H ₂ SO ₄	Electro-deposition	Inter-digitated	0.8		0.8 (10 V s ⁻¹)	-65	2015 [13]
Graphene/conducting polymer	PET/Au	PVA/H ₂ SO ₄	Spray coating	Flexible	0.472	6.3	0.15 (100 Hz)	-75	2015 [12]
Graphene	Au	1 M H ₂ SO ₄	Cu mediated GO reduction	Inter-digitated	0.35	7.5	0.316	-75.4	2015 [33]
N-doped holey graphene	Au	6 M KOH	Doctor blading, annealing, etching	Sandwich	0.203	0.22	0.478	81.2	2016 [34]
IrCND	Stainless steel	0.1 M TBAPF ₆	Drop casting, laser-reduction	Sandwich	0.29	3.95	0.259	-78	This work

determined by Raman spectroscopy. Higher defects and open pores cause a decrease in sheet conductivity and an increase in capacitance. In the absence of atmospheric oxygen, higher structural integrity of the 3D-carbon films are achieved, subsequently leading to better frequency response in HF-EDLCs. A minimum phase angle of -84° and an RC time constant of 0.29 ms make the electrodes interesting candidates for line filtering applications.

4. Experimental

4.1. Sample preparation

CNDs were synthesized according to previously published protocols [19,35]. CNDs were synthesized by reacting citric acid and urea in a 1:1 mass ratio in deionized H₂O heated in a standard 700 W microwave oven until the solvent evaporated. The CNDs from this reaction were annealed at 300 °C (CND300) under argon for 2 h. 100 mg of CND300 was suspended in 10 mL of a 1:1 (v/v) mixture of *N*-methyl-2-pyrrolidone (NMP) and propan-2-ol (*i*-PrOH) by vigorous stirring overnight. Films were prepared by drop-casting 0.025 mL onto stainless-steel discs and evaporating the solvent at 150 °C. The uniform films were then converted with a Full Spectrum laser engraver in a laser-reaction chamber based on the example discussed in reference 27. The gas inlet was opposite to the gas outlet. A 50 mm diameter zinc selenide window was incorporated in the reaction chamber lid, allowing the CO₂ laser (10.6 μ m) to pass into the gas-reaction chamber. The sample was placed in the center of the chamber. A continuous gas flow of 0.1 L s⁻¹ during the reaction was used. The substrate-supported films were washed by immersing into either NMP or 1 M KOH. After the unreacted CND300 was dissolved, the electrodes were thoroughly rinsed with deionized water and methanol.

4.2. Characterization

Raman spectra were recorded with a Renishaw InVia Raman Microscope using a 633 nm laser as the excitation source. The spectra shown are averaged from 49 spots on a film. Scanning electron microscopy (SEM) was conducted on a Jeol JSM-6700F

with an electron acceleration voltage of 3 kV. Samples were prepared on stainless steel substrates. XPS spectra were recorded using a Kratos Axis Ultra DLD spectrometer equipped with a monochromatic Al K α X-ray source ($h\nu = 1486.6$ eV). High-resolution spectra were calibrated using carbon tape (Ted Pella) with a known C1s binding energy of 284.6 eV. Raw data were processed using CasaXPS software (version 2.3.16). C1s spectra were fit using Gaussian–Lorentzian line-shapes for all spectral components except for the sp² C–C component, which was fitted with an asymmetric line shape to reflect the metallic character of the respective samples. Conductivity measurements were performed on a defined area on a Si substrate. Active surface areas were determined by stirring measured amounts of IrCND300 in solutions of methylene blue in DI water with known concentrations for at least 24 h [36]. The suspended material was then removed by centrifugation at 16 kG and UV–vis absorption spectra of the supernatant recorded. The number of methylene blue molecules adsorbed onto the surfaces was calculated from the difference in absorption at 665 nm with respect to the reference solution. Every methylene blue molecule was assumed to occupy 1.35 nm² of active surface area [37]. For all experiments, polypropylene beakers and vials were used.

EDLCs were assembled in coin cells with electrode diameters of 15 mm and tested under sealed conditions. Electrochemical measurements were conducted on a Biologic VMP3 electrochemical workstation. The areal capacitance C_A was obtained from electrochemical impedance measurements. The RC time constants were determined from the product of the resistance and the capacitance at 120 Hz according to $\tau_{RC} = RC = Z' \cdot 1/2\pi f \cdot Z''$.

Acknowledgments

This work was supported by the Deutsche Forschungsgemeinschaft (German Academic Research Society), grant number STR1508/1-2 (V.S.) and the UCLA Dr. Myung Ki Hong Endowed Chair in Materials Innovation (R.B.K.). We thank the microscopy facility in the UCLA Department of Materials Science and Engineering led by Dr. S.V. Prikhodko for use of their Raman spectrometer.

References

- [1] F. Wang, X. Wu, X. Yuan, Z. Liu, Y. Zhang, L. Fu, Y. Zhu, Q. Zhou, Y. Wu, W. Huang, Latest advances in supercapacitors: from new electrode materials to novel device designs, *Chem. Soc. Rev.* 46 (2017) 6816–6854, <https://doi.org/10.1039/C7CS00205J>.
- [2] D. Premathilake, R.A. Outlaw, S.G. Parler, S.M. Butler, J.R. Miller, Electric double layer capacitors for ac filtering made from vertically oriented graphene nanosheets on aluminum, *Carbon* 111 (2017) 231–237, <https://doi.org/10.1016/j.carbon.2016.09.080>.
- [3] Z. Gao, Y. Zhang, N. Song, X. Li, Biomass-derived renewable carbon materials for electrochemical energy storage, *Mater. Res. Lett.* 5 (2017) 69–88, <https://doi.org/10.1080/21663831.2016.1250834>.
- [4] Q. Wang, J. Yan, Z. Fan, Carbon materials for high volumetric performance supercapacitors: design, progress, challenges and opportunities, *Energy Environ. Sci.* 9 (2016) 729–762, <https://doi.org/10.1039/C5EE03109E>.
- [5] Q. Ke, J. Wang, Graphene-based materials for supercapacitor electrodes – a review, *J. Mater.* 2 (2016) 37–54, <https://doi.org/10.1016/j.jmat.2016.01.001>.
- [6] P.L. Taberna, P. Simon, J.F. Fauvarque, Electrochemical characteristics and impedance spectroscopy studies of carbon-carbon supercapacitors, *J. Electrochem. Soc.* 150 (2003) A292, <https://doi.org/10.1149/1.1543948>.
- [7] Z. Fan, N. Islam, S.B. Bayne, Towards kilohertz electrochemical capacitors for filtering and pulse energy harvesting, *Nano Energy* 39 (2017) 306–320, <https://doi.org/10.1016/j.nanoen.2017.06.048>.
- [8] D. Pech, M. Brunet, H. Durou, P. Huang, V. Mochalin, Y. Gogotsi, P.-L. Taberna, P. Simon, Ultrahigh-power micrometre-sized supercapacitors based on onion-like carbon, *Nat. Nanotechnol.* 5 (2010) 651–654, <https://doi.org/10.1038/nnano.2010.162>.
- [9] J. Lin, C. Zhang, Z. Yan, Y. Zhu, Z. Peng, R.H. Hauge, D. Natelson, J.M. Tour, 3-Dimensional graphene carbon nanotube carpet-based microsupercapacitors with high electrochemical performance, *Nano Lett.* 13 (2013) 72–78, <https://doi.org/10.1021/nl3034976>.
- [10] K. Sheng, Y. Sun, C. Li, W. Yuan, G. Shi, Ultrahigh-rate supercapacitors based on electrochemically reduced graphene oxide for ac line-filtering, *Sci. Rep.* 2 (2012), <https://doi.org/10.1038/srep00247>.
- [11] M. Beidaghi, C. Wang, Micro-supercapacitors based on interdigital electrodes of reduced graphene oxide and carbon nanotube composites with ultrahigh power handling performance, *Adv. Funct. Mater.* 22 (2012) 4501–4510, <https://doi.org/10.1002/adfm.201201292>.
- [12] Z.-S. Wu, Z. Liu, K. Parvez, X. Feng, K. Müllen, Ultrathin printable graphene supercapacitors with AC line-filtering performance, *Adv. Mater.* 27 (2015) 3669–3675, <https://doi.org/10.1002/adma.201501208>.
- [13] N. Kurra, M.K. Hota, H.N. Alshareef, Conducting polymer micro-supercapacitors for flexible energy storage and AC line-filtering, *Nano Energy* 13 (2015) 500–508, <https://doi.org/10.1016/j.nanoen.2015.03.018>.
- [14] P. Kossyrev, Carbon black supercapacitors employing thin electrodes, *J. Power Sources* 201 (2012) 347–352, <https://doi.org/10.1016/j.jpowsour.2011.10.106>.
- [15] M. Cai, R.A. Outlaw, R.A. Quinlan, D. Premathilake, S.M. Butler, J.R. Miller, Fast response, vertically oriented graphene nanosheet electric double layer capacitors synthesized from C₂H₂, *ACS Nano* 8 (2014) 5873–5882, <https://doi.org/10.1021/nn5009319>.
- [16] J.R. Miller, R.A. Outlaw, B.C. Holloway, Graphene double-layer capacitor with ac line-filtering performance, *Science* 329 (2010) 1637–1639, <https://doi.org/10.1126/science.1194372>.
- [17] Y. Zhou, Q. Bao, B. Varghese, L.A.L. Tang, C.K. Tan, C.-H. Sow, K.P. Loh, Microstructuring of graphene oxide nanosheets using direct laser writing, *Adv. Mater.* 22 (2010) 67–71, <https://doi.org/10.1002/adma.200901942>.
- [18] V. Abdelsayed, S. Moussa, H.M. Hassan, H.S. Aluri, M.M. Collinson, M.S. El-Shall, Photothermal deoxygenation of graphite oxide with laser excitation in solution and graphene-aided increase in water temperature, *J. Phys. Chem. Lett.* 1 (2010) 2804–2809, <https://doi.org/10.1021/jz1011143>.
- [19] V. Strauss, K. Marsh, M.D. Kowal, M.F. El-Kady, R.B. Kaner, A simple Route to porous graphene from carbon nanodots for supercapacitor applications, *Adv. Mater.* 30 (2018) 1704449, <https://doi.org/10.1002/adma.201704449>.
- [20] M. Li, M.F. El-Kady, J.Y. Hwang, M.D. Kowal, K. Marsh, H. Wang, Z. Zhao, R.B. Kaner, Embedding hollow Co₃O₄ nanoboxes into a three-dimensional macroporous graphene framework for high-performance energy storage devices, *Nano Res.* 11 (2018) 2836–2846, <https://doi.org/10.1007/s12274-017-1914-7>.
- [21] V. Strong, S. Dubin, M.F. El-Kady, A. Lech, Y. Wang, B.H. Weiller, R.B. Kaner, Patterning and electronic tuning of laser scribed graphene for flexible all-carbon devices, *ACS Nano* 6 (2012) 1395–1403, <https://doi.org/10.1021/nn204200w>.
- [22] M.F. El-Kady, R.B. Kaner, Scalable fabrication of high-power graphene micro-supercapacitors for flexible and on-chip energy storage, *Nat. Commun.* 4 (2013) 1475, <https://doi.org/10.1038/ncomms2446>.
- [23] J.Y. Hwang, M.F. El-Kady, M. Li, C.-W. Lin, M. Kowal, X. Han, R.B. Kaner, Boosting the capacitance and voltage of aqueous supercapacitors via redox charge contribution from both electrode and electrolyte, *Nano Today* 15 (2017) 15–25, <https://doi.org/10.1016/j.nantod.2017.06.009>.
- [24] V. Strauss, A. Roth, M. Sekita, D.M. Guldi, Efficient energy-conversion materials for the future: understanding and tailoring charge-transfer processes in carbon nanostructures, *Chem* 1 (2016) 531–556, <https://doi.org/10.1016/j.chempr.2016.09.001>.
- [25] V. Strauss, A. Kahnt, E.M. Zolnhofer, K. Meyer, H. Maid, C. Placht, W. Bauer, T.J. Nacken, W. Peukert, S.H. Etschel, M. Halik, D.M. Guldi, Assigning electronic states in carbon nanodots, *Adv. Funct. Mater.* 26 (2016) 7975–7985, <https://doi.org/10.1002/adfm.201602325>.
- [26] V. Strauss, Ecofriendly carbon nanomaterials for future electronic applications, *Chem* 2 (2017) 319–321, <https://doi.org/10.1016/j.chempr.2017.02.012>.
- [27] W.-W. Liu, Y.-Q. Feng, X.-B. Yan, J.-T. Chen, Q.-J. Xue, Superior micro-supercapacitors based on graphene quantum dots, *Adv. Funct. Mater.* 23 (2013) 4111–4122, <https://doi.org/10.1002/adfm.201203771>.
- [28] Y. Li, D.X. Luong, J. Zhang, Y.R. Tarkunde, C. Kittrell, F. Sargunara, Y. Ji, C.J. Arnsch, J.M. Tour, Laser-induced graphene in controlled atmospheres: from superhydrophilic to superhydrophobic surfaces, *Adv. Mater.* 29 (2017) 1700496, <https://doi.org/10.1002/adma.201700496>.
- [29] L.M. Malard, M.A. Pimenta, G. Dresselhaus, M.S. Dresselhaus, Raman spectroscopy in graphene, *Phys. Rep.* 473 (2009) 51–87, <https://doi.org/10.1016/j.physrep.2009.02.003>.
- [30] A.C. Ferrari, J. Robertson, Raman spectroscopy of amorphous, nanostructured, diamond-like carbon, and nanodiamond, *Philos. Trans. A Math. Phys. Eng. Sci.* 362 (2004) 2477–2512, <https://doi.org/10.1098/rsta.2004.1452>.
- [31] The “high-frequency hooks” are artefacts due to inaccurate calibration of the instrument, very likely a inductive effect from the cable. The Non-zero Capacitance at Zero Potential Is Due to a Defect Electrical Connection in the Instrument. (n.d.).
- [32] Y. Rangom, X. (Shirley) Tang, L.F. Nazar, Carbon nanotube-based supercapacitors with excellent ac line filtering and rate capability via improved interfacial impedance, *ACS Nano* 9 (2015) 7248–7255, <https://doi.org/10.1021/acs.nano.5b02075>.
- [33] Z. Wu, L. Li, Z. Lin, B. Song, Z. Li, K.-S. Moon, C.-P. Wong, S.-L. Bai, Alternating current line-filter based on electrochemical capacitor utilizing template-patterned graphene, *Sci. Rep.* 5 (2015) 10983, <https://doi.org/10.1038/srep10983>.
- [34] Q. Zhou, M. Zhang, J. Chen, J.D. Hong, G. Shi, Nitrogen-doped holey graphene film-based ultrafast electrochemical capacitors, *ACS Appl. Mater. Interfaces* 8 (2016) 20741–20747, <https://doi.org/10.1021/acsami.6b05601>.
- [35] J.T. Margraf, F. Lodermeier, V. Strauss, P. Haines, J. Walter, W. Peukert, R.D. Costa, T. Clark, D.M. Guldi, Using carbon nanodots as inexpensive and environmentally friendly sensitizers in mesoscopic solar cells, *Nanoscale Horiz.* 1 (2016) 220–226, <https://doi.org/10.1039/C6NH00010J>.
- [36] S. Naeem, V. Baheti, J. Wiener, J. Marek, Removal of methylene blue from aqueous media using activated carbon web, *J. Text. Inst.* 108 (2017) 803–811, <https://doi.org/10.1080/00405000.2016.1191745>.
- [37] P.T. Hang, Methylene blue absorption by clay minerals. Determination of surface areas and cation exchange capacities (clay-organic studies XVIII), *Clays Clay Miner.* 18 (1970) 203–212, <https://doi.org/10.1346/CCMN.1970.0180404>.



Cite this: DOI: 10.1039/c9nr01719d

Patching laser-reduced graphene oxide with carbon nanodots†

Volker Strauss,^{ID} *^{a,b} Mit Muni,^a Arie Borenstein,^{ID} ^{a,c} Bolortuya Badamdorj,^b Tobias Heil,^b Matthew D. Kowal^a and Richard Kaner^{ID} *^{a,d}

Three-dimensional graphenes are versatile materials for a range of electronic applications and considered among the most promising candidates for electrodes in future electric double layer capacitors (EDLCs) as they are expected to outperform commercially used activated carbon. Parameters such as electrical conductivity and active surface area are critical to the final device performance. By adding carbon nanodots to graphene oxide in the starting material for our standard laser-assisted reduction process, the structural integrity (*i.e.* lower defect density) of the final 3D-graphene is improved. As a result, the active surface area in the hybrid starting materials was increased by 130% and the electrical conductivity enhanced by nearly an order of magnitude compared to pure laser-reduced graphene oxide. These improved material parameters lead to enhanced device performance of the EDLC electrodes. The frequency response, *i.e.* the minimum phase angle and the relaxation time, were significantly improved from -82.2° and 128 ms to -84.3° and 7.6 ms, respectively. For the same devices the specific gravimetric device capacitance was increased from 110 to a maximum value of 214 F g⁻¹ at a scan rate of 10 mV s⁻¹.

Received 25th February 2019,

Accepted 20th June 2019

DOI: 10.1039/c9nr01719d

rsc.li/nanoscale

Introduction

Tailored carbon nanomaterials are gaining significance for electronics and energy conversion and storage applications because of carbon's low cost and structural and electronic tunability.¹ In particular, graphene and its derivatives are expected to play a decisive role.² With respect to energy storage, during the past few years interest in designing graphene electrodes for capacitor and battery applications has grown rapidly.^{3,4} This is mainly due to their promising materials characteristics such as extraordinary electronic conductivity and high theoretical active surface area.⁵ Both these properties are fundamental for electric double layer capacitor (EDLC) electrodes and graphene has been shown to outperform commercially used activated carbon in terms of capacitance, charging rates, and cycle life at least in the laboratory.⁶ A major drawback, however, is that after exfoliation 2D-graphene sheets tend to reagglomerate which impedes the exploitation of their intrinsic

high surface area.⁷ Therefore, different methods have been developed to arrange the graphene sheets in a 3D-arrangement to ensure interconnectivity and electrical conductance between the layers, while enabling the larger part of the sheets exposure to the electrolyte.^{8,9} Due to the resulting structure, these porous graphenes are often referred to as graphene aerogels or graphene foams. In some cases porous 3D-carbon monoliths are a more appropriate description as the materials only partially possess a graphenic nature.¹⁰ Summaries and categorizations of fabrication methods for 3D-graphenes are found in several review articles and books.^{4,8,9,11}

Most fabrication methods for porous 3D-graphenes fall in either of two categories, namely the template-assisted or the template-free approach. In the first category, soft or hard templates like surfactants or metal/metal oxides or salts are used as templates for graphene oxide reduction or CVD graphene growth.^{12–16} These approaches, in general, allow for control over the pore size and structure. Template-free approaches, on the other hand, include chemical activation of carbon or thermal or photo-induced reduction of graphene oxide as well as graphitization or carbonization of small molecules or polymers.^{17–20}

A particularly interesting approach is the direct laser-assisted conversion of graphene oxide (GO) or carbon nanodots (CNDs).^{21–27} In the past years, laser-reduction of GO has been studied as a versatile method to fabricate and micro-pattern nanoelectronic devices.²⁸ Laser-reduced GO is composed of randomly oriented single graphene sheets that are partially stacked with specific surface areas (SSA) of

^aDepartment of Chemistry and Biochemistry and California NanoSystems Institute, University of California, Los Angeles (UCLA), Los Angeles, CA, USA.

E-mail: kaner@chem.ucla.edu

^bMax Planck Institut für Kolloid – und Grenzflächenforschung Am Mühlenberg 1, 14476 Potsdam, Germany. E-mail: volker.strauss@mpikg.mpg.de

^cChemistry Department, Ariel University, Ariel, Israel

^dDepartment of Materials Science and Engineering, UCLA, Los Angeles, CA, USA

†Electronic supplementary information (ESI) available. See DOI: 10.1039/c9nr01719d

800–1500 m² g⁻¹.^{26,27} On the other hand, laser-reduced CNDs form a porous material with a more bubble-like appearance featuring lower SSAs of ~230 m² g⁻¹.^{23,24} Despite the low surface area, the benefits of CNDs or reduced CNDs, in particular, are higher electrical conductivity and faster frequency response in the final electrodes.^{29–32} Moreover, they act as suitable starting materials for uniform functional composite materials.²⁵

In general, CNDs and GO can be considered related materials. Both consist of two-dimensional π -conjugated carbon with oxygen containing functional groups. According to XPS data, the carbon content in GO is typically between 65–75%, while in CNDs the carbon content is between 55–75%, but values differ depending on the analysis methods and preparation routes used.^{33,34} The remaining elemental fraction includes functional groups like hydroxyls, carboxylates, and/or epoxides attached to the carbon skeleton. Depending on the synthesis method for CNDs, nitrogen-containing functional groups like amines and amides may also be present. Thermal or photo-induced removal of these functional groups leads to a restoration of the π -conjugation and an opening of pores due to evaporating gases.²⁸

In this work we investigate the impact of CNDs as additives to GO in the starting material for creating laser-reduced 3D-graphene electrodes. The uniform GO/CND mixtures were simultaneously reduced in our standard CO₂-laser-assisted reduction process to obtain thin films of 3D-graphene. To gain insights into the reaction mechanism, we carefully analyzed these films in terms of mass loss and structure. Structural information about the porous material was obtained using scanning electron microscopy (SEM), transmission electron microscopy (TEM), electron energy loss spectroscopy (EELS), and Raman spectroscopy. Electrical and structural characterization of the films yielded improvements in electrical conductivity and SSA by a factor of ten and 130%, respectively. Electrochemical impedance spectroscopy revealed improvements of the minimum phase angle and the relaxation time from -82.2° and 128 ms to -84.3° and 7.6 ms, respectively. Finally, the performance of the films as electrodes in EDLCs in terms of capacitance was tested by cyclic voltammetry. A maximum specific gravimetric device capacitance of 214 F g⁻¹ at 10 mV s⁻¹ was achieved, which is an improvement of more than twice the original value of pure laser-reduced GO.

Results and discussion

A set of GO-containing solutions with different amounts of CNDs ranging from 0–65 wt% were prepared to test the effect of CNDs during the laser-assisted reduction of graphene oxide. Seven aqueous solutions with a constant amount of GO and variable amounts of CNDs were prepared. To this end, homogeneous mixtures of CNDs and GO were prepared by stirring both components in the solvent (NMP/*i*-PrOH (1:1 v/v) or H₂O) for at least 24 h. As CNDs are added to GO, a mixture of both materials is established, *i.e.* both materials are dispersed in the solvent. The resulting dispersions are stable for weeks (Fig. S1†).³⁵ Interactions between the two materials are most likely van der Waals interactions and π - π -stacking along with ionic interactions due to the polar nature of the carbon-oxygen bonds and carboxyl-centered surface charges of both components.^{36–38} After 24 h, highly homogeneous mixtures are established. From these solutions uniform films were prepared by drop-casting on defined areas. The GO/CND films were then reduced in our standard laser assisted process as depicted in Fig. 1.^{23–26}

To ensure equal mass loading throughout the samples on the substrates prior to the laser-reduction step, the amount of applied solution was adjusted accordingly (Table 1). Solutions were either prepared in H₂O or in a 1:1 mixture of *N*-methyl-2-pyrrolidone (NMP) and iso-propanol (*i*-PrOH) (NMP/*i*-PrOH (1:1 v/v)) to produce uniform films. When using H₂O as the solvent, slow vacuum-assisted drying helped to avoid delamination during the drying process. When using NMP/*i*-PrOH as the solvent, drying was achieved by evaporating the solvent at an elevated temperature (~100 °C) using a precision hotplate. Solutions with a higher CND content (>30 wt%) dried faster and tended to delaminate upon drying or laser-reduction. GO is known to swell in water and traps a substantial number of water molecules between the layers. The small CNDs also intercalate between the GO layers and, thereby, displace water molecules. Presumably, during solvent evaporation surface tension due to a drying gradient between the upper and the lower layer causes delamination.

The cast films were analyzed in terms of mass before and after the laser-reduction process. In general, higher laser power causes more material to be removed (evaporated) during

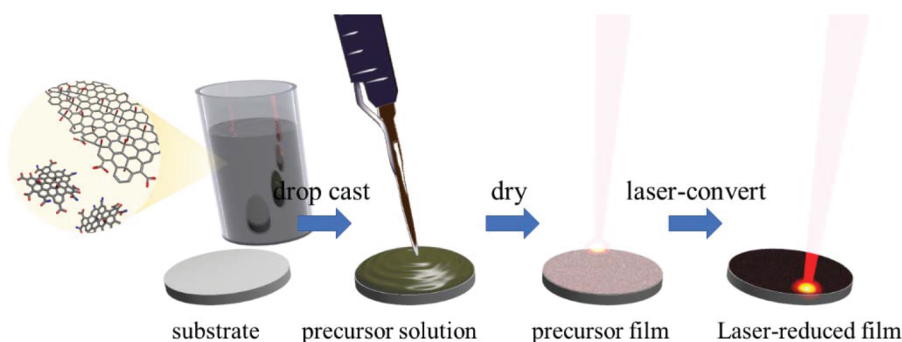


Fig. 1 Illustration of the preparation procedures for the sample films.

Table 1 Concentrations of GO and CNDs Used^a

Sample	c(GO) (mg mL ⁻¹)	c(CND) (mg mL ⁻¹)	m(GO) (mg cm ⁻²)	m(CND) (mg cm ⁻²)	m _{overall} (mg cm ⁻²)	mass fraction CND (wt%)
1	3.63	0.00	0.51	0.00	0.51	0
2	3.63	0.25	0.48	0.03	0.51	6
3	3.63	0.50	0.45	0.06	0.51	12
4	3.63	1.09	0.39	0.12	0.51	23
5	3.63	1.67	0.35	0.16	0.51	32
6	3.63	3.35	0.27	0.25	0.51	48
7	3.63	6.69	0.18	0.33	0.51	65

^aThe concentrations of GO and CND used in the precursor solutions 1–7 are given in columns 2 and 3. The mass loading of components in a typical film for EDLCs are given in columns 4–6. The final mass fraction of CND in the solutions and the films are provided in column 7.

the laser-reduction process. Detailed structural characterization and reaction mechanisms of the laser-reduction process of GO or CNDs have been published previously.^{22,23,26,27} In all our experiments the same laser power was used, and it was found that the investigated samples react differently upon laser impact. The precursor films with higher CND mass fractions are more stable against laser-induced evaporation (Fig. S2†). This effect is most likely caused by a synergistic influence of both GO and CNDs, which is explained based on our experimental findings in the following paragraphs. For all experiments this mass difference was taken into account and the films with equal mass loadings in regard to the final active films on the substrates were analyzed.

The laser-reduced GO/CND films were characterized by means of SEM, TEM, EELS, and Raman spectroscopy. In Fig. 2a representative SEM images of six laser-reduced samples with different mass fractions of CNDs are shown. Comparing the images reveals that increasing the mass fraction of CNDs in the precursor mixture leads to an apparent increase in the

structural integrity of the films. This trend is seen throughout the samples. Higher and lower magnification images are shown in Fig. S3.† Notably, in the high CND mass fraction precursor film (6) bubble-like objects are found (Fig. S4†), that are typical of purely reduced CND phases.^{23,24} These patterns are presumably formed by enclosed aggregates of CNDs.

The graph in Fig. 2b shows a set of representative normalized Raman spectra of samples 1–6 (black to red). All spectra are composed of four major peaks assigned to the D, G, D' and G' bands at 1329, 1576, 1607 and 2647 cm⁻¹, respectively. The entire spectra of representative samples are presented in Fig. S5.† In general, the pattern is similar for all tested samples. However, differences in the D-band intensity are striking. The D-band diminishes with increasing CND mass fraction until ~65% in the precursor solution. As the D-band is related to defects within the graphitic network, we conclude that the defect density is lower when higher amounts of CNDs are present in a given sample. In the film with 70 wt% CNDs, the D-band starts to increase which is attributed to an excess

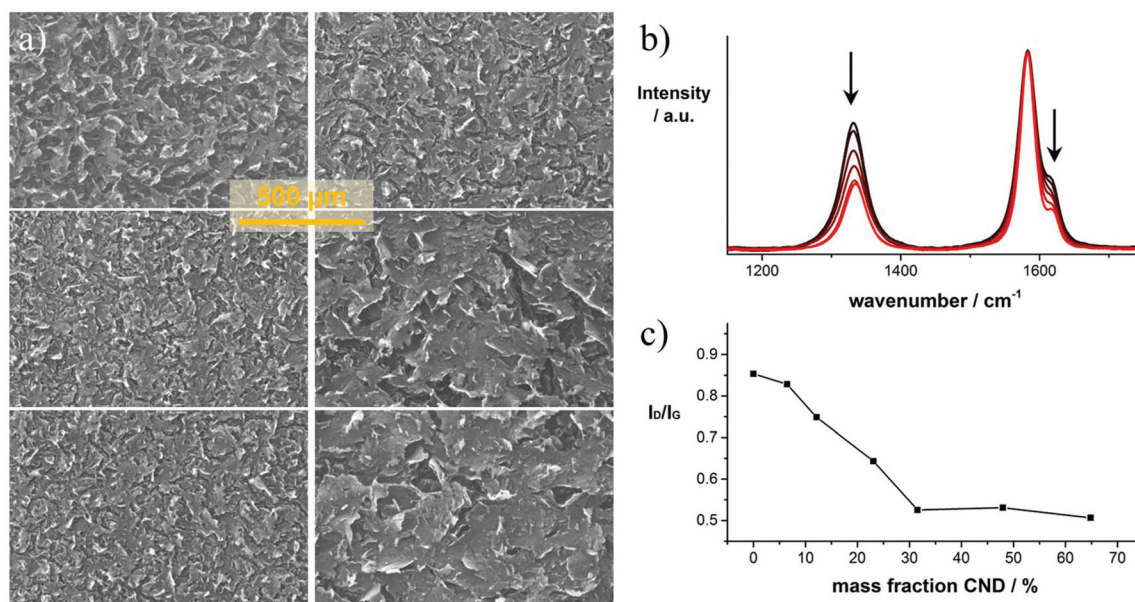


Fig. 2 Structural characterization of laser-reduced GO/CND films; (a) low-magnification SEM images of laser-converted films of samples (1, 3, 4, 5, 6, 7) from top left down to bottom right. (b) Raman spectra of samples 1–6 (black to red) obtained upon excitation at 633 nm; (c) plot showing the D/G-intensity ratios versus the mass fraction of CNDs in the precursor solution.

of CNDs that do not interconnect with the reduced GO layers, but rather form purely reduced CNd phases (Fig. S4†). The position of the G-band is maintained throughout the samples as determined by systematic fitting of the Raman spectra (Fig. S6†). Only minor shifts in the range between 1582.6 to 1583.5 cm^{-1} are observed, but no clear trend is found.

Deeper insights into the microscopic structure and chemical composition of the samples were obtained by TEM and EELS. In Fig. S7† representative TEM images of samples 1, 3, and 6 are shown. Samples 1 and 3 consist of flat reduced GO sheets as typically seen for reduced GO.²⁸ Likewise, in sample 3, sheets of monolayer graphene were observed. Upon taking a closer look, blobs in a size regime of 5–10 nm on the converted carbon sheets were observed. These are not seen in sample 1, in the absence of CNds. In sample 6, with a CNd mass fraction of 48%, a significant amount of bubble-like objects stemming from the laser reduction of pure CNd phases, as already shown in Fig. S4† are observed. Several spots in the tested samples were analyzed by EELS to gain information about the chemical composition. Sample 1 is composed of 99% carbon. In samples 3 and 6, traces of nitrogen and oxygen on the order of 1–4% were identified as shown in Fig. S8.† Notably, the carbon peaks in all samples show a typical graphene structure, indicating a successful conversion into graphitic/graphenic materials.

In the next step, the SSA of the laser-converted films from samples 1–7 were determined. Due to the low mass loadings of only $\sim 0.1 \text{ mg cm}^{-2}$ the methylene blue (MB) adsorption method (see Experimental section) rather than BET measurements was chosen. The data of the MB absorption measurements are presented in Fig. S9.† As a general trend, we observe that up to a mass fraction of $\sim 30\%$ CNds, the SSA increases from 782 to 1010 $\text{m}^2 \text{g}^{-1}$ with an increasing amounts of CNds in the precursor solution (Fig. 3a). This effect can be attributed

to the higher structural integrity and the CNds acting as spacers between the laser-reduced GO sheets in the reduced film. The decrease of the SSA for CNd mass fractions of $>40\%$ is attributed, again, to purely reduced CNd phases (Fig. S4†). Pure laser-reduced CNds exhibit a SSA of $230 \text{ m}^2 \text{g}^{-1}$.²³

The electrical conductivities were obtained from laser-reducing a series of films with equal mass from solutions 1–7 on defined areas of electronically insulating SiO_2 wafers. The thus determined sheet conductivities are plotted in Fig. 3b. With an increasing mass fraction of CNd, the conductivity increases from 118 to 904 S m^{-1} for samples 1 through 7, respectively. The increase follows a nearly linear trend.

The above results show improved materials' characteristics for the laser-reduced 3D-graphene obtained from simultaneous reduction of GO and CNds during the laser-assisted reduction process. Mechanistically, the impacting laser energy is dissipated across the GO sheets, which subsequently de-oxygenates the GO. Excess heat leads to ripping apart of the GO sheets and partial carbon removal by an oxidation/combustion process. A probable explanation is a synergistic effect of both reactive components, CNds and GO, during the laser-induced reaction. As the GO sheets are de-oxygenated, reduced CNds or their reaction products occurring during the laser treatment react with the reactive sites on the GO sheets and thus reduce the defects induced during laser-reduction. From the blobs observed in the TEM analysis, an interaction of this kind may be inferred. This "patching" results in a lower defect density in the 3D-carbon network. Similar effects regarding the healing of defects in GO have been observed in chemical vapor deposition experiments.³⁹ Another positive effect on the SSA and the electrical conductivity that may be hypothesized in a mechanistic model is the improved inter-layer heat dissipation during the laser-reduction due to the presence of CNds between the GO layers. Their presence may promote the establishment of improved interconnections between the GO layers, which leads to a milder de-oxygenation upon absorption of excess heat energy across the layers and thus, the reduction of occurring defects. At the same time, CNds between the GO layers could act as spacers and increase the SSA during the laser-reduction by forming conductive bridges between these layers. These assumptions will require more detailed future analysis of the laser-reduced GO/CNd hybrids.

The positive effect of the structural and electronic properties points to improved performance in EDLC electrodes. To test the electrochemical properties of the carbon electrodes, three-electrode electrochemical measurements were conducted with samples 1, 3, and 6. To this end, defined amounts of precursor solution were applied on top of stainless steel current collectors and subsequently laser-reduced. Fig. S11† shows the cyclic voltammograms of sample 3 in 1.0 M Na_2SO_4 as the electrolyte. In the tested voltage window, no apparent redox peaks were observed, indicating a purely capacitive charge storage mechanism. This is supported by the quasi-triangular shapes of the galvanostatic charge–discharge curves. In the impedance measurements shown in Fig. S11† additional evidence for the capacitive charge storage mechanism is found.

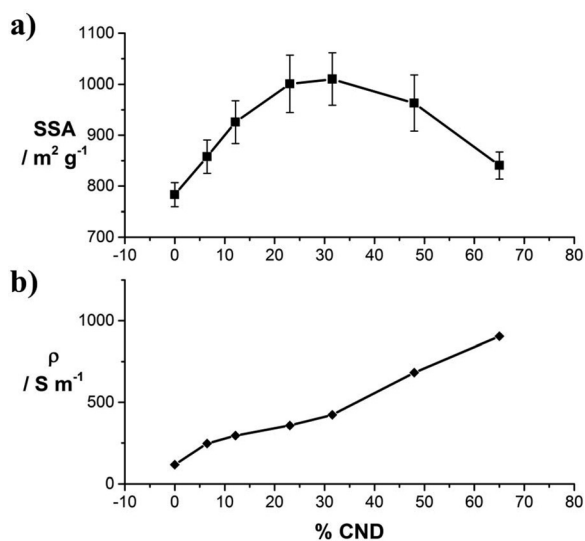


Fig. 3 (a) Specific surface areas of 1–7 obtained by the methylene blue adsorption method; (b) sheet conductivity of samples 1–7, plotted as a function of the mass fraction of CNds.

The increase in electrical conductivity and SSA upon adding CNDs is beneficial for the performance of laser-reduced GO as electrode materials in EDLCs. To quantify the effect on the electrochemical properties symmetric device assemblies of our electrodes with equal amounts of active material were tested under sealed conditions in coin cells. The active material was directly laser converted on stainless steel discs that served as the current collectors (Fig. S10[†]). A full characterization of the cells is shown for two example cells, produced from samples 1 (0 wt% CNDs) and 5 (32 wt% CNDs), in Fig. 4. The data of the other samples are shown in the ESI.[†] The mass loading of the active material on the current collector was 0.1 mg, used equally for all samples.

In Fig. 4a, the mass normalized cyclic voltammograms of 1 and 5 in 6.0 M KOH are shown. Both curves have a rectangular shape typical for purely capacitive behavior. Addition of CNDs to GO in 5 leads to an increase in capacitance and a slightly improved curve shape. From the CV curves of samples 1–9 we calculated the specific gravimetric capacitance, which is plotted *versus* the CND mass fraction in the precursor solution in Fig. 4b. Due to rather low mass loadings on the electrodes, the measurement error is potentially high, however, a clear trend towards higher capacitance upon addition of CNDs to GO is noticeable. Maximum values are achieved with a CND

mass fraction of 32%. The same trend was also observed in reference measurements using 0.5 M TBAPF₆ in acetonitrile as the electrolyte (Fig. S12[†]). The specific capacitance in organic electrolytes is generally lower. Here, a maximum capacitance was also achieved with a CND mass fraction of 32%. The entire data set for the gravimetric capacitances determined in dependence of the scan rate are plotted in Fig. S13.[†]

In galvanostatic charge–discharge measurements of the same cells at different current densities (Fig. S14[†]), quasi-triangular curve shapes were obtained for all tested samples. Small internal resistance (*IR*) drops of, for example, 0.125 or 0.027 V upon discharging at 76 A g⁻¹ for 1 or 5, respectively, are observed at the beginning of the discharge curves. From these values equivalent series resistances of 2.19 Ω or 0.47 Ω for 1 or 5 in 6.0 M KOH are obtained, respectively. Specific gravimetric capacitances determined from these charge–discharge curves (Fig. S15[†]) are in good agreement with the values obtained from cyclic voltammetry. Notably, the presence of CNDs also supports the cycling stability of the cells. Sample 1 exhibits excellent cycling stability with retention of the initial capacitance of 90.5% after 20 000 cycles. Upon addition of a mass fraction of 32% CNDs (sample 5), a significant improvement with retention up to 98.5% after 20 000 cycles is observed (Fig. S16[†]).

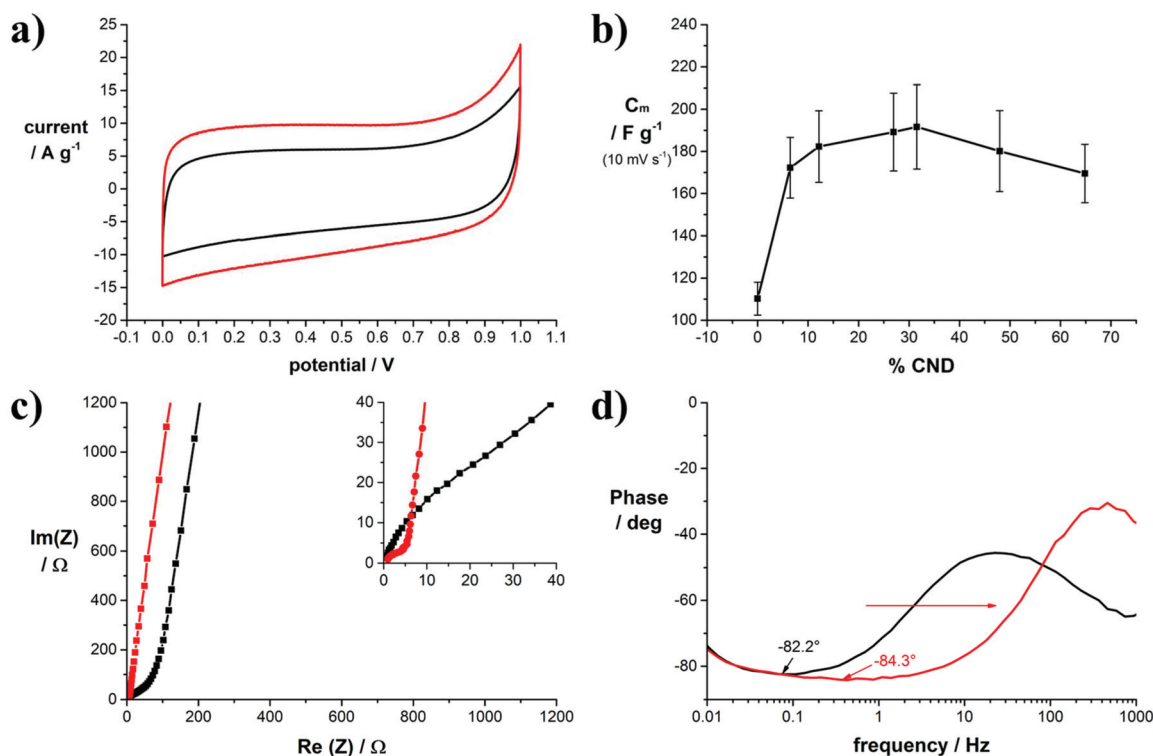


Fig. 4 Electrochemical characterization of symmetric coin cell capacitors with different GO/CND mass ratios; (a) representative cyclic voltammograms of coin cell capacitors assembled with electrodes of 1 (black) and 5 (red) in 6.0 M KOH as the electrolyte at a scan rate of 100 mV s⁻¹; (b) specific gravimetric capacitance *versus* mass fraction of CNDs contained in the precursor solution determined by cyclic voltammetry at a scan rate of 10 mV s⁻¹; (c) representative Nyquist impedance plots of coin cell capacitors assembled with electrodes of 1 (black) and 5 (red) in 6.0 M KOH as the electrolyte; inset: zoom-in to the high-frequency region; (d) representative phase angle plots of coin cell capacitors assembled with electrodes of 1 (black) and 5 (red) in 6.0 M KOH as the electrolyte.

The frequency response of the cells was tested subsequently by electrochemical impedance spectroscopy. The graph in Fig. 4c compares the Nyquist plots of samples 1 and 5. Clearly, in sample 1 the high frequency region up to $\text{Re}(Z) = 80 \Omega$ is dominated by Warburg-type impedance as indicated by a 45° phase angle. The absence of this Warburg-type element in sample 5 points to a change in pore structure compared to sample 1.

The minimum phase angle of 84.3° in sample 5 is reached at a frequency of 1 Hz, while the minimum phase angle of 82.2° in sample 1 is reached at a phase angle of only 0.1 Hz. As shown in Fig. 4d, addition of CNDs to the precursor material results in lower minimum phase angles and a wider capacitive frequency region with minimum phase angles close to -90° ,⁴⁰ thereby widening the operative frequency region of the capacitor. As a reference, in commercial activated carbon-based EDLCs, a minimum phase angle of -85.6° was measured; however, this showed a smaller active frequency region (Fig. S17†). The improved frequency response is also reflected in the phase angle diagram presented in Fig. 4d. For example, the capacitive frequency window of the capacitors made from sample 5 is larger by more than one order of magnitude in Hz. Throughout the tested cells an improvement towards wider capacitive frequency windows is noted as shown in Fig. S18.† Typically, the frequency value at a phase angle of -45° between the resistive and the capacitive region translates to the relaxation time of the cell. This is a measure for the transition from capacitive to resistive behavior in a capacitor (RC circuit). Without the addition of CNDs, the relaxation time is 128 ms, while the lowest value measured for a CND mass fraction of 32% is 7.6 ms. Therefore, addition of CNDs to reduced GO electrodes enables operation at higher frequencies.

These trends were also observed in reference cells using an organic electrolyte. The minimum phase angles measured in the organic electrolyte are generally higher throughout all the cells. An improvement from -73.9° for sample 1 to -78.1° for samples 3 and 6 was achieved. The relaxation times improve from 100.8 ms for sample 1 to 26.9 ms for sample 5.

Conclusions

We have conducted a comprehensive study on the role of carbon nanodots (CNDs) as additives to graphene oxide (GO) in the starting material for laser-reduced GO in EDLC electrodes. In a complementary analysis of scanning electron microscopy (SEM), transmission electron microscopy (TEM), electron energy loss spectroscopy (EELS) and Raman spectroscopy, we found that the addition of CNDs to the starting material helps maintain a high structural integrity of the final 3D-graphene in the laser-assisted reduction process. Independent of the amount of CNDs, the chemical analysis yields a carbon content of $>96\%$. Raman spectroscopy of a range of samples with different amounts of CNDs added show that the defect density in the final 3D-graphene films is significantly reduced at a CND mass fraction of $\sim 30\%$. Moreover,

electrical conductivity was improved by one order of magnitude and the active surface area was enhanced by 130%. These structural improvements lead to an increase in gravimetric device capacitance from 110 to 214 F g^{-1} at a scan rate of 10 mV s^{-1} and an enhanced frequency response, determined by the minimum phase angle and the relaxation time. The simultaneous laser-reduction mechanism of graphene and carbon nanodots is currently under investigation.

Experimental

Synthesis

Carbon nanodots (CNDs). For CND synthesis we followed previously published protocols in which a detailed description is available.^{23,37,41,42} CNDs were prepared by reacting equal masses of citric acid and urea in H_2O in a regular household microwave oven (700 W) until the solvent was completely evaporated. The residue was annealed at 300°C in a tube furnace in an argon atmosphere for 2 h.

Graphene oxide (GO). Graphene oxide was synthesized *via* a modified version of Hummers' method. 10 g of graphite (Asbury 3775) was added to 500 ml of prechilled, 0°C conc. sulfuric acid (EMD). 60 g of KMnO_4 (Sigma Aldrich) was then added to the mixture slowly while cooling externally, maintaining a temperature below 15°C . The reaction was left to stir with external cooling for 2 h, followed by a dropwise addition of deionized water over an additional hour, reaching an average temperature of $65 \pm 5^\circ\text{C}$. The reaction continued to be stirred for an additional hour followed by quenching with 2.8 L of deionized H_2O and 30 ml of H_2O_2 (30%). Purification was performed by washing the GO 5 times with 1 L of 10% HCl, followed by 2 washes with 1 L of deionized water. Finally, GO was dialyzed (Spectrum, Spectrum/POR membrane MWCO 6–8000) for 2 weeks.

Sample preparation

In H_2O . 17 mg of GO and different amounts of CNDs ranging from 0 to 40 mg (samples 1–10) were stirred in deionized H_2O for at least 24 h at room temperature. Defined amounts of these solutions were drop-cast on defined areas of substrates and the solvent was evaporated at room temperature under reduced pressure to ensure homogeneous drying.

In NMP/i-PrOH (1:1 v/v). 17 mg of GO and different amounts of CNDs ranging from 0 to 40 mg (samples 1–10) were stirred in NMP/i-PrOH (1:1 v/v) for at least 24 h at room temperature. Defined amounts of these solutions were drop-cast on defined areas of substrates and the solvent was evaporated on a hotplate at 100°C to ensure homogeneous drying.

The films were then reduced using a 40 W CO_2 Laser engraver (Full Spectrum – glass tube laser source). To compensate for the instrument intrinsic laser intensity deviations, we conducted arrays of experiments, all on the same day and under the same conditions. However, some stray results due to the laser instrument cannot be ruled out.

Microscopy

Scanning electron microscopy (SEM) was conducted on a JEOL JSM-6700F with an electron acceleration voltage of 3 kV. Samples were prepared on either stainless steel or SiO₂ substrates.

Transmission electron microscopy (TEM) and electron energy loss spectroscopy (EELS) were conducted using a double-cs-corrected Jeol ARM200F, equipped with a cold field emission gun. The acceleration voltage was put to 200 kV, the emission was set to 5 μ A and a condenser aperture with a diameter of 150 μ m was used. Samples were transferred by dipping the Lacey carbon grid onto the as-prepared laser-reduced films.

Determination of the I_D/I_G -ratios

Raman spectra were recorded with a Renishaw InVia Raman Microscope. For each sample 16 Raman spectra were recorded in mapping mode. The separation between the spots was 10 μ m. The obtained spectra were baseline corrected and averaged using Wire 3.4 software. The D and G-band regions between 1150 and 1750 cm^{-1} of the averaged spectra were fit with three Lorentzians.

Determination of the sheet conductivity

Defined amounts of precursor solutions were drop-cast on a defined area (5 \times 17 mm) of an insulating SiO₂ substrate. After evaporation of the solvent, the films were laser-reduced. The short ends of the films were connected to measure the resistance of the films. From the resistance of the films, the sheet resistance was determined using the thickness and the area of the films. The lead and contact resistance from the probing electrodes was neglected as they were two orders of magnitude smaller than the resistance of the film.

Determination of the active surface area

The GO/CND films were laser-reduced on substrates with defined areas and the mass was determined. The substrates with the laser-reduced films were immersed into solutions of methylene blue (MB) in DI water with known concentrations and stirred vigorously. After 24 h the solutions were centrifuged at 16 000 rpm to remove any suspended material.⁴³ The number of MB molecules adsorbed onto the surfaces was calculated from the difference in absorption at 665 nm with respect to the reference solution. Every MB molecule is assumed to occupy 1.35 nm² of the active surface area.⁴⁴ For all experiments involving MB, polypropylene beakers and vials were used. The spectra are shown in Fig. S9.†

Electrochemical measurements

All electrochemical measurements were performed with a Biologic VMP3 electrochemical workstation.

Solution-based measurements were conducted with a three-electrode setup using an Ag/AgCl reference electrode and platinum foil as a counter electrode. The active material was applied on a stainless steel strip which was used as the working electrode.

Quantitative measurements were conducted in a symmetric device geometry. Cyclic voltammetry, charge–discharge curves, and electrochemical impedance spectroscopy was recorded with a Biologic VMP3 electrochemical workstation. Symmetric electrochemical capacitors were assembled in coin cells with electrode diameters of 15 mm and tested under sealed conditions.

Determination of the volumetric capacitance. The volumetric capacitance C_V was determined by dividing the positive integrated current $\int IdV$ by the volume of the film V , the scan rate ν and the potential scan range ($E_1 - E_0$).

Conflicts of interest

There are no conflicts to declare.

Acknowledgements

This work was supported by the Deutsche Forschungsgemeinschaft (German Academic Research Society), grant number STR1508/1-2 (V. S.) and the Dr Myung Ki Hong Endowed Chair in Materials Innovation (R. B. K.). We thank the microscopy facility in the UCLA Department of Materials Science and Engineering led by Dr S. V. Prikhodko for use of their Raman spectrometer.

References

- 1 V. Georgakilas, J. a. Perman, J. Tucek and R. Zboril, *Chem. Rev.*, 2015, **115**, 4744–4822.
- 2 J. K. Wassei and R. B. Kaner, *Acc. Chem. Res.*, 2013, **46**, 2244–2253.
- 3 M. F. El-Kady, Y. Shao and R. B. Kaner, *Nat. Rev. Mater.*, 2016, **1**, 16033.
- 4 *Nanocarbons for Advanced Energy Storage*, ed. X. Feng, Wiley-VCH Verlag GmbH & Co. KGaA, Weinheim, Germany, 2015.
- 5 Y. Sun, Q. Wu and G. Shi, *Energy Environ. Sci.*, 2011, **4**, 1113.
- 6 Y. Shao, M. F. El-Kady, L. J. Wang, Q. Zhang, Y. Li, H. Wang, M. F. Mousavi and R. B. Kaner, *Chem. Soc. Rev.*, 2015, **44**, 3639–3665.
- 7 S. He and W. Chen, *Nanoscale*, 2015, **7**, 6957–6990.
- 8 X. Yao and Y. Zhao, *Chem*, 2017, **2**, 171–200.
- 9 S. Han, D. Wu, S. Li, F. Zhang and X. Feng, *Adv. Mater.*, 2014, **26**, 849–864.
- 10 A.-H. Lu, G.-P. Hao, Q. Sun, X.-Q. Zhang and W.-C. Li, in *Chemical Synthesis and Applications of Graphene and Carbon Materials*, Wiley-VCH Verlag GmbH & Co. KGaA, Weinheim, Germany, 2016, pp. 115–157.
- 11 *Chemical Synthesis and Applications of Graphene and Carbon Materials*, ed. M. Antonietti and K. Müllen, Wiley-VCH Verlag GmbH & Co. KGaA, Weinheim, Germany, 2017.

- 12 H. Zhan, D. J. Garrett, N. V. Apollo, K. Ganesan, D. Lau, S. Prawer and J. Cervenka, *Sci. Rep.*, 2016, **6**, 19822.
- 13 Z. Chen, W. Ren, L. Gao, B. Liu, S. Pei and H.-M. Cheng, *Nat. Mater.*, 2011, **10**, 424–428.
- 14 Y. Wang, L. Tao, Z. Xiao, R. Chen, Z. Jiang and S. Wang, *Adv. Funct. Mater.*, 2018, **28**, 1705356.
- 15 S. Dou, X. Wang and S. Wang, *Small Methods*, 2018, 1800211.
- 16 D. Liu, L. Tao, D. Yan, Y. Zou and S. Wang, *ChemElectroChem*, 2018, **5**, 1775–1785.
- 17 Y. Xu, K. Sheng, C. Li and G. Shi, *ACS Nano*, 2010, **4**, 4324–4330.
- 18 X.-F. Jiang, X.-B. Wang, P. Dai, X. Li, Q. Weng, X. Wang, D.-M. Tang, J. Tang, Y. Bando and D. Golberg, *Nano Energy*, 2015, **16**, 81–90.
- 19 D. Ge, L. Yang, L. Fan, C. Zhang, X. Xiao, Y. Gogotsi and S. Yang, *Nano Energy*, 2015, **11**, 568–578.
- 20 J. Lin, Z. Peng, Y. Liu, F. Ruiz-Zepeda, R. Ye, E. L. G. Samuel, M. J. Yacaman, B. I. Yakobson and J. M. Tour, *Nat. Commun.*, 2014, **5**, 5714.
- 21 M. F. El-Kady, V. Strong, S. Dubin and R. B. Kaner, *Science*, 2012, **335**, 1326–1330.
- 22 V. Strong, S. Dubin, M. F. El-Kady, A. Lech, Y. Wang, B. H. Weiller and R. B. Kaner, *ACS Nano*, 2012, **6**, 1395–1403.
- 23 V. Strauss, K. Marsh, M. D. Kowal, M. F. El-Kady and R. B. Kaner, *Adv. Mater.*, 2018, **30**, 1704449.
- 24 V. Strauss, M. Anderson, C. L. Turner and R. B. Kaner, *Mater. Today Energy*, 2019, **11**, 114–119.
- 25 V. Strauss, M. Anderson, C. Wang, A. Borenstein and R. B. Kaner, *Small*, 2018, 1803656.
- 26 A. Borenstein, V. Strauss, M. D. Kowal, M. Yoonessi, M. Muni, M. Anderson and R. B. Kaner, *J. Mater. Chem. A*, 2018, **6**, 20463–20472.
- 27 K. Griffiths, C. Dale, J. Hedley, M. D. Kowal, R. B. Kaner and N. Keegan, *Nanoscale*, 2014, **6**, 13613–13622.
- 28 R. Kumar, R. K. Singh, D. P. Singh, E. Joanni, R. M. Yadav and S. A. Moshkalev, *Coord. Chem. Rev.*, 2017, **342**, 34–79.
- 29 Y.-Q. Dang, S.-Z. Ren, G. Liu, J. Cai, Y. Zhang and J. Qiu, *Nanomaterials*, 2016, **6**, 212.
- 30 Q. Li, H. Cheng, X. Wu, C.-F. F. Wang, G. Wu and S. Chen, *J. Mater. Chem. A*, 2018, **6**, 14112–14119.
- 31 G. Yuan, X. Zhao, Y. Liang, L. Peng, H. Dong, Y. Xiao, C. Hu, H. Hu, Y. Liu and M. Zheng, *J. Colloid Interface Sci.*, 2019, **536**, 628–637.
- 32 S. Bak, D. Kim and H. Lee, *Curr. Appl. Phys.*, 2016, **16**, 1192–1201.
- 33 M. Nováček, O. Jankovský, J. Luxa, D. Sedmidubský, M. Pumera, V. Fila, M. Lhotka, K. Klímová, S. Matějková and Z. Sofer, *J. Mater. Chem. A*, 2017, **5**, 2739–2748.
- 34 *Graphene Oxide*, ed. A. M. Dimiev and S. Eigler, John Wiley & Sons, Ltd, Chichester, UK, 2016.
- 35 D. Konios, M. M. Stylianakis, E. Stratakis and E. Kymakis, *J. Colloid Interface Sci.*, 2014, **430**, 108–112.
- 36 F. Baskoro, C.-B. Wong, S. R. Kumar, C.-W. Chang, C.-H. Chen, D. W. Chen and S. J. Lue, *J. Membr. Sci.*, 2018, **554**, 253–263.
- 37 V. Strauss, J. T. Margraf, C. Dolle, B. Butz, T. J. Nacken, J. Walter, W. Bauer, W. Peukert, E. Spiecker, T. Clark and D. M. Guldi, *J. Am. Chem. Soc.*, 2014, **136**, 17308–17316.
- 38 P. Yu, X. Wen, Y.-R. Toh, Y.-C. Lee, K.-Y. Huang, S. Huang, S. Shrestha, G. Conibeer and J. Tang, *J. Mater. Chem. C*, 2014, **2**, 2894.
- 39 S. Grimm, M. Schweiger, S. Eigler and J. Zaumseil, *J. Phys. Chem. C*, 2016, **120**, 3036–3041.
- 40 A. Noori, M. F. El-Kady, M. S. Rahmanifar, R. B. Kaner and M. F. Mousavi, *Chem. Soc. Rev.*, 2019, **48**, 1272–1341.
- 41 J. T. Margraf, F. Lodermeier, V. Strauss, P. Haines, J. Walter, W. Peukert, R. D. Costa, T. Clark and D. M. Guldi, *Nanoscale Horiz.*, 2016, **1**, 220–226.
- 42 V. Strauss, A. Kahnt, E. M. Zolnhofer, K. Meyer, H. Maid, C. Placht, W. Bauer, T. J. Nacken, W. Peukert, S. H. Etschel, M. Halik and D. M. Guldi, *Adv. Funct. Mater.*, 2016, **26**, 7975–7985.
- 43 S. Naeem, V. Baheti, J. Wiener and J. Marek, *J. Text. Inst.*, 2017, **108**, 803–811.
- 44 P. T. Hang, *Clays Clay Miner.*, 1970, **18**, 203–212.

Supporting Information to
Patching Laser-Reduced Graphene Oxide with Carbon
Nanodots

Volker Strauss, Mit Muni, Arie Borenstein, Bolortuya Badamdorj, Tobias Heil, Matthew D. Kowal,
Richard Kaner

Sample overview	19
Scanning electron microscopy	20
Raman spectroscopy.....	21
Transmission electron microscopy and electron energy loss spectroscopy.....	22
Specific surface area measurements	23
Voltammetry	23
Three-electrode measurements.....	24
Reference measurements in organic electrolyte	25
Capacitance	25
Galvanostatic charge-discharge measurements.....	26
Electrochemical impedance spectroscopy.....	27

Sample overview

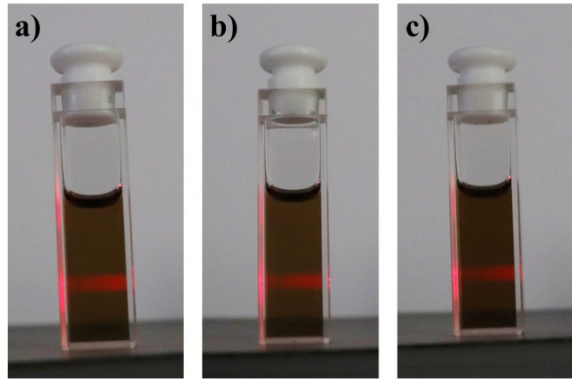


Figure S1. Photograph of precursor solutions of 1, 3, and 6 in NMP after one week under illumination with a laser pointer demonstrating the Tyndall effect.

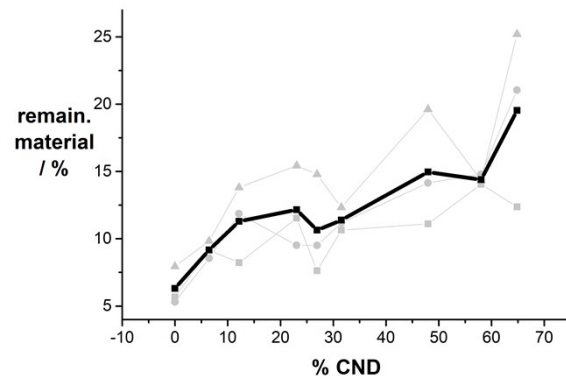


Figure S2. Percentage of the remaining mass of the films after laser-reduction obtained from a series of experiments (shown in gray).

Scanning electron microscopy

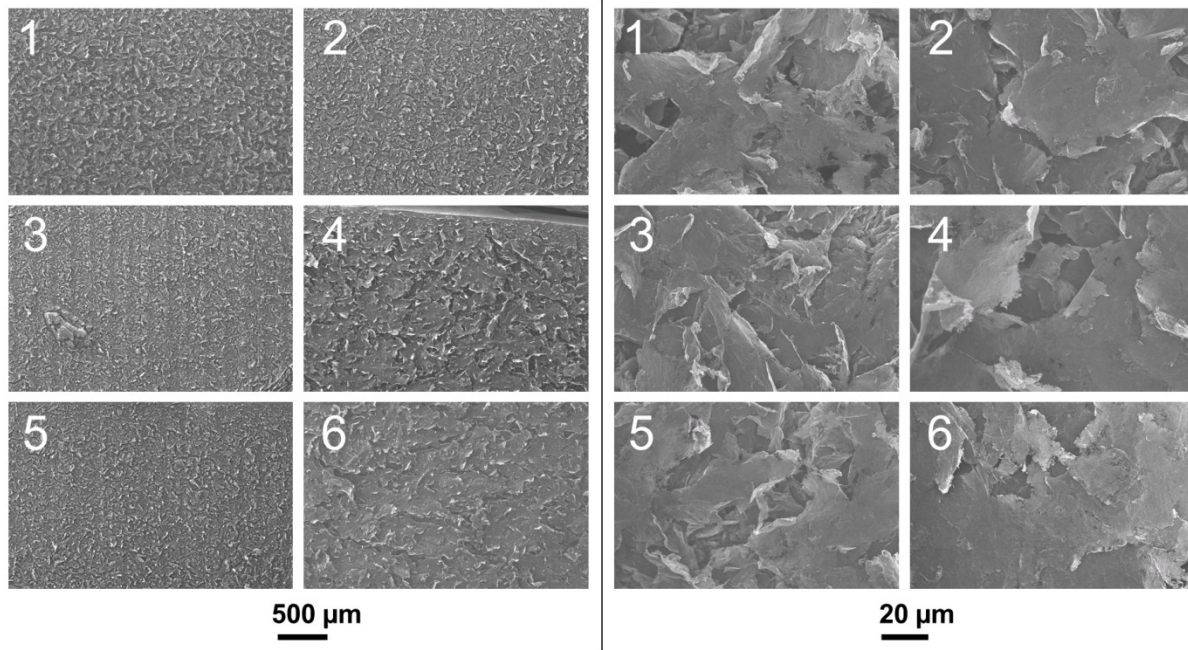


Figure S3. SEM images of laser-converted films of samples 1 – 6 from top left down to bottom right at low-magnification (left) and high-magnification (right), see scale bars.

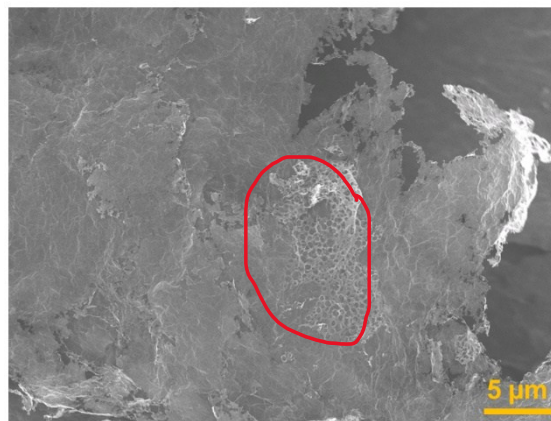


Figure S4. SEM image of a laser-converted film of sample 6 showing a converted pattern with excess CNDs.

Raman spectroscopy

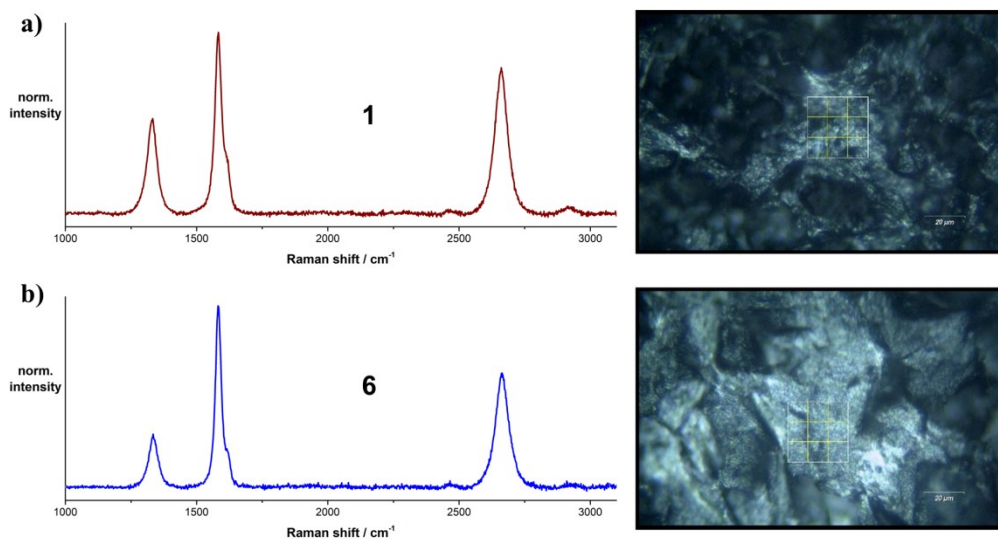


Figure S5. Averaged Raman spectrum obtained from a map composed of 16 spots (depicted on the right) of laser-reduced samples a) **1** and b) **6** using a 633 nm laser as the excitation source.

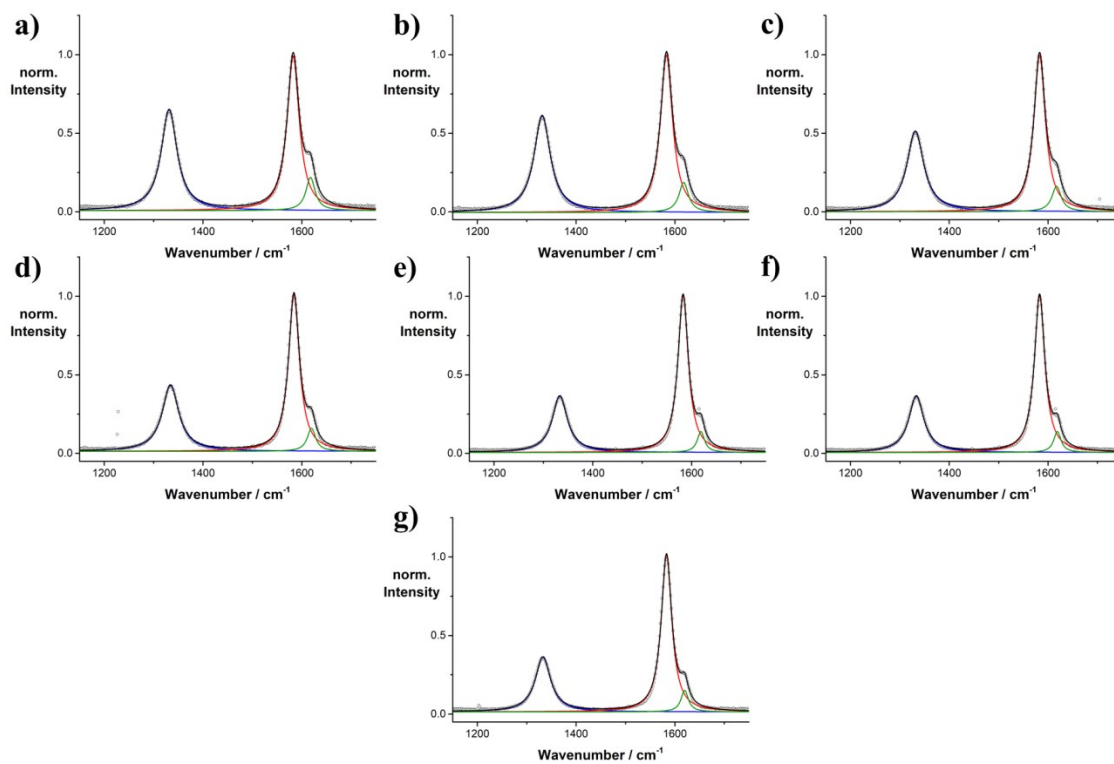


Figure S6. Lorentz fitting of averaged Raman spectra of laser-reduced samples **1** – **7** (a – g).

Transmission electron microscopy and electron energy loss spectroscopy

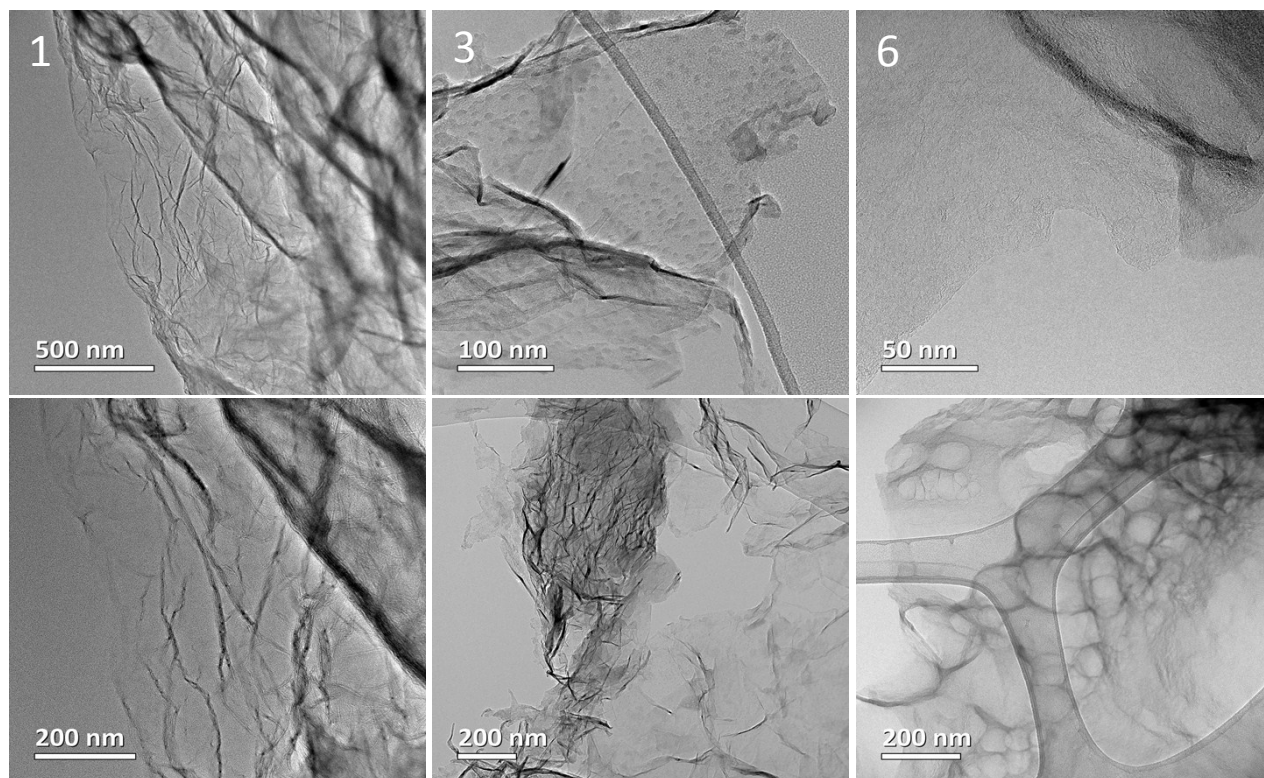


Figure S7. Representative TEM images of samples **1**, **3** and **6** obtained at an acceleration voltage of 200 kV.

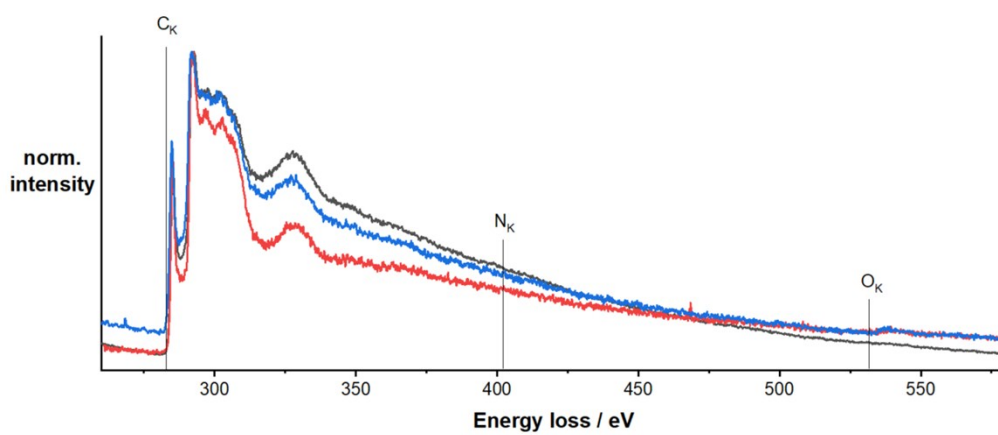


Figure S8. Electron energy loss spectra of samples **1** (black), **3** (red) and **6** (blue).

Specific surface area measurements

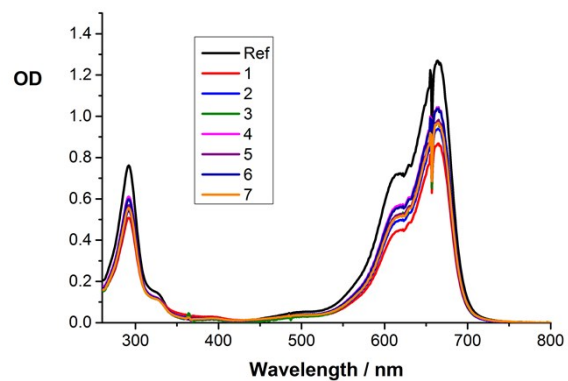


Figure S9. UV-vis absorption spectra of the methylene blue stock solution ($c = 4.3 \times 10^{-5} M$) in black and the same solution after adsorbing ~ 0.1 mg of samples **1** – **7**.

Voltammetry

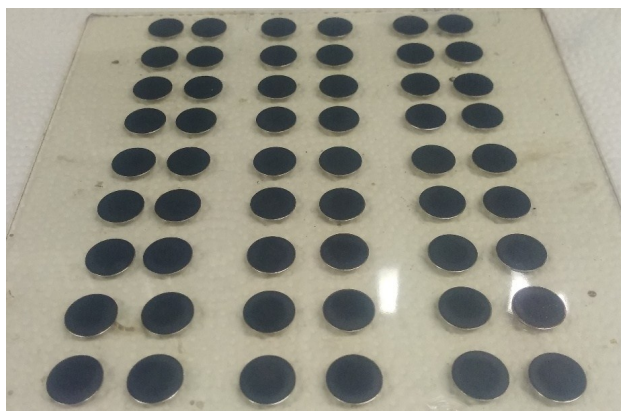


Figure S10. Photograph of the laser-reduced films on stainless-steel disks.

Three-electrode measurements

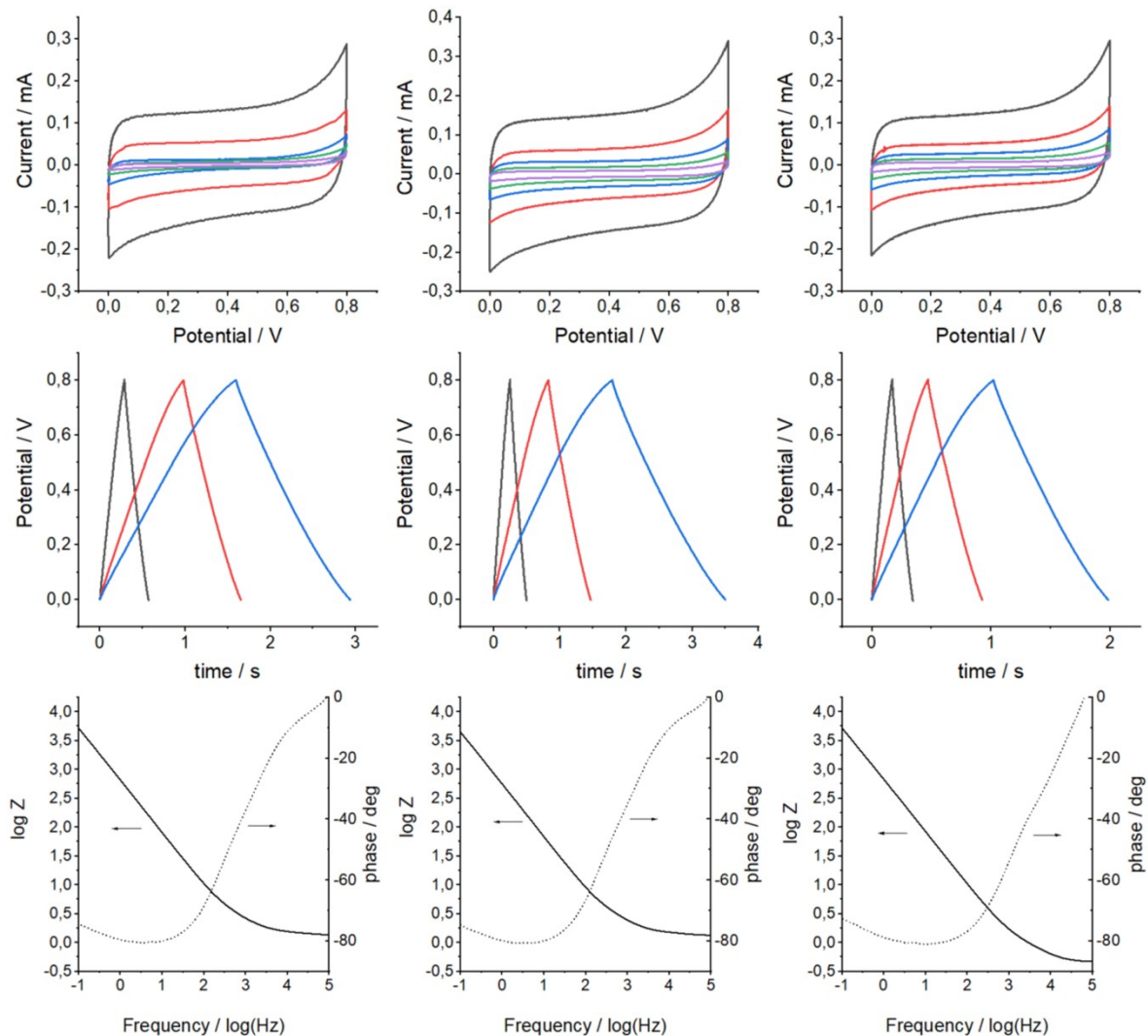


Figure S11. Electrochemical characterization electrodes fabricated from samples **1** (left column), **3** (center), and **6** (right) in 1.0 M Na_2SO_4 using an Ag/AgCl reference electrode; a) Cyclic voltammograms in 1.0 M Na_2SO_4 as electrolyte at different scan rates between 500 and 10 mV s^{-1} ; b) Galvanostatic charge discharge curves obtained at different current densities of 7 (blue), 9 (red), and 10 (Ag^{-1}) in 1.0 M Na_2SO_4 ; c) Representative Bode impedance plots of the electrodes in 1.0 M Na_2SO_4 as the electrolyte.

Reference measurements in organic electrolyte

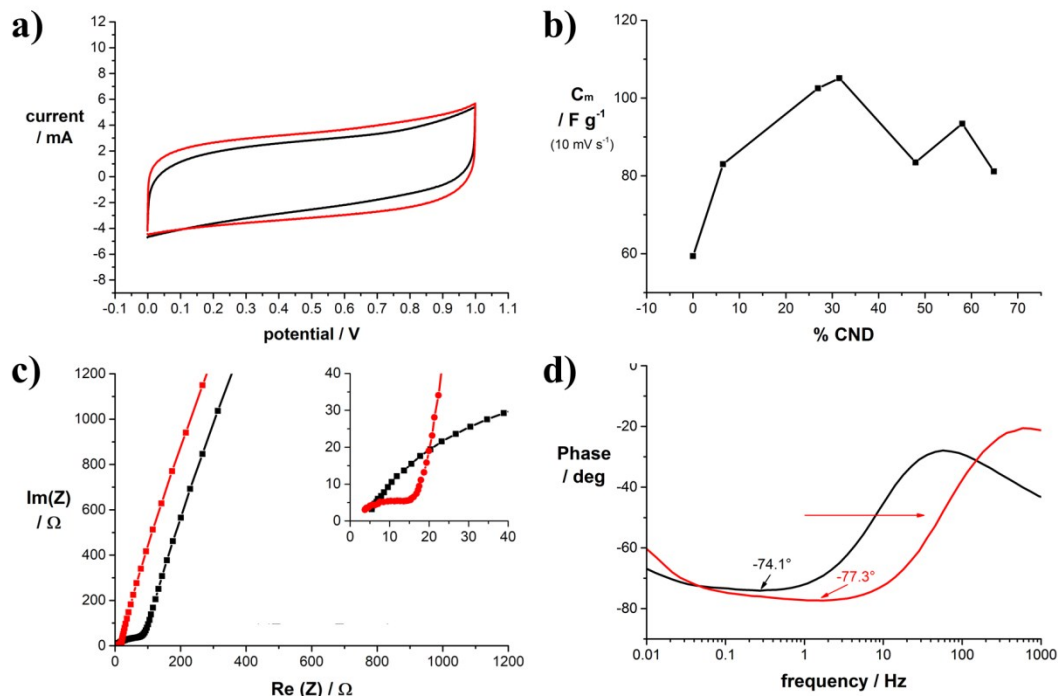


Figure S12. Electrochemical characterization of symmetric coin cell capacitors with different CND/GO mass ratios; a) Representative cyclic voltammograms of coin cell capacitors assembled with electrodes of sample 1 (black) and sample 5 (red) in 0.5 M TBAPF₆ in acetonitrile as electrolyte at a scan rate of 100 mV s⁻¹; b) Specific gravimetric capacitance versus mass fraction of CNDs contained in the precursor solution determined by cyclic voltammetry at a scan rate of 10 mV s⁻¹; c) Representative Nyquist impedance plots of coin cell capacitors assembled with electrodes of sample 1 (black) and sample 5 (red) in 0.5 M TBAPF₆ in acetonitrile as the electrolyte; d) Representative Phase-angle diagrams of coin cell capacitors assembled with electrodes of sample 1 (black) and sample 5 (red) in 0.5 M TBAPF₆ in acetonitrile as the electrolyte;

Capacitance

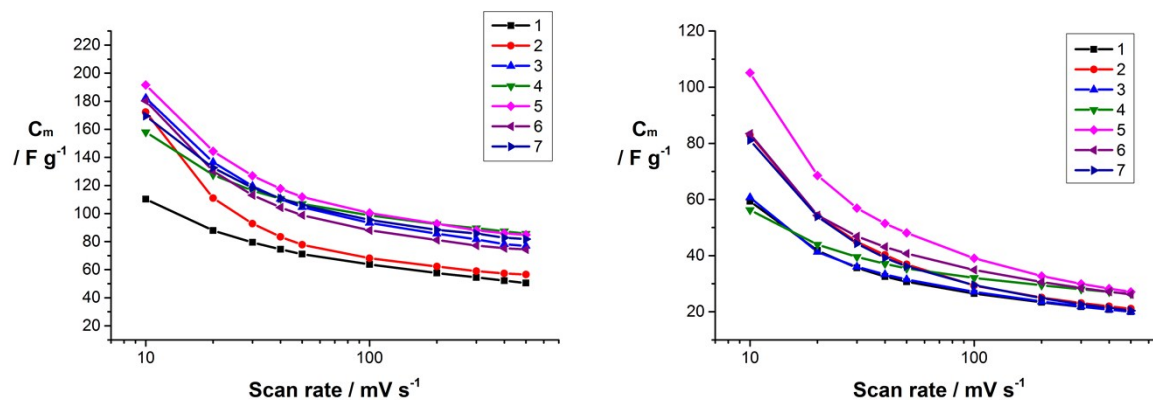


Figure S13. Specific gravimetric capacitances of samples 1 – 7 as a function of the scan rate in 6.0 M KOH (left) and in 0.5 M TBAPF₆ in acetonitrile as electrolyte (right).

Galvanostatic charge-discharge measurements

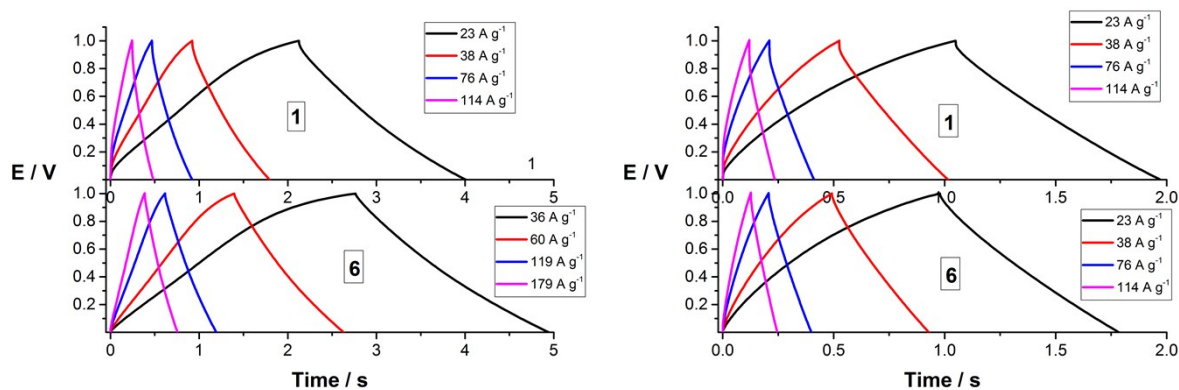


Figure S14. Galvanostatic charge discharge curves of samples **1** and **6** obtained at different current densities in 6.0 M KOH (left) and 0.5 M TBAPF₆ in acetonitrile (right).

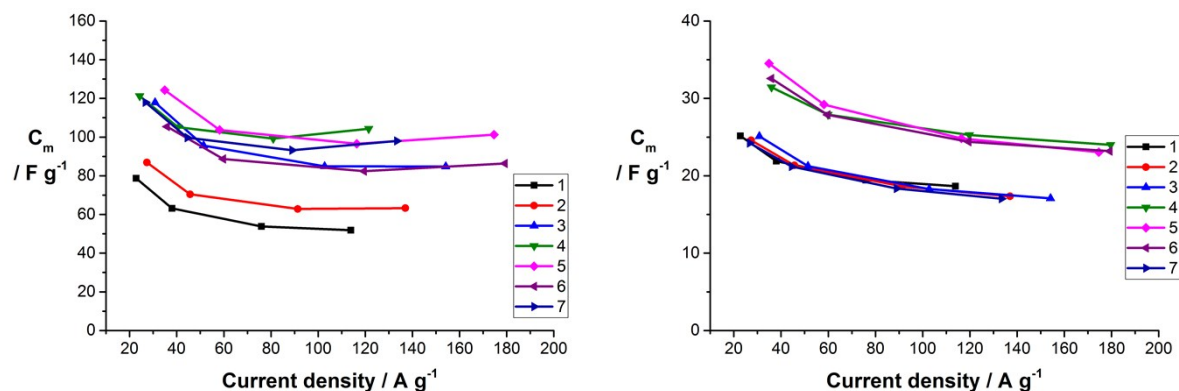


Figure S15. Specific gravimetric capacitances of samples **1** – **7** as a function of the current density in 6.0 M KOH (left) and in 0.5 M TBAPF₆ in acetonitrile as electrolyte (right).

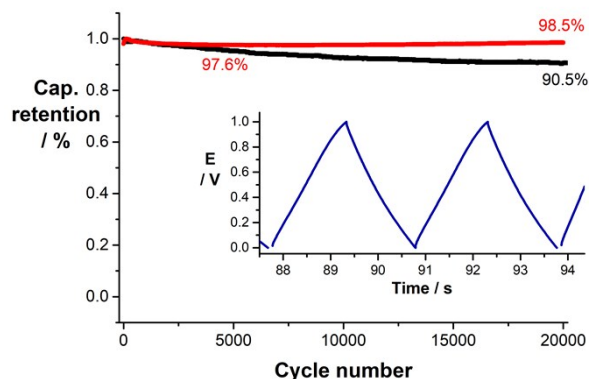


Figure S16. Capacitance retention of capacitor cells with sample **1** (black) and sample **6** (red) in 6.0 M KOH after 20,000 charge discharge cycles. Inset: Galvanostatic charge discharge curves of sample **6** obtained with a current density of 7.5 A g⁻¹.

Electrochemical impedance spectroscopy

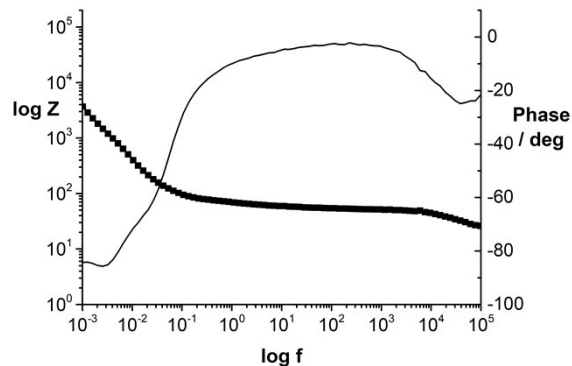


Figure S17. Representative Bode plot of a commercial activated carbon based EDLC.

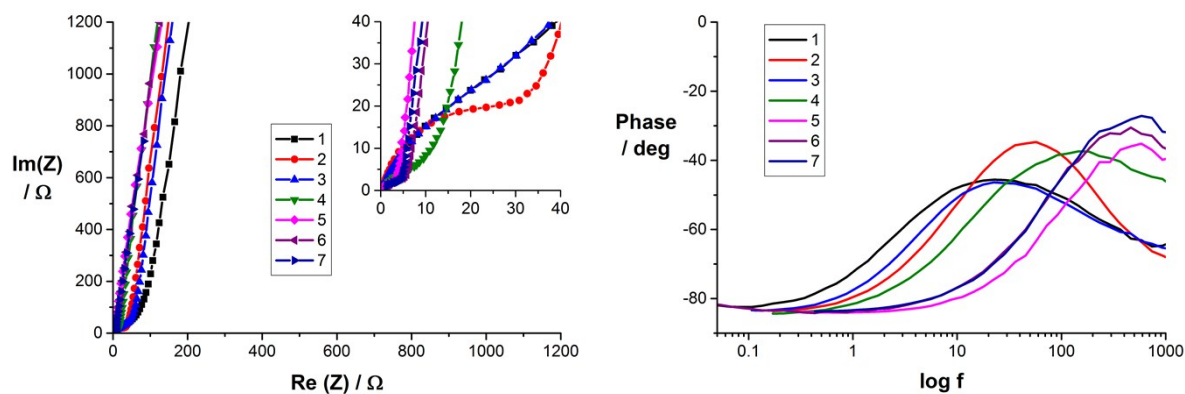


Figure S18. Left: Nyquist impedance plots of coin cell capacitors assembled with electrodes of samples 1 – 7 in 6.0 M KOH as electrolyte; Right: Phase angle plots of coin cell capacitors assembled with electrodes of samples 1 – 7 in 6.0 M KOH as the electrolyte.

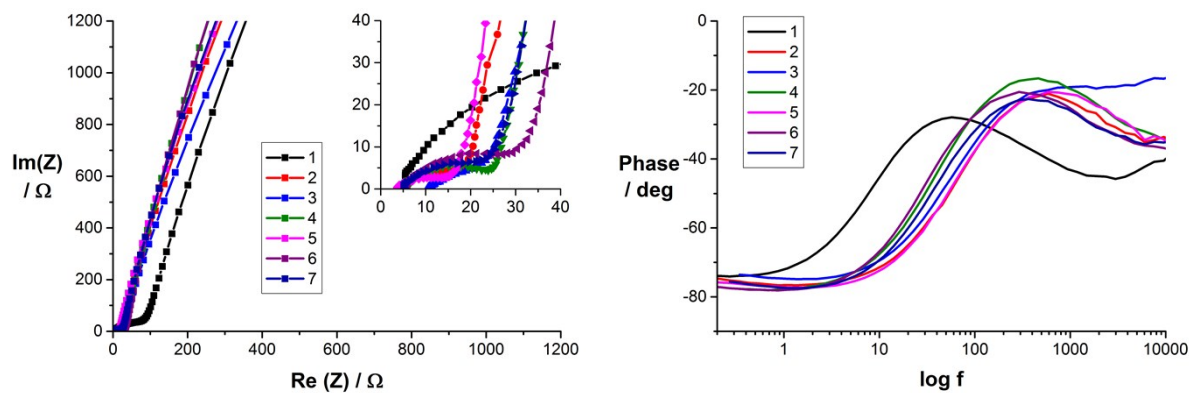


Figure S19. Left: Nyquist impedance plots of coin cell capacitors assembled with electrodes of samples 1 – 7 in 0.5 M TBAPF₆ in acetonitrile as the electrolyte; Right: Phase angle plots of coin cell capacitors assembled with electrodes of samples 1 – 7 with 0.5 M TBAPF₆ in acetonitrile as the electrolyte.

On-Chip Direct Laser Writing of PAN-Based Carbon Supercapacitor Electrodes

Andreas Hoffmann, Pablo Jiménez-Calvo, Joachim Bansmann, Volker Strauss,*
and Alexander J. C. Kuehne*

The carbonization of polyacrylonitrile (PAN) by direct laser writing to produce microsupercapacitors directly on-chip is reported. The process is demonstrated by producing interdigitated carbon finger electrodes directly on a printed circuit board (PCB), which is then employed to characterize the supercapacitor electrodes. By varying the laser power, the process can be tuned from carbonization to material ablation. This allows to not only convert pristine PAN films into carbon electrodes, but also to pattern and cut away non-carbonized material to produce completely freestanding carbon electrodes. While the carbon electrodes adhere well to the printed circuit board, non-carbonized PAN is peeled off the substrate. Specific capacities as high as $260 \mu\text{F cm}^{-2}$ are achieved in a supercapacitor with 16 fingers.

materials have been explored for carbon-based microsupercapacitors electrodes, with the aim of increasing the surface area to yield acceptable capacitance despite their small size.^[7–12] However, fabrication techniques to produce the required electrode geometries are limited to off-chip methods. The solvents or high processing temperatures employed to obtain carbonized, conductive electrode material are incompatible with typical electronic chip materials. Certainly, patterning and carbonization of carbon precursor materials remain possible off-chip; however, off-chip carbonization, in turn, requires precise and

1. Introduction

Miniaturized electric double-layer capacitors—termed microsupercapacitors—enable integrated energy storage directly on the chip, facilitating self-sufficient devices without a large periphery for external power supply and management systems.^[1–3] Such devices for on-chip energy storage could potentially transform the way we employ wearable and textile electronics and foster the development of autonomous microrobots.^[4–6] Different classes of organic and inorganic

complicated placing, interfacing, and integration of the manufactured supercapacitor on the dedicated chip.^[13]

We and others have previously reported on laser-induced carbonization of PAN-based carbon-fibers and other carbon-precursors.^[14–18] Conventional carbonization of PAN is performed in convection ovens at temperatures $>1000 \text{ }^\circ\text{C}$.^[19,20] By contrast, laser-induced carbonization is beneficial, as heat is locally produced in the focus of the laser, preventing exposure to high temperatures in undesired areas. Moreover, laser-carbonization is fast, potentially allowing pattern formation of carbonized PAN when scanning the laser focus across a film.^[21]

However, pristine PAN is transparent in the visible and near IR spectrum, which requires the addition of a photosensitizer to enable its laser carbonization. CNTs are robust laser-absorbers and have previously been shown to improve the performance of carbonized materials by increasing their electrical conductivity^[22] and surface area.^[23]

Here, we demonstrate how interdigitated carbon electrodes can be directly laser-patterned into a film of CNT sensitized PAN to produce microsupercapacitors. We perform direct laser-writing on commercially available PCB to demonstrate that the laser-written carbon structures are well interfaced with the metallic current collectors on the PCB and that our laser process does not interfere with the materials of the substrate. The resulting supercapacitor electrodes are then characterized and benchmarked using an ionic liquid electrolyte.

A. Hoffmann, A. J. C. Kuehne
Institute of Organic and Macromolecular Chemistry
Ulm University

Albert-Einstein-Allee 11, 89081 Ulm, Germany
E-mail: alexander.kuehne@uni-ulm.de

P. Jiménez-Calvo, V. Strauss
Department of Colloid Chemistry
Max-Planck-Institute of Colloids and Interfaces
Am Mühlenberg 1, 14476 Potsdam, Germany
E-mail: volker.strauss@mpikg.mpg.de

J. Bansmann
Institute of Surface Chemistry and Catalysis
Ulm University
Albert-Einstein-Allee 47, 89069 Ulm, Germany

 The ORCID identification number(s) for the author(s) of this article can be found under <https://doi.org/10.1002/marc.202100731>

© 2022 The Authors. Macromolecular Rapid Communications published by Wiley-VCH GmbH. This is an open access article under the terms of the Creative Commons Attribution-NonCommercial-NoDerivs License, which permits use and distribution in any medium, provided the original work is properly cited, the use is non-commercial and no modifications or adaptations are made.

DOI: 10.1002/marc.202100731

2. Results and Discussion

PAN is a transparent polymer, which shows no absorption in the visible and near-infrared spectrum. To enable laser carbonization, an absorber is added, to facilitate absorption of the laser energy and transfer heat into the exposed PAN material. We have

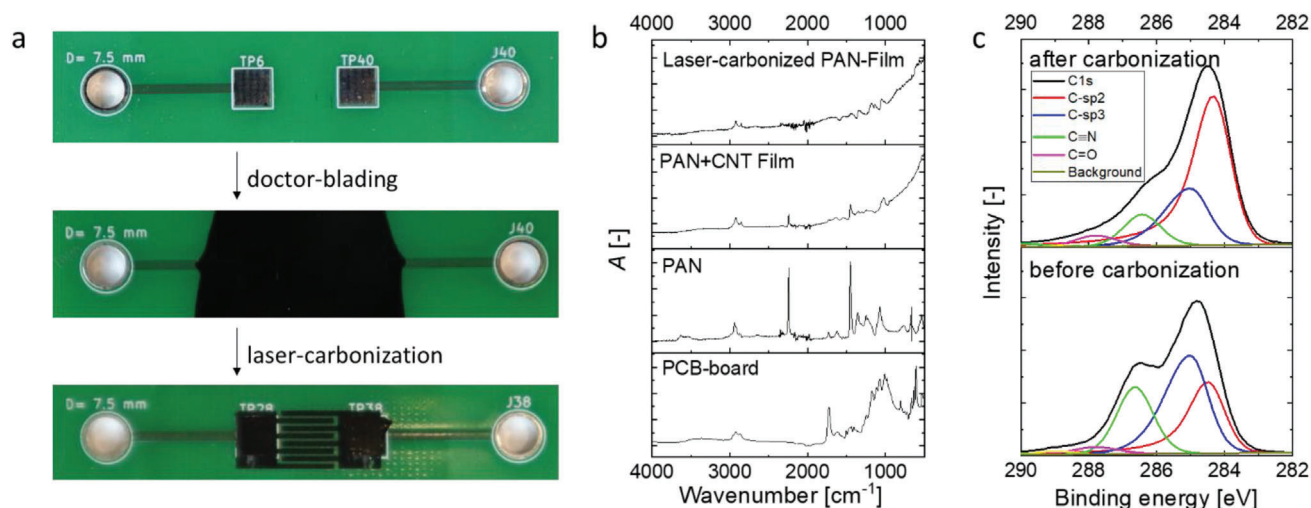


Figure 1. a) Photographs of the microcaps during progressing manufacturing stages. Bare PCBs containing the square silver electrodes, which act as current collectors. The current collectors connect the carbon electrodes to a read-out device via banana clips. The space between the collectors, as well as the current collectors themselves, are coated with a PAN-CNT composite film. In a second step, the film is laser-carbonized and patterned producing interdigitating electrodes. b) FT-IR-absorbance spectra of the bare PCB-board, PAN, the laser-absorbing PAN-CNT composite film, and laser-carbonized electrodes. c) XPS-spectra of PAN-CNT films before (bottom) and after (top) laser-carbonization.

previously employed graphene nanoplatelets as absorbers^[14]; however, these fillers strongly increase the viscosity of the PAN solution, which is beneficial for fiber spinning but not necessarily beneficial for casting films. Therefore, we here make use of CNTs, which come as a dispersion in dimethyl sulfoxide. CNTs exhibit high conductivity, which is why we do not expect detrimental effects of the filler on the conductivity of the carbonized PAN material. We employ a concentration of 3 wt% of CNT per weight PAN, while the concentration of PAN in DMSO is 12 wt%. The concentration of 3 wt% CNT is optimized for sufficient absorption at the laser wavelength (CO_2 , 10.6 μm) and maximum capacitance in the resulting carbon structures (see Figure S1, Supporting Information). We can spin-coat this PAN/CNT solution in DMSO onto almost any desired flat substrate and the resulting film thickness can be precisely tuned through the speed of rotation or the concentration of PAN in solution (see Figure S2, Supporting Information). However, to avoid coating the entire chip or PCB board with PAN/CNT in undesired areas, we here turn to pipette printing and subsequent doctor blading of the PAN/CNT solution. This way we are able to precisely deposit PAN/CNT onto the desired areas. As a substrate, we employ PCB with square silver collector electrodes of 16 mm^2 in area, which are separated by a distance of 7.5 mm. The collector electrodes are connected to a potentiostat via banana clips, which fit drillings in the PCB (see Figure 1).

We deposit the viscous PAN/CNT solution onto the PCB, by pipetting 2.5 mL of the viscous PAN/CNT solution as a grid of individual droplets. Closed films are drawn by doctor blading with a 30 μm gap into an ≈ 3 cm long stripe across the collector electrodes. The resulting films have a thickness of 20–21 μm after drying (see Figure S3, Supporting Information).

These films are irradiated with a CO_2 laser with a wavelength of 10.6 μm . In an attempt to replicate the thermal two-step treatment of stabilization and carbonization, we conduct laser exposure at an increasing power density in the air to generate laser-induced stabilization. However, we are not able to separate the

exothermic stabilization event from carbonization. In contrast to carbonization, where increasing laser power density produces higher degrees of carbonization, for the stabilization step, there seems to exist a sharp threshold of 0.26 J mm^{-2} . Below this threshold, we do not see a change in the material properties or the infrared spectrum, in which stabilization is detectable by the disappearance of the corresponding nitrile band at 2442 cm^{-1} (see Figure 1b). Above the threshold we obtain conductive structures, indicating that we can conduct stabilization and carbonization in one step, despite the presence of air. Typically, thermal carbonization is conducted in the absence of air to avoid oxidation of the carbon material to CO_2 . However, our laser carbonization is sufficiently fast, so that oxidation does not occur and the amount of sp^2 -carbon increases to 52%, confirming successful laser carbonization (see Figure 1c). When we further increase the laser dose to 0.7 J mm^{-2} then we do no longer observe converted carbon structures, but instead, we observe the bare substrate, indicating the occurrence of an ablation process rather than pyrolytic carbonization (see Figure 2). This interval in power density is beneficial, as we can perform precise carbonization within this parameter window, while we can also employ the ablation process with power densities beyond this interval for precise removal of the PAN-precursor films. The underlying PCB board is not harmed by either process, as no visible or measurable material changes in infrared spectroscopy or conductivity occur.

We carry on to pattern interdigitated electrodes with eight or 16 fingers at 0.63 J mm^{-2} , which is the ideal dose for carbonization. In a second patterning step, we increase the power density to ablation and follow a trace between the electrode fingers to remove any non-carbonized material between the carbonized electrode fingers (see Figure 3).

Now that the carbonized electrode pattern is separated from the pristine area, the excessive non-carbonized PAN film can simply be peeled off the PCB (see Figure 3a). By contrast, the carbonized interdigitating supercapacitor electrodes adhere to the PCB (see Figure 3a: Video S1, Supporting Information). This

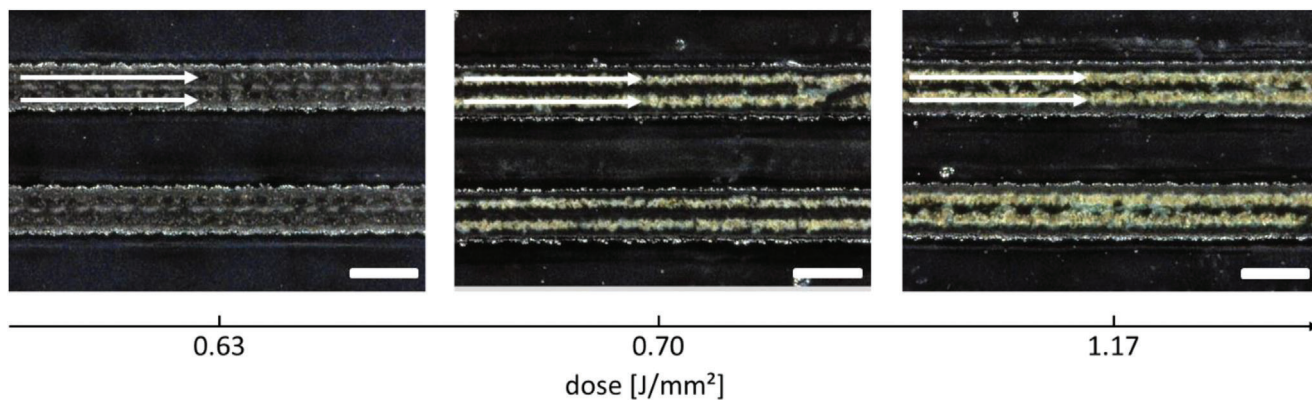


Figure 2. Variation of the laser dose for carbonization or ablation of PAN-films. White arrows indicate the pathway of the laser beam. A laser dose of 0.63 J mm^{-2} leads to carbonized structures, whereas increasing the dose to 0.70 J mm^{-2} leads to ablation of PAN material revealing the yellow/golden color of the PCB board. Doses higher than 1.17 J mm^{-2} lead to large area ablation, which limits the quality of the remaining PAN and carbon patterns. The scale bars represent $200 \mu\text{m}$.

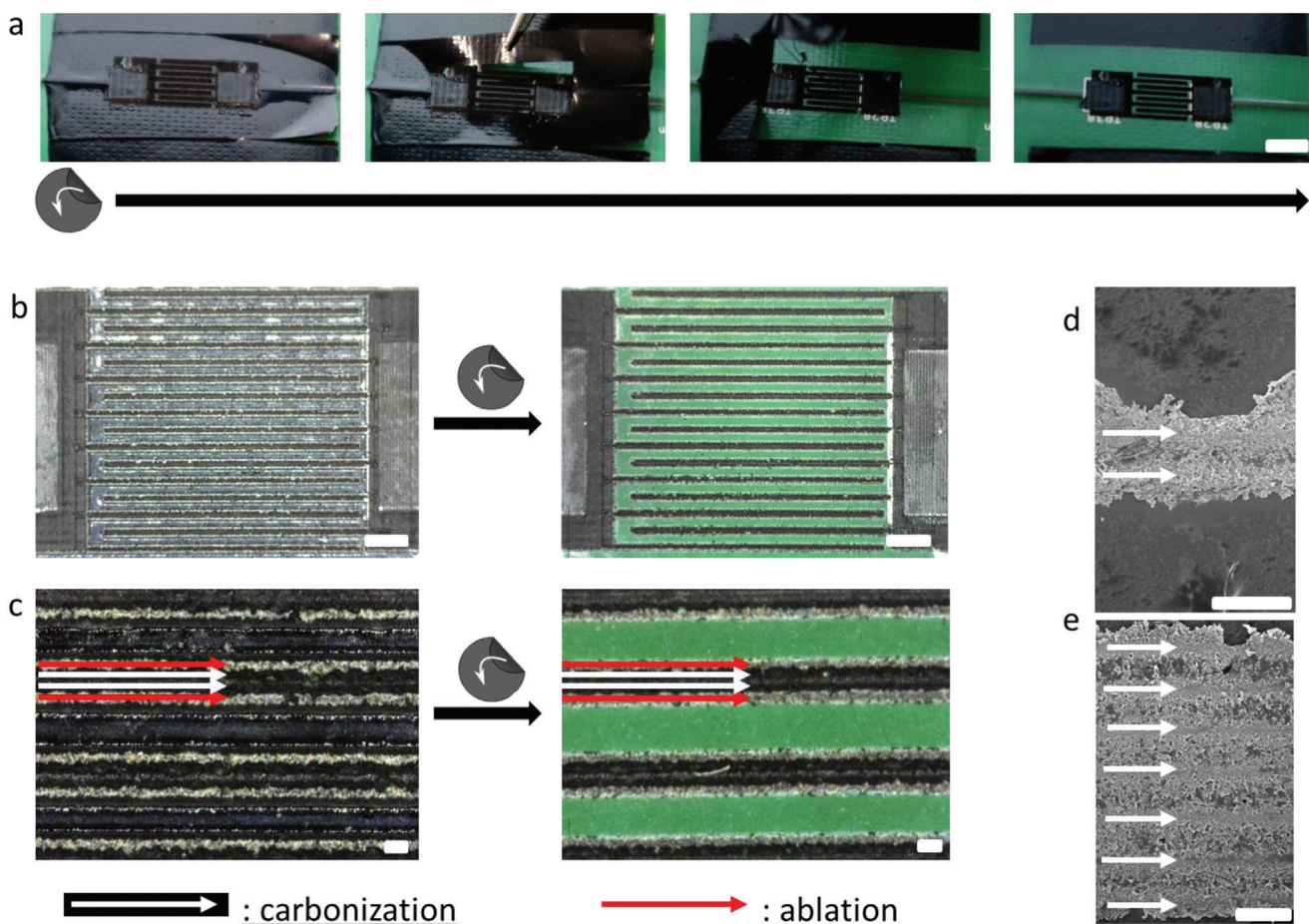


Figure 3. Laser carbonization and ablation to separate carbonized pattern from the non-carbonized film: a) The non-carbonized film is removed by peeling off with a pair of tweezers. The carbonized interdigitated electrode structure remains attached to the PCB. The scale bar represents 5 mm . b) Micrographs of the laser carbonized and ablated films before and after removal of the non-carbonized material. The scale bar represents 1 mm . c) Close-up on four electrodes and arrows indicating the laser paths for carbonization (white arrow) and ablation (red arrow) before and after removal of the non-carbonized PAN film. Scale bars indicate $100 \mu\text{m}$. d) SEM-images of electrodes of 16-finger microcaps and e) 8-finger microcaps. The white arrows indicate the laser pathways for carbonization, producing electrodes of different widths. The scale bar indicates $100 \mu\text{m}$.

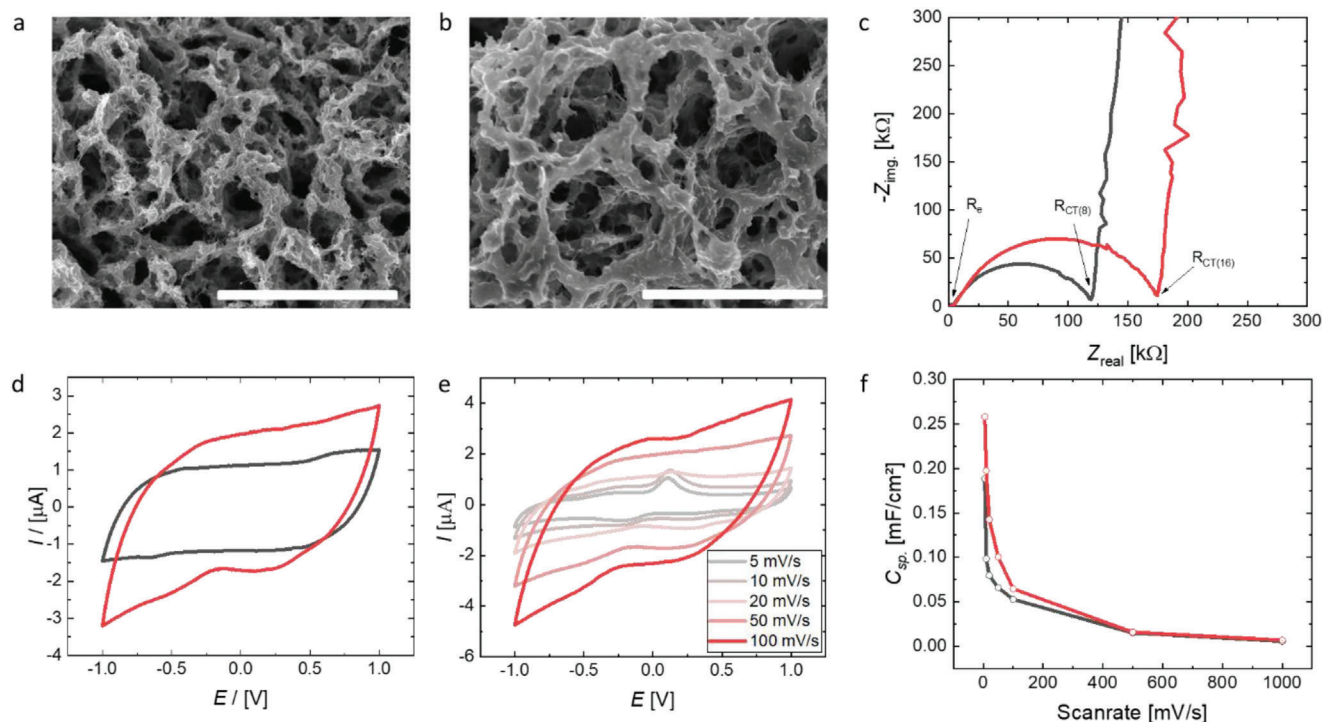


Figure 4. a) SEM-images of laser carbonized electrodes of the 8-finger and b) 16-finger pattern. The scale bars indicate 5 μm . c) Nyquist plots of laser-carbonized microcaps with 8- (black) and 16-finger (red) patterns. d) Cyclic voltammograms of 8- (black) and 16-finger (red) microcaps, recorded at 50 mV s^{-1} . e) Cyclic voltammograms of 16-finger microcaps, recorded at various scan rates. f) Specific capacitance of 8- (black) and 16-finger (red) microcaps at scan rates from 5 to 1000 mV s^{-1} .

way, the entire electrode structures including the sides of the electrode fingers down to the PCB substrate become accessible for the electrolyte in the final supercapacitor device. For 16 finger electrodes, the individual fingers are produced by scanning twice with the laser beam, followed by two additional scans for ablation and separation of the carbonized electrodes from the pristine PAN film (see Figure 3b–d). The eight finger devices are produced by seven laser traces next to each other (see Figure 3e). For eight fingers, the electrode width is $w = 510 \mu\text{m}$ with a height of $h = 9.4 \mu\text{m}$ at a spacing of $d = 290 \mu\text{m}$ between electrodes; and for 16 fingers the dimensions are $w = 145 \mu\text{m}$, $h = 10.9 \mu\text{m}$, and $d = 263 \mu\text{m}$ (see Figure S3, Supporting Information). The laser carbonization process produces electrodes of hierarchical porosity (see Figure 4a,b). This is a well-known feature of the fast laser carbonization process, where the gasses produced during carbonization are formed instantaneously, leading to the porous foam-like structure, with high surface area, which is beneficial for the capacitor performance.^[14] Additionally, the compounded CNTs should contribute to the electrode performance. Analysis by scanning electron microscopy (SEM) shows that the remaining CNTs are intact after laser treatment and seem to percolate within the porous carbon structure, which could contribute to the electrical conductivity of the laser-carbonized material (Figure S4, Supporting Information).

Next, we test the performance of electrodes in electrochemical measurements. As electrolyte, we employ 20 μL of the ionic liquid 1-ethyl-3-methylimidazolium bis(trifluoromethylsulfonyl)imide (EMIM TFSI), which we deposit on the interdigitated finger electrodes in an inert nitrogen atmosphere. After an equilibration pe-

riod of 12 h, we conduct electrochemical impedance spectroscopy and cyclic voltammetry. Nyquist plots of our eight or 16 finger electrodes show a semicircle at high frequencies and a steep increase with 85° phase angle at lower frequencies, indicating capacitive behavior (see Figure 4c). The semicircles intercept the x -axis at 2.3 $\text{k}\Omega$ for the eight finger electrodes and at 2.8 $\text{k}\Omega$ for the 16 finger electrodes. We interpret these values as the electrode resistance R_e (see Figure 4c).^[24] By contrast, the charge transfer resistance R_{CT} is increased for the 16-finger microsupercapacitor (170 $\text{k}\Omega$) compared to the eight-finger device (116 $\text{k}\Omega$), which we account to the increased surface area in the 16-finger device (see Figure 4c). For the same reason, cyclic voltammetry shows that the double layer capacitance C_{sp} of the 16-finger device is much higher than in the 8-fingered device (see Figure 4d).

When we plot the specific area capacitance C_{sp} against the scan rate, we observe a similar trend for the 8 and 16-fingered electrode devices. However, the microsupercapacitor with 16-fingers achieves significantly higher $C_{sp} = 260 \mu\text{F cm}^{-2}$ at low scan rates compared to $C_{sp} = 190 \mu\text{F cm}^{-2}$ in the 8-finger device (see Figure 4d–f). This difference in performance indicates that there might be a greater number of accessible pores in the 16-finger device, which improves the capacitance compared to the 8-fingered microsupercapacitors with less overall interface. The achieved capacitances are of the same order of magnitude as for recently reported graphene-based finger capacitors of similar dimensions.^[17] The microsupercapacitors retain their capacitance for 2000 cycles, which is comparable to other carbon electrodes (see Figure S5, Supporting Information).^[25] Prolonged exposure of the electrodes to the ionic liquid electrolyte over the course of

7 days, does not lead to their delamination or changes in their electrochemical performance.

3. Conclusion

We have demonstrated how to achieve direct on-chip laser-carbonization of PAN films. Our specifically designed process has been used to fabricate carbon supercapacitor electrodes. We can precisely tune the process from carbonization to ablation, allowing us to remove any non-carbonized material to obtain free-standing interdigitating electrodes.

The developed process gives access to highly integrated energy storage devices of on-chip applications, which in the future might become even further miniaturized. Tuning of the exact porosity and potential post carbonization treatment to further activate the materials to increase the porosity might lead to even larger capacitances and better performance.

4. Experimental Section

Materials: Acrylonitrile homopolymer ($M_w = 150\,000\text{ g mol}^{-1}$) was obtained from Dralon GmbH, Dimethylsulfoxide (DMSO) was obtained from Fisher Scientific, Acetone was obtained from Sigma-Aldrich, a CNT dispersion in DMSO with a weight content of 2 wt.% CNTs was obtained from Future Carbon GmbH, and 1-Ethyl-3-methylimidazolium bis(trifluoromethylsulfonyl)imide (EMIM TFSI; 99.5%) was obtained from Iolitec GmbH.

PAN-Deposition: The PCB board was designed with KiCad-software and manufactured by Aisler B.V. (Germany). PAN-CNT composite films were deposited on the PCB from a 12 wt.% homo-PAN solution in a mixture of DMSO:Acetone ($V_{\text{DMSO}}:V_{\text{Acetone}} = 4:1$), containing 3 wt.% CNTs (related to the mass of PAN). PAN-CNT dispersion (2.5 mL) was deposited in a grid of droplets (microdrop technologies GmbH, Germany) between the collector electrodes over a length of 3 cm. A film was produced on the PCB, by moving a doctor blade (with a distance of 30 μm between the blade and the substrate) through the reservoir. The resulting film had a length of 3–6 cm and a width of 1–2 cm, covering the current collector and the space in between them. The coated PCB dried for 10 min at 110 $^{\circ}\text{C}$ prior to laser-carbonization.

Carbonization: Laser-carbonization was conducted with a high-precision laser engraver setup (Speedy 100, Trotec) equipped with a 60 W CO_2 laser. The laser beam was focused with a 2.5 in. lens providing a focal depth of $\approx 3\text{ mm}$ and a focus diameter of 170 μm . The center wavelength of the laser was $10.6 \pm 0.03\ \mu\text{m}$. The laser was operated in a pulsed vector mode at 1000 Hz. Therefore, the resulting energy input onto the film (dose) was given per area in J mm^{-2} . The areal energy density results from the effective linewidth d (170 μm) of the carbonized structures obtained in the laser focus. The scanning speed v' , generically given in %, was converted into s m^{-1} . The effective output power P of the laser was measured with a Solo 2 (Gentec Electro-Optics) power meter. The line separation for the patterning of the interdigitated electrodes was 75 μm .

$$F = P \times v' \times d^{-1} \quad (1)$$

The unexposed, non-carbonized PAN-film was removed by peeling off.

Electrochemical Measurements: The produced microsupercapacitors were connected to an IviumStat.h potentiostat (Ivium technologies) via banana clips. All measurements were performed in a glove box, with a two-electrode setup and 20 μL of EMIM TFSI as an electrolyte. The electrolyte covered the whole electrode structure. The cyclic voltammograms were recorded at scan rates from 5 to 1000 mV s^{-1} . The specific capacitance was calculated by $C_{\text{sp}} = \frac{\int_{-1V}^{1V} I dU}{2 \cdot v \cdot 2U \cdot A}$, with the scan rate v and the electrode area A . Impedance spectra were recorded from 5 MHz to 0.01 Hz

at a voltage U of 0.1 V. The capacitance fatigue was determined by cycling 2000 voltammograms and displaying the capacity of every 100th cycle in Figure S5 (Supporting Information).

Instruments: IR-spectra were recorded on a PerkinElmer Spectrum two. SEM images were recorded on a Hitachi S-5200.

XPS was performed on a PHI 5800 ESCA system (Physical Electronics), using monochromatized Al $K\alpha$ radiation (1486 eV). The pass energy for survey spectra was 93.9 eV, for detail spectra, 29.35 eV was used. The binding energies (BEs) of all spectra were calibrated with respect to the C (1s) peak. The data evaluation and peak convolution were performed using the commercial software CasaXPS 2.3.23PR1.0 (www.casaxps.com). A Tougaard-type background was subtracted before the peak-fitting process.

Supporting Information

Supporting Information is available from the Wiley Online Library or from the author.

Acknowledgements

The authors thank Carsten Johnigk and Dr. Christian Vedder both at ILT – Fraunhofer Institute for Laser Technology, Aachen, Germany for measuring the laser absorbance of PAN-CNT dispersions. The authors thank Dr. Christian Herbert and Dr. Andreas Wego both at Dralon GmbH for donating the PAN homopolymer. The authors thank Krisztian Herman for capacitance and conductivity measurements of CNT/C composites with various amounts of CNT. The authors thankfully acknowledge funding from the BMBF SuperCarbon (13XP5036E) and the Cluster of Excellence EXC2154 POLIS and the Max Planck Society for financial support.

Open Access funding enabled and organized by Projekt DEAL.

Conflict of Interest

The authors declare no conflict of interest.

Data Availability Statement

The data that support the findings of this study are available from the corresponding author upon reasonable request.

Keywords

carbonization, laser-induced carbonization, laser-pyrolysis, microcapacitors, polyacrylonitrile

Received: November 2, 2021

Revised: January 19, 2022

Published online: February 3, 2022

- [1] P. Huang, C. Lethien, S. Pinaud, K. Brousse, R. Laloo, V. Turq, M. Respaud, A. Demortière, B. Daffos, P. L. Taberna, B. Chaudret, Y. Gogotsi, P. Simon, *Science* **2016**, 351, 691.
- [2] N. A. Kyeremateng, T. Brousse, D. Pech, *Nat. Nanotechnol.* **2017**, 12, 7.
- [3] F. Bu, W. Zhou, Y. Xu, Y. Du, C. Guan, W. Huang, *npj Flexible Electron.* **2020**, 4, 31.
- [4] R. Jia, G. Shen, F. Qu, D. Chen, *Energy Storage Mater.* **2020**, 27, 169.
- [5] Y. Lee, V. K. Bandari, Z. Li, M. Medina-Sánchez, M. F. Maitz, D. Kar-naushenko, M. V. Tsurkan, D. D. Kar-naushenko, O. G. Schmidt, *Nat. Commun.* **2021**, 12, 4967.

- [6] C. C. Mayorga-Martinez, J. G. S. Moo, B. Khezri, P. Song, A. C. Fisher, Z. Sofer, M. Pumera, *Adv. Funct. Mater.* **2016**, *26*, 6662.
- [7] J. Ye, H. Tan, S. Wu, K. Ni, F. Pan, J. Liu, Z. Tao, Y. Qu, H. Ji, P. Simon, Y. Zhu, *Adv. Mater.* **2018**, *30*, 1801384.
- [8] E. Hourdakis, A. G. Nassiopoulou, *PHYS STATUS SOLIDI A* **2020**, *217*, 1900950.
- [9] J. Han, Y.-C. Lin, L. Chen, Y.-C. Tsai, Y. Ito, X. Guo, A. Hirata, T. Fujita, M. Esashi, T. Gessner, M. Chen, *Adv. Sci.* **2015**, *2*, 1500067.
- [10] J.-H. Sung, S.-J. Kim, K.-H. Lee, *J. Power Sources* **2003**, *124*, 343.
- [11] A. Eftekhari, L. Li, Y. Yang, *J. Power Sources* **2017**, *347*, 86.
- [12] Y.-Z. Zhang, Y. Wang, T. Cheng, L.-Q. Yao, X. Li, W.-Y. Lai, W. Huang, *Chem. Soc. Rev.* **2019**, *48*, 3229.
- [13] M. F. El-Kady, R. B. Kaner, *Nat. Commun.* **2013**, *4*, 1475.
- [14] D. Go, P. Lott, J. Stollenwerk, H. Thomas, M. Möller, A. J. C. Kuehne, *ACS Appl. Mater. Interfaces* **2016**, *8*, 28412.
- [15] D. Go, M. Opitz, P. Lott, K. Rahimi, J. Stollenwerk, H. Thomas, M. Möller, B. Roling, A. J. C. Kuehne, *J. Appl. Polym. Sci.* **2018**, *135*, 46398.
- [16] S. Delacroix, H. Wang, T. Heil, V. Strauss, *Adv. Electron. Mater.* **2020**, *6*, 2000463.
- [17] V. Strauss, M. Anderson, C. L. Turner, R. B. Kaner, *Mater. Today Energy* **2019**, *11*, 114.
- [18] R. D. Rodriguez, S. Shchadenko, G. Murastov, A. Lipovka, M. Fatkullin, I. Petrov, T.-H. Tran, A. Khalelov, M. Saqib, N. E. Villa, V. Bogoslovskiy, Y. Wang, C.-G. Hu, A. Zinovyev, W. Sheng, J.-J. Chen, I. Amin, E. Sheremet, *Adv. Funct. Mater.* **2021**, *31*, 2008818.
- [19] S. K. Nataraj, K. S. Yang, T. M. Aminabhavi, *Prog. Polym. Sci.* **2012**, *37*, 487.
- [20] L. Zhang, A. Aboagye, A. Kelkar, C. Lai, H. Fong, *J. Mater. Sci.* **2014**, *49*, 463.
- [21] H. Wang, S. Delacroix, O. Osswald, M. Anderson, T. Heil, E. Lepre, N. Lopez-Salas, R. B. Kaner, B. Smarsly, V. Strauss, *Carbon* **2021**, *176*, 500.
- [22] T. Maitra, S. Sharma, A. Srivastava, Y. K. Cho, M. Madou, A. Sharma, *Carbon* **2012**, *50*, 1753.
- [23] Y. Jeong, K. Lee, K. Kim, S. Kim, *Materials* **2016**, *9*, 995.
- [24] B.-A. Mei, O. Munteshari, J. Lau, B. Dunn, L. Pilon, *J. Phys. Chem. C* **2018**, *122*, 194.
- [25] C. Zequine, C. K. Ranaweera, Z. Wang, S. Singh, P. Tripathi, O. N. Srivastava, B. K. Gupta, K. Ramasamy, P. K. Kahol, P. R. Dvornic, R. K. Gupta, *Sci. Rep.* **2016**, *6*, 31704.

[M]acro-
[M]olecular
Rapid Communications

Supporting Information

for *Macromol. Rapid Commun.*, DOI 10.1002/marc.202100731

On-Chip Direct Laser Writing of PAN-Based Carbon Supercapacitor Electrodes

Andreas Hoffmann, Pablo Jiménez-Calvo, Joachim Bansmann, Volker Strauss
and Alexander J. C. Kuehne**

Supporting Information

On-chip Direct Laser Writing of Carbon Supercapacitor Electrodes

Andreas Hoffmann, Pablo Jiménez-Calvo, Joachim Bansmann, Volker Strauss* and Alexander J. C. Kuehne*

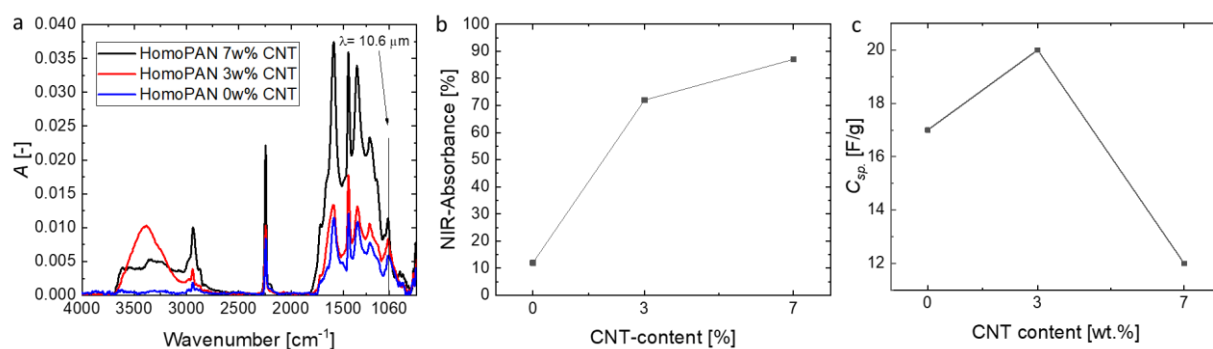


Figure S1: a) IR-spectra of homo-PAN-films with 0 wt%, 3 wt% and 7 wt%, recorded by attenuated total reflectance. b) The total laser-absorbance of different CNT loadings in PAN, quantified by transmission IR-spectroscopy. c) Specific capacitance of CNT/C composites with CNT-contents of 0, 3 and 7 wt%.

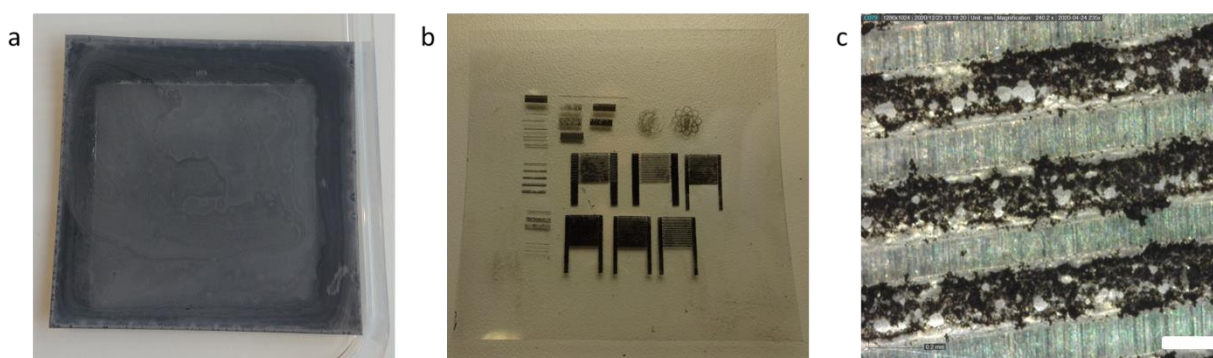


Figure S2: a) PAN/CNT-composite film spin-coated on a 7 x 7 cm PET foil. The concentration was 16 wt% PAN-CNT in 2 mL dispersion I DMSO deposited at 1200 rpm. b) Photograph of spin-coated PAN-CNT composite films, after carbonization to dedicated patterns. c) Close up of the carbon electrodes. The scale bar indicates 200 μm .

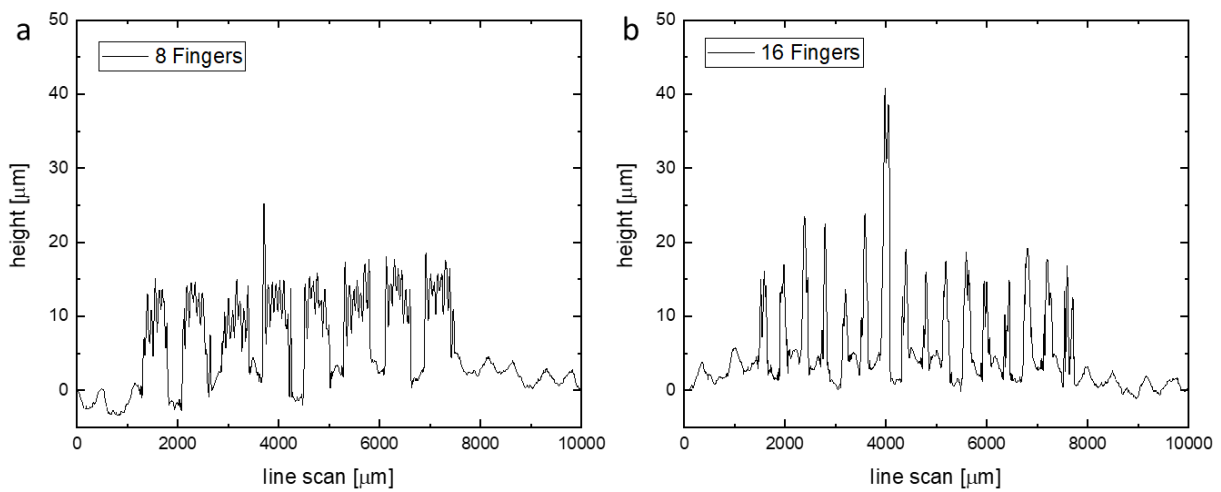


Figure S3: a) Height profiles of microsupercapacitors on PCB with the eight-finger pattern and b) the 16-finger pattern determined using a Dektak profilometer.

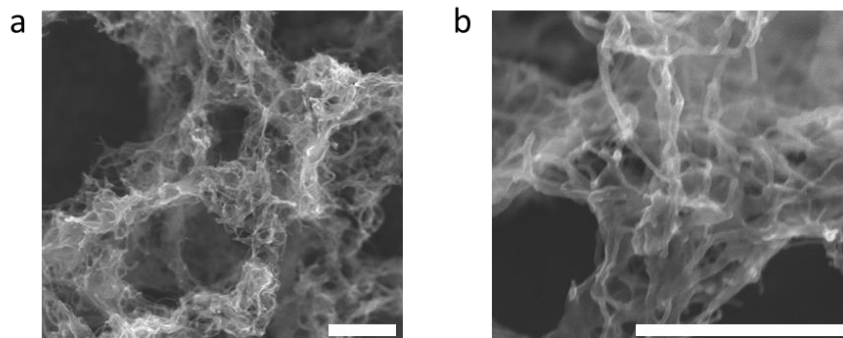


Figure S4: SEM-images of PAN-CNT films after laser-carbonization. A) Overview and b) close up on the carbonized electrode finger. The scale bars indicate 500 nm.

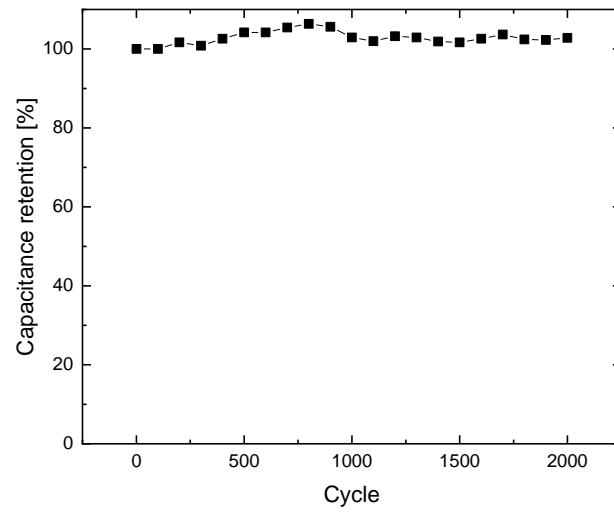


Figure S5: The carbon electrodes of a microsupercapacitor with 16 fingers show no capacitance fatigue over the course of 2000 charging and discharging cycles.